IMMUNOLOGICAL EFFECTS OF NANO-IMAGING MATERIALS

EDITED BY: Yang Li, Diana Boraschi, Ben Zhong Tang and Pengfei Zhang

PUBLISHED IN: Frontiers in Immunology,
Frontiers in Bioengineering and Biotechnology and
Frontiers in Molecular Biosciences

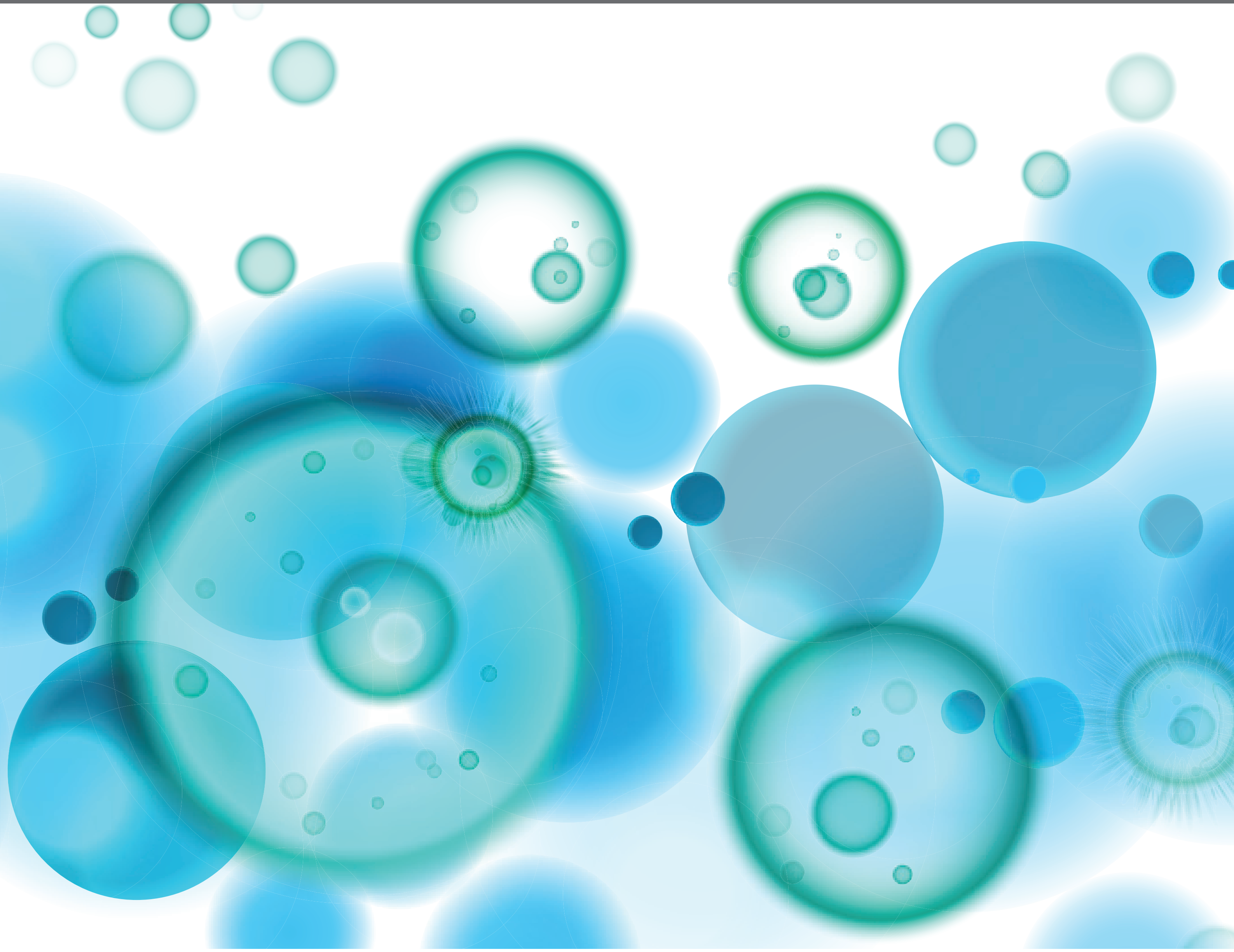

frontiers Research Topics

ISSN 1664-8714
ISBN 978-2-88974-932-4
DOI 10.3389/978-2-88974-932-4

About Frontiers

Frontiers is more than just an open-access publisher of scholarly articles: it is a pioneering approach to the world of academia, radically improving the way scholarly research is managed. The grand vision of Frontiers is a world where all people have an equal opportunity to seek, share and generate knowledge. Frontiers provides immediate and permanent online open access to all its publications, but this alone is not enough to realize our grand goals.

Frontiers Journal Series

The Frontiers Journal Series is a multi-tier and interdisciplinary set of open-access, online journals, promising a paradigm shift from the current review, selection and dissemination processes in academic publishing. All Frontiers journals are driven by researchers for researchers; therefore, they constitute a service to the scholarly community. At the same time, the Frontiers Journal Series operates on a revolutionary invention, the tiered publishing system, initially addressing specific communities of scholars, and gradually climbing up to broader public understanding, thus serving the interests of the lay society, too.

Dedication to Quality

Each Frontiers article is a landmark of the highest quality, thanks to genuinely collaborative interactions between authors and review editors, who include some of the world's best academicians. Research must be certified by peers before entering a stream of knowledge that may eventually reach the public - and shape society; therefore, Frontiers only applies the most rigorous and unbiased reviews.
Frontiers revolutionizes research publishing by freely delivering the most outstanding research, evaluated with no bias from both the academic and social point of view. By applying the most advanced information technologies, Frontiers is catapulting scholarly publishing into a new generation.

What are Frontiers Research Topics?

Frontiers Research Topics are very popular trademarks of the Frontiers Journals Series: they are collections of at least ten articles, all centered on a particular subject. With their unique mix of varied contributions from Original Research to Review Articles, Frontiers Research Topics unify the most influential researchers, the latest key findings and historical advances in a hot research area! Find out more on how to host your own Frontiers Research Topic or contribute to one as an author by contacting the Frontiers Editorial Office: frontiersin.org/about/contact

IMMUNOLOGICAL EFFECTS OF NANO-IMAGING MATERIALS

Topic Editors:
Yang Li, Shenzhen Institutes of Advanced Technology, Chinese Academy of Sciences (CAS), China
Diana Boraschi, Shenzhen Institute of Advanced Technology (SIAT), Chinese Academy of Science (CAS), China
Ben Zhong Tang, Hong Kong University of Science and Technology, Hong Kong, SAR China
Pengfei Zhang, Shenzhen Institutes of Advanced Technology, Chinese Academy of Sciences (CAS), China

Citation: Li, Y., Boraschi, D., Tang, B. Z., Zhang, P., eds. (2022). Immunological Effects of Nano-Imaging Materials. Lausanne: Frontiers Media SA.
doi: 10.3389/978-2-88974-932-4

Table of Contents

frontiers in Immunology

EDITORIAL
published: 24 March 2022
doi: 10.3389/fimmu.2022.886415

Editorial: Immunological Effects of Nano-Imaging Materials

Yang Li[1,2]*, Pengfei Zhang[1], Ben Zhong Tang[3] and Diana Boraschi[1,2,4,5]*

[1] Shenzhen Institute of Advanced Technology (SIAT), Chinese Academy of Science (CAS), Shenzhen, China, [2] Laboratory of Immunology and Nanomedicine & China-Italy Joint Laboratory of Pharmacobiotechnology for Medical Immunomodulation, Shenzhen Institute of Advanced Technology (SIAT), Chinese Academy of Sciences (CAS), Shenzhen, China, [3] Shenzhen Institute of Aggregate Science and Technology, School of Science and Engineering, The Chinese University of Hong Kong, Shenzhen, China, [4] Institute of Biochemistry and Cell Biology (IBBC), National Research Council (CNR), Napoli, Italy, [5] Stazione Zoologica Anton Dohrn, Napoli, Italy

Keywords: nanomaterials, immunity, imaging, inflammation, cancer, diagnosis, immunotherapy

Editorial on the Research Topic

Immunological Effects of Nano-Imaging Materials

Edited and reviewed by:
Francesca Granucci,
University of Milano-Bicocca, Italy

****Correspondence:***
Yang Li
yang.li@siat.ac.cn
Diana Boraschi
diana.boraschi@ibbc.cnr.it

Specialty section:
This article was submitted to
Molecular Innate Immunity,
a section of the journal
Frontiers in Immunology

Received: *28 February 2022*
Accepted: *04 March 2022*
Published: *24 March 2022*

Citation:
Li Y, Zhang P, Tang BZ and Boraschi D (2022) Editorial: Immunological Effects of Nano-Imaging Materials. Front. Immunol. 13:886415. doi: 10.3389/fimmu.2022.886415

The biomedical application of novel engineered nanomaterials (ENM) has substantially expanded in the last years in many areas, including imaging-based diagnostic approaches and use as imaged-guided carriers for chemotherapeutic drugs and vaccines. In this context, the interaction between nanomaterials for biomedical imaging (nano-imaging materials) and the immune system is a key issue in the safety perspective, as nanomaterial-induced changes in immune reactivity may pose health problems and even participate to disease development. On the other side, such interaction, in particular with cells of the innate immune system, can be exploited for the targeted activation of beneficial immune functions, thereby opening the way to new immunotherapeutic strategies targeting innate immunity.

The Research Topic "*Immunological Effects of Nano-Imaging Materials*" aims at providing new information and perspectives of the immune-related effects of nano-imaging materials, used or developed for diagnostic procedures, which allow us to predict a much wider exploitation that encompasses immunotherapeutic and immunopreventive purposes. The synergy between three different research areas and related Frontiers journals (Frontiers in Immunology, Frontiers in Bioengineering and Biotechnology, Frontiers in Molecular Biosciences) provides a wide interdisciplinary view of different technological and conceptual strategies and underlines the need for a comprehensive approach for successfully addressing and exploiting the capacity of nanomaterials to interact with the immune system (**Figure 1**).

Safety, in particular immunosafety, is the primary issue for any new nanomaterial to be used in nanomedicine. Our immune system is devoted to surveillance and protection of the body integrity from endogenous and exogenous agents, such as senescent/anomalous cells, pathogens and particles. In this scenario, ENMs used in medical applications may trigger a defensive immune reaction, which may cause immune-related adverse effects and/or the failure of medical treatment. Thus, the immunological effects and immunosafety of the nano-imaging materials should be carefully evaluated before their clinical application, so as to allow for their optimal application in the medical practice through a safer-by-design ENM optimisation.

We have examined here the immune-related toxicity and effects of some new nanomaterials with unique physico-chemical and optical characteristics, in particular Aggregation-Induced Emission

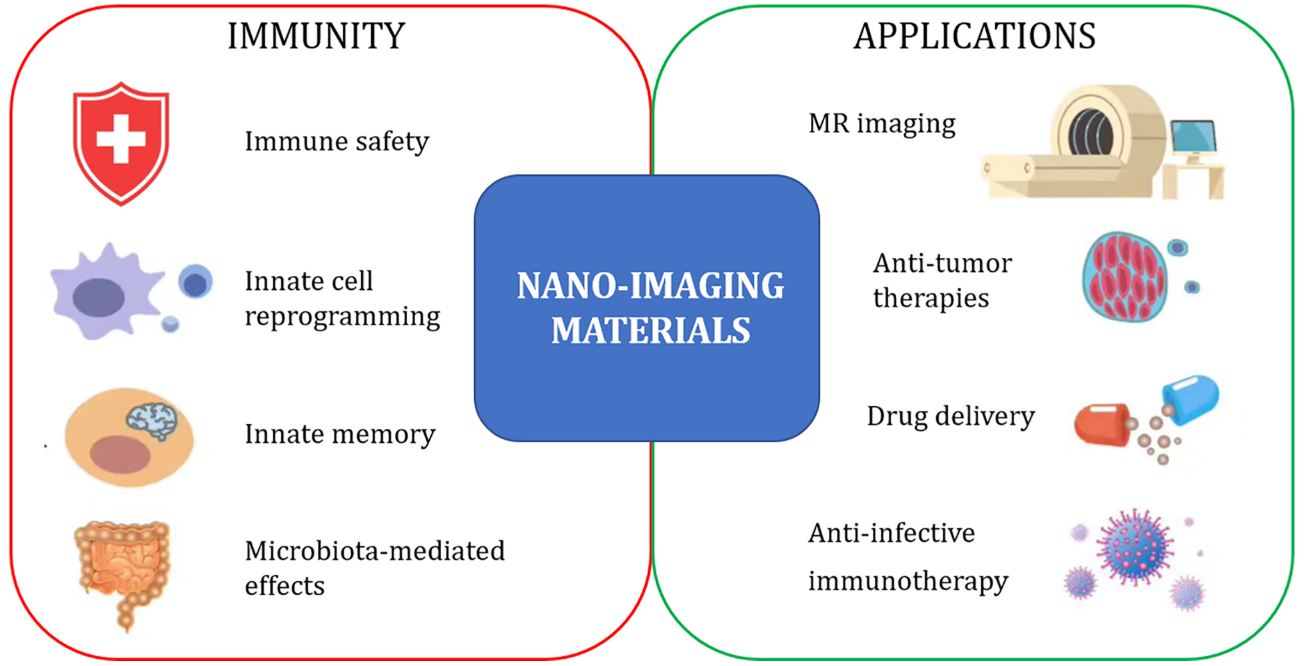

FIGURE 1 | Immunological effects and biomedical application of nano-imaging materials.

(AIE) imaging materials, 2D nano-imaging materials, quantum dots, and perovskite nanomaterials (Wu et al., Da Silva et al., Geppert and Himly, and Wei et al.).

Numerous organic and nanomaterial-based fluorophores possess excellent fluorescent properties when dispersed in solution. However, aggregation of these materials is likely to result in fluorescent quenching due to the ACQ effect, which is largely responsible for nonradiative energy transfer induced by strong π-π stack. Since the discovery of AIE effects in 2001, great efforts have been made to exploit AIE-active materials in medical applications for diagnosis and treatment, as summarized by Wu et al.

The group of Diego Martinez reviewed the most recent advances relative to the immunological effects of the two dimensional (2D) ENM applied to bio-imaging, and highlighted to use nanoinformatics approaches/computational modelling for nano-immunosafety evaluation, aiming at providing key information towards immunologically safer design of 2D-ENM (Da Silva et al.).

Geppert and Himly discussed the immunological effects induced by iron oxide nanoparticles (IONP) used as MRI contrast agent, and described how the physico-chemical properties of IONP are crucial in determining their biological and immunological effects. Notably, they stressed an important issue in the assessment of nano-immunosafety, *i.e.*, the undetected presence of endotoxin (lipopolysaccharide, LPS), a ubiquitous bacterial molecule with strong inflammatory/toxic effects (1). Thus, the association of immunoactive agents such as LPS to the surface of nanoimaging materials (usually occurring during nanomaterial synthesis or storage) must be assessed and prevented, in order to improve the material safety and correctly assess its biological effects. In this respect, Anna Chiara De Luca's group has developed a highly sensitive surface-enhanced Raman spectroscopy (SERS) method for accurate endotoxin detection in nano-imaging gold ENM, which overcomes the many issues of optical interference experienced when the current endotoxin detection assays are applied to ENM (Verde et al.) Such evaluation is fundamental for toxicological evaluation of nanomaterials, in order to discriminate between nano-dependent and contaminant-dependent toxicity. On the other hand, the interaction of nanomaterials with bacteria can also have very promising health-improving applications, as in the case of interaction with gut microbiota, which can change the microbial composition in the gut and modulate in a positive fashion the microbiota-dependent immune functions, as pointed out by Liang Li's group (Tang et al.).

The group of Shanze Chen reviewed the biomedical application and immunological responses of a traditional nano-imaging material, quantum dots (QD), with focus on the respiratory apparatus (Ren et al.). They highlighted the adverse effects and immunosafety concerns caused by QD, which are mainly related to oxidative stress caused by the release of toxic metal ions and reactive surface charge. Reactive oxygen species generated by ENM could be considered as a common reason for ENM-induced cyto/immuno-toxicity, as they seem to also account for the immuno-toxic effects of Perovskite NM observed by the Liming Wang's group (Wei et al.). However, there are reports on many other potentially toxic effects of medical ENM, relevant to immunotoxicity, for instance the specific molecular interference with cell duplication (2), an effect that may hamper lymphocyte proliferation during adaptive immune responses. This asks for a deeper molecular analysis of nano-immune interactions, in order to clearly define the possible immunotoxicity risks on different types of immune cells/organs/responses.

Thus, by examining the effects of nanoimaging materials on immunity, we can foresee the possibility of activating or modulating some specific immune-related functions for bioimaging-guided therapeutic purposes.

This is the case of nano-based strategies for modulating innate memory, reported by Paola Italiani's group, strategies that would make possible to change/improve the capacity of innate immune cells to mount a defensive response to infections or diseases (Della Camera et al.). The effect on innate immunity has the advantage of being largely non-specific, meaning that a positive nano-effect would apply to a range of different diseases, but it seems to depend on the individual subject (*i.e.*, each human being has her/his own individual way to generate innate memory in response to nanoparticles), calling for a personalized profiling and nano-application (Italiani et al.).

The capacity of EMNs to induce and direct innate immune cells activation (*e.g.*, anti-inflammatory macrophage polarization) can be harnessed for improving tissue replacement integration. The use of nano-patterned titania described by Ting Zhang and colleagues can induce macrophage anti-inflammatory activation with the release of exosomes able to facilitate bone cell differentiation and bone apposition (Zhang et al.), thereby opening the way to the design of "intelligent" biomaterials for tissue replacement that facilitate transplant take and integration.

In the case of immunotherapeutic approaches to cancer, IONP can be of particular interest for their ability to drive the anti-tumor capacity of tumor-associated macrophages, in addition to direct cytotoxic effects on tumor cells, as reported by Yang Li's group (Song et al.). Other novel "intelligent" photoreactive bimetallic nanoparticles can be designed, able to induce tumor cell death by inducing a strong oxidative burst and localized hyperthermia within the hypoxic tumor microenvironment (Li et al.). Particles can be designed with different characteristics for adding functional properties, as shown in the exosome-camouflaged particles that can act as chemotherapeutic drug carriers in addition to their photothermal therapeutic properties (Tian et al.). Other particles, such as the self-assembling amphiphilic nanodots reported by Yang et al., can unite their ability to deliver chemotherapeutic agents with the AIE-based capacity for cancer imaging and accurate targeting.

Lastly, nano-probes sensitive to changes in pH and/or oxidation can be used for imaging of pathological innate immune reactions, such as trauma-induced neuroinflammation, which can be identified by detection of hypoxia-induced pH decrease and the sustained production of reactive oxygen species, as described by Lu et al., while AIE luminogen-based nanodots are being applied to improving the specificity and sensitivity of detection assays for SARS-CoV-2, because of their high stability and lack of non-specific luminescence, as reported by Liu et al.

While our current knowledge on nano-immune interactions is fostering the development of many tools and strategies for using nano-imaging materials for the targeted therapeutic activation of immunity, it is also clear that much basic information is still missing, which would need a stricter collaboration between immunologists, nanotechnologists, pharmacologists, toxicologists and clinicians in order to tackle and overcome current gaps and weaknesses. This Research Topic aims to be a first practical step in this direction.

AUTHOR CONTRIBUTIONS

All authors contributed to writing and revised the manuscript.

FUNDING

YL is supported by National Natural Science Foundation of China (32171390), International Partnership Program (IPP) of CAS (172644KYSB20210011), National Key R&D Program of China (2021YFE0113000), Shenzhen Science and Technology Program (GJHZ20190821155803877), CAS President's International Fellowship Initiative (PIFI, 2021PB0060, 2022VBA0008). PZ is supported by National Key R&D Program of China (2019YFE0198700), Shenzhen Science and Technology Program (JCYJ20210324120011030). DB is supported by the EU H2020 project PANDORA (GA 671881) and by CAS-PIFI (2020VBA0028).

ACKNOWLEDGMENTS

The authors are grateful to Mr. Wenjie Yang from SIAT-CAS for his kind help with the Figure preparation.

REFERENCES

1. Li Y, Boraschi D. Endotoxin Contamination: A Key Element in the Interpretation of Nanosafety Studies. *Nanomedicine* (2016) 11:269–87. doi: 10.2217/nnm.15.196
2. Shao X, Ding Z, Zhou W, Li Y, Li Z, Ciu H, et al. Intrinsic Bioactivity of Black Phosphorus Nanomaterials on Mitotic Centrosome Destabilization Through Suppression of PLK1 Kinase. *Nat Nanotechnol* (2021) 16:1150–60. doi: 10.1038/s41565-021-00952-x

frontiers
in Bioengineering and Biotechnology

ORIGINAL RESEARCH
published: 08 May 2020
doi: 10.3389/fbioe.2020.00423

Intelligent Bimetallic Nanoagents as Reactive Oxygen Species Initiator System for Effective Combination Phototherapy

***Hongfeng Li*[1,2†], *Ying Li*[2,3†], *Jingjing Xiang*[2,4†], *Xing Yang*[2,4], *Chunbing Li*[2], *Chuangjun Liu*[2], *Qi Zhao*[5], *Lihua Zhou*[2], *Ping Gong*[2,6*] and *Jiahao Huang*[1*]**

[1] Biomaterials Research Center, School of Biomedical Engineering, Southern Medical University, Guangzhou, China, [2] Guangdong Key Laboratory of Nanomedicine, CAS Key Lab for Health Informatics, Shenzhen Engineering Laboratory of Nanomedicine and Nanoformulations, Shenzhen Institutes of Advanced Technology (SIAT), Chinese Academy of Sciences, Shenzhen, China, [3] School of Materials Science and Engineering, Guilin University of Electronic Technology, Guilin, China, [4] University of Chinese Academy of Sciences, Beijing, China, [5] Faculty of Health Sciences, University of Macau, Macau, China, [6] Dongguan Key Laboratory of Drug Design and Formulation Technology, Key Laboratory for Nanomedicine, Guangdong Medical University, Dongguan, China

Phototherapy is a promising oncotherapy method. However, there are various factors greatly restricted phototherapy development, including poor tumor-specific accumulation, the hypoxia in solid tumor, and the systemic phototoxicity of photosensitizer. Herein, a tumor microenvironment (TME)-responsive intelligent bimetallic nanoagents (HSA-Pd-Fe-Ce6 NAs) composed of human serum albumin (HSA), palladium-iron (Pd-Fe) bimetallic particles, and chlorin e6 (Ce6) was designed for effective combination phototherapy. The Pd-Fe part in the HSA-Pd-Fe-Ce6 NAs would react with the endogenous hydrogen peroxide (H_2O_2) in an acidic ambiance within tumor to generate cytotoxic superoxide anion free radical through the "Fenton-like reaction." H_2O_2, coupled with highly toxic singlet oxygen ($^1O_2$) caused by the Ce6 component under the irradiation of 660 nm laser, resulted in synergistic cancer therapy effects in hypoxia surroundings. Besides, this nanoagents could result in hyperpyrexia-induced cell apoptosis because of superior absorption performance in near-infrared wavelength window bringing about excellent photothermal conversion efficiency. The cell cytotoxicity results showed that the survival rate after treated by 40 μg mL^{-1} nanoagents was only 17%, which reveals that the HSA-Pd-Fe-Ce6 NAs had the advantage of efficient and controllable phototherapy. In short, it exhibited excellent hypoxia-resistant combination phototherapy efficacy *in vitro*. Therefore, the multifunctional nanoagents are powerful and provide a new avenue for effective combination phototherapy.

Keywords: bimetallic nanoagents, photosensitizers, tumor microenvironment, reactive oxygen species, phototherapy

Edited by:
Ben Zhong Tang,
Hong Kong University of Science and Technology, Hong Kong

Reviewed by:
Zhaohui Li,
Zhengzhou University, China
Zhihe Qing,
Changsha University of Science and Technology, China
Zonghai Sheng,
Chinese Academy of Sciences (CAS), China
Lei Ye,
Huazhong University of Science and Technology, China

***Correspondence:**
Ping Gong
ping.gong@siat.ac.cn
Jiahao Huang
jhuangaf@connect.ust.hk

† These authors have contributed equally to this work

Specialty section:
This article was submitted to Nanobiotechnology, a section of the journal Frontiers in Bioengineering and Biotechnology

Received: *02 February 2020*
Accepted: *14 April 2020*
Published: *08 May 2020*

Citation:
Li H, Li Y, Xiang J, Yang X, Li C, Liu C, Zhao Q, Zhou L, Gong P and Huang J (2020) Intelligent Bimetallic Nanoagents as Reactive Oxygen Species Initiator System for Effective Combination Phototherapy. Front. Bioeng. Biotechnol. 8:423. doi: 10.3389/fbioe.2020.00423

INTRODUCTION

Cancer has become an important cause of morbidity and mortality worldwide. As the GLOBOCAN 2018 reported, there were 18.1 million new cases of cancer and 9.6 million deaths resulting from cancer in 2018 (Bray et al., 2018). The conventional cancer treatment options are chemotherapy, surgery resection, and radiotherapy. However, chemotherapy often comes with systemic side effects and high recurrence rate,which is associated with surgical resection (Sun et al., 2019). Meanwhile, radiation therapy is limited by the cumulative radiation dose. Therefore, it is an urgent issue to develop a smart, safe, efficient, and cost-effective alternative strategy to treat cancer (Liu et al., 2018; Pu et al., 2019).

As one of the non-invasive tumor therapy, phototherapy has become a hot research topic in recent years (Ma et al., 2020). It can be devided into two categories: photothermal therapy (PTT) and photodynamic therapy (PDT) (Meng et al., 2018; Zhou et al., 2018). PTT is an efficient cancer treatments that artificially elevates tissue temperatures to take advantage of cells with a weak defense against heat, causing minimal side effects. Many PTT delivery materials, including nanocomposites, have been developed for the applications in oncotherapy (Robinson et al., 2011; Jung et al., 2015; Lim et al., 2015; Hu et al., 2019). PDT, a typical phototherapy, involves the administration of a photosensitizer (PS) followed by local illumination of the tumor with light in a specific wavelength to active the PS, which converts molecular oxygen into cytotoxic reactive oxygen species (ROS) resulting in tumor cell ablation (Dougherty et al., 1975; Dolmans et al., 2003). Obviously, such a light-triggered and oxygen-dependent therapy has better selectivity to the target site and less toxic side effects on the biological system than the traditional therapy (Hu et al., 2016). However, neither PTT nor PDT can realize the perfect cancer treatment, since they have their own weakness. For example, most of the small molecule PSs such as phthalocyanines, porphin, and porphyrin derivatives which are currently available in the clinical practice (Brown et al., 2004) generally have various drawbacks, such as the lack of specificity, rapid metabolism, and phototoxicity (Hu et al., 2015). It is known that the rapid growth of tumor cells and abnormal vascularization would confine oxygen supply, aggravate hypoxia, and acidization tumor microenvironment (TME), which not only promote the angiogenesis and metastasis, but also could be main causes for the therapeutic resistance and failure of phototherapy (Semenza, 2003, 2012; Bertout et al., 2008; Rademakers et al., 2008; Lou et al., 2011) especially for PDT, which requires oxygen to be maximally cytotoxic. Therefore, it is highly demanded to develop intelligent phototherapy nanoagents that are sensitive to TME for better phototherapy effect.

In recent years, various strategies have been explored to overcome therapeutic resistance of phototherapy (Qing et al., 2019a), including the application of artificial blood substitutes (such as perfluorocarbons) to transport oxygen into tumors (Song et al., 2016) and inorganic nanocatalysts to generate oxygen *in situ* within the tumor (Prasad et al., 2014; Chen et al., 2015a). Moreover, Fenton-like catalytic reaction also plays an essential role in cancer therapy. For example, Liu et al. (2020) fabricated a biodegradable nanoscale coordination polymers for chemodynamic therapy. And Chen et al. (2019) developed AFeNPs@CAI nanocomposites to accelerate the Fenton reaction for amplified oxidative damage to cells. Herein, we have developed a self-assembling intelligent bimetallic nanoagents, HSA-Pd-Fe-Ce6 nanoagents (NAs) for effective combination phototherapy (**Scheme 1**). The HSA-Pd-Fe-Ce6 NAs are composed of human serum albumin (HSA), which is the most abundant plasma protein in human body and a multifunctional biocompatible drug delivery carrier to tumor (Xie et al., 2010; Elzoghby et al., 2012; Mertz et al., 2012a,b; Chen et al., 2014a,b, 2015b,c; Gause et al., 2015), palladium-iron bimetallic particles (Pd-Fe NPs) which have high reactivity toward hydrogen peroxide (H_2O_2) to genrate superoxide anion free radicals, and chlorin e6 (Ce6), a commercial photosensitizer, which converts molecular oxygen into cytotoxic singlet molecular oxygen ($^1O_2$) by PDT (Yoon et al., 2012; Huang et al., 2016; Liu et al., 2016). It is possible that the hydrophobic Ce6 and Fe-Pd nanoparticles enter the hydrophobic chamber of HSA, thereby forming an amphiphilic molecular system.

In this system, we took advantages of high loading capacity, biocompatibility of HSA, which could overcome the potential problems carused from Ce6, such as poor solubility in an aqueous solution and lack of tumor targeting. So this nanoagents were able to be enriched in tumor by passive targeting (enhanced permeability and retention effect). The experimental results demonstrated that subacid and excessive hydrogen peroxide of TME enabled Pd-Fe bimetallic NPs to generate hydroxyl radical by the "Fenton-like" reaction (Chand et al., 2009; Pang et al., 2011). Simultaneously, the Ce6 would convert oxygen into $^1O_2$ under irradiation. In addition, the results indicated that HSA-Pd-Fe-Ce6 NAs could produce topical heat under the irradiation of 660 nm laser and near infrared absorption induced cell apotosis. Thus, this nanoagents could resolve the problems of traditional photosensitizer, such as poor solubility in aqueous solution, poor specific accumulation, and insufficient treatment effect. Therefore, the nanoagents are promising smart multifunctional integrated NAs for effective combination phototherapy.

MATERIALS AND METHODS

Materials and Instruments

Ni(acac)$_2$, PdCl$_2$, oleylamine (OA, 90%), dichloromethane (DCM, 99%), Tetraoctylamine bromide (TOAB) were obtained from Sigma– Aldrich (United States). HSA was purchased from biomatrik (CHN). Triphenylphosphine (PPh$_3$) and Tetrahydrofuran (THF) were obtained from Aladdin (CHN). Hoechst 33258 and Dihydroethidium (DHE) were purchased from Thermo Fisher Scientific (United States). Cell Counting Kit-8 (CCK-8) and 2,7-Dichlorofluorescein (DCFH-DA) were obtained from Dojindo laboratories (JPN). Penicillin–streptomycin, fetal bovine serum, PBS, DMEM medium, and trypsin were acquired from Gibco Life Technologies (United States). MCF-7 were obtained from Shanghai cell bank of Chinese Academy of Sciences.

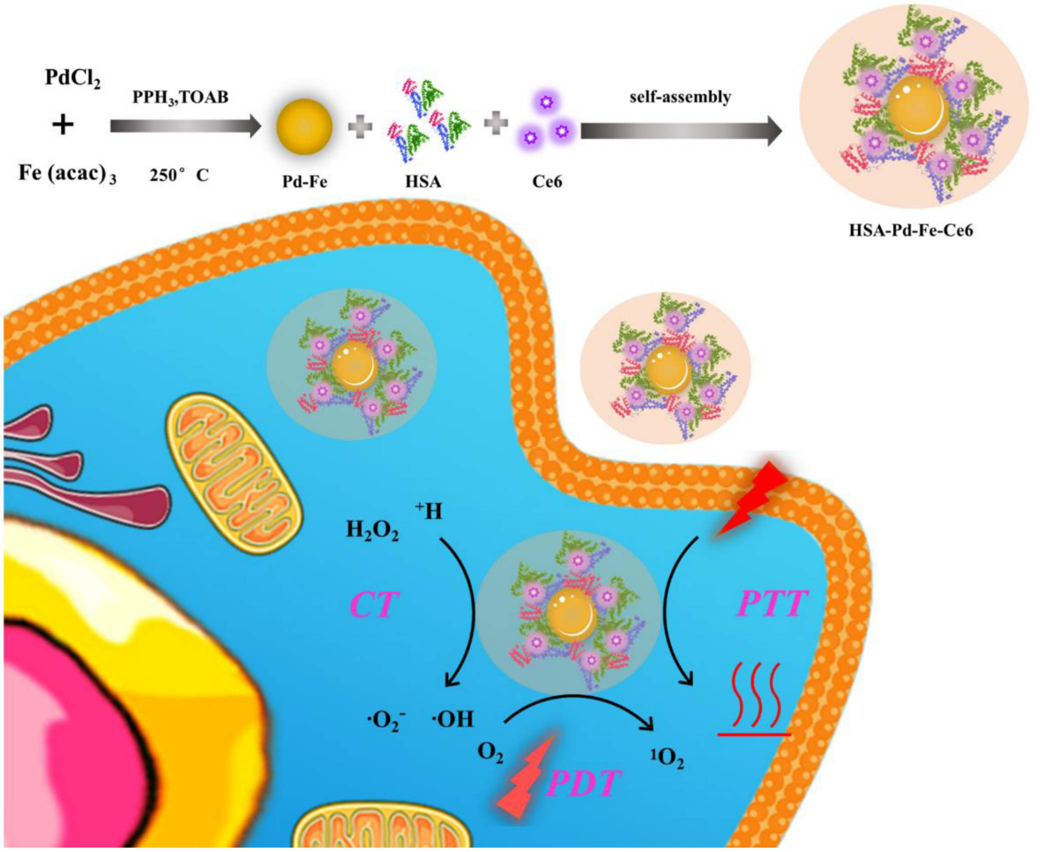

SCHEME 1 | The process of HSA-Pd-Fe-Ce6 NAs synthesis and its application for synergistic phototherapy. The Pd-Fe NPs react with the endogenous hydrogen peroxide (H_2O_2) within tumor cell to generate cytotoxic superoxide anion free radical through the "Fenton-like reaction". Moreover, Ce6 also turns O_2 into a highly toxic singlet oxygen ($^1O_2$) by photodynamic reaction under 660 nm laser. Other than this, the nanoagents result in hyperpyrexia induced cell apoptosis.

Preparation of Pd-Fe

The Pd-Fe nanoparticles were synthesized by the previously reported procedure (Xiang et al., 2014; Chen et al., 2018). In short, a mixture of $PdCl_2$ (0.01 g), Fe $(acac)_3$ (0.04 g), Triphenylphosphine (50 mg) and TOAB (0.03 g) were dissolved in a mixed solution of tetrahydrofuran (5 mL) and oleylamine (6 mL), placed in a 100 mL three-neck round-bottom flask and was stirred at room temperature for 10 min. Then its temperature was increased to 90°C for 10 min. It was subsequently heated up to 250°C. After a 30 min reaction, the solution was cooled down to room temperature. Obtained Pd-Fe (**Supplementary Figure S1**) nanoparticles were washed and centrifuged several times with dichloromethane and then dispersed in the dichloromethane for further use.

Preparation and Characterization of HSA-Pd-Fe-Ce6

The as-prepared hydrophobic Pd-Fe nanoparticles were transferred into aqueous solution by coating with HSA amphiphilic copolymer. The Pd-Fe nanoparticles (10 mg mL^{-1}, 500 μL) were mixed with powder of Ce6 (5 mg) and HSA (80 mg) in dichloromethane (2 mL) as solvent. Ultrapure water (2 mL) was added in to mixed solution forms a biphasic system. Then, nitrogen was bubbled in the solution and mixture changed cloudy to be an emulsion. After bubbled for 30 min, emulsion became clearly because of completely evaporation of the dichloromethane. As acquired HSA-Pd-Fe-Ce6 NAs were purified by a membrane filter (0.22 μm) to remove clustered large nanoparticles and a centrifugal filtration device (Millipore, M_w cutoff = 100 kDa) to get rid of excess HSA for several times. Purified HSA-Pd-Fe-Ce6 NAs were concentrated for further characterization and application. The UV–vis absorbance spectra and photoluminescence (PL) spectra of HSA-Pd-Fe-Ce6 NAs were measured using PerkinElmer Lambda 25 UV–vis absorption spectrophotometer and Edinburgh FS920 fluorescent spectrometer, respectively. TEM images of HSA-Pd-Fe-Ce6 NAs and Pd-Fe NPs were recorded using FEI Tecnai G20 transmission microscope at 200 kV. Dynamic light scattering (DLS) analysis was taken using a Zeta sizer Nano ZS (Malvern Instruments).

Photothermal Property of HSA-Pd-Fe-Ce6 Nanoagents

HSA-Pd-Fe-Ce6 (3.0 mg) nanoparticles were mixed with dichloromethane (2 mL) and irradiated (0.5 w/cm^2, 660 nm, 2 min). Then the solution was cooled down to room temperature. And then repeat the above steps five times while using a thermal infrared hand-held viewer (Ti27, Fluke, United States) to record temperature changes every 10 s.

ROS Generation of HSA-Pd-Fe-Ce6 Nanoagents

HSA-Pd-Fe-Ce6 (3.0 mg) NAs and HSA-Ce6 NPs (3.0 mg) were mixed with DNA (1 mg/mL) and DHE (4 mg/mL) in PBS (2 mL, pH 5.5). The fluorescence intensity was measured using Edinburgh FS920 fluorescent spectrometer before and after mixing with H_2O_2 (1 mM) for 8 min, respectively. Group of HSA-Pd-Fe-Ce6 + H_2O_2: HSA-Pd-Fe-Ce6 (3.0 mg) NAs were mixed with DCFH-DA (4 mg/mL) and H_2O_2 (1 mM) in PBS (2 mL). Group of HSA-Pd-Fe-Ce6: HSA-Pd-Fe-Ce6 (3.0 mg) NAs were mixed with DCFH-DA (4 mg/mL) in PBS (2 mL). Group HSA-Ce6 + H_2O_2: HSA-Ce6 (3.0 mg) NPs were mixed with DCFH-DA (4 μg/mL) and H_2O_2 (1 mM) in PBS (2 mL). All groups were irradiated (660 nm, 0.5 w/cm^2) for 30 s and then measured by Edinburgh FS920 fluorescent spectrometer per 30 s.

In vitro Cellular and 3D-Spheroids Cell Uptake of HSA-Pd-Fe-Ce6 Nanoagents

Flow cytometric assay and CLSM were employed to investigate the cell uptake. The typical procedure was described as follows. Tumor cell (MCF-7) were seeded in six-well plates and cultured for 24 h. The density of various cells is consistent before experiment. Then, the medium was replaced with fresh medium containing HSA-Pd-Fe-Ce6 NAs (1.6 μg mL^{-1}) or HSA-Ce6 (1.6 μg mL^{-1}). After 2 h incubation, cells were washed thrice with PBS and then digested by trypsin and harvested by centrifugation. The fluorescence of histograms of Ce6 were recorded by flow cytometer (Becton Dickinson, San Jose, CA, United States).

For CLSM observation (Qing et al., 2019b), MCF-7 cells (5000 cells per well) were seeded in eight-well chambered cover glasses (Lab-Tek, Nunc, United States). The old medium at 24 h was changed by the medium with HSA-Pd-Fe-Ce6 NAs (1.6 μg mL^{-1}). After 2 h, PBS washed the cells thrice and then stained with Hoechst 33258 and PBS rinsed thrice. Finally, Leica TCS SP5 confocal laser scanning microscope (GER) was used to observe cellular uptake and subcellular distribution.

Intracellular ROS

The MCF-7 cells were seeded in six-well plate, incubated for 24 h in 5% CO_2 at 37°C. Next, added to PBS, HSA-Ce6, HSA-Pd-Fe-Ce6 NAs and H_2O_2 (50 μM) in medium make the final concentrations consistent. After irradiation treatment (0.5 w/cm^2 laser 20 min), cells were promptly washed with PBS and incubated with 10 μmol L^{-1} 2′,7′-dichloro-fluoreseindiacetate (DCFH-DA) and dihydroethidium for 30 min, and intracellular ROS generation was evaluated by flow cytometry.

Cytotoxicity Assay

For PTT, the MCF-7 cells were then incubated with HSA -Ce6 or HSA-Pd-Fe -Ce6 at a Ce6 equiv concentration from 0 to 40 μg mL^{-1} for 4 h. Then, treated with non-irradiated, irradiated (808 nm, 0.5 w/cm^2, 20 min). In order to achieve PTT only effect, Vitamin C (2 × 10^{-3} M) was added to scavenge intracellular ROS.

For combined treatment (CBT), the MCF-7 cells were then incubated with HSA -Ce6 or HSA-Pd-Fe -Ce6 at a Ce6 equiv concentration from 0 to 40 μg mL^{-1} for 4 h. Then, treated with or without 50 μM H_2O_2 for 2 h.

For PDT, the MCF-7 cells were then incubated with HSA -Ce6 or HSA-Pd-Fe -Ce6 at a Ce6 equiv concentration from 0 to 40 μg mL^{-1} for 4 h. Then, treated with non-irradiated, irradiated (660 nm, 0.5 w/cm^2, 20 min). In order to achieve PDT only effect, cells were cooled at 4°C during the irradiation.

For combination therapy, MCF-7 cells were incubated with HSA-Ce6 or HSA-Pd-Fe-Ce6 at a Ce6 equiv concentration from 0 to 40 μg mL^{-1} for 4 h. Then, treated with all above treatment.

After rinsing three times with PBS, all groups were incubated with new culture medium. CCK-8 assay was carried out to investigate the cell survival of different groups after 4 h. At 4 h post laser irradiation, 10 μL CCK-8 mixed with 90 μL of DMEM were added to each well of the plate. Incubated the plates for an hour in the incubate. Then measured the absorbance at 450 nm using a multimode microplate reader (Synergy4, BioTek, United States).

To obtain visible results, *in vitro* cell cytotoxicity of HSA-Ce6 and HSA-Pd-Fe-Ce6 NAs were also investigated by Dead cell staining via confocal laser scanning microscope (FV3000, Olympus, Japan) observation. MCF-7 cells (5 × 10^3) were added into each well of a chamber slide with different treatment. Control: MCF-7 cells incubated with HSA -Ce6 or HSA-Pd-Fe -Ce6 for an hour. PTT: The cells incubated with HSA -Ce6 or HSA-Pd-Fe -Ce6 after irradiation (808 nm, 0.5 w/cm^2) for an hour. In order to achieve PTT only effect, Vitamin C (2 × 10^{-3} M) was added to scavenge intracellular ROS. CT: The cells incubated with HSA -Ce6 or HSA-Pd-Fe-Ce6 after incubation with 50 μM H_2O_2 for 1 h. PDT: The cells incubated with HSA -Ce6 orHSA-Pd-Fe-Ce6 after irradiation (660 nm, 0.5 w/cm^2) for an hour. In order to achieve PDT only effect, cells were cooled at 4°C during the irradiation. CBT: The cells incubated with HSA -Ce6 or HSA-Pd-Fe -Ce6 after above treatment. dividing into five groups [PBS, HSA-Ce6, HSA-Pd-Fe-Ce6, HSA-Ce6(+), and HSA-Pd-Fe-Ce6(+)] and cultured for 24 h. After that, the PBS, HSA-Ce6, and HSA-Pd-Fe-Ce6 NAs (20 μg mL^{-1}) were added into relative wells of chamber slide. 2 h later, groups HSA-Ce6(+) and HSA-Pd-Fe-Ce6(+) were irradiated (660 nm, 0.5 W cm^{-2}, 20 min). After incubation for another 2 h, the PI was added into the well. After 35 min, the cells were observed by a confocal laser scanning microscope.

Statistical Analysis

All the results are reported as mean ± SD. The differences among groups were determined using one-way ANOVA analysis and student's *t*-test; $^{*}P < 0.05$, $^{**}P < 0.01$, $^{***}P < 0.001$.

RESULTS AND DISCUSSION

Characteristics of HSA-Pd-Fe-Ce6 NAs

As revealed by transmission electron microscope (TEM) (**Figure 1A**), the synthesized HSA-Pd-Fe-Ce6 NAs showed

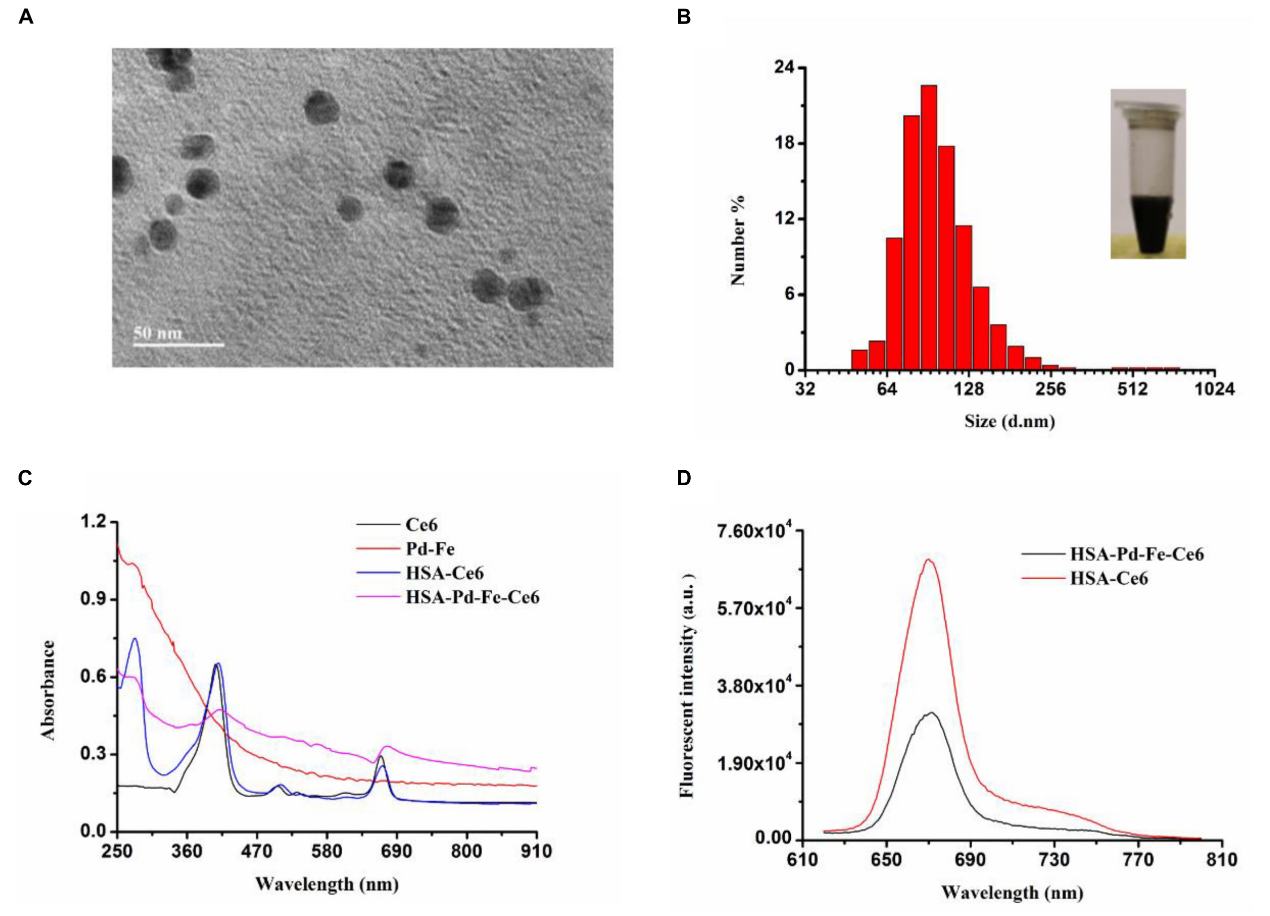

FIGURE 1 | (A) A TEM image of HSA-Pd-Fe-Ce6. **(B)** Hydrodynamic diameters of HSA-Pd-Fe-Ce6 NAs and optical image (insert) of the nanoparticles. **(C)** Normalized UV–vis-NIR absorption spectra of Pd-Fe (dichloromethane), Ce6 (dichloromethane), HSA-Ce6 (Deionized water), and HSA-Pd-Fe-Ce6 (Deionized water) **(D)** fluorescence spectra at 600 nm of (a) HSA-Pd-Fe-Ce6 (70 μg/mL) and (b) HSA-Ce6 (70 μg/mL).

average sizes at ≈20 nm and it can be observed that Pd-Fe NPs (deep black) are wrapped by HSA (light gray). As revealed by Malvern Particle Sizer, HSA-Pd-Fe-Ce6 NAs are stable and dispersed well in distilled deionized (DDI) water with an average NP size of 105 nm (**Figure 1B**). As illustrated by UV–vis spectra (**Figure 1C**), the Ce6 characteristic peaks (410 and 660 nm) and the characteristic peaks at 300 nm, which corresponded to HSA both are seen in the spectrum of the synthesized HSA-Pd-Fe-Ce6 NPs. It was also shown that HSA-Pd-Fe-Ce6 NAs have higher absorption than Ce6 and HSA-Ce6 absorption in the range of 700 and 1000 nm, similar to the way Pd-Fe NPs. The above mentioned results indicated the successful synthesis of HSA-Pd-Fe-Ce6 NAs in which Ce6 was conjugated onto Pd-Fe NPs coated with HSA. The absorption in the range of 750 to 1000 nm may render HSA-Pd-Fe-Ce6 NAs the photothermal effect that individual Ce6 does not have. At the same concentration, the fluorescence intensity stimulated by 600 nm of HSA-Ce6 NAs at 672 nm is more than twice that of HSA-Pd-Fe-Ce6 NAs (**Figure 1D**), which indicates that may have better phototherapy effect than HSA-Ce6 NAs. In terms of stability, the size of HSA-Pd-Fe-Ce6 NAs stabilized at 105 nm within a week (**Supplementary Figure S2**), while the size of HSA-Ce6 NAs maintained the trend of increasing (**Supplementary Figures S3, S4**).

To investigate photothermal effect of HSA-Pd-Fe-Ce6 NPs, they were tested under the irradiation of 808 nm. As shown in **Figures 2A,B**, HSA-Pd-Fe-Ce6 NAs had increased in temperature up to 27.3°C and reached 51.8°C, which was high enough for tumor cell ablation. No obvious change was observed during the five cycles of heating/cooling, implying the great potential of HSA-Pd-Fe-Ce6 NAs as a durable photothermal agent (**Figure 2C**).

The ROS generation in solution was studied with superoxide anion (SOA) indicators, DHE and DCFH-DA. As shown in **Supplementary Figure S5**, though the group HSA-Ce6 exhibited a stronger fluorescence intensity after mixing with H_2O_2 compared with group HSA-Pd-Fe-Ce6, the latter showed more than four times relative intensity of the former implying great generation of SOD resulting from "Fenton-like" reaction (**Figure 3A**). To further investigate total ROS generation, group HSA-Pd-Fe-Ce6 + H_2O_2, HSA-Pd-Fe-Ce6 and HSA-Ce6 were studied with ROS indicator, DCFH-DA.

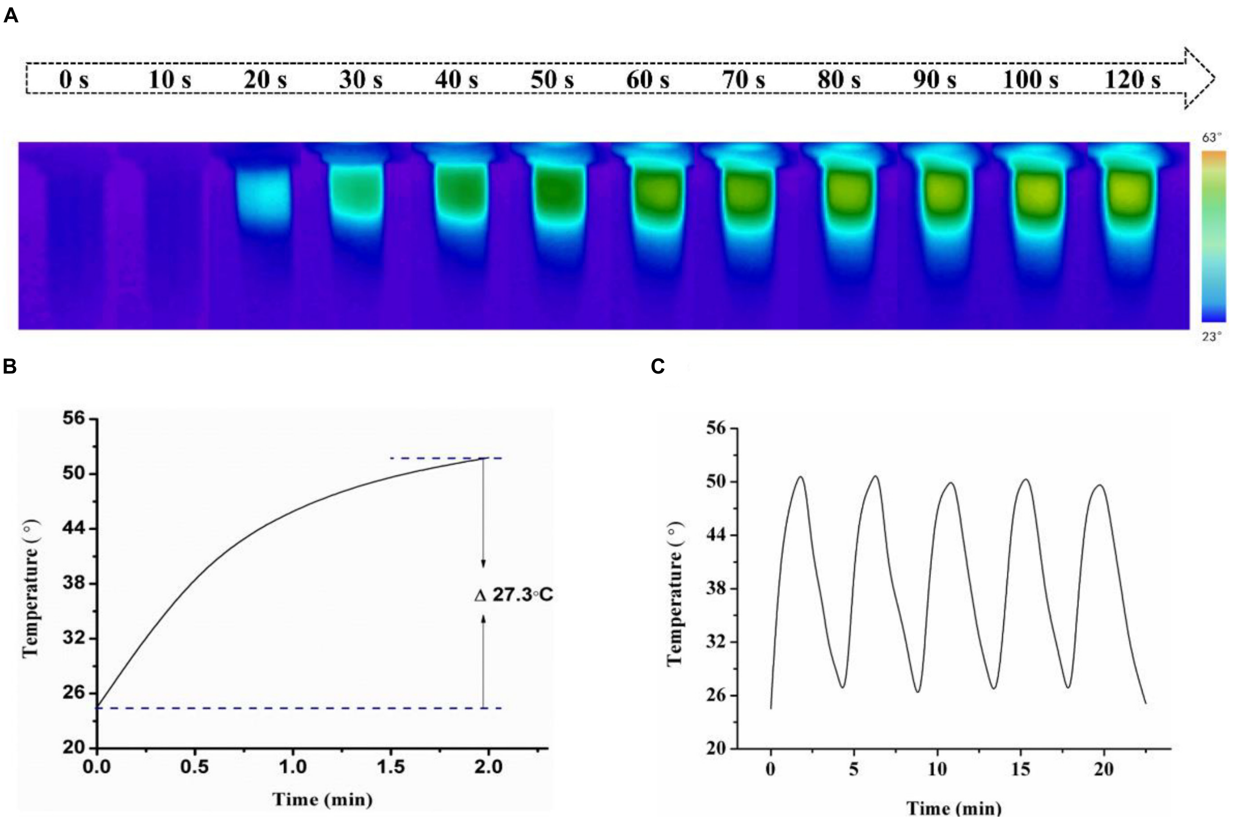

FIGURE 2 | (A) Infrared images of HSA-Pd-Fe-Ce6 NAs (1.5 mg/mL) within 2 min under 808 nm laser (0.5 w/cm^2) irradiation per 10 s and **(B)** Temperature growth curve of **(A)**. **(C)** A temperature cycling test of HSA-Pd-Fe-Ce6 NAs.

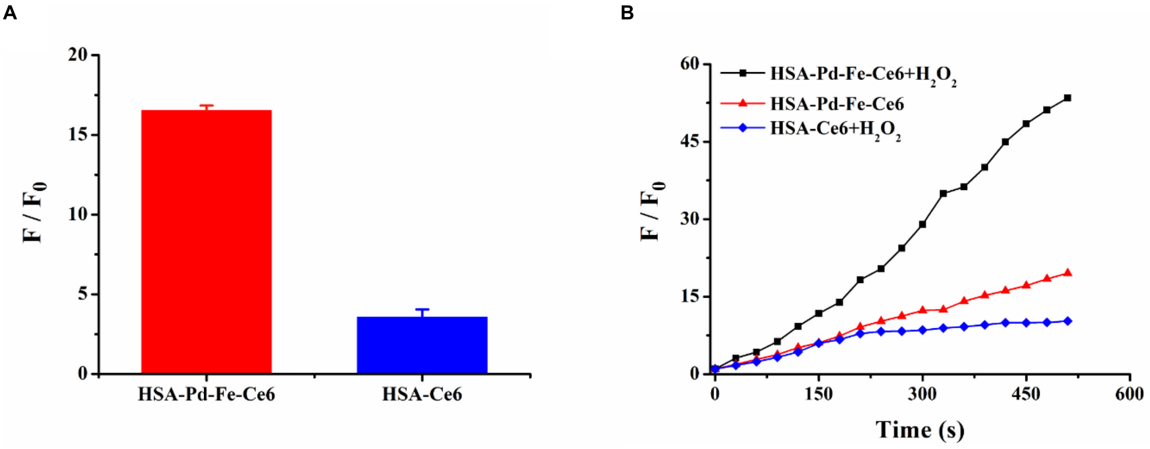

FIGURE 3 | (A) The fluorescence intensity changes of dihydroethidium (DHE) between HSA-Pd-Fe-Ce6 NAs and HSA-Ce6 NPs after mixed with H_2O_2 (1 mM), DNA (1 mg/mL) and DHE (4 mg/mL) in PBS (pH 5.0). F_0 refers to the fluorescence intensity before mixed with H_2O_2. **(B)** The fluorescence intensity changes of 2′,7′-dichlorofluorescein diacetate (DCFH-DA) between group HSA-Pd-Fe-Ce6 + H_2O_2, group HSA-Pd-Fe-Ce6 and group HSA-Ce6 + H_2O_2 NPs under 660 nm laser (0.5 w/cm^2, 30 s) irradiation per 30 s. F_0 refers to the fluorescence intensity before irradiation.

As shown in **Figure 3B** and **Supplementary Figure S6**, group HSA-Pd-Fe-Ce6 + H_2O_2 showed nearly three times relative fluorescence intensity of group HSA-Pd-Fe-Ce6 and six times of HSA-Ce6 + H_2O_2 at 510 s point. In addition, intensity growth of group HSA-Ce6 seemed bog down since 270 s point while other two group seemed to continuous increase suggesting great and enduring ROS generation of HSA-Pd-Fe-Ce6.

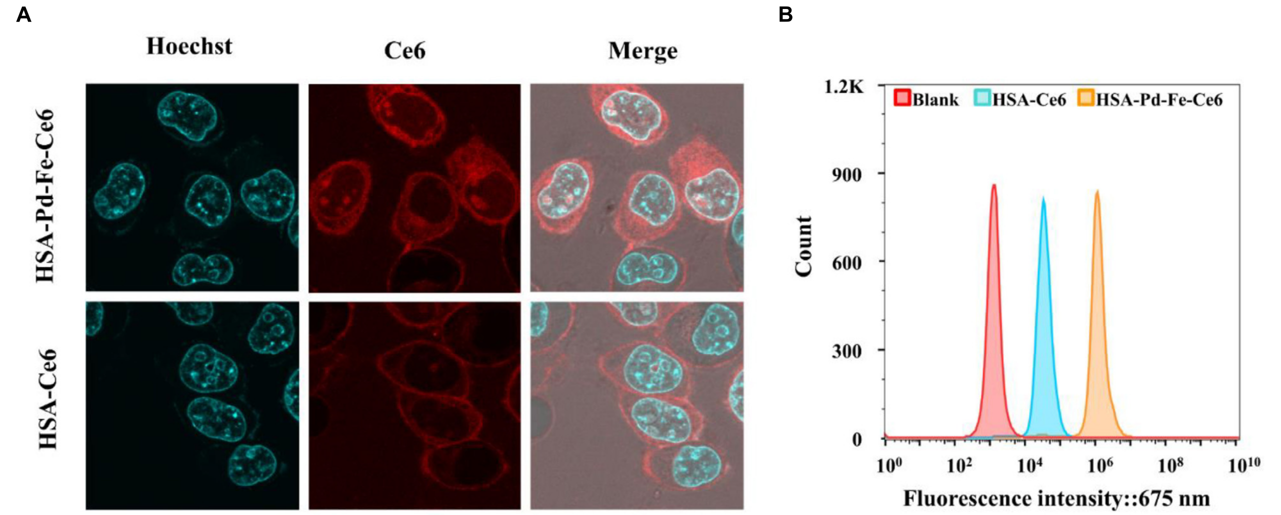

FIGURE 4 | (A) The location of HSA-Pd-Fe-Ce6 in MCF-7. **(B)** Flow cytometric analysis of uptake of HSA-Pd-Fe-Ce6 and HSA-Ce6 by MCF-7 cells.

Uptake of HSA-Pd-Fe-Ce6 NAs

The human breast cancer cell line MCF-7 cells were incubated with HSA-Pd-Fe-Ce6 NAs or HSA-Ce6 NAs (20 μg mL^{-1}) for 2 h at 37°C, and cell uptake was visualized using confocal laser scanning microscopy. The cell nucleus was stained greenish-blue to differentiate cellular compartments. The images show uniform distribution of HSA-Pd-Fe-Ce6 NAs and Ce6 in the cytoplasm and around the nucleus of the cells, while the former intracellular fluorescence intensity corresponding to assimilated particles amount was much higher than the latter (**Figure 4A**), indicating HSA enhanced the efficiency of the internalization of HSA-Pd-Fe-Ce6 NPs. To further certify it, flow cytometric analysis was carried out to analyze and quantify cellular uptake. The fluorescence intensity associated with Ce6 of HSA-Pd-Fe-Ce6 NAs was several orders of magnitude higher than Ce6 and blank (**Figure 4B**), which was consistent with the results above. These results demonstrate that HSA-Pd-Fe-Ce6 NAs was more easily taken up by tumor cells than free Ce6.

To understand the intratumoral transport behavior, *in vitro* 3D tumor spheroids were used to further investigate intratumoral transport of HSA-Pd-Fe-Ce6 NAs and HSA-Ce6. Tumor spheroids were formed using MCF-7 cells incubated with HSA-Pd-Fe-Ce6 NAs or HSA-Ce6 NAs. Confocal quantitative image cytometer CQ1 was used to image tumor spheroids every hour. As shown in **Supplementary Figure S7**, the fluorescence intensity of group HSA-Pd-Fe-Ce6 was obviously stronger than that from HSA-Ce6 at 4 h and the former maintained strong pink signal afterward while the latter was attenuated over time, indicating great intratumoral permeability and retention of HSA-Pd-Fe-Ce6 NAs.

Intracellular Generation of ROS

It has been known that the vigorous metabolism and restricted blood supply for cancer cells resulting in significant increase of the H_2O_2 level in the tumor sites (Kuang et al., 2011), so a ROS probe 2′,7′-dichlorofluorescein diacetate (DCFH-DA) was then used to assessed the intracellular generation of ROS. MCF-7 cells were incubated with HSA-Ce6 NAs, HSA-Pd-Fe-Ce6 NAs, and H_2O_2 for 2 h, respectively, followed by incubation with DCFH-DA and treatment with the 660 nm laser. As shown in **Supplementary Figure S8**, The fluorescence intensity of HSA-Pd-Fe-Ce6 NAs was several orders of magnitude higher than HSA-Ce6 and blank, which was attributed to T the *in situ* production of ROS by the reaction of Pd-Fe with the H_2O_2 in the tumor under the acidic condition and the ROS produced by Ce6. Meanwhile, another superoxide indicator, dihydroethdium, was also used to evaluate the generation of superoxide anion free radical. It exhibits blue-fluorescence in the cytosol until oxidized in the nucleus, where it intercalates within the cell's DNA and emits a bright red fluorescence. As shown in **Supplementary Figure S9**, MCF-7 cells, when incubated with 20 μg mL^{-1} HSA-Pd-Fe-Ce6 and H_2O_2, produced the strongest fluorescence signal, indicting the most efficient in the generation of intracellular superoxide anion free radical.

Cytotoxicity Assay of HSA-Pd-Fe-Ce6 NAs

In vitro cell cytotoxicity of HSA-Pd-Fe-Ce6 NAs was investigated using Cell Counting Kit-8 (CCK-8). The amount of water-soluble formazan was directly proportional to the number of living cells. To investigate the PTT effect of HSA-Pd-Fe-Ce6 NAs, MCF-7 cells were incubated with HSA -Ce6 or HSA-Pd-Fe -Ce6 at a Ce6 equiv concentration from 0 to 40 μg mL^{-1} for 4 h. Then, treated with non-irradiated, irradiated (808 nm, 0.5 w/cm^2, 20 min). In order to achieve PTT only effect, Vitamin C (2×10^{-3} M) was added to scavenge intracellular ROS. Compared with other groups, group HSA-Pd-Fe-Ce6 under irradiation had significantly lower cell viability with about 61% cells survived when the concentration reached 40 μg mL^{-1}, as shown in **Figure 5A**. For CBT, the MCF-7 cells were incubated

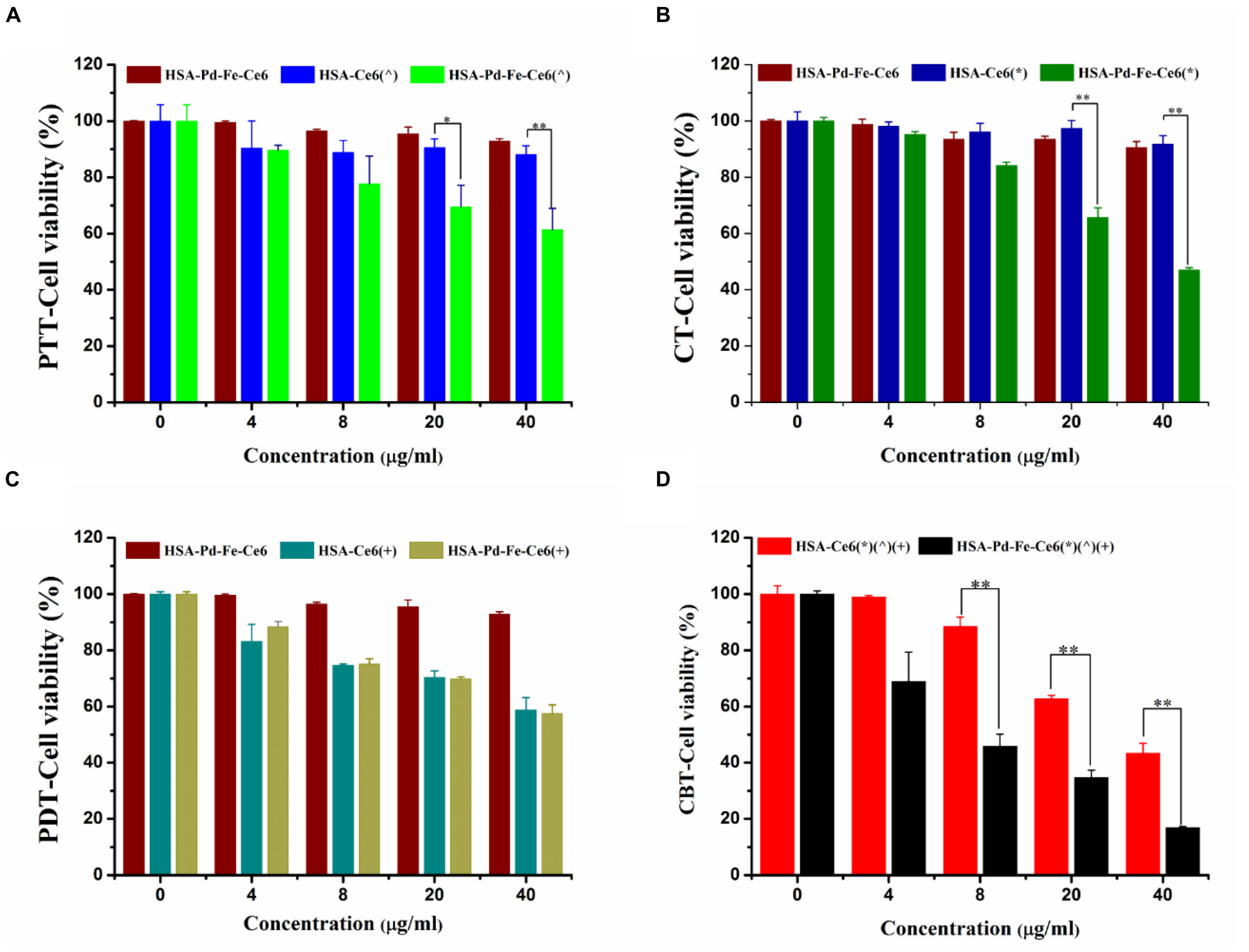

FIGURE 5 | (A) The cell cytotoxicity of HSA-Pd-Fe-Ce6 only, HSA -Ce6 and HSA-Pd-Fe -Ce6 after irradiation (808 nm, 0.5 w/cm^2) for an hour (n = 6). In order to achieve PTT only effect, Vitamin C (2×10^{-3} M) was added to scavenge intracellular ROS **(B)** The cell cytotoxicity of HSA-Pd-Fe-Ce6 only, HSA -Ce6 and HSA-Pd-Fe-Ce6 after incubation with 50 μM H_2O_2 for 4 h (n = 6). **(C)** The cell cytotoxicity of HSA-Pd-Fe-Ce6 only, HSA-Ce6 and HSA-Pd-Fe-Ce6 after irradiation (660 nm, 0.5 w/cm^2) for an hour (n = 6). In order to achieve PDT only effect, cells were cooled at 4°C during the irradiation **(D)** The cell cytotoxicity of MCF-7 incubated with HSA -Ce6 or HSA-Pd-Fe -Ce6 after above treatment (n = 6). (^) refers to 808 nm laser irradiation. (+) refers to 660 nm laser irradiation. (*) refers to incubation with 50 μM H_2O_2 for 4 h. P-values were calculated by Tukey's post-test ($^{**}P < 0.01$ or $^{*}P < 0.05$). The error bars represent the standard error of six independent measurements.

with HSA -Ce6 or HSA-Pd-Fe -Ce6 at a Ce6 equiv concentration from 0 to 40 μg mL^{-1} for 4 h. Then, treated with or without 50 μM H_2O_2 for 2 h. Group HSA-Pd-Fe-Ce6 with H_2O_2 showed significantly low cell viability up to around 47% at 40 μg mL^{-1} concentration while the other groups kept considerable high percent survival within investigated concentration seen in **Figure 5B**. We could see the negative results of group HSA-Pd-Fe-Ce6 without treatment and HSA-Ce6 with relative treatment in both studies comparing with positive results of group HSA-Pd-Fe-Ce6 with treatment, implying Pd-Fe bimetallic part with irradition and Pd-Fe with H_2O_2 were the sufficient condition of PTT and CBT, respectively. To investigate PDT effect, MCF-7 cells were incubated with HSA -Ce6 or HSA-Pd-Fe -Ce6 at a Ce6 equiv concentration from 0 to 40 μg mL^{-1} for 4 h. Then, treated with non-irradiated, irradiated (660 nm, 0.5 w/cm^2, 20 min). In order to achieve PDT only effect, cells were cooled at 4°C during the irradiation. As seen in **Figure 5C**, group HSA-Pd-Fe-Ce6 and HSA-Ce6 with irradiation showed identical results, which was because of the equivalent Ce6. For the combination therapy, MCF-7 cells were incubated with HSA-Ce6 or HSA-Pd-Fe-Ce6 at a Ce6 equiv concentration from 0 to 40 μg mL^{-1} for 4 h. Then, treated with all above treatment. As shown in **Figure 5D**, both groups showed positive outcomes but group HSA-Pd-Fe-Ce6 possessed significant lower cell survival than group HSA-Ce6 had from 8 to 40 μg mL^{-1} concentration and at the 40 μg mL^{-1} concentration the survival rate of groups were 17 and 43%, which were consistent to results above, revealing that the HSA-Pd-Fe-Ce6 NAs had the advantage of efficient and controllable phototherapy.

We further investigated *in vitro* cell cytotoxicity of HSA-Pd-Fe-Ce6 and HSA-Ce6 by dead cell staining, in which red fluorescent PI were used as dyes. As shown in **Figure 6**, groups

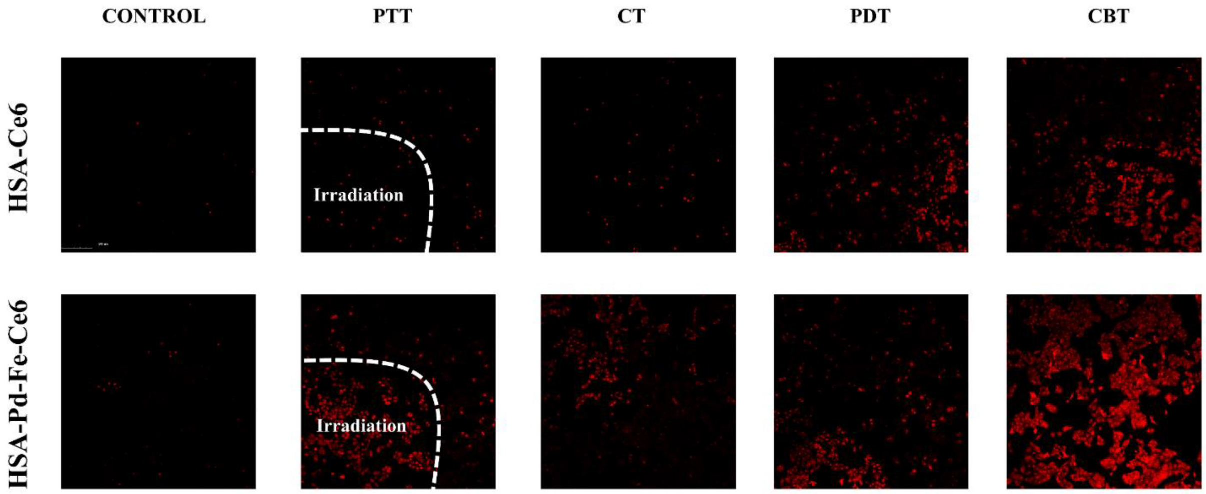

FIGURE 6 | The Dead cell staining results of HSA-Ce6 NPs, HSA-Pd-Fe-Ce6 NPs with different treatment. Control: MCF-7 cells incubated with HSA -Ce6 or HSA-Pd-Fe -Ce6 for an hour. PTT: The cells incubated with HSA -Ce6 or HSA-Pd-Fe -Ce6 after irradiation (808 nm, 0.5 w/cm^2) for an hour. In order to achieve PTT only effect, Vitamin C (2×10^{-3} M) was added to scavenge intracellular ROS. CT: The cells incubated with HSA -Ce6 or HSA-Pd-Fe-Ce6 after incubation with 50 μM H_2O_2 for 1 h. PDT: The cells incubated with HSA -Ce6 orHSA-Pd-Fe-Ce6 after irradiation (660 nm, 0.5 w/cm^2) for an hour. In order to achieve PDT only effect, cells were cooled at 4°C during the irradiation. CBT: The cells incubated with HSA -Ce6 or HSA-Pd-Fe -Ce6 after above treatment.

HSA-Pd-Fe-Ce6 with treatment showed obvious red signal, implying cellular death were positive. Especially CBT treatment, a huge area was stained. However, there was barely red single seen in the group HSA-Ce6 with PTT or CT treatment. Though the area of group HSA-Ce6 with PDT treatment was the same as the area of HSA-Pd-Fe-Ce6, the area of HSA-Ce6 with CBT treatment was significantly smaller than HSA-Pd-Fe-Ce6's, which were in agreement with the CCK8 assay.

In order to test the potential application of HSA-Pd-Fe-Ce6 NPs, they were injected subcutaneously into left lower abdomen of the mouse imaging by micro-ultrasound Imaging System. As shown in **Supplementary Figure S10**, HSA-Pd-Fe-Ce6 NPs had near-infrared (NIR) absorption photoacoustic signals from 700 to 970 nm. Moreover, it was clear that the longer the wavelength was, the less the background signals were, and the signal intensity didn't weaken much at NIR wavelength. Unlike the visible spectrum, in which most tissue chromophores (hemoglobin, melanin, fat etc.) absorb light strongly, wavelength of the irradiated beam in the NIR region has a deeper tissue penetration into tissues. HSA-Pd-Fe-Ce6 is a promising photoacoustic contrast agent, which makes it possible to realize further applications, such as real-time imaging guidance and therapeutic evaluation.

CONCLUSION

In conclusion, we have constructed self-assembling intelligent bimetallic nanoagents for effective combination phototherapy via reductive co-precipitation method. The presence of Pd-Fe and Ce6 offers HSA-Pd-Fe-Ce6 NAs two ways to generate ROS leading to superior ROS production, in which superoxide anion free radicals are produced by the reaction between Pd-Fe bimetallic NPs and H_2O_2 in acidic TME and singlet molecular oxygen converted from molecular oxygen though photodynamic reaction caused by the Ce6. Additionally, the results show that HSA-Pd-Fe-Ce6 NAs can produce topical heat under the irradiation and near infrared absorption bringing about excellent photothermal conversion efficiency. Overall, this nanoagents could resolve the problems of traditional photosensitizer, such as poor solubility in aqueous solution, poor specific enrichment, and insufficient treatment effect. Therefore, the nanoagents are promising smart multifunctional integrated nanophotosensitive agent for effective combination phototherapy.

DATA AVAILABILITY STATEMENT

All datasets generated for this study are included in the article/**Supplementary Material**.

ETHICS STATEMENT

The animal study was reviewed and approved by Chinese Academy of Sciences.

AUTHOR CONTRIBUTIONS

HL and YL: data curation, validation, visualization, investigation, writing-original draft. JX, XY, CnL, CaL, QZ, LZ: writing-original draft. PG: funding acquisition, project administration, methodology, writing-review and editing. JH: funding acquisition, project administration, supervision, writing-review and editing.

FUNDING

This work was financially supported by the National Natural Science Foundation of China (81671758, 21705076, 31571013, and 21975117), Guangdong Natural Science Foundation of Research Team (2016A030312006), and the Shenzhen Science and Technology Program (JCYJ20160429191503002, JCYJ20170818162522440, JCYJ20170818154843625, and JCYJ20170818113538482).

ACKNOWLEDGMENTS

We thank the Instrumental Analysis Center of Shenzhen University (Xili Campus).

SUPPLEMENTARY MATERIAL

The Supplementary Material for this article can be found online at: https://www.frontiersin.org/articles/10.3389/fbioe.2020.00423/full#supplementary-material

FIGURE S1 | A TEM image of Pd-Fe.

FIGURE S2 | Stability of HSA-Pd-Fe-Ce6 NAs in DI water.

FIGURE S3 | Stability of HSA-Ce6 NAs in DI water.

FIGURE S4 | Size change curve of S2 and S3.

FIGURE S5 | The fluorescence intensity of dihydroethidium (DHE) of **(A)** HSA-Ce6 NPs and **(B)** HSA-Pd-Fe-Ce6 NAs after mixed with H_2O_2 (100 μM), DNA (1 mg/mL) and DHE (4 mg/mL) in PBS (pH 5.5). 0: refers to the fluorescence intensity before mixed with DHE.

FIGURE S6 | The fluorescence intensity of 2′,7′-dichlorofluorescein diacetate (DCFH-DA) **(A)** group HSA-Pd-Fe-Ce6 + H_2O_2, **(B)** group HSA-Pd-Fe-Ce6, and **(C)** group HSA-Ce6 + H_2O_2 NPs under 660 nm laser (0.5 w/cm^2, 30 s) irradiation per 30 s.

FIGURE S7 | Images of the 3D spheroids of MCF-7 cells incubated with HSA-Pd-Fe-Ce6 or HSA-Ce6 per hour.

FIGURE S8 | The generation of ROS determined by the DCFH-DA fluorescence of MCF-7 cells after coincubated with PBS or HSA-Ce6 nanoparticles (20 μg/mL) or HSA-Pd-Fe-Ce6 NAs (20 μg/mL) with H_2O_2 (50 μM) for 2 h and further 20 min laser irradiation.(660 nm,0.5 w/cm^2).

FIGURE S9 | Use of a free radical indicator to evaluate the production of ROS (·OH,·O_2^-) after incubation of MCF-7 cells with dihydroethidium and H_2O_2 (50 μM).

FIGURE S10 | Photoacoustic signals of HSA-Pd-Fe-Ce6 nanoparticles at 700, 760, 820, 880, 930, and 970 nm.

REFERENCES

Bertout, J. A., Patel, S. A., and Simon, M. C. (2008). Hypoxia and metabolism series-timeline the impact of O2 availability on human cancer. *Nat. Rev. Cancer* 8, 967–975. doi: 10.1038/nrc2540

Bray, F., Ferlay, J., Soerjomataram, I., Siegel, R. L., Torre, L. A., and Jemal, A. (2018). Global cancer statistics 2018: GLOBOCAN estimates of incidence and mortality worldwide for 36 cancers in 185 countries. *CA Cancer J. Clin.* 68, 394–424. doi: 10.3322/caac.21492

Brown, S. B., Brown, E. A., and Walker, I. (2004). The present and future role of photodynamic therapy in cancer treatment. *Lancet Oncol.* 5, 497–508. doi: 10.1016/s1470-2045(04)01529-23

Chand, R., Ince, N. H., Gogate, P. R., and Bremner, D. H. (2009). Phenol degradation using 20, 300 and 520 kHz ultrasonic reactors with hydrogen peroxide, ozone and zero valent metals. *Sep. Purif. Technol.* 67, 103–109. doi: 10.1016/j.seppur.2009.03.035

Chen, H., Tian, J., He, W., and Guo, Z. (2015a). H2O2-Activatable and O-2-evolving nanoparticles for highly efficient and selective photodynamic therapy against hypoxic tumor cells. *J. Am. Chem. Soc.* 137, 1539–1547. doi: 10.1021/ja511420n

Chen, Q., Liang, C., Wang, C., and Liu, Z. (2015b). An imagable and photothermal "Abraxane-Like" nanodrug for combination cancer therapy to treat subcutaneous and metastatic breast tumors. *Adv. Mater.* 27, 903–910. doi: 10.1002/adma.201404308

Chen, Q., Wang, X., Wang, C., Feng, L., Li, Y., and Liu, Z. (2015c). Drug-Induced self-assembly of modified albumins as nano-theranostics for tumor-targeted combination therapy. *ACS Nano* 9, 5223–5233. doi: 10.1021/acsnano.5b00640

Chen, Q., Liang, C., Wang, X., He, J., Li, Y., and Liu, Z. (2014a). An albumin-based theranostic nano-agent for dual-modal imaging guided photothermal therapy to inhibit lymphatic metastasis of cancer post surgery. *Biomaterials* 35, 9355–9362. doi: 10.1016/j.biomaterials.2014.07.062

Chen, Q., Wang, C., Zhan, Z., He, W., Cheng, Z., Li, Y., et al. (2014b). Near-infrared dye bound albumin with separated imaging and therapy wavelength channels for imaging-guided photothermal therapy. *Biomaterials* 35, 8206–8214. doi: 10.1016/j.biomaterials.2014.06.013

Chen, X., Zhang, H., Zhang, M., Zhao, P., Song, R., Gong, T., et al. (2019). Amorphous Fe-based nanoagents for self-enhanced chemodynamic therapy by re-establishing tumor acidosis. *Adv. Funct. Mater.* 30:1908365. doi: 10.1002/adfm.201908365

Chen, Z., Wu, C., Zhang, Z. F., Wu, W. P., Wang, X. F., and Yu, Z. Q. (2018). Synthesis, functionalization, and nanomedical applications of functional magnetic nanoparticles. *Chin. Chem. Lett.* 29, 1601–1608. doi: 10.1016/j.cclet.2018.08.007

Dolmans, D., Fukumura, D., and Jain, R. K. (2003). Photodynamic therapy for cancer. *Nat. Rev. Cancer* 3, 380–387. doi: 10.1038/nrc1071

Dougherty, T. J., Grindey, G. B., Fiel, R., Weishaupt, K. R., and Boyle, D. G. (1975). Photoradiation therapy cure of animal tumors with hematoporphyrin and light. *J. Natl. Cancer Inst.* 55, 115–121. doi: 10.1093/jnci/55.1.115

Elzoghby, A. O., Samy, W. M., and Elgindy, N. A. (2012). Albumin-based nanoparticles as potential controlled release drug delivery systems. *J. Control Release* 157, 168–182. doi: 10.1016/j.jconrel.2011.07.031

Gause, K. T., Yan, Y., Cui, J., O'Brien-Simpson, N. M., Lenzo, J. C., Reynolds, E. C., et al. (2015). Physicochemical and immunological assessment of engineered pure protein particles with different redox states. *ACS Nano* 9, 2433–2444. doi: 10.1021/acsnano.5b00393

Hu, D., Sheng, Z., Gao, G., Siu, F., Liu, C., Wan, Q., et al. (2016). Activatable albumin-photosensitizer nanoassemblies for triple-modal imaging and thermal-modulated photodynamic therapy of cancer. *Biomaterials* 93, 10–19. doi: 10.1016/j.biomaterials.2016.03.037

Hu, J., Tang, Y. A., Elmenoufy, A. H., Xu, H., Cheng, Z., and Yang, X. (2015). Nanocomposite-Based photodynamic therapy strategies for deep tumor treatment. *Small* 11, 5860–5887. doi: 10.1002/smll.201501923

Hu, S. Q., Tong, L. J., Wang, J. X., Yi, X. Y., and Liu, J. W. (2019). NIR light-responsive hollow porous gold nanospheres for controllable pressure-based sensing and photothermal therapy of cancer cells. *Anal. Chem.* 91, 15418–15424. doi: 10.1021/acs.analchem.9b02871

Huang, Y., Qiu, F., Shen, L., Chen, D., Su, Y., Yang, C., et al. (2016). Combining two-photon-activated fluorescence resonance energy transfer and near-infrared photothermal effect of unimolecular micelles for enhanced photodynamic therapy. *ACS Nano* 10, 10489–10499. doi: 10.1021/acsnano.6b06450

Jung, H. S., Han, J., Lee, J. H., Lee, J. H., Choi, J. M., Kweon, H. S., et al. (2015). Enhanced NIR radiation-triggered hyperthermia by mitochondrial targeting. *J. Am. Chem. Soc.* 137, 3017–3023. doi: 10.1021/ja5122809

Kuang, Y., Baakrishnan, K., Gandhi, V., and Peng, X. (2011). Hydrogen peroxide inducible DNA cross-linking agents: targeted anticancer prodrugs. *J. Am. Chem. Soc.* 133, 19278–19281. doi: 10.1021/ja2073824

Lim, E. K., Kim, T., Paik, S., Haam, S., Huh, Y. M., and Lee, K. (2015). Nanomaterials for theranostics: recent advances and future challenges. *Chem. Rev.* 115, 327–394. doi: 10.1021/cr300213b

Liu, J., Wu, M., Pan, Y., Duan, Y., Dong, Z., Chao, Y., et al. (2020). Biodegradable nanoscale coordination polymers for targeted tumor combination therapy with oxidative stress amplification. *Adv. Funct. Mater.* 30:1908865. doi: 10.1002/adfm.201908865

Liu, K., Xing, R., Li, Y., Zou, Q., Moehwald, H., and Yan, X. (2016). Mimicking primitive photobacteria: sustainable hydrogen evolution based on peptide-porphyrin co-assemblies with a self-mineralized reaction center. *Angewandte Chem Int. Ed.* 55, 12503–12507. doi: 10.1002/anie.201606795

Liu, Y. R., Kim, Y. J., Siriwon, N., Rohrs, J. A., Yu, Z. Q., and Wanga, P. (2018). Combination drug delivery via multilamellar vesicles enables targeting of tumor cells and tumor vasculature. *Biotechnol. Bioeng.* 115, 1403–1415. doi: 10.1002/bit.26566

Lou, Y., McDonald, P. C., Oloumi, A., Chia, S., Ostlund, C., Ahmadi, A., et al. (2011). Targeting tumor hypoxia: suppression of breast tumor growth and metastasis by novel carbonic anhydrase IX inhibitors. *Cancer Res.* 71, 3364–3376. doi: 10.1158/0008-5472.can-10-4261

Ma, W., Sha, S. N., Chen, P. L., Yu, M., Chen, J. J., Huang, C. B., et al. (2020). A cell membrane-targeting self-delivery chimeric peptide for enhanced photodynamic therapy and in situ therapeutic feedback. *Adv. Healthcare Mater.* 9:e1901100. doi: 10.1002/adhm.201901100

Meng, H., Hu, X., Kong, G., Yang, C., Fu, T., Li, Z., et al. (2018). Aptamer-functionalized nanoscale metal-organic frameworks for targeted photodynamic therapy. *Theranostics* 8, 4332–4344. doi: 10.7150/thno.26768

Mertz, D., Cui, J., Yan, Y., Devlin, G., Chaubaroux, C., Dochter, A., et al. (2012a). Protein capsules assembled via isobutyramide grafts: sequential growth, biofunctionalization, and cellular uptake. *ACS Nano* 6, 7584–7594. doi: 10.1021/nn302024t

Mertz, D., Wu, H., Wong, J. S., Cui, J., Tan, P., Alles, R., et al. (2012b). Ultrathin, bioresponsive and drug-functionalized protein capsules. *J. Mater. Chem.* 22, 21434–21442. doi: 10.1039/c2jm33737a

Pang, S.-Y., Jiang, J., and Ma, J. (2011). Oxidation of Sulfoxides and Arsenic(III) in corrosion of nanoscale zero valent iron by oxygen: evidence against ferryl ions (Fe(IV)) as active intermediates in fenton reaction. *Environ. Sci. Technol.* 45, 307–312. doi: 10.1021/es102401d

Prasad, P., Gordijo, C. R., Abbasi, A. Z., Maeda, A., Ip, A., Rauth, A. M., et al. (2014). Multifunctional Albumin-MnO2 nanoparticles modulate solid tumor microenvironment by attenuating hypoxia, acidosis, vascular endothelial growth factor and enhance radiation response. *ACS Nano* 8, 3202–3212. doi: 10.1021/nn405773r

Pu, X. H., Li, J., Qiao, P., Li, M. M., Wang, H. Y., Zong, L. L., et al. (2019). Mesoporous silica nanoparticles as a prospective and promising approach for drug delivery and biomedical applications. *Curr. Cancer Drug. Targets* 19, 285–295. doi: 10.2174/1568009619666181206114904

Qing, Z. H., Bai, A. L., Xing, S. H., Zou, Z., He, X. X., Wang, K. M., et al. (2019a). Progress in biosensor based on DNA-templated copper nanoparticles. *Biosens. Bioelectron.* 137, 96–109. doi: 10.1016/j.bios.2019.05.014

Qing, Z. H., Xu, J. Y., Hu, J. L., Zheng, J., He, L., Zou, Z., et al. (2019b). In situ amplification-based imaging of RNA in living cells. *Angewandte Chem Int. Ed.* 58, 11574–11585. doi: 10.1002/anie.201812449

Rademakers, S. E., Span, P. N., Kaanders, J. H. A. M., Sweep, F. C. G. J., van der Koyel, A. J., and Bussink, J. (2008). Molecular aspects of tumour hypoxia. *Mol. Oncol.* 2, 41–53. doi: 10.1016/j.molonc.2008.03.006

Robinson, J. T., Tabakman, S. M., Liang, Y. Y., Wang, H. L., Casalongue, H. S., Vinh, D., et al. (2011). Ultrasmall reduced graphene oxide with high near-infrared absorbance for photothermal therapy. *J. Am. Chem. Soc.* 133, 6825–6831. doi: 10.1021/ja2010175

Semenza, G. L. (2003). Targeting HIF-1 for cancer therapy. *Nat. Rev. Cancer* 3, 721–732. doi: 10.1038/nrc1187

Semenza, G. L. (2012). Hypoxia-inducible factors: mediators of cancer progression and targets for cancer therapy. *Trends Pharmacol. Sci.* 33, 207–214. doi: 10.1016/j.tips.2012.01.005

Song, G., Liang, C., Yi, X., Zhao, Q., Cheng, L., Yang, K., et al. (2016). Perfluorocarbon-Loaded Hollow Bi2Se3 nanoparticles for timely supply of oxygen under near-infrared light to enhance the radiotherapy of cancer. *Adv. Mater.* 28, 2716–2723. doi: 10.1002/adma.201504617

Sun, Y. B., Ma, W., Yang, Y. Y., He, M. X., Li, A. M., Bai, L., et al. (2019). Cancer nanotechnology: enhancing tumor cell response to chemotherapy for hepatocellular carcinoma therapy. *Asian J. Pharm. Sci.* 14, 581–594. doi: 10.1016/j.ajps.2019.04.005

Xiang, J., Li, P., Chong, H., Feng, L., Fu, F., Wang, Z., et al. (2014). Bimetallic Pd-Ni core-shell nanoparticles as effective catalysts for the Suzuki reaction. *Nano Res.* 7, 1337–1343. doi: 10.1007/s12274-014-0498-498

Xie, J., Wang, J., Niu, G., Huang, J., Chen, K., Li, X., et al. (2010). Human serum albumin coated iron oxide nanoparticles for efficient cell labeling. *Chem. Commun.* 46, 433–435. doi: 10.1039/b917195a

Yoon, H. Y., Koo, H., Choi, K. Y., Lee, S. J., Kim, K., Kwon, I. C., et al. (2012). Tumor-targeting hyaluronic acid nanoparticles for photodynamic imaging and therapy. *Biomaterials* 33, 3980–3989. doi: 10.1016/j.biomaterials.2012.02.016

Zhou, L. H., Wu, Y. Y., Meng, X. Q., Li, S. P., Zhang, J. L., Gong, P., et al. (2018). Dye-Anchored MnO nanoparticles targeting tumor and inducing enhanced phototherapy effect via mitochondria-mediated pathway. *Small* 14:e1801008. doi: 10.1002/smll.201801008

Conflict of Interest: The authors declare that the research was conducted in the absence of any commercial or financial relationships that could be construed as a potential conflict of interest.

frontiers
in Bioengineering and Biotechnology

ORIGINAL RESEARCH
published: 31 August 2020
doi: 10.3389/fbioe.2020.01010

Tumor Exosome Mimicking Nanoparticles for Tumor Combinatorial Chemo-Photothermal Therapy

Ran Tian[1,2,3], Zhaosong Wang[3], Ruifang Niu[3], Hanjie Wang[1,2]*, Weijiang Guan[4]* and Jin Chang[1,2]*

[1] School of Life Sciences, Tianjin University, Tianjin, China, [2] Tianjin Key Laboratory of Function and Application of Biological Macromolecular Structures, Tianjin Engineering Center of Micro-Nano Biomaterials and Detection-Treatment Technology, Tianjin, China, [3] Public Laboratory, Tianjin Medical University Cancer Institute and Hospital, National Clinical Research Center for Cancer, Key Laboratory of Cancer Prevention and Therapy, Tianjin's Clinical Research Center for Cancer, Tianjin, China, [4] State Key Laboratory of Chemical Resource Engineering, College of Chemistry, Beijing University of Chemical Technology, Beijing, China

Edited by:
Pengfei Zhang,
Shenzhen Institutes of Advanced Technology (CAS), China

Reviewed by:
Kanyi Pu,
Nanyang Technological University, Singapore
Xianglong Hu,
South China Normal University, China

***Correspondence:**
Hanjie Wang
wanghj@tju.edu.cn
Weijiang Guan
wjguan@mail.buct.edu.cn
Jin Chang
jinchang@tju.edu.cn

Specialty section:
This article was submitted to Nanobiotechnology, a section of the journal Frontiers in Bioengineering and Biotechnology

***Received:** 01 July 2020*
***Accepted:** 03 August 2020*
***Published:** 31 August 2020*

Citation:
Tian R, Wang Z, Niu R, Wang H, Guan W and Chang J (2020) Tumor Exosome Mimicking Nanoparticles for Tumor Combinatorial Chemo-Photothermal Therapy. Front. Bioeng. Biotechnol. 8:1010. doi: 10.3389/fbioe.2020.01010

The development of biomimetic nanoparticles with functionalities of natural biomaterial remains a major challenge in cancer combination therapy. Herein, we developed a tumor-cell-derived exosome-camouflaged porous silicon nanoparticles (E-MSNs) as a drug delivery system for co-loading ICG and DOX (ID@E-MSNs), achieving the synergistic effects of chemotherapy and photothermal therapy against breast cancer. Compared with ID@MSNs, the biomimetic nanoparticles ID@E-MSNs can be effectively taken up by the tumor cell and enhance tumor accumulation with the help of the exosome membrane. ID@E-MSNs also retain the photothermal effect of ICG and cytotoxicity of DOX. Under 808 nm near infrared irradiation, ICG can produce hyperthermia to collapse E-MSNs nanovehicles, accelerate drug release, and induce tumor ablation, achieving effective chemo-photothermal therapy. *In vivo* results of 4T1 tumor-bearing BALB/c mice showed that ID@E-MSNs could accumulate tumor tissue and inhibit the growth and metastasis of tumor. Thus, tumor exosome-biomimetic nanoparticles indicate a proof-of-concept as a promising drug delivery system for efficient cancer combination therapy.

Keywords: tumor exosome, biomimetic, nanovehicles, breast cancer, combination therapy

INTRODUCTION

Cancer with high mortality has become the leading cause of fatality worldwide (Bray et al., 2018), mainly due to the limited drug delivery system (Gelband et al., 2016). An ideal drug delivery achieves therapeutic efficacy in cancer with enhanced thermal target and long blood circulation (Maeda et al., 2013). In order to improve the capacity of targeting tumor tissues, nanoparticles have been surface-modified by peptides or chemical biomacromolecules (Cheng et al., 2015). However, nanoparticles as allogenic substances might be rapidly recognized and cleared away by the immune system (Salvati et al., 2013). Moreover, the targeting ligands are not valid for all types of tumors because of the complexity of tumors and heterogeneity of human beings (Zhao et al., 2013).

Biomimetic nanoparticles (Luk and Zhang, 2015; Tan et al., 2015; Zhen et al., 2019) are assembled by natural biomaterials such as cell membranes from cancer cells (Chen et al., 2016; Zhang et al., 2020), red blood cells (Gao et al., 2013; Piao et al., 2014), white blood cells (Parodi et al., 2013), platelets (Wei et al., 2016), and various synthetic nanoparticles, and this might be a promising strategy for anti-tumor drug delivery (Li et al., 2018). The biomimetic nanoparticles have displayed target-homing capacity, prolonged circulation, and good biocompatibility, in accordance with properties of cell membranes (Gao et al., 2016; Deng et al., 2018; He et al., 2018). Recently, exosomes as endogenous nanovesicles are secreted by various cells which have been developed as a novel drug delivery system (Batrakova and Kim, 2015; Vader et al., 2016). Moreover, numerous studies have reported that the exosomes 30–100 nm in diameter possess retention effects, and the membrane protein, target-homing and escaping phagocytosis (Kamerkar et al., 2017; Teng et al., 2017). Given all of these excellent characteristics, exosomes can be used as a drug delivery due to biocompatibility, low immunogenicity, and target-homing (Cheng et al., 2018). However, the exosomes used as a drug carrier are limited to the low drug-loading capacity (Yong et al., 2019), and porous silicon nanoparticles (MSNs) have been widely used for drug delivery owing to their excellent drug loading capacity (Wang et al., 2015). Therefore, it is desired to construct exosome-biomimetic nanoparticles with good biocompatibility and high drug loading for cancer therapy in present research.

The strategy of exosome-biomimetic nanoparticles with chemotherapy and photothermal therapy (Li J. et al., 2019; Cong et al., 2020; Guo et al., 2020; Li and Pu, 2020) could provide a novel approach for the combined treatment of tumors (Wan et al., 2018; Tang et al., 2019). As one of the commonly used photosensitizers, ICG is designed to exhibit PTT efficiency to induce the tumor cell apoptosis under 808 nm laser irradiation (Xin et al., 2017; Li X. et al., 2019). The utilization of ICG in combination with doxorubicin (DOX), a broad-spectrum chemotherapeutic drug, can improve anticancer effects (Ye et al., 2020; Wu et al., 2020). However, the hydrophobic characteristic of ICG and the toxicity of DOX *in vivo* limit its clinical applications (Zheng et al., 2013; Yan et al., 2016). Therefore, ICG and DOX can be co-loaded into exosome-biomimetic nanoparticles, which can improve drug stability, utilization, and effectivity so as to achieve the anti-tumor treatment.

In this study, we developed a tumor-cell-derived exosome-camouflaged porous silicon nanoparticles (E-MSNs) by extrusion method (Pan et al., 2020) as a drug delivery system for co-loading ICG and DOX (ID@E-MSNs), to achieve targeted cancer combined therapy. Compared with ID@MSNs, the biomimetic nanoparticles ID@E-MSNs can be taken up by the tumor cell effectively, which could also enhance tumor accumulation owing to the characteristics of exosome membrane. Besides, ID@E-MSNs also retain the photothermal effect of ICG and cytotoxicity of DOX. Under 808 nm near infrared irradiation, ICG can produce hyperthermia to collapse nanovehicles, accelerate drug release, and induce tumor ablation, achieving effective chemo-photothermal therapy. *In vivo* results of 4T1 tumor-bearing BALB/c mice, it showed that ID@E-MSNs could accumulate tumor tissue and inhibit its growth and metastasis. Thus, tumor exosome-biomimetic nanoparticles indicate that a proof-of-concept could be concerned as a promising drug delivery system for efficient cancer combination therapy (shown in **Figure 1**).

RESULTS AND DISCUSSION

Synthesis and Characterization of ID@E-MSN Nanoparticles

In this study, a biomimetic nanocarrier system was assembled based on 4T1 tumor exosome-modified MSNs for the co-loading of ICG and DOX, thus hoping to combine chemotherapy and photothermal therapy against breast cancer efficiently. The formulation of E-MSNs was composed of three processes: 4T1 exosomes were derived from the culture supernatants of 4T1 cells by ultracentrifugation; the mesoporous silica nanoparticles (MSNs) were synthetized under the guidance of previous methods; 4T1 exosomes were mixed with MSNs and then processed through extrusion, thus preparing E-MSNs. The typical morphological structure of these particles was observed by transmission electron microscope (TEM). The images of TEM (**Figure 2A**) revealed exosomes which had a typical morphology, MSNs particles displayed irregular morphology, and E-MSNs had 20 nm thick membrane appearing on the surface comparing with MSNs, confirming the presence of the membrane sheathed on MSNs in E-MSNs. In addition, the histogram of size distribution is shown in **Figures 2B–D**. NTA analysis displayed that the size of 4T1 exosomes was within 50–100 nm, MSNs and E-MSNs were 125 ± 15 nm and 150 ± 11 nm, in accordance with the result attained from TEM. To further prove that MSNs were coated with 4T1 exosomes membrane structure in E-MSNs, 3,3′-dioctadecyloxacarbocyanine perchlorate (DiO), a commonly used cell membrane fluorescent probe, was used to stain 4T1 exosomes, and 1,1′-Dioctadecyl-3,3,3′,3′-tetramethylindocarbocyanine perchlorate (DiI) was loaded in MSNs. What's more, colocalization of green DiO fluorescence with red DiI fluorescence was observed in DiI@E-MSNs by confocal laser scanning microscopy (CLSM) (**Figure 2E**).

Apart from those, Western blot experiments further showed that similar to the whole cell lysates and the purified exosomes obtained by differential ultracentrifugation, exosome biomarkers CD63 and CD81 were also detected in E-MSNs (**Figure 2F**), confirming the presence of 4T1 exosomes in E-MSNs. In contrast to exosome biomarkers, calnexin, a protein located in the endoplasmic reticulum (ER), was only detected in whole cell lysates, but not in both E-MSNs and the purified exosomes, revealing the high purity of the exosomes sheathed on MSNs in E-MSNs.

E-MSNs was used as a drug carrier by co-loading ICG and DOX for combined therapy. ICG/DOX were loaded into MSNs and then ID@E-MSNs were also obtained by an extrusion method in a similar fashion to E-MSNs. In order to prove that E-MSNs successfully had loaded ICG and DOX, compared with the single MSNs, free ICG, and free DOX, ID@E-MSNs successfully detected two drugs with peaks of 488 and 780 nm, respectively (**Supplementary Figure S1**). Moreover,

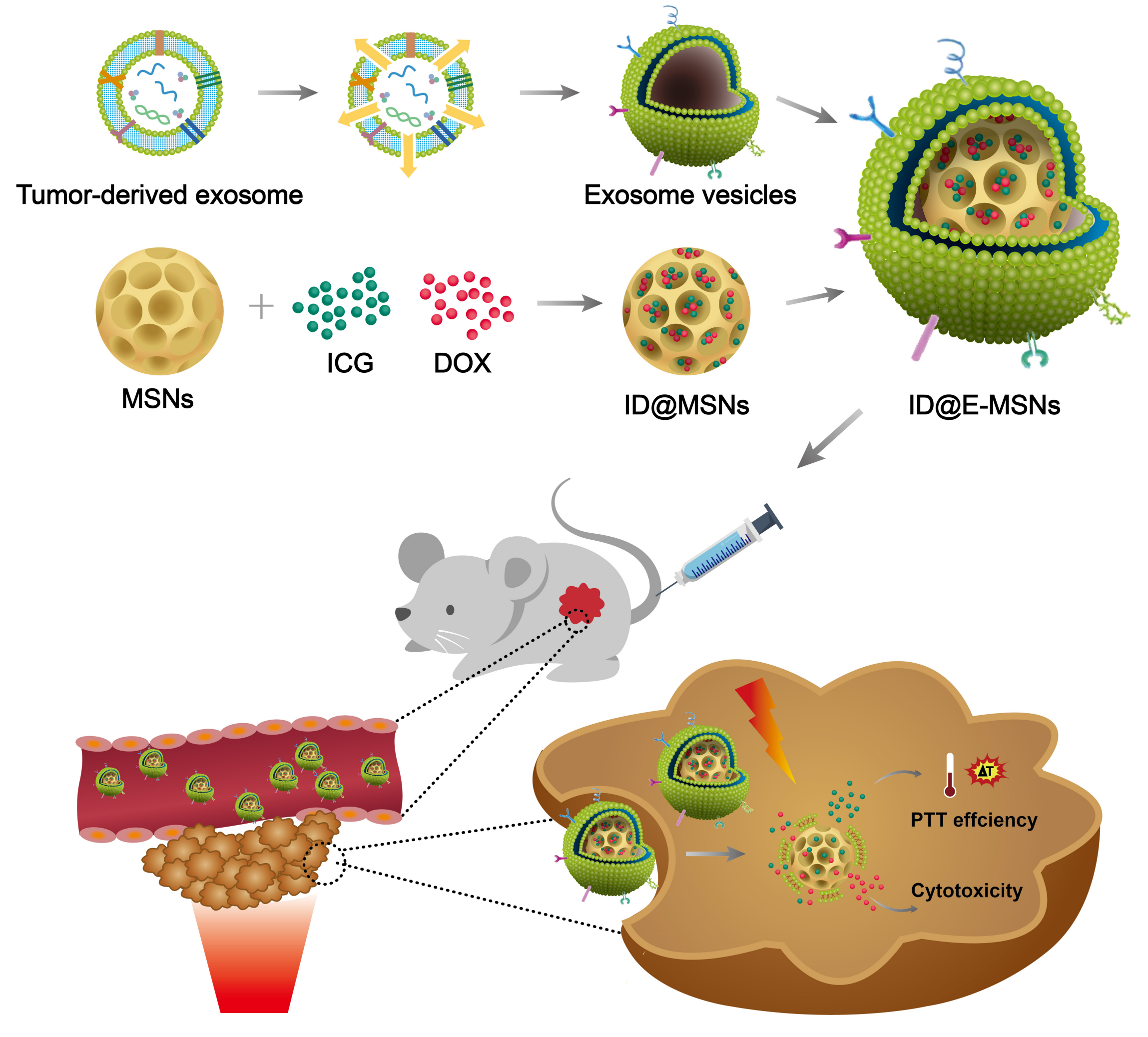

FIGURE 1 | Schematic illustration of ID@E-MSNs nanovehicles for cancer-targeted chemo-photothermal therapy.

the zeta potential (ζ) values provided further evidence for the successful construction of nanoparticles co-loading drugs in each procedure, with a value of −20.5 ± 1.2 mV for MSNs, −5.8 ± 1.5 mV for ID@MSNs and −28.9 ± 3 mV for ID@E-MSNs (**Figure 2G**).

Meanwhile, ICG/DOX loading did not significantly change the size of E-MSNs. Moreover, the size of ID@E-MSNs remained almost constant even after incubating in PBS with or without 10% fetal bovine serum (FBS) for 7 days (**Supplementary Figure S2**). These results demonstrated that ID@E-MSNs were featured with excellent stability, which can be further applied for *in vitro* and *in vivo* study.

Cellular Internalization of ID@E-MSNs

Cellular internalization plays a key role in therapy. To evaluate the cellular uptake efficiency of ID@MSNs, 4T1 cells were treated with free DOX+ICG, ID@MSNs and ID@E-MSNs. As shown in **Supplementary Figure S3**, the red fluorescence of DOX and the green fluorescence of ICG were observed in cells. After the 6 h incubation, compared with other treatments, ID@E-MSNs exhibited the highest fluorescence, indicating that exosome membrane coating enhanced the cellular uptake of ID@E-MSNs.

Combination Therapy Effects of ID@E-MSNs *in vitro*

To evaluate the photothermal efficiency of ID@E-MSNs *in vitro* by detecting the temperature changes in 10 min laser irradiation, the images of infrared thermal and curve of temperature were shown in **Figures 3A,B**. According to the result, the free ICG, ID@MSNs, ID@E-MSNs showed similar temperature changes, with the maximum temperature about 60°C, which was enough to kill tumor cells. These results indicated that ID@E-MSNs had the capacity of photothermal conversion equal to free ICG, and the exosome membrane coating exerted little impact on the ability to transfer light to heat, then to evaluate the release of DOX from ID@MSNs and ID@E-MSNs in different conditions (**Supplementary Figure S4**). The

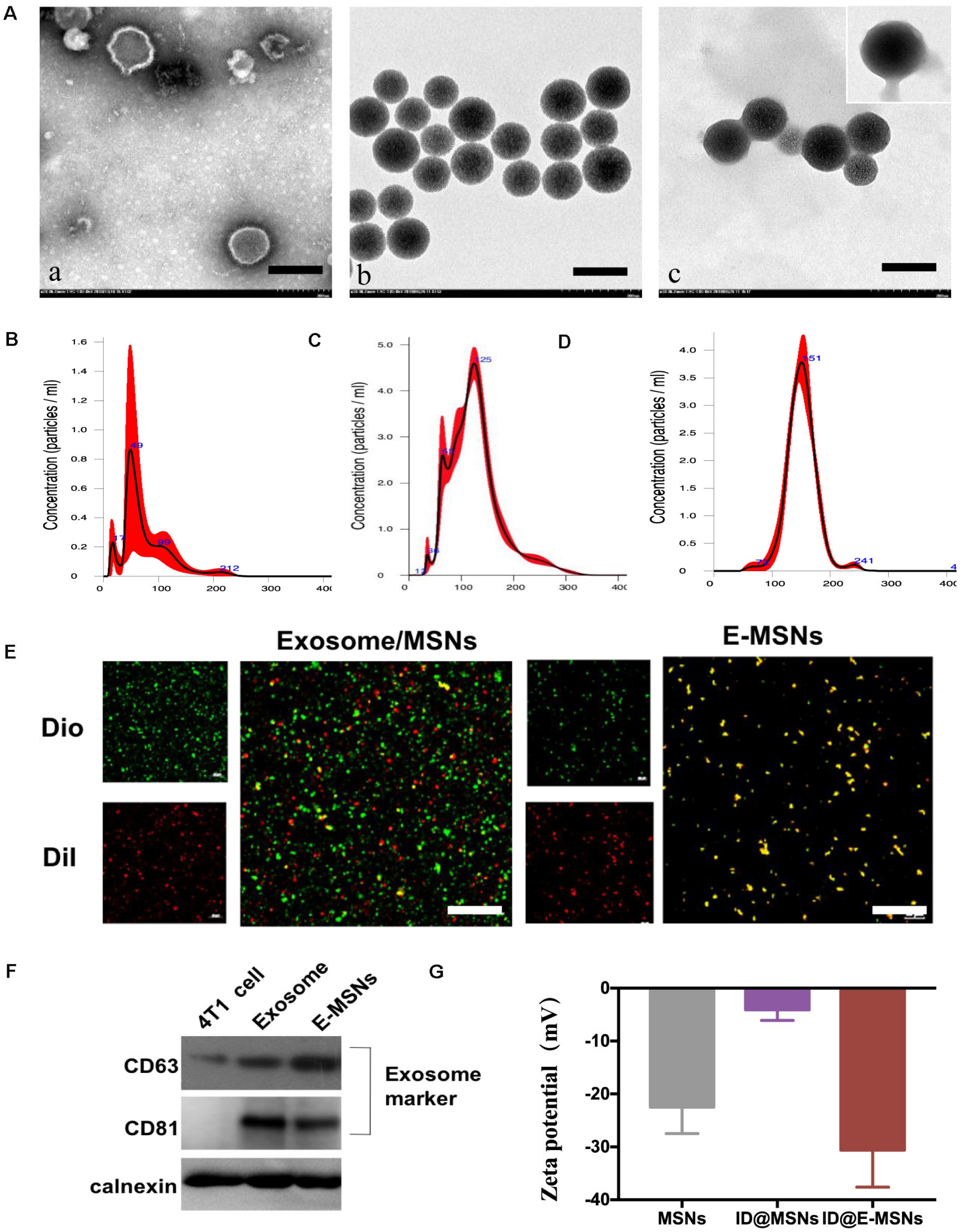

FIGURE 2 | Synthesis and characterization. **(A)** TEM images of (a) 4T1 exosomes, (b) MSNs, and (c) E-MSNs, the membrane of E-MSNs with the average value of 20 nm. Scale bar: 100 nm. **(B–D)** The size distribution of 4T1 exosomes, MSNs, and E-MSNs was measured by NTA. **(E)** Confocal images of exosome membrane labeled by DiO dye (λ_{em} = 488 nm), DiI loaded in MSNs (λ_{em} = 560 nm), a mixture of exosome and MSNs, fused E-MSNs nanovesicles (Scale bar = 42 μm). **(F)** Western blot analysis of protein expression (CD63, CD81, calnexin) of 4T1 cells, 4T1 exosome, and E-MSNs nanovehicles. **(G)** Zeta potential (ζ) of MSNs, ID@MSNs, and ID@E-MSNs.

results showed the acidic condition and laser irradiation played a key role in stimulating the release of DOX from ID@E-MSNs. The cytotoxicity of free DOX, free ICG, and irradiation were evaluated by CCK-8 assay (**Supplementary Figure S5**). What's more, the 808 nm laser at power densities of 1.0, 2.0, and 2.5 W/cm^2 did not influence the growth of 4T1 during continuous irradiation for 10 min. Besides, the IC50 of free DOX was about 0.5 μg/mL, and that of free ICG and NIR

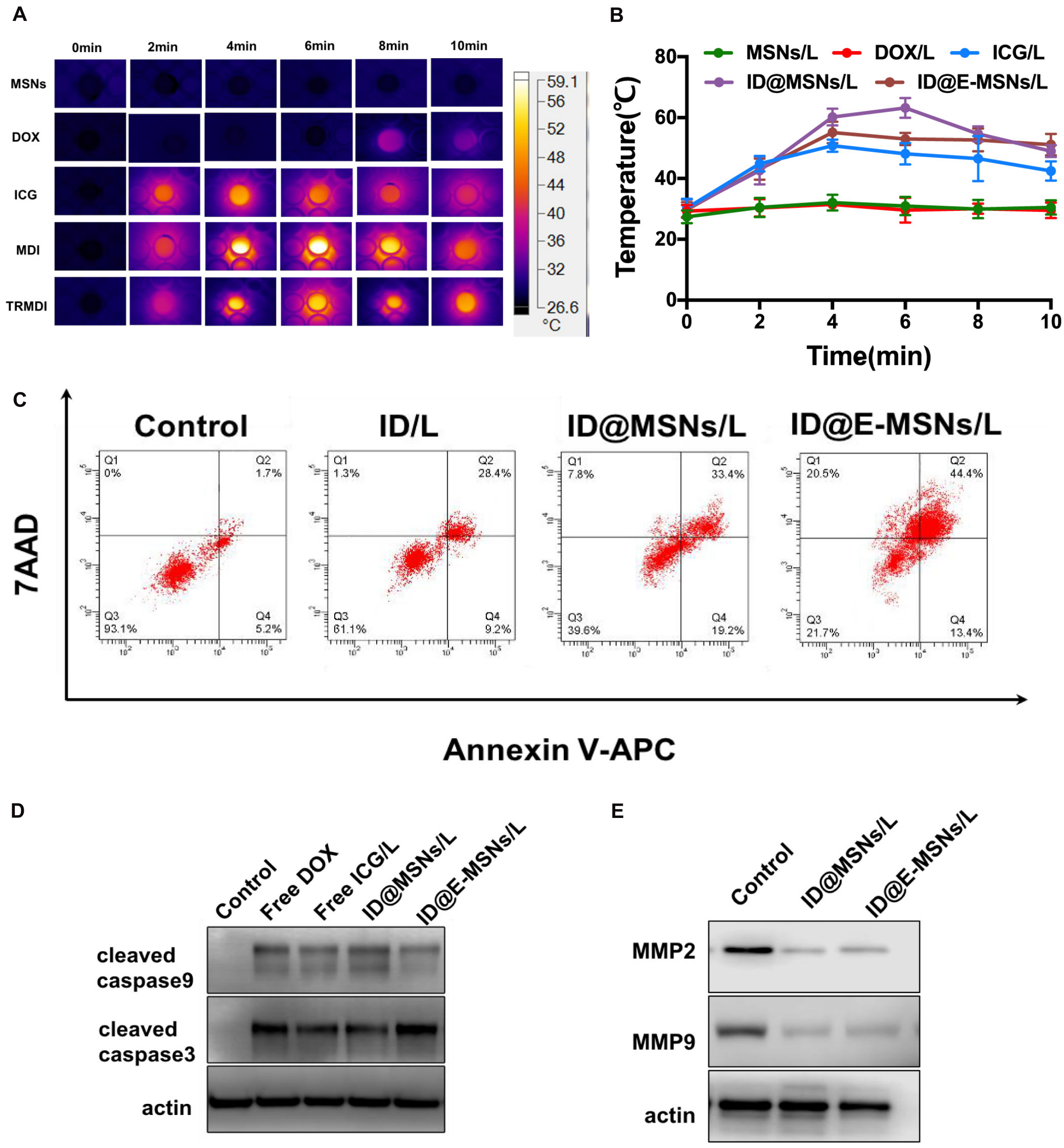

FIGURE 3 | Combination therapy effects of ID@E-MSNs *in vitro*. **(A)** The IR thermal images of PBS, free DOX, free ICG, ID@MSNs, and ID@E-MSNs during laser irradiation for 10 min. **(B)** The temperature change curves of PBS, free DOX, free ICG, ID@MSNs, and ID@E-MSNs during laser irradiation. **(C)** The cell apoptosis quantified by the flow cytometry at 48 h after various treatments (Q1: live cells; Q2: early apoptotic cells; Q3: late apoptotic cells; Q4: dead cells). **(D)** The Western blot analysis of the protein expressions of cleaved caspase-9/-3 in 4T1 cells at 48 h after various treatments. **(E)** The Western blot analysis of the protein expressions of MMP2/9 in 4T1 cells at 48 h after various treatments.

irradiation was 2 μg/mL. ID@E-MSNs exhibited combined therapy efficiency under laser irradiation to 4T1 breast cancer cells. To evaluate the effect of synergistic cytotoxicity, clone formation assay of 4T1 was performed. The results showed that 808 nm laser irradiation induced cell death. Moreover, the effect of synergistic cytotoxicity was assessed by the flow cytometry (**Figure 3C**). After laser irradiation, the total rate of cell apoptosis induced by ID@MSNs was 60.4%, while that of ID@E-MSNs was 78.3%. The cytotoxicity of ID@MSNs was more significant than the other treatments. Altogether, ID@E-MSNs mediated combinatorial chemo-photothermal therapy which induced 4T1 cell apoptosis. In addition, apoptosis-associated proteins and metastases-associated proteins were also detected. As shown in **Figures 3D,E**, after laser irradiation, the caspase-9/-3 expressions level in the 4T1 treated with ID@MSNs and ID@E-MSNs were increasing obviously, while the MM2/MMP9 level was declining, demonstrating that these treatments had activated the signaling pathway.

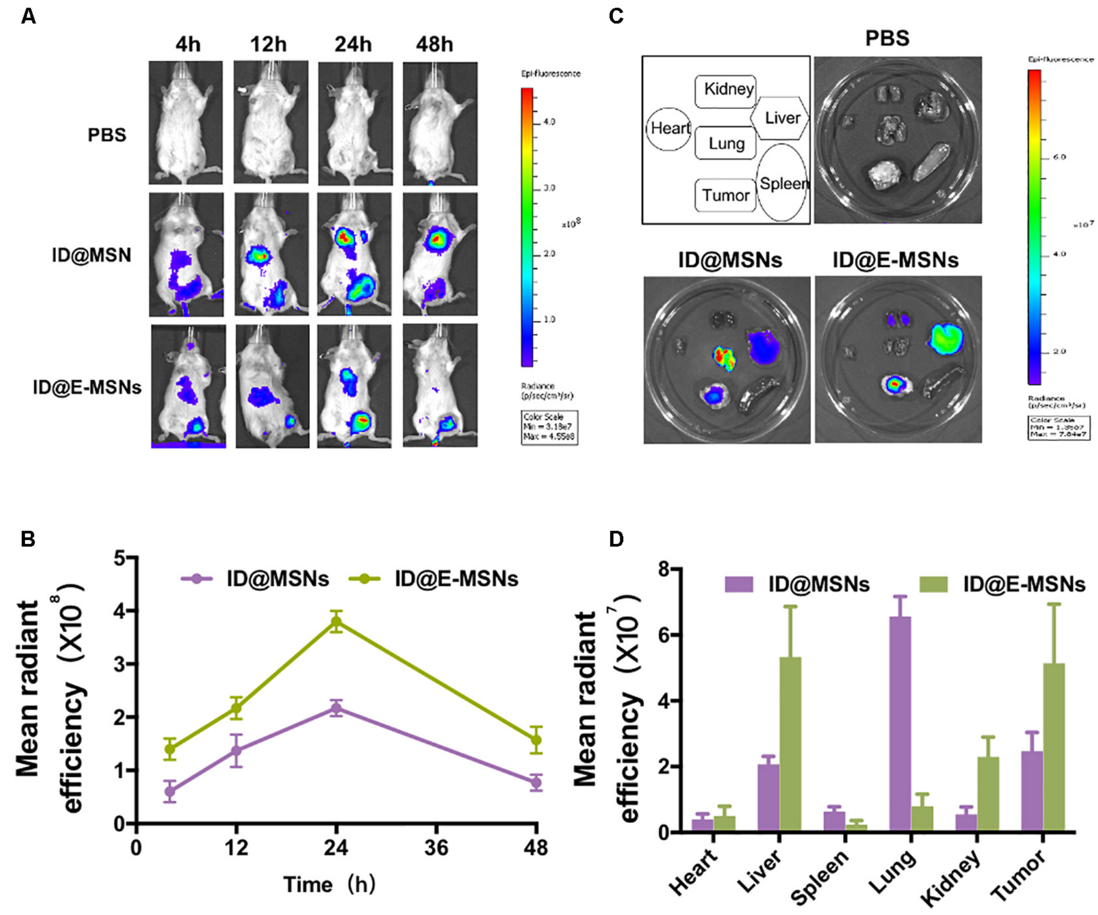

FIGURE 4 | Distribution of ID@E-MSNs *in vivo*. **(A)** Imaging of 4T1 tumor-bearing mice at time points 4, 12, 24, 48 h after intravenous injection with ID@MSNs and ID@E-MSNs. Schematic diagram of experiment for 16 days of treatment. **(C)** Fluorescence images of organs harvest from 4T1 tumor-bearing mice were injected by ID@MSNs and ID@E-MSNs after 24 h. Schematic diagram of experiment for 16 days of treatment. **(B)** The fluorescence intensity of ID@MSNs and ID@E-MSNs *in vivo*. **(D)** The fluorescence intensity of ID@MSNs and ID@E-MSNs in organs.

Evaluation of ID@E-MSNs *in vivo*

According to the above results, the biodistribution of ID@E-MSNs was then taking a further investigation. The ID@MSNs and ID@E-MSNs were injected via tail veins of the 4T1 tumor-bearing mice to compare tumor accumulation capacity and photothermal capacity. As shown in **Figures 4A,B**, the fluorescent intensity of ID@E-MSNs gradually got enhanced at the tumor site during the first 24 h and were maintained for more than 24 h, which was always higher than that of the ID@MSNs group. These results showed that the tumor-targeting ability of ID@E-MSNs was from the modification of 4T1 exosome. Furthermore, the fluorescent intensity of tumors tissue injected by ID@E-MSNs was 3.1-fold higher than those injected by ID@MSNs (**Figures 4C,D**), proving the strong accumulation capacity of ID@E-MSNs. Nevertheless, the photothermal capacity of ID@E-MSNs and ID@MSNs was evaluated in **Supplementary Figure S6**. Upon NIR irradiation 24 h after injection, the tumor tissue administered by ID@E-MSN temperature gradually increased, reaching 50°C, which was powerful enough to kill tumor cells.

Combination Therapy Effects of ID@E-MSNs *in vivo*

To investigate the impact on the therapeutic effect and the inhibition of the metastasis of ID@E-MSNs, chemo-photothermal therapy schedule conducted in 4T1-tumor-bearing BALB/c mice is shown in **Figure 5A**. Tumor-bearing mice were administered with PBS, Free DOX, Free ICG+NIR laser, ID@MSNs+NIR laser, and ID@E-MSNs+NIR laser. In all treatment groups, ID@E-MSNs-based chemo-photothermal therapy obviously inhibited the growth of tumor after 16 days of treatment (**Figures 5B,C**), in accordance with the photograph of tumors (**Figure 5D**). Also, there were no significant alterations shown in the body weight of mice with the injected ID@E-MSNs and exposed to NIR laser (**Figure 5E**). In addition, compared with the other groups, tumor cell proliferation was also observed in the groups by the Ki67 assay (**Figure 5F**), in which the ability of proliferation was repressed by the treatment of ID@E-MSNs+NIR laser. Therefore, ID@E-MSNs represented a very effective chemo-photothermal nanomedicine for the preventing growth and metastasis of breast cancer.

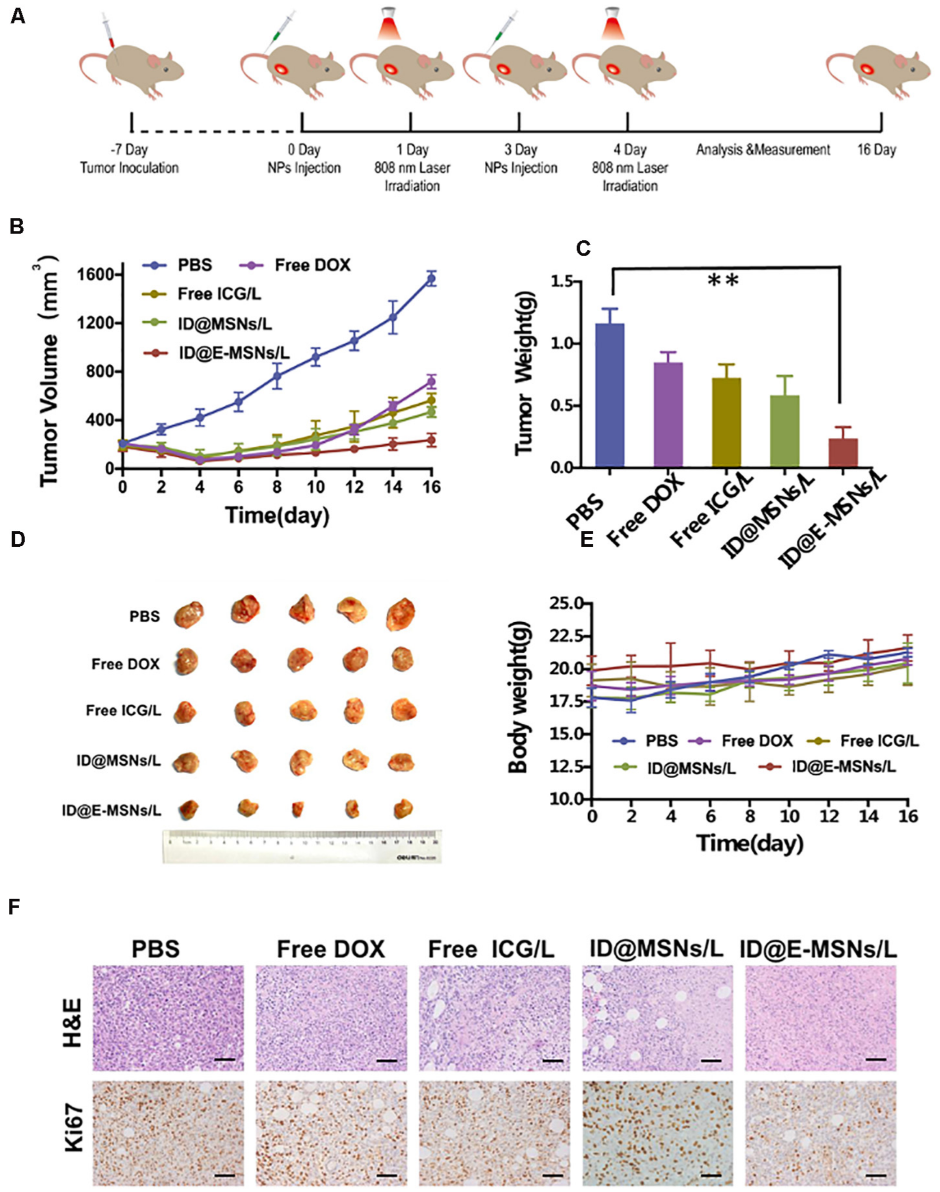

FIGURE 5 | Combination therapy effects of ID@E-MSNs *in vivo*. **(A)** Schematic diagram of experiment for 16 days of treatment. **(B)** The curves of tumor volumes, $n = 5$. **(C)** The photograph of tumor, $n = 5$. **(D)** Tumor weight, $n = 5$. Data are characterized as mean ± *SD*, $^{**}p < 0.01$. **(E)** The curves of body weight, $n = 5$. **(F)** HE and Ki67 staining of tumor tissues after 16 days of treatment, Scale bar = 1 mm.

To further evaluate the systematic toxicity of ID@MSNs and ID@E-MSNs *in vivo*, we injected the particles into healthy BALB/c mice by means of a tail-intravenous injection at a dosage of 20 mg/kg and harvested the blood at 24 h for biochemistry assay. As shown in **Figure 6A**, the weight of mice did not change significantly. The levels of liver function markers such as AST\ALT, and the kidney marker such as BUN\CRE, were all in the normal range (**Figures 6B,C**). Furthermore, in **Figure 6D**, compared with control, organs and tissues such as heart, liver, spleen, lung, and kidney had no obvious pathological change in ID@MSNs- and ID@E-MSNs-treated groups, which suggested that there was no evidence of inflammatory response caused by ID@E-MSNs. Altogether, ID@E-MSNs-mediated combinatorial chemo-photothermal therapy can be deemed as a safe drug carrier against tumors.

CONCLUSION

In summary, we have successfully developed a biocompatible tumor exosome-sheathed MSNs-based drug delivery platform for targeted tumor chemo-photothermal therapy, in which ID@E-MSNs are constructed by combining 4T1 exosomes and ID@MSNs via an extruding method to an achieve enhanced

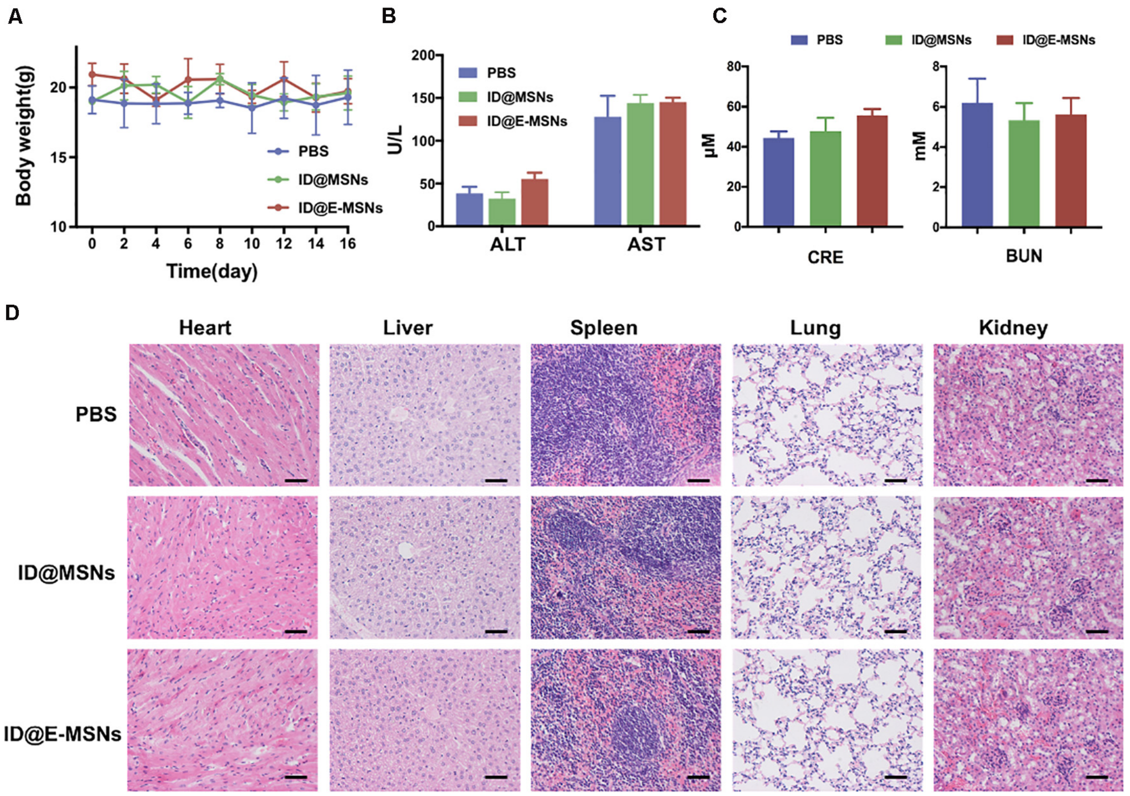

FIGURE 6 | Biosafety assay verification of ID@E-MSNs. **(A)** Body weight curve of mice during 16 days of treatment. **(B)** Blood analysis of the levels of liver function markers ALT and AST. **(C)** Blood analysis of the levels of kidney function markers CRE and BUN. **(D)** H&E staining of major organs showing no obvious histology changes comparing with control, Scale bar = 1 mm.

combined therapy for cancer. Compared with free ICG/DOX, the drug loaded on MSNs and cloaked by 4T1 exosomes has shown superior performance in targeting, long-term retention, and favorable biocompatibility. These results mainly originate from the nature characteristics and the component of exosomes. Our study clearly demonstrates that exosome-biomimetic nanoparticles can be used in combined therapy, and this approach provides a new idea for developing natural drug carriers to improve the efficacy of anticancer therapy.

MATERIALS AND METHODS

Materials

Doxorubicin (DOX), indocyanine green (ICG), bovine serum albumin (BSA), tetraethylorthosilicate (TEOS), and cetyltrimethylammonium bromide (CTAB) were obtained from Sigma-Aldrich (United States). 3,3′-Dioctadecyloxacarbocyanine perchlorate (Dio) and 1,1′-dioctadecyl-3,3,3′,3′-tetramethylindocarbocyanine perchlorate (DiI) were bought from Biyuntian (China). Polyvinylidene fluoride membranes (PVDF) were acquired from Millipore (United States). MTT and Ki67 reagents were provided by Yeasen Corporation (China). RPMI 1640 medium, FBS, penicillin, and streptomycin were provided by Hyclone (United States). You Ning Wei Corporation (China) offered the other reagents, including acrylamide, mouse anti-MMP2 (Santa Cruz, United States), mouse anti-MMP9 (Santa Cruz, United States), rabbit anti-calnexin (Santa Cruz, United States), rabbit anti-CD81 (ProteinTech, Chicago, IL, United States), and rabbit anti-CD63 (Abcam, Cambridge, Britain).

Characterization

The particle size of exosomes and membrane-coated nanoparticles were measured by Nanosight3300 (Malvern, Britain). The morphology of the particle was observed by a Transmission Electron Microscope (Hitachi, Japan). The content of drugs and granules is calculated by UV-Vis absorption spectroscopy (BioTek, United States). The cells were observed by inverted fluorescence microscope and laser scanning confocal microscope (Leica, Germany). The 808 nm laser irradiation instrument was obtained from Changchun New Industries (China). Exosome-encapsulated nanoparticles were constructed by an Avanti mini extruder (Avanti Polar Lipids). Ultrapure water was prepared by the Millipore Milli-Q system (Merck, Germany).

Preparation of MSNs and ID@MSNs

The MSNs were synthesized by a previous protocol (Cheng et al., 2018). Briefly, 0.25 g of CTAB was added into 25 mL of deionized water, 7 mL of absolute ethanol, and

70 μL of diethanolamine. The mixture was stirred at 70°C for 30 min and then quickly added 0.8 mL of TEOS. The action lasted for 1 h, then the template was removed to obtain the MSNs. After being freeze-dried, 10 mg of MSNs was weighted and mixed with 2 mg of DOX and 4 mg of ICG in 2 mL of deionized water, then stirred overnight at room temperature to prepare ID@MSNs. The ID@MSNs were centrifuged at 5000 rpm for 10 min to collect precipitate and gently washed with deionized water twice to eliminate free drug.

Preparation of Purified 4T1 Exosome Vesicles

Firstly, 1×10^6 4T1 cells were seeded in 10 mL of 1640 supplemented with 10% no-nanovesicle FBS at standard condition for 48 h. The medium was then centrifuged at 5000 × *g* for 30 min, 10,000 × *g* for 30 min, and 100,000 × *g* for 1 h. The isolated exosomes were resuspended in cooling PBS. All the experiments were completed under 4°C. The preparation of 4T1 exosome vesicles used a previous method (Xin et al., 2017). In short, exosomes were sonicated at 5 W for 5 s, and then extruded with polycarbonate membrane to obtain exosomes vesicles. The protein of exosome vesicles was detected by Western blot.

Fabrication of ID@E-MSNs Nanovehicles

ID@MSNs were embedded into 4T1 exosomes vehicles to fabricate the ID@E-MSNs nanovehicles by an extruding process. Briefly, 500 μL of exosomes (2×10^9 particles/mL) were mixed with the equal particles of ID@MSNs in an Avanti mini extruder. Then the mixture was sonicated at 5 W for 5 s, and then extruded with polycarbonate membrane to obtain ID@E-MSNs. The protein of ID@E-MSNs was detected by Western blot, and the stability of ID@E-MSNs in PBS was tested for 7 days at room temperature.

Cell Culture and Animals

Tumor cell 4T1 and mononuclear macrophage RAW264.7 cells bought from the American Type Culture Collection were cultured by a standard method (RPMI 1640 with 10% FBS and 1% penicillin and streptomycin at 37°C, 5% CO_2); 18–20 g of BALB/c mice (female) were purchased from Beijing HFK Bioscience Co., Ltd. All of the animal experiments were compiled by relevant ethical regulations and were authorized by the Institutional Animal Care and Use Committee of Tianjin Medical University Cancer Institute.

Cell Uptake Assay

1×10^6 4T1 cells and RAW264.7 cells were seeded into 10 cm dishes, respectively, supplemented with RIPM 1640 and 10% FBS at standard condition for 48 h. The cells were incubated with ID@MSNs and ID@E-MSNs for 4 h at the ICG concentrations of 10 μg/mL. After incubation, the free particles were washed three times by PBS, and the cells were stained with DAPI for 20 min for observation. Analysis was performed by a confocal microscope. Moreover, the uptakes of ID@MSNs and ID@E-MSNs in 4T1 cells and RAW264.7 were evaluated by the flow cytometry. In short, 1×10^6 the cells were cultured in 6 cm dishes and incubated with ID@MSNs and ID@E-MSNs for 4 h at the ICG concentrations of 10 μg/mL. After incubation, the free particles were washed three times by PBS, and the cells were stained with DAPI for 20 min for observation. Analysis was performed by flow cytometry.

Cell Safety Assay

5×10^3 4T1 cells were cultured into a 96-well plate for 24 h, then exposed to 808 nm laser irradiation at power density of 0.5, 1.5, and 2.5 W/cm^2 for 10 min.

Subsequently, the cells were incubated for another 24 h. Then, the cells were processed by CCK8 assay to analyze the toxicity of irradiation, and the absorbance was detected by a microplate reader. The same method was used to evaluate the toxicity of dosing.

Biodistribution Study of ID@E-MSNs in Tumor-Bearing Mice

To construct the tumor-bearing mice, 1×10^5 4T1 cells were implanted in female BALB/c mice. When the tumor volumes reached 150 mm^3, the biodistribution studies of ID@E-MSNs were evaluated. The experiments were divided into two groups (five mice for each group): 100 μL of ID@MSNs and ID@E-MSNs (ICG concentration: 100 μg/mL) was injected via tail veins to the 4T1 tumor-bearing mice. Fluorescent images were acquired by IVIS Spectrum imaging systems at desired time points – 1, 4, 8, and 24 h pre-injection. Under the same condition, the excised tumor and organs such as heart, liver, spleen, lung, and kidney were also imaged by the IVIS fluorescent system.

In vivo Anti-tumor Assay of ID@E-MSNs

Orthotropic 4T1 tumor-bearing mode were constructed for assessing efficacy of combined therapy *in vivo*. When the tumor volumes reached about ∼150 mm^3, the mice were randomized into two groups. The mice were intravenously injected with: PBS, free ICG/DOX, ID@MSNs, and ID@E-MSNs at an ICG dosage of 2 mg/kg and DOX of 0.5 mg/kg via the tail vein, respectively. The amount of ICG was 2 mg/kg and DOX was 0.5 mg/kg; 808 nm laser treatment was performed next day. The body weight of mice was recorded every day after treatment, and the dimensions of tumor were measured every 3 days. At 16 days after treatments, the mice were euthanized. Then, the tumor tissues and organs, such as the heart, kidney, liver, spleen, and lung were collected for histopathological examination (H&E) or Ki67 staining. At 24 h post-injection, the levels of liver function markers such as AST\ALT and the kidney marker such as BUN\CRE were detected by kit.

Statistical Analysis

All values represented mean ± *SD*. Statistical analyses between two paired groups using the Tukey comparative test (ANOVA) were carried out by the GraphPad Prism 5.0 software. $P < 0.05$ indicates statistically significant data.

DATA AVAILABILITY STATEMENT

The original contributions presented in the study are included in the article/**Supplementary Material**, further inquiries can be directed to the corresponding author/s.

ETHICS STATEMENT

The animal study was reviewed and approved by the Institutional Animal Care and Use Committee of Tianjin Medical University Cancer Institute.

AUTHOR CONTRIBUTIONS

JC, WG, and RN designed the project. RT and ZW performed the experiments and analyzed data. HW interpreted the data and wrote the manuscript. All authors contributed to the article and approved the submitted version.

FUNDING

This work was sponsored by the National Key Research and Development Program of China (No. 2017YFA0205104), National Natural Science Foundation of China (Nos. 81903092, 51873150, 31971300, 817719709, and 81772804), Tianjin Natural Science Foundation (No. 19JCYBJC28800), Changjiang Scholars and Innovative Research Team (No. IRT_14R40), Young Elite Scientists Sponsorship Program by Tianjin, and Cancer Translational Research Seed Fund (No. 1703).

SUPPLEMENTARY MATERIAL

The Supplementary Material for this article can be found online at: https://www.frontiersin.org/articles/10.3389/fbioe.2020.01010/full#supplementary-material

REFERENCES

Batrakova, E. V., and Kim, M. S. (2015). Using exosomes, naturally-equipped nanocarriers, for drug delivery. *J. Control. Release* 219, 396–405. doi: 10.1016/j.jconrel.2015.07.030

Bray, F., Ferlay, J., Soerjomataram, I., Siegel, R. L., Torre, L. A., and Jemal, A. (2018). Global cancer statistics 2018: GLOBOCAN estimates of incidence and mortality worldwide for 36 cancers in 185 countries. *CA Cancer J. Clin.* 68, 394–424. doi: 10.3322/caac.21492

Chen, Z., Zhao, P., Luo, Z., Zheng, M., Tian, H., Gong, P., et al. (2016). Cancer cell membrane-biomimetic nanoparticles for homologous-targeting dual-modal imaging and photothermal therapy. *ACS Nano* 10, 10049–10057. doi: 10.1021/acsnano.6b04695

Cheng, C. J., Tietjen, G. T., Saucier-Sawyer, J. K., and Saltzman, W. M. (2015). A holistic approach to targeting disease with polymeric nanoparticles. *Nat. Rev. Drug Discov.* 14, 239–247. doi: 10.1038/nrd4503

Cheng, G., Li, W., Ha, L., Han, X., Hao, S., Wan, Y., et al. (2018). Self-assembly of extracellular vesicle-like metal-organic framework nanoparticles for protection and intracellular delivery of biofunctional proteins. *J. Am. Chem. Soc.* 140, 7282–7291. doi: 10.1021/jacs.8b03584

Cong, Z., Zhang, L., Ma, S. Q., Lam, K. S., Yang, F. F., and Liao, Y. H. (2020). Size-transformable hyaluronan stacked self-assembling peptide nanoparticles for improved transcellular tumor penetration and photo-chemo combination therapy. *ACS Nano* 14, 1958–1970. doi: 10.1021/acsnano.9b08434

Deng, G., Sun, Z., Li, S., Peng, X., Li, W., Zhou, L., et al. (2018). Cell-membrane immunotherapy based on natural killer cell membrane coated nanoparticles for the effective inhibition of primary and abscopal tumor growth. *ACS Nano* 12, 12096–12108. doi: 10.1021/acsnano.8b05292

Gao, C., Lin, Z., Wu, Z., Lin, X., and He, Q. (2016). Stem-cell-membrane camouflaging on near-infrared photoactivated upconversion nanoarchitectures for in vivo remote-controlled photodynamic therapy. *ACS Appl Mater Interfaces* 8, 34252–34260. doi: 10.1021/acsami.6b12865

Gao, W., Hu, C. M., Fang, R. H., Luk, B. T., Su, J., and Zhang, L. (2013). Surface functionalization of gold nanoparticles with red blood cell membranes. *Adv. Mater.* 25, 3549–3553. doi: 10.1002/adma.201300638

Gelband, H., Sankaranarayanan, R., Gauvreau, C. L., Horton, S., Anderson, B. O., Bray, F., et al. (2016). Costs, affordability, and feasibility of an essential package of cancer control interventions in low-income and middle-income countries: key messages from Disease Control Priorities, 3rd edition. *Lancet* 387, 2133–2144. doi: 10.1016/S0140-6736(15)00755-2

Guo, X., Cao, B., Wang, C., Lu, S., and Hu, X. (2020). In vivo photothermal inhibition of methicillin-resistant Staphylococcus aureus infection by in situ templated formulation of pathogen-targeting phototheranostics. *Nanoscale* 12, 7651–7659. doi: 10.1039/d0nr00181c

He, H., Guo, C., Wang, J., Korzun, W. J., Wang, X. Y., Ghosh, S., et al. (2018). Leutusome: a biomimetic nanoplatform integrating plasma membrane components of leukocytes and tumor cells for remarkably enhanced solid tumor homing. *Nano Lett.* 18, 6164–6174. doi: 10.1021/acs.nanolett.8b01892

Kamerkar, S., LeBleu, V. S., Sugimoto, H., Yang, S., Ruivo, C. F., Melo, S. A., et al. (2017). Exosomes facilitate therapeutic targeting of oncogenic KRAS in pancreatic cancer. *Nature* 546, 498–503. doi: 10.1038/nature22341

Li, J., Cui, D., Huang, J., He, S., Yang, Z., Zhang, Y., et al. (2019). Organic Semiconducting Pro-nanostimulants for near-infrared photoactivatable cancer immunotherapy. *Angew. Chem. Int. Ed. Engl.* 58, 12680–12687. doi: 10.1002/anie.201906288

Li, J., and Pu, K. (2020). Semiconducting polymer nanomaterials as near-infrared photoactivatable protherapeutics for cancer. *Acc. Chem. Res.* 53, 752–762. doi: 10.1021/acs.accounts.9b00569

Li, J., Zhen, X., Lyu, Y., Jiang, Y., Huang, J., and Pu, K. (2018). Cell membrane coated semiconducting polymer nanoparticles for enhanced multimodal cancer phototheranostics. *ACS Nano* 12, 8520–8530. doi: 10.1021/acsnano.8b04066

Li, X., Bottini, M., Zhang, L., Zhang, S., Chen, J., Zhang, T., et al. (2019). Core-satellite nanomedicines for in vivo real-time monitoring of enzyme-activatable drug release by fluorescence and photoacoustic dual-modal imaging. *ACS Nano* 13, 176–186. doi: 10.1021/acsnano.8b05136

Luk, B. T., and Zhang, L. (2015). Cell membrane-camouflaged nanoparticles for drug delivery. *J. Control. Release* 220, 600–607. doi: 10.1016/j.jconrel.2015.07.019

Maeda, H., Nakamura, H., and Fang, J. (2013). The EPR effect for macromolecular drug delivery to solid tumors: improvement of tumor uptake, lowering of systemic toxicity, and distinct tumor imaging in vivo. *Adv. Drug Deliv. Rev* 65, 71–79. doi: 10.1016/j.addr.2012.10.002

Pan, S., Pei, L., Zhang, A., Zhang, Y., Zhang, C., Huang, M., et al. (2020). Passion fruit-like exosome-PMA/Au-BSA@Ce6 nanovehicles for real-time fluorescence imaging and enhanced targeted photodynamic therapy with deep penetration and superior retention behavior in tumor. *Biomaterials* 230:119606. doi: 10.1016/j.biomaterials.2019.119606

Parodi, A., Quattrocchi, N., van de Ven, A. L., Chiappini, C., Evangelopoulos, M., Martinez, J. O., et al. (2013). Synthetic nanoparticles functionalized with biomimetic leukocyte membranes possess cell-like functions. *Nat. Nanotechnol.* 8, 61–68. doi: 10.1038/nnano.2012.212

Piao, J. G., Wang, L., Gao, F., You, Y. Z., Xiong, Y., and Yang, L. (2014). Erythrocyte membrane is an alternative coating to polyethylene glycol for prolonging the circulation lifetime of gold nanocages for photothermal therapy. *ACS Nano* 8, 10414–10425. doi: 10.1021/nn503779d

Salvati, A., Pitek, A. S., Monopoli, M. P., Prapainop, K., Bombelli, F. B., Hristov, D. R., et al. (2013). Transferrin-functionalized nanoparticles lose their targeting capabilities when a biomolecule corona adsorbs on the surface. *Nat. Nanotechnol.* 8, 137–143. doi: 10.1038/nnano.2012.237

Tan, S., Wu, T., Zhang, D., and Zhang, Z. (2015). Cell or cell membrane-based drug delivery systems. *Theranostics* 5, 863–881. doi: 10.7150/thno.11852

Tang, Y., Li, Y., Li, S., Hu, H., Wu, Y., Xiao, C., et al. (2019). Transformable nanotherapeutics enabled by ICG: towards enhanced tumor penetration under NIR light irradiation. *Nanoscale* 11, 6217–6227. doi: 10.1039/c9nr01049a

Teng, Y., Ren, Y., Hu, X., Mu, J., Samykutty, A., Zhuang, X., et al. (2017). MVP-mediated exosomal sorting of miR-193a promotes colon cancer progression. *Nat. Commun.* 8:14448. doi: 10.1038/ncomms14448

Vader, P., Mol, E. A., Pasterkamp, G., and Schiffelers, R. M. (2016). Extracellular vesicles for drug delivery. *Adv. Drug Deliv. Rev.* 106, 148–156. doi: 10.1016/j.addr.2016.02.006

Wan, G., Chen, B., Li, L., Wang, D., Shi, S., Zhang, T., et al. (2018). Nanoscaled red blood cells facilitate breast cancer treatment by combining photothermal/photodynamic therapy and chemotherapy. *Biomaterials* 155, 25–40. doi: 10.1016/j.biomaterials.2017.11.002

Wang, Y., Zhao, Q., Han, N., Bai, L., Li, J., Liu, J., et al. (2015). Mesoporous silica nanoparticles in drug delivery and biomedical applications. *Nanomedicine* 11, 313–327. doi: 10.1016/j.nano.2014.09.014

Wei, X., Gao, J., Fang, R. H., Luk, B. T., Kroll, A. V., Dehaini, D., et al. (2016). Nanoparticles camouflaged in platelet membrane coating as an antibody decoy for the treatment of immune thrombocytopenia. *Biomaterials* 111, 116–123. doi: 10.1016/j.biomaterials.2016.10.003

Wu, M., Mei, T., Lin, C., Wang, Y., Chen, J., Le, W., et al. (2020). Melanoma cell membrane biomimetic versatile CuS nanoprobes for homologous targeting photoacoustic imaging and photothermal chemotherapy. *ACS Appl. Mater. Interfaces* 12, 16031–16039. doi: 10.1021/acsami.9b23177

Xin, Y., Yin, M., Zhao, L., Meng, F., and Luo, L. (2017). Recent progress on nanoparticle-based drug delivery systems for cancer therapy. *Cancer Biol. Med.* 14, 228–241. doi: 10.20892/j.issn.2095-3941.2017.0052

Yan, F., Duan, W., Li, Y., Wu, H., Zhou, Y., Pan, M., et al. (2016). NIR-laser-controlled drug release from DOX/IR-780-loaded temperature-sensitive-liposomes for chemo-photothermal synergistic tumor therapy. *Theranostics* 6, 2337–2351. doi: 10.7150/thno.14937

Ye, H., Wang, K., Lu, Q., Zhao, J., Wang, M., Kan, Q., et al. (2020). Nanosponges of circulating tumor-derived exosomes for breast cancer metastasis inhibition. *Biomaterials* 242:119932. doi: 10.1016/j.biomaterials.2020.119932

Yong, T., Zhang, X., Bie, N., Zhang, H., Zhang, X., Li, F., et al. (2019). Tumor exosome-based nanoparticles are efficient drug carriers for chemotherapy. *Nat. Commun.* 10:3838. doi: 10.1038/s41467-019-11718-4

Zhang, S., Deng, G., Liu, F., Peng, B., Bao, Y., Du, F., et al. (2020). Autocatalytic delivery of brain tumor-targeting, size-shrinkable nanoparticles for treatment of breast cancer brain metastases. *Adv. Funct. Mater.* 30:1910651. doi: 10.1002/adfm.201910651

Zhao, Y., Alakhova, D. Y., and Kabanov, A. V. (2013). Can nanomedicines kill cancer stem cells? *Adv. Drug Deliv. Rev.* 65, 1763–1783. doi: 10.1016/j.addr.2013.09.016

Zhen, X., Cheng, P., and Pu, K. (2019). Recent advances in cell membrane-camouflaged nanoparticles for cancer phototherapy. *Small* 15:e1804105. doi: 10.1002/smll.201804105

Zheng, M., Yue, C., Ma, Y., Gong, P., Zhao, P., Zheng, C., et al. (2013). Single-step assembly of DOX/ICG loaded lipid–polymer nanoparticles for highly effective chemo-photothermal combination therapy. *ACS Nano* 7, 2056–2067. doi: 10.1021/nn400334y

Conflict of Interest: The authors declare that the research was conducted in the absence of any commercial or financial relationships that could be construed as a potential conflict of interest.

frontiers
in Bioengineering and Biotechnology

ORIGINAL RESEARCH
published: 02 October 2020
doi: 10.3389/fbioe.2020.00903

Small Molecular Prodrug Amphiphile Self-Assembled AIE Dots for Cancer Theranostics

Xing Yang[1,2†], Yuan Luo[1†], Sanpeng Li[1†], Xiuli Xu[1,3], Yingxia Bao[4], Jiaming Yang[5], Defang Ouyang[6], Xingxing Fan[7], Ping Gong[1] and Lintao Cai[1]**

[1] Guangdong Key Laboratory of Nanomedicine, CAS-HK Joint Lab for Biomaterials, Shenzhen Institutes of Advanced Technology, Chinese Academy of Sciences, Shenzhen, China, [2] University of Chinese Academy of Sciences, Beijing, China, [3] Nano Science and Technology Institute, University of Science and Technology of China, Hefei, China, [4] Guangzhou Baiyunshan Pharmaceutical Co., Ltd., Baiyunshan Pharmaceutical General Factory, Guangzhou, China, [5] Livzon Mabpharm Inc., Zhuhai, China, [6] State Key Laboratory of Quality Research in Chinese Medicine, Institute of Chinese Medical Sciences (ICMS), University of Macau, Macau, China, [7] State Key Laboratory of Quality Research in Chinese Medicine, Macau Institute for Applied Research in Medicine and Health, Macau University of Science and Technology, Macau, China

OPEN ACCESS

Edited by:
Ben Zhong Tang,
Hong Kong University of Science and Technology, Hong Kong

Reviewed by:
Guangle Niu,
Shandong University, China
Weijiang Guan,
Beijing University of Chemical Technology, China

Correspondence:
Lintao Cai
lt.cai@siat.ac.cn
Ping Gong
ping.gong@siat.ac.cn;
pinggong861@126.com

† These authors have contributed equally to this work

Specialty section:
This article was submitted to Nanobiotechnology, a section of the journal Frontiers in Bioengineering and Biotechnology

Received: *11 June 2020*
Accepted: *13 July 2020*
Published: *02 October 2020*

Citation:
Yang X, Luo Y, Li S, Xu X, Bao Y, Yang J, Ouyang D, Fan X, Gong P and Cai L (2020) Small Molecular Prodrug Amphiphile Self-Assembled AIE Dots for Cancer Theranostics. Front. Bioeng. Biotechnol. 8:903. doi: 10.3389/fbioe.2020.00903

A simple and facile one-step method was developed to construct a small molecular prodrug amphiphile self-assembled organic dots CPPG with aggregation-induced emission (AIE) characteristics. Diphenylalanine peptide (FF), which is the essential moiety of the self-assembling peptide-drug conjugate and as its core recognition motifs for molecular self-assembly. In addition, the D-glucose transported protein (GLUT), which is one of the important nutrient transporters and is overexpressed in cancer cells. The conjugation of glycosyl further endues the nanoparticle with good biocompatibility and tumor-targeting ability. Taking advantages of both the cancer cell-targeting capability of small molecular prodrug amphiphile CPPG and the AIE aggregates with strong emission, the prepared CPPG AIE dots can target cancer cells specifically and inhibit the proliferation of cancer cells with good biocompatibility and photostability. Based on the general approach, types of universal organic fluorescent nanoprobes could be facilely constructed for imaging applications and biological therapeutics, which possess the properties of specific recognition and high brightness.

Keywords: prodrug, self-assembly, AIE, cancer, theranostics

INTRODUCTION

Fluorescence imaging is a low-cost and highly sensitive method for the diagnosis of early tumors, visualization of tumor margins, and evaluation of treatment effects (Ozawa et al., 2013; Weissleder and Nahrendorf, 2015; Antaris et al., 2016). A variety of nanomaterials have been developed as fluorescence nanoprobes for cancer diagnosis which bring excellent optical characteristics, as the rapid development of nanotechnology in the past few decades (Chinen et al., 2015; Wolfbeis, 2015; Fu et al., 2017). Compared with the traditional organic molecules, nanoparticles usually possess better photostability, higher brightness, and larger absorption coefficients, which make them able to enhance the versatility and sensitivity of fluorescence-based imaging and diagnosis. Unfortunately, most fluorescent nanoparticles are made by highly toxic heavy metal cations, which increase the concerns of long-time toxicity and limits further clinical transition (Tsoi et al., 2013). Considering the biocompatibility, organic fluorescent nanoparticles, composed of organic molecules decorated on a matrix of biocompatible polymers or encapsulated inside, are usually considered more suitable than the inorganic nanoparticles (Li and Liu, 2014; Yu et al., 2017).

To develop organic dye nanoparticles with significantly enhanced biocompatibility and photostability have taken great efforts (Wang et al., 2013). However, the brightness of the organic nanoparticles, gradually decrease along with the increase of dye concentration. This phenomenon has been known as aggregation-caused quenching (ACQ), which presents a barrier for fabricating organic nanoparticles (Reisch and Klymchenko, 2016). In 2001, a breakthrough in luminescent materials was made. Tang et al. reported a kind of propeller-shaped molecule with aggregation-induced emission (AIE) characteristics, such as hexaphenylsilole and tetraphenylethylene, in which the AIE luminogens generally exhibited weak or no emissions in solution but strong emissions in the solid or aggregated states (Luo et al., 2001). From then on, several AIEgens have been developed (Ding et al., 2013; Mei et al., 2015; Zhang W. et al., 2015; Yu et al., 2016; Gu et al., 2017). Furthermore, the strong emissions of the solid-state AIEgens offer a great opportunity for developing highly bright organic nanoparticles, also known as AIE dots, without blemishing their emissions (Zhang X. et al., 2015; Xu et al., 2016; Yan et al., 2016; Li H. et al., 2017; Niu et al., 2019).

A universal way of generating AIE-nanoparticles is the reprecipitation method, in which AIE molecules in gentle solvents (such as DMSO and THF) were mixed with a poor solvent (e.g., water). However, in this method, the gentle solvent is usually poisonous, which limits the applications of AIE-nanoparticles in biological environments. To solve the biocompatibility and water solubility of AIE fluorescent organic nanoparticles, the conventional methods were facilely prepared by mixing AIE material with different surfactants. A variety of strategies, such as polymerization of other monomers with AIE dyes, covalent conjugation of hydrophilic molecules with AIE dyes, and encapsulation in silica nanoparticles were considered (Zhang X. et al., 2015). The general surface functional groups facilitated further functionalization to achieve the goal of multimodal imaging, which consisted of $-NH_2$, $-COOH$, −maleimide (−Mal) and the DSPE-PEG derivatives (distearoyl-sn-glycero-3-phosphoethanolamine poly ethylene glycol) (Li K. et al., 2013). However, the surfactant for AIE dye based nanoprobes reported previously are focused on solving the biocompatibility problem. As for the theranostic systems, use of the small molecular prodrug amphiphile, which can be self-assembled, as the surfactant of the AIE nanoprobes has not been reported yet.

In this research, we try to develop a simple and facile way to fabricate small molecular prodrug amphiphilic AIE-dots based on a self-assembly approach which is also known as CPPG AIE dots. As illustrated in **Scheme 1**, the CPPG AIE dots were prepared by a one-step self-assembly method through mixing the AIEgens-TTF and CPPG under sonication. The aggregates of hydrophobic AIEgens tend to embed themselves in the hydrophobic prodrugs while the hydrophilic glucosamine chains stretch themselves into the aqueous solution to offer the AIE dots enhanced stability and good water dispersibility. The specific synthesis steps are as shown in **Scheme 2**.

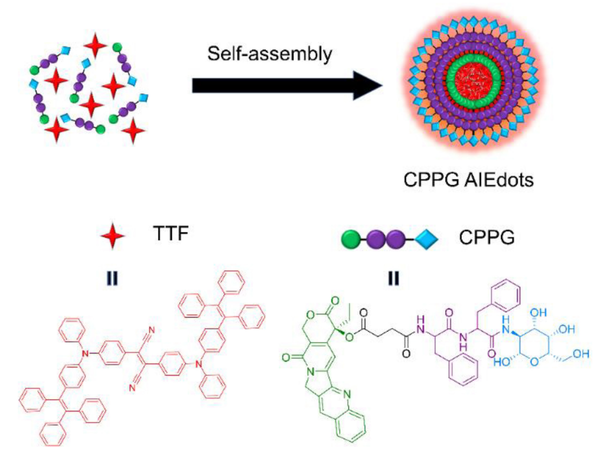

SCHEME 1 | Schematic illustration of CPPG AIE dots preparation by one-pot self-assembly method.

Herein, we successfully generated the CPPG AIE dots system, the small molecular prodrug amphiphilic CPPG consists of three parts, CPT, glucosamine, and the connecting element diphenylalanine peptide (also termed as FF), and their structures were characterized by High Resolution Mass Spectrometry (HRMS), ^1H NMR and ^{13}C NMR, respectively (**Supplementary Figures S1–S11**). TTF, a typical AIE luminogen were added into the hydrophobic core of the CPPG, which came from Tang's lab (Geng et al., 2014; Wang et al., 2014; Li D. et al., 2017). Camptothecin (CPT), an inhibitor of DNA topoisomerase I, (Sen et al., 2004) has been widely used to induce apoptosis under experimental conditions. Owing to its hydrophobicity, the CPT molecule acted as a self-assembly inducer by adding diphenylalanine peptide (FF), which is the essential moiety of the self-assembling peptide-drug conjugate and as its core recognition motifs for molecular self-assembly, have attracted much attention due to their biocompatibility, easy chemical modification, simple structure, and especially great capability of assembly under different conditions (Reches and Gazit, 2003; Li J. et al., 2013; Zhang H. et al., 2015). It has been widely utilized as a remarkable component to self-assemble various functional nanomaterials for biomedical applications, such as drug delivery. However, the delivery system, combining the FF with both prodrug and AIE, was rarely reported before. In addition, the D-glucose transported protein (GLUT), which is one of the important nutrient transporters and is overexpressed in cancer cells (Zhang et al., 2019). The conjugation of glycosyl further endues the nanoparticle with good biocompatibility and tumor-targeting ability (Zhao et al., 2017).

EXPERIMENTAL

Materials and Instruments

Reagents were purchased from commercial sources and were used as received unless mentioned otherwise. Reactions were monitored by TLC. ^1H NMR and ^{13}C NMR spectra were

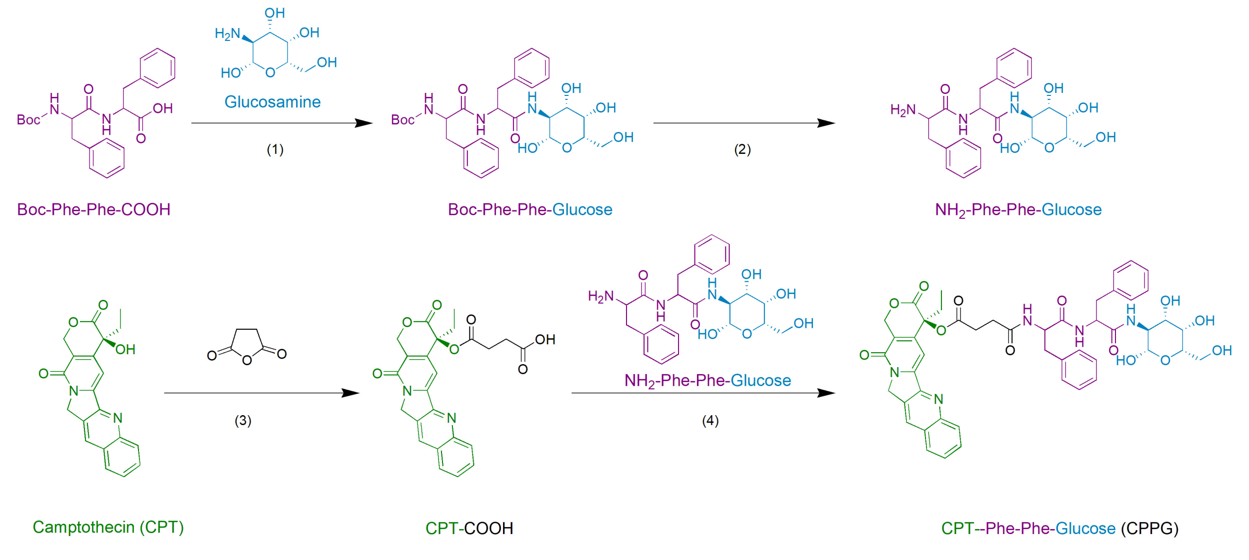

SCHEME 2 | The synthesis route of small molecular drug amphiphile CPPG.

obtained by a Bruker ARX 400 MHz spectrometer in DMSO-d_6. ^{1}H NMR chemical shifts are reported in ppm relative to tetramethylsilane (TMS) with the solvent resonance employed as the internal standard (DMSO-d_6 at 2.50 ppm). Data are reported as follows: chemical shift, multiplicity (s = singlet, br s = broad singlet, d = doublet, t = triplet, q = quartet, m = multiplet), coupling constants (Hz), and integration. ^{13}C NMR chemical shifts are reported in ppm from tetramethylsilane (TMS) with the solvent resonance as the internal standard (DMSO-d_6 at 39.51 ppm). High Resolution Mass Spectra (HRMS) were obtained by a GCT Premier CAB 048 mass spectrometer operating in MALDI-TOF mode. Absorption spectra were measured on a Varian 50 Conc UV-Visible spectrophotometer at 25°C. Fluorescence spectra were recorded on an Edinburgh FS5 fluorescence spectrophotometer at 25°C. Cellular imaging experiments were performed with a confocal laser scanning microscope (LSM880, ZEISS, Germany) equipped with Argon, red HeNe, and green HeNe lasers. A Cell Counting Kit-8 (CCK-8) was obtained from Dojindo Laboratories (Japan). Penicillin–streptomycin, fetal bovine serum, PBS, DMEM medium, and trypsin were acquired from Gibco Life Technologies (United States). MCF-7 and LO2 cell lines were obtained from the Shanghai cell bank of the Chinese Academy of Sciences.

Synthesis of Compound CPT-COOH

In an ordinary vial equipped with a magnetic stirring bar, 1,8-Diazabicycloundec-7-ene (DBU, 1 mL, 0.6 mmol) was slowly at 0°C added to a mixture of (S)-(+)-camptothecin (70 mg, 0.2 mmol) and succinic anhydride (60 mg, 0.6 mmol) in 6 mL of dichloromethane. The reaction mixture was stirred at room temperature for few hours, until the reaction completed (monitored by TLC). After evaporation of the solvent, the crude product was recrystallized with methanol to obtain the pale yellow crystalline product.

^{1}H NMR (400 MHz, DMSO-d_6) δ 12.29 (s, 1H), 8.70 (s, 1H), 8.22 – 8.10 (m, 2H), 7.92 – 7.83 (m, 1H), 7.77 – 7.68 (m, 1H), 7.14 (s, 1H), 5.57 – 5.42 (m, 2H), 5.37 – 5.23 (m, 2H), 2.86 – 2.66 (m, 2H), 2.50 – 2.44 (m, 2H), 2.23 – 2.09 (m, 2H), 0.92 (t, J = 7.0 Hz, 3H).

^{13}C NMR (101 MHz, DMSO-d_6) δ 173.5, 171.7, 167.7, 157.0, 152.9, 148.3, 146.4, 145.7, 132.0, 130.9, 130.3, 129.5, 129.0, 128.4, 128.2, 119.4, 95.6, 76.3, 66.8, 50.7, 30.8, 29.0, 28.8, 8.0.

HRMS (ESI) calcd. for C24H20N2NaO7 [M + Na]$^{+}$ 471.1168, found: 471.1161.

Synthesis of Compound CPPG

Boc-Phe-Phe-Glucose: Boc-Diphenylalanine (82.4 mg, 0.2 mmol) and HATU (80.0 mg, 0.2 mmol) were dissolved in DCM (1.2 mL). Diisopropylethylamine (44 μL, 0.24 mmol) was added at 0°C, and the mixture was stirred at room temperature for 10 min. Then the solution was added to a suspension of glucosamine hydrochloride (64.7 mg, 0.3 mmol) in a mixture of DCM (1.2 mL) and diisopropylethylamine (80 μL, 0.44 mmol). After stirring at room temperature overnight, the resulting mixture was then poured into saturated brine. The insoluble solids in the dichloromethane phase were collected by centrifugation. The precipitate was washed with water (2 × 1 mL) and DCM (2 × 1 mL), and dried under vacuum to afford Boc-Phe-Phe-Glucose as a white solid.

^{1}H NMR (400 MHz, DMSO-d_6) δ 8.23 – 8.06 (m, 1H), 7.95 – 7.77 (m, 1H), 7.32 – 7.16 (m, 10H), 7.02 – 6.90 (m, 1H), 6.62 – 6.43 (m, 1H), 5.16 – 5.04 (m, 1H), 5.04 – 4.80 (m, 2H), 4.75 – 4.63 (m, 1H), 4.52 (s, 1H), 4.13 – 3.99 (m, 1H), 3.60 (s, 3H), 3.54 – 3.47 (m, 1H), 3.18 – 3.07 (m, 2H), 2.88 – 2.76 (m, 2H), 2.69 (s, 1H), 2.66 – 2.56 (m, 1H), 1.27 (s, 9H).

^{13}C NMR (101 MHz, DMSO-d_6) δ 171.5, 155.5, 138.7, 138.1, 130.1, 130.0, 129.6, 128.4, 128.3, 128.3, 126.5, 91.1, 78.6, 77.3, 72.6, 71.4, 71.2, 70.8, 61.5, 56.6, 55.0, 53.8, 49.0, 38.9, 38.7, 38.0, 28.5, 28.2.

HRMS (ESI) calcd. for C29H39N3NaO9 [M + Na]$^+$ 596.2584, found: 596.2568.

Procedure for the Boc Deprotection: Boc-Phe-Phe-Glucose (28.7 mg, 0.05 mmol) was dissolved in DCM (1 mL) and cooled to 0°C. TFA (trifluoroacetic acid) (2 mL, 26 mol) was added dropwise, and the stirring was continued for 1 h at room temperature. After the reaction was completed, the solvent and TFA were removed by evaporation. To the residue, cold diethyl ether was added whereupon the product precipitated. The product was filtered off via a sinter funnel and dried in a vacuum leaving the Phe-Phe-Glucose trifluoroacetate as a white powder.

To compound CPT-COOH (22.4 mg, 0.05 mmol) in 1 mL anhydrous DMSO the following was added: NHS (N-Hydroxysuccinimide) (6.9 mg, 0.06 mmol), DIC (N,N′-Diisopropylcarbodiimide) (7.6 mg, 0.06 mmol), and DMAP (4-Dimethylaminopyridine) (7.3 mg, 0.06 mmol), at room temperature. After the reaction was stirred for 12 h at room temperature, Phe-Phe-Glucose trifluoroacetate (29.3 mg, 0.05 mmol) was added, and then stirred for 2 h. The resulting mixture was then poured into DCM and deionized H_2O. The insoluble solids in the dichloromethane phase were collected by centrifugation. The precipitate was washed with water and DCM, and dried under a vacuum to create CPPG as a pale yellow solid.

^{1}H NMR (400 MHz, DMSO-d_6) δ 8.74 – 8.67 (m, 1H), 8.22 – 8.13 (m, 3H), 7.92 – 7.80 (m, 2H), 7.76 – 7.70 (m, 1H), 7.28 – 7.21 (m, 2H), 7.22 – 7.09 (m, 10H), 7.09 – 7.04 (m, 1H), 6.71 – 6.65 (m, 1H), 5.56 – 5.43 (m, 3H), 5.33 – 5.23 (m, 2H), 4.95 (s, 1H), 4.73 – 4.37 (m, 4H), 3.66 – 3.55 (m, 3H), 3.52 – 3.46 (m, 1H), 3.00 (s, 3H), 2.72 (s, 2H), 2.37 (s, 2H), 2.35 – 2.30 (m, 2H), 2.10 – 2.04 (m, 2H), 0.89 (t, *J* = 7.0 Hz, 3H).

^{13}C NMR (101 MHz, DMSO-d_6) δ 173.3, 171.7, 171.4, 170.7, 167.7, 157.0, 152.8, 148.4, 147.4, 146.4, 145.8, 138.4, 138.2, 132.0, 130.9, 130.2, 129.9, 129.6, 129.5, 129.0, 128.4, 128.4, 128.3, 126.6, 119.2, 107.2, 95.6, 91.2, 76.5, 76.2, 72.6, 71.6, 71.0, 66.8, 61.6, 54.8, 54.4, 54.0, 50.7, 47.8, 38.4, 37.7, 30.8, 30.0, 29.4, 25.7, 23.8, 8.0.

HRMS (ESI) calculated for $C_{48}H_{49}N_5NaO_{13}$ [M + Na]$^+$ 926.3225, found: 926.3196.

Preparation and Characterization of CPPG AIE Dots

The as-prepared hydrophobic AIEgens (2,3-bis(4-(phenyl(4-(1,2,2-triphenylvinyl) phenyl) amino) phenyl) fumaronitrile),

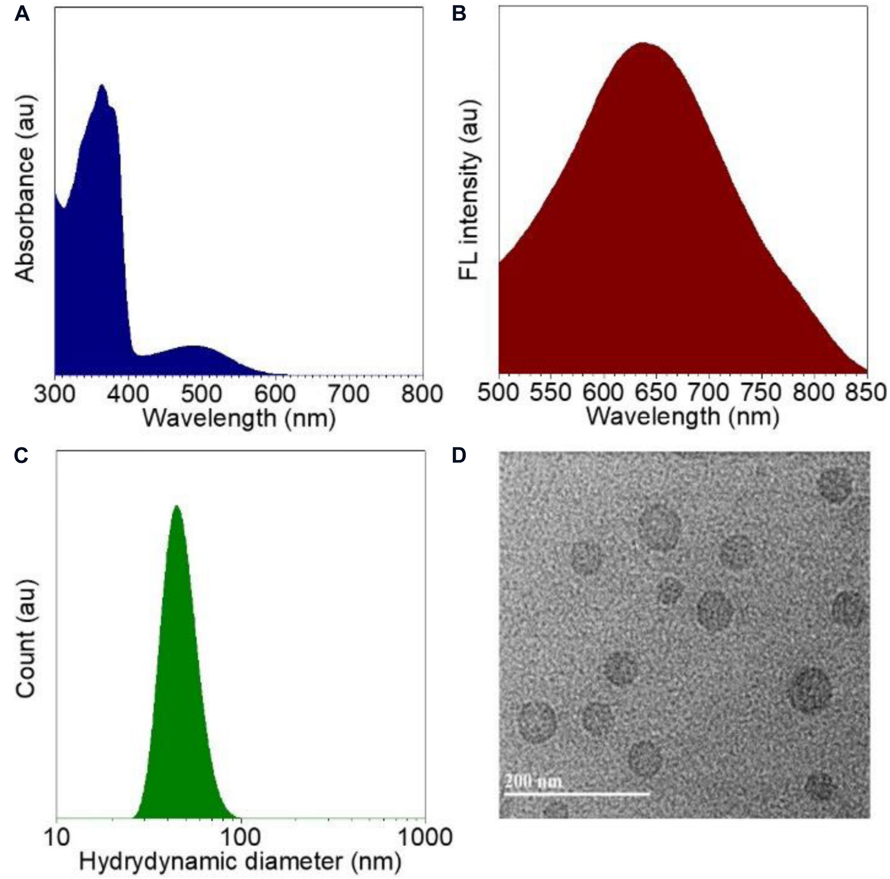

FIGURE 1 | Characterizations of CPPG AIE dots. **(A)** Absorption spectra recorded for CPPG AIE dots. **(B)** Fluorescence emission spectra for CPPG AIE dots. **(C)** Hydrodynamic diameter distribution obtained for CPPG AIE dots. **(D)** TEM image obtained for CPPG AIE dots. Synthesis route of small molecular drug amphiphile CPPG.

also known as TTF, were transferred into an aqueous solution by coating with a CPPG amphiphilic molecular. A combination of 1 mg CPPG and 1 mg TTF were then dissolved in tetrahydrofuran (THF), then CPPG was added dropwise to water under an ultrasonic environment, and repeatedly pipetted with a pipette to remove THF, so that the amphiphilic molecules self-assembled to form a water-soluble nano skeleton. Then, under the same conditions, according to the volume of 1:1, an equal volume of the TTF solution was drawn, added drop by drop, and repeatedly pipetted to remove THF to make amphiphilic molecules through self-assembly to form a water-soluble nano skeleton. The liquid in the beaker was then transferred to a dialysis bag with a molecular weight of 1 KD, and dialyzed against distilled water for 48 h, during which the water was changed every 8 h to remove free single molecules that did not form particles. Then the purified CPPG AIE dots were concentrated for further characterization and application. The UV–vis absorbance spectra and photoluminescence (PL) spectra of CPPG AIE dots were measured using PerkinElmer Lambda 25 UV–vis absorption spectrophotometer and Edinburgh FS920 fluorescent spectrometer, respectively. TEM images of CPPG AIE dots were recorded using the FEI Tecnai G20 transmission microscope at 200 kV. Dynamic light scattering (DLS) analysis was taken using a Zetasizer Nano ZS (Malvern Instruments).

Cell Treatment and Cell Imaging

For the imaging of AIE, the MCF7 and LO2 cells were incubated with CPPG AIE dots at 37°C. For glucosamine pre-block cell imaging, a solution of glucosamine (10 mg/mL) was prepared

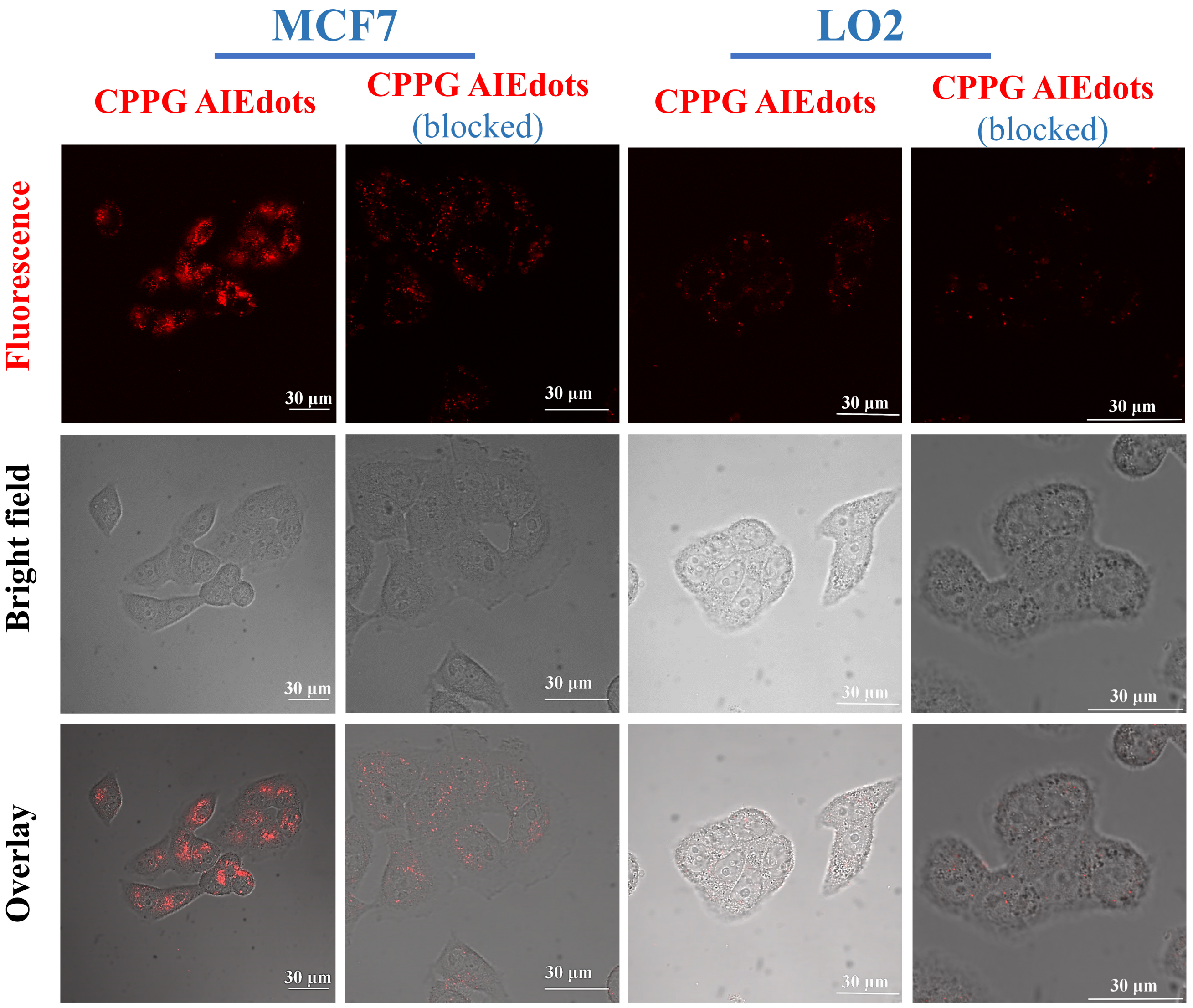

FIGURE 2 | Cancer cell targeting property of CPPG AIE dots. CLSM (Confocal Laser Scanning Microscopy) images of MCF7 cells (GLUT high-concentration) and LO2 cells (GLUT low-concentration) after incubating with CPPG AIE dots under different treatments for 3 h at 37°C. For the pre-blocking experiment, cells were pretreated with 10 mg/mL free glucosamine hydrochloride (dissolved in DMEM) for 30 min before incubation with CPPG AIE dots.

(dissolved in DMEM) and added to each pore, then incubated at 37°C for 30 min. The imaging was acquired using a confocal laser scanning microscope (LSM 880, ZEISS, Germany). For cell imaging, the cells were washed with PBS three times. A 480 nm laser was used as the light source and emission was collected from 600 to 700 nm.

Cell Viability

Cell viability was determined by a CCK-8 assay. Firstly, 150 μL cell suspension was prepared in a 96-well plate and incubated in the incubator for 24 h (37°C, 5% CO_2). Then 2 μL of different concentrations of (0–10 mg/mL) CPT and CPPG-AIE were, respectively added to the plate and incubated for 48 h. After removing the solution, 100 μL 10% CCK-8 (dissolved in DMEM) was added to each pore (attention was paid to not generate bubbles) and incubated for 40 min. Finally, the absorbance at 450 nm was measured by a microplate reader. Cell Survival Rate = [(As-Ab)/(Ac-Ab)] × 100% [As: Laboratory pore (medium containing cells, CCK-8, CPT, and CPT or CPPG-AIE); Ac: Control pore (medium containing cells, CCK-8, without CPT or CPPG-AIE); Ab: Blank pore (medium without cells and CPT or CPPG-AIE, CCK-8)].

Statistical Analysis

All the results are reported as mean ± SD. The differences among groups were determined using one-way ANOVA analysis and student's *t*-test.

RESULTS AND DISCUSSION

Characteristics of CPPG AIE Dots

With the CPPG AIE dots in hand, we first investigated the spectral characteristics, all the test samples are from 4 mg/mL CPPG AIE dots, the UV/Vis absorption spectrum of CPPG AIE dots dispersion displayed typical signals of TTF at ~480 nm and the peak of CPPG at ~370 nm (**Figure 1A** and **Supplementary Figure S12**), as for the fluorescence emission spectra, CPPG AIE dots show a emission peak at ~650 nm (**Figure 1B**), which further confirmed the successfully synthesized of CPPG AIE dots. Furthermore, DLS analysis revealed that the average diameter of CPPG AIE dots was ~57 nm (**Figure 1C**), the uniform spherical morphology was confirmed by transmission electron microscopy (TEM) analysis (**Figure 1D**). In terms of stability, the size of CPPG AIE dots stabilized within a week (**Supplementary Figure S13**) and the fluorescence intensity remains unchanged under excitation light which indicated good photostability (**Supplementary Figure S14**). To study the fluorescence performance of AIE dots in the poor solvent, we changed the fraction of water and THF (**Supplementary Figure S15**) which showed poor solubility when the percentage of water increased. In addition, to study the loading capacity and versatility of the nanodots formed by CPPG, we tested the different volume mixing ratio of CPPG with TTF (**Supplementary Figures S16A,B**) and two other AIEgens in the CPPG dots, they are DCPP-TPA (**Supplementary Figures S16C,D**) and

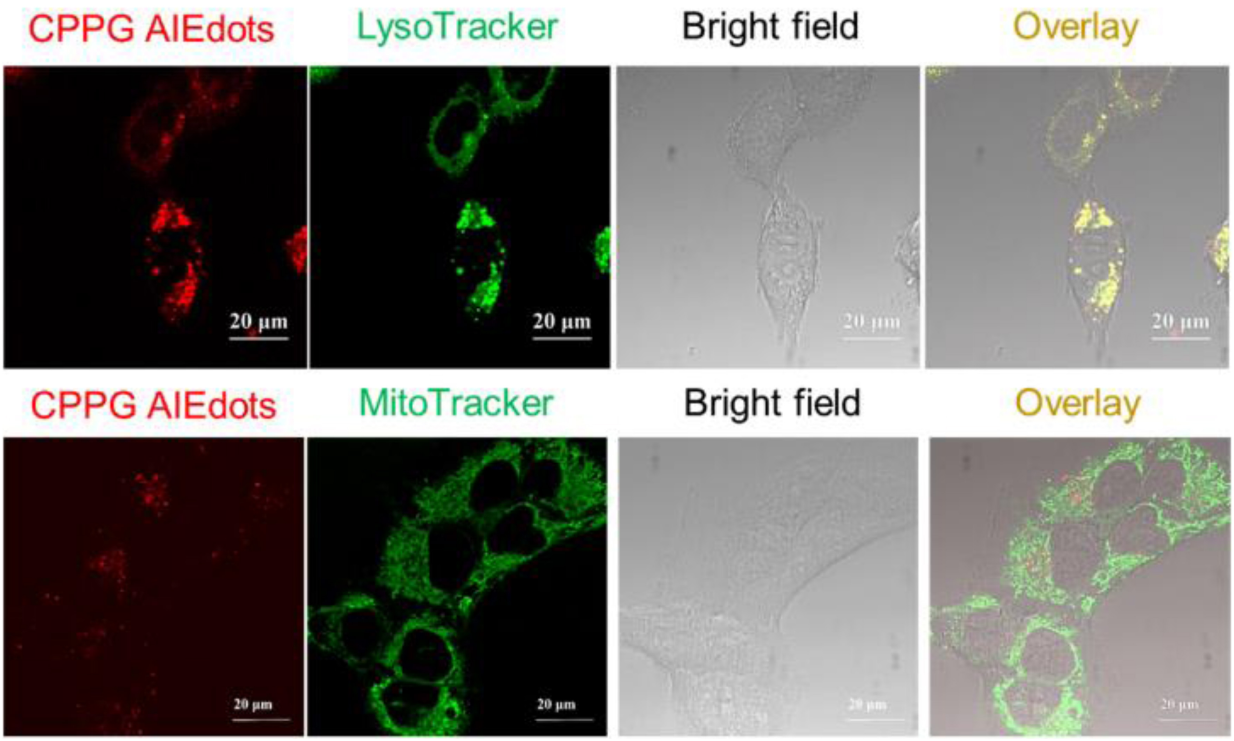

FIGURE 3 | Colocalization studies of CPPG AIE dots with LysoTracker Green DND-99 or MitoTracker Green FM in MCF7 cells, respectively.

MEH-PPV (**Supplementary Figures S16E,F**), respectively. The results indicated that the optimal loading capacity when the mixing ratio is 1:1.

Cell Imaging of CPPG AIE Dots

Since GLUT presents high concentration in cancer cells, the property of CPPG AIE dots as cancer cell specific fluorescence light-up probes was studied for live cell imaging. Herein, the human breast cancer cell line MCF7 and human hepatocytes normal cell line LO2 were selected as the model for fluorescence imaging research. As displayed in **Figure 2**, under a fluorescence microscope, a strong red fluorescence was detected after MCF7 cells were incubated with 4 mg/mL CPPG AIE dots. However, compared to the MCF7 cells, a weak red fluorescence was observed in LO2 cells. Furthermore, when both MCF7 and LO2 cells were pre-treated with excess free glucosamine hydrochloride for 30 min before the addition of CPPG AIE dots, only a very weak red fluorescence was detected (**Figure 2**). These results suggested that the intracellular fluorescence light-up of CPPG AIE dots almost came from the endocytosis mediated by the GLUT pathway. Moreover, the localization of CPPG AIE dots was tracked by Lysotracker and Mitotracker (**Figure 3**), as it matched very well with the Lysotracker, which also suggested that the entry of CPPG AIE dots into cells was at least partially GLUT receptor-mediated endocytosis. Herein, CPPG AIE dots can aggregated much more in the cancer cells, which revealed a potential way to distinguish cancer cell from normal cells.

Cell Viability

In order to assess the possibility of using the AG-targeted prodrug CPPG AIE dots to inhibit cancer cells, the cell viabilities of MCF7 and LO2 were studied using CCK8 (Cell Count Kits-8). As is shown in **Figure 4**, when treated with the same concentration of the CPPG AIE dots, the cell viability of MCF7 was much lower than LO2, which suggests that our design of nanoprobe CPPG AIE dots works well in targeting the cancer cell and also significantly inhibiting the cell growth.

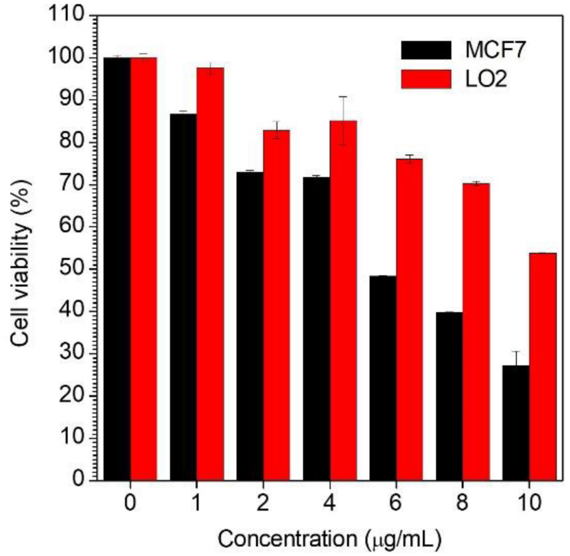

FIGURE 4 | Cell viability determined by CCK-8 assay against MCF7 cells and LO2 cells upon 48 h treatment with CPPG-AIE dots.

CONCLUSION

In summary, taking advantage of the characteristics of the AIEgens, we have successfully synthesized AIE-based intracellular light-up nanoprobe CPPG AIE dots with self-assemble and cancer cell targeted prodrug properties. The CPPG AIE dots nanoprobe was selected for cancer cell targeted imaging and selective suppression of the growth of cancer cells. As far as we know, the strategies to combine the AIEgens with prodrug by the FF element have not been widely used yet. Herein, such an AIE-based nanoprobe offers a new choice for the development of fluorescence light-up imaging and anticancer therapeutics.

DATA AVAILABILITY STATEMENT

The raw data supporting the conclusions of this article will be made available by the authors, without undue reservation.

AUTHOR CONTRIBUTIONS

XY and YL: data curation, validation, visualization, investigation and writing–original draft. SL, XX, YB, JY, DO, and XF: writing-original draft. PG and LC: funding acquisition, supervision, project administration, methodology, and writing–review and editing.

FUNDING

This work was financially supported by the National Natural Science Foundation of China (81671758 and 31571013), Guangdong Natural Science Foundation of Research Team (2016A030312006), the Shenzhen Science and Technology Program (JCYJ20160429191503002, JCYJ20170818162522440, JCYJ20170818154843625, and JCYJ20170818113538482), China Postdoctoral Science Foundation (2019M660219), Special Research Assistant Project of the Chinese Academy of Sciences (Y959101001), and Guangdong Basic and Applied Basic Research Fund Project (2019A1515110222).

ACKNOWLEDGMENTS

We thank the Instrumental Analysis Center of Shenzhen University (Xili Campus).

SUPPLEMENTARY MATERIAL

The Supplementary Material for this article can be found online at: https://www.frontiersin.org/articles/10.3389/fbioe.2020.00903/full#supplementary-material

REFERENCES

Antaris, A. L., Chen, H., Cheng, K., Sun, Y., Hong, G., Qu, C., et al. (2016). A small-molecule dye for NIR-II imaging. *Nat. Mater.* 15, 235–242. doi: 10.1038/nmat4476

Chinen, A. B., Guan, C. M., Ferrer, J. R., Barnaby, S. N., Merkel, T. J., and Mirkin, C. A. (2015). Nanoparticle probes for the detection of cancer biomarkers. Cells, and Tissues by fluorescence. *Chem. Rev.* 115, 10530–10574. doi: 10.1021/acs.chemrev.5b00321

Ding, D., Li, K., Liu, B., and Tang, B. Z. (2013). Bioprobes based on AIE fluorogens. *Acc. Chem. Res.* 46, 2441–2453. doi: 10.1021/ar3003464

Fu, X., Chen, L., and Choo, J. (2017). Optical nanoprobes for ultrasensitive immunoassay. *Anal. Chem.* 89, 124–137. doi: 10.1021/acs.analchem.6b02251

Geng, J., Zhu, Z., Qin, W., Ma, L., Hu, Y., Gurzadyan, G. G., et al. (2014). Near-infrared fluorescence amplified organic nanoparticles with aggregation-induced emission characteristics for in vivo imaging. *Nanoscale* 6, 939–945. doi: 10.1039/c3nr04243j

Gu, X., Kwok, R. T. K., Lam, J. W. Y., and Tang, B. Z. (2017). AIEgens for biological process monitoring and disease theranostics. *Biomaterials* 146, 115–135. doi: 10.1016/j.biomaterials.2017.09.004

Li, D., Qin, W., Xu, B., Qian, J., and Tang, B. Z. (2017). AIE nanoparticles with high stimulated emission depletion efficiency and photobleaching resistance for long-term super-resolution bioimaging. *Adv. Mater.* 29:1703643. doi: 10.1002/adma.201703643

Li, H., Wang, C., Hou, T., and Li, F. (2017). Amphiphile-mediated ultrasmall aggregation induced emission dots for ultrasensitive fluorescence biosensing. *Anal. Chem.* 89, 9100–9107. doi: 10.1021/acs.analchem.7b01797

Li, J., Kuang, Y., Gao, Y., Du, X., Shi, J., and Xu, B. (2013). D-amino acids boost the selectivity and confer supramolecular hydrogels of a nonsteroidal anti-inflammatory drug (NSAID). *J. Am. Chem. Soc.* 135, 542–545. doi: 10.1021/ja310019x

Li, K., Ding, D., Prashant, C., Qin, W., Yang, C. T., Tang, B. Z., et al. (2013). Gadolinium-functionalized aggregation-induced emission dots as dual-modality probes for cancer metastasis study. *Adv. Healthc. Mater.* 2, 1600–1605. doi: 10.1002/adhm.201300135

Li, K., and Liu, B. (2014). Polymer-encapsulated organic nanoparticles for fluorescence and photoacoustic imaging. *Chem. Soc. Rev.* 43, 6570–6597. doi: 10.1039/c4cs00014e

Luo, J., Xie, Z., Lam, J. W., Cheng, L., Chen, H., Qiu, C., et al. (2001). Aggregation-induced emission of 1-methyl-1,2,3,4,5-pentaphenylsilole. *Chem. Commun.* 21, 1740–1741. doi: 10.1039/b105159h

Mei, J., Leung, N. L., Kwok, R. T., Lam, J. W., and Tang, B. Z. (2015). Aggregation-induced emission: together we shine, united we soar! *Chem. Rev.* 115, 11718–11940. doi: 10.1021/acs.chemrev.5b00263

Niu, G., Zheng, X., Zhao, Z., Zhang, H., Wang, J., He, X., et al. (2019). Functionalized acrylonitriles with aggregation-induced emission: structure tuning by simple reaction-condition variation, efficient red emission, and two-photon bioimaging. *J. Am. Chem. Soc.* 141, 15111–15120. doi: 10.1021/jacs.9b06196

Ozawa, T., Yoshimura, H., and Kim, S. B. (2013). Advances in fluorescence and bioluminescence imaging. *Anal. Chem.* 85, 590–609. doi: 10.1021/ac3031724

Reches, M., and Gazit, E. (2003). Casting metal nanowires within discrete self-assembled peptide nanotubes. *Science* 300, 625–627. doi: 10.1126/science.1082387

Reisch, A., and Klymchenko, A. S. (2016). Fluorescent polymer nanoparticles based on dyes: seeking brighter tools for bioimaging. *Small* 12, 1968–1992. doi: 10.1002/smll.201503396

Sen, N., Das, B. B., Ganguly, A., Mukherjee, T., Bandyopadhyay, S., and Majumder, H. K. (2004). Camptothecin-induced imbalance in intracellular cation homeostasis regulates programmed cell death in unicellular hemoflagellate *Leishmania donovani*. *J. Biol. Chem.* 279, 52366–52375. doi: 10.1074/jbc.M406705200

Tsoi, K. M., Dai, Q., Alman, B. A., and Chan, W. C. W. (2013). Are quantum dots toxic? Exploring the discrepancy between cell culture and animal studies. *Acc. Chem. Res.* 46, 662–671. doi: 10.1021/ar300040z

Wang, D., Qian, J., Qin, W., Qin, A., Tang, B. Z., and He, S. (2014). Biocompatible and photostable AIE dots with red emission for in vivo two-photon bioimaging. *Sci. Rep.* 4:4279. doi: 10.1038/srep04279

Wang, K., He, X., Yang, X., and Shi, H. (2013). Functionalized silica nanoparticles: a platform for fluorescence imaging at the cell and small animal levels. *Acc. Chem. Res.* 46, 1367–1376. doi: 10.1021/ar3001525

Weissleder, R., and Nahrendorf, M. (2015). Advancing biomedical imaging. *Proc. Natl. Acad. Sci. U.S.A.* 112, 14424–14428. doi: 10.1073/pnas.1508524112

Wolfbeis, O. S. (2015). An overview of nanoparticles commonly used in fluorescent bioimaging. *Chem. Soc. Rev.* 44, 4743–4768. doi: 10.1039/c4cs00392f

Xu, S., Bai, X., Ma, J., Xu, M., Hu, G., James, T. D., et al. (2016). Ultrasmall organic nanoparticles with aggregation-induced emission and enhanced quantum yield for fluorescence cell imaging. *Anal. Chem.* 88, 7853–7857. doi: 10.1021/acs.analchem.6b02032

Yan, L., Zhang, Y., Xu, B., and Tian, W. (2016). Fluorescent nanoparticles based on AIE fluorogens for bioimaging. *Nanoscale* 8, 2471–2487. doi: 10.1039/c5nr05051k

Yu, J., Rong, Y., Kuo, C. T., Zhou, X. H., and Chiu, D. T. (2017). Recent advances in the development of highly luminescent semiconducting polymer dots and nanoparticles for biological imaging and medicine. *Anal. Chem.* 89, 42–56. doi: 10.1021/acs.analchem.6b04672

Yu, Y., Huang, Y., Hu, F., Jin, Y., Zhang, G., Zhang, D., et al. (2016). Self-assembled nanostructures based on activatable red fluorescent dye for site-specific protein probing and conformational transition detection. *Anal. Chem.* 88, 6374–6381. doi: 10.1021/acs.analchem.6b00774

Zhang, H., Fei, J., Yan, X., Wang, A., and Li, J. (2015). Enzyme-responsive release of doxorubicin from monodisperse dipeptide-based nanocarriers for highly efficient cancer treatment in vitro. *Adv. Funct. Mater.* 25, 1193–1204. doi: 10.1002/adfm.201403119

Zhang, W., Liu, W., Li, P., Huang, F., Wang, H., and Tang, B. (2015). Rapid-response fluorescent probe for hydrogen peroxide in living cells based on increased polarity of C-B bonds. *Anal. Chem.* 87, 9825–9828. doi: 10.1021/acs.analchem.5b02194

Zhang, X., Wang, K., Liu, M., Zhang, X., Tao, L., Chen, Y., et al. (2015). Polymeric AIE-based nanoprobes for biomedical applications: recent advances and perspectives. *Nanoscale* 7, 11486–11508. doi: 10.1039/c5nr01444a

Zhang, W., Hu, X., Shen, Q., and Xing, D. (2019). Author correction: mitochondria-specific drug release and reactive oxygen species burst induced by polyprodrug nanoreactors can enhance chemotherapy. *Nat. Commun.* 10:2597. doi: 10.1038/s41467-019-10186-0

Zhao, X., Yang, C. X., Chen, L. G., and Yan, X. P. (2017). Dual-stimuli responsive and reversibly activatable theranostic nanoprobe for precision tumor-targeting and fluorescence-guided photothermal therapy. *Nat. Commun.* 8:14998. doi: 10.1038/ncomms14998

Conflict of Interest: YB was employed by the company Guangzhou Baiyunshan Pharmaceutical General Factory. JY was employed by the company Livzon Mabpharm Inc., Zhuhai, China.

The remaining authors declare that the research was conducted in the absence of any commercial or financial relationships that could be construed as a potential conflict of interest.

frontiers
in Immunology

MINI REVIEW
published: 06 October 2020
doi: 10.3389/fimmu.2020.575816

Immunological Effects of Aggregation-Induced Emission Materials

Haibo Wu[1,2*†], *Wen Huang*[1,2†], *Xingyu Zhou*[3,4†] *and Yuanzeng Min*[3,4,5,6*]

[1] *Department of Pathology, The First Affiliated Hospital of USTC, Division of Life and Sciences and Medicine, University of Science and Technology of China, Hefei, China,* [2] *Intelligent Pathology Institute, The First Affiliated Hospital of USTC, Division of Life Sciences and Medicine, University of Science and Technology of China, Hefei, China,* [3] *CAS Key Lab of Soft Matter Chemistry, University of Science and Technology of China, Hefei, China,* [4] *Department of Chemistry, University of Science and Technology of China, Hefei, China,* [5] *Department of Endocrinology, The First Affiliated Hospital of USTC, Anhui Provincial Hospital, University of Science and Technology of China, Hefei, China,* [6] *Hefei National Laboratory for Physical Science at the Microscale, University of Science and Technology of China, Hefei, China*

OPEN ACCESS

Edited by:
Ben Zhong Tang,
Hong Kong University of Science and Technology, Hong Kong

Reviewed by:
Dan Ding,
Nankai University, China
Meng Gao,
South China University of Technology, China
Xian-Zheng Zhang,
Wuhan University, China
Xinggui Gu,
Beijing University of Chemical Technology, China
Yunlu Dai,
University of Macau, China

****Correspondence:***
Haibo Wu
wuhaibo@ustc.edu.cn
Yuanzeng Min
minyz@ustc.edu.cn

†These authors have contributed equally to this work

Specialty section:
This article was submitted to Molecular Innate Immunity, a section of the journal Frontiers in Immunology

Received: *24 June 2020*
Accepted: *14 September 2020*
Published: *06 October 2020*

Citation:
Wu H, Huang W, Zhou X and Min Y (2020) Immunological Effects of Aggregation-Induced Emission Materials. Front. Immunol. 11:575816. doi: 10.3389/fimmu.2020.575816

Nanotechnology is widely used in the fields of biology and medicine. Some special nanoparticles with good biocompatibility, hydrophilicity, and photostability can be used as ideal systems for biomedical imaging in early diagnosis and treatment of diseases. Among them, aggregation-induced emission materials are new antiaggregation-caused quenching nano-imaging materials, which have advantages in biocompatibility, imaging contrast, and light stability. Meanwhile, heterogeneity of nanoparticles may cause various adverse immune reactions. In response to the above problems, many researchers have modified nano-materials to be multifunctional nano-composites, aiming at combining diagnosis and treatment with simultaneous imaging and targeted therapy and additionally avoiding immune reactions, which is of great potential in imaging-guided therapy. This review discusses the application of aggregation-induced emission materials, and other nano-imaging materials are also mentioned. We hope to provide new ideas and methods for the imaging of nano-materials in diagnosis and treatment.

Keywords: aggregation-induced emission, immunity, inflammation, biomedical imaging, application of aggregation-induced emission

INTRODUCTION

Nanotechnology is widely used in the fields of biology and medicine. Among them, nanoparticles (NPs) play a key role in biomedical imaging and the therapeutic fields of modern medicine due to their special physical and chemical properties, such as electrical conductivity, stability, and optical properties. Some NPs, called nano-imaging materials, can be used as imaging agents (with diagnostic capability) in ideal imaging systems. The nano-imaging materials commonly used include carbon nanotubes (CNTs), nano-materials with metal ions, rare earth elements, and a new kind of imaging material named aggregation-induced emission (AIE) materials (1). With the improvement of biomedical imaging technology, nano-imaging materials enable the achievement of early diagnosis and visualization during the treatment process based on their unique optical properties. For example, in order to achieve the efficiency and visualization of the diagnosis and treatment, the multifunctional nano-probes with good photothermal property, high imaging contrast, biological safety, and accurate drug delivery are mainly developed. The multifunctional nano-probes not only realize the various ways of imaging, but also achieve an efficient treatment of neoplastic and non-neoplastic disease by combination therapy (2); nano-imaging material with metal ions can convert absorbed light energy into heat energy, leading to the apoptosis or necrosis of specific lesions, which is often used in the photothermal therapy of tumors at present (3).

In recent years, people have been devoted to the research of a new type of nano-imaging material, namely AIE materials. AIE materials are essential materials about antiaggregation-caused quenching (anti-ACQ), which were first reported in the study by Tang et al. (4) in 2001. It is mentioned in the report that AIE materials can be emitted more efficiently in an aggregated (rather than dispersed) state. In accordance with the advantages of AIE luminogens (AIEgens) in biocompatibility, imaging contrast with biological background, and photostability (5, 6), their potential applications in the fields of fluorescence bioimaging and chemical sensors have attracted widespread attention for research (7) by implementing multimodal imaging, synergistic therapy, and tumor immunotherapy for monitoring as well as effectively generating reactive oxygen species (ROS) as aggregates in order to achieve high-performance fluorescence (FL) imaging-guided photodynamic therapy (PDT) (8). As a result, AIE materials may play an important role in the diagnosis and treatment of neoplastic disease. In addition, AIEgens can be used in the treatment of non-neoplastic diseases. In recent years, antibiotics have been used frequently to cure bacterial infection (9). It is critical to prepare a multifunctional system that has both rapid bacterial differentiation and effective antibacterial properties and to quickly identify gram-positive bacteria in order to achieve an accurate and efficient antibacterial effect (10, 11) (**Scheme 1**).

With the wide application of nano-imaging materials, there are some problems in the safety of these special materials. Some nano-imaging materials can communicate with biological components (like cells, receptors, and proteins) and trigger cell signaling cascades, which can cause an unpredictable immune reaction (activation or suppression) or other negative results (17), such as nondegradability, normal tissue damage, potential immunogenicity, and even cell and systematic immunoreaction and inflammatory reaction (both innate immunity and immunological adaptive reactions) (18). After NPs get into the body, the complement system can be activated by nano-imaging

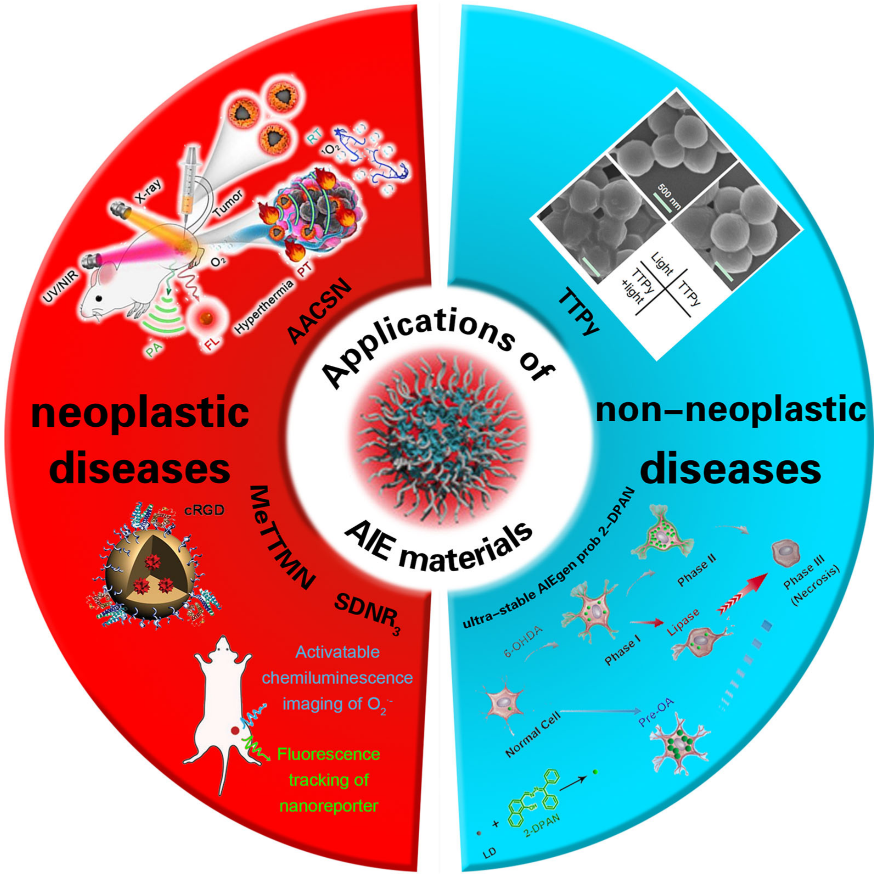

SCHEME 1 | The application of AIE materials in neoplastic and non-neoplastic diseases. cited from Ref (12), Ref (13), Ref (14), Ref (15) and Ref (16).

materials, and then they interact with the innate immune system and cause an immunomodulation reaction based on their physical and chemical properties (19). Furthermore, when exposed to the X-ray, an amount of electrons and free radicals damage cell DNA due to the toxic potentially of nano-imaging materials with heavy metal ions. The aqueous solution or physiological solution of the nano-imaging materials used in MRI is less stable and easy to accumulate and precipitate (20), react with plasma proteins, and be phagocytosed by monocytes and macrophages. The damage of some nano-imaging materials, like Ag NPs and Au NPs, to the human body derives from ROS, which break mitochondria function, lysosomes, and cytomembranes and causes apoptosis (21, 22). These imaging materials interact with the cells of the liver, lung, spleen, and skin directly, which will lead to oxidative damage and inflammation (23). Therefore, the key to nanotechnology is to solve heterogeneity when designing nano-materials in order to extend circulation time in the body and achieve long-term immune escape (3). This review emphatically sums up the immunobiological applications related to AIE materials and the solution of potential risks as well as summarizes the recent developments, biological effects, and biomedical applications of other nano-imaging materials.

THE LATEST DEVELOPMENTS AND BIOMEDICAL APPLICATIONS OF AIE MATERIALS

NPs with integrated multiple imaging and therapeutic modalities have great potential in accurate diagnosis and improvement of curative effect for tumors. Compared with traditional organic fluorescent materials, AIEgens have higher luminous intensity, photobleaching resistance, and biocompatibility so that they have become a superior tool for biosensing and bioimaging (24, 25).

AIEgens Can Realize Multimodal Imaging and Synergistic Therapy

Hypoxia in the tumor microenvironment often leads to reduced effectiveness of radiation therapy (RT) for some malignant tumors. However, photothermal therapy (PTT) under near infrared irradiation (NIR) can increase the blood flow and promote the oxygen supply of tumor tissue (26). Resulting from the uneven distribution of heat in tumor tissue, the tumor cannot be eradicated effectively by PTT alone (26). Therefore, combining the uniform irradiation of RT with the oxygen pump effect of PTT is an ideal choice to achieve synergetic treatment of tumors and improve the therapeutic effect. For tumor therapeutics, integrating multiple imaging and treatment modes into a single structural unit in order to attain an accurate diagnosis and improve the therapeutic effect is a promising research interest with profound clinical value (27).

The simple Ag @ AIE core-shell nanoparticles (AACSN) were prepared by Xue et al. (28) using the simple silver core/AIE shell NPs, which realize a new strategy of multimodal imaging and cooperative therapy. The adjustability of shell thickness could help to overcome the incompatibility between FL and plasma noble-metal NP while the excellent performance of FL and CT imaging can also be maintained. More importantly, an additional function is generated on the core-shell interface to achieve outstanding properties of PT and PA. The experimental results show that five types of imaging and therapy modes based on FL, PA, CT, PTT, and RT are successfully constructed in core @ shell nanostructure. This simplifies the complex preparation process and avoids the potential incompatibility between different components. This strategy provides an effective way to design multifunctional nanomaterials for disease diagnosis and synergetic treatment.

AIEgens Can Improve the Therapeutic Efficiency of PTT and PDT

For optical materials, photophysical properties play key roles in determining the biomedical function and efficacy of optical agents. When an optical material is in an excited state, it dissipates the energy through three pathways (29): fluorescence emission (FE), intersystem crossing (ISC), and thermal deactivation (TD), which are utilized as FL, luminescence, and PA imaging or PTT, respectively. Regulating the optical agents through a nano-engineering approach or molecular design can enhance one of the three pathways of these agents and improve one of their imaging effects. For the nano-engineering approach, an optical agent can be delivered and aggregated in the tumor and then reacts with the tumor microenvironment and opens up the radiative pathway. For molecular design, one can improve the molecular structure to narrow the energy gap, decrease energy loss, or control the agent's release, thus enhancing cancer phototheranostics. As is mentioned in previous research (30), one can control the imaging effect of AIEgens by regulating FE, ISC, or TD. Dan Ding et al. use calix arene and AIEgens to form supramolecular AIE dots, which are encapsulated by PEG-12C. These kinds of NPs could restrict ISC and TD, so the light excitation energy will only release by FE (see **Figure 1**), causing highly emissive, photosensitive supramolecular AIE nano-dots.

PDT is an emerging means for tumor treatment. Under the function of a photosensitizer (PS), the cytotoxic ROS are generated, leading to the death of tumor cells (31). This method has the distinct advantages of minimal invasion and high spatiotemporal precision (32, 33). Although preliminary results have been achieved by PDT in the treatment of tumors, there are still the following deficiencies. First, traditional PSs such as rose bengal and methylene blue have the problem of low generation efficiency of ROS, which limits the antitumor activity of PDT (34). Second, the PSs mentioned above exhibit intrinsically weak FL (35) while the lack of FE is not conducive to manipulate FL imaging-guided PDT. Consequently, multifunctional materials need to be designed to improve the therapeutic efficiency of PDT. In recent years, the emergence of PSs with AIE features has promoted the new development of PDT. It is proved that AIEgens can effectively generate ROS as aggregates and then realize high-performance FL imaging-guided PDT (36). Inspired by the advantages of stimuli-responsive nano-micelles and AIE PSs in tumor treatment, the team of You ML and Ben ZT designed two kinds of stimuli-responsive nano-micelles carrying a

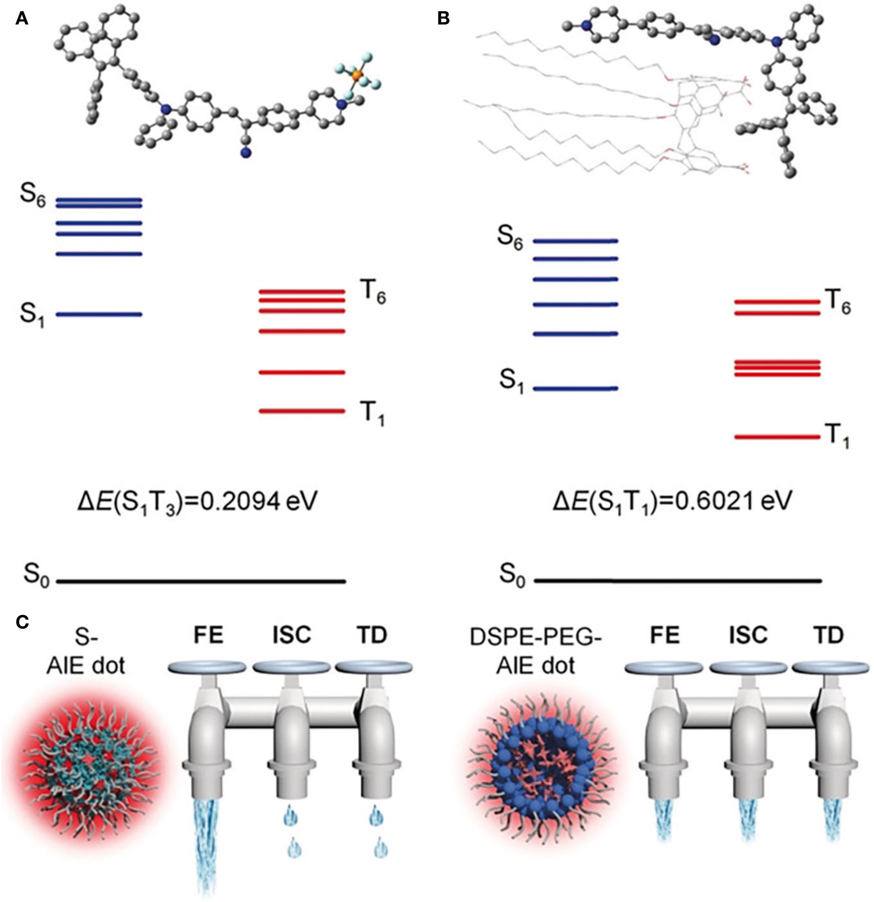

FIGURE 1 | Optimized molecular structures and calculated energy diagrams of **(A)** 1 and **(B)** 1+CC5A-12C complex. **(C)** The three dissipation pathways of the absorbed excitation energy for different AIE dots, which are likened to three water taps. FE, fluorescence emission; TD, thermal deactivation. (Reprinted with permission from Ref (30). Copyright © 2019 WILEY-VCH Verlag GmbH & Co. KGaA, Weinheim).

far red–emissive AIE PS (MeTTMN) to improve the generation efficiency of ROS and the PDT effect (37). Two kinds of stimuli-responsive polymer, mPEG-Hyd-PCL-CIN (P-Hyd) and mPEG-SS-PCL-CIN (P-SS), were successfully synthesized (8). The results show that the synthesized polymer has good biocompatibility, spontaneous assembly into nano-micelles in aqueous solution, and good drug-loading ability (AIE-PS-MeTTMN with high drug loading). In addition, compared to the control group, the generation efficiency of ROS can be significantly improved by using stimulus-responsive nano-micelle carriers at a simulative cancer environment. These MeTTMN-loaded stimuli-responsive nano-micelles have an efficient inducing effect on the apoptosis of tumor cells. Jun D and Ben ZT et al. (38) efficiently made fluorogen TTB with AIE properties encapsulated within a polymeric matrix and modified with RGD-4R peptide to prepare RGD-4R-MPD/TTB NPs with NIR emission, high photostability, and low dark cell toxicity. The results show that the PDT based on RGD-4R-MPD/TTB NPs T can effectively inhibit the growth of cervical, prostatic, and ovarian cancer. By observing changes of tumor histology and protein levels, it was found that it could effectively promote the apoptosis and necrosis of tumor cells, inhibit the proliferation of tumor cells, and thereby promote the death of cells. These results suggest that the efficiency of FL imaging-guided PDT could be improved in different ways, and the NIR PS with AIE character might be used as a substitute for nano-probes and nano-medicines in the clinical treatment of various tumors.

The Monitoring of AIEgens in Tumor Immunotherapy

As a new type of luminescent material, AIEgens has become a powerful tool for biological sensing and monitoring, including long-term tracking (39). The tumor immunotherapy provides new options for the treatment of various types of malignant tumors. It aims to train the immune cells in the host so as to destroy the tumor cells, but the response in patients is generally limited (40). Hence, the immune reaction needs to be monitored *in vivo* in volunteers to optimize the immunotherapeutic effect. At present, the existing methods include the determination of whole blood lymphocytes and immunocytokine and biopsy of tumor tissue. However, these measures are invasive and cannot effectively reflect the data of dynamic therapy (41). ROS plays a key role in regulating biological functions from intracellular homeostasis to cell death. What is more, it is essential for ROS to activate immune reactions (42). In innate immunity, the phagocytes (such as neutrophils and macrophages) can spontaneously promote the generation of ROS and fight against infection through an oxidation mechanism (17). In an adaptive immune reaction, the activation of T cell receptors triggers the generation of ROS in T cells, leading to the activation of T cells and cytokine secretion (19). In conclusion, the ROS can be used as a biomarker to monitor immune activation. Dan Ding et al. (12) carried out a novel PS, which reduced intermolecular interaction with a twisted donor-π-acceptor (D-π-A) molecular structure, which could also restrict the excited-state intramolecular motion due to the steric hindrance (see **Figure 2**). With consumption of absorbed excitation energy decreasing, more ROS were induced, and immunogenic cell death was massively evoked. In recent years, molecular imaging technology has wide prospective application in real-time evaluation of immunoactivation *in vivo* in volunteers. Although fluorescent probes can be used to detect ROS (13), they are rarely used to detect ROS in immune cells because of their inadequate biodistribution and poor sensitivity, let alone for *in vivo* imaging of immune activation. D. Cui and K. Pu et al. (14) synthesized a kind of semiconducting polymer nano-reporters (SPNRs) with superoxide anion ($O_2\bullet^-$), which can activate chemiluminescence signals for *in vivo* imaging of immunoactivation during tumor immunotherapy. Among them, SPNR3 represents the first $O_2\bullet^-$-activatable near-infrared chemiluminescent reporter. Owing to its high selectivity and sensitivity, the SPNR3 can distinguish the higher $O_2\bullet^-$ levels in immune cells from that in other cells (including tumor and normal cells). After systemic administration, SPNR3 preferentially accumulates in the tumor cells of living mice and activates the chemiluminescence signal in the tumor microenvironment. In addition, the improvement of *in vivo* chemiluminescence signals after tumor immunotherapy is related to the increase of T cells in tumors, which indicate the feasibility of SPNR3 tracking T cell activation. Therefore, this

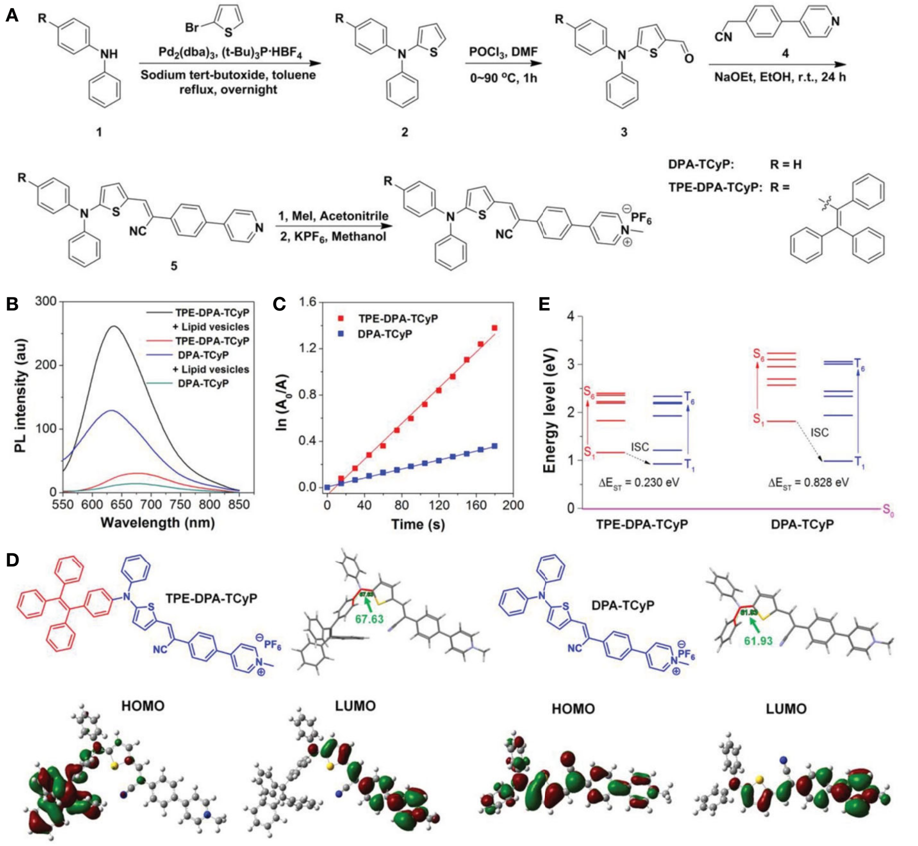

FIGURE 2 | **(A)** Synthetic route to TPE-DPA-TCyP and DPA-TCyP. **(B)** Photoluminescence (PL) spectra of TPE-DPA-TCyP and DPA-TCyP (10×10^{-6} M) in the presence and absence of lipid vesicles (22×10^{-6} M) in PBS. **(C)** Plot of $\ln(A_0/A)$ against light exposure time, where A_0 and A are the ABDA absorbance (378 nm) before and after irradiation, respectively. **(D)** Chemical structures, dihedral angles, and HOMO-LUMO distributions by DFT calculations of TPE-DPA-TCyP and DPA-TcyP. **(E)** Energy levels of S_1-S_6 and T_1-T_6 calculated by the vertical excitation of the optimized structures in **(D)**. (Reprinted with permission from (12) Copyright © 2020 Wiley-VCH Verlag GmbH & Co. KGaA, Weinheim).

kind of AIEgens can be used for real-time imaging of tumor immunotherapy *in vivo*, and it has great prospective application for high-throughput screening of immunotherapeutics of immunotherapy drugs.

In recent years, much research has been done on the biomedical applications of AIEgens involved immunological effects. For example, Wang et al. (43) discovered an FL self-reporting approach based on AIE properties to monitor polymeric fluorescent particles (PFPs). PFPs with uniform and tunable sizes harboring the abilities of biolabeling and photosensitizing, can be employed as superior optical nano-agents for photo-controllable immunotherapy. NK cells keep their original immunocompetence after coating with low-concentration PFPs, and such immunocompetence could be promoted by PFPs under light irradiation in PFP-coated NK cells. In addition, PFP-coated NK cells promote immunotherapy efficiency to cancer cells. Thus, excellent optical nano-agents greatly boost the extensive applications of precipitation polymerization in various science and technology areas.

The Role of AIEgens in the Treatment of Non-Neoplastic Diseases

AIEgens for the Diagnosis and Treatment of Bacterial Infectious Diseases

Human health is seriously threatened by bacterial infectious diseases, especially those caused by gram-positive bacteria (44). Millions of people are infected with gram-positive bacteria every year (45); furthermore, such bacteria causes 25% of surgical-site infections in nosocomial infections (46). In addition, in some kinds of tumors, the gram-positive bacteria can significantly enhance the resistance of chemotherapy drugs, reduce the curative effect of chemotherapy drugs (2), and promote tumor growth and metastasis (47). The traditional methods of bacterial identification include a gram-staining test, plate-culture, polymerase chain reaction, and immunological methods (48), but the implementation of them requires complex instruments, much time, large amounts of labor, and expensive fees (49). In recent years, antibiotics have been used frequently to cure bacterial infection (9). Although they are capable of killing bacteria and are easily accessible, excessive use and abuse of antibiotics inhibit their effectiveness and develop drug resistance (50). Therefore, in the case of no drug resistance, it is critical to prepare a multifunctional system that has both rapid bacterial differentiation and effective antibacterial properties and to quickly identify gram-positive bacteria in order to achieve an accurate and efficient antibacterial effect (10, 11). FL imaging-guided photodynamic antibacterial technology serves as an effective method to solve this problem in recent years (15). Michelle M.S. Lee et al. (15, 51) use AIE-active molecules called TTVP with good water solubility, NIR emission, and extremely high generation efficiency of ROS for the first time to carry out bacterial identification and photodynamic antibacterial research. The research indicates that TTVP can selectively target gram-positive bacteria through a washing-free and ultrafast staining procedure after the incubation period of 3 s, which shows ultrafast bacterial identification. The results of *in vitro* and *in vivo* experiments show that TTVP can completely inactivate gram-positive bacteria under white light irradiation *in vitro*, so it is a kind of super strong light-mediated antibacterial. More significantly, it also has a significant effect on photodynamic antibacterial treatment in a rat model of skin wound infection. This was the first time it has been reported that NIR-emissive AIEgen as a multifunctional agent can effectively kill gram-positive bacteria *in vivo* and *in vitro* with both specific identification and photodynamics, which provide guidance for the rational design of easy-to-operate and time-saving bacterial identification reagents and the promotion of the development of high-performance antibacterial materials.

The Diagnosis and Treatment of Parkinson's Disease (PD) With AIEgens

PD is one of the most common progressive neurodegenerative diseases, which often occurs in people aged 60 years and over with symptoms of shaking palsy and involuntary tremble (52). However, the exact cause of the disease is unknown (53). Recently, studies have shown that lipid droplets (LDs) serve as containers of triglycerides and cholesteryl esters as well as the dynamic organelles for lipid metabolism, protein storage, signal regulation, and cell apoptosis (54). It was found by Liu et al. (55) that mitochondrial disorder and oxidative stress lead to accumulation of LDs, and the oxidized lipid metabolites further promote mitochondrial disorder and cause neuronal death and PD, which indicates LDs may play an important role in PD's progress. Thus, the real-time monitoring of LDs from PD patients is of great value. Li HL et al. (16) synthesized ultra-stable AIEgen probe 2-DPAN to monitor the dynamic process of LDs in PD model cells. The results show that LDs are closely related to the change of mitochondrial activity; that is, lipase can accelerate the process of cell death, prestimulate LDs through unsaturated fat acid oleic acid (OA), and reduce the process of cell death by inhibiting the production of excess ROS and fat acid so as to protect the mitochondria. Therefore, real-time behavior monitoring of LDs is important and necessary in the early stage of PD prevention. The application of 2-DPAN proves the importance of LDs in neuronal homeostasis, and the effective regulation of LDs may prevent or inhibit the progress of PD. Benefiting from its good specificity, photostability, and biocompatibility, the probe may become a useful tool for studying LD-related diseases.

THE DISADVANTAGE AND IMPROVEMENT OF AIE MATERIALS AND NANO-IMAGING MATERIALS

Deficiencies and Modification of AIEgens

Based on the research on AIEgens in the past 20 years, it can be seen that the introduction of AIE can solve the problem of fluorescent quenching. However, there are still some limitations, such as high hydrophobicity, poor cell compatibility, short emission wavelength, low penetration, long latency (> 5 min), and being time-consuming (56, 57), which severely limit the biological applications of AIE materials *in vivo*. To develop and promote the biomedical applications of fluorescent organic NPs based on AIE materials, their biocompatibility and the application of cell imaging are further studied. The hydrophobic surface of NPs can be modified to be hydrophilic so that they can have good water dispersibility and novel AIE properties. Xi QZ et al. (58) have designed a new system of FL bioprobes based on nano-aggregates combining AIE-based organic fluorogens An18 (derived from 9,10-distyrylanthracene with an alkoxyl end group) and surfactant Pluronic F127. It was also the first time to propose a simple method for preparing AIE-based fluorescent organic nanoparticles (FONs) by mixing AIE units (An18) and surfactant F127. Originating from the hydrophobic interaction between An18 and F127, water-soluble An18-F127 NPs are widely used in cell imaging. The research shows that the modified AIE-based NPs are biocompatible with cells and easy to observe. It means that the surfactant-modified AIE-based FONs have good water solubility, biocompatibility, and a convenient preparation method, which can be used as a new kind of bioimaging dye.

Deficiencies and Modification of Nano-Imaging Materials

As an important part of innate immunity, the complement system is the first defense to deal with invaders and protect the body, and it can be activated by three pathways, i.e., the classical, alternative, and mannan-binding lectin (MBL) pathways. After NPs get into the body, they interact with the innate immune system and generate the immunomodulation reaction based on their physical and chemical properties (19). With the participation of the complement members (see **Figure 3**), the acute anaphylactoid reaction or anaphylactic reaction would be triggered. In order to reduce the adverse reactions and toxicity, it is feasible to use surface modification technology and restrain the formation of complement C3 and C5 invertase so as to improve innate immune compatibility and safety *in vivo*.

Because of high X-ray absorbance, metal nano-imaging materials can be used as radio sensitizers. Nevertheless, this is potentially toxic because of the heavy metal ions. The aqueous or physiological solution of the magnetic NPs (MNPs) used in MRI is less stable and easy to accumulate and precipitate (20), resulting in the decrease of effective concentration in the tissue. Thus, ligand choosing is the premise and basis for optimizing and stabilizing the optical properties of a nanocluster and reducing its toxicity. In addition, according to the physical and chemical properties of NPs, the multifunctional NPs of biocompatibility would be manufactured after the modification (59) for the immune escape and *in vivo* longevity.

The damage of some nano-imaging materials, like Ag NPs and Au NPs, to the human body derives from ROS, which could interact with the cells of the liver, lung, spleen, and skin directly, leading to oxidative damage and inflammation (23). Cytoskeleton damage, mitochondrial activity, and the changes of protein and nucleus metabolism are the main effects of NPs on the cells. Studies of cytotoxicity and genotoxicity show that toxicity of some nano-imaging materials to tumor cells led to cytoskeleton damage and impact cell division, which explain the potential applications and mechanism of nano-imaging materials on malignant tumor therapy.

CONCLUSION

With the rapid development of the emerging field of nanomedicine, nano-imaging materials are applied to daily life and medicine. Functional/smart AIEgen probes have made great progress in specific bacterial imaging and killing, targeted cell/intracellular organelle imaging and ablation, and targeted tumor therapy. At present, biomedical imaging is mainly used for the diagnosis and therapy for image capture. Previous studies demonstrate that most of AIEgens harbor low *in vitro* cytotoxicity, and one of the limitations of AIEgens is that they are not good at building FL "turn-on" nanoprobes. Therefore, complex molecular design and modification must be carried out to obtain multi-functional nano-imaging materials (60). Great efforts have been made to modify new AIEgens and traditional nano-imaging materials for the decrease of the immune reaction and to synthesize multifunctional nano-composite particles through the design of nanostructures, which provides a new method for realizing image-guided tumor therapy and multimode imaging and collaborative therapy. Researchers

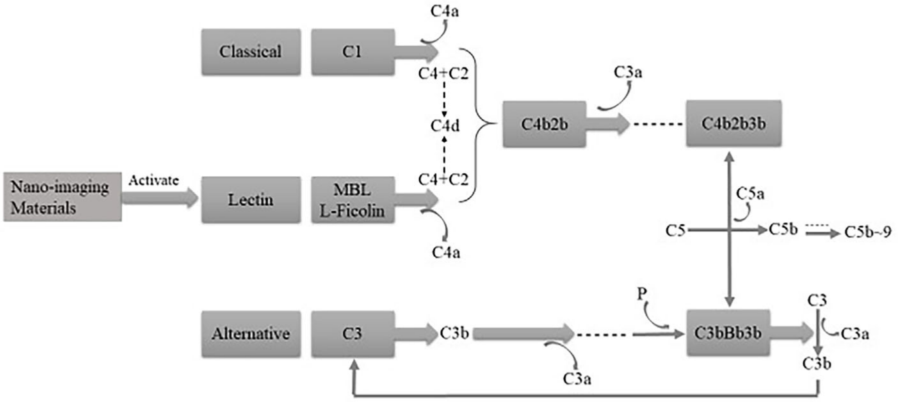

FIGURE 3 | The complement system can be activated by three pathways, that is, classical, alternative, and MBL pathways.

have designed various multifunctional nano-composite particles based on photothermal conversion and the improvement of mediating tumor oxygen levels, which are beneficial for the therapy of combination photothermal and radiation. Additionally, nano-imaging materials can enhance the targeting of drug delivery as the chemotherapy drug carrier and make tumor targeting imaging and combined therapy (chemotherapy and radiotherapy) possible by combining PTT and MRI diagnosis. Similarly, the synthesis and modification of AIEgens through different ways could improve the efficiency of FL imaging-guided PDT, NIR PS with AIE character could be the substitutes of nano-probes and nanomedicines for multiple tumor clinical therapies and real-time supervision and imaging during tumor immune therapy, optimizing the effect of the immune therapy. Nano-imaging materials can not only be used in malignant tumor therapy, but also in benign diseases as probes, which has a high prospective application in diagnosis and treatment.

Nano-imaging materials should be given more attention and research in the future due to their high medical and biomedical value as well as the new ideas and possibilities for people in the field of disease therapy.

AUTHOR CONTRIBUTIONS

HW, WH, and XZ contributed equally. All authors contributed to the article and approved the submitted version.

REFERENCES

1. Aghebati-Maleki A, Dolati S, Ahmadi M, Baghbanzhadeh A, Asadi M, Fotouhi A, et al. Nanoparticles and cancer therapy: Perspectives for application of nanoparticles in the treatment of c ancers. *J Cell Physiol* (2020) 235:1962–72. doi: 10.1002/jcp.29126
2. Yu T, Guo F, Yu Y, Sun T, Ma D, Han J, et al. Fusobacterium nucleatum Promotes Chemoresistance to Colorectal Cancer by Modulating Autophagy. *Cell* (2017) 170:548–63.e16. doi: 10.1016/j.cell.2017.07.008`
3. Wang G, Inturi S, Serkova NJ, Merkulov S, Mccrae K, Russek SE, et al. High-relaxivity superparamagnetic iron oxide nanoworms with decreased immune recognition and long-circulating properties. *ACS Nano* (2014) 8:12437–49. doi: 10.1021/nn505126b
4. Luo J, Xie Z, Lam JWY, Cheng L, Tang BZ, Chen H, et al. Aggregation-induced emission of 1-methyl-1,2,3,4,5-pentaphenylsilole. *Chem Commun* (2001) 18:1740–41. doi: 10.1039/b105159h
5. Wang D, Tang BZ. Aggregation-Induced Emission Luminogens for Activity-Based Sensing. *Acc Chem Res* (2019) 52:2559–70. doi: 10.1021/acs.accounts.9b00305
6. Wong Y, Wang H, Xue M, Zhang P, Lu W, Chen S, et al. Rational design of ratiometric and lysosome-targetable AIE dots for imaging endogenous HClO in live cells. *Mater Chem Front* (2019) 3:203–8. doi: 10.1039/C8QM00511G
7. Gao L, Lin X, Chen X. Ionic liquid decorated AIE luminogen for selective detection of HSA in biofluids and early disease sc reening. *Talanta* (2020) 212:120763. doi: 10.1016/j.talanta.2020.120763
8. Li Y, Wu Q, Kang M, Song N, Wang D, Tang BZ. Boosting the photodynamic therapy efficiency by using stimuli-responsive and AIE-featured nanoparticl es. *Biomaterials* (2020) 232:119749. doi: 10.1016/j.biomaterials.2019.119749
9. Hu Y, Liu J, Xia D, Chen S. Simultaneous analysis of foodborne pathogenic bacteria by an oligonucleotide microarray assay. *J Basic Microbiol* (2012) 52:27–34. doi: 10.1002/jobm.201000458
10. Wen CY, Jiang YZ, Li XY, Tang M, Wu LL, Hu J, et al. Efficient Enrichment and Analyses of Bacteria at Ultralow Concentration with Quick-Response Magnetic Nanospheres. *ACS Appl Mater Interf* (2017) 9:9416–25. doi: 10.1021/acsami.6b16831
11. Baker SJ, Payne DJ, Rappuoli R, De Gregorio E. Technologies to address antimicrobial resistance. *Proc Natl Acad Sci U.S.A.* (2018) 115:12887–95. doi: 10.1073/pnas.1717160115
12. Chen C, Ni X, Jia S, Liang Y, Wu X, Kong D, et al. Massively Evoking Immunogenic Cell Death by Focused Mitochondrial Oxidative Stress using an AIE Lumin ogen with a Twisted Molecular Structure. *Adv Mater* (2019) 31: e1904914. doi: 10.1002/adma.201904914
13. Banda NK, Mehta G, Chao Y, Wang G, Inturi S, Fossati-Jimack L, et al. Mechanisms of complement activation by dextran-coated superparamagnetic iron oxide (SPIO) nanoworms in mouse versus human serum. *Particle Fibre Toxicol* (2014) 11:64. doi: 10.1186/s12989-014-0064-2
14. Cui D, Li J, Zhao X, Pu K, Zhang R. Semiconducting Polymer Nanoreporters for Near-Infrared Chemiluminescence Imaging of Immunoactivation. *Adv Mater* (2020) 32:e1906314. doi: 10.1002/adma.201906314
15. Lee MMS, Xu W, Zheng L, Yu B, Leung ACS, Kwok RTK, et al. Ultrafast discrimination of Gram-positive bacteria and highly efficient photodynamic antibacterial th erapy using near-infrared photosensitizer with aggregation-induced emission characteristics. *Biomaterials* (2020) 230:119582. doi: 10.1016/j.biomaterials.2019.119582
16. Li L, Zhou F, Gao Q, Lu Y, Xu X, Hu R, et al. Visualizing Dynamic Performance of Lipid Droplets in a Parkinson's Disease Model via a Smart Photosta ble Aggregation-Induced Emission Probe. *iScience* (2019) 21:261–72. doi: 10.1016/j.isci.2019.10.027
17. Dobrovolskaia MA, Shurin M, Shvedova AA. Current understanding of interactions between nanoparticles and the immune system. *Toxicol Appl Pharmacol* (2016) 299:78–89. doi: 10.1016/j.taap.2015.12.022
18. Shou P, Yu Z, Wu Y, Feng Q, Zhou B, Xing J, et al. Zn2+ Doped Ultrasmall Prussian Blue Nanotheranostic Agent for Breast Cancer Photothermal Therapy unde r MR Imaging Guidance. *Adv Healthc Mater* (2020) 9: e1900948. doi: 10.1002/adhm.201900948
19. Kononenko V, Narat M, Drobne D. Nanoparticle interaction with the immune system. *Arh Hig Rada Toksikol* (2015) 66:97–108. doi: 10.1515/aiht-2015-66-2582
20. Boyer C, Whittaker MR, Bulmus V, Liu J, Davis TP. The design and utility of polymer-stabilized iron-oxide nanoparticles for nanomedicine applications. *Npg Asia Mater* (2010) 2:23–30. doi: 10.1038/asiamat.2010.6
21. Jiang X, Wang L, Ji Y, Tang J, Tian X, Cao M, et al. Interference of Steroidogenesis by Gold Nanorod Core/Silver Shell Nanostructures: Implications for Re productive Toxicity of Silver Nanomaterials. *Small* (2017) 13:1602855. doi: 10.1002/smll.201602855
22. De Matteis V, Cascione M, Toma CC, Leporatti S. Morphomechanical and organelle perturbation induced by silver nanoparticle exposure. *J Nanopart Res* (2018) 20:273. doi: 10.1007/s11051-018-4383-3
23. Chen L, Wu M, Jiang S, Zhang Y, Li R, Lu Y, et al. Skin Toxicity Assessment of Silver Nanoparticles in a 3D Epidermal Model Compared to 2D Keratinocytes. *Int J Nanomed* (2019) 14:9707–19. doi: 10.2147/IJN.S225451
24. Wang Y, Zhang Y, Wang J, Liang XJ. Aggregation-induced emission (AIE) fluorophores as imaging tools to trace the biological fate of nano -based drug delivery systems. *Adv Drug Delivery Rev* (2019) 143:161–76. doi: 10.1016/j.addr.2018.12.004
25. Xiong LH, He X, Zhao Z, Kwok RTK, Xiong Y, Gao PF, et al. Ultrasensitive Virion Immunoassay Platform with Dual-Modality Based on a Multifunctional Aggregation- Induced Emission Luminogen. *ACS Nano* (2018) 12:9549–57. doi: 10.1021/acsnano.8b05270
26. Kai Z, Xiangdan M, Yu C, Zhou Y, Haifeng D, Yuedong Z, et al. Metal-Organic Framework Nanoshuttle for Synergistic Photodynamic and Low-Temperature Photothermal Therapy. *Adv Funct Mater* (2018) 28 1804634–. doi: 10.1002/adfm.201804634
27. Gambhir SS, Ge TJ, Vermesh O, Spitler R. Toward achieving precision health. *Sci Transl Med* (2018) 10:eaao3612. doi: 10.1126/scitranslmed.aao3612

28. He X, Peng C, Qiang S, Xiong LH, Zhao Z, Wang Z, et al. Less is more: Silver-AIE core@shell nanoparticles for multimodality cancer imaging and synergistic therapy. *Biomaterials* (2020) 238:119834. doi: 10.1016/j.biomaterials.2020.119834
29. Chen C, Ou H, Liu R, Ding D. Regulating the Photophysical Property of Organic/Polymer Optical Agents for Promoted Cancer Phototheranostics. *Adv Mater* (2020) 32:e1806331. doi: 10.1002/adma.201806331
30. Chen C, Ni X, Tian HW, Liu Q, Guo DS, Ding D. Calixarene-Based Supramolecular AIE Dots with Highly Inhibited Nonradiative Decay and Intersystem Crossing for Ultrasensitive Fluorescence Image-Guided Cancer Surgery. *Angew Chem Int Ed Engl* (2020) 59:10008–12. doi: 10.1002/anie.201916430
31. Wu HB, Yang S, Weng HY, Chen Q, Zhao XL, Fu WJ, et al. Autophagy-induced KDR/VEGFR-2 activation promotes the formation of vasculogenic mimicry by glioma stem cells. *Autophagy* (2017) 13:1528–42. doi: 10.1080/15548627.2017.1336277
32. Ibrahim KE, Al-Mutary MG, Bakhiet AO, Khan HA. Histopathology of the Liver, Kidney, and Spleen of Mice Exposed to Gold Nanoparticles. *Molecules* (2018) 23:1848. doi: 10.3390/molecules23081848
33. Ansari MA, Khan HM, Khan AA, Alzohairy MA. Biochemical and histopathological ultrastructural changes caused by ZnO nanoparticles in mice. *Toxicol Environ Chem* (2015) 97:1025–40. doi: 10.1080/02772248.2015.1077960
34. Yang L, Kuang H, Zhang W, Aguilar ZP, Wei H, Xu H. Comparisons of the biodistribution and toxicological examinations after repeated intravenous administration of silver and gold nanoparticles in mice. *Sci Rep* (2017) 7:3303. doi: 10.1038/s41598-017-03015-1
35. Merritt E. *The Relation Between Intensity Of Fluorescence And Concentration In Solid Solutions*. (1926), josa/12/6/josa-12-6-613.pdf.
36. Hu F, Xu S, Liu B. Photosensitizers with Aggregation-Induced Emission: Materials and Biomedical Applications. *Adv Mater* (2018) 30:e1801350. doi: 10.1002/adma.201801350
37. Wang D, Su H, Kwok RTK, Shan G, Leung ACS, Lee MMS, et al. Facile Synthesis of Red/NIR AIE Luminogens with Simple Structures, Bright Emissions, and High Photostabilities, and Their Applications for Specific Imaging of Lipid Droplets and Image-Guided Photodynamic Therapy. *Adv Funct Mater* (2017) 27:1704039. doi: 10.1002/adfm.201704039
38. Liu Y, Hardie J, Zhang X, Rotello VM. Effects of engineered nanoparticles on the innate immune system. *Semin Immunol* (2017) 34:25–32. doi: 10.1016/j.smim.2017.09.011
39. Qi J, Chen C, Ding D, Tang BZ. Aggregation-Induced Emission Luminogens: Union Is Strength, Gathering Illuminates Healthcare. *Adv Healthc Mater* (2018) 7:e1800477. doi: 10.1002/adhm.201800477
40. Jeffrey K, Mariana L, Caleb C, Lawrence C, Joseph G, Denise H, et al. Immunotherapies: Exploiting the Immune System for Cancer Treatment. *J Immunol Res* (2018) 2018:1–16. doi: 10.1155/2018/9585614
41. Wei W, Jiang D, Ehlerding EB, Luo Q, Cai W. Noninvasive PET Imaging of T cells. *Trends Cancer* (2018) 4:359–73. doi: 10.1016/j.trecan.2018.03.009
42. Park EJ, Bae E, Yi J, Kim Y, Choi K, Lee SH, et al. Repeated-dose toxicity and inflammatory responses in mice by oral administration of silver nanoparticles. *Environ Toxicol Pharmacol* (2010) 30:162–8. doi: 10.1016/j.etap.2010.05.004
43. Wang G, Zhou LY, Zhang PF, Zhao EG, Zhou LH, Chen D, et al. Fluorescence Self-Reporting Precipitation Polymerization Based on Aggregation-Induced Emission for Constructing Optical Nanoagents. *Angewandte Chem Internat Ed* (2020) 59:10122–8. doi: 10.1002/anie.201913847
44. Bartell JA, Sommer LM, Haagensen J, Loch A, Espinosa R, Molin S, et al. Evolutionary highways to persistent bacterial infection. *Nat Commun* (2019) 10:629. doi: 10.1038/s41467-019-08504-7
45. Lehar SM, Pillow T, Xu M, Staben L, Kajihara KK, Vandlen R, et al. Novel antibody-antibiotic conjugate eliminates intracellular S. aureus. *Nature* (2015) 527:323–8. doi: 10.1038/nature16057
46. Manian FA, Meyer PL, Setzer J, Senkel D. Surgical site infections associated with methicillin-resistant Staphylococcus aureus: do postoperative factors play a role? *Clin Infect Dis* (2003) 36:863–8. doi: 10.1086/368195
47. Bullman S, Pedamallu CS, Sicinska E, Clancy TE, Zhang X, Cai D, et al. Analysis of Fusobacterium persistence and antibiotic response in colorectal cancer. *Science* (2017) 358:1443–8. doi: 10.1126/science.aal5240
48. Wang J, Wang X, Li Y, Yan S, Zhou Q, Gao B, et al. A novel, universal and sensitive lateral-flow based method for the detection of multiple bacterial contamination in platelet concentrations. *Anal Sci* (2012) 28:237–41. doi: 10.2116/analsci.28.237
49. Lam SJ, O'brien-Simpson NM, Pantarat N, Sulistio A, Wong EH, Chen YY, et al. Combating multidrug-resistant Gram-negative bacteria with structurally nanoengineered antimicrobial peptide polymers. *Nat Microbiol* (2016) 1:16162. doi: 10.1038/nmicrobiol.2016.162
50. Arias CA, Murray BE. Antibiotic-resistant bugs in the 21st century–a clinical super-challenge. *N Engl J Med* (2009) 360:439–43. doi: 10.1056/NEJMp0804651
51. Kang M, Zhou C, Wu S, Yu B, Zhang Z, Song N, et al. Evaluation of Structure-Function Relationships of Aggregation-Induced Emission Luminogens for Simultaneous Dual Applications of Specific Discrimination and Efficient Photodynamic Killing of Gram-Positive Bacteria. *J Am Chem Soc* (2019) 141:16781–89. doi: 10.1021/jacs.9b07162
52. Dauer W, Przedborski S. Parkinson's disease: mechanisms and models. *Neuron* (2003) 39:889–909. doi: 10.1016/S0896-6273(03)00568-3
53. Collier TJ, Kanaan NM, Kordower JH. Ageing as a primary risk factor for Parkinson's disease: evidence from studies of non-human primates. *Nat Rev Neurosci* (2011) 12:359–66. doi: 10.1038/nrn3039
54. Martin S, Parton RG. Lipid droplets: a unified view of a dynamic organelle. *Nat Rev Mol Cell Biol* (2006) 7:373–8. doi: 10.1038/nrm1912
55. Liu L, Zhang K, Sandoval H, Yamamoto S, Jaiswal M, Sanz E, et al. Glial lipid droplets and ROS induced by mitochondrial defects promote neurodegeneration. *Cell* (2015) 160:177–90. doi: 10.1016/j.cell.2014.12.019
56. Hu R, Zhou F, Zhou T, Shen J, Wang Z, Zhao Z, et al. Specific discrimination of gram-positive bacteria and direct visualization of its infection towards mammalian cells by a DPAN-based AIEgen. *Biomaterials* (2018) 187:47–54. doi: 10.1016/j.biomaterials.2018.09.019
57. Kang M, Kwok RTK, et al. A multifunctional luminogen with aggregation-induced emission characteristics for selective imaging and photodynamic killing of both cancer cells and Gram-positive bacteria. *J Mater Chem B* (2018) 6:3894–903. doi: 10.1039/C8TB00572A
58. Zhang X, Zhang X, Wang S, Liu M, Tao L, Wei Y. Surfactant modification of aggregation-induced emission material as biocompatible nanoparticles: facile preparation and cell imaging. *Nanoscale* (2013) 5:147–50. doi: 10.1039/C2NR32698A
59. El-Sayed N, Trouillet V, Clasen A, Jung G, Hollemeyer K, Schneider M. NIR-Emitting Gold Nanoclusters-Modified Gelatin Nanoparticles as a Bioimaging Agent in Tissue. *Adv Healthc Mater* (2019) 8:e1900993. doi: 10.1002/adhm.201900993
60. Gao H, Zhang X, Chen C, Kai L, Dan D. Unity Makes Strength: How Aggregation-Induced Emission Luminogens Advance the Biomedical Field. *Adv Biosyst* (2018) 2:1800074. doi: 10.1002/adbi.201800074

Conflict of Interest: The authors declare that the research was conducted in the absence of any commercial or financial relationships that could be construed as a potential conflict of interest.

frontiers in Immunology

MINI REVIEW
published: 16 February 2021
doi: 10.3389/fimmu.2021.635558

The Promise of Aggregation-Induced Emission Luminogens for Detecting COVID-19

Zongwei Liu[1], **Ting Meng**[2], **Xiaofang Tang**[3], **Ran Tian**[4*] and **Weijiang Guan**[3*]

[1] Department of Respiratory Medicine, Lianyungang Hospital of Traditional Chinese Medicine, Affiliated Hospital of Nanjing University of Chinese Medicine, Lianyungang, China, [2] The First Clinical Medical College, Nanjing University of Chinese Medicine, Nanjing, China, [3] State Key Laboratory of Chemical Resource Engineering, College of Chemistry, Beijing University of Chemical Technology, Beijing, China, [4] Public Laboratory, Tianjin Medical University Cancer Institute and Hospital, National Clinical Research Center for Cancer, Key Laboratory of Cancer Prevention and Therapy, Tianjin's Clinical Research Center for Cancer, Tianjin, China

The long-term pandemic of coronavirus disease 2019 (COVID-19) requires sensitive and accurate diagnostic assays to detect severe acute respiratory syndrome coronavirus 2 (SARS-CoV-2) virus and SARS-CoV-2 antibodies in infected individuals. Currently, RNA of SARS-CoV-2 virus is mainly detected by reverse transcription-polymerase chain reaction (RT-PCR)-based nucleic acid assays, while SARS-CoV-2 antigen and antibody are identified by immunological assays. Both nucleic acid assays and immunological assays rely on the luminescence signals of specific luminescence probes for qualitative and quantitative detection. The exploration of novel luminescence probes will play a crucial role in improving the detection sensitivity of the assays. As innate probes, aggregation-induced emission (AIE) luminogens (AIEgens) exhibit negligible luminescence in the free state but enhanced luminescence in the aggregated or restricted states. Moreover, AIEgen-based nanoparticles (AIE dots) offer efficient luminescence, good biocompatibility and water solubility, and superior photostability. Both AIEgens and AIE dots have been widely used for high-performance detection of biomolecules and small molecules, chemical/biological imaging, and medical therapeutics. In this review, the availability of AIEgens and AIE dots in nucleic acid assays and immunological assays are enumerated and discussed. By building a bridge between AIE materials and COVID-19, we hope to inspire researchers to use AIE materials as a powerful weapon against COVID-19.

Keywords: COVID-19, diagnosis, aggregation-induced emission, immunoassay, nucleic acid

Edited by:
Pengfei Zhang,
Shenzhen Institutes of Advanced Technology (CAS), China

Reviewed by:
Xiaoding Lou,
China University of Geosciences Wuhan, China
Lei Zheng,
Southern Medical University, China

***Correspondence:**
Ran Tian
rantian@tmu.edu.cn
Weijiang Guan
wjguan@mail.buct.edu.cn

Specialty section:
This article was submitted to Molecular Innate Immunity, a section of the journal Frontiers in Immunology

Received: *30 November 2020*
Accepted: *25 January 2021*
Published: *16 February 2021*

Citation:
Liu Z, Meng T, Tang X, Tian R and Guan W (2021) The Promise of Aggregation-Induced Emission Luminogens for Detecting COVID-19. Front. Immunol. 12:635558. doi: 10.3389/fimmu.2021.635558

INTRODUCTION

Coronavirus disease 2019 (COVID-19), caused by severe acute respiratory syndrome coronavirus 2 (SARS-CoV-2) virus, has spread over 216 countries/regions and resulted in more than 84 million infected cases and nearly 1.8 million deaths (1). SARS-CoV-2 is an RNA virus and has five open reading frames (ORFs) to encode the hemagglutinin esterase dimer protein (HE), the spike protein (S), the envelope protein (E), the glycosylated membrane protein (M), and the nucleocapsid protein (N), respectively (2, 3). The pathogenesis of SARS-CoV-2 infection contains two courses: virus entry cell and virus replicates. During the cellular entry of the virus, the S protein plays a key role through host recognition and is closely associated with the human receptor angiotensin-converting enzyme 2 (ACE2), which is highly expressed in the lung, stomach, small intestine, colon, kidney, and lymph nodes (4–6). The human immune system responds to viral infection *via* the innate and adaptive immune systems, gradually producing antibodies against SARS-CoV-2 (7). Despite the use of multiple therapies over nearly a year, there are still no effective treatments for SARS-CoV-2 infection. Thus, the most effective and economical strategy is to identify infected individuals and prevent healthy individuals from coming into contact with infected individuals.

Current detection methods can be divided into two categories: nucleic acid assays and immunological assays (8–12). Nucleic acid assays directly detect the presence of SARS-CoV-2 virus in the upper respiratory tract during the first days of infection. Among nucleic acid assays, reverse transcription-polymerase chain reaction (RT-PCR)-based assays are currently considered the gold standard and are generally composed of six steps: (1) collection of respiratory samples using swabs, (2) inactivation of SARS-CoV-2 using lysis buffer, (3) purification of the SARS-CoV-2 RNA, (4) conversion of the purified RNA to complementary DNA (cDNA) using reverse transcriptase, (5) amplification of the specific regions of cDNA using primers, and (6) detection of the amplified cDNA using luminescence probes (11). The design of primers and probes targeting different regions of the SARS-CoV-2 genome can significantly affect the detection sensitivity, as low-performance nucleic acid amplifications and probes may generate false negatives. Moreover, nucleic acid assays require specialized instruments and complicated operations and are of little help in identifying past infections and monitoring infection status and immune progress (13). On the other hand, immunological assays with simpler design enable convenient and rapid detection of SARS-CoV-2 antigen, immunoglobulin M (IgM) and immunoglobulin G (IgG) antibodies in the serum of infected individuals (8). IgM and IgG are generally produced after 5–10 d upon SARS-CoV-2 infection and last for several weeks (8). Immunological assays rely on the formation of immune complexes between the antibody and antigen. In the presence of appropriate substrates, luminescence probes labeled on the antibody or antigen can be activated to produce a given luminescence that is capable of both qualitative observation under a UV lamp and qualitative analysis on a spectrophotometer. Obviously, the detection sensitivity of nucleic acid assays and immunological assays is closely related to the performance of the luminescence probes. However, conventional luminescence probes inevitably encounter the aggregation-caused quenching (ACQ) problem at high target concentrations, greatly limiting their performance.

Aggregation-induced emission (AIE), first proposed by Tang in 2001, is a diametrically opposite phenomenon to ACQ (14). The luminogen with AIE characteristics is named AIEgen, which has no/low luminescence in the molecularly dispersed state but enhanced luminescence in the aggregated state (14–18). Further mechanistic studies indicate that strong luminescence can be also achieved by restricting the intramolecular motions (RIM) of the AIEgens in the molecularly dispersed state (16–18). After 20 years of outstanding development, a great family of AIEgens has been established, ranging from twisted conjugated AIEgens to planar conjugated AIEgens and irregular non-conjugated AIEgens (14–21). Moreover, AIEgen-based nanoparticles (AIE dots) have been well-developed to obtain highly efficient luminescence (22–25). Both AIEgens and AIE dots are widely used for the high-performance detection of small molecules and biomolecules, chemical/biological imaging, and medical therapeutics (15, 22–33). Undoubtedly, some of them can be used for nucleic acid assays and immunological assays. Therefore, this review aims to bridge the gap between AIE materials and COVID-19 detection and proposes AIE materials as potential diagnostic weapons against COVID-19. Possible candidates for nucleic acid assays and immunological assays are summarized. This knowledge may contribute to the development of advanced diagnostic kits that are effective for more sensitive assays.

AIEgens EXHIBIT GREAT POTENTIAL FOR NUCLEIC ACID ASSAYS

Since the number of viruses reach the maximum in the first few days of infection, nucleic acid assays can provide the earliest information to determine the presence or absence of the SARS-CoV-2 virus (9). Although the protocols and advances of nucleic acid assays have been reviewed (8–12), little attention is paid to the design of luminescence probes for highly sensitive detection of the amplified cDNA. Typically, commercial double-stranded DNA (dsDNA) binding dyes (e.g., SYBR Green) show low luminescence in the free state but enhanced luminescence upon insertion into the dsDNA sequence (9). Their luminescence intensity increases quantitatively with the exponential amplification of cDNA. However, the short Stokes shift (<30 nm) allows a large overlap between the absorption and emission spectra, which leads to self-absorption or inner-filter effects, thus reducing the signal-to-noise ratio and the detection sensitivity (30). There is no doubt that further innovations in producing more efficient luminescence signals and outputs could significantly improve the detection sensitivity. Therefore, this section focuses on the great potential of using AIEgen-based DNA probes to improve the sensitivity of current nucleic acid assays.

Similar to SYBR Green, AIEgen-based DNA probes show low luminescence in the free state but enhanced luminescence upon binding to dsDNA, which is caused by RIM (32–51). AIEgen-based DNA probes (**Figure 1**) consist of two parts: AIE-active groups for producing light-up signals and targeting groups for binding to DNA (34–53). The AIE-active groups have a larger Stokes shift (>100 nm) compared to SYBR Green, which prevents the reabsorption or inner-filter effects as well as aggregation-caused quenching, thereby improving sensitivity. The effect of AIEgen structures on DNA detection has been systematically revealed by studying the number of binding groups, the length of hydrophobic linking groups and the molecular conformation. Taking the AIEgens **1**, **3**, and **5** as examples (39, 42), their cationic amino-groups can endow them with good water solubility to avoid the aggregation and fluorescence of the AIE-active tetraphenylethene (TPE) groups. Meanwhile, these amino-modified AIEgens can firmly bind

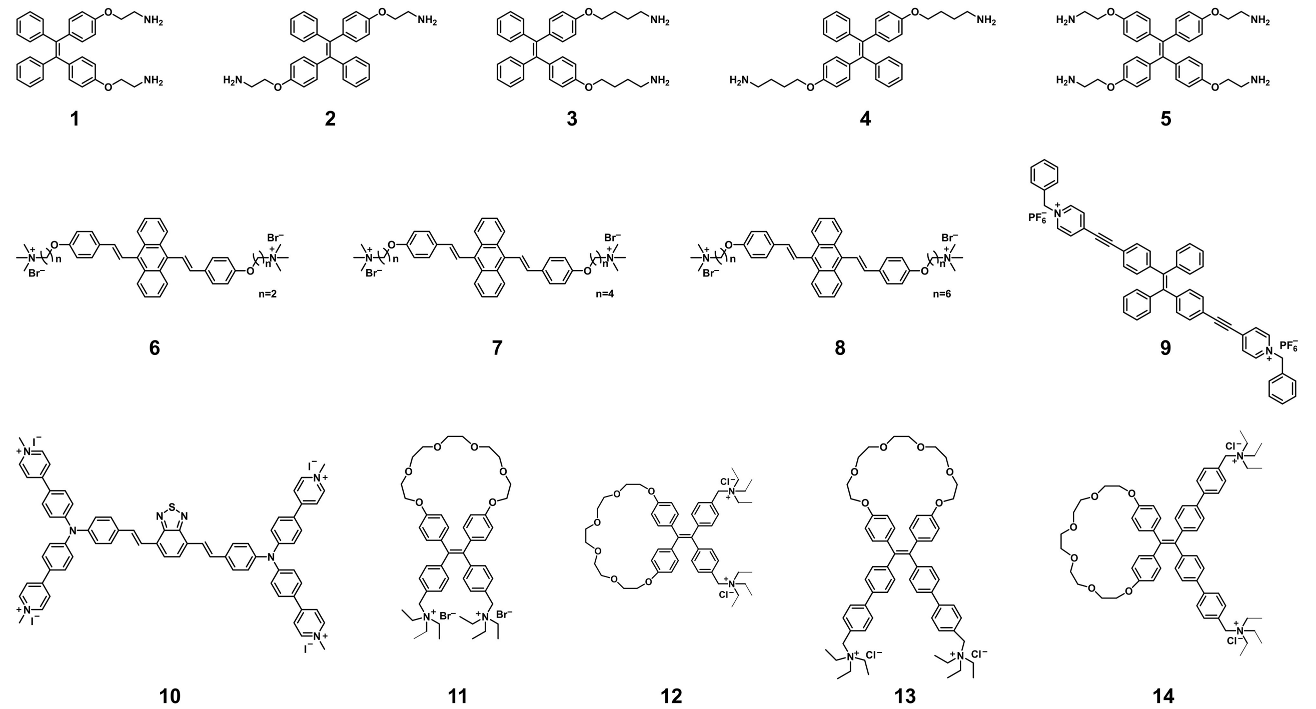

FIGURE 1 | Chemical structures of AIEgens for the detection of nucleic acids. Adapted and modified with permission from Xu et al. (39) (Copyright 2014 American Chemical Society), Wang et al. (44) (Copyright 2016 Wiley-VCH Verlag GmbH & Co. KGaA, Weinheim), Wang et al. (47) (Copyright 2018 Royal Society of Chemistry), Gao et al. (48) (Copyright 2019 American Chemical Society), and Yuan et al. (52) (Copyright 2020 American Chemical Society).

negatively charged dsDNA through electrostatic interactions and hydrogen bonds, resulting in TPE aggregation to display strong fluorescence. The detection limit of AIEgen **1** and AIEgen **3** with two amino-groups were much lower than that of AIEgen **5** with four amino-groups, indicating that the extra two amino-groups cannot make AIEgens bind dsDNA more firmly but reduce the aggregation of TPE groups. On the other hand, AIEgen **3** with longer hydrophobic linking groups showed higher sensitivity than AIEgen **1** with shorter hydrophobic linking groups. This result demonstrated that stronger hydrophobic interactions between AIEgens can facilitate the aggregation of TPE groups, leading to the enhanced fluorescence and higher sensitivity. Based on the revealed relationship between the AIEgen structures and detection sensitivity, AIEgens **11–14** with restriction of double-bond rotation were developed to further improve the sensitivity of sensing DNA (52). In addition, the conformational change of AIEgen **10** results in a two-color fluorescent signal from red to green, enabling selective and sensitive determination of dsDNA (48). When bound to anionic macromolecules, AIEgen **10** emits a bright red fluorescence at about 640 nm. Interestingly, dsDNA can wrap around AIEgen **10** and change its molecular conformation, resulting in a change in conjugation and bright green fluorescence of about 537 nm. From these published studies, it is understood that AIEgens with two binding sites, proper hydrophobicity and variable conformation enable sensitive detection of dsDNA. To facilitate the utilization of AIEgen-based DNA probes, their detection limits for dsDNA are summarized in **Table 1**. It is clear that AIEgen-based DNA probes are like a vast treasure trove, and some of them can serve as reliable and sensitive fluorescence probes that can be quickly adapted to SARS-CoV-2 PCR assays after proper calibration. At the same time, more efforts are needed to develop new AIEgens for other nucleic acid-based SARS-CoV-2 assays.

AIEgens EXHIBIT GREAT POTENTIAL FOR IMMUNOLOGICAL ASSAYS

Theoretically, if the luminescence signals can increase with the concentrations of luminescent labels without the ACQ problem, the detection sensitivity for immunological assays will be continuously improved. This is exactly the strength of AIE, therefore, this section focuses on the great potential of using AIEgens and AIE dots to improve the sensitivity of current immunoassays, such as enzyme-linked immunosorbent assays (ELISA) and lateral flow immunoassays.

ELISA is typically performed on the plate wells coated with the SARS-CoV-2 viral protein. The SARS-CoV-2 antibody (if present) can specifically bind the SARS-CoV-2 viral protein to form antibody–protein complex, which can be detected by an additional tracer antibody. This assay is very fast and results can be obtained within 1–5 h. Various AIEgens with switchable luminescence have been successfully used in ELISA (54–58), and can be good candidates for constructing ELISA to detect

TABLE 1 | Summary of detection limits for dsDNA.

AIEgens	Target analyte	LOD	References
1	75–300 bp	4 ng/band	(39)
	50 bp	10.5 ng/band	
	35 bp	15 ng/band	
5	50 bp	>42 ng/band	
3	75–300 bp	1 ng/band	
	50 bp	<3.5 ng/band	
	35 bp	5 ng/band	
	25 bp	7.5 ng/band	
	20 bp	8 ng/band	
	15 bp	19 ng/band	
	10 bp	<24 ng/band	
1	75–300 bp	1 ng/band	(42)
	50 bp	<3.5 ng/band	
	35 bp	2.5 ng/band	
	25 bp	5 ng/band	
	20 bp	5.3 ng/band	
	15 bp	9.5 ng/band	
	10 bp	12 ng/band	
6 + GO1	T1	0.17×10^{-9} M	(44)
6 + GO2		11.8×10^{-9} M	
6 + GO3		15.5×10^{-9} M	
7 + GO1		2.7×10^{-9} M	
7 + GO2		22.9×10^{-9} M	
7 + GO3		26.1×10^{-9} M	
8 + GO1		2.1×10^{-9} M	
8 + GO2		24.1×10^{-9} M	
8 + GO3		22.4×10^{-9} M	
9	DNA (cas: 9007-49-2)	0.02 μg/mL	(47)
10	ct DNA	1.75 ng/mL	(48)
	WT HIV DNA	7.2×10^{-11} M	
11	FS-DNA	123 pM	(52)
13		74 pM	
12		496 pM	
14		235 pM	
11	ct DNA	7.3 ng/mL	
13		1.6 ng/mL	
12		22 ng/mL	
14		2.1 ng/mL	

SARS-CoV-2 infection. For example, a dual-modality readout immunoassay platform was developed using AIEgen-based signal unit consisting of streptavidin-alkaline phosphatase (SA-ALP), TPE-APP with enzyme cleavage sites, and gold nanoparticles (56). When the immunocapture unit composed of magnetic beads, anti-VP1 monoclonal antibodies (mAb-VP1), rabbit polyclonal antibodies (P-Ab) and biotinylated antibodies (Biotin-Ab) captures the target EV71 virus, SA-ALP will promote the hydrolysis of the water-soluble TPE-APP to produce the water-insoluble TPE-DMA, resulting in the aggregation of TPE-DMA in water and the emission of bright fluorescence (**Figures 2A,B**). The fluorescence turn-on mode gives the immunoassay platform a lower detection limit, as low as 1.4 copies/μL (56). At the same time, the hydrolysis of TPE-APP can mediate the reduction of silver ions, thereby generating silver nanoshells on the surface of gold nanoparticles. The resulting nanoshells cause a significant plasmon color change, which can be clearly recognized by the naked eye in a wide range from 1.3×10^3 to 2.5×10^6 copies/μL (56). Additionally, the immunocapture unit can capture different wanted targets (e.g., H7N9 virus and Zika virus) through conjugating suitable antibodies to achieve accurate and ultrasensitive detection. It can be anticipated that the proposed protocol could inspire and stimulate new developments in clinical diagnosis of SARS-CoV-2 viral protein with high accuracy and sensitivity by varying AIEgens with switchable luminescence. Compared to most turn-off fluorescent probes, the fluorescence turn-on property gives AIEgens a unique advantage in terms of signal reliability and sensitivity.

Lateral flow immunoassay is typically performed in a paper-like membrane strip with two lines (8). The test line is coated with colorimetric or fluorescent material-antibody conjugates, and the control line is coated with capture antibodies. After depositing the test person's blood on the membrane strip, the SARS-CoV-2 antibody (if present) can specifically bind to the colorimetric or fluorescent material-antibody conjugate while flowing through the test line. The resulting complex continues to move until it is immobilized by the capture antibodies on the control line, causing a visible line under daylight or ultraviolet (UV) light. It is worth noting that the sensitivity of the fluorescent signal is much higher than that of the colorimetric signal. By virtue of the AIE feature, AIEgens can be integrated into nanoparticles at high concentrations, resulting in one AIE dot for labeling in response to one binding unit (59–61). For example, AIEgen-based fluorescent microsphere (AIEFM) was obtained by self-assembly of poly(methyl methacrylate) (PMMA), poly (maleic anhydride-alt-1-octadecene) (PMAO), sodium dodecyl sulfate (SDS), and AIE-active TCBPE (**Figures 2C,D**). The hydrophilic part of PMAO acts outward as a functional group to conjugate with anti-*E. coli* O157:H7 monoclonal antibody, forming the fluorescent immunoprobe (AIEFM-mAb) (59). Anti-*E. coli* O157:H7 polyclonal antibody (pAb) was immobilized on the test line (T) of the nitrocellulose membrane while goat anti-mouse antibody (sAb) was immobilized on the control line (C). The target *E. coli* O157:H7 (if present) can be specifically captured by mixing with AIEFM-mAb to generate bright fluorescence on both the test line and control line. Otherwise, AIEFM-mAb can only be captured by sAb on the control line to emit bright fluorescence. The advantage of using AIE-active TCBPE is that the higher the loading of TCBPE, the stronger the fluorescence signal and the higher the detection sensitivity. As a result, the AIEFM endows the lateral flow immunosensor with a very low detection limit, down to 3.98×10^3 CFU/mL, which is about 10 times lower than that of the two commercial FMs (59). Undoubtedly, the above strategy is also applicable to the construction of lateral flow immunoassay kits for detecting SARS-CoV-2 antigen and antibody. Higher performance detection can be achieved not only by using different AIEgens for AIEFM, but also by using other AIE dots. In addition, some news reported that lateral flow immunoassay

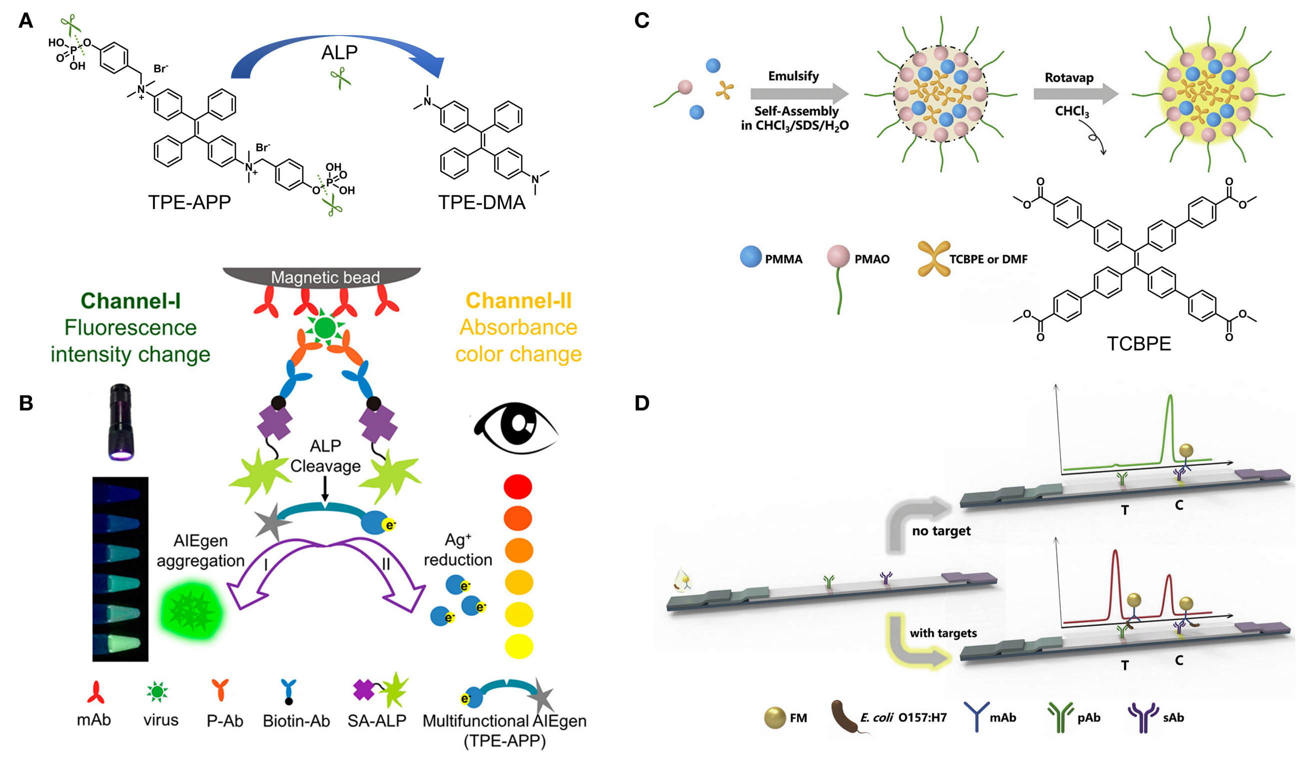

FIGURE 2 | (A) ALP-catalyzed hydrolysis of TPE-APP to TPE-DMA. **(B)** Schematic illustration of fluorescent and plasmonic colorimetric dual-modality for virus detection based on the ALP-catalyzed hydrolysis of TPE-APP. Reprinted with permission from Xiong et al. (56). Copyright 2018 American Chemical Society. **(C)** One-pot synthesis strategy and **(D)** the principle of the immunochromatographic assay based on AIEFM. Reprinted with permission from Zhang et al. (59). Copyright 2019 Elsevier B.V.

kits for SARS-CoV-2 antigen or antibody detection have been developed through the use of highly luminescent AIE dots (62, 63). Therefore, it is reasonable to conclude that AIEgens-/AIE dots-based SARS-CoV-2 immunoassay kits can be designed and produced with higher sensitivity and lower detection limit.

To facilitate the understanding and utilization of AIE dots, current AIE dots are divide into two categories: pure AIE dots and composite AIE dots (22–25). The commonly used preparation method is anti-solvent precipitation, which is achieved by adding an anti-solvent in which AIEgens are poorly soluble or by reducing the volume of a solvent in which AIEgens are well soluble. This method is convenient and principally applicable to any AIEgen to form the pure AIE dots. However, the formed pure AIE dots usually have difficult to control particle morphology (e.g., spheres, ellipsoids, and bulk amorphous), particle size, and surface modification, making them difficult to perform desired and specific applications. To overcome these difficulties, more sophisticated molecular designs and synthetic efforts are required to obtain functional AIEgens. On the other hand, the composite AIE dots are formed from encapsulating various AIEgens into the different amphiphile matrices. The amphiphile matrices provide not only stability for the AIE dots and water solubility for the organic AIEgens, but also enhance the control of morphology and size of AIE dots. By simultaneously precipitating AIEgens and amphiphilic matrices, spherical AIE dots of uniform particle sizes are usually produced, which can be easily further modified. The commercial matrices include, but are not limited to: poly(ethylene glycol) derivatives (e.g., 1,2-distearoyl-sn-glycero-3-phosphoethanolamine-N-[methoxy(polyethylene glycol)-2000] (DSPE-PEG$_{2000}$), poly(ethylene glycol)-*b*-polystyrene (PEG-*b*-PS), 1,2-distearoyl-sn-glycero-3-phosphoethanolamine-N-[folate(polyethylene glycol)-5000] (DSPE-PEG$_{5000}$-folate), etc.), bovine serum albumin (BSA), and biocompatible surfactants (e.g., pluronic F127 and lecithin). It is worth noting that the internal dispersion of AIEgens throughout the amphiphilic matrix may be stochastic and vary from molecular to aggregate distributions when preparing and using the composite AIE dots. Compared to the pure AIE dots, the composite AIE dots preserve the properties of both materials to offer a number of unique advantages: (1) synthetic efforts are minimized by reducing the hydrophilic groups; (2) luminescence performance are well-tuned by mixing various AIEgens in different concentrations; and (3) high specificity and responsiveness are achieved by using the amphiphilic matrices to conjugate with diverse linkers.

CONCLUSION

Global health is facing the most dangerous situation regarding the COVID-19 pandemic. Owing to the large number of infected cases worldwide, the rapid long-term spread, and lack of effective treatments, there is a continuing need for more sensitive, low-cost, rapid, and point-of-care diagnostic kits to

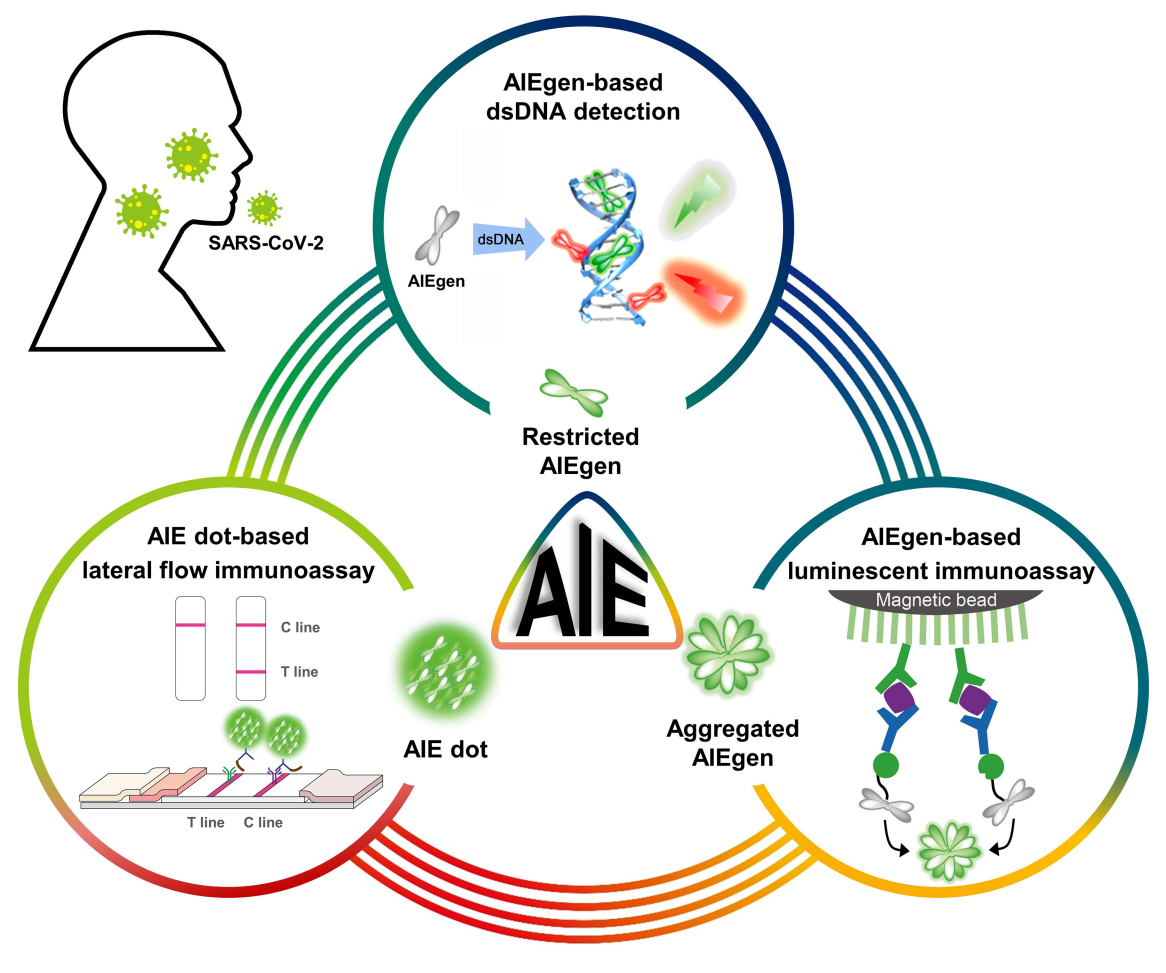

SCHEME 1 | Schematic diagram of AIEgens and AIE dots as potential tools for COVID-19 detection. Partially cited from Gao et al. (48), Xiong et al. (56), and Zhang et al. (59).

identify cases of SARS-CoV-2 infection in communities and individuals without advanced facilities. To date, while RT-PCR assays have become the primary technique for detection of SARS-CoV-2 RNA, other nucleic acid assays including isothermal amplification assays, hybridization microarray assays, amplicon-based metagenomics sequencing, and the cutting-edge CRISPR-related technologies have also been developed (64). Challenges related to current nucleic acid assays mainly include improving detection sensitivity to eliminate false negatives and performing rapid and point-of-care tests outside of sophisticated laboratories. On the other hand, immunological assays are capable of detecting both SARS-CoV-2 antigens and antibodies. Immunoassays for antigens enable direct, rapid, low-cost, and point-of-care detection of SARS-CoV-2 infection at an early stage. Since antigen proteins are unable to be amplified like viral genes, it is crucial to develop new fluorescent probes to improve sensitivity. Immunoassays for antibodies can provide valuable knowledge about the course and extent of the immune response, which are useful in further identifying infected individuals and their close contacts. In particular, the immune persistence of healthy participants can be well-tracked during the vaccination phase. Based on the challenges present in these assays, this review highlights the inherent advantages of AIEgens and AIE dots that can help improve sensitivity (**Scheme 1**). AIEgens used in nucleic acid assays show negligible fluorescence in the free state but turn-on fluorescence upon binding to dsDNA, and the fluorescence signals increase with the binding numbers without the ACQ problem. Similarly, the AIE dots used in the immunoassays can continuously increase the fluorescence intensity by increasing the loading concentration of AIEgens.

In addition, there are some issues that need further improvement when AIE materials are used to COVID-19 detection: (1) development of the sequence-specific DNA probes labeled with AIE dots and quenchers; (2) promotion of AIE dots-based lateral flow immunoassay kits for COVID-19 clinical testing; (3) diversification of AIEgens and AIE dots that can be directly labeled with highly targeted molecules (e.g., antibodies); and (4) further attempts to use AIE materials for studying immune mechanisms and pharmacological treatment of COVID-19 infection (65). With these solid foundations and promising possibilities, there is no doubt that AIE materials should be regarded as a promising anti-SARS-CoV-2 weapon.

AUTHOR CONTRIBUTIONS

All authors listed have made a substantial, direct and intellectual contribution to the work, and approved it for publication.

FUNDING

This work was supported by the National Natural Science Foundation of China (21804006 and 81903092), Beijing Natural Science Foundation (2212013), Science Foundation of Tianjin Health Bureau (RC20190), the Fundamental Research Funds for the Central Universities (buctrc201820), and Changjiang Scholars and Innovative Research Team (No. IRT_14R40).

REFERENCES

1. World Health Organization. *WHO Coronavirus Disease (COVID-19) Dashboard*. (2020). Available online at: https://covid19.who.int (accessed January 5, 2021).
2. Kumari P, Singh A, Ngasainao MR, Shakeel I, Singh IK, MI H, et al. Potential diagnostics and therapeutic approaches in COVID-19. *Clin Chim Acta.* (2020) 510:488–97. doi: 10.1016/j.cca.2020.08.013
3. Carter-Timofte ME, Jorgensen SE, Freytag MR, Thomsen MM, Hait AS, Mogensen TH, et al. Deciphering the role of host genetics in susceptibility to severe COVID-19. *Front Immunol.* (2020) 11:1606. doi: 10.3389/fimmu.2020.01606
4. Wiersinga WJ, Rhodes A, Cheng AC, Peacock SJ, Prescott HC. Pathophysiology, transmission, diagnosis, and treatment of coronavirus disease 2019 (COVID-19). *J Am Med Assoc.* (2020) 324:782–93. doi: 10.1001/jama.2020.12839
5. Freeman TL, Swartz TH. Targeting the NLRP3 Inflammasome in Severe COVID-19. *Front. Immunol.* (2020) 11:1518. doi: 10.3389/fimmu.2020.01518
6. Li F, Li W, Farzan M, Harrison SC. Structure of SARS coronavirus spike receptor-binding domain complexed with receptor. *Science.* (2005) 309:1864–1868. doi: 10.1126/science.1116480
7. Aoshi T, Koyama S, Kobiyama K, Akira S, Ishii KJ. Innate and adaptive immune responses to viral infection and vaccination. *Curr Opin Virol.* (2011) 1:226–232. doi: 10.1016/j.coviro.2011.07.002
8. Carter LJ, Garner LV, Smoot JW, Li Y, Zhou Q, Saveson CJ, et al. Assay techniques and test development for COVID-19 diagnosis. *ACS Cent Sci.* (2020) 6:591–605. doi: 10.1021/acscentsci.0c00501
9. Esbin MN, Whitney ON, Chong S, Maurer A, Darzacq X, Tjian R. Overcoming the bottleneck to widespread testing: a rapid review of nucleic acid testing approaches for COVID-19 detection. *RNA.* (2020) 26:771–83. doi: 10.1261/rna.076232.120
10. Thompson D, Lei Y. Mini review: recent progress in RT-LAMP enabled COVID-19 detection. *Sensors Actuat Rep.* (2020) 2:100017. doi: 10.1016/j.snr.2020.100017
11. Jayamohan H, Lambert CJ, Sant HJ, Jafek A, Patel D, Feng H, et al. SARS-CoV-2 pandemic: a review of molecular diagnostic tools including sample collection and commercial response with associated advantages and limitations. *Anal Bioanal Chem.* (2021) 413:49–71. doi: 10.1007/s00216-020-02958-1
12. Sharifi M, Hasan A, Haghighat S, Taghizadeh A, Attar F, Bloukh SH, et al. Rapid diagnostics of coronavirus disease 2019 in early stages using nanobiosensors: challenges and opportunities. *Talanta.* (2021) 223:121704. doi: 10.1016/j.talanta.2020.121704
13. Tang YW, Schmitz JE, Persing DH, Stratton CW. Laboratory diagnosis of COVID-19: current issues and challenges. *J Clin Microbiol.* (2020) 58: e00512-20. doi: 10.1128/JCM.00512-20
14. Luo J, Xie Z, Lam JWY, Cheng L, Chen H, Tang BZ, et al. Aggregation-induced emission of 1-methyl-1,2,3,4,5-pentaphenylsilole. *Chem Commun.* (2001) 18:1740–41. doi: 10.1039/b105159h
15. Mei J, Leung NLC, Kwok RTK, Lam JWY, Tang BZ. Aggregation-induced emission: together we shine, united we soar. *Chem Rev.* (2015) 115:11718–940. doi: 10.1021/acs.chemrev.5b00263
16. Zhao Z, Zhang H, Lam JWY, Tang BZ. Aggregation-induced emission: new vistas at the aggregate level. *Angew Chem Int Ed.* (2020) 59:9888–907. doi: 10.1002/anie.201916729
17. Liu B, Zhang H, Liu S, Sun J, Zhang X, Tang BZ. Polymerization-induced emission. *Mater Horiz.* (2020) 7:987–98. doi: 10.1039/c9mh01909j
18. Suzuki S, Sasaki S, Sairi AS, Iwai R, Tang BZ, Konishi G. Principles of aggregation-induced emission: design of deactivation pathways for advanced AIEgens and applications. *Angew Chem Int Ed.* (2020) 59:9856–67. doi: 10.1002/anie.202000940
19. Li X, Li M, Yang M, Xiao H, Wang L, James TD, et al. "Irregular" aggregation-induced emission luminogens. *Coord Chem Rev.* (2020) 418:213358. doi: 10.1016/j.ccr.2020.213358
20. Wang Y, Nie J, Fang W, Yang L, Hu Q, Tang BZ, et al. Sugar-based aggregation-induced emission luminogens: design, structures, and applications. *Chem Rev.* (2020) 120:4534–77. doi: 10.1021/acs.chemrev.9b00814
21. Xu S, Duan Y, Liu B. Precise molecular design for high-performance luminogens with aggregation-induced emission. *Adv Mater.* (2020) 32:1903530. doi: 10.1002/adma.201903530
22. Li K, Liu B. Polymer-encapsulated organic nanoparticles for fluorescence and photoacoustic imaging. *Chem Soc Rev.* (2014) 43:6570–97. doi: 10.1039/c4cs00014e
23. Chen S, Wang H, Hong Y, Tang BZ. Fabrication of fluorescent nanoparticles based on AIE luminogens (AIE dots) and their applications in bioimaging. *Mater Horiz.* (2016) 3:283–93. doi: 10.1039/c6mh00060f
24. Feng G, Liu B. Aggregation-induced emission (AIE) dots: emerging theranostic nanolights. *Acc Chem Res.* (2018) 51:1404–14. doi: 10.1021/acs.accounts.8b00060
25. Liu H, Xiong LH, Kwok RTK, He X, Lam JWY, Tang BZ. AIE bioconjugates for biomedical applications. *Adv Optical Mater.* (2020) 8:2000162. doi: 10.1002/adom.202000162
26. Wang D, Tang BZ. Aggregation-induced emission luminogens for activity-based sensing. *Acc Chem Res.* (2019) 52:2559–70. doi: 10.1021/acs.accounts.9b00305
27. Zhang MM, Li K, Zang SQ. Progress in atomically precise coinage metal clusters with aggregation-induced emission and circularly polarized luminescence. *Adv Optical Mater.* (2020) 8:1902152. doi: 10.1002/adom.201902152
28. Cai X, Liu B. Aggregation-induced emission: recent advances in materials and biomedical applications. *Angew Chem Int Ed.* (2020) 59:9868–86. doi: 10.1002/anie.202000845
29. Song N, Zhang Z, Liu P, Yang YW, Wang D, Tang BZ, et al. Nanomaterials with supramolecular assembly based on AIE luminogens for theranostic applications. *Adv Mater.* (2020) 32:2004208. doi: 10.1002/adma.202004208
30. Jiang M, Gu X, Lam JWY, Zhang Y, Kwok RTK, Tang BZ, et al. Two-photon AIE bio-probe with large Stokes shift for specific imaging of lipid droplets. *Chem Sci.* (2017) 8:5440–6. doi: 10.1039/c7sc01400g
31. Yao W, Tebyetekerwa M, Bian X, Li W, Qin A, Tang BZ, et al. Materials interaction in aggregation-induced emission (AIE)-based fluorescent resin for smart coatings. *J Mater Chem C.* (2018) 6:12849–57. doi: 10.1039/c8tc04175j
32. Li W, Ding Y, Tebyetekerwa M, Xie Y, Qin A, Tang BZ, et al. Fluorescent aggregation-induced emission (AIE)-based thermosetting electrospun nanofibers: fabrication, properties and applications. *Mater Chem Front.* (2019) 3:2491–8. doi: 10.1039/c9qm00342h
33. Guan W, Yang T, Lu C. Measurement of solubilization location in micelles using anchored aggregation-induced emission donors. *Angew Chem Int Ed.* (2020) 59:12800–5. doi: 10.1002/anie.202005085
34. Tong H, Hong Y, Dong Y, Haußler M, Lam JWY, Tang BZ, et al. Fluorescent "light-up" bioprobes based on tetraphenylethylene derivatives

with aggregation-induced emission characteristics. *Chem Commun.* (2006) 42:3705–7. doi: 10.1039/b608425g

35. Hong Y, Haußler M, Lam JWY, Li Z, Sin KK, Tang BZ, et al. Label-free fluorescent probing of G-quadruplex formation and real-time monitoring of DNA folding by a quaternized tetraphenylethene salt with aggregation-induced emission characteristics. *Chem Eur J.* (2008) 14:6428–37. doi: 10.1002/chem.200701723
36. Hong Y, Xiong H, Lam JWY, Hußler M, Liu J, Tang BZ, et al. Fluorescent bioprobes: structural matching in the docking processes of aggregation-induced emission fluorogens on DNA surfaces. *Chem Eur J.* (2010) 16:1232–45. doi: 10.1002/chem.200900778
37. Li S, Langenegger SM, Haner R. Control of aggregation-induced emission by DNA hybridization. *Chem Commun.* (2013) 49:5835–7. doi: 10.1039/c3cc42706d
38. Hong Y, Chen S, Leung CWT, Lam JWY, Tang BZ. Water-soluble tetraphenylethene derivatives as fluorescent "light-up" probes for nucleic acid detection and their applications in cell imaging. *Chem Asian J.* (2013) 8:1806–12. doi: 10.1002/asia.201300065
39. Xu L, Zhu Z, Wei D, Zhou X, Qin J, Yang C. Amino-modified tetraphenylethene derivatives as nucleic acid stain: relationship between the structure and sensitivity. *ACS Appl Mater Interfaces.* (2014) 6:18344–51. doi: 10.1021/am505791f
40. Xu X, Yan S, Zhou Y, Huang R, Chen Y, Zhou X, et al. A novel aggregation-induced emission fluorescent probe for nucleic acid detection and its applications in cell imaging. *Bioorg Med Chem Lett.* (2014) 24:1654–6. doi: 10.1016/j.bmcl.2014.02.071
41. Chen J, Wang Y, Li W, Zhou H, Li Y, Yu C. Nucleic acid-induced tetraphenylethene probe noncovalent self-assembly and the superquenching of aggregation-induced emission. *Anal Chem.* (2014) 86:9866–72. doi: 10.1021/ac502496h
42. Xu L, Zhu Z, Zhou X, Qin J, Yang C. A highly sensitive nucleic acid stain based on amino-modified tetraphenylethene: the influence of configuration. *Chem Commun.* (2014) 50:6494–7. doi: 10.1039/c4cc02671c
43. Zhao Y, Yu CYY, Kwok RTK, Chen S, Lam JWY, Tang BZ, et al. Photostable AIE fluorogens for accurate and sensitive detection of S-phase DNA synthesis and cell proliferation. *J Mater Chem B.* (2015) 3:4993–6. doi: 10.1039/c5tb00458f
44. Wang H, Ma K, Xu B, Tian W. Tunable supramolecular interactions of aggregation-induced emission probe and graphene oxide with biomolecules: an approach toward ultrasensitive label-free and "turn-on" DNA sensing. *Small.* (2016) 12:6613–22. doi: 10.1002/smll.201601544
45. Tyagi A, Chu KL, Abidi IH, Cagang AA, Leung NLC, Tang BZ, et al. Single-probe multistate detection of DNA via aggregation-induced emission on a graphene oxide platform. *Acta Biomater.* (2017) 50:334–43. doi: 10.1016/j.actbio.2016.12.003
46. Ou X, Hong F, Zhang Z, Gao P, Lou X, Xia F, et al. A highly sensitive and facile graphene oxide-based nucleic acid probe: label-free detection of telomerase activity in cancer patient's urine using AIEgens. *Biosens Bioelectron.* (2017) 89:417–21. doi: 10.1016/j.bios.2016.05.035
47. Wang Z, Gu Y, Liu J, Cheng X, Sun JZ, Tang BZ, et al. A novel pyridinium modified tetraphenylethene: AIE-activity, mechanochromism, DNA detection and mitochondrial imaging. *J Mater Chem B.* (2018) 6:1279–85. doi: 10.1039/c7tb03012f
48. Gao Y, He Z, He X, Zhang H, Weng J, Tang BZ, et al. Dual-color emissive AIEgen for specific and label-free double-stranded DNA recognition and single-nucleotide polymorphisms detection. *J Am Chem Soc.* (2019) 141:20097–106. doi: 10.1021/jacs.9b09239
49. Kotras C, Fossepre M, Roger M, Gervais V, Richeter S, Clementr S, et al. A cationic tetraphenylethene as a light-up supramolecular probe for DNA G-quadruplexes. *Front Chem.* (2019) 7:493. doi: 10.3389/fchem.2019.00493
50. Liu H, Zhang Z, Zhao Y, Zhou Y, Zhou X, Li Z, et al. A water-soluble two-dimensional supramolecular organic framework with aggregation-induced emission for DNA affinity and live-cell imaging. *J Mater Chem B.* (2019) 7:1435–41. doi: 10.1039/c8tb03206h
51. Shen J, Zhang Y, Hu R, Kwok RTK, Qin A, Tang BZ, et al. Dual-mode ultrasensitive detection of nucleic acids via an aqueous "Seesaw" srategy by combining aggregation-induced emission and plasmonic colorimetry. *ACS Appl Nano Mater.* (2019) 2:163–9. doi: 10.1021/acsanm.8b01773
52. Yuan YX, Zhang HC, Hu M, Zhou Q, Wu BX, Zheng YS, et al. Enhanced DNA sensing and chiroptical performance by restriction of double-bond rotation of AIE *cis*-tetraphenylethylene macrocycle diammoniums. *Org Lett.* (2020) 22:1836–40. doi: 10.1021/acs.orglett.0c00174
53. Yu KK, Li K, He HZ, Liu YH, Bao JK, Yu XQ. A label-free fluorescent probe for accurate mitochondrial G-quadruplex structures tracking via assembly hindered rotation induced emission. *Sens Actuators B.* (2020) 321:128479. doi: 10.1016/j.snb.2020.128479
54. Wang X, Hu J, Zhang G, Liu S. Highly selective fluorogenic multianalyte biosensors constructed via enzyme-catalyzed coupling and aggregation-induced emission. *J Am Chem Soc.* (2014) 136:9890–3. doi: 10.1021/ja505278w
55. Engels JF, Roose J, Zhai DS, Yip KM, Tang BZ, Renneberg R, et al. Aggregation-induced emissive nanoparticles for fluorescence signaling in a low cost paper-based immunoassay. *Colloids Surf B.* (2016) 143:440–6. doi: 10.1016/j.colsurfb.2016.03.051
56. Xiong LH, He X, Zhao Z, Kwok RTK, Zhang R, Tang BZ, et al. Ultrasensitive virion immunoassay platform with dual-modality based on a multifunctional aggregation-induced emission luminogen. *ACS Nano.* (2018) 12:9549–57. doi: 10.1021/acsnano.8b05270
57. Yu W, Li Y, Xie B, Ma M, Tang BZ, Shen J, et al. An aggregation-induced emission-based indirect competitive immunoassay for fluorescence "turn-on" detection of drug residues in foodstuffs. *Front Chem.* (2019) 7:228. doi: 10.3389/fchem.2019.00228
58. Wu W, Shen M, Liu X, Shen L, Ke X, Li W. Highly sensitive fluorescence-linked immunosorbent assay based on aggregation-induced emission luminogens incorporated nanobeads. *Biosens. Bioelectron.* (2020) 150:111912. doi: 10.1016/j.bios.2019.111912
59. Zhang G, Xu S, Xiong Y, Duan H, Yuan M, Lai W, et al. Ultrabright fluorescent microsphere and its novel application for improving the sensitivity of immunochromatographic assay. *Biosens Bioelectron.* (2019) 135:173–80. doi: 10.1016/j.bios.2019.04.023
60. Wang Z, Hu S, Zhang G, Liu J, Peng J, Lai W, et al. Aggregation-induced emission-based competitive lateral flow immunoassay for rapid detection of sulfamethazine in honey. *Food Agric Immunol.* (2019) 30:1303–17. doi: 10.1080/09540105.2019.1689929
61. Hu S, Liu J, Zhang G, Wang Z, Peng J, Lai W, et al. Reliable performance of aggregation-induced emission nanoparticle-based lateral flow assay for norfloxacin detection in nine types of animal-derived food. *Talanta.* (2020) 219:121245. doi: 10.1016/j.talanta.2020.121245
62. Office of Alumni Relations. *Solutions for a Brighter, Post-pandemic Future.* (2020). Available online at: http://www.nus.edu.sg/alumnet/thealumnus/issue-122/perspectives/frontiers/solutions-for-a-brighter-post-pandemic-future (accessed January 5, 2021).
63. The Hong Kong University of Science and Technology. *What Do Tests for Fertility and COVID-19 Have in Common?* (2020). Available online at: https://hkust.edu.hk/news/entrepreneurship/what-do-tests-fertility-and-covid-19-have-common?cn=1 (accessed November 24, 2020).
64. Feng W, Newbigging AM, Le C, Zhang XE, Zhang H, Le XC, et al. Molecular diagnosis of COVID-19: challenges and research needs. *Anal Chem.* (2020) 92:10196–209. doi: 10.1021/acs.analchem.0c02060
65. Kang M, Zhang Z, Song N, Li M, Wang D, Tang BZ, et al. Aggregation-enhanced theranostics: AIE sparkles in biomedical field. *Aggregate.* (2020) 1:80–106. doi: 10.1002/agt2.7

Conflict of Interest: The authors declare that the research was conducted in the absence of any commercial or financial relationships that could be construed as a potential conflict of interest.

frontiers
in Immunology

ORIGINAL RESEARCH
published: 22 April 2021
doi: 10.3389/fimmu.2021.676773

Induced Autophagy of Macrophages and the Regulation of Inflammatory Effects by Perovskite Nanomaterial $LaNiO_3$

Yang Wei[1,2†], Xuejiao Gao[1†], Feng Zhao[2†], Didar Baimanov[2,3], Yalin Cong[2,3,4], Yingying Jiang[2,5], Saima Hameed[2], Yixin Ouyang[2,6], Xingfa Gao[1], Xiaoying Lin[7*] and Liming Wang[2,3*]*

[1] College of Chemistry and Chemical Engineering, Jiangxi Normal University, Nanchang, China, [2] CAS Key Laboratory for Biological Effects of Nanomaterials and Nanosafety & CAS-HKU Joint Laboratory of Metallomics on Health and Environment, and Beijing Metallomics Facility, Institute of High Energy Physics, Chinese Academy of Sciences, Beijing, China, [3] University of Chinese Academy of Sciences, Beijing, China, [4] CAS Key Laboratory for Biological Effects of Nanomaterials and Nanosafety, National Center for Nanoscience and Technology, Beijing, China, [5] School of Public Health, Qingdao University, Qingdao, China, [6] School of Public Health, Capital Medical University, Beijing, China, [7] College of Pharmacy, Jilin Medical University, Jilin, China

Edited by:
Yang Li,
Shenzhen Institutes of Advanced Technology (CAS), China

Reviewed by:
Xin Wang,
Brigham and Women's Hospital and Harvard Medical School,
United States
Liang Chen,
University of Science and Technology of China, China

***Correspondence:**
Liming Wang
wangliming@ihep.ac.cn
Xiaoying Lin
linxytime@163.com
Xingfa Gao
gaoxf@jxnu.edu.cn

†These authors have contributed equally to this work

Specialty section:
This article was submitted to Molecular Innate Immunity, a section of the journal Frontiers in Immunology

Received: 06 March 2021
Accepted: 25 March 2021
Published: 22 April 2021

Citation:
Wei Y, Gao X, Zhao F, Baimanov D, Cong Y, Jiang Y, Hameed S, Ouyang Y, Gao X, Lin X and Wang L (2021) Induced Autophagy of Macrophages and the Regulation of Inflammatory Effects by Perovskite Nanomaterial $LaNiO_3$. Front. Immunol. 12:676773. doi: 10.3389/fimmu.2021.676773

Perovskite nanomaterials (NMs) possess excellent physicochemical properties and have promising applications in light-emitting diodes (LEDs), lasers, photodetectors, and artificial synapse electronics. Potential exposure to these NMs happens in the manufacture and application of the perovskite-based products, however, the biological safety of these NMs is still unknown. Here, we used the $LaNiO_3$ NM (LNO), a typical kind of perovskite nanostructures to study the interaction with macrophages (J774A.1) and to explore its biological effects at the cellular level. Firstly, we characterized the properties of LNO including the size, shape, and crystal structure using Transmission electronic microscope (TEM), Dynamic lighting scattering (DLS), and X-ray diffraction (XRD). Secondly, to gain a better understanding of the biological effect, we evaluated the effect of LNO on cell viability and found that LNO induced cell autophagy at a concentration of 5 μg/ml and influenced the inflammatory response based on RT-PCR result. Finally, we demonstrated the mechanism that LNO causes cell autophagy and immune response is probably due to the metal ions released from LNO in acidic lysosomes, which triggered ROS and increased lysosomal membrane permeation. This study indicates the safety aspect of perovskite NMs and may guide the rational design of perovskite NMs with more biocompatibility during their manufacture and application.

Keywords: perovskite nanomaterials, $LaNiO_3$, autophagy, dissolution, inflammation response

INTRODUCTION

The crystal structure of perovskite nanomaterials (NMs) can be described as ABX_3 octahedron (1). The cation of A is composed of lanthanide including La, Sc, Y, Ce, Pr, Nd, Pm, Sm, etc., while the B cation origins from transition element including Ni, Cr, Co, Fe, etc. X is constituted as anion, halogen and chalcogen are the dominating elements (2, 3). Perovskite oxide NMs exhibit more stable and higher electron conduction efficiency compared to conventional NMs with low cost (4, 5), which endows promising application in the fields of energy storage and electronic devices including light-emitting diodes (LEDs), lasers, photodetectors, artificial synapse electronics, wearable electronics, and intelligent vehicles (6–8). During the manufacture and consumption, the latent exposure of such perovskite NMs to human being increases; however, the biological safety of perovskite NMs is still uncertain. Until now, few reports have reported biological effects of the perovskite LNO.

As we know, mononuclear-macrophage system (MPS) is a class of cells including macrophages, dendritic cells (derived from monocytes) and granulocytes (9) that are widely separated in the human body with the property of phagocytosis, in which the cells engulf and destroy bacteria, viruses, and other foreign substances such as nanomaterials (10, 11). As one of the most important barriers, macrophages are responsible for engulfing nanomaterials and removing them *in vivo*. NMs will thus end up in the macrophages of the tissues and organs during their exposure and long-term residence (12, 13). In addition, MPS cells participate in the innate immune responses, through which cells are activated by the NMs and pathogens and then secrete pro-inflammatory cytokines and promote their clearance (14). Thus, it is crucial to evaluate how LNO interact with MPS and the potential effects of LNO on the functions and viability of macrophages after the exposure.

Herein, we investegated the interaction of LNO perovskite oxide NMs with macrophages and potential effects on cytotoxicity and immunological responses. First, we characterized the morphology, size distribution, surface charge, and the component of LNO NMs. Second, we evaluated the effects of LNO on the viability of the macrophage cell line J774A.1 and confirmed that LNO NMs induced cell autophagy. Thirdly, to explore cell autophagy mechanism, we utilized TEM to capture the engulfment, accumulation, and the location of LNO NMs within J774A.1 cells. We also employed inductively coupled plasma mass spectrometry (ICP-MS) to evaluate the release of metallic ions from LNO in an artificial lysosomal fluid (ALF). After the exposure to LNO, we further introduced AO assays by means of Laser scanning confocal microscopic (CLSM) imaging to assess lysosomal membrane integrity (LMP). Finally, we demonstrated that due to the metal ions released from LNO NMs, intracellular Reactive Oxygen Species (ROS) elevated that caused the impairment of LMP. Furthermore, LNO NMs mediated the secretion of cytokines including interleukin, tumor necrosis factor, etc. according to ELISA kit and RT-PCR which suggested immunological effects of LNO NMs. We concluded that LNO-based perovskite materials are chemically active that caused the autophagy of macrophages and mediated immune responses.

MATERIALS AND METHODS

Materials and Chemicals

$LaNiO_3$ nanomaterials were prepared according to previous publication (15) and donated by Prof. Hui Wei in Nanjing University. DMEM medium (Hyclone, USA), streptomycin/penicillin(Sigma, USA), Fetal bovine serum (FBS) (BI, Israel), Trypsin-EDTA (TE) (Hyclone, USA), phosphate-buffered saline (PBS) (Hyclone, USA), phenol red-free medium (Hyclone, USA), TBST(Sigma, USA), SDS-PAGE (Hyclone, USA), SDS-polyacrylamide (Hyclone, USA), HNO_3 (BV-III, Beijing Institute of Chemical Reagents, China), H_2O_2 (MOS level, Beijing Institute of Chemical Reagents, China), OsO_4 (Sigma, USA), and DCFH-DA (Invitrogen, USA). All chemicals were analytical grades and artificial lysosomal fluid was prepared by Milli-Q water.

Characterization of $LaNiO_3$

The morphology of LNO materials were characterized by (TEM, a Tecnai G2 20 S-TWIN) at an accelerating voltage of 200 kV. Zeta potential and hydrodynamic diameter of the materials were measured by a Zeta Sizer Nano series Nano-ZS (Malvern Instruments Ltd., UK); TZY-XRD(D/MAX-TTRIII(CBO) was utilized to acquire the crystal configuration. LNO differences in water and the artificial lysosomal fluids(ALF), which was prepared according to previous publication.

Cell Culture

Mouse monocytic cell lines or mouse macrophages (J774A.1) were obtained from ATCC, USA. Cells were cultured in a complete medium containing 90% DMEM medium, 10% FBS, and streptomycin (100 μg/ml)/penicillin (100 U/ml) at 37°C in a humidified 5% CO_2 incubator.

Cytotoxicity Assay

Cytotoxicity of LNO was determined by a Cell Counting-Kit 8 (CCK-8) assay (Dojindo, Japan). In brief, J774A.1 cells were seeded in 96-well plates at a density of 2.5×10^3/well overnight. And then, the cell medium was replaced by the fresh DMEM medium containing a series of concentrations (1.25, 2.5, 5, 10, 20, 40, and 80 μg/ml) of LNO. After 24 h treatment, the cells were rinsed twice with PBS at pH 7.4 and further incubated with a 100 μL of mixture including 10% CCK-8 and 90% complete medium (v/v) at 37°C for 1 h in a humidified 5% CO_2 incubator. The absorbance of the mixture at 450 nm was obtained by a microplate reader (Enspire, USA), while the absorbance of the same sample at 600 nm was used for the reference. Each sample contains five repeated wells for CCK-8 assay.

Autophagy Fluorescent Probe Analysis

J774A.1 cells were seeded on a petri dish at a density of 5×10^5 cells/well overnight. After twice rinsing with PBS, the probe for autophagy, DAL Green (Costar, Corning, NY) (16), was incubated with cells for 30 minutes under a 37°C incubator. After twice rinsing with phenol red-free medium, cells were treated with lno(2.5, 5 μg/ml) for 12 h, respectively. Then, a confocal microscope was used to detect the fluorescence signal of DAL Green. The cells were observed under confocal microscope and samples were excited at 488 nm (Perkin Elmer Ultra View Vox system, USA).

Subcellular Structures Observation by TEM

The cells were seeded in six-well plates and exposed to LNO (5 μg/ml) for 12 h. Then, cells were digested by TE, washed three times with PBS, and collected as cell pellets. About 200 μl of 2.5% (w/w) glutaraldehyde in PBS solution was added to the cell pellets and stored at 4°C overnight. Afterward, the cells were sequentially fixed with 1% (w/w) OsO_4 in PBS for 1 h, dehydrated with ethanol, embedded in resin, cut into ultrathin sections, placed on the copper grids, and stained with osmic acid before the observation. Finally, the images of the subcellular localization of LNO and the subcellular structures were observed using a bio-transmission electron microscope (HT7700).

Western Blotting

J774A.1 cells were treated with LNO at 2.5 and 5 μg/ml for 12 h and then lysed in a RIPA lysis buffer (containing protein inhibitor). To obtain the total protein concentration, BCA Kit (Pierce) was employed. For each sample, 20 μg protein was loaded on SDS-PAGE and electrophoresed. The proteins were separated on a 12% or 5% SDS-polyacrylamide gel at 120 V and transferred to a nitrocellulose membrane at 250 mA. At room temperature, the membranes were blocked for 2 h by the solution containing 0.05% Tween-20 (TBST) and 5% non-fat milk that was diluted by TBS buffer. After rinsing with TBST three times, the membranes were incubated with various primary antibodies against β-actin, LC3 I, LC3 II, and p62 (Cell Signaling Technologies, USA) that were diluted by 1:1000, overnight at 4°C. After washing three times with TBST, the secondary antibodies in a blocking solution with a dilution of 1:3000 were added. After 2 h incubation, the membranes were rinsed three times with TBST, followed by chemiluminescence, and finally detected using a gel-imaging analysis system (Bio-Rad, UK).

Cellular Uptake and Efflux of LNO

To comprehend the process of uptake, the cells were seeded in 6-well plates at a density of 5×10^5/well and exposed to 5 μg/ml LNO for 3, 6, 12 and 24 h. For the exocytosis, cells were first exposed to 5 μg/ml LNO for 12 h and then rinsed twice with PBS. After that, cells were further cultured for 12, 24 and 36 h in a DMEM medium containing 1% FBS. Each sample had five replicate wells. After rinsing with PBS three time, cells were collected, counted, and centrifuged. Then, the samples were incubated with 4 ml HNO_3 overnight within conical flasks. Next, the samples were heated for 2 h with a temperature maintaining at 150°C During the heating, the 30% H_2O_2 was gradually added to the flasks drop by drop until the solution became colorless. Afterwards, the solution was cooled to room temperature and diluted by a 2% HNO_3 solution to a final volume of 3 ml. A series of concentrations containing 0.1, 0.5, 1, 5, 10, 50, 100, 500, and 1000 ng/ml lanthanum and nickel were prepared as standard solutions. In addition, a final concentration of 40 ng/ml indium was added as the internal standard. All the solutions were measured three times by ICP-MS (Thermo, USA) and the data were shown as mean value and standard error (17–19).

Detection of Metal Ion Release in ALF

LNO at 200 μg/ml (10 ml) were incubated with the ALF with a pH value of 4.5 for 3, 6, 12 and 24 h, respectively. After different incubation time, the sample were collected by a centrifugation at 9000 rpm for 15 min. The supernatant was digested according to the procedure mentioned above and diluted by a 2% HNO_3 solution to a final volume of 3 ml before the measurement by ICP-MS. The ratio of La and Ni was used to evaluate the ion release.

Analysis of Lysosomal Membrane Integrity

Acridine orange (AO, Sigma, USA) assay (20) was used to assess the lysosomal membrane integrity (21). Cells were first seeded in a 6-well plate at a density of 5×10^5 cells/well, stained with 1 μg/ml AO for 15 min, rinsed with PBS, and then exposed to 5 μg/ml LNO for 12 h in a complete medium. Then rinsed with PBS, dispersed in a serum-free and phenol red-free medium. Finally, the cells were observed under confocal microscope (Perkin Elmer Ultra View Vox system, USA) and samples were excited at 488 nm, and emission was detected at 537 nm (green) and 615 nm (red).

Reactive Oxygen Species (ROS) Assay

Cells were seeded on a petri dish with a density of 5×10^5 cells/well. After 24 h culture, cells were exposed to 2.5 and 5 μg/ml LNO for 12 h. After twice rinsing with PBS, the cells were incubated with PBS containing 10 μM DCFH-DA for 25 min at 37°C. After twice rinsing with PBS, cells were cultured with serum-free and phenol red-free medium and then observed by a microscope with the excitation wavelength at 488 and the emission at 525 nm.

Real-Time Reverse Transcription Quantitative PCR (Real-Time RT-qPCR) and Inflammation Effects

Cells were differentiated onto 6-well plates at a density of 1×10^5 cell/well for 48 h. To prime the macrophages, the cells were treated with 5 μg/ml lno for 12 h. RT-PCR experiments were done to determine the level of mRNA expression. The TRIZOL reagent method (Life Technology, CA, USA) was utilized to isolate RNA from cells. About 10 p mol oligonucleotide (Oligo dT)(Sigma, USA) primer and Moloney murine leukemia virus reverse transcriptase (M-MLV, Promega, Madison, USA) added 2 μg of RNA was used to generate cDNA. Each sample was prepared for real-time quantitative PCR in a final reaction volume of 20 μl by adding Master Mix (Promega, Madison, USA) and SYBR Green (Invitrogen, Paisley, UK). The amplification cycle was performed by Realplex4 (Eppendof, Germany). The primers synthesized by Sangon Biotech (China) were shown as below:

TNFα:

F-CATCTTCTCAAAATTCGAGTGACAA
R-TGGGAGTAGACAAGGTACAACCC

IL10:

F-CTTACTGACTGGCATGAGGATCA
R-GCAG CTCTAGGAGCATGTGG

IL-1β:

F-TGAAATGCCACCTTTTGACAGTG
R-ATGTGCTGCTGCGAGATTTG

NF-κB:

F-GGGCTATAATCCTGGACTTCTGG
R-AGTTTCCAGGTCTGATTTCCTCC

IL-8:

F-CACCTCAAGAACATCCAGAGT
R-CAAGCAGAACTGAACTACCATCG

IL-6:

F-GAGGATACCACTCCCAACAGACC
R-CAAGCAGAACTGAACTACCATCG

GAPDH:

F-GACCCCTTCATTGACCTCAAC
R-CTTCTCCATGGTGGTGAAGA

Statistical Analysis

All the data were statistically analyzed using Origin 9 software by one-way ANOVA or Student *t* test. Significant difference based on that *p* value is less than 0.05. Data were shown as mean value ± standard error of three replicated experiments at least.

RESULTS

Characterization of LaNiO$_3$

TEM was employed to characterize the morphology of LNO in water and artificial lysosomal fluids (ALF) at pH 4.5 as shown in **Figure 1A**. The result indicated that there was structural variation in LNO NMs from the water to the ALF after 24 h exposure LNO displayed long tentacle-like shape in ALF rather than in the water, which meant physical or chemical changes in LNO within the acidic ALF environment. This result was further confirmed by XRD results. Compared with XRD pattern of LNO NMs dispersed in water, the characteristic peaks for 101, 021, 122 and 220 crystal facets disappeared in the ALF (**Figure 1B**), which suggested the impaired structure of LNO in the acidic lysosome. Based on DLS measurement, we found that the average of hydrodynamic size of LNO NMs in water was 350 ± 20 nm (**Figure 1C**).

Cytotoxicity and Cellular Location of LaNiO$_3$

We then investigated the effect of LNO on the viability of j774a.1 cells after 24 $_h$ exposure (**Figures 2A, B**). CCK-8 results indicated that LNO NMs decreased cell viability in a dose-dependent manner with an IC50 concentration of 5.08 ± 0.14 μg/ml (**Figure 2B**). For the following experiments, the concentrations of 2.5 and 5 μg/ml were chosen to evaluate the cellular effects of LNO NMs. Compared with the control, multiple and large intracellular vesicles with a size of several micrometers (labeled by yellow arrows) formed after LNO NMs treatment, which were observed by optical microscope (**Figure 2A**). TEM images show

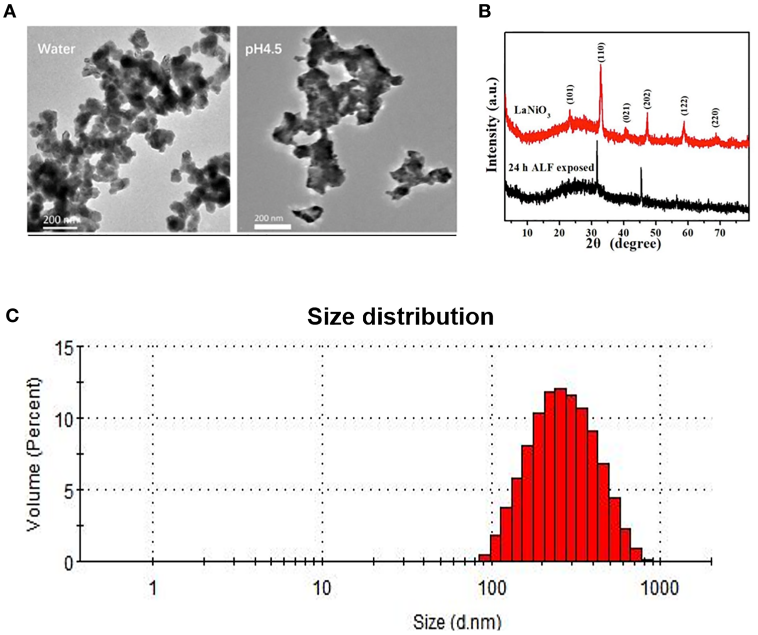

FIGURE 1 | Characterization of LNO. **(A)** TEM images of LNO NMs as dispersed in water and ALF. **(B)** Powder X-ray diffraction patterns of LNO NMs as dispersed in water (red line) and ALF (black line). **(C)** Size distribution of LNO NMs in water as determined by DLS.

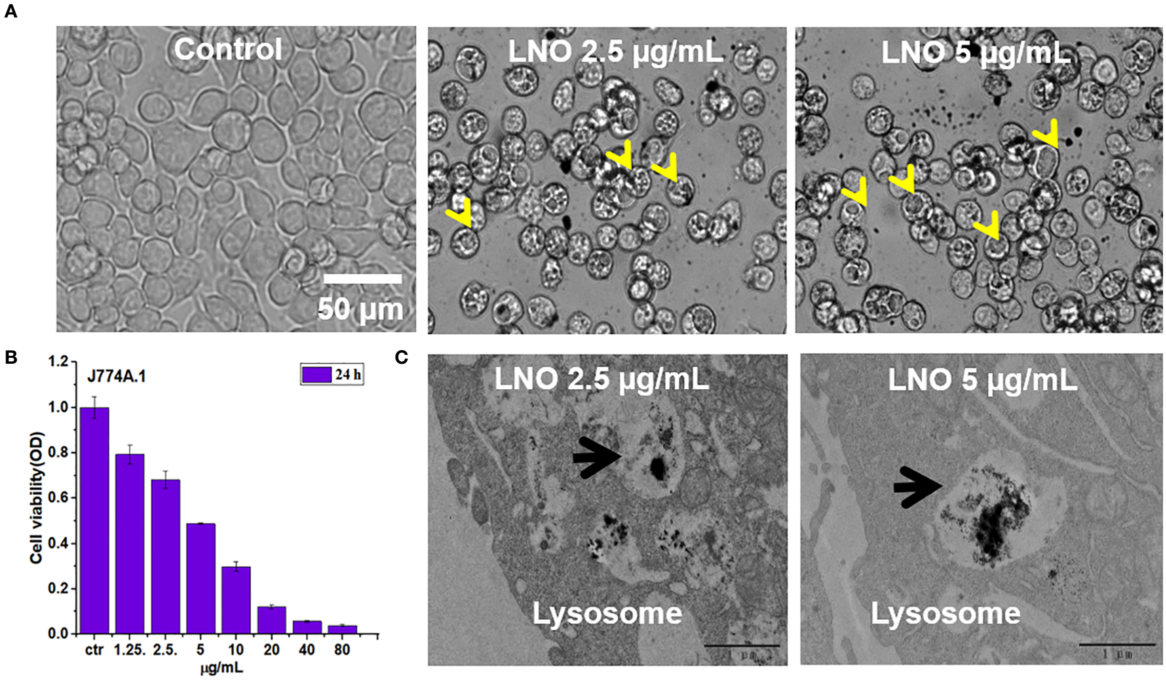

FIGURE 2 | Cytotoxicity and localization of lno nms. **(A)** Images of j774a.1 cells before and after treatment with 2.5 and 5 µg/ml LNO as observed by an optical microscope. **(B)** Dosage-dependent effects of LNO on J774A.1 viability after 24 h exposure as determined by cck-8 assay (*n*=6). **(C)** TEM images of subcellular structures and intracellular location of LNO after 24 h treatment. The arrows indicate the lysosomes.

the formation of large vesicles and the accumulation of LNO NMs in the lysosomes or the phagolysosomes. Within the organelles, the most of LNO aggregated. At a higher dosage of 5 µg/ml, the exposure of LNO NMs resulted in much more and larger intracellular vesicles compared to the control and that at 2.5 µg/ml. In addition, the mitochondrial structure turned to be swelling (**Figures 2C**, **3A**). Thus, TEM results suggest that LNO NMs might influence the structure of organelles such as lysosomes, phagolysosomes, and mitochondria.

Autophagy Induced by LaNiO$_3$

We further checked death pathways of LNO-treated for J774A.1 cells at the morphological and molecular levels. Autophagy plays a crucial role in the processes of removal, degradation, and recycling of misfolding proteins or damaged organelles. When cells sense the signals for misfolding proteins and damaged organelles, the autophagy is triggered and the autophagosomes will form that is a type of vesicles composed of double-layer membrane with engulfed matters (22). In an acidic environment, autophagosomes fuse with lysosomes to form autophagolysosomes, and the contents of autophagolysosomes will be degraded by digestive enzymes in the lysosomes (23). After the exposure to LNO at the sub-lethal doses such as 2.5 and 5 µg ml^{-1} for 12 h, both the autophagosomes and autolysosomes were visible based on TEM images (**Figure 3A**).

In addition, DAL Green is a small-molecule probe that is specific for autophagy, which is capable of emitting fluorescence in hydrophobic and acidic environments and can be thus used to identify autophagolysosomes (24). After the exposure to 2.5 and 5 µg ml^{-1} LNO for 12 h, obvious fluorescence signal appeared compared to the control that suggested the induced autophagic lysosomes by LNO (**Figure 3B**).

Moreover, we verified the autophagy at the protein level by analyzing the conversion of the autophagy-related protein, microtubule-associated protein 1 light chain 3 (LC3). LC3 has two isoforms: LC3-I is cytosolic, while LC3-II is associated with autophagosome membranes. Autophagy is featured as an increase ratio of LC3-II protein (25). WB results show that both the level of LC3-II and the ratio of LC3-II to LC3-I expression enhanced with the increasing dosage of LNO (**Figures 3C, E**). As we know, p62, or SQSTM1/sequestosome1, is a substrate that is preferentially degraded during the autophagy (26). The expression of p62 was downregulated with the increasing LNO concentration (**Figures 3C, D**). Taken together, LNO induced the autophagy of J774A.1 cells.

Impairment in Lysosomal Membrane Integrity Induced by LNO

Acridine orange (AO) is a pH-sensitive probe for that is proper for the assessment of lysosomal membrane integrity. AO can penetrate cell membrane and distributes in the different organelles where it exhibits distinct fluorescence signals. With an excitation at 488 nm, at the acidic environment such as lysosomes/endosomes, AO emits bright red color while it shows green color at the neutral or basic environment such as the

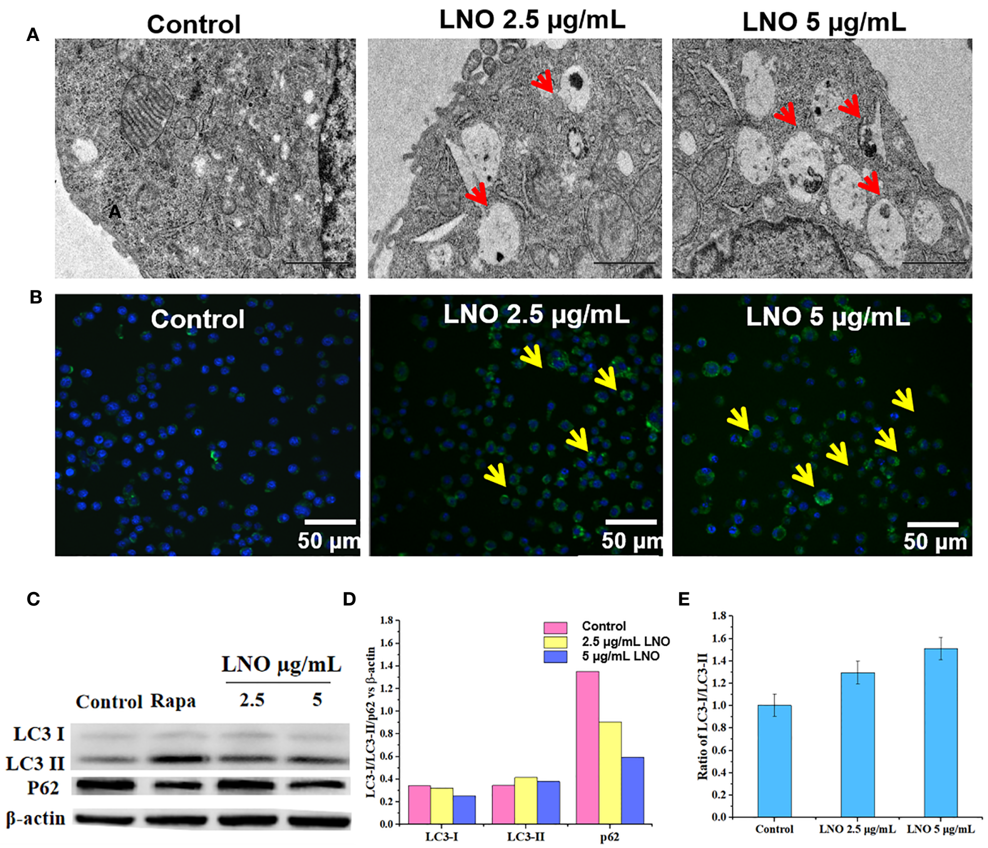

FIGURE 3 | Cell autophagy induced by LNO. **(A)** TEM images for the subcellular structures indicating the induced autophagolysosome in J774A.1 cells after 12 h exposure to 5 μg/ml LNO. **(B)** Images of the autophagy-specific fluorescent probe when J774A.1 cells were exposed to LNO for 12 h and labeled with the probes as observed by CLSM. **(C)** The expression of autophagy-related proteins including lC3-i, lC3-ii, and p62 in J774A.1 cells after LNO exposure for 12 has detected by western blotting. **(D)** The ratio of intensity of the lC3-i, lC3-ii, and p62 protein expression compared to β-actin as calculated by the gray value according to Image J software. **(E)** The ratio of the lC3-ii VS lC3-i *expression* calculated by the gray value according to Image J software.

cytoplasm and the nucleus. When the lysosomal membrane integrity decreased, the pH will increase and then there was significant color change in the lysosome from red to green or yellow (27). Confocal images for AO staining show that LNO increases lysosomal membrane permeation at 5 μg/ml, in which the fluorescence of lysosomes changed from red to green (**Figure 4**).

Release of La and Ni Ions in the Acidic ALF Environment

The degradation and dissolution of perovskite materials in the organisms and the release of metal ions is a crucial way to induce toxicity (28, 29). To understand why LNO influence the lysosome membrane, it is necessary to explore chemical behaviors of LNO in the lysosomes. We then used ICP-MS to determine the release of La and Ni ions within the artificial lysosomal fluid. After the exposure to LNO for 24 h at 5 μg/ml, the amount of intracellular lanthanum and nickel ions increased in a time-dependent manner within 12 h while it decreased at 24 h, suggesting the uptake reached an equilibrium at 12 h and cells removed LNO or metal ions after the uptake (**Figure 5A**). The accumulation of La was much higher than that of Ni in the cells, which may be due to much more removal of Ni than La during the internalization of LNO. After 12 h uptake, time-dependent removal by cells was evaluated after the withdraw of LNO in the cell culture media. ICP-MS results indicated that both La and Ni were released in the media with the increasing time (**Figure 5B**). We calculated the percentage of the metal ions released from the accumulated LNO at 12 h uptake and found that the efflux ratio of Ni was much higher than La during 36 h exocytosis, which suggested faster removal of Ni than La during the cell-LNO interaction (**Figure 5C**). The reason may be that a part of La ions may form LaPO$_4$ in the cytoplasm that decreased the exclusion process, while Ni can be excluded by cells by means of metal ion transporters and pump (30, 31).

Furthermore, we evaluated the dissolution of LNO and the release of ions in ALF fluid with a pH of 4.5. When LNO NMs were centrifuged and the supernatant was collected to quantify the dissolved metal ions from LNO. After continuous incubation of LNO with ALF for 36 h, the released La and Ni from 200 μg/ml

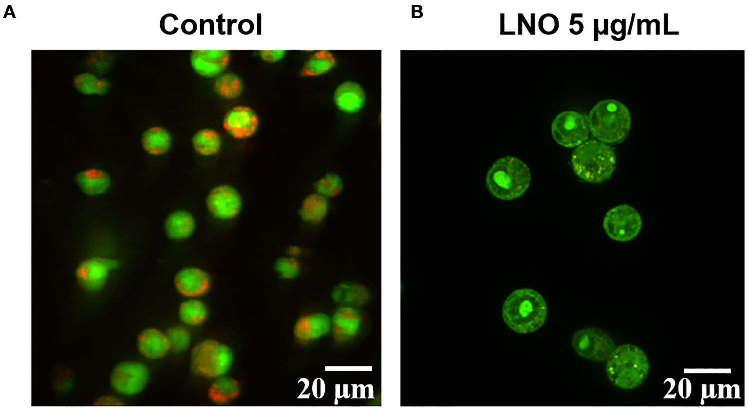

FIGURE 4 | Influence of LNO on the lysosomal membrane permeation. The lysosomal membrane integrity of J774A.1 before **(A)** and after the exposure **(B)** to 5 μg/ml LNO 12 h using AO staining. The scale bar represents 20 μm.

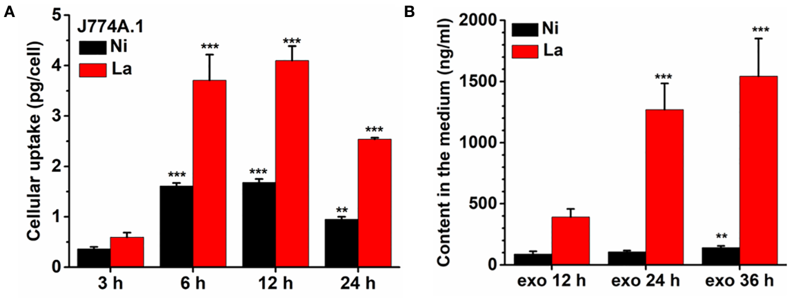

C

Efflux ratio of La and Ni after cell incubation for 12 h and then 12, 24, 36 h efflux		
	Ni	La
12 h	38.49%±2.45%	24.11%±7.56%
24 h	51.06%±4.71%	34.43%±5.51%
36 h	55.12%±6.38%	39.33%±4.35%

D

Efflux ratio of La and Ni in ALF		
	Ni	La
3 h	12.25%±1.22%	6.76%±2.34%
6 h	17.86%±3.15%	16.21%±3.21%
12 h	29.43%±1.41%	29.15%±3.08%
24 h	48.32%±3.74%	44.33%±4.73%

FIGURE 5 | Cellular uptake of LNO and the release of La and Ni from LNO. **(A)** The uptake of LNO in J774A.1 cells after exposure to 5 μg/ml LNO as determined by ICP-MS (*n*=5). The signs (** and ***) indicates significant different for the level of La and Ni between the group and that at 3h uptake with $p < 0.01$ an $p < 0.001$, respectively. **(B)** The exocytosis of La and Ni elements in the supernatant as detected by ICP-MS. Cells were exposed to 5 μg/ml LNO for 12 h and then further cultured in fresh medium for 36 h (*n*=5). The signs (** and ***) indicates significant different for the level of La and Ni between the group and that at exo 12h with $p < 0.01$ an $p < 0.001$, respectively. **(C)** The percentage of the released La ions and Ni ions in J774A.1 cells that was calculated by the formula of the amount of element released/the uptaken element amount. **(D)** The persistent release of metal ions from LNO when LNO was incubated with ALF solution as detect by ICP-MS (*n*=5). The sign *** indicates the very significant difference between samples and control ($p < 0.001$).

LNO suspension was shown in **Figure 5D**. At such an acidic buffer, LNO gradually released metal ions with the time and the dissolution rate for La and Ni kept the same.

Triggering High Level of Oxidative Stress by LNO

To verify the effects of metal ions derived of LNO, we evaluated the production of ROS in J774A.1 cells after the exposure to LNO. After the incubation with 2.5 and 5 μg/ml LNO, DCF, a ROS-specific fluorescent probe was used to determine the level of ROS in J774A.1 cells at 12 h. Optical microscopic images show that LNO significantly promotes the production of ROS in a dose-dependent manner (**Figure 6**). After the exposure to 2.5 and 5 μg/ml LNO, intracellular ROS levels separately elevated to ~2.2 and ~3.2 folds compared to control, which may be explained by the uptake of LNO and the release of metal ions. As we know, transition metal ion may cause oxidative stress by interacting with antioxidant systems in the cells and taking part in catalytic reactions (32). Oxidative stress refers to the imbalance between oxidation and antioxidation in the body, which can be caused by the massive production of reactive oxygen species (ROS) that tends to oxidize biological molecules, leads to inflammatory infiltration of neutrophils and increases secretion of proteases. ROS directly participates in the regulation of cell survival and death (33–35). The overloaded free radicals can oxidize proteins, lipids, and nucleic acids within cells and impair their structures and functions. In the case of high level of oxidative stress, the damage in the organelle membrane structure such as proteins/enzymes and phospholipids may increase LMP and trigger the release of cathepsin B and D from lysosomes. As a result, the damage in lysosomes/endosome membrane promotes the release of lysosomal contents that activates cell autophagy (24).

Promoting the Immune Responses by LNO

Cytokines include blood cell growth factors and interleukins, abbreviated as IL that refers to the lymphokine, which are involved in the cell-cell interaction for white blood cells and

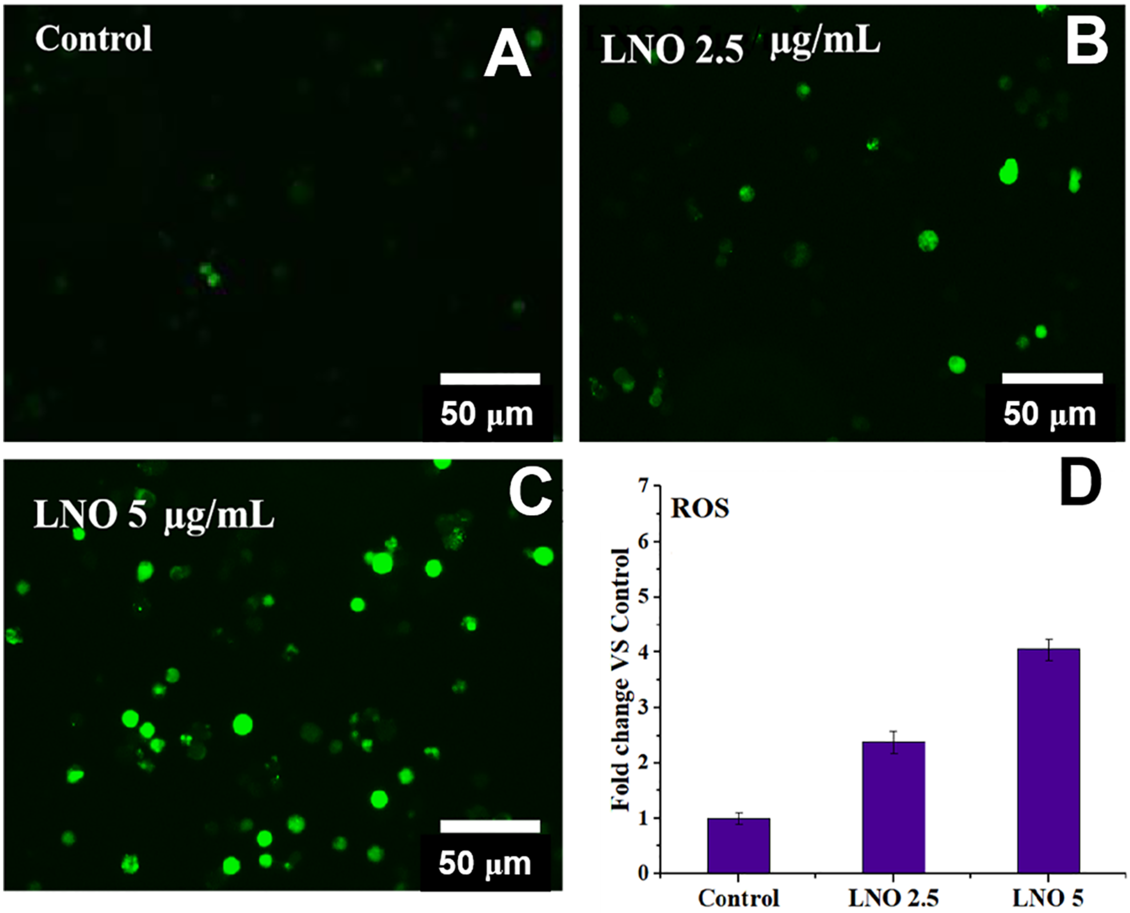

FIGURE 6 | Intracellular ROS level after the exposure to LNO. **(A–C)** Optical images for intracellular ROS stained by DCFHDA when cells are treated by 2.5 and 5 μg/ml LNO for 12 h. **(D)** Quantitative analysis of relative intensity of intracellular DCF fluorescence based on optical images. Data are expressed by mean value and standard errors (*n*=3).

immune cells in order to regulate immune responses (36, 37). Cytokines play crucial roles in the activation and regulation of immunological system, which mediate the activation, proliferation and differentiation of T and B cells, and also affect inflammatory responses (38, 39). The activation of nuclear factor kappa beta (NF-κB) pathway is an upstream event that mediates inflammatory responses, which may be involved in the occurrence and development of multiple diseases (40). Both the increased lysosomal membrane permeation and the autophagy are related to immunological effects of macrophages (41, 42). We thus tested the expression of inflammatory response-related factors including tumor necrosis factor-α (TNF-α), Interleukin-6(IL-6)/Interleukin-1β (IL-1β), and NF-κB by RT-PCR when the cells were treated with 2.5 and 5 μg/ml LNO for 12 h.

RT-PCR results show that LNO at 5 μg/ml suppressed the expression of NF-κB after 12 h treatment (**Figure 7A**). Moreover, the expression of proinflammatory cytokines including TNF-α (**Figure 7B**), IL-6 (**Figure 7C**), and IL-1β (**Figure 7D**) at mRNA level was decreased after the LNO treatment. The gene expression of these factors at mRNA level thus indicated that LNO exhibited immunosuppressive effect by inhibiting NF-κB pathway and the expression of several inflammatory factors (**Figure 7**). For classical NF-κB pathway, NF-κB molecule enters the nucleus through p65 and p50 to regulate inflammatory activation which can be induced by cytokines, ROS, and metal ions etc. However, selective autophagy can modulate p100/p52 stability that inhibits the activation of non-canonical NF-κB pathway (43), by which we can understand the reason why LNO induced autophagy efficiently suppressed the inflammatory responses. Moreover, TNF-α is mainly secreted by macrophages and plays an important role in the onset of inflammation (44), which and involved in the regulation of tumor microenvironment and the development in diseases (45). IL-6 can be produced by macrophages and has pleiotropic functions in immune system, which activates immune cells to remove pathogens, to repair damaged tissues, to regulate acute immune response (46) and is also involved in autoimmune diseases and chronic inflammation (47). As an inflammatory cytokine, IL-1β is widely involved in a variety of pathological damage processes such as human tissue destruction and edema formation as well as inflammation response (48, 49). In summary, the decreased expression of proinflammatory cytokines suggests that LNO may serve as a potential inhibitor for the inflammation therapy.

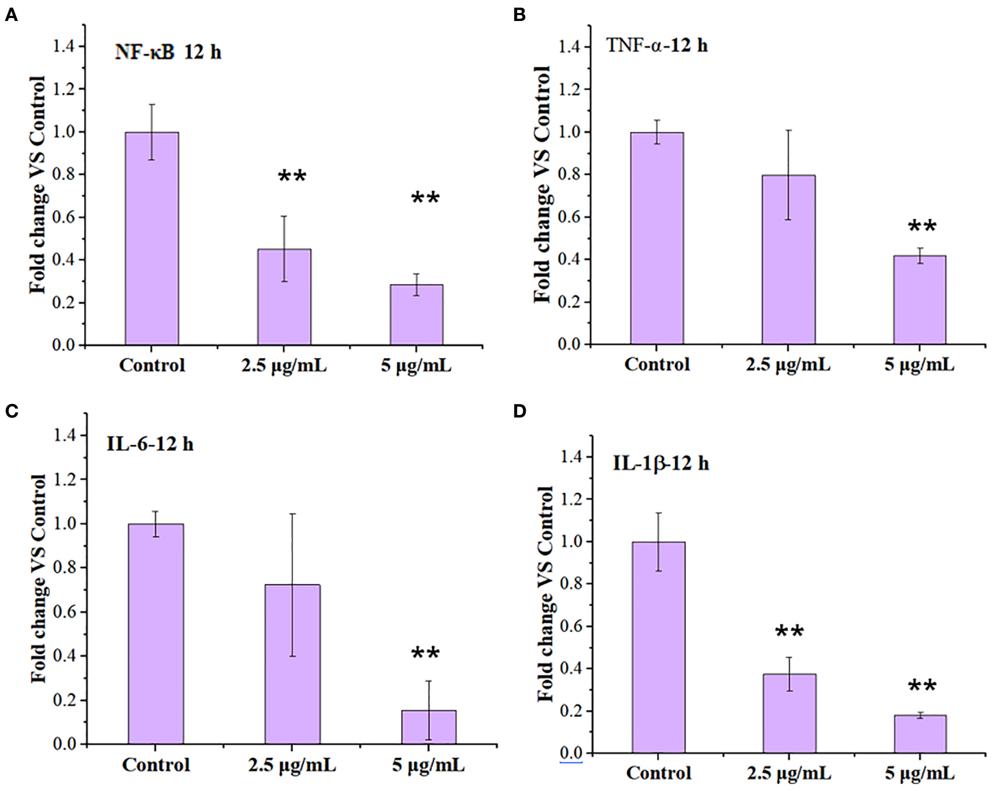

FIGURE 7 | Regulation of immune response in the macrophages by LNO. The expression of NF-κB **(A)**,TNF-α **(B)**, IL-6 **(C)**, and IL-1β **(D)** in J774A.1 cells after the exposure to 2.5 and 5 μg/ml LNO for 12 h as measured by RT-PCR (*n*=3). The sign ** indicates the significant difference between the LNO-treated group and the control.

DISCUSSIONS

The study about the dissolution and release of heavy metal ions from LaNiO$_3$ is crucial to understand the safety of LNO perovskite nanomaterial. The toxic effects of metal ions on tissue and cells are well-known in many studies (28, 29). The quantitative results for intracellular La and Ni by ICP-MS show that both of La and Ni can be internalized by macrophages quickly and then a half of them can be released at least within 24 h. These metal ions contribute to the lysosomal membrane impairment. One of the major reasons is that the released La ions from LNO can react with the phosphate groups of phospholipid heads on the lysosomal membrane (50), which probably destroys the structure of the lysosomal membrane and triggers autophagy. In addition, the released Ni ions may also contribute to ROS production through Fenton-like catalytic reaction.

Under the exposure to stressors such as pathogens and inflammatory signals, autophagy plays crucial roles in innate and adaptive immunity as an effector and mediator, during which autophagy-related proteins act to achieve a balance between activation and inactivation of innate immune signaling (51, 52). For example, the formation of NLRP3 inflammasomes can be suppressed due to the degradation of NOD-like receptor (NLR), a key component of NLRP3 inflammasomes during the autophagy As a result, the maturation and secretion of IL-1β and IL-18 decreased and the inflammation is suppressed (52, 53). In addition, under the stimulation by the stressors, pathogen-recognition receptors (PRR) such as toll-like receptor (TLRs) can form a complex with MyD88 and TRIF but are recognized by autophagy-related receptors, such as SQSTM1, HDAC-6, NDP52, which triggers the degradation of the TLR-containing complex in the autolysosomes (54). The other autophagy-related receptors, such as OPTN and UBQLN1, can promote the degradation of TRIF and TRAF in the autolysosomes. As a result, TLRs signaling is negatively regulated in the autophagy (52, 53). Thus, LNO can not only induce macrophage autophagy but also is capable of suppressing inflammation.

Macrophage autophagy regulates the physiological and pathological process. For example, autophagy can targeted degrade IL-1β, inhibits the activation of inflammasome NLRP3 and reduces the release of inflammatory cytokines. Induced autophagy may weaken sepsis inflammation according to immunosuppression in the late stage of sepsis to a certain extent (36). In addition, macrophage autophagy plays a vital role in the physiological functions of the pulmonary system and its inflammatory response during the infection, pathogenesis, and chronic lung diseases. In a mouse model of acute lung injury induced by hemorrhagic shock, the autophagy of macrophages can inhibit inflammation and reduce acute lung injury (37). By starvation or rapamycin treatment, the autophagy of macrophages promotes the elimination of Mycobacterium tuberculosis (55). Furthermore, macrophage autophagy has been shown to be highly related to the regulation of intestinal natural immune response. AMPK activator GL-V9 can trigger macrophage autophagy, degrade NLRP3 inflammasomes, and have a protective effect on colitis and tumor formation in mouse colitis-related colorectal cancer (56, 57). Therefore, based on the capability of inducing autophagy of macrophages, LNO may serve as a nanomedicine to inhibit inflammation for the therapy purpose in immune regulation diseases, such as tumors, lung injury, and intestinal immune diseases.

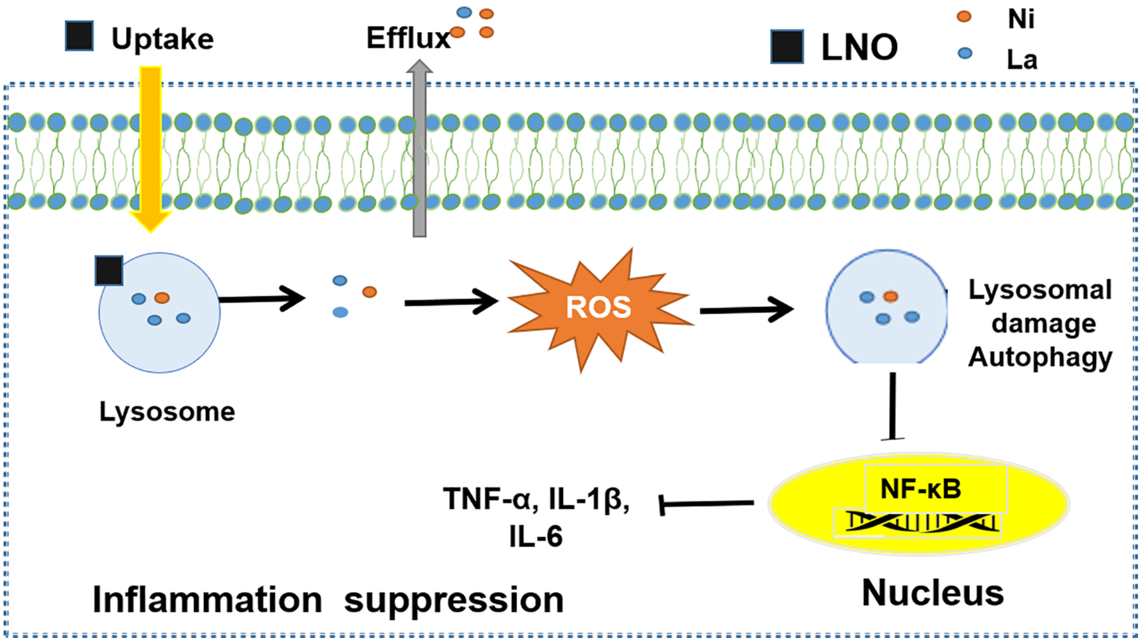

FIGURE 8 | The mechanism of LNO induces protective autophagy of monocytes by inhibiting the expression of inflammatory factors to promote immune response.

CONCLUSION

In summary, we studied the interaction of a typical perovskite $LaNiO_3$ (LNO) with the macrophages and biological effects. We found that LNO nanomaterials reduced the viability of macrophages *via* the autophagy and show the autophagy evidences from cellular morphology, intracellular structures, and the expression of autophagy-related proteins after the exposure of LNO. We further explored the biological and chemical mechanism about the autophagy. We found that cellular uptake of LNO was time-dependent and then LNO was dissolved in the lysosomes or artificial lysosome fluid due to the acidic environment where metal La and Ni ions were released. Next, the release of metal ions induced ROS production and resulted in oxidative stress that increased lysosomal membrane permeation to induce the autophagy. The possible mechanism about how $LaNiO_3$ causes autophagy in the macrophages is shown in **Figure 8**. Moreover, we also evaluated the immune response after the LNO exposure and observed that LNO inhibit the expression of NF-κB, TNF-α, IL-6, and IL-1β at mRNA level, which suggested suppressive effect of LNO on inflammation responses with potential application for the pathogen infection intervene, disease therapy, and tissue repairment. This study revealed the safety and biological effects of perovskite nanomaterials, such as $LaNiO_3$ on the macrophages, which will guide the manufacture and design of safe nanomaterials during the production and consumption.

DATA AVAILABILITY STATEMENT

The raw data supporting the conclusions of this article will be made available by the authors, without undue reservation.

AUTHOR CONTRIBUTIONS

Conception and design: LW, XL, and XFG. Development of methodology: LW and XL. Acquisition of data: YW, XJG, DB, YC, and FZ. Analysis and interpretation of data: YW, XJG, FZ, YJ, DB, SH, and YO. Writing, review, and/or revision of the manuscript: LW, XL, and YW. All authors contributed to the article and approved the submitted version.

FUNDING

We appreciated the funding from Science and Technology Research Project of Jilin Province Education Department (JJKH20210496KJ), the National Basic Research Program of China (2016YFA0203200, 2020YFA0710702), the National Natural Science Foundation of China (31971322), the Users with Excellence Project of Hefei Science Center CAS (2018HSC-UE004), CAS President's International Fellowship Initiative (PIFI, 2021PM0059), and the College Students' Science and Technology Innovation Project in IHEP and UCAS (H95120P0U7). This work was partly supported by the State Key Laboratory of Natural and Biomimetic Drugs, Peking University.

SUPPLEMENTARY MATERIAL

The Supplementary Material for this article can be found online at: https://www.frontiersin.org/articles/10.3389/fimmu.2021.676773/full#supplementary-material

REFERENCES

1. Tong L, Xiong Z, Shen Y, Peng Y, Zhu X. Metasurfaces: an acoustic meta-skin insulator. *Adv Mater* (2020) 32(37):2002251. doi: 10.1002/adma.202002251
2. Zhou C, Lin H, Sujin L, Maya C, Ma B. Organic-inorganic metal halide hybrids beyond perovskites. *Mater Res Lett* (2018) 6(10):552–69. doi: 10.1080/21663831.2018.1500951
3. Saparov B, Mitzi DB. Organic-inorganic perovskites: structural versatility for functional materials design. *Chem Rev* (2016) 116(7):4558–96. doi: 10.1021/acs.chemrev.5b00715
4. Ahmad S, Husain A, AliKhan MM, Khan I, Khan A, Asiri AM. Perovskite-based material for sensor applications. *Hybrid Perovskite Compos Mat* (2021) 135–45. doi: 10.1016/B978-0-12-819977-0.00005-6
5. Stoerzinger KA, Hong W, Wang X, Rao RR, Shao-Horn Y. Decreasing hydroxylation affinity of La(1-x)SrxMnO_3 perovskites to promote oxygen reduction electrocatalysis. *Chem Mater* (2017) 29(23):9990–7. doi: 10.1021/acs.chemmater.7b03399
6. Jin HH, Dong HS, Min HJ, Lee ML, Sang HI. Highly flexible, high-performance perovskite solar cells with adhesion promoted $AuCl_3$-doped graphene electrodes. *J Mater Chem A* (2017) 5(40):21146–52. doi: 10.1039/C7TA06465A
7. Howard JM, Lahoti R, Leite M. Imaging metal halide perovskites material and properties at the nanoscale. *Adv Energy Mater* (2019) 10(26):1903161. doi: 10.1039/C7TA06465A
8. Wang K, Zheng L, Zhu T, Yao X, Yi C, Zhang X, et al. Efficient perovskite solar cells by hybrid perovskites incorporated with heterovalent neodymium cations. *Nano Energy* (2019) 61:352–60. doi: 10.1016/j.nanoen.2019.04.073
9. Wegrowski Y, Milard AL, Kotlarz G, Toulmonde E, Maquart FX, Bernard J. Cell surface proteoglycan expression during maturation of human monocytes-derived dendritic cells and macrophages. *Clin Exp Immunol* (2010) 144(3):485–93. doi: 10.1111/j.1365-2249.2006.03059.x
10. Walkey CD, Olsen JB, Guo H, Emili J. Chan WCW Nanoparticle size and surface chemistry determine serum protein adsorption and macrophage uptake. *J Am Chem Soc* (2012) 134(4):2139–47. doi: 10.1021/ja2084338
11. Jiang J, Oberdörster J, Biswas P. Characterization of size, surface charge, and agglomeration state of nanoparticle dispersions for toxicological studies. *J Nanopart Res* (2009) 11(1):77–89. doi: 10.1007/s11051-008-9446-4
12. Xiao B, Laroui H, Ayyadurai S, Viennois E, Charania MA, Zhang Y, et al. Mannosylated bioreducible nanoparticle-mediated macrophage-specific TNF-α RNA interference for IBD therapy. *Biomater* (2013) 34(30):7471–82. doi: 10.1016/j.biomaterials.2013.06.008
13. Jason RM, Farouc A. A macrophage-targeted theranostic nanoparticle for biomedical applications. *Small* (2006) 2(8-9):983–7. doi: 10.1002/smll.200600139
14. Grekova SP, Aprahamian M, Giese N, Schmitt S, Giese T, Falk C, et al. Immune cells participate in the oncosuppressive activity of parvovirus H-1PV and are activated as a result of their abortive infection with this agent. *Cancer Biol Ther* (2010) 10(12):1280–9. doi: 10.4161/cbt.10.12.13455
15. Tsounis C, Wang Y, Arandiyan H, Wong RJ, Toe CY, Amal R, et al. Tuning the selectivity of $LaNiO_3$ perovskites for CO_2 hydrogenation through potassium substitution. *Catalysts* (2020) 10(4):409. doi: 10.3390/catal10040409
16. Klionsky DJ, Abdalla FC, Abeliovich H, Agrawal DK, Aliev G, Askew DS, et al. Guidelines for the use and interpretation of assays for monitoring autophagy. *Autophagy* (2008) 4(2):151–75. doi: 10.4161/auto.19496

17. Li H, Yan J, Meng D, Cai R, Gao X, Wang L, et al. Gold nanorod-based nanoplatform catalyzes constant NO neneration and protects from cardiovascular injury. *ACS Nano* (2020) 14(10):12854–65. doi: 10.1021/acsnano.0c03629
18. Wang L, Zhang T, Li P, Huang W, Tang J, Wang P, et al. Use of synchrotron radiation-analytical techniques to reveal chemical origin of silver-nanoparticle cytotoxicity. *ACS Nano* (2015) 9(6):532–6547. doi: 10.1021/acsnano.5b02483
19. Wang L, Liu Y, Li W, Jiang X, Ji Y, Wu X, et al. selective targeting of gold nanorods at the mitochondria of cancer cells: implications for cancer therapy. *Nano Lett* (2011) 11(2):772–80. doi: 10.1021/nl103992v
20. Mirshafiee V, Sun B, Chang C, Liao Y, Jiang W, Jiang J, et al. Toxicological profiling of metal oxide nanoparticles in liver context reveals pyroptosis in kupffer cells and macrophages versus apoptosis in hepatocytes. *ACS Nano* (2018) 12(4):3836–52. doi: 10.1021/acsnano.8b01086
21. Liu K, Liu P, Liu R, Wu X. Dual AO/EB staining to detect apoptosis in osteosarcoma cells compared with flow cytometry. *Med Sci Monit Basic Res* (2015) 21(9):15–20. doi: 10.12659/MSMBR.893327
22. Shen H, Mizushima N. At the end of the autophagic road: an emerging understanding of lysosomal functions in autophagy. *Trends Biochem Sci* (2014) 39(2):61–71. doi: 10.1016/j.tibs.2013.12.001
23. Mizushima N. Autophagy: process and function. *Genes Dev* (2007) 21 (22):2861–73. doi: 10.1101/gad.1599207
24. Li H, Chen J, Fan H, Cai R, Gao X, Meng D, et al. Initiation of protective autophagy in hepatocytes by gold nanorod core/silver shell nanostructures. *Nanoscale* (2020) 12(11):6429–37. doi: 10.1039/c9nr08621h
25. Mizushima N, Yoshimori T, Levine B. Methods in mammalian autophagy research. *Cell* (2010) 140(3):313–26. doi: 10.1016/j.cell.2010.01.028
26. Ichimura Y, Komatsu M. Selective degradation of p62 by autophagy. *Semin Immunopathol* (2010) 32(4):431–6. doi: 10.1007/s00281-010-0220-1
27. Wang K, Gong Q, Zhan Y, Chen B, Yin T, Lu Y, et al. Blockage of autophagic flux and induction of mitochondria fragmentation by paroxetine hydrochloride in lung cancer cells promotes apoptosis *via* the ROS-MAPK pathway. *Front Cell Dev Bio* (2019) 7:397. doi: 10.3389/fcell.2019.00397
28. Egorov VM, Smirnova SV, Formanovsky AA, Pletnev IV, Zolotov A. Dissolution of cellulose in ionic liquids as a way to obtain test materials for metal-ion detection. *Anal Bioanal Chem* (2007) 387(6):2263–9. doi: 10.1007/s00216-006-1114-x
29. Heidenau F, Mittelmeier W, Detsch R, Haenle M, Stenzel F, Ziegler G, et al. A novel antibacterial titania coating: metal ion toxicity and in vitro surface colonization. *J Matr Sci Mater Med* (2005) 16(10):883–8. doi: 10.1007/s10856-005-4422-3
30. Yoshinobu F, Hisayoshi IB, Tsugio S, Alkitugu O. Synthesis of monodispersed LaPO$_4$ particles using the hydrothermal reaction of an La(edta)-chelate precursor and phosphate ions. *J Alloy Compd* (1997) 252:103–9. doi: 10.1016/S0925-8388(96)02612-6
31. Greie J. The KdpFABC complex from Escherichia coli : A chimeric K$^+$ transporter merging ion pumps with ion channels. *Eur J Cell Biol* (2011) 90 (9):705–10. doi: 10.1016/j.ejcb.2011.04.011
32. Yan L, Zhao F, Wang J, Zu Y, Gu Z, Zhao Y. A safe-by-design strategy towards safer nanomaterials in nanomedicines. *Adv Mater* (2019) 31(45):e1805391. doi: 10.1002/adma.201805391
33. Scherz SR, Elazar Z. Regulation of autophagy by ROS: physiology and pathology. *Trends Biochem Sci* (2011) 36(1):30–8. doi: 10.1016/j.tibs.2010.07.007
34. Tan H, Wang N, Li S, Hong M, Wang X, Feng Y. The reactive oxygen species in macrophage polarization: reflecting its dual role in progression and treatment of human diseases. *Oxid Med Cell Longev* (2016) 2016:2795090. doi: 10.1155/2016/2795090
35. Kumar P, Swain MM, Pal A. Hyperglycemia-induced inflammation caused down-regulation of 8-oxoG-DNA glycosylase levels in murine macrophages is mediated by oxidative-nitrosative stress-dependent pathways. *Int J Biochem Cell Biol* (2016) 73:82–98. doi: 10.1016/j.biocel.2016.02.006
36. Wu M, Lu J. Autophagy and macrophage functions: inflammatory response and phagocytosis. *Cells* (2019) 9(1):70. doi: 10.3390/cells9010070
37. Racanelli AC, Kikkers SA, Choi AMK, Cloonan SM. Autophagy and inflammation in chronic respiratory disease. *Autophagy* (2018) 14(2):221–32. doi: 10.1080/15548627.2017.1389823
38. Frissora F, Chen H, Durbin JE, Bondada S. IFN-mediated inhibition of antigen receptor-induced B cell proliferation and CREB-1 binding activity requires STAT-1 transcription factor. *Eur J Immunol* (2003) 33(4):907–12. doi: 10.1002/eji.200323657
39. Ehrenstein MR, Evans JG, Singh A, Moore S, Warnes G, Isenber DA, et al. Compromised function of regulatory T cells in rheumatoid arthritis and reversal by anti-TNFα therapy. *J Exp Med* (2004) 200(3):277–85. doi: 10.1084/jem.20040165
40. Xu K, Chen W, Wang X, Peng Y, Liang A, Huang D, et al. Autophagy attenuates the catabolic effect during inflammatory conditions in nucleus pulposus cells, as sustained by NF-κB and JNK inhibition. *Int J Mol Med* (2015) 36(3):661–8. doi: 10.3892/ijmm.2015.2280
41. Lukashevich IS, Maryankova R, Vladyko AS, Nashkevich N, Koleda S, Djavani M, et al. Lassa and mopeia virus replication in human monocytes/macrophages and in endothelial cells: Different effects on IL-8 and TNF-gene expression. *J Med Viro* (1999) 59(4):552–60. doi: 10.1002/(SICI)1096-9071(199912)59:4<552::AID-JMV21>3.0.CO;2-A
42. Luo M, Wong S, Chan M, Chan M, Yu L, Yu S, et al. Autophagy mediates HBx-induced nuclear factor-κB Activation and Release of IL-6, IL-8, and CXCL2 in Hepatocytes. *J Cell Physiol* (2015) 230(10):2382–9. doi: 10.1002/jcp.24967
43. Chen M, Zhao Z, Meng Q, Liang P, Su Z, Wu Y, et al. TRIM14 promotes non-canonical NF-κB activation by modulating p100/p52 stability *via* selective Autophagy. *Adv Sci* (2020) 7(1):1901261. doi: 10.1002/advs.201901261
44. Jia G, Gang G, Gangahar DM, Agrawal DK. Insulin-like growth factor-1 and TNF-α regulate autophagy through c-jun N-terminal kinase and Akt pathways in human atherosclerotic vascular smooth cells. *Immunol Cell Biol* (2006) 84(5):448–54. doi: 10.1111/j.1440-1711.2006.01454.x
45. Prokesch A, Blaschitz A, Bauer T, Moser G, Hiden U, Zadora J, et al. Placental DAPK1 and autophagy marker LC3B-II are dysregulated by TNF-α in a gestational age-dependent manner. *Histochem Cell Biol* (2017) 147(6):695–705. doi: 10.1007/s00418-016-1537-1
46. Chen R, Sun Y, Cui X, Ji Z, Kong X, Wu S, et al. Autophagy promotes aortic adventitial fibrosis via the IL-6/Jak1 signaling pathway in Takayasu's arteritis. *J Autoimmun* (2019) 99:39–47. doi: 10.1016/j.jaut.2019.01.010
47. Zhang H, Mccarty N. Tampering with cancer chemoresistance by targeting the TGM2-IL6-autophagy regulatory network. *Autophagy* (2017) 13(3):627–8. doi: 10.1080/15548627.2016.1271516
48. Maedler K, Joachim S, Sturis J, Zuelling RA. Glucose- and interleukin-1β-induced β-Cell apoptosis requires Ca^{2+} influx and extracellular signal-regulated kinase (ERK) 1/2 activation and is prevented by a sulfonylurea receptor 1/inwardly rectifying K$^+$ channel 6.2 (SUR/Kir6.2) selective potassium channel opener in human islets. *Diabetes* (2004) 53(7):1706–171. doi: 10.2337/diabetes.53.7.1706
49. Meissner F, Molawi K, Zychlinsky A. Mutant superoxide dismutase 1-induced IL-1β accelerates ALS pathogenesis. *Proc Natl Acad Sci* (2010) 107(29):13046–50. doi: 10.1073/pnas.1002396107
50. Li R, Ji Z, Qin H, Kang X, Sun B, Wang M, et al. Interference in autophagosome fusion by rare earth nanoparticles disrupts autophagic flux and regulation of an interleukin-1β producing inflammasome. *ACS Nano* (2014) 8(10):10280–92. doi: 10.1021/nn505002w
51. Levine B, Mizushima N, Virgin HW. Autophagy in immunity and inflammation. *Nature* (2011) 469:323–35. doi: 10.1038/nature07383
52. Virgin HW, Levine B. Autophagy genes in immunity. *Nat Immunol* (2009) 10 (5):461–70. doi: 10.1038/nature09782
53. Into T, inomata M, Takayama M, Takjgawa T. Autophagy in regulation of Toll-like receptor signaling. *Cell Signal* (2012) 24(6):1150–62. doi: 10.1016/j.cellsig.2012.01.020
54. Saitoh T, Fujita N, Jang MH, Yang BG, Satoh T, Omori H, et al. Loss of the autophagy protein Atg16L1 enhances endotoxin-induced IL-1 beta production. *Nature* (2008) 456(7219):264–8. doi: 10.1038/ni.1726
55. Lodder J, Denaës T, Chobert MN, Wan J, El-Benna J, Pawlotsky JM, et al. Macrophage autophagy protects against liver fibrosis in mice. *Autophagy* (2015) 11(8):1280–92. doi: 10.1080/15548627.2015.1058473
56. Denaës T, Lodder J, Chobert MN, Ruiz I, Pawlotsky JM, Lotersztajn S. Teixeira-Clerc F. The cannabinoid receptor 2 protects against alcoholic liver disease via a macrophage autophagy-dependent pathway. *Sci Rep* (2016) 6:28806. doi: 10.1038/srep28806

57. Stopford W, Turner J, Cappellini D, Brock T. Bioaccessibility testing of cobalt compounds. *J Environ Monit* (2003) 5(4):675–80. doi: 10.1039/b302257a

Conflict of Interest: The authors declare that the research was conducted in the absence of any commercial or financial relationships that could be construed as a potential conflict of interest.

frontiers
in Molecular Biosciences

MINI REVIEW
published: 26 May 2021
doi: 10.3389/fmolb.2021.660993

Recent Advances in Fluorescence Imaging of Traumatic Brain Injury in Animal Models

Fei Lu[1], Jiating Cao[2], Qinglun Su[1], Qin Zhao[1], Huihai Wang[1], Weijiang Guan[3] and Wenjuan Zhou[2]**

[1]Department of Rehabilitation Medicine, The First People's Hospital of Lianyungang, The First Affiliated Hospital of Kangda College of Nanjing Medical University, Lianyungang, China, [2]Department of Chemistry, Capital Normal University, Beijing, China, [3]State Key Laboratory of Chemical Resource Engineering, College of Chemistry, Beijing University of Chemical Technology, Beijing, China

Traumatic brain injury (TBI) is one of the top three specific neurological disorders, requiring reliable, rapid, and sensitive imaging of brain vessels, tissues, and cells for effective diagnosis and treatment. Although the use of medical imaging such as computed tomography (CT) and magnetic resonance imaging (MRI) for the TBI detection is well established, the exploration of novel TBI imaging techniques is of great interest. In this review, recent advances in fluorescence imaging for the diagnosis and evaluation of TBI are summarized and discussed in three sections: imaging of cerebral vessels, imaging of brain tissues and cells, and imaging of TBI-related biomarkers. Design strategies for probes and labels used in TBI fluorescence imaging are also described in detail to inspire broader applications. Moreover, the multimodal TBI imaging platforms combining MRI and fluorescence imaging are also briefly introduced. It is hoped that this review will promote more studies on TBI fluorescence imaging, and enable its use for clinical diagnosis as early as possible, helping TBI patients get better treatment and rehabilitation.

Keywords: traumatic brain injury, inflammation, molecular diagnostics, biomarkers, nanomaterial, imaging

OPEN ACCESS

Edited by:
Yang Li,
Shenzhen Institutes of Advanced Technology, Chinese Academy of Sciences (CAS), China

Reviewed by:
Shuhui Liu,
Icahn School of Medicine at Mount Sinai, United States
Pengfei Zhang,
Shenzhen Institutes of Advanced Technology, Chinese Academy of Sciences (CAS), China

***Correspondence:**
Weijiang Guan
wjguan@mail.buct.edu.cn
Wenjuan Zhou
zhouwenjuan@cnu.edu.cn

Specialty section:
This article was submitted to Nanobiotechnology, a section of the journal Frontiers in Molecular Biosciences

Received: *30 January 2021*
Accepted: *11 May 2021*
Published: *26 May 2021*

Citation:
Lu F, Cao J, Su Q, Zhao Q, Wang H, Guan W and Zhou W (2021) Recent Advances in Fluorescence Imaging of Traumatic Brain Injury in Animal Models. Front. Mol. Biosci. 8:660993. doi: 10.3389/fmolb.2021.660993

INTRODUCTION

Traumatic brain injury (TBI) refers to a brain damage caused by trauma, usually occurring in traffic accidents, falls, violent blows, sports, and combat (Leeds et al., 2014; Treble-Barna et al., 2017; Li et al., 2018). As one of the top three specific neurological disorders worldwide, TBI has become a huge public problem that threatens human health and life. Currently, more than 50 million people suffer from TBI every year, which puts a heavy burden on their families and the whole society (Maas et al., 2017). During the TBI process, the initial impact causes both primary and secondary injuries. Primary injuries include cerebral concussion, cerebral contusion, laceration, and penetrating wounds that occur immediately as a result of direct mechanical damage (Katzenberger et al., 2013; Kwon et al., 2016; Barbacci et al., 2017). On the other hand, some pathophysiological processes, such as post-traumatic neurotransmitter release, free radical generation, mitochondrial dysfunction, inflammatory response, abnormal coagulation function, and blood–brain barrier damage, subsequently cause secondary brain injuries and lead to cerebrovascular and neurological disorders (Brown et al., 2019; Glotfelty et al., 2019; Ghosh et al., 2020). Therefore, rapid and sensitive imaging of brain tissues, cerebrovascular vessels, and cells is particularly important for the diagnosis and treatment of TBI.

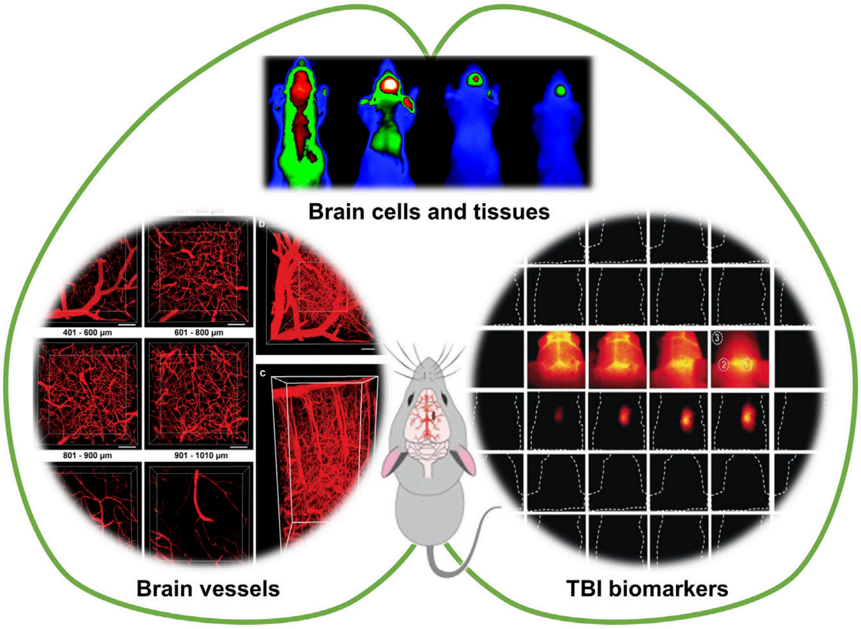

SCHEME 1 | Fluorescence imaging for visualizing cerebral vessels, brain tissues and cells, and TBI-related biomarkers. Partially cited from ref (Li et al., 2018), ref (Wang et al., 2019), ref (Xie et al., 2013), ref (Maas et al., 2017).

Medical imaging including computed tomography (CT) and magnetic resonance imaging (MRI) is the most used imaging modality for TBI (Brody et al., 2015; Shin et al., 2018; Lindberg et al., 2019). CT is capable of objectively reflecting the size, shape, and distribution of brain tissues, while MRI can provide a higher level of anatomical detail of brain tissues for noninvasive and longitudinal assessment of vessel occlusion, tissue injury, and hemodynamics (Kim and Gean, 2011; Bouts et al., 2017). However, the radiation and carcinogenic risks to the CT examiners cannot be ignored, especially for special populations such as pediatric patients (Brix and Nekolla, 2012). Moreover, challenges remain in the MRI technology concerning the scanning protocols (e.g., spatial vs. temporal resolution), analytical approaches, contrast agents, and sensitivity (Lelyveld et al., 2010; Li et al., 2018). Therefore, the development and application of new imaging techniques for TBI is of great interest.

Fluorescence imaging has attracted increasing attention in biological imaging because of its high spatial and temporal resolution, remarkable contrast, sensitivity, simplicity, and noninvasiveness (Ozawa et al., 2013; Liu et al., 2018; Li et al., 2020; Shah et al., 2020). With the rapid development of optical technology in the past two decades, the resolution of fluorescence imaging has experienced a dramatical improvement and reached up to the single nanometer scale (Wöll and Flors, 2017; Wilson et al., 2020; Zhang et al., 2020). The probes and labels employed for fluorescence imaging have also flourished, offering excitation ranges from single photon to two and even three photons, while the emission window has been extended to the near-infrared II (NIR-II, 1000–1700 nm) region (Wolfbeis, 2015; Li et al., 2019; Deng et al., 2020; Ji et al., 2020; Liu et al., 2020; Liu et al., 2021; Yang et al., 2021). Herein, we review recent advances in fluorescence imaging as a promising technique for the diagnosis and evaluation of TBI. To be specific, this review summarizes the current utilization and performance of fluorescence imaging for visualizing cerebral vessels, brain tissues and cells, and TBI-related biomarkers (**Scheme 1**). The design strategies for TBI imaging since 2008 are described and discussed in detail. Additionally, multimodal imaging platforms based on the combination of MRI and fluorescence imaging for the detection of TBI are also briefly presented. Our goal is to help researchers stay abreast of current advances of TBI fluorescence imaging and understand the potential opportunities and challenges.

IMAGING OF CEREBRAL VESSELS

In patients with craniocerebral injury, cerebral ischemia is the most common pathological change in secondary brain injuries, and is caused by the immediate decrease in cerebral blood flow (CBF). Peri-contusion ischemia is suggested to be induced by vasoconstriction, microvascular compression, and cerebral microvascular obstruction. To achieve sufficient spatial and temporal resolution, earlier studies raised the utility of *in vivo* fluorescence microscopy (IVM) for the investigation of vascular activities and vessel diameters in the microcirculation after TBI (Schwarzmaier et al., 2010; Obenaus et al., 2017). For example, visualization of the microvessels was performed by intravenously injecting fluorescein isothiocyanate-dextrane (FITC-dextrane) as the fluorescent plasma marker (Schwarzmaier et al., 2010). Meanwhile, white blood cells and platelets were stained with the fluorescent rhodamine 6G. With the help of fluorescent dyes with different emitting colors, multiple parameters of the microcirculation (e.g., vessel diameter, leukocyte-endothelial interactions, and microthrombus formation) can be analyzed in the same vessel segment.

The challenges of *in vivo* fluorescence imaging include light absorption and scattering, autofluorescence, and low depth penetration. To overcome these obstacles, near-infrared (NIR, 650–1700 nm) fluorescence imaging techniques, especially NIR-II (1000–1700 nm) fluorescence imaging, have been developed successively. The development of NIR fluorophores is closely related to the application of NIR fluorescence imaging in biological and medical fields. An effective strategy for constructing NIR fluorophores is to incorporate donor–acceptor–donor structures to reduce the band gap of fluorophores. For instance, a NIR-II fluorophore (IR-E1) was designed with benzo[1,2-c:4,5-c′]bis([1,2,5] thiadiazole) (BBTD) as the acceptor and thiophene-based moiety as the donor (Zhang et al., 2016). Under 808 nm excitation, IR-E1 showed NIR-II emission at 1071 nm, which was applied to *in vivo* cerebral imaging of hypoperfusion in a TBI mouse model. Compared to conventional fluorescence imaging, NIR-II fluorescence imaging allows dynamic *in vivo* imaging of the brain without craniotomy.

Besides the NIR emission, NIR excitation can also be used for deep tissue imaging. Two-photon fluorescence (2PF) imaging is usually performed by two-photon NIR excitation, which is a nonlinear process with a square dependence on the intensity of excitation light, allowing for three-dimensional (3D) tissue imaging with high spatial and temporal resolution. Meanwhile, the low-energy two-photon NIR excitation light has less damages to the tissues and deeper penetration depth. Schwarzmaier et al. (Schwarzmaier et al., 2015) applied *in vivo* two-photon microscopy to investigate vascular leakage in a clinically relevant model of TBI via green fluorescent protein (GFP) expression in vascular endothelial cells and intravenous injection of fluorescent plasma marker tetramethylrhodamine-dextran (TMRM). Arterioles and venules can be distinguished based on the levels of GFP expression. A penetration depth of 300 μm was achieved through the cranial window.

In addition, organic fluorophores with large multiphoton absorption cross section and high fluorescence quantum efficiency are capable of achieving both NIR excitation and emission. For example, Liu group developed an ultrasmall single-chain conjugated polymer dots (CPdots) with NIR-II excitation and bright NIR-I (700–950 nm) emission for deep *in vivo* two-photon fluorescence imaging of intact mouse brain (Wang et al., 2019). The vasculature was labeled by retro-orbital injection of CPdots, followed by 2PF imaging of brain blood vessels under 1200 nm fs laser excitation. With a cranial window, the maximal imaging depth reaches 1010 μm. Moreover, Tang group developed three-photon fluorescence (3PF) microscopy imaging technique for the *in vivo* brain vascular imaging by using a far-red/near-infrared (FR/NIR) luminogen (BTF) with remarkable aggregation-induced emission (AIE) characteristics (Qin et al., 2020). Through the further construction of BTF-based nanodots with a large three-photon absorption cross section, *In vivo* 3PF images and 3D high-resolution images of the mouse brain vessels with intact skull was obtained before/after brain thrombosis. Undoubtedly, these pioneering studies have a great potential for clinical applications.

IMAGING OF BRAIN CELLS AND TISSUES

TBI could induce the blood–brain barrier (BBB) disruption and neuroinflammations via regulating the lipid peroxidation and induction of oxidative stress to induce cell death and further disability of patient as the results of the secondary injury of TBI (Li et al., 2020). Observation or tracking of brain cells and tissues promote deeper understanding of injury mechanism, providing guidance for the prognosis and treatment of TBI. Various kinds of fluorescent labels including fluorescent proteins, small molecules, and nanoparticles have been developed for the fluorescence imaging of brain cells and tissues.

Neuroinflammatory responses (e.g., microglia/macrophage activation) could be induce by TBI, which is regarded as a key factor in the secondary injury cascade following TBI. Immunofluorescence staining is a classic method to investigate the mechanism of TBI-induced neuroinflammatory responses (Readnower et al., 2010; Villapol et al., 2017; Takahata et al., 2019; Mao et al., 2021). By double-labeling immunofluorescence, the levels of the lipid peroxidation marker 4-hydroxynonenal (4-HNE) and the protein nitration marker 3-nitrotyrosine (3-NT) in brain sections after exposure to blast have been determined (Readnower et al., 2010). The temporal course of brain oxidative stress following exposure to blast was obtained, which was rapidly increased at 3 h postexposure and were resolved by 24 h postexposure. The activation of microglial/macrophages could also be observed using double-labeling technique with two primary antibodies (polyclonal anti-rabbit P2Y12 for microglial cells and polyclonal anti-rat F4/80 for macrophages), and then corresponding fluorescent-dye conjugated secondary antibodies (anti-rabbit Alexa Fluor 568-conjugated IgG and anti-rat Alexa Fluor 488-conjugated IgG) (Villapol et al., 2017).

Another efficient methodology for the visual analysis of TBI is fluorescence protein expression. Yellow fluorescent protein (YFP) has been expressed under the promoter for the classically activated (M1) and alternatively activated (M2) macrophages for the identification of macrophage subset, demonstrating the heterogeneous polarization of the macrophage response to TBI (Hsieh et al., 2013). If YFP is expressed cortical neurons, the fluorescent protein can be used for the assessment of axonal injury over time within a well-defined axonal population, enabling an evaluation of the axonal injury pathobiology induced by TBI (Hånell et al., 2015). Moreover, fluorescent protein-expressing mesenchymal stem cells (MSCs) can be used for the location tracking of the MSCs during the TBI recovery progress (Hung et al., 2010; Lam et al., 2013).

Cerebral cell death is the major neuropathological basis in TBI, and apoptosis and autophagic cell death account for a considerable proportion. Molecular imaging for selective detection of apoptosis in experimental TBI was reported as early as 2008 (Reshef et al., 2008). Following intravenous administration *in vivo*, the animals with TBI were sacrificed, and brain tissues labelled with the apoptosis-sensitive N,N-didansyl-L-cystine (DDC) can be imaged via fluorescent microcopy. In addition, whole-body fluorescence imaging of cell death could be achieved using NIR fluorescent probes in a mouse model of TBI (Smith et al., 2012; Xie et al., 2013). A NIR fluorescent conjugate of a synthetic heat shock protein-90 (Hsp-90) alkylator, (4-N-S-glutathionylacetyl amino) phenylarsonous acid (GSAO), was utilized for labeling of apoptotic and necrotic cells (Xie et al., 2013). The GSAO can covalently bind with the Cys597 and Cys598 residues of Hsp-90 in mammalian cells through the cross-links of As(III) atom of GSAO and sulphur atoms of Hsp-90, Cys597, and Cys598. For healthy individuals, GSAO exists in the extracellular environment and is largely unreactive because there are few appropriately spaced cysteines thiols. When the plasma membrane is damaged (mid-to late-stage apoptotic cells), GSAO could enter the cell freely and display high reactivity. The selectivity of the fluorescent probe for dying and dead cells provides high signal-to-noise ratio and reliability for *in vivo* imaging of brain lesion cell death. Moreover, multiple biochemical changes in the early stage of TBI can be reported by using multiple probes in a single animal (Smith et al., 2012). A binary mixture of a NIR fluorescent probe (PSS-794) for detecting cell death and a deep-red dye (Tracer-653) for monitoring BBB disruption was described for multicolor imaging of cell death and blood-brain-barrier permeability in a single animal.

IMAGING OF BIOMARKERS

Medical imaging techniques hardly provide an accurate prediction of the effects of brain injury (secondary injury) due to long-term impacts and heterogeneous nature of TBI (Mondello et al., 2011; Maas et al., 2017; Mondello et al., 2018). Biomarkers of brain injury refer to substances that can be detected and released into the cerebrospinal fluid and blood during brain injury. The level of biomarkers changes in the early stage of brain injury, which plays a crucial role in predicting early brain injury, identifying brain injury areas, and evaluating prognosis (Wang et al., 2018). Generally, brain injury is usually associated with neuroinflammation or nerve damage, which produces a number of associated biomarkers, such as acidity (pH) change, hypochlorous acid (HOCl), peroxynitrite ($ONOO^-$), and calproteinase-1 (Zhai et al., 2019; Kudryashev et al., 2020; Li et al., 2020; Song et al., 2020). The sensitivity and specificity of biomarker detection are often more advantageous than imaging examination.

Neuroinflammation as one of the earliest hallmark features of TBI can cause an increased oxygen consumption and a hypoxic state in BV-2 cells. A dramatic decrease in mitochondrial pH appears as a result of cellular anaerobic respiration. To monitor pH changes, a ratiometric fluorescence probe (FRET-pH) was developed by covalently linking 6-hydroxy-quinoline-2-benzothiazole (ADN) as a fluorescent donor to a derivative of Rh6G (SRhB) as a fluorescent acceptor and a response group (Zhai et al., 2019). The fluorescence of ADN (λ_{em} = 454 nm) could be excited by absorption of one photon (λ_{abs} = 350 nm) or simultaneous absorption of two photons (λ_{abs} = 700 nm). SRhB exhibited intense orange-red fluorescence (λ_{em} = 562 nm) through energy transfer from AND and was highly sensitive in the pH range of 4.6–7.4. FRET-pH was able to clearly detect pH changes in both BV-2 cells and rat brain tissues using 2PF microscopy.

TBI-associated neuroinflammation can also cause sustained oxidative stress (OT) to produce reactive oxygen species (ROS), including HOCl, $ONOO^-$, etc. The general strategy for detecting mitochondrial ROS is similar to that for detecting mitochondrial pH. For example, Liu et al. synthesized a ratiometric two-photon fluorescence probe (Mito-P-OCl) consisting of three moieties: a rhodanol moiety (Rhod-c), a dihydrazide moiety, and a quaternized pyridine moiety (Song et al., 2020). They acted as the two-photon fluorophore, the HOCl response group, and the mitochondrial-targeting group, respectively. The as-prepared Mito-P-OCl itself had blue fluorescence due to the occurrence of excited-state intramolecular proton transfer (ESIPT) in the molecule. In the presence of HOCl, the rhodol ring on Mito-P-OCl could be opened to form Rhod-c, in which the ESIPT process was inhibited, thus showing a strong red fluorescence. Taking advantages of the rhodol ring-opening/ring-closing switch, Mito-P-OCl successfully achieved the monitoring of endogenous HOCl in living cells and brain tissue. To further expand the above strategy to *in vivo* imaging, a novel targeted activatable NIR-II nanoprobe (V&A@Ag_2S) with emission at the range of 1000–1800 nm was designed and synthesized (Li et al., 2020). The V&A@Ag_2S includes three components: VCAM1 binding peptide (VHPKQHR) for targeting the inflamed endothelium expressing VCAM1 in TBI regions, a NIR absorber A1094 for responding $ONOO^-$ changes, and Ag_2S QD for emitting NIR-II fluorescence. Due to the large overlap between the absorption spectrum of A1094 and the emission spectrum of Ag_2S QD, the fluorescence of V&A@Ag_2S is quenched through the energy transfer from Ag_2S QD to A1094. On the contrary, the presence of $ONOO^-$ oxidized A1094 to decrease the absorbance at 1094 nm, turning on fluorescence signal of the Ag_2S QD at 1050 nm. The unique optical properties of NIR-II imaging enabled real-time dynamic measurement of $ONOO^-$ in live mice with brain vascular injury.

MULTIMODAL IMAGING

Medical imaging including CT, MRI, X-ray is the most used imaging modality for TBI without any surgery (James and Dasarathy, 2014; Du et al., 2016; Kaur and Singh, 2020). Due to different imaging principles, a single imaging modality often has limitations in terms of sensitivity, specificity, targeting ability, and spatial resolution. Multimodal imaging probes can provide diagnostic information combining different imaging modalities, which overcomes the deficiency of traditional single-modal imaging, and widens the application range of imaging technology. Multimodal imaging enables rapid and accurate imaging at specific target sites to provide a comprehensive assessment of functional, structural, and metabolic changes *in vivo* (Feng et al., 2019). Therefore, the development of multimodal probes for TBI has become the focus of research (Guo et al., 2019; Bony et al., 2020; Schomann et al., 2020). Among them, fluorescence/MRI bimodal probes have attracted much attention with the superior advantages of high tissue

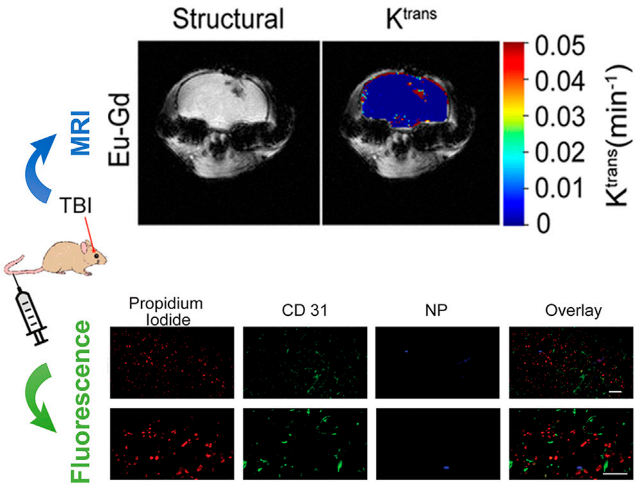

FIGURE 1 | Multimodal fluorescence and magnetic resonance imaging of passive accumulation and retention in a mouse traumatic brain injury model. Adapted and modified with permission from ref (Bony et al., 2020) (Copyright 2020 American Chemical Society).

resolution and imaging sensitivity. A feasible attempt is to use the mixed lanthanide oxide magnetic nanoparticles (MNPs) containing europium (Eu) for fluorescence imaging and gadolinium (Gd) for MRI in TBI (Bony et al., 2020). Moreover, these Eu–Gd NPs can be modified with different functional poly(ethylene glycol) (PEG) to not only tune their hydrodynamic dimensions and surface charge, but also to improve targeting ability and biocompatibility. In a controlled cortical impact (CCI) mouse model of TBI, MRI data showed that Eu-Gd NPs were rapidly accumulated and retained in the mouse brain after intravenous injection, while fluorescence imaging revealed their spatial distribution on cells and tissues (**Figure 1**). It is worthwhile to expect that more NIR and multiphoton fluorophores suitable for tri-modal or even quad-modal imaging can be designed and synthesized TBI.

CONCLUSION AND OUTLOOK

Over the past decade, various fluorescence imaging techniques for TBI diagnosis have made considerable progress due to their abilities to directly detect and visualize brain microstructures (e.g., blood vessels, tissues, and cells) and to track dynamic changes during TBI injury, treatment, and rehabilitation. It overcomes the deficiency of strong radiation, low resolution and low sensitivity of conventional brain MRI and CT, showing great clinic potentials in the diagnosis and treatment of TBI. Superior to conventional fluorescence imaging in the visible and NIR-I spectral range (400–900 nm), NIR II fluorescence imaging greatly reduces tissue scattering, light absorption, and autofluorescence, allowing deeper tissue penetration, higher spatial resolution, and dynamic *in vivo* imaging of the brain without craniotomy. In addition, the appearance of organic fluorophores with large photon absorption cross sections and high fluorescence quantum efficiency has also greatly promoted the development of two-photon or even three-photon imaging for TBI diagnosis. With the continuous development of fluorescence imaging technology, researchers have begun to explore novel multimodal probes (e.g., fluorescence/MRI dual-modal probe) to achieve complementary parameters, so as to make more accurate diagnosis and effective treatment of TBI.

Notably, challenges remain in translating the TBI fluorescence imaging platform from the research setting to more practical devices and clinical applications. Hence, more investigations and innovations are necessary to develop universal fluorescent dyes, improve the operability of the method, and reduce professional and technical requirements. NIR II or multi-photon fluorescence imaging can be regarded an ideal candidate for *in vivo* and *in situ* imaging of brain. In order to achieve full-scale and high-quality imaging of the brain through the scalp and skull, fluorophores with higher quantum yield should be designed and developed. Another promising strategy is the combining of fluorescence imaging with other imaging techniques (e.g., MRI, CT, and X-ray). The multimodal imaging system can provide a more accurate and comprehensive reference for the diagnosis and treatment of TBI, especially for the secondary brain injury after TBI. In addition, the neurotoxicity of fluorescent probes must be considered when performing brain imaging. The effects of the developed fluorescent probes on human health and brain function are unclear, which also limits the pace of clinical applications of fluorescent imaging.

Compared with brain structure (blood vessel, tissue, etc.) imaging, the identification and detection of TBI-associated biomarkers can provide a more accurate molecular level diagnosis of TBI, which is the key to the early diagnosis of craniocerebral injury. The identified biomarkers allow us to measure the extent of damage and monitor the recovery process from brain injury. It is worth noting that the biomarkers released at different time periods of the occurrence and development of TBI are different, thus further explore about the optimum detection moment for different types of biomarkers is of great significance in assessing the injury and prognosis of patients with TBI.

AUTHOR CONTRIBUTIONS

All authors listed have made a substantial, direct, and intellectual contribution to the work and approved it for publication.

FUNDING

This work was supported by the National Natural Science Foundation of China (21804094 and 21804006), the Scientific Research Project of Beijing Educational Committee (KM201910028015), the Beijing Natural Science Foundation (2212013), and the Fundamental Research Funds for the Central Universities (buctrc201820).

REFERENCES

Barbacci, D. C., Roux, A., Muller, L., Jackson, S. N., Post, J., Baldwin, K., et al. (2017). Mass Spectrometric Imaging of Ceramide Biomarkers Tracks Therapeutic Response in Traumatic Brain Injury. *ACS Chem. Neurosci.* 8, 2266–2274. doi:10.1021/acschemneuro.7b00189

Bony, B. A., Miller, H. A., Tarudji, A. W., Gee, C. C., Sarella, A., Nichols, M. G., et al. (2020). Ultrasmall Mixed Eu-Gd Oxide Nanoparticles for Multimodal Fluorescence and Magnetic Resonance Imaging of Passive Accumulation and Retention in TBI. *ACS Omega* 5, 16220–16227. doi:10.1021/acsomega.0c01890

Bouts, M. J. R. J., Wu, O., and Dijkhuizen, R. M. (2017). "Magnetic Resonance Imaging of Stroke," in *"Magnetic Resonance Imaging of Stroke" in Primer on Cerebrovascular Diseases*. Editor L. R. Caplan (Amsterdam, Netherlands: Elsevier Inc., Academic Press), 328–332. doi:10.1016/b978-0-12-803058-5.00069-2

Brix, G., and Nekolla, E. A. (2012). in *"Radiation Exposure and Risk Associated with CT Examinations" in Multislice-CT of the Abdomen*. Editor C. J. Zech (New York Dordrecht London: Springer Heidelberg Academic Press), 25–36. doi:10.1007/174_2011_405

Brody, D. L., Mac Donald, C. L., and Shimony, J. S. (2015). "Current and Future Diagnostic Tools for Traumatic Brain Injury," in *Handbook of Clinical Neurology*. Editors J. Grafman and A. M. Salazar (Amsterdam, Netherlands: Elsevier B.V.Academic Press), 267–275. doi:10.1016/b978-0-444-52892-6.00017-9

Brown, A. C., Lavik, E., and Stabenfeldt, S. E. (2019). Biomimetic Strategies to Treat Traumatic Brain Injury by Leveraging Fibrinogen. *Bioconjug. Chem.* 30, 1951–1956. doi:10.1021/acs.bioconjchem.9b00360

Deng, G., Peng, X., Sun, Z., Zheng, W., Yu, J., Du, L., et al. (2020). Natural-Killer-Cell-Inspired Nanorobots with Aggregation-Induced Emission Characteristics for Near-Infrared-II Fluorescence-Guided Glioma Theranostics. *ACS Nano* 14, 11452–11462. doi:10.1021/acsnano.0c03824

Du, J., Li, W., Lu, K., and Xiao, B. (2016). An Overview of Multi-Modal Medical Image Fusion. *Neurocomputing* 215, 3–20. doi:10.1016/j.neucom.2015.07.160

Feng, Y., Zhang, X. D., Zheng, G., and Zhang, L. J. (2019). Chemotherapy-Induced Brain Changes in Breast Cancer Survivors: Evaluation with Multimodality Magnetic Resonance Imaging. *Brain Imaging Behav.* 13, 1799–1814. doi:10.1007/s11682-019-00074-y

Ghosh, S., Garg, S., and Ghosh, S. (2020). Cell-Derived Exosome Therapy: A Novel Approach to Treat Post-Traumatic Brain Injury Mediated Neural Injury. *ACS Chem. Neurosci.* 11, 2045–2047. doi:10.1021/acschemneuro.0c00368

Glotfelty, E. J., Delgado, T. E., Tovar-Y-Romo, L. B., Luo, Y., Hoffer, B. J., Olson, L., et al. (2019). Incretin Mimetics as Rational Candidates for the Treatment of Traumatic Brain Injury. *ACS Pharmacol. Transl. Sci.* 2, 66–91. doi:10.1021/acsptsci.9b00003

Guo, B., Feng, Z., Hu, D., Xu, S., Middha, E., Pan, Y., et al. (2019). Precise Deciphering of Brain Vasculatures and Microscopic Tumors with Dual NIR-II Fluorescence and Photoacoustic Imaging. *Adv. Mater.* 31, 1902504–1902508. doi:10.1002/adma.201902504

Hånell, A., Greer, J. E., McGinn, M. J., and Povlishock, J. T. (2015). Traumatic Brain Injury-Induced Axonal Phenotypes React Differently to Treatment. *Acta Neuropathol.* 129, 317–332. doi:10.1007/s00401-014-1376-x

Hsieh, C. L., Kim, C. C., Ryba, B. E., Niemi, E. C., Bando, J. K., Locksley, R. M., et al. (2013). Traumatic Brain Injury Induces Macrophage Subsets in the Brain. *Eur. J. Immunol.* 43, 2010–2022. doi:10.1002/eji.201243084

Hung, C.-J., Yao, C.-L., Cheng, F.-C., Wu, M.-L., Wang, T.-H., and Hwang, S.-M. (2010). Establishment of Immortalized Mesenchymal Stromal Cells with Red Fluorescence Protein Expression for In Vivo Transplantation and Tracing in the Rat Model with Traumatic Brain Injury. *Cytotherapy* 12, 455–465. doi:10.3109/14653240903555827

James, A. P., and Dasarathy, B. V. (2014). Medical Image Fusion: A Survey of the State of the Art. *Inf. Fusion* 19, 4–19. doi:10.1016/j.inffus.2013.12.002

Ji, Y., Jones, C., Baek, Y., Park, G. K., Kashiwagi, S., and Choi, H. S. (2020). Near-Infrared Fluorescence Imaging in Immunotherapy. *Adv. Drug Deliv. Rev.* 167, 121–134. doi:10.1016/j.addr.2020.06.012

Katzenberger, R. J., Loewen, C. A., Wassarman, D. R., Petersen, A. J., Ganetzky, B., and Wassarman, D. A. (2013). A Drosophila Model of Closed Head Traumatic Brain Injury. *Proc. Natl. Acad. Sci.* 110, E4152–E4159. doi:10.1073/pnas.1316895110

Kaur, M., and Singh, D. (2020). Multi-Modality Medical Image Fusion Technique Using Multi-Objective Differential Evolution Based Deep Neural Networks. *J. Ambient Intell. Hum. Comput.* 12, 2483–2493. doi:10.1007/s12652-020-02386-0

Kim, J. J., and Gean, A. D. (2011). Imaging for the Diagnosis and Management of Traumatic Brain Injury. *Neurotherapeutics* 8, 39–53. doi:10.1007/s13311-010-0003-3

Kudryashev, J. A., Waggoner, L. E., Leng, H. T., Mininni, N. H., and Kwon, E. J. (2020). An Activity-Based Nanosensor for Traumatic Brain Injury. *ACS Sens.* 5, 686–692. doi:10.1021/acssensors.9b01812

Kwon, E. J., Skalak, M., Lo Bu, R., and Bhatia, S. N. (2016). Neuron-Targeted Nanoparticle for SiRNA Delivery to Traumatic Brain Injuries. *ACS Nano* 10, 7926–7933. doi:10.1021/acsnano.6b03858

Lam, P. K., Lo, A. W. I., Wang, K. K. W., Lau, H. C. H., Leung, K. K. C., Li, K. T. C., et al. (2013). Transplantation of Mesenchymal Stem Cells to the Brain by Topical Application in an Experimental Traumatic Brain Injury Model. *J. Clin. Neurosci.* 20, 306–309. doi:10.1016/j.jocn.2012.03.028

Leeds, P. R., Yu, F., Wang, Z., Chiu, C.-T., Zhang, Y., Leng, Y., et al. (2014). A New Avenue for Lithium: Intervention in Traumatic Brain Injury. *ACS Chem. Neurosci.* 5, 422–433. doi:10.1021/cn500040g

Lelyveld, V. S., Atanasijevic, T., and Jasanoff, A. (2010). Challenges for Molecular Neuroimaging with MRI. *Int. J. Imaging Syst. Technol.* 20, 71–79. doi:10.1002/ima.20221

Li, B., Zhou, X., Yi, T.-L., Xu, Z.-W., Peng, D.-W., Guo, Y., et al. (2020). Bloodletting Puncture at Hand Twelve Jing-Well Points Improves Neurological Recovery by Ameliorating Acute Traumatic Brain Injury-Induced Coagulopathy in Mice. *Front. Neurosci.* 14, 403. doi:10.3389/fnins.2020.00403

Li, C., Chen, G., Zhang, Y., Wu, F., and Wang, Q. (2020). Advanced Fluorescence Imaging Technology in the Near-Infrared-II Window for Biomedical Applications. *J. Am. Chem. Soc.* 142, 14789–14804. doi:10.1021/jacs.0c07022

Li, C., Li, W., Liu, H., Zhang, Y., Chen, G., Li, Z., et al. (2020). An Activatable NIR-II Nanoprobe for In Vivo Early Real-Time Diagnosis of Traumatic Brain Injury. *Angew. Chem. Int. Ed.* 59, 247–252. doi:10.1002/anie.201911803

Li, W., Chen, R., Lv, J., Wang, H., Liu, Y., Peng, Y., et al. (2018). In Vivo Photoacoustic Imaging of Brain Injury and Rehabilitation by High-Efficient Near-Infrared Dye Labeled Mesenchymal Stem Cells with Enhanced Brain Barrier Permeability. *Adv. Sci.* 5, 1700277. doi:10.1002/advs.201700277In

Li, X., Shi, L., Li, L., Dong, C., Li, C.-z., and Shuang, S. (2019). Recent Advances in Carbon Nanodots: Properties and Applications in Cancer Diagnosis and Treatment. *J. Anal. Test.* 3, 37–49. doi:10.1007/s41664-019-00089-w

Lindberg, D. M., Stence, N. V., Grubenhoff, J. A., Lewis, T., Mirsky, D. M., Miller, A. L., et al. (2019). Feasibility and Accuracy of Fast MRI versus CT for Traumatic Brain Injury in Young Children. *Pediatrics* 144, e20190419. doi:10.1542/peds.2019-0419

Liu, H.-W., Chen, L., Xu, C., Li, Z., Zhang, H., Zhang, X.-B., et al. (2018). Recent Progresses in Small-Molecule Enzymatic Fluorescent Probes for Cancer Imaging. *Chem. Soc. Rev.* 47, 7140–7180. doi:10.1039/c7cs00862g

Liu, M., Gu, B., Wu, W., Duan, Y., Liu, H., Deng, X., et al. (2020). Binary Organic Nanoparticles with Bright Aggregation-Induced Emission for Three-Photon Brain Vascular Imaging. *Chem. Mater.* 32, 6437–6443. doi:10.1021/acs.chemmater.0c01577

Liu, X., Duan, Y., and Liu, B. (2021). Nanoparticles as Contrast Agents for Photoacoustic Brain Imaging. *Aggregate* 2, 4–19. doi:10.1002/agt2.26

Maas, A. I. R., Menon, D. K., Adelson, P. D., Andelic, N., Bell, M. J., Belli, A., et al. (2017). Traumatic Brain Injury: Integrated Approaches to Improve Prevention, Clinical Care, and Research. *Lancet Neurol.* 16, 987–1048. doi:10.1016/S1474-4422(17)30371-X

Maas, A. I. R., Menon, D. K., Adelson, P. D., Andelic, N., Bell, M. J., Belli, A., et al. Traumatic Brain Injury: Integrated Approaches to Improve Prevention, Clinical Care, and Research. *Lancet Neurol.* 16, 987–1048. doi:10.1016/S1474-4422(17)30371-X

Mao, L., Sun, L., Sun, J., Sun, B., Gao, Y., and Shi, H. (2021). Ethyl Pyruvate Improves White Matter Remodeling in Rats after Traumatic Brain Injury. *CNS Neurosci. Ther.* 27, 113–122. doi:10.1111/cns.13534

Mondello, S., Muller, U., Jeromin, A., Streeter, J., Hayes, R. L., and Wang, K. K. (2011). Blood-Based Diagnostics of Traumatic Brain Injuries. *Expert Rev. Mol. Diagn.* 11, 65–78. doi:10.1586/erm.10.104

Mondello, S., Thelin, E. P., Shaw, G., Salzet, M., Visalli, C., Cizkova, D., et al. (2018). Extracellular Vesicles: Pathogenetic, Diagnostic and Therapeutic Value in Traumatic Brain Injury. *Expert Rev. Proteomics* 15, 451–461. doi:10.1080/14789450.2018.1464914

Obenaus, A., Ng, M., Orantes, A. M., Kinney-Lang, E., Rashid, F., Hamer, M., et al. (2017). Traumatic Brain Injury Results in Acute Rarefication of the Vascular Network. *Sci. Rep.* 7, 239. doi:10.1038/s41598-017-00161-4

Ozawa, T., Yoshimura, H., and Kim, S. B. (2013). Advances in Fluorescence and Bioluminescence Imaging. *Anal. Chem.* 85, 590–609. doi:10.1021/ac3031724

Qin, W., Alifu, N., Lam, J. W. Y., Cui, Y., Su, H., Liang, G., et al. (2020). Facile Synthesis of Efficient Luminogens with AIE Features for Three-Photon Fluorescence Imaging of the Brain through the Intact Skull. *Adv. Mater.* 32, 2000364. doi:10.1002/adma.202000364

Readnower, R. D., Chavko, M., Adeeb, S., Conroy, M. D., Pauly, J. R., McCarron, R. M., et al. (2010). Increase in Blood-Brain Barrier Permeability, Oxidative Stress, and Activated Microglia in a Rat Model of Blast-Induced Traumatic Brain Injury. *J. Neurosci. Res.* 88, 3530–3539. doi:10.1002/jnr.22510

Reshef, A., Shirvan, A., Shohami, E., Grimberg, H., Levin, G., Cohen, A., et al. (2008). Targeting Cell Death In Vivo in Experimental Traumatic Brain Injury by a Novel Molecular Probe. *J. Neurotrauma* 25, 569–580. doi:10.1089/neu.2007.0341

Schomann, T., Iljas, J. D., Que, I., Li, Y., Suidgeest, E., Cruz, L. J., et al. (2020). Multimodal Imaging of Hair Follicle Bulge-Derived Stem Cells in a Mouse Model of Traumatic Brain Injury. *Cell Tissue Res.* 381, 55–69. doi:10.1007/s00441-020-03173-1

Schwarzmaier, S. M., Gallozzi, M., and Plesnila, N. (2015). Identification of the Vascular Source of Vasogenic Brain Edema Following Traumatic Brain Injury Using In Vivo 2-Photon Microscopy in Mice. *J. Neurotrauma* 32, 990–1000. doi:10.1089/neu.2014.3775

Schwarzmaier, S. M., Kim, S.-W., Trabold, R., and Plesnila, N. (2010). Temporal Profile of Thrombogenesis in the Cerebral Microcirculation after Traumatic Brain Injury in Mice. *J. Neurotrauma* 27, 121–130. doi:10.1089/neu.2009.1114

Shah, J. V., Gonda, A., Pemmaraju, R., Subash, A., Bobadilla Mendez, C., Berger, M., et al. (2020). Shortwave Infrared-Emitting Theranostics for Breast Cancer Therapy Response Monitoring. *Front. Mol. Biosci.* 7, 569415. doi:10.3389/fmolb.2020.569415

Shin, S. S., Huisman, T. A. G. M., and Hwang, M. (2018). Ultrasound Imaging for Traumatic Brain Injury. *J. Ultrasound Med.* 37, 1857–1867. doi:10.1002/jum.14547

Smith, B. A., Xie, B.-W., Van Beek, E. R., Que, I., Blankevoort, V., Xiao, S., et al. (2012). Multicolor Fluorescence Imaging of Traumatic Brain Injury in a Cryolesion Mouse Model. *ACS Chem. Neurosci.* 3, 530–537. doi:10.1021/cn3000197

Song, X., Li, C., Wang, Y., Wang, D., and Liu, Z. (2020). A Ratiometric Two-Photon Fluorescence Probe for Monitoring Mitochondrial HOCl Produced during the Traumatic Brain Injury Process. *Sensors Actuators B: Chem.* 311, 127895. doi:10.1016/j.snb.2020.127895

Takahata, K., Kimura, Y., Sahara, N., Koga, S., Shimada, H., Ichise, M., et al. (2019). PET-detectable Tau Pathology Correlates with Long-Term Neuropsychiatric Outcomes in Patients with Traumatic Brain Injury. *Brain* 142, 3265–3279. doi:10.1093/brain/awz238

Treble-Barna, A., Zang, H., Zhang, N., Taylor, H. G., Yeates, K. O., and Wade, S. (2017). Long-Term Neuropsychological Profiles and Their Role as Mediators of Adaptive Functioning after Traumatic Brain Injury in Early Childhood. *J. Neurotrauma* 34, 353–362. doi:10.1089/neu.2016.4476

Villapol, S., Loane, D. J., and Burns, M. P. (2017). Sexual Dimorphism in the Inflammatory Response to Traumatic Brain Injury. *Glia* 65, 1423–1438. doi:10.1002/glia.23171

Wang, K. K., Yang, Z., Zhu, T., Shi, Y., Rubenstein, R., Tyndall, J. A., et al. (2018). An Update on Diagnostic and Prognostic Biomarkers for Traumatic Brain Injury. *Expert Rev. Mol. Diagn.* 18, 165–180. doi:10.1080/14737159.2018.1428089

Wang, S., Liu, J., Feng, G., Ng, L. G., and Liu, B. (2019). NIR-II Excitable Conjugated Polymer Dots with Bright NIR-I Emission for Deep In Vivo Two-Photon Brain Imaging through Intact Skull. *Adv. Funct. Mater.* 29, 1808365. doi:10.1002/adfm.201808365

Wilson, A. J., Devasia, D., and Jain, P. K. (2020). Nanoscale Optical Imaging in Chemistry. *Chem. Soc. Rev.* 49, 6087–6112. doi:10.1039/d0cs00338g

Wolfbeis, O. S. (2015). An Overview of Nanoparticles Commonly Used in Fluorescent Bioimaging. *Chem. Soc. Rev.* 44, 4743–4768. doi:10.1039/c4cs00392f

Wöll, D., and Flors, C. (2017). Super-Resolution Fluorescence Imaging for Materials Science. *Small Methods* 1, 1700191. doi:10.1002/smtd.201700191

Xie, B.-W., Park, D., Van Beek, E. R., Blankevoort, V., Orabi, Y., Que, I., et al. (2013). Optical Imaging of Cell Death in Traumatic Brain Injury Using a Heat Shock Protein-90 Alkylator. *Cell Death Dis.* 4, e473. doi:10.1038/cddis.2012.207

Yang, L., Guo, L., Yu, H., Wang, G., Sun, J., Zhang, P., et al. (2021). Organic Nanocrystals Based on a Solid-Emission-Tunable AIEgen for Cell Imaging. *Chem. Res. Chin. Univ.* 37, 129–136. doi:10.1007/s40242-020-0346-1

Zhai, B., Zhai, S., Hao, R., Xu, J., and Liu, Z. (2019). A FRET-Based Two-Photon Probe for In Vivo Tracking of pH during a Traumatic Brain Injury Process. *New J. Chem.* 43, 17018–17022. doi:10.1039/c9nj04049h

Zhang, X.-D., Wang, H., Antaris, A. L., Li, L., Diao, S., Ma, R., et al. (2016). Traumatic Brain Injury Imaging in the Second Near-Infrared Window with a Molecular Fluorophore. *Adv. Mater.* 28, 6872–6879. doi:10.1002/adma.201600706

Zhang, Y., Schroeder, L. K., Lessard, M. D., Kidd, P., Chung, J., Song, Y., et al. (2020). Nanoscale Subcellular Architecture Revealed by Multicolor Three-Dimensional Salvaged Fluorescence Imaging. *Nat. Methods* 17, 225–231. doi:10.1038/s41592-019-0676-4

Conflict of Interest: The authors declare that the research was conducted in the absence of any commercial or financial relationships that could be construed as a potential conflict of interest.

frontiers
in Immunology

MINI REVIEW
published: 03 June 2021
doi: 10.3389/fimmu.2021.689519

Recent Advances in Immunosafety and Nanoinformatics of Two-Dimensional Materials Applied to Nano-imaging

Gabriela H. Da Silva[1], Lidiane S. Franqui[1,2], Romana Petry[1,3], Marcella T. Maia[1], Leandro C. Fonseca[4], Adalberto Fazzio[1,3], Oswaldo L. Alves[4*] and Diego Stéfani T. Martinez[1,2*]

[1] Brazilian Nanotechnology National Laboratory (LNNano), Brazilian Center for Research in Energy and Materials (CNPEM), Campinas, Brazil, [2] School of Technology, University of Campinas (Unicamp), Limeira, Brazil, [3] Center of Natural and Human Sciences, Federal University of ABC (UFABC), Santo Andre, Brazil, [4] NanoBioss Laboratory and Solid State Chemistry Laboratory (LQES), Institute of Chemistry, University of Campinas (Unicamp), Campinas, Brazil

OPEN ACCESS

Edited by:
Diana Boraschi,
Shenzhen Institutes of Advanced Technology, Chinese Academy of Sciences (CAS), China

Reviewed by:
Paola Italiani,
National Research Council (CNR), Italy
Mariusz Piotr Madej,
OcellO B.V., Netherlands

***Correspondence:**
Oswaldo L. Alves
izolas@unicamp.br
Diego Stéfani T. Martinez
diego.martinez@lnnano.cnpem.br

Specialty section:
This article was submitted to Molecular Innate Immunity, a section of the journal Frontiers in Immunology

Received: 01 April 2021
Accepted: 10 May 2021
Published: 03 June 2021

Citation:
Da Silva GH, Franqui LS, Petry R, Maia MT, Fonseca LC, Fazzio A, Alves OL and Martinez DST (2021) Recent Advances in Immunosafety and Nanoinformatics of Two-Dimensional Materials Applied to Nano-imaging. Front. Immunol. 12:689519. doi: 10.3389/fimmu.2021.689519

Two-dimensional (2D) materials have emerged as an important class of nanomaterials for technological innovation due to their remarkable physicochemical properties, including sheet-like morphology and minimal thickness, high surface area, tuneable chemical composition, and surface functionalization. These materials are being proposed for new applications in energy, health, and the environment; these are all strategic society sectors toward sustainable development. Specifically, 2D materials for nano-imaging have shown exciting opportunities in *in vitro* and *in vivo* models, providing novel molecular imaging techniques such as computed tomography, magnetic resonance imaging, fluorescence and luminescence optical imaging and others. Therefore, given the growing interest in 2D materials, it is mandatory to evaluate their impact on the immune system in a broader sense, because it is responsible for detecting and eliminating foreign agents in living organisms. This mini-review presents an overview on the frontier of research involving 2D materials applications, nano-imaging and their immunosafety aspects. Finally, we highlight the importance of nanoinformatics approaches and computational modeling for a deeper understanding of the links between nanomaterial physicochemical properties and biological responses (immunotoxicity/biocompatibility) towards enabling immunosafety-by-design 2D materials.

Keywords: nanomaterials, bioimaging, immunotoxicity, nanobiotechnology, nanosafety

INTRODUCTION

Two-dimensional (2D) materials constitutes an emerging class of nanomaterials, characterized mainly by their high surface-area-to-mass ratio due to a sheet-like morphology; responsible for their outstanding physicochemical properties (e.g., electronic, optical, mechanical, and magnetic) with a currently leading position in materials science and technology (1, 2). Since the pioneering work of

Novoselov et al. (3) in 2004, several 2D materials have been produced for many applications in energy, catalysis, composites, sensors, biomedicine, agriculture, and environmental remmediation (4–7).

Beyond graphene-based materials (GBMs), other 2D materials have also emerged, by replacing carbon elements for other heteroatoms (P, B, O, and N) (8). Black phosphorus (BP), transition metal dichalcogenides (TMDs), transition metal carbides, nitrides, and carbonitrides (MXenes), layered double hydroxides (LDHs), antimonenes (AM), boron nitride nanosheets (BNNs) are the most common graphene analogs under investigation (9–17).

Among several applications, 2D materials have attracted special interest to be applied in the bioimaging field because of their high electrical and thermal conductivity, high degree of anisotropy, exceptional mechanical strength, and unique optical properties (18). Due to such properties, 2D materials have been developed to be applied in molecular imaging techniques, such as computed tomography (CT), magnetic resonance imaging (MRI), optical imaging (fluorescence and luminescence), and nuclear imaging including positron emission tomography (PET) and single photon emission computed tomography (SPECT) (19). Besides, 2D materials allow multimodal imaging by providing a variety of properties useful for more than one imaging technique and/or because of their facility to combine them to form nanocomposites and hybrid materials (20). Given the applicability and growing interests in 2D materials, unveiling their impact on the immune system is a key step towards safe use and responsible innovation (21, 22). These materials' intrinsic characteristics, such as chemical composition, surface chemistry, functionalization, morphology, lateral size, purity, and crystallinity are directed related to their degradability, dispersion stability, and protein corona profile; hence, their adverse effects in a biological system (23–26). Such parameters modulate the biotransformation and biodistribution of 2D materials under *in vitro* and *in vivo* models, influencing their interaction with the immune system, fate, and toxicological profile (27–30).

Biocompatibility, biodegradability, and eliciting an adequate biological effect in the organisms are crucial to the applicability of 2D materials (22, 24, 31). Indeed, the complexity of toxicokinetic and toxicodynamic events of 2D materials under physiological conditions associated with a lack of harmonized protocols for experimental research represents majors challenges for clinical translation and safety regulation involving these emerging materials (32–35). Therefore, combining systems toxicology and nanoinformatics is a foremost strategy in the integration of 2D material design on a safe and sustainable basis (36–38).

In this mini-review, we present the recent advances involving 2D materials, nano-imaging, and immunosafety. Briefly, the main findings associated with the adverse immunological effects were shown in *in vitro* and *in vivo* models. Finally, we highlight the great potential of nanoinformatics approaches towards immunosafety-by-design 2D materials (**Figure 1**).

TECHNOLOGICAL APPLICATIONS AND INNOVATION OF 2D MATERIALS

A literature review on the Web of Science™ database was performed, considering articles published from 2000 to 2021 (25/03/2021), and over these last 20 years, many 2D materials have been synthesized as exemplified in **Figure 2A**. The number of publications of 2D materials and their applications is growing, in which nano-imaging and drug release systems stand out and are present mostly in the health sector (**Figures 2B, D**). For energy application, the structural and electronic properties of 2D materials have been shown to improve the energy accumulation in devices such as lithium-ion, metal-air batteries (LIBs) (9, 39, 49, 50) and electrochemical devices (51, 52). Moreover, these 2D materials are of particular interest as catalysts and nanoscale substrates, replacing transition, or noble metals normally used to catalyze an acid-basic reaction, producing metal free-catalysts (53, 54). In environment, the 2D materials have been used as adsorbents for removing pollutants to treat contaminated water (55–57). Their atomic thickness and antibacterial activity contribute to superior water permeability and anti-fouling capacity in the development of membranes for desalination (58–62) and cleaning purposes (63–65). Sensing has covered both environmental and health sectors, contributing to the detection and monitoring of traces of pollutants (66, 67) and blood biomarkers (68–71). The thin structure, large surface area, chemical modifications and quenching ability of 2D materials provide high sensitivity, durability, stability, selectivity, and conductivity for sensors and biosensors (72–82).

Considering biomedical applications, 2D materials have been applied in bone tissue engineering, conferring improved mechanical characteristics and great osteoconductivity for scaffold design (83–87). However, due to the higher surface area of 2D materials and distinguish light-material interactions, research has mostly given attention to their usefulness in nano-imaging and therapeutics (theranostics) (88) (**Figures 2B, C**), including early detection, monitoring, and treatment of diseases, which are the main examples described in this mini-review (89). For example, in cancer, malign tumors are sensitive to heating when compared to healthy tissues. Graphene oxide decorated with gold nanoparticles (GO-AuNPs), TMDs (MoS_2, WS_2), and MXenes (MoC_2, Ti_3C_2) have shown effective agents in photothermal and photodynamic therapy for inducing tumor necrosis (40, 41, 90–92). 2D materials have been successfully modified with numerous polymers to enhance their cytocompatibility and dispersibility (90) and used as nanoplatforms carrying active molecules or imaging agents to improve their biological function (93) and clinical visualization for imaging-drug delivery guiding (12, 94). MoS_2 and BNNs have been employed as effective fluorescence quenchers and associated with aptamers, substituting antibody-based therapy (69, 95–97). Compared to the other 2D inorganic materials, and in addition to the previous features, the ultrathin structure of the BP nanosheets results in an exceptional biodegradability in physiological media it shows promising in theranostics (98, 99). Magnetic nanoparticles have been used as contrast agents

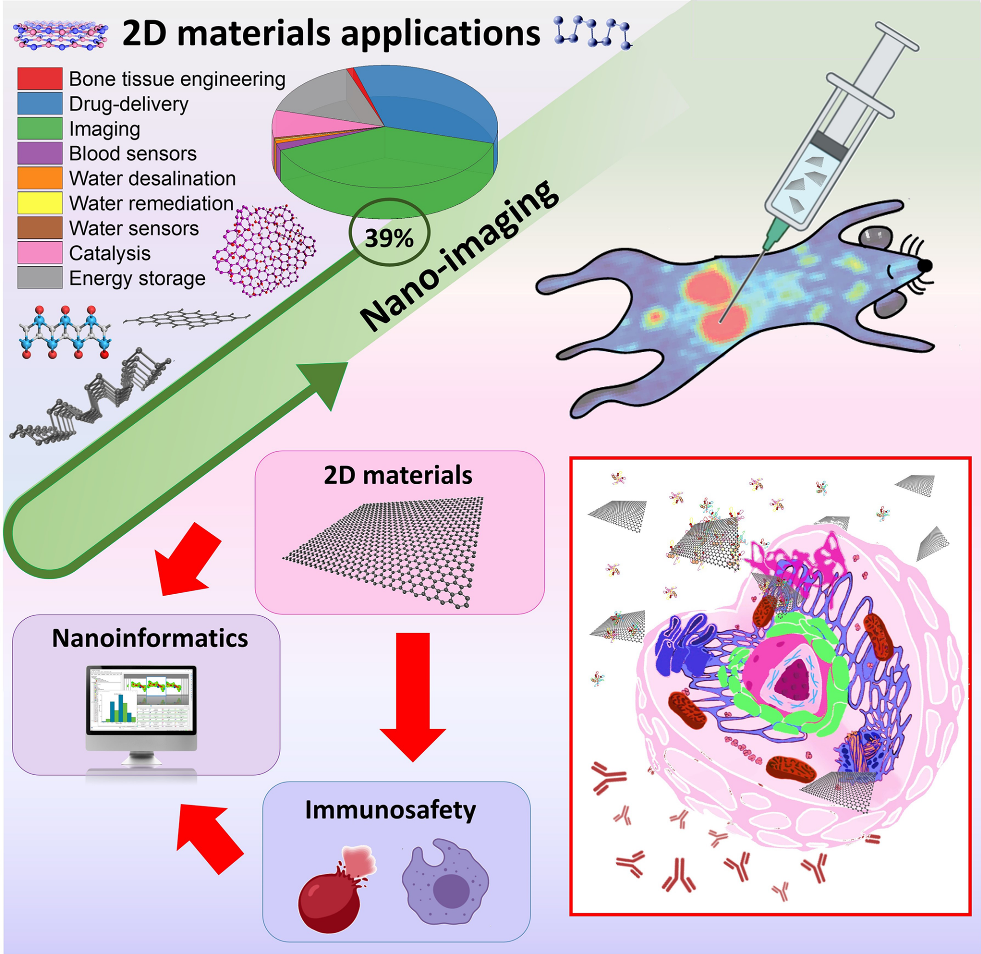

FIGURE 1 | Two-dimensional materials applications, nano-imaging and their links with immunosafety and nanoinformatics approaches.

and incorporated into 2D materials in MRI, in place of conventional ones (100, 101). In this respect, 2D magnetic materials production can be very useful for accurate bioimaging and therapy of diseases *in vivo* using MRI and CT techniques (10, 102).

2D MATERIALS AND THE IMMUNE SYSTEM: ADVERSE EFFECTS IN *IN VITRO* AND *IN VIVO* MODELS

As far as it is known, 2D materials have proven their significance and innovation perspective in almost all industrial areas and sectors, making it imperative to assess their environmental health risks and safety aspects (24, 103–105). However, toxicological studies, including immunotoxicity, are still in their infancy for GBMs and 2D inorganic materials (31). **Table 1** is an extensive literature revision reporting major findings of 2D materials and their adverse effects in the immunological system considering *in vitro* and *in vivo* models. The terms used for the literature research is detailed in the supplementary material.

Studies have demonstrated that 2D materials can induce immunological system activation with a consequent induction of an inflammatory response (145). This immunological system activation showed itself to be dependent of the 2D materials' physicochemical properties, such as size (106–109, 144), surface chemistry (114, 115, 123), number of layers, shape (118, 119), and functionalization (109, 112, 114, 128, 135, 139). For example, Yue et al. (106) demonstrated that larger graphene oxide (GO) (2 µm) has induced a higher immunological activation than smaller GO (350 nm) both *in vitro* (peritoneal macrophages) and *in vivo* (C57BL/6 mice). Similarly, Ma et al. (107) showed a lateral-size-dependent pro-inflammatory effect of GO under *in vitro* and *in vivo* conditions, wherein the largest GO (L-GO; 750–1300 nm) elicit higher inflammatory response than smallest GO (S-GO; 50–350 nm). Moreover, the mechanism of inflammation has also differed according to the lateral size, with L-GO being more prone to plasma membrane adsorption and the toll-like receptors

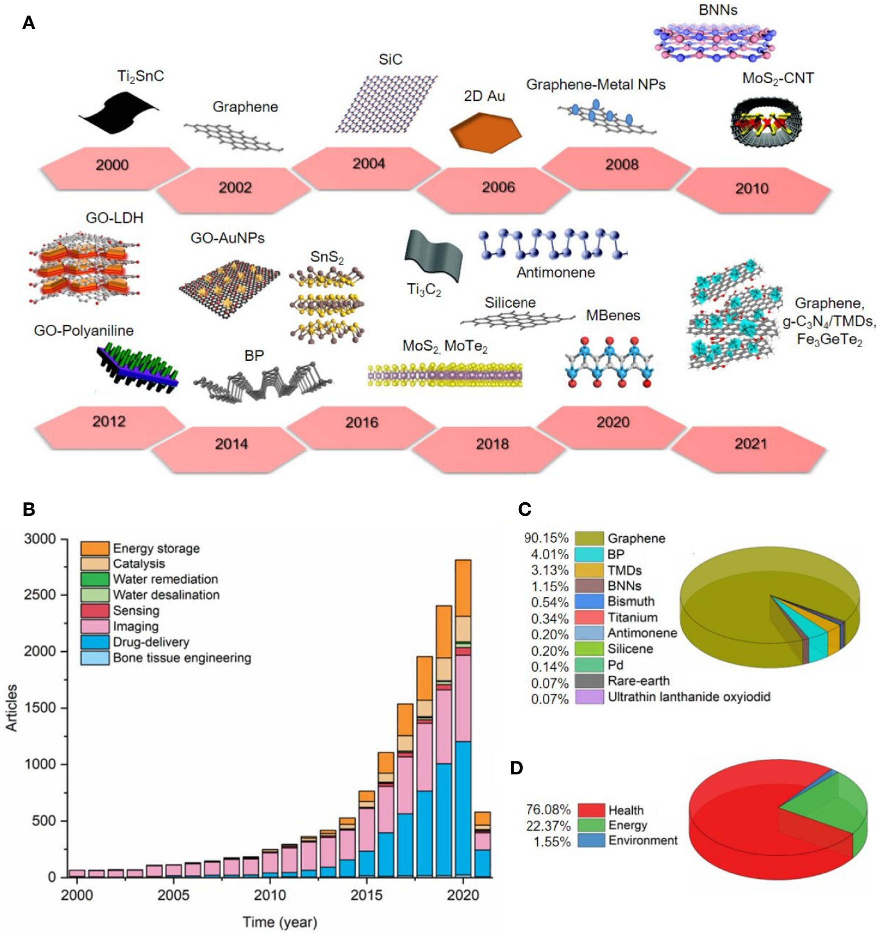

FIGURE 2 | The data obtained previously was organized into the following sectors: health (bone tissue engineering, drug delivery, imaging, sensing blood markers), energy (catalysis and energy storage), and environment (water remediation and desalination, and water sensing contaminants). **(A)** Timeline showing examples of 2D materials produced over the period established (from 2000 to 2021). **(B)** Number of articles from 2000 to 2021 (25/03/2021) **(C)** 2D materials used in nano-imaging applications (see supporting information) **(D)** Percentage of 2D materials applied in health, energy and environment sectors.

(TLRs) and nuclear factor-κB (NF-κB) pathways activation, whereas S-GO was mostly taken up by macrophages. In another study that investigated the effects of small GO (S-GO < 1 μm) and large GO (L-GO, 1–10 μm) on human peripheral immune cells, it was found that the S-GO has a more significant impact on the upregulation of critical genes implicated in immune responses and the release of cytokines IL1β and TNFα compared to L-GO (108). However, it is important to clarify here that the S-GO in this study presented similar lateral size of the L-GO in the previous studies cited, which means that all these studies are in agreement, and we may erroneously interpret them because attention to the lateral size was not devoted. Indeed, a nomenclature harmonization of GBMs is urgently needed to allow a clear understanding on the impacts of GBM physicochemical properties on their biocompatibility.

Besides to assess the effect of lateral size, Duarte and coworkers (109) investigated the impacts of two different surfaces functionalization: pegylated graphene oxide (GO-PEG, 200–500 nm) and flavin mononucleotide-stabilized pristine graphene with two different sizes (200–400 nm and 100–200 nm). Their results showed that the cellular uptake of GBMs was mainly influenced by their lateral size, with smaller particles showing greater internalization, while the inflammatory response depended also on the type of functionalization, with GO-PEG showing the lower pro-inflammatory potential. This study corroborates in number previous ones that also showed an increased biocompatibility of GO due to the pegylation (GO-PEG) (110, 111). Similarly, Xie et al. (139) studied PEG coated 2D titanium nanosheets (TiNS-PEG) and reported no indication of inflammation and other negative impacts. Moreover, the material was promising for photothermal tumor therapy and presented a high contrast for *in vivo* imaging. However, Gu et al. (129) found that MoS$_2$ and PEGylated MoS$_2$ induced a robust macrophage immune response, with PEG-MoS$_2$ eliciting stronger cytokine secretion than the pristine MoS$_2$. By performing molecular dynamics simulations, they

TABLE 1 | Relevant studies addressing the adverse immunological effects of 2D materials in *in vitro* and *in vivo* models from 2000 to 2021.

Nanomaterial	Dose	Exposure time	*in vivo/in vitro* models	Method or endpoints	Adverse immunological effects	Ref.
Graphene oxide (GO) (lateral size of 350 nm and 2 μm)	2, 4, and 6 μg ml^{-1}	24, 48, and 96 h	peritoneal macrophage	Secretion of pro-inflammatory cytokines (IL-6, IL-10, IL-12, TNF-α, MCP-1, and IFN-ɤ)	Dose-dependent release of cytokines induced in a higher extent by 2 μm GO than 350 nm GO.	(106)
	–	21 days	C57BL/6 male mice	Histological micrographics	Mononuclear cells (i.e. macrophages and lymphocytes) infiltration and inflammation response induced by 2 μm GO, but not by 350 nm GO.	
GO (smallest S-GO 50–350 nm; intermediate I-GO 350–750 nm; largest L-GO 750–1300 nm)	Viability: 1-300 μg ml^{-1}; Others: 20 μg ml^{-1}	12, 24 h	J774.A1 and THP-1 macrophages	Live/dead assay, TNF-α, IL-6 and IL1β release; and macrophage polarization, NF-κB signaling activation.	All GO materials have induced a decrease in cell viability, and a production of cytokines. The L-GO significantly elicited higher response than S-GO. Higher macrophage polarization to the M1 phenotype by L-GO than S-GO.	(107)
	Ip^1*:* 5000 μg kg^{-1} bw; Lung^2: 2500 μg kg^{-1} bw; It^3: 5000 μg kg^{-1} bw	Ip: 72 h; Lung: 72 h; It: 24 h	BALB/c male mice	Local and systemic inflammation: TNF-α, IL6 release, recruitment of immune cell.	Both S-GO and L-GO have induced an inflammatory response by cytokines production and leukocytes recruitment, been the L-GO response higher than the S-GO response in all endpoints.	
GO S-GO (<1 μm) L-GO (1-10 μM)	25, 50, and 75 μg ml^{-1}	24 h	PBMCs, Jurkat and THP-1 cells	Annexin-V FITC (apoptosis), LIVE/DEAD FITC (late apoptosis and necrosis), and propidium iodide (necrosis), cell activation (expression of CD69 and CD25 markers), cytokine release, expression of 84 genes related to innate and adaptive immune responses	Only S-GO presented a decrease in cell viability at highest dose (75 μg/ml). None of GO tested have induced the cell activation (expression of CD69 and CD25 markers). However, both GO induced cytokines release and upregulation of genes related to immune response, being that the S-GO response was significantly higher compared to L-GO response.	(108)
GO-PEG (200-500 nm) and PG-FMN (L) (200-400 nm) and PG-FMN (S) (100-200 nm)	10 μg ml^{-1}	24 h	RAW-264.7 macrophages	Cellular uptake, nitric oxide production, NMR metabolic profiling, expression of cell surface markers CD80 and CD206.	PG-FMN (S) was internalized in a greater extent compared to GO-PEG and PG-FMN (L), which presented a similar uptake. GO-PEG did not induce NO production, whereas PG-FMN (S) and PG-FMN (L) caused significant NO increases of 21% and 12%, respectively. Only PG-FMN (S) caused increases in intracellular succinate and itaconate, similarly to LPS, while PG-FMN (L) did not alter the levels of TCA cycle intermediates and GO-PEG caused a decrease of succinate. Besides, GO-PEG decreased the TNF-α secretion compared to control cell, and do not affected the cell surface markers.	(109)
GO-PEG (200-500 nm)	40 and 80 μg ml^{-1}	24 and 48 h	Murine peritoneal macrophages	Cell surface markers of M1 (CD80 and iNOS) and M2 (CD206 and CD163) phenotypes.	PEG-GO did not induce the macrophage polarization towards the M1 pro-inflammatory phenotype, with a slight shift towards M2 reparative phenotype.	(110)
GO-1PEG (~100 nm) GO-6PEG (~300 nm)	2.3–75 μg ml^{-1}	24 h	RAW-264.7 macrophages and primary splenocytes (B-cells and T-cells)	Proinflammatory cytokine secretion (IL-1β, TNF-α and IL-6) and proliferation of immune cells.	Only GO-6PEG increased the secretion of TNF-α by RAW-264.7 macrophages without alteration of IL-6 and IL-1β levels. The treatment of primary splenocytes with GO-1PEG and GO-6PEG in the presence of concanavalin A, anti-CD3 antibody, and LPS, produced significant dose-dependent decrease of cell proliferation and IL-6 levels.	(111)
GO and PVP coated-GO	25, 50, and 100 μg ml^{-1}	48 h	Human DC, macrophages and T cells	Differentiation and maturation of DC cells, cytokine release, apoptosis of T cells, and phagocytosis	GO induced the differentiation and maturation of DC cells; a dose-dependent release of pro-inflammatory cytokines by DC cells; a dose-dependent apoptosis of T cells; and a susceptibility of phagocytosis by macrophages. The coating with PVP has reduced the cytokines secretion and the differentiation and maturation of DC cells; delayed the apoptotic process of T cells; and avoid the phagocytosis by macrophages.	(112)

(Continued)

TABLE 1 | Continued

Nanomaterial	Dose	Exposure time	*in vivo/in vitro* models	Method or endpoints	Adverse immunological effects	Ref.
GO GO-NH$_2$, GO-PAM, GO-PAA GO-PEG	1, 2, 4, 10, 20, 50, 100, or 200 μg ml^{-1}	1, 6, and 24 h	J774A.1 cell line	Viability, cellular adhesion, uptake, membrane permeability and fluidity, Ca^{2+} flux and transcriptome analysis.	GO caused the impairment of cell membrane integrity and functions including regulation of membrane- and cytoskeleton- associated genes, membrane permeability, fluidity, and ion channels. The -NH$_2$ and -PAA showed similar toxicity to GO, but -PEG and -PAA significantly decreased the GO cytotoxicity.	(113)
	It: 1 mg kg^{-1}	24 h	Male BALB/c mice	Survival, body weight increase, complete blood count (numbers of RBC, WBC, PLT, neutrophils, lymphocyte), blood biochemistry, GO distribution, histological analysis of lung, liver and spleen.	GO induced platelet depletion, pro-inflammatory response and pathological changes of lung and liver in mice. The -NH$_2$, -PAA and -PEG modifications greatly reduced the toxicity of GO in mice. The -PAM modification was more toxic than pristine GO.	
GO and reduced GO (rGO) (100 nm)	20, 40, 60, 80, and 100 µg ml^{-1}	24 h	THP-1 cells	Cellular viability, proliferation, oxidative stress, mitochondrial membrane potential, ATP synthesis, antioxidants, apoptosis, DNA damage, and the inflammation response	Both GO and rGO caused dose-dependent loss of cell viability and proliferation, increased level of LDH, MMP, decreased level of ATP content, redox imbalance, mitochondria-mediated apoptosis, cell death due to oxidative stress, increased secretion of various cytokines and chemokines. Overall, the toxic response of rGO was more severe than GO for all endpoints.	(114)
GO nanoplatelets (GONPs) and reduced GONPs (rGONPs)	GONP (5 µg ml^{-1}) or rGONP (50 µg ml^{-1}	24 h	THP-1 cells	Cell viability, ROS production, expression of genes related to the oxidative and inflammatory response, cellular uptake, endocytosis and phagocytosis, Rho/ROCK pathway, cytoskeleton analysis, differentiation of THP-1 cells into macrophage-like cells (THP-1a)	Both GO induced a dose-dependent loss in cell viability, an increase in ROS production, and a disruption of the F-actin cytoskeletons leading to the loss of the adherence ability of THP-1a and a reduction in the phagocytosis capability of THP-1a cells. GONP presented higher upregulation of HO-1 and SOD-2 expressions, and higher levels of IL-1β, TNF-α, IL-8, and MCP-1, compared to rGONP. rGONP exhibited a greater expression of NF-κB (p65), higher uptake and a higher decrease of Rho/ROCK expression than GONP.	(115)
Pristine graphene with 1% pluronic F108	20 µg ml^{-1}	24 h	Primary and immortalize (RAW264.7) macrophages	Quantification of cytokines and chemokines (IFNɣ, IL-1α, IL-2, IL-4, IL-5, IL-6, IL-10, IL-17, TNFα, and GM-CSF, MCP-1, MCP-3, RANTES, MIP-1α and MIP-1β). RT-PCR analysis of the mRNA levels of TNF-α, IL-1β, IL-6, iNOS and COX-2. Adhesion, phagocytosis and cytoskeleton assay.	Increased transcription and secretion of cytokines and chemokines, which is triggered by activation of the NF-kB signaling pathway; The cytokines and chemokines secreted by graphene-exposed macrophages further impaired the morphology of naïve macrophages by affect the actin structures and podosomes expansion, decreasing the adhesion and phagocytosis.	(116)
Pristine graphene with 1% pluronic F108 (500–1000 nm)	20 µg ml^{-1}	12, 24, and 48 h	Murine RAW 264.7 macrophages	Cell viability, ROS production, MMP, apoptosis, expression of proteins (Phospho-p38 MAPKinase (P-p38), p38 MAPKinase (p38), Phospho-JNK (P-JNK), JNK, Phospho-ERK (P-ERK), ERK, Phospho- Smad2, Smad2, Bim, Bax, caspase 3, Bcl-2, PARP and β-actin) and genes (TNF-α, TGF-β TGF-β receptor I, TGF-β receptor II, Smad2, Smad3, Smad4, Smad7, β-Actin)	Loss of cell viability at highest concentration (100 µg/mL); induction of intracellular ROS generation, depletion of MMP and apoptosis, all in a time- and dose-dependent way; activation of the mitochondrial pathways: MAPKs (JNK, ERK and p38) as well as the TGF- β-related signaling pathways.	(117)
Graphene nanoplatelets (1-10 layers)	1, 5 and 10 µg cm^2	24 h	THP-1 macrophages	Phagocytosis, cytokine release and the involvement of the NALP3 inflammasome.	Frustrated phagocytosis, loss of membrane integrity at higher concentration, increase in cytokines expression, and activation of the NALP3 inflammasome.	(118)
	pharyngeal aspiration: 50 µg per mouse.	24 h	C57BL/6 strain mice	BAL cells analysis, Histological sections of lungs. Pleural space lavage: total and differential cell	BAL and pleural lavage showed an increased number of polymorphonuclear leucocytes (neutrophils and eosinophils); and an increase in the levels of cytokines.	

(Continued)

TABLE 1 | Continued

Nanomaterial	Dose	Exposure time	*in vivo/in vitro* models	Method or endpoints	Adverse immunological effects	Ref.
	intrapleural injection: 5 µg per mouse			count, histological examination of the parietal pleura.	Histological analysis: presence of granulomatous lesions in the bronchiole lumen and near the alveolar region; presence of histiocytic aggregates along the mesothelium.	
Graphene nanoplatelets (~10 layers; particle size ~ 2 µm; thickness ~3–4 nm)	Intratracheal instillation: 1.25, 2.5 and 5 mg kg^{-1}	90 days	ICR mice	Blood and BAL analysis: concentrations of pro-inflammatory cytokines (IL-1β, TNF-α, IL-6, IL-2, Th1-type cytokines, Th2-type cytokines) and chemokines (MIP)-1α, MCP-1, and GM-CSF in BAL fluids and immunoglobulins (Ig, IgE, IgG, and IgM) in serum. Expression of genes encoding actin family cytoskeletal proteins, calcium-binding proteins, and natriuretic-related genes. Histopathological analysis of lung.	BAL: increased number of lymphocytes, GNP-engulfed macrophages and apoptotic cells; general increase in cytokine and chemokine secretion; blood: increased number of macrophages and neutrophils, and elevated production of IgG, IgM and IgA. Gene expression: elevated expression of gens related to actin family cytoskeletal proteins and calcium-binding proteins; and alteration of natriuretic-related genes expression. Histopathological analysis: presence of GNP-engulfed macrophages without pathological lesion	(119)
Single- and multi-layered GO (SLGO and MLGO) in the presence or absence of Pluronic F-127	10, 20, 40, 80 and 100 µg ml^{-1}	6 h	THP-1 cells	Cell viability, membrane integrity, cell morphology levels of cytokine and ROS production, phagocytosis, and cytometric apoptosis.	SLGO induced ROS and IL-1β production, necrosis, and apoptosis to a lesser extent than MLGO. However, SLGO induced higher membrane damage and decrease in cell viability.	(120)
	Iv: 10 mg kg^{-1}	24 h (acute toxicity) or 10 days (chronic toxicity)	Mice	Histological analysis of lung and kidney: immunohistochemistry (IHC) for MCP-1 and TGF-β.	Both SLGO and MLGO induced acute and chronic damage to the lung and kidney in the presence or absence of Pluronic F-127.	
GO-PEG with mean thickness of 1.1 nm and lateral dimension ranged from 20 to 80 nm	It: 25 mg/kg	28 days	Balb/c mice: Age: 6 - 8 weeks; Weight: 18–22g	Blood circulation test; Hematologic and Biochemical marker analysis; Histopathological evaluation: trace element biodistribution observation in heart, liver spleen, lung, kidney and lymph.	Blood exposure to GO under the maximum safe starting dose caused accidental death in 1/5 *Macaca fascicularis* and 7/221 mice, while remains general amenable in others. Elevated levels of immunoglobulin E and severe lung injury were found in dead animals, suggesting the GO-induced acute anaphylactic reactions.	(121)
	4 mg/kg	90 days	*Macaca fascicularis*: Age; 4–5 years; weight: 4–5 kg			
Graphene oxide – silver nanoparticles hybrid material (GOAg)	5, 10, and 25 mg mL^{-1}	24 h	J774 and primary murine macrophages	Cell viability, apoptosis/necrosis, mitochondrial depolarization, lipid peroxidation, cytokines release (IL-1β, TNF-α and IL-10), ratio between CD80 and CD206 macrophage populations and NO production.	GOAg induced a dose-dependent mitochondrial depolarization, apoptosis, and lipid peroxidation to J774 macrophages. However, no effects were observed on cytokines release, macrophages polarization toward M1 and NO production.	(122)
Bimetallic oxide FeWOx -PEG nanosheet (FeWOx-PEG)	0-200 µg ml^{-1}	24 h	4T1 and CT26 cells	Cell viability, internalization, ROS generation.	No significant toxicity was observed, however FeWOx-PEG could internalize *via* cell endocytosis and efficiently active OH generation and GSH depletion.	(123)
	Toxicity: 10 mg kg^{-1} Biodistribution: 120 mg kg^{-1}		BALB/c mice	Body weight, histological analysis, blood chemistry, cytokines secretion (IL-6, IL-12 and TNFα) and biodistribution.	No significant differences in blood chemistry were observed for FeWOx-PEG treated mice. Also, H&E staining and histology analysis showed no obvious tissue damages and adverse effects and no significative body weight changes. However, FeWOx-PEG induce strong immune responses, showed by the increase levels of IL-6, IL-12 and TNFα. Biodistribution analyses showed that the material could accumulate in liver and spleen, however, it was observed a decrease concentration after 7 and 14 days indicating the biodegradable and clearable behavior of FeWO$_X$ -PEG nanosheets.	

(Continued)

TABLE 1 | Continued

Nanomaterial	Dose	Exposure time	*in vivo/in vitro* models	Method or endpoints	Adverse immunological effects	Ref.
FePSe$_3$@APP@CCM	0-160 μg ml^{-1}	Viability: 6 h Cytokine secretion: 48 h	PBMC, CT26 and RAW-264.7 cells	Viability and cytokines secretion (IL-10, IL-12 and IFN- γ)	No obvious cytotoxicity was caused by the nanomaterial However, taken together, upon NIR laser irradiation, FePSe$_3$@APP@CCM matured and activated immature DCs, enhanced the secretion of IFN-γ and IL-12, and decreased the expression and the consequent inhibitory effect of IL-10 on T cells, resulting in the enhanced immunity of T cells for killing CT26 cancer cells in the coculture system.	(124)
	10 mg kg^{-1}	25 days	C57BL/6J mice	Body weight, blood biochemical parameters (ALT, AST, BUN, CRE, LDH and PLT), histological analysis and cytokines secretion.	No obvious abnormality, inflammation and exudation or other pathological lesions were observed. Also, it was observed the increased expression of DC-secreted cytokines, including IFN-γ and IL-12, while the level of IL-10 was found to be decreased.	
Ferrimagnetic vortex-domain iron oxide nanoring and graphene oxide (FVIOs-GO) hybrid nanoparticle	50 or 75 μg ml^{-1} Fe	8 and 24 h	4T1 breast cancer cell and RAW264.7	Cell viability, uptake, apoptosis/ necrosis, ROS generation, macrophages polarization.	Increased ROS generation and macrophage polarization to pro-inflammatory M1 phenotypes.	(125)
	Iv: 3 mg kg^{-1}	24 days	Balb/c mice Subcutaneous 4T1 Breast Tumor Model	Measurement of tumor width and length for 24 days.	Control group exhibited a rapid increase in the tumor volume, while FVIOs-GO group had tumor growth inhibition by 97.1%.	
Borophene nanosheets (B NSs), graphene nanosheets (GR NSs) and phosphorene nanosheets (BP NSs)	Viability: 60, 80, and 100 μg ml^{-1} Membrane damage: 100 μg ml^{-1} Uptake: 200 μg ml^{-1}	Viability: 24 h Uptake: 6 h	dTHP-1 and SC cells	Cell viability, membrane damage, cell uptake, intracellular localization, inflammatory cytokines secretion (IL-1β, IL-6, IL-8, IFN- γ and TNFα).	Corona coated 2D monoelemental nanosheets decreases cytotoxicity and cell membrane damage. For B NSs it was observed an increase in cellular uptake when the material was coronated, therefore corona may promote phagocytosis. Protein corona also stimulates the secretion of inflammatory cytokines. GR NSs and B NSs had immunoregulation behaviors only in the presence of plasma corona, while BP NSs had stronger immunoregulation behavior regardless of the absence and presence of corona.	(126)
Aggregated MoS$_2$ and 2D MoS$_2$ (exfoliated by lithiation or dispersed by Pluronic F87)	6.25–50 μg ml^{-1}	24 h	THP-1 and BEAS-2B cells	Measurement of IL-8, TNF-α, and IL-1β levels	Aggregated MoS$_2$ induced significant increases in IL-8, TNF-α, and IL-1β production, while there were significantly less effects of 2D MoS$_2$ on cytokine and chemokine production.	(127)
	2 mg kg^{-1}	40 h and 21 days	C57Bl/6 mice	BALF and lung tissue were collected for measurement of LIX, MCP-1, IL-6, TGF-β1, and PDGF-AA levels and performance of Hematoxylin and Eosin (H&E) or Masson's trichrome staining.	Aggregated MoS$_2$ induced robust increasing in LIX, MCP-1 and IL-6 responses along with neutrophilic exudation into the BALF; while 2D MoS$_2$ did not trigger cytokine or chemokine production in the lung. Histopathological changes were observed with aggregated MoS$_2$ inducing focal areas of inflammation around small airways, while 2D MoS$_2$ had little or no effect.	
Exfoliated pristine and covalently functionalized MoS$_2$	1, 10, 25, 50, 75, and 100 μg ml^{-1}	24 h	Raw-264.7 and human monocyte-derived macrophages	Cell viability, CD86 expression and secretion of TNFα and IL6.	Cell viability was reduced only at high concentration; no variation of CD86 levels in both RAW 264.7 cells and human monocyte-derived macrophages was registered; no increase in cytokine secretion was observed for both cell lines.	(128)
Pristine MoS$_2$ and PEGylated MoS$_2$	10 μg ml^{-1}	24 h	Primary mouse macrophages	Cytokine secretion (IL-6, IL-10, MCP-1, IFN-γ, TNF-α and IL-12).	Both materials significantly increased the secretion of cytokines such as IL-6, IL-12, TNF-α, IFN-γ and MCP-1. Interestingly, MoS$_2$-PEG was found to elicit stronger cytokine secretion than the pristine MoS$_2$, particularly involving IL-6, TNF-α, IFN-γ, and MCP-1.	(129)
MoS$_2$ alone, MoS$_2$–PEG or MoS$_2$–PEG–CpG	0, 5, 10, 20, 30, 40 and 50 μg mL^{-1}	48 h	RAW-264.7 cells and 4T1 cells	Cell viability, Cytokine release (TNF-α and IL-6),	MoS$_2$ alone, MoS$_2$–PEG or CpG alone had no effect on cytokine release while the MoS$_2$–PEG–CpG significantly elevate the cytokine level. MoS$_2$–PEG–CpG could elevate the expression of CD86 & CD80 and the percentage of matured DCs (CD80+ CD86+ DCs) was remarkably raised to 79.8% when combined with NIR irradiation.	(130)

(Continued)

TABLE 1 | Continued

Nanomaterial	Dose	Exposure time	*in vivo/in vitro* models	Method or endpoints	Adverse immunological effects	Ref.
Protein coated with different proteins (HSA, Tf, Fg and IgG) MoS_2 NSs	500 µg ml^{-1}	12 and 24 h	THP-1 cells	Cellular viability, cellular uptake and cytokine release.	Protein coated MoS_2 NSs increase viability and decrease cytoplasmic membrane damage comparing with MoS_2 NSs. Also, the presence of a protein corona decreased the secretion of cytokines. Among the four NSs the IgG coated MoS_2 NSs enhanced uptake and cause more inflammatory cytokines.	(31)
MoS_2 nanosheets (100 and 500 nm)	0 – 128 µg ml^{-1}	48 h	DC cells	Cell viability, apoptosis, ROS generation, expression of CD40, CD80, CD86 and CCR7, secretion of proinflammatory cytokines (IL-12p70, IL6, IL-1β and TNF-α, DC homing ability.	Overall, there were no significant differences in cytotoxicity assays, however high doses could promote DC maturation as observed by the expression of CD40, CD80 and CD86 and enhanced secretion of IL-6 and TNF- α. Also, MSNs upregulate ROS generation in DCs, further promoting cytoskeletal rearrangement and promoting the local lymphoid homing ability of DCs.	(131)
Black phosphorus nanosheet (BPNSs) and black phosphorus quantum dot (BPQDs) (~300 nm)	100, 50, 25, 12.5 µg ml^{-1}	48 h	H1299, L0-2, 293T, THP-1 cell line and SC human macrophages	Cell viability, cellular uptake (1, 3, or 6 h), intracellular localization, ROS generation, cytokines release (IL-1 β, IL-6, IL-8, IL-9, IL-10, IFN- γ), NO and TNF- α generation.	A reduction of cytotoxicity was observed when BPNSs and BPQDs were coated with protein corona reduced. However, the corona facilitated the BP internalization and induced an increase in inflammatory cytokines and in ROS generation. Also, an induction of NO and TNF- α production were provoked by BP and corona coated BP.	(132)
Black phosphorus nanosheet (128 nm)	15 µg ml^{-1}	24 h	4T1, F10, CT26 and Raw-264.7 cell lines	Cell morphology, cell expression differences, expression of the surface marker CD80 using flow cytometry, proteomic analysis, western blot analysis and immunofluorescence to analyze, expression of IL-10 (M2-related marker) and TNF- α (M1-related marker).	Corona coated black phosphorus nanosheet increase the expression of calcium signaling pathways and interact with STIM2 protein facilitating Ca^{2+} influx promoting macrophage polarization.	(133)
Few-layer two-dimensional black phosphorous (2D BP)	10 to 500 µg.ml^{-1}	24 h (acute toxicity) or 21 days (chronic toxicity)	SAOS-2, HOb, L929 and hMSC cell lines	Cell viability and proliferation, ROS production, immunofluorescence to analyze cell morphology, inflammatory marker expression tested by LPS to analyzed cytokine generation (IL-10 and IL-6).	Black phosphorus did not show cytotoxicity on human mesenchymal stem cells and inhibits the metabolic activity of SAOS-2 cell line while inducing both proliferation and osteogenic differentiation in HOb cell and mesenchymal stem cells. Also, the presence of BP inhibits the ALP (an early marker of osteogenesis) expression in SAOS-2 cells and induces antiproliferative and apoptotic effects by increasing the production of ROS on SAOS-2 cells. Besides, increase the inflammatory cytokine generation but inhibits proinflammatory mediators for the co-culture of SAOS-2 and HOb.	(134)
Black Phosphorus nanoflakes functionalized with TGF-β inhibitor and neutrophil membrane (NG/BP-PEI-LY)	20 µg ml^{-1}	24 h (*in vitro*) 72 h (*in vivo*)	4T1 and HUVEC cell line BALB/c mice	Cell viability, ROS production, apoptosis, cytokine generation (IL-6 and TNF-α) Mice NIR fluorescent imaging, immunofluorescent staining of CD31 (red) and ICAM-1 (green).	NG/BP-PEI-LY induced acute inflammatory responses, cause a decrease in viability, and increase apoptosis and ROS production when laser irradiated. Besides, when laser irradiated increased the ICAM-1 expression, enhancing intracellular delivery by adhesion molecule mediated targeting.	(135)
Black Phosphorus nanosheet (BPNS) and Black Phosphorus nanocomposite (BPCP) modified with PEG and OD CpG or CpG-Cy5.5	Up to 100 µg ml^{-1}	24 h	4T1, RAW-264.7 and Hep62	Cell viability, necroptosis, protein expression, cytokine generation (IL-6 and TNF-α) and hemocytolysis.	No obvious cytotoxicity was observed, also no significant hemolysis. For BPTT treatments it was observed that necroptosis play an important role, mediating death process in cancer cells. These results were confirmed by the expression of necroptosis-related proteins, where it was observed a significantly expression of RIP1 and RIP3. Caspase-8 and Caspase-3 levels were not significantly changed.	(136)

(Continued)

TABLE 1 | Continued

Nanomaterial	Dose	Exposure time	*in vivo/in vitro* models	Method or endpoints	Adverse immunological effects	Ref.
	2 mg/kg	Up to 16 days	BALB/c mice	Biodistribution, expression of immune factors (FOXP3, IL-2, TNF- α and INF- γ), histological analysis, hematological toxicity.	No body weight loss and no systemic toxicity were observed. Also, no tissue damage and blood physiological indicators were within normal range. After BPTT treatments the immune responses were activated as observed by detection of T lymphocytes and various immune cytokines.	
DSPE-PEG coated Tao nanosheet (92.5 nm)	1 mg ml^{-1}	30 days	C57 mice	Body weight, biodistribution, immunogenicity, hematological toxicity, liver and spleen histopathology, oxidative stress response.	DSPE-PEG coated TiO_2 nanosheet cause a decrease in body weight after 14 to 30 days of the injection, also, it was observed a that the particles were accumulated in liver and cause liver toxicity by inducing oxidative stress. Besides, an obvious decrease in HTC and significant increase in MCH and MCHC indicate that the particles may induce blood system damage.	(137)
Two-Dimensional Core – Shell MXene@Gold Nanocomposites	*In vitro*: 3.1 to 100 μg ml^{-1}	24 h	4T1 cell line	Cell viability, immunohistochemistry and immunofluorescence staining.	Overall, the particle did not show apparent cytotoxicity, and no toxic side effect was observed in mice after 30 days of injection.	(138)
	In vivo: 20 mg kg^{-1}	30 days	Balb/c mice	Body weight and biodistribution.	No height loss and no notable abnormality on major organs were observed.	
2D titanium nanosheets (TiNS) and polyethylene glycol coated titanium nanosheets (TiNS-PEG)	*In vitro*: 10-100 ppm	4 h	A1 cell line, J774A.1 cell line and SMMC-7721.	Cell viability.	TiNS and TiNS-PEG did not significantly affect cell viability.	(139)
	In vivo: 5 mg kg^{-1}	19 days	Balb/c mice	Histopathology, body weight, biodistribution and hematological toxicity.	Any significant differences on mice body weight, no histological abnormalities, and no impact on hematological parameters, indicating no inflammation and other negative impact on blood and organs was observed.	
PEGylated molybdenum dichalcogenides (MoS_2-PEG), tungsten dichalcogenides (WS_2-PEG) and titanium dichalcogenides (TiS_2-PEG) nanosheets	*In vitro*: 25 – 200 μg ml^{-1}	24 h	RAW-264.7, 4T1 and 293T.	Cell viability and ROS generation.	No significant *in vitro* cytotoxicity was observed for all the three types of PEG functionalized TMDCs.	(140)
	In vivo: 10 mg kg^{-1}	up to 60 days post injection	Balb/c mice.	biodistribution, hematological toxicity, biochemical parameters (ALP, ALT, AST and BUN) and histopathology.	The materials show dominate accumulation in reticuloendothelial systems (RES) such as liver and spleen after intravenous injection. Also, no significant results were observed for the analyzed biochemical and hematological parameters and no obvious sign of abnormality, such as inflammation, was noticed in all examined major organs.	
Two-dimensional polyethylene glycol modified TiS_2 nanosheets (TiS_2-PEG)	*In vitro*: 0.0015 - 0.1 mg ml^{-1}	24 h	4T1 cell and	Cell viability	No significant cytotoxicity of TiS_2-PEG was observed.	(141)
	In vivo: 20 mg kg^{-1}	60 days	Balb/c mice	*In vivo* toxicity, histopathology.	No histological abnormalities and no obvious toxicity to Balb/c mice was observed.	
BSA coated 2D silicene nanosheets (SNSs-BSA)	*In vitro*: 12.5 - 200 μg ml^{-1}	24 h	4T1 and U87 cell lines	Cell viability	SNSs-BSA exhibit insignificant effect on cell viability of either 4T1 or U87 cancer cells.	(142)
	In vivo: 20 mg kg^{-1}	4 weeks	Kunming mice and Balb/c mice	Body weight, histopathology, hematological toxicity, biochemical parameters (ALT, AST, ALP, urea, CREA, and UA).	In a four-week duration, the mice present no significant abnormality, body weight differences, and no significant behavioral alterations. The histological observations of major organs showed no significant acute pathological toxicity. Furthermore, hematological parameters showed no obvious sign of abnormalities indicating that the SNSs-BSA induce negligible renal and hepatic toxicity in mice model.	
Poly (vinylpyrrolidone)-encapsulated Bi_2Se_3 nanosheets (diameter 31.4 nm and thickness 1.7 nm)	*In vitro*: 5 - 200 ppm	48 h	MCF7 cell line	Cell viability	It was not observed any cytotoxicity effects caused by Bi_2Se_3 nanosheets.	(143)
	In vivo: 27 – 1168 mg kg^{-1}	14 days	Balb/c mice	*in vivo* toxicity and biodistribution.	At the dose of 750 or less no mice mortality nor any reaction was observed. The nanomaterial mainly accumulated in liver, spleen and kidney, however, the concentration decreases with time.	

(Continued)

TABLE 1 | Continued

Nanomaterial	Dose	Exposure time	*in vivo/in vitro* models	Method or endpoints	Adverse immunological effects	Ref.
Pd nanosheets (diameter ranging from 5 to 80 nm)	*In vitro*: up to 100 μg ml^{-1}	24 h	NIH-3T3, 4T1, Raw-264.7, QSG-7701 and QGY-7703 cell lines	Cell viability, mitochondrial membrane depolarization and ROS generation.	Pd nanosheets have no effect on cell viability, apoptosis, ROS generation, or mitochondrial depolarization.	(144)
	In vivo: 10 mg kg^{-1}	30 days	Balb/c mice	Biodistribution, blood chemistry and hematology analysis and histopathology.	The *in vivo* results show that the particle is primarily trapped by reticuloendothelial system (RES). Also, no significant hepatotoxicity was induced by Pd nanosheets of different sizes. The activity of ALP, ALT, AST and BUN observed was within normal range and no apparent histopathological abnormalities or lesions were observed in any major organ.	
PEGylated ultrathin boron nanosheets (B-PEG NSs)	25 to 500 μg mL^{-1}	48 h	HeLa, PC3, MCF7, and A549	Cell viability, ROS generation.	No significant cytotoxicity was observed for B-PEG NSs. However, when exposed to an 808 nm NIR laser (1 Wcm^{-2}) for 5 min it was notices a strong concentration-dependent cytotoxicity. Also, when the B-PEG NSs were combined with DOX and NIR laser irradiation, over 95% of the cells died at a DOX concentration of 100 μg mL^{-1}.	(89)
	5.3 mg kg^{-1}	24 h	Mice	Body weight, histopathology, hematological toxicity (HGB, WBC, RBC, MCV, MCHC, PLT, MCH, HCT, Cr, NEU, LYM, MPV), biochemical parameters (ALP, AST, BUN and ALT) and cytokine generation (TNF-α, IL-6, IFN-γ, and IL-12+P40)	No obvious side effects were noted, also the levels of TNF-α, IL-6, IFN-γ, and IL-12+P40 were similar to those in the PBS control group indicating that B-PEG NSs did not induce obvious cytokine response. Compared with the control group, there is no statistically significant difference of the NSs-treated groups with PBS-treated groups in all the parameters, no obvious induction on cytokine response, no change in biochemical parameter and no hematological toxicity, therefore, B-PEG NSs do not cause obvious infection and inflammation in the treated mice. Moreover, no noticeable signal of inflammation or tissue damage was observed in major organs.	

[1]Ip, intraperitoneal; [2]Lung, oropharyngeal aspiration; [3]It, intratail.

GO-PEG, poly-(ethylene glycol)-functionalized GO; PG-FMN, flavin mononucleotide-stabilized pristine graphene; GO-NH2, aminated GO; GO-PAM, poly(acrylamide)-functionalized GO; GO-PAA, poly(acrylic acid)-functionalized GO; PEG, polyethylene glycol; DSPE-PEG, N-(carbonyl-methoxypolyethyleneglycol 5000)-1,2-distearoyl-sn-glycero-3-phosphoethanolamine; HSA, human serum albumin; Tf, transferrin; Fg, fibrinogen; IgG, immunoglobulin G; NSs, Nanosheets; ALP, aspartate aminotransferase; ALT, alanine aminotransferase; LDH, lactate dehydrogenase; BUN, blood urea nitrogen; CRE, creatinine; lactate dehydrogenase; PLT, platelet; NO, nitric oxide; IHC, immunohistochemistry; Nuclear NMR, magnetic resonance spectroscopy; TCA, tricarboxylic acid cycle; PVP, polyvinyl chloride; LPS, lipopolysaccharide; Rho/ROCK, Rho-associated protein kinase; RBC, red blood cells; WBC, white blood cells; MMP, mitochondrial membrane potential; MAPKs, mitogen–activated protein kinase; ERK, extracellular signal-regulated kinase; JNK, c-Jun N-terminal kinase; GSH, glutathione; BALF, bronchoalveolar lavage fluid; LYM, lymphocytes; MPV, mean platelets volume; HTC, hematocrit count; HGB, hemoglobin; MVC, mean volume cell; MCH, mean cell hemoglobin; MCHC, MCH concentration; NEU, neutrophil count; DOX, doxorubicin; NIR, near infrared light; UA, uric acid; CpG, cytosine–phosphate–guanine; BPTT, black phosphorus based photothermal therapy; TMDC, transition metal dichalcogenides.

demonstrated that small MoS_2 nanoflakes can penetrate the macrophage membrane, and that the PEG chain on PEG-MoS_2 lead to a prolonged passage throughout the membrane. Such a result might explain why PEG-MoS_2 triggers sustained more stimulation of macrophages than pristine MoS_2.

Other types of functionalization have also been studied in respect to their biocompatibility to immune cells. For instance, Zhi et al. (112) reported that the polyvinylpyrrolidone (PVP) coating of GO has exhibited lower immunogenicity when compared with pristine GO in relation to the inducing differentiation and maturation of dendritic cells (DCs), provoking a delaying in apoptotic process of T lymphocytes and the anti-phagocytosis ability against macrophages.

Surface chemistry has also been shown to influence on the immunotoxicity of 2D materials. Gurunathan et al. (114) reported that both GO and reduced GO (rGO) induced a dose-dependent loss of cell viability and proliferation, cell membrane damage, a loss of mitochondrial membrane potential, a decreased level of ATP, a redox imbalance, and an increased secretion of various cytokines and chemokines (IL1-β, TNF-α, GM-CSF, IL-6, IL-8, and MCP-1) by THP-1 cells. However, to all these toxic effects the rGO presented a significantly worse response compared to GO. In a previous study, Yan et al. (115) showed that different oxidation degrees resulted in the toxicity of monocytes *via* different signaling pathways, with GO nanoplatelets (GONPs) inducing the expression of antioxidative enzymes and inflammatory factors, whereas the reduced GO nanoplatelets (rGONPs) activated the NF-κB pathway. The contradictory results between these two studies, in relation to cytokine and chemokine expression, may be due to differences in the GBMs studied (i.e. GO sheets *versus* GO nanoplatelets), and they raise the need for further investigation concerning the effects of the oxidative degree of GBMs on immune cells.

In order to investigate the pristine graphene effects *in vitro* (THP-1 cell line) and *in vivo* (C57BL/6 strain mice), Schinwald et al. (118) have assessed the impacts of the shape of graphene nanoplatelets (GNPs) on their inflammatory potential. This large few-layer graphene presented as inflammogenic both *in vitro* and *in vivo*, which was attributed to its large size that led to frustrated phagocytosis. The authors highlighted that the potential hazard of GNPs could be minimized by producing GNPs small enough to be phagocytosed by macrophages. Moreover, the number of GO layers has been shown to affect its immunotoxicity, in which single-layer GO (SLGO) caused a more pronounced decrease in cell viability due to membrane damage of THP-1 cells, while multi-layer GO (MLGO) induced higher reactive oxygen species (ROS) and IL-1β production, leading to necrosis and apoptosis (120). In addition, the histological animal analysis revealed that SLGO and MLGO induced acute and chronic damage to the lungs and kidneys in the presence or absence of Pluronic F-127 (120).

Another important parameter, when approaching nanomaterial biosafety, is colloidal stability. Aggregation can influence the immunological response as observed by Wang et al. (127), when compared the toxicological profile of 2D MoS_2 versus aggregated MoS_2 in lung cells and mice. In their *in vitro* evaluation, in THP-1 and BEAS-2B cells, they found that aggregated MoS_2 induces strong proinflammatory and profibrogenic responses, while 2D MoS_2 have little or no effect. In agreement with *in vitro* results, an acute toxicity study *in vivo* showed that aggregated MoS_2 induced an acute lung inflammation, while 2D MoS_2 had no or a slight effect.

To increase the stability of 2D materials, studies have shown that proteins can be used as a dispersant agent. Lin et al. (142) studied silicene nanosheets modified with a bovine albumin serum protein corona (SNSs-BSA) and observed a significant increase in the colloidal stability in several physiological media (0.9% saline, phosphate buffered saline and Dulbecco's modified Eagle medium). Furthermore, SNSs-BSA did not cause significant toxicity *in vitro* neither significant acute toxicity *in vivo*. Only meaningless hematological changes were observed during the treatment duration, and no significant inflammation or infection were caused by the SNSs-BSA.

It is imperative that in a physiological environment, the nanomaterials will interact with biomolecules, forming a complex biomolecular corona. Those biomolecules (e.g., proteins, lipids, carbohydrates) can change the identity of the nanomaterials and influence their interaction with biological systems, causing an increase or decrease in internalization, toxicity, and biocompatibility as well as in colloidal stability over time. Thus, the biotransformation of nanomaterials in a physiological environment is an important parameter to be studied (146). The most common and highly studied component of biomolecular corona is the protein corona. In this sense, Mo et al. (132) studied the effect of the human plasma protein corona on the cytotoxicity of BP nanosheets and BP quantum dots (BPQDs) observing a reduction in cell viability for both nanomaterials when coated with proteins. However, protein corona facilitated BP nanosheet internalization and induced an increase in inflammatory cytokines (IL-1β, IL-6, IL-8 and IFN-γ) and in ROS generation. Besides, it was observed that protein corona coated BP caused an induction on the nitric oxide (NO) and tumour necrosis factor. Further, Mo et al. (133) studied the effect of the human plasma protein corona in BP toxicity, and observed an increased macrophage polarization due to the adsorption of opsonins present in the plasma, increasing the uptake of BP and the interaction with stromal interaction molecule 2 (STIM2) protein facilitating Ca^{2+} influx.

Similarly, Han et al. (126) studied the effect of plasma corona-coated 2D monoelemental nanosheets and observed that the protein corona decreases cytotoxicity and cell membrane damage for borophene, phosphorene, and graphene nanosheets. The corona coating induced the secretion of inflammatory cytokines (IL-1β, IL-6, IL-8, and IFN-γ) for all three materials. Also, for BNNs, it was observed an increase in cellular uptake when the material was coronated, and therefore, the corona may promote phagocytosis. Baimanov et al. (31) also investigated the effect of four different blood protein coronas (human serum albumin (HSA), transferrin (Tf), fibrinogen (Fg), and immunoglobulin G (IgG) corona) on cell viability, uptake, and pro-inflammatory effects of MoS_2 nanosheets (NSs) in the macrophages cell line. Their results demonstrate that blood proteins contribute to uptake and inflammatory effects, as protein coated MoS_2 NSs increase cell viability and decrease cytoplasmic membrane damage when compared to non-coated MoS_2 NSs. Besides, it was observed that the type of protein influences cytokine secretion, as IgG-coated MoS_2 NSs causes more inflammatory cytokine secretion (TNF-α, IL-6 and IL-1β). The highest proportion of β-sheets on IgG led to fewer secondary structure changes on MoS_2 NSs, facilitating uptake and producing a stronger pro-inflammatory response in macrophages due to the recognition of an MoS_2 NSs–IgG complex by Fc gamma receptors and the subsequent activation of the NF-κB pathways. Another interesting finding is that in a serum-containing medium, cellular uptake of MoS_2 NSs–protein complexes was higher than that in a serum-free medium. Also, the MoS_2 NSs–Fg, and MoS_2 NSs–serum complexes had similar results in serum-free conditions and different results in a serum-containing medium, suggesting the formation of the protein corona layer above the previously formed MoS_2 NSs–protein complexes. Those studies can help to elucidate the mechanisms in which protein corona can affects the toxicity of 2D materials.

One important ability of the immune system is the innate immune memory, where cells from the innate immune system react to secondary stimulus, which mostly includes an increased or decreased production of inflammation-related factors (147). With regard to 2D materials studies, there is yet a little research on this topic. Liu et al. (148) functionalize GO with lentinan (LNT) and observed that GO-LNT was able to promote macrophage activation by NF-κB and TLR signaling pathway, as well as enhance antigen protein processing after initial contact with macrophage. Moreover, the efficiency of this material was investigated, as a vaccine adjuvant for ovalbumin (OVA), in this sense GO-LNT induced robust long-term OVA-specific antibody responses due to the prolonged release of OVA. Besides this, GO-LNT was able to sustain a long-term immune response because it facilitated the uptake and slowed the release rate of antigen in macrophage. Further, Lebre et al. (149), demonstrated that pristine graphene can promote the innate immune training, enhancing the secretion of IL-6 and TNF-α and a decrease in IL-10 after toll-like receptor ligand stimulation 5 days after graphene exposure, indicating that pristine graphene can activate the immune innate memory.

Immune cells, such as macrophages and neutrophils, are one of the first line of defense of the immune system; they are capable of engulf the foreign material (or pathogen), degrading it and producing cytokines to enhanced the immune response (150). The uptake of 2D materials by immune system cells have been reported in various studies (31, 109, 115, 126, 132); however, there are few studies that address the degradation of those materials after internalization. Mukherjee et al. (151) studied the degradation of large and small GO by neutrophils and observed that not only both GO be degraded by neutrophils but also that the product of the degradation was non-toxic to human cells. Similarly, Moore et al. (152) studied the degradation of few-layer MoS_2 in human macrophage-like cells and observed that internalization occurred following 4 h of exposure and after 24 h the *in vitro* degradation of the material was confirmed, which occurred within lipidic vesicles and associated with enzymatic regions containing lysozyme.

As presented above, 2D nanomaterials may have an inflammogenic potential and immunotoxicity, which may impair their successful clinical translation; however, the immunological system activation can also be useful for theragnostic purposes. This application uses the immune responses to protect the body and eliminate cancer cells. The advantage of immunotherapy is that it engages the immune system to kill tumor cells without damaging healthy cells, additionally, it may induce immunological memory, causing long-lasting protection (153).

Nanoinformatics Approaches Toward Immunosafety-by-Design

In materials science, theory, computational modeling and informatics have a substantial role in accelerating and discovering new materials with interesting properties and applications (154–156). Due to the growing interest in 2D nanomaterials, computational approaches are extensively used in the discovery, development and application of these materials by detailed study of their structure/property relationships (156–158).

The nano-bio interface phenomena are directly related to the physicochemical properties of nanomaterials. However, tracing general correlations and delineating predictive models of nanomaterials biological effects remains challenging. Some issues include the complexity of nano-bio interactions, nanomaterials structural heterogeneity, lack of standard methodologies, absence of systematic studies and low-quality nanomaterial characterization (159–161). In this context, computational methods have been incorporated into the nanotoxicology field to support the understanding of the nano-bio interface to enable the development of safe-by-design principles applied to nanomaterials (162, 163). Theoretical modeling (i.e., molecular dynamics, density functional theory) enables precise control of critical parameters of the nanomaterials surface to study their individual effects in nano-bio interactions, providing mechanistic knowledge (164–166). On the other hand, machine learning (ML) techniques are used to assess datasets of nanomaterials biological outcomes in order to find patterns and correlations between physicochemical properties and biological effects, often undetectable through other types of analysis (167–169).

Applications of data-driven strategies include data filling, grouping, and predictive modeling. Quantitative nanostructure–activity relationships (QNAR) consist of the main strategy to delineate prediction models based on correlations between nanomaterial structural characteristics to their properties and biological activities (170, 171). It is based on the assumption that nanomaterials in their properties present similar biological effects. Diverse algorithms can be used in QNAR models, including support vector machine (172), artificial neural network (173), and decision trees (174), among others, and depending of the level of algorithms interpretability may enable the outline of causal relationships.

The scarcity of quality data and comprehensive databases is the major bottleneck in the application of ML to predict nanomaterials immune reactions (175, 176). Data-driven strategies have been making important advances in modeling biological phenomena that have potential usage to evaluate nano-immune interactions, such as predicting biomolecular corona compositions (177–181), and nanomaterials and cell interactions (e.g., cell uptake, cytotoxicity, membrane integrity, oxidative stress) (182–185). Furthermore, the exploration of omics approaches (e.g., genomics, transcriptomics, and metabolomics) has promoting the development of ML models to process the complex data generated by these techniques and enables a better understanding of the molecular mechanisms of nanomaterials adverse effects in a systemic context, defining and predicting adverse outcome pathways (186–189). The omics' potential of data generation is demonstrated by Kinaret et al. (190), who were able to connect immune responses to observed transcriptomic alterations in mouse airway exposed to 28 engineered nanomaterials. Together with cytological and histological analyses (imaging processing), they generated an extensive *in vivo* data set of nanomaterial adverse effects.

Allied with quality data infrastructure and processing, computational methods are sizeable to deal with complexity of nano-bio interface to assess and model the toxicity of nanomaterials in a variety of environments (163, 191–194). To support safe-by-design approaches, international efforts have been made to provide data integration and sharing, modeling tools, standard protocols, and ontologies, to ensure Findable, Accessible, Interoperate, and Reusable (FAIR) data (195, 196). For example, European projects, such as NanosolveIT and NanoCommons, and more recently CompSafeNano are initiatives facing on this direction (164, 165, 197, 198). In accordance with these initiatives, Gazzi et al. (199) recently presented the nanoimmunity-by-design concept developed inside G-IMMUNOMICS and CARBO-IMmap projects, which aim to bridge the knowledge gaps in the immune characterization of carbon-based materials, integrating data-driven methodologies which are extendable to other 2D materials.

CONCLUSIONS AND FUTURE PERSPECTIVES

Two-dimensional materials are key elements for nanoscience and innovation in energy, health, and the environment. This can lead to a broad range of technological applications, especially nano-imaging, which has been growing exponentially in recent years. The wide number of 2D materials with different physicochemical properties make immunotoxicity and safety evaluation a challenge. There are therefore still gaps and controversial data in the literature. For example, within the same material category (i.e., graphene oxide) different properties were observed that might affect immunological and toxicological responses. It is imperative to evaluate the biological effects of biomolecular corona formation on 2D materials at nanobiointerfaces. Only by the identification of these material properties (intrinsic and extrinsic) and an integrated understanding on how they may influence its immunological response, we can manage immunotoxicity/biocompatibility and then benefit from their unique properties for many applications. Furthermore, it is very important to highlight the critical influence of endotoxin contamination prior immunological studies and toxicity testing. Special attention on this topic will avoid misinterpretation of immunosafety results involving 2D materials (148). In addition, it is important to advance in the understanding of the links between nanomaterials and the immune system across environmental species; this being a future challenge for immunosafety research associated with 2D materials (200). Nanoinformatics and computational modeling will have a decisive role on immunotoxicological studies with nanomaterials toward the practical implementation of immunosafety-by-design. However, it is very important to develop harmonized protocols, ontologies, and public databases to facilitate and promote a global research community for the collaboration and an exchange of knowledge in this field, focusing efforts on FAIR data principles.

AUTHOR CONTRIBUTIONS

All authors listed have made a substantial, direct and intellectual contribution to the work, and approved it for publication. GS and LFr: literature research, data curation, writing, and editing. RP, LFo, and MM: literature research and writing. DM, AF, and OA: funding acquisition, supervision, project administration, and writing. All authors contributed to the article and approved the submitted version.

FUNDING

This work was funded by the Sao Paulo Research Foundation (FAPESP, grant no. 18/25103-0; 17/02317-2; 14/50906-9), the National Council for Scientific and Technological Development (CNPq, grant no. 315575/2020-4; 301358/2020-6), and the Coordination for the Improvement of Higher Education Personnel (CAPES, Finance code 001).

ACKNOWLEDGMENTS

The authors thank the National System of Laboratories in Nanotechnologies (SisNANO/MCTI), the National Institute for Research and Development in Complex Functional Materials (INCT-Inomat) and the National Institute for Research and Development in Carbon nanomaterials (INCT-NanoCarbono).

SUPPLEMENTARY MATERIAL

The Supplementary Material for this article can be found onlineat: https://www.frontiersin.org/articles/10.3389/fimmu.2021.689519/full#supplementary-material

REFERENCES

1. Nicolosi V, Chhowalla M, Kanatzidis MG, Strano MS, Coleman JN. Liquid Exfoliation of Layered Materials. *Sci (80-)* (2013) 340:1226419–1226419. doi: 10.1126/science.1226419
2. Hu T, Mei X, Wang Y, Weng X, Liang R, Wei M. Two-Dimensional Nanomaterials: Fascinating Materials in Biomedical Field. *Sci Bull* (2019) 64:1707–27. doi: 10.1016/j.scib.2019.09.021
3. Novoselov KS, Geim AK, Morozov SV, Jiang D, Zhang Y, Dubonos SV, et al. Electric Field in Atomically Thin Carbon Films. *Sci (80-)* (2004) 306:666–9. doi: 10.1126/science.1102896
4. Hao S, Zhao X, Cheng Q, Xing Y, Ma W, Wang X, et al. A Mini Review of the Preparation and Photocatalytic Properties of Two-Dimensional Materials. *Front Chem* (2020) 8:582146. doi: 10.3389/fchem.2020.582146
5. Mohammadpour Z, Majidzadeh-a K. Applications of Two-Dimensional Nanomaterials in Breast Cancer Theranostics. *ACS Biomater Sci Eng* (2020) 6(4):1852–73. doi: 10.1021/acsbiomaterials.9b01894
6. Rohaizad N, Mayorga-Martinez CC, Fojtů M, Latiff NM, Pumera M. Two-Dimensional Materials in Biomedical, Biosensing and Sensing Applications. *Chem Soc Rev* (2021) 50:619–57. doi: 10.1039/d0cs00150c
7. Bolotsky A, Butler D, Dong C, Gerace K, Glavin NR. Two-Dimensional Materials in Biosensing and Healthcare: From In Vitro Diagnostics to Optogenetics and Beyond. *ACS Nano* (2019) 13:9781–810. doi: 10.1021/acsnano.9b03632
8. Samorì P, Feng X, Palermo V. Introduction to 'Chemistry of 2D Materials: Graphene and Beyond.'. *Nanoscale* (2020) 12:24309–10. doi: 10.1039/d0nr90263b
9. Ostadhossein A, Guo J, Simeski F, Ihme M. Functionalization of 2D Materials for Enhancing OER/ORR Catalytic Activity in Li–oxygen Batteries. *Commun Chem* (2019) 2:1–11. doi: 10.1038/s42004-019-0196-2

10. Och M, Martin M, Dlubak B, Mattevi C, Martin M, Martin M. Synthesis of Emerging 2D Layered Magnetic Materials. *Nanoscale* (2021) 13:2157–80. doi: 10.1039/d0nr07867k
11. Tao W, Ji X, Zhu X, Li L, Wang J, Zhang Y, et al. Two-Dimensional Antimonene-Based Photonic Nanomedicine for Cancer Theranostics. *Adv Mater* (2018) 30:1–11. doi: 10.1002/adma.201802061
12. Tao W, Zhu X, Yu X, Zeng X, Xiao Q, Zhang X, et al. Black Phosphorus Nanosheets as a Robust Delivery Platform for Cancer Theranostics. *Adv Mater* (2017) 29:1–9. doi: 10.1002/adma.201603276
13. Ares P, Palacios JJ, Abellán G, Gómez-Herrero J, Zamora F. Recent Progress on Antimonene: A New Bidimensional Material. *Adv Mater* (2018) 30:1–27. doi: 10.1002/adma.201703771
14. Wang H, Wang X, Xia F, Wang L, Jiang H, Xia Q, et al. Black Phosphorus Radio-Frequency Transistors. *Nano Lett* (2014) 14:6424–9. doi: 10.1021/nl5029717
15. Ugeda MM, Bradley AJ, Shi SF, Da Jornada FH, Zhang Y, Qiu DY, et al. Giant Bandgap Renormalization and Excitonic Effects in a Monolayer Transition Metal Dichalcogenide Semiconductor. *Nat Mater* (2014) 13:1091–5. doi: 10.1038/nmat4061
16. Huang C, Wu S, Sanchez AM, Peters JJP, Beanland R, Ross JS, et al. Lateral Heterojunctions Within Monolayer MoSe2-WSe2 Semiconductors. *Nat Mater* (2014) 13:1096–101. doi: 10.1038/nmat4064
17. Abo El-Reesh GY, Farghali AA, Taha M, Mahmoud RK. Novel Synthesis of Ni/Fe Layered Double Hydroxides Using Urea and Glycerol and Their Enhanced Adsorption Behavior for Cr(VI) Removal. *Sci Rep* (2020) 10:1–20. doi: 10.1038/s41598-020-57519-4
18. Zhu C, Du D, Lin Y. Graphene and Graphene-Like 2D Materials for Optical Biosensing and Bioimaging: A Review. *2D Mater* (2015) 2:32004. doi: 10.1088/2053-1583/2/3/032004
19. Eom S, Choi G, Nakamura H, Choy J-H. 2-Dimensional Nanomaterials With Imaging and Diagnostic Functions for Nanomedicine; A Review. *Bull Chem Soc Jpn* (2020) 93:1–12. doi: 10.1246/bcsj.20190270
20. Wang X, Cheng L. Multifunctional Two-Dimensional Nanocomposites for Photothermal-Based Combined Cancer Therapy. *Nanoscale* (2019) 11:15685–708. doi: 10.1039/C9NR04044G
21. Cai X, Liu X, Jiang J, Gao M, Wang W, Zheng H, et al. Molecular Mechanisms, Characterization Methods, and Utilities of Nanoparticle Biotransformation in Nanosafety Assessments. *Small* (2020) 1907663:1–19. doi: 10.1002/smll.201907663
22. Fadeel B, Bussy C, Merino S, Vázquez E, Flahaut E, Mouchet F, et al. Safety Assessment of Graphene-Based Materials: Focus on Human Health and the Environment. *ACS Nano* (2018) 12:10582–620. doi: 10.1021/acsnano.8b04758
23. Chetwynd AJ, Wheeler KE, Lynch I. Best Practice in Reporting Corona Studies: Minimum Information About Nanomaterial Biocorona Experiments (Minbe). *Nano Today* (2019) 28:100758. doi: 10.1016/j.nantod.2019.06.004
24. Ma B, Martín C, Kurapati R, Bianco A. Degradation-by-Design: How Chemical Functionalization Enhances the Biodegradability and Safety of 2D Materials. *Chem Soc Rev* (2020) 49:6224–47. doi: 10.1039/c9cs00822e
25. Ganguly P, Breen A, Pillai SC. Toxicity of Nanomaterials: Exposure, Pathways, Assessment, and Recent Advances. *ACS Biomater Sci Eng* (2018) 4:2237–75. doi: 10.1021/acsbiomaterials.8b00068
26. Orecchioni M, Bedognetti D, Newman L, Fuoco C, Spada F, Hendrickx W, et al. Single-Cell Mass Cytometry and Transcriptome Profiling Reveal the Impact of Graphene on Human Immune Cells. *Nat Commun* (2017) 8(1):1–14. doi: 10.1038/s41467-017-01015-3
27. Kämpfer AAM, Busch M, Schins RPF. Advanced In Vitro Testing Strategies and Models of the Intestine for Nanosafety Research. *Chem Res Toxicol* (2020) 33:1163–78. doi: 10.1021/acs.chemrestox.0c00079
28. Cronin JG, Jones N, Thornton CA, Jenkins GJS, Doak SH, Clift MJD. Nanomaterials and Innate Immunity: A Perspective of the Current Status in Nanosafety. *Chem Res Toxicol* (2020) 33:1061–73. doi: 10.1021/acs.chemrestox.0c00051
29. Franqui LS, De Farias MA, Portugal RV, Costa CAR, Domingues RR, Souza Filho AG, et al. Interaction of Graphene Oxide With Cell Culture Medium: Evaluating the Fetal Bovine Serum Protein Corona Formation Towards In Vitro Nanotoxicity Assessment and Nanobiointeractions. *Mater Sci Eng C* (2019) 100:363–77. doi: 10.1016/J.MSEC.2019.02.066
30. Cao M, Cai R, Zhao L, Guo M, Wang L, Wang Y, et al. Molybdenum Derived From Nanomaterials Incorporates Into Molybdenum Enzymes and Affects Their Activities In Vivo. *Nat Nanotechnol* (2021) 1–9. doi: 10.1038/s41565-021-00856-w
31. Baimanov D, Wu J, Chu R, Cai R, Wang B, Cao M, et al. Immunological Responses Induced by Blood Protein Coronas on Two-Dimensional Mos 2 Nanosheets. *ACS Nano* (2020) 14:5529–42. doi: 10.1021/acsnano.9b09744
32. Ede JD, Lobaskin V, Vogel U, Lynch I, Halappanavar S, Doak SH, et al. Translating Scientific Advances in the AOP Framework to Decision Making for Nanomaterials. *Nanomaterials* (2020) 10:1–22. doi: 10.3390/nano10061229
33. Chen C, Leong DT, Lynch I. Rethinking Nanosafety: Harnessing Progress and Driving Innovation. *Small* (2020) 16:2–5. doi: 10.1002/smll.202002503
34. Miernicki M, Hofmann T, Eisenberger I, Von Der KF, Praetorius A. Legal and Practical Challenges in Classifying Nanomaterials According to Regulatory Definitions. *Nat Nanotechnol* (2019) 14(3):208–16. doi: 10.1038/s41565-019-0396-z
35. Shatkin JA. The Future in Nanosafety. *Nano Lett* (2020) 20:1479–80. doi: 10.1021/acs.nanolett.0c00432
36. Varsou D, Afantitis A, Tsoumanis A, Melagraki G, Sarimveis H, Valsamijones E. Nanoscale Advances A Safe-by-Design Tool for Functionalised Nanomaterials Through the Enalos Nanoinformatics. *Nanoscale Adv* (2019) 1:706–18. doi: 10.1039/c8na00142a
37. Singh AV, Maharjan RS, Kanase A, Siewert K, Rosenkranz D, Singh R, et al. Machine-Learning-Based Approach to Decode the Influence of Nanomaterial Properties on Their Interaction With Cells. *ACS Appl Mater Interfaces* (2021) 13:1943–55. doi: 10.1021/acsami.0c18470
38. Sturla SJ, Boobis AR, FitzGerald RE, Hoeng J, Kavlock RJ, Schirmer K, et al. Systems Toxicology: From Basic Research to Risk Assessment. *Chem Res Toxicol* (2014) 27:314–29. doi: 10.1021/tx400410s
39. Li B, Wu Y, Li N, Chen X, Zeng X, Arramel, et al. Single-Metal Atoms Supported on MBenes for Robust Electrochemical Hydrogen Evolution. *ACS Appl Mater Interfaces* (2020) 12:9261–7. doi: 10.1021/acsami.9b20552
40. Wang Y, Polavarapu L, Liz-Marzán LM. Reduced Graphene Oxide-Supported Gold Nanostars for Improved SERS Sensing and Drug Delivery. *ACS Appl Mater Interfaces* (2014) 6:21798–805. doi: 10.1021/am501382y
41. Yin W, Yan L, Yu J, Tian G, Zhou L, Zheng X, et al. High-Throughput Synthesis of Single-Layer MoS2 Nanosheets as a Near-Infrared Photothermal-Triggered Drug Delivery for Effective Cancer Therapy. *ACS Nano* (2014) 8:6922–33. doi: 10.1021/nn501647j
42. Garcia-Gallastegui A, Iruretagoyena D, Gouvea V, Mokhtar M, Asiri AM, Basahel SN, et al. Graphene Oxide as Support for Layered Double Hydroxides: Enhancing the CO2 Adsorption Capacity. *Chem Mater* (2012) 24:4531–9. doi: 10.1021/cm3018264
43. Warner JH, Rümmeli MH, Bachmatiuk A, Büchner B. Atomic Resolution Imaging and Topography of Boron Nitride Sheets Produced by Chemical Exfoliation. *ACS Nano* (2010) 4:1299–304. doi: 10.1021/nn901648q
44. Huang Y, Sutter E, Sadowski JT, Cotlet M, Monti OLA, Racke DA, et al. Tin Disulfide-an Emerging Layered Metal Dichalcogenide Semiconductor: Materials Properties and Device Characteristics. *ACS Nano* (2014) 8:10743–55. doi: 10.1021/nn504481r
45. Naguib M, Mashtalir O, Carle J, Presser V, Lu J, Hultman L, et al. Two-Dimensional Transition Metal Carbides. *ACS Nano* (2012) 6:1322–31. doi: 10.1021/nn204153h
46. Shwetharani R, Kapse S, Thapa R, Nagaraju DH, Balakrishna RG. Dendritic Ferroselite (FeSe2) With 2D Carbon-Based Nanosheets of rGO and G-C3n4as Efficient Catalysts for Electrochemical Hydrogen Evolution. *ACS Appl Energy Mater* (2020) 3:12682–91. doi: 10.1021/acsaem.0c02619
47. Wang Z, Li H, Liu Z, Shi Z, Lu J, Suenaga K, et al. Mixed Low-Dimensional Nanomaterial: 2D Ultranarrow MoS2 Inorganic Nanoribbons Encapsulated in quasi-1D Carbon Nanotubes. *J Am Chem Soc* (2010) 132:13840–7. doi: 10.1021/ja1058026
48. Wang L, Ye Y, Lu X, Wen Z, Li Z, Hou H, et al. Hierarchical Nanocomposites of Polyaniline Nanowire Arrays on Reduced Graphene Oxide Sheets for Supercapacitors. *Sci Rep* (2013) 3:5019–26. doi: 10.1038/srep03568

49. Li S, Liu Y, Zhao X, Shen Q, Zhao W, Tan Q, et al. Sandwich-Like Heterostructures of MoS2/Graphene With Enlarged Interlayer Spacing and Enhanced Hydrophilicity as High-Performance Cathodes for Aqueous Zinc-Ion Batteries. *Adv Mater* (2021) 2007480:1–9. doi: 10.1002/adma.202007480
50. Wang C, Yu X, Park HS. Boosting Redox-Active Sites of 1T MoS2Phase by Phosphorus-Incorporated Hierarchical Graphene Architecture for Improved Li Storage Performances. *ACS Appl Mater Interfaces* (2020) 12:51329–36. doi: 10.1021/acsami.0c12414
51. Vaghasiya JV, Mayorga-Martinez CC, Sofer Z, Pumera M. Mxene-Based Flexible Supercapacitors: Influence of an Organic Ionic Conductor Electrolyte on the Performance. *ACS Appl Mater Interfaces* (2020) 12:53039–48. doi: 10.1021/acsami.0c12879
52. Shen J, Chen X, Wang P, Zhou F, Lu L, Wang R, et al. Electrochemical Performance of Zinc Carbodiimides Based Porous Nanocomposites as Supercapacitors. *Appl Surf Sci* (2021) 541:148355. doi: 10.1016/j.apsusc.2020.148355
53. Chen LX, Chen W, Jiang M, Lu Z, Gao C. Insights on the Dual Role of Two-Dimensional Materials as Catalysts and Supports for Energy and Environmental Catalysis. *J Mater Chem A* (2021) 9:2018–42. doi: 10.1039/d0ta08649e
54. Deng D, Novoselov KS, Fu Q, Zheng N, Tian Z, Bao X. Catalysis With Two-Dimensional Materials and Their Heterostructures. *Nat Nanotechnol* (2016) 11:218–30. doi: 10.1038/nnano.2015.340
55. Huang H, Wang Y, Zhang Y, Niu Z, Li X. Amino-Functionalized Graphene Oxide for Cr(VI), Cu(Ii), Pb(II) and Cd(II) Removal From Industrial Wastewater. *Open Chem* (2020) 18:97–107. doi: 10.1515/chem-2020-0009
56. Ahmad H, Huang Z, Kanagaraj P, Liu C. Separation and Preconcentration of Arsenite and Other Heavy Metal Ions Using Graphene Oxide Laminated With Protein Molecules. *J Hazard Mater* (2020) 384:121479. doi: 10.1016/j.jhazmat.2019.121479
57. Li DO, Gilliam MS, Debnath A, Chu XS, Yousaf A, Green AA, et al. Interaction of Pb2+ Ions in Water With Two-Dimensional Molybdenum Disulfide. *J Phys Mater* (2020) 3:024007. doi: 10.1088/2515-7639/ab7ab3
58. Oliveira NC, Maia MT, Noronha VT, Petry R, Aquino YMLO, Paula AJ. Nanomaterials for Desalination. *Elsevier Inc* (2019) 227–62. doi: 10.1016/B978-0-12-814829-7.00006-9
59. Liu G, Shen J, Liu Q, Liu G, Xiong J, Yang J, et al. Ultrathin Two-dimensional Mxene Membrane for Pervaporation Desalination. *J Memb Sci* (2017) 548:548–58. doi: 10.1016/j.memsci.2017.11.065
60. Safaei J, Xiong P, Wang G. Progress and Prospects of Two-Dimensional Materials for Membrane- Based Water Desalination. *Mater Today Adv* (2020) 8:100108. doi: 10.1016/j.mtadv.2020.100108
61. Heiranian M, Farimani AB, Aluru NR. Water Desalination With a Single-Layer MoS2 Nanopore. *Nat Commun* (2015) 6(1):1–6. doi: 10.1038/ncomms9616
62. Caglar M, Silkina I, Brown BT, Thorneywork AL, Burton OJ, Babenko V, et al. Tunable Anion-Selective Transport Through Monolayer Graphene and Hexagonal Boron Nitride. *ACS Nano* (2020) 14:2729–38. doi: 10.1021/acsnano.9b08168
63. Ye S, Wang B, Pu Z, Liu T, Feng Y, Han W, et al. Flexible and Robust Porous Thermoplastic Polyurethane / Reduced Graphene Oxide Monolith With Special Wettability for Continuous Oil / Water Separation in Harsh Environment. *Sep Purif Technol* (2021) 266:118553. doi: 10.1016/j.seppur.2021.118553
64. Li Q, Zhang N, Yang Y, Wang G, Ng DHL. High Efficiency Photocatalysis for Pollutant Degradation With MoS2/ C3n4 Heterostructures. *Langmuir* (2014) 30:8695–972. doi: 10.1021/la502033t
65. Online VA, Yang X, Li J, Liang T, Zhang Y, Chen H, et al. Antibacterial Activity of Two-Dimensional MoS 2 Sheets. *Nanoscale* (2014) 6:10126–33. doi: 10.1039/c4nr01965b
66. Guo X, Yue G, Huang J, Liu C, Zeng Q, Wang L. Label-Free Simultaneous Analysis of Fe (III) and Ascorbic Acid Using Fluorescence Switching of Ultrathin Graphitic Carbon Nitride Nanosheets. *ACS Appl Mater Interfaces* (2018) 10:26118–27. doi: 10.1021/acsami.8b10529
67. Huang H, Chen R, Ma J, Yan L, Zhao Y, Wang Y, et al. Graphitic Carbon Nitride Solid Nanofilms for Selective and Recyclable Sensing of Cu2+ and Ag+ in Water and Serum. *Chem Commun* (2014) 50:15415–8. doi: 10.1039/c4cc06659f
68. Ou JZ, Chrimes AF, Wang Y, Tang S, Strano MS, Kalantar-zadeh K. Ion-Driven Photoluminescence Modulation of Quasi-Two- Dimensional MoS 2 Nano Fl Akes for Applications in Biological Systems. *Nano Lett* (2014) 14:857–63. doi: 10.1021/nl4042356
69. Deng H, Yang X, Gao Z. MoS2 Nanosheets as an Effective Fluorescence Quencher for DNA Methyltransferase Activity Detection. *Analyst* (2015) 140:3210–5. doi: 10.1039/c4an02133a
70. Wang L, Wang Y, Wong JI, Palacios T, Kong J, Yang HY. Functionalized MoS2 nanosheet-based field-effect biosensor for label-free sensitive detection of cancer marker proteins in solution.. *Small* (2014) 10(6):1101–5. doi: 10.1002/smll.201302081
71. Lee KT, Liang YC, Lin HH, Li CH, Lu SY. Exfoliated SnS2 Nanoplates for Enhancing Direct Electrochemical Glucose Sensing. *Electrochim Acta* (2016) 219:241–50. doi: 10.1016/j.electacta.2016.10.003
72. Singh C, Ali A, Kumar V, Ahmad R, Sumana G. Chemical Functionalized MoS2 Nanosheets Assembled Microfluidic Immunosensor for Highly Sensitive Detection of Food Pathogen. *Sensors Actuators B Chem* (2018) 259:1090–8. doi: 10.1016/j.snb.2017.12.094
73. Elumalai S, Mani V, Jeromiyas N, Ponnusamy VK, Yoshimura M. A Composite Film Prepared From Titanium Carbide Ti3C2Tx (Mxene) and Gold Nanoparticles for Voltammetric Determination of Uric Acid and Folic Acid. *Microchim Acta* (2020) 187:1–10. doi: 10.1007/s00604-019-4018-0
74. Hernández-Sánchez D, Villabona-Leal G, Saucedo-Orozco I, Bracamonte V, Pérez E, Bittencourt C, et al. Stable Graphene Oxide-Gold Nanoparticle Platforms for Biosensing Applications. *Phys Chem Chem Phys* (2018) 20:1685–92. doi: 10.1039/c7cp04817c
75. Ji J, Wen J, Shen Y, Lv Y, Chen Y, Liu S, et al. Simultaneous Noncovalent Modification and Exfoliation of 2D Carbon Nitride for Enhanced Electrochemiluminescent Biosensing. *J Am Chem Soc* (2017) 139:11698–701. doi: 10.1021/jacs.7b06708
76. Lei Y, Butler D, Lucking MC, Zhang F, Xia T, Fujisawa K, et al. Single-Atom Doping of MoS2 With Manganese Enables Ultrasensitive Detection of Dopamine: Experimental and Computational Approach. *Sci Adv* (2020) 6:1–9. doi: 10.1126/sciadv.abc4250
77. Fu Y, Zhang Y, Zheng S, Jin W. Bifunctional Electrochemical Detection of Organic Molecule and Heavy Metal At Two-Dimensional Sn-In2S3 Nanocomposite. *Microchem J* (2020) 159:105454. doi: 10.1016/j.microc.2020.105454
78. Peng Y, Zhou J, Song X, Pang K, Samy A, Hao Z, et al. A Flexible Pressure Sensor With Ink Printed Porous Graphene for Continuous Cardiovascular Status Monitoring. *Sensors (Switzerland)* (2021) 21:1–12. doi: 10.3390/s21020485
79. Ramalingam S, Elsayed A, Singh A. An Electrochemical Microfluidic Biochip for the Detection of Gliadin Using MoS2/graphene/gold Nanocomposite. *Microchim Acta* (2020) 187(12):1–11. doi: 10.1007/s00604-020-04589-w
80. Moghzi F, Soleimannejad J, Sañudo EC, Janczak J. Dopamine Sensing Based on Ultrathin Fluorescent Metal-Organic Nanosheets. *ACS Appl Mater Interfaces* (2020) 12:44499–507. doi: 10.1021/acsami.0c13166
81. Noronha VT, Aquino YMLO, Maia MT, Freire RM. Sensing of Water Contaminants: From Traditional to Modern Strategies Based on Nanotechnology. *Elsevier Inc* (2019) 109–50. doi: 10.1016/B978-0-12-814829-7.00003-3
82. Kokulnathan T, Kumar EA, Wang TJ. Design and in Situ Synthesis of Titanium Carbide/Boron Nitride Nanocomposite: Investigation of Electrocatalytic Activity for the Sulfadiazine Sensor. *ACS Sustain Chem Eng* (2020) 8:12471–81. doi: 10.1021/acssuschemeng.0c03281
83. Purohit SD, Singh H, Bhaskar R, Yadav I, Bhushan S. Fabrication of Graphene Oxide and Nanohydroxyapatite Reinforced Gelatin – Alginate Nanocomposite Scaffold for Bone Tissue Regeneration. *Front Mater* (2020) 7:1–10. doi: 10.3389/fmats.2020.00250
84. Ramani D, Sastry TP. Bacterial Cellulose-Reinforced Hydroxyapatite Functionalized Graphene Oxide: A Potential Osteoinductive Composite. *Cellulose* (2014) 21:3585–95. doi: 10.1007/s10570-014-0313-4
85. Fu Y, Zhang JB, Lin H, Mo A. 2D Titanium Carbide(Mxene) Nanosheets and 1D Hydroxyapatite Nanowires Into Free Standing Nanocomposite

Membrane: In Vitro and In Vivo Evaluations for Bone Regeneration. *Mater Sci Eng C* (2021) 118:111367. doi: 10.1016/j.msec.2020.111367

86. Liu X, George MN, Li L, Gamble D, Miller AL, Gaihre B, et al. Injectable Electrical Conductive and Phosphate Releasing Gel With Two-Dimensional Black Phosphorus and Carbon Nanotubes for Bone Tissue Engineering. *ACS Biomater Sci Eng* (2020) 6:4653–65. doi: 10.1021/acsbiomaterials.0c00612
87. Liu H, Yang G, Yin H, Wang Z, Chen C, Liu Z, et al. *In Vitro* and *In Vivo* Osteogenesis Up-Regulated by Two-Dimensional Nanosheets Through a Macrophage-Mediated Pathway. *Biomater Sci* (2021) 9:780–94. doi: 10.1039/d0bm01596b
88. Le HuX, Kwon N, Yan KC, Sedgwick AC, Chen GR, He XP, et al. Bio-Conjugated Advanced Materials for Targeted Disease Theranostics. *Adv Funct Mater* (2020) 30:1–25. doi: 10.1002/adfm.201907906
89. Ji X, Kong N, Wang J, Li W, Xiao Y, Gan ST, et al. A Novel Top-Down Synthesis of Ultrathin 2d Boron Nanosheets for Multimodal Imaging-Guided Cancer Therapy. *Adv Mater* (2018) 30:1803031. doi: 10.1002/adma.201803031
90. Feng W, Wang R, Zhou Y, Ding L, Gao X, Zhou B, et al. Ultrathin Molybdenum Carbide MXene With Fast Biodegradability for Highly Efficient Theory-Oriented Photonic Tumor Hyperthermia. *Adv Funct Mater* (2019) 29:1–15. doi: 10.1002/adfm.201901942
91. Lin H, Wang X, Yu L, Chen Y, Shi J. Two-Dimensional Ultrathin Mxene Ceramic Nanosheets for Photothermal Conversion. *Nano Lett* (2017) 17:384–91. doi: 10.1021/acs.nanolett.6b04339
92. Murugan C, Sharma V, Murugan RK, Malaimegu G, Sundaramurthy A. Two-Dimensional Cancer Theranostic Nanomaterials: Synthesis, Surface Functionalization and Applications in Photothermal Therapy. *J Control Release* (2019) 299:1–20. doi: 10.1016/j.jconrel.2019.02.015
93. Chen L, Chen C, Chen W, Li K, Chen X, Tang X, et al. Biodegradable Black Phosphorus Nanosheets Mediate Specific Delivery of hTERT siRNA for Synergistic Cancer Therapy. *ACS Appl Mater Interfaces* (2018) 10:21137–48. doi: 10.1021/acsami.8b04807
94. Kang Y, Ji X, Li Z, Su Z, Zhang S. Boron-Based Nanosheets for Combined Cancer Photothermal and Photodynamic Therapy. *J Mater Chem B* (2020) 8:4609–19. doi: 10.1039/d0tb00070a
95. Sekhon SS, Kaur P, Kim Y-H, Sekhon SS. 2D Graphene Oxide – Aptamer Conjugate Materials for Cancer Diagnosis. *Nat Partn Journals 2D Mater Appl* (2021) 5(1):1–19. doi: 10.1038/s41699-021-00202-7
96. Zhan Y, Yan J, Wu M, Guo L, Lin Z, Qiu B, et al. Wong K Yin. Boron Nitride Nanosheets as a Platform for Fluorescence Sensing. *Talanta* (2017) 174:365–71. doi: 10.1016/j.talanta.2017.06.032
97. Wang Q, Wang W, Lei J, Xu N, Gao F, Ju H. Fluorescence Quenching of Carbon Nitride Nanosheet Through its Interaction With DNA for Versatile Fluorescence Sensing. *Anal Chem* (2013) 85:12182–8. doi: 10.1021/ac403646n
98. Qian X, Gu Z, Chen Y. Two-Dimensional Black Phosphorus Nanosheets for Theranostic Nanomedicine. *Mater Horizons* (2017) 4:800–16. doi: 10.1039/c7mh00305f
99. Yang X, Wang D, Shi Y, Zou J, Zhao Q, Zhang Q, et al. Black Phosphorus Nanosheets Immobilizing Ce6 for Imaging-Guided Photothermal/Photodynamic Cancer Therapy. *ACS Appl Mater Interfaces* (2018) 10:12431–40. doi: 10.1021/acsami.8b00276
100. Zhang N, Wang Y, Zhang C, Fan Y, Li D, Cao X, et al. Theranostics LDH-stabilized Ultrasmall Iron Oxide Nanoparticles as a Platform for Hyaluronidase-Promoted MR Imaging and Chemotherapy of Tumors. *Theranostics* (2020) 10(6):2791–802. doi: 10.7150/thno.42906
101. Gonzalez-Rodriguez R, Campbell E, Naumov A. Multifunctional Graphene Oxide/Iron Oxide Nanoparticles for Magnetic Targeted Drug Delivery Dual Magnetic Resonance/ Fluorescence Imaging and Cancer Sensing. *PloS One* (2019) 14:1–19. doi: 10.1371/journal.pone.0217072
102. Guo Jj, Xia Ql, Wang Xg, Nie Yz, Xiong R, Guo Gh. Temperature and Thickness Dependent Magnetization Reversal in 2D Layered Ferromagnetic Material Fe3GeTe2. *J Magn Magn Mater* (2021) 527:167719. doi: 10.1016/j.jmmm.2020.167719
103. Xu Z, Lu J, Zheng X, Chen B, Luo Y, Nauman M, et al. A Critical Review on the Applications and Potential Risks of Emerging MoS2 Nanomaterials. *J Hazard Mater* (2020) 399:123057. doi: 10.1016/j.jhazmat.2020.123057
104. Wang Z, Zhu W, Qiu Y, Yi X, Von Dem Bussche A, Kane A, et al. Biological and Environmental Interactions of Emerging Two-Dimensional Nanomaterials. *Chem Soc Rev* (2016) 45:1750–80. doi: 10.1039/c5cs00914f
105. Zhou X, Sun H, Bai X. Two-Dimensional Transition Metal Dichalcogenides: Synthesis, Biomedical Applications and Biosafety Evaluation. *Front Bioeng Biotechnol* (2020) 8:236. doi: 10.3389/fbioe.2020.00236
106. Yue H, Wei W, Yue Z, Wang B, Luo N, Gao Y, et al. The Role of the Lateral Dimension of Graphene Oxide in the Regulation of Cellular Responses. *Biomaterials* (2012) 33:4013–21. doi: 10.1016/j.biomaterials.2012.02.021
107. Ma J, Liu R, Wang X, Liu Q, Chen Y, Valle RP, et al. Crucial Role of Lateral Size for Graphene Oxide in Activating Macrophages and Stimulating Pro-Inflammatory Responses in Cells and Animals. *ACS Nano* (2015) 9:10498–515. doi: 10.1021/acsnano.5b04751
108. Orecchioni M, Jasim DA, Pescatori M, Manetti R, Fozza C, Sgarrella F, et al. Molecular and Genomic Impact of Large and Small Lateral Dimension Graphene Oxide Sheets on Human Immune Cells From Healthy Donors. *Adv Healthc Mater* (2016) 5:276–87. doi: 10.1002/adhm.201500606
109. Cicuéndez M, Fernandes M, Ayán-Varela M, Oliveira H, Feito MJ, Diez-Orejas R, et al. Macrophage Inflammatory and Metabolic Responses to Graphene-Based Nanomaterials Differing in Size and Functionalization. *Colloids Surf B Biointerfaces* (2020) 186:110709. doi: 10.1016/j.colsurfb.2019.110709
110. Feito MJ, Diez-Orejas R, Cicuéndez M, Casarrubios L, Rojo JM, Portolés MT. Characterization of M1 and M2 Polarization Phenotypes in Peritoneal Macrophages After Treatment With Graphene Oxide Nanosheets. *Colloids Surf B Biointerfaces* (2019) 176:96–105. doi: 10.1016/j.colsurfb.2018.12.063
111. Feito MJ, Vila M, Matesanz MC, Linares J, Gonçalves G, Marques PAAP, et al. *In Vitro* Evaluation of Graphene Oxide Nanosheets on Immune Function. *J Colloid Interface Sci* (2014) 432:221–8. doi: 10.1016/j.jcis.2014.07.004
112. Zhi X, Fang H, Bao C, Shen G, Zhang J, Wang K, et al. The Immunotoxicity of Graphene Oxides and the Effect of PVP-Coating. *Biomaterials* (2013) 34:5254–61. doi: 10.1016/j.biomaterials.2013.03.024
113. Xu M, Zhu J, Wang F, Xiong Y, Wu Y, Wang Q, et al. Improved In Vitro and *In Vivo* Biocompatibility of Graphene Oxide Through Surface Modification: Poly(Acrylic Acid)-Functionalization is Superior to Pegylation. *ACS Nano* (2016) 10:3267–81. doi: 10.1021/acsnano.6b00539
114. Gurunathan S, Kang M-H, Jeyaraj M, Kim J-H. Differential Immunomodulatory Effect of Graphene Oxide and Vanillin-Functionalized Graphene Oxide Nanoparticles in Human Acute Monocytic Leukemia Cell Line (Thp-1). *Int J Mol Sci* (2019) 20:247. doi: 10.3390/ijms20020247
115. Yan J, Chen L, Huang C-C, Lung S-CC, Yang L, Wang W-C, et al. Consecutive Evaluation of Graphene Oxide and Reduced Graphene Oxide Nanoplatelets Immunotoxicity on Monocytes. *Colloids Surf B Biointerfaces* (2017) 153:300–9. doi: 10.1016/j.colsurfb.2017.02.036
116. Zhou H, Zhao K, Li W, Yang N, Liu Y, Chen C, et al. The Interactions Between Pristine Graphene and Macrophages and the Production of Cytokines/Chemokines *Via* TLR- and NF-κb-Related Signaling Pathways. *Biomaterials* (2012) 33:6933–42. doi: 10.1016/j.biomaterials.2012.06.064
117. Li Y, Liu Y, Fu Y, Wei T, Le Guyader L, Gao G, et al. The Triggering of Apoptosis in Macrophages by Pristine Graphene Through the MAPK and TGF-beta Signaling Pathways. *Biomaterials* (2012) 33:402–11. doi: 10.1016/j.biomaterials.2011.09.091
118. Schinwald A, Murphy FA, Jones A, MacNee W, Donaldson K. Graphene-Based Nanoplatelets: A New Risk to the Respiratory System as A Consequence of Their Unusual Aerodynamic Properties. *ACS Nano* (2012) 6:736–46. doi: 10.1021/nn204229f
119. Park E-J, Lee SJ, Lee K, Choi YC, Lee B-S, Lee G-H, et al. Pulmonary Persistence of Graphene Nanoplatelets may Disturb Physiological and Immunological Homeostasis. *J Appl Toxicol* (2017) 37:296–309. doi: 10.1002/jat.3361
120. Cho YC, Pak PJ, Joo YH, Lee H-S, Chung N. In Vitro and In Vivo Comparison of the Immunotoxicity of Single- and Multi-Layered Graphene Oxides With or Without Pluronic F-127. *Sci Rep* (2016) 6:38884. doi: 10.1038/srep38884

121. Lin Y, Zhang Y, Li J, Kong H, Yan Q, Zhang J, et al. Blood Exposure to Graphene Oxide May Cause Anaphylactic Death in Non-Human Primates. *Nano Today* (2020) 35:100922. doi: 10.1016/j.nantod.2020.100922
122. de Luna LAV, Zorgi NE, de Moraes ACM, da Silva DS, Consonni SR, Giorgio S, et al. *In Vitro* Immunotoxicological Assessment of A Potent Microbicidal Nanocomposite Based on Graphene Oxide and Silver Nanoparticles. *Nanotoxicology* (2019) 13:189–203. doi: 10.1080/17435390.2018.1537410
123. Gong F, Chen M, Yang N, Dong Z, Tian L, Hao Y, et al. Bimetallic Oxide Fewo X Nanosheets as Multifunctional Cascade Bioreactors for Tumor Microenvironment-Modulation and Enhanced Multimodal Cancer Therapy. *Adv Funct Mater* (2020) 30:2002753. doi: 10.1002/adfm.202002753
124. Fang X, Wu X, Li Z, Jiang L, Lo W, Chen G, et al. Biomimetic Anti-PD-1 Peptide-Loaded 2d FePSe 3 Nanosheets for Efficient Photothermal and Enhanced Immune Therapy With Multimodal Mr/Pa/Thermal Imaging. *Adv Sci* (2021) 8:2003041. doi: 10.1002/advs.202003041
125. Liu X, Yan B, Li Y, Ma X, Jiao W, Shi K, et al. Graphene Oxide-Grafted Magnetic Nanorings Mediated Magnetothermodynamic Therapy Favoring Reactive Oxygen Species-Related Immune Response for Enhanced Antitumor Efficacy. *ACS Nano* (2020) 14:1936–50. doi: 10.1021/acsnano.9b08320
126. Han M, Zhu L, Mo J, Wei W, Yuan B, Zhao J, et al. Protein Corona and Immune Responses of Borophene: A Comparison of Nanosheet–Plasma Interface With Graphene and Phosphorene. *ACS Appl Bio Mater* (2020) 3:4220–9. doi: 10.1021/acsabm.0c00306
127. Wang X, Mansukhani ND, Guiney LM, Ji Z, Chang CH, Wang M, et al. Differences in the Toxicological Potential of 2D Versus Aggregated Molybdenum Disulfide in the Lung. *Small* (2015) 11:5079–87. doi: 10.1002/smll.201500906
128. Kurapati R, Muzi L, de Garibay APR, Russier J, Voiry D, Vacchi IA, et al. Enzymatic Biodegradability of Pristine and Functionalized Transition Metal Dichalcogenide MoS 2 Nanosheets. *Adv Funct Mater* (2017) 27:1605176. doi: 10.1002/adfm.201605176
129. Gu Z, Chen SH, Ding Z, Song W, Wei W, Liu S, et al. The Molecular Mechanism of Robust Macrophage Immune Responses Induced by PEGylated Molybdenum Disulfide. *Nanoscale* (2019) 11:22293–304. doi: 10.1039/C9NR04358F
130. Han Q, Wang X, Jia X, Cai S, Liang W, Qin Y, et al. Cpg Loaded MoS 2 Nanosheets as Multifunctional Agents for Photothermal Enhanced Cancer Immunotherapy. *Nanoscale* (2017) 9:5927–34. doi: 10.1039/C7NR01460K
131. Deng L, Pan X, Zhang Y, Sun S, Lv L, Gao L, et al. Immunostimulatory Potential of MoS2 Nanosheets: Enhancing Dendritic Cell Maturation, Migration and T Cell Elicitation. *Int J Nanomed* (2020) 15:2971–86. doi: 10.2147/IJN.S243537
132. Mo J, Xie Q, Wei W, Zhao J. Revealing the Immune Perturbation of Black Phosphorus Nanomaterials to Macrophages by Understanding the Protein Corona. *Nat Commun* (2018) 9:2480. doi: 10.1038/s41467-018-04873-7
133. Mo J, Xu Y, Wang X, Wei W, Zhao J. Exploiting the Protein Corona: Coating of Black Phosphorus Nanosheets Enables Macrophage Polarization *Via* Calcium Influx. *Nanoscale* (2020) 12:1742–8. doi: 10.1039/C9NR08570J
134. Raucci MG, Fasolino I, Caporali M, Serrano-Ruiz M, Soriente A, Peruzzini M, et al. Exfoliated Black Phosphorus Promotes *In Vitro* Bone Regeneration and Suppresses Osteosarcoma Progression Through Cancer-Related Inflammation Inhibition. *ACS Appl Mater Interfaces* (2019) 11:9333–42. doi: 10.1021/acsami.8b21592
135. Su Y, Wang T, Su Y, Li M, Zhou J, Zhang W, et al. A Neutrophil Membrane-Functionalized Black Phosphorus Riding Inflammatory Signal for Positive Feedback and Multimode Cancer Therapy. *Mater Horizons* (2020) 7:574–85. doi: 10.1039/C9MH01068H
136. Zhao H, Chen H, Guo Z, Zhang W, Yu H, Zhuang Z, et al. *In Situ* Photothermal Activation of Necroptosis Potentiates Black Phosphorus-Mediated Cancer Photo-Immunotherapy. *Chem Eng J* (2020) 394:124314. doi: 10.1016/j.cej.2020.124314
137. Song S-S, Xia B-Y, Chen J, Yang J, Shen X, Fan S-J, et al. Two Dimensional TiO 2 Nanosheets: In Vivo Toxicity Investigation. *RSC Adv* (2014) 4:42598–603. doi: 10.1039/C4RA05953K
138. Tang W, Dong Z, Zhang R, Yi X, Yang K, Jin M, et al. Multifunctional Two-Dimensional Core–Shell MXene@Gold Nanocomposites for Enhanced Photo–Radio Combined Therapy in the Second Biological Window. *ACS Nano* (2019) 13:284–94. doi: 10.1021/acsnano.8b05982
139. Xie Z, Chen S, Duo Y, Zhu Y, Fan T, Zou Q, et al. Biocompatible Two-Dimensional Titanium Nanosheets for Multimodal Imaging-Guided Cancer Theranostics. *ACS Appl Mater Interfaces* (2019) 11:22129–40. doi: 10.1021/acsami.9b04628
140. Hao J, Song G, Liu T, Yi X, Yang K, Cheng L, et al. In Vivo Long-Term Biodistribution, Excretion, and Toxicology of PEGylated Transition-Metal Dichalcogenides Ms 2 (M = Mo, W, Ti) Nanosheets. *Adv Sci* (2017) 4:1600160. doi: 10.1002/advs.201600160
141. Qian X, Shen S, Liu T, Cheng L, Liu Z. Two-Dimensional TiS 2 Nanosheets for In Vivo Photoacoustic Imaging and Photothermal Cancer Therapy. *Nanoscale* (2015) 7:6380–7. doi: 10.1039/C5NR00893J
142. Lin H, Qiu W, Liu J, Yu L, Gao S, Yao H, et al. Silicene: Wet-Chemical Exfoliation Synthesis and Biodegradable Tumor Nanomedicine. *Adv Mater* (2019) 31:1903013. doi: 10.1002/adma.201903013
143. Xie H, Li Z, Sun Z, Shao J, Yu X-F, Guo Z, et al. Metabolizable Ultrathin Bi 2 Se 3 Nanosheets in Imaging-Guided Photothermal Therapy. *Small* (2016) 12:4136–45. doi: 10.1002/smll.201601050
144. Chen M, Chen S, He C, Mo S, Wang X, Liu G, et al. Safety Profile of Two-Dimensional Pd Nanosheets for Photothermal Therapy and Photoacoustic Imaging. *Nano Res* (2017) 10:1234–48. doi: 10.1007/s12274-016-1349-6
145. Orecchioni M, Ménard-Moyon C, Delogu LG, Bianco A. Graphene and the Immune System: Challenges and Potentiality. *Adv Drug Delivery Rev* (2016) 105:163–75. doi: 10.1016/j.addr.2016.05.014
146. Corbo C, Molinaro R, Parodi A, Toledano Furman NE, Salvatore F, Tasciotti E. The Impact of Nanoparticle Protein Corona on Cytotoxicity, Immunotoxicity and Target Drug Delivery. *Nanomedicine* (2016) 11:81–100. doi: 10.2217/nnm.15.188
147. Italiani P, Della Camera G, Boraschi D. Induction of Innate Immune Memory by Engineered Nanoparticles in Monocytes/Macrophages: From Hypothesis to Reality. *Front Immunol* (2020) 11:566309. doi: 10.3389/fimmu.2020.566309
148. Liu Z, He J, Zhu T, Hu C, Bo R, Wusiman A, et al. Lentinan-Functionalized Graphene Oxide Is an Effective Antigen Delivery System That Modulates Innate Immunity and Improves Adaptive Immunity. *ACS Appl Mater Interfaces* (2020) 12:39014–23. doi: 10.1021/acsami.0c12078
149. Lebre F, Boland JB, Gouveia P, Gorman AL, Lundahl MLE, I Lynch R, et al. Pristine Graphene Induces Innate Immune Training. *Nanoscale* (2020) 12:11192–200. doi: 10.1039/C9NR09661B
150. Su Y, Gao J, Kaur P, Wang Z. Neutrophils and Macrophages as Targets for Development of Nanotherapeutics in Inflammatory Diseases. *Pharmaceutics* (2020) 12:1222. doi: 10.3390/pharmaceutics12121222
151. Mukherjee SP, Gliga AR, Lazzaretto B, Brandner B, Fielden M, Vogt C, et al. Graphene Oxide is Degraded by Neutrophils and the Degradation Products are non-Genotoxic. *Nanoscale* (2018) 10:1180–8. doi: 10.1039/C7NR03552G
152. Moore C, Harvey A, Coleman JN, Byrne HJ, McIntyre J. *In Vitro* Localisation and Degradation of Few-Layer MoS 2 Submicrometric Plates in Human Macrophage-Like Cells: A Label Free Raman Micro-Spectroscopic Study. *2D Mater* (2020) 7:025003. doi: 10.1088/2053-1583/ab5d98
153. Grimaldi AM, Incoronato M, Salvatore M, Soricelli A. Nanoparticle-Based Strategies for Cancer Immunotherapy and Immunodiagnostics. *Nanomedicine* (2017) 12:2349–65. doi: 10.2217/nnm-2017-0208
154. De Pablo JJ, Jones B, Kovacs CL, Ozolins V, Ramirez AP. The Materials Genome Initiative, the Interplay of Experiment, Theory and Computation. *Curr Opin Solid State Mater Sci* (2014) 18:99–117. doi: 10.1016/j.cossms.2014.02.003
155. Schmidt J, Marques MRG, Botti S, Marques MAL. Recent Advances and Applications of Machine Learning in Solid-State Materials Science. *NPJ Comput Mater* (2019) 5:83. doi: 10.1038/s41524-019-0221-0
156. Schleder GR, Padilha ACM, Acosta CM, Costa M, Fazzio A. From DFT to Machine Learning: Recent Approaches to Materials Science–a Review. *J Phys Mater* (2019) 2:032001. doi: 10.1088/2515-7639/ab084b
157. Liu C, Chen H, Wang S, Liu Q, Jiang Y-G, Zhang DW, et al. Two-Dimensional Materials for Next-Generation Computing Technologies. *Nat Nanotechnol* (2020) 15:545–57. doi: 10.1038/s41565-020-0724-3

158. Tawfik SA, Isayev O, Stampfl C, Shapter J, Winkler DA, Ford MJ. Efficient Prediction of Structural and Electronic Properties of Hybrid 2d Materials Using Complementary DFT and Machine Learning Approaches. *Adv Theory Simul* (2019) 2:1800128. doi: 10.1002/adts.201800128
159. Giusti A, Atluri R, Tsekovska R, Gajewicz A, Apostolova MD, Battistelli CL, et al. Nanomaterial Grouping: Existing Approaches and Future Recommendations. *NanoImpact* (2019) 16:100182. doi: 10.1016/j.impact.2019.100182
160. Basei G, Hristozov D, Lamon L, Zabeo A, Jeliazkova N, Tsiliki G, et al. Making Use of Available and Emerging Data to Predict the Hazards of Engineered Nanomaterials by Means of in Silico Tools: A Critical Review. *NanoImpact* (2019) 13:76–99. doi: 10.1016/j.impact.2019.01.003
161. Karcher S, Willighagen EL, Rumble J, Ehrhart F, Evelo CT, Fritts M, et al. Integration Among Databases and Data Sets to Support Productive Nanotechnology: Challenges and Recommendations. *NanoImpact* (2018) 9:85–101. doi: 10.1016/j.impact.2017.11.002
162. Lynch I, Afantitis A, Leonis G, Melagraki G, Valsami-Jones E. Strategy for Identification of Nanomaterials' Critical Properties Linked to Biological Impacts: Interlinking of Experimental and Computational Approaches. InAdvances in QSAR Modeling 2017. (pp. 385–424). Springer, Cham.
163. Singh AV, Rosenkranz D, Ansari MHD, Singh R, Kanase A, Singh SP, et al. Artificial Intelligence and Machine Learning Empower Advanced Biomedical Material Design to Toxicity Prediction. *Adv Intell Syst* (2020) 2:2000084. doi: 10.1002/aisy.202000084
164. Afantitis A, Melagraki G, Isigonis P, Tsoumanis A, Varsou DD, Valsami-Jones E, et al. Nanosolveit Project: Driving Nanoinformatics Research to Develop Innovative and Integrated Tools for in Silico Nanosafety Assessment. *Comput Struct Biotechnol J* (2020) 18:583–602. doi: 10.1016/j.csbj.2020.02.023
165. Haase A, Klaessig F. Eu US Roadmap Nanoinformatics 2030. *EU Nanosafety Clust* (2018), 0–127. doi: 10.5281/zenodo.1486012
166. Cui Q, Hernandez R, Mason SE, Frauenheim T, Pedersen JA, Geiger F. Sustainable Nanotechnology: Opportunities and Challenges for Theoretical/Computational Studies. *J Phys Chem B* (2016) 120:7297–306. doi: 10.1021/acs.jpcb.6b03976
167. Winkler DA. Role of Artificial Intelligence and Machine Learning in Nanosafety. *Small* (2020) 16:2001883. doi: 10.1002/smll.202001883
168. Lynch I, Afantitis A, Exner T, Himly M, Lobaskin V, Doganis P, et al. Can An Inchi for Nano Address the Need for a Simplified Representation of Complex Nanomaterials Across Experimental and Nanoinformatics Studies? *Nanomaterials* (2020) 10:1–44. doi: 10.3390/nano10122493
169. Rajan K. Nanoinformatics: data-driven materials design for health and environmental needs. InNanotechnology Environmental Health and Safety 2014 Jan 1 (pp. 173–198). William Andrew Publishing.
170. Muratov EN, Bajorath J, Sheridan RP, Tetko IV, Filimonov D, Poroikov V, et al. QSAR Without Borders. *Chem Soc Rev* (2020) 49:3525–64. doi: 10.1039/d0cs00098a
171. Winkler DA. Recent Advances, and Unresolved Issues, in the Application of Computational Modelling to the Prediction of the Biological Effects of Nanomaterials. *Toxicol Appl Pharmacol* (2016) 299:96–100. doi: 10.1016/j.taap.2015.12.016
172. Trinh TX, Ha MK, Choi JS, Byun HG, Yoon TH. Curation of Datasets, Assessment of Their Quality and Completeness, and nanoSAR Classification Model Development for Metallic Nanoparticles. *Environ Sci Nano* (2018) 5:1902–10. doi: 10.1039/c8en00061a
173. Choi J-S, Ha MK, Trinh TX, Yoon TH, Byun H-G. Towards a Generalized Toxicity Prediction Model for Oxide Nanomaterials Using Integrated Data From Different Sources. *Sci Rep* (2018) 8:6110. doi: 10.1038/s41598-018-24483-z
174. Gajewicz A, Puzyn T, Odziomek K, Urbaszek P, Haase A, Riebeling C, et al. Decision Tree Models to Classify Nanomaterials According to the DF4nanoGrouping Scheme. *Nanotoxicology* (2018) 12:1–17. doi: 10.1080/17435390.2017.1415388
175. Feng R, Yu F, Xu J, Hu X. Knowledge Gaps in Immune Response and Immunotherapy Involving Nanomaterials: Databases and Artificial Intelligence for Material Design. *Biomaterials* (2021) 266:120469. doi: 10.1016/j.biomaterials.2020.120469
176. Burello E. A Mechanistic Model for Predicting Lung Inflammogenicity of Oxide Nanoparticles. *Toxicol Sci* (2017) 159:339–53. doi: 10.1093/toxsci/kfx136
177. Ban Z, Yuan P, Yu F, Peng T, Zhou Q, Hu X. Machine Learning Predicts the Functional Composition of the Protein Corona and the Cellular Recognition of Nanoparticles. *Proc Natl Acad Sci U.S.A.* (2020) 117:10492–9. doi: 10.1073/pnas.1919755117
178. Quan X, Liu J, Zhou J. Multiscale Modeling and Simulations of Protein Adsorption: Progresses and Perspectives. *Curr Opin Colloid Interface Sci* (2019) 41:74–85. doi: 10.1016/j.cocis.2018.12.004
179. Duan Y, Coreas R, Liu Y, Bitounis D, Zhang Z, Parviz D, et al. Prediction of Protein Corona on Nanomaterials by Machine Learning Using Novel Descriptors. *NanoImpact* (2020) 17:100207. doi: 10.1016/j.impact.2020.100207
180. Alsharif SA, Power D, Rouse I, Lobaskin V. In Silico Prediction of Protein Adsorption Energy on Titanium Dioxide and Gold Nanoparticles. *Nanomaterials* (2020) 10:1–21. doi: 10.3390/nano10101967
181. Findlay MR, Freitas DN, Mobed-Miremadi M, Wheeler KE. Machine Learning Provides Predictive Analysis Into Silver Nanoparticle Protein Corona Formation From Physicochemical Properties. *Environ Sci Nano* (2018) 5:64–71. doi: 10.1039/C7EN00466D
182. Le TC, Yin H, Chen R, Chen Y, Zhao L, Casey PS, et al. An Experimental and Computational Approach to the Development of ZnO Nanoparticles That are Safe by Design. *Small* (2016) 12:3568–77. doi: 10.1002/smll.201600597
183. Mikolajczyk A, Gajewicz A, Mulkiewicz E, Rasulev B, Marchelek M, Diak M, et al. Nano-QSAR Modeling for Ecosafe Design of Heterogeneous TiO 2 -Based Nano-Photocatalysts. *Environ Sci Nano* (2018) 5:1150–60. doi: 10.1039/C8EN00085A
184. Puzyn T, Rasulev B, Gajewicz A, Hu X, Dasari TP, Michalkova A, et al. Using nano-QSAR to Predict the Cytotoxicity of Metal Oxide Nanoparticles. *Nat Nanotechnol* (2011) 6:175–8. doi: 10.1038/nnano.2011.10
185. Wang W, Sedykh A, Sun H, Zhao L, Russo DP, Zhou H, et al. Predicting Nano-Bio Interactions by Integrating Nanoparticle Libraries and Quantitative Nanostructure Activity Relationship Modeling. *ACS Nano* (2017) 11:12641–9. doi: 10.1021/acsnano.7b07093
186. Martins C, Dreij K, Costa PM. The State-of-the Art of Environmental Toxicogenomics: Challenges and Perspectives of "Omics" Approaches Directed to Toxicant Mixtures. *Int J Environ Res Public Health* (2019) 16:1–16. doi: 10.3390/ijerph16234718
187. Peng T, Wei C, Yu F, Xu J, Zhou Q, Shi T, et al. Predicting Nanotoxicity by an Integrated Machine Learning and Metabolomics Approach. *Environ Pollut* (2020) 267:115434. doi: 10.1016/j.envpol.2020.115434
188. Serra A, Fratello M, Cattelani L, Liampa I, Melagraki G, Kohonen P, et al. Transcriptomics in Toxicogenomics, Part III: Data Modelling for Risk Assessment. *Nanomaterials* (2020) 10:708. doi: 10.3390/nano10040708
189. Ahmad F, Mahmood A, Muhmood T. Machine Learning-Integrated Omics for the Risk and Safety Assessment of Nanomaterials. *Biomater Sci* (2021) 9:1598–608. doi: 10.1039/D0BM01672A
190. Kinaret PAS, Ndika J, Ilves M, Wolff H, Vales G, Norppa H, et al. Toxicogenomic Profiling of 28 Nanomaterials in Mouse Airways. *Adv Sci* (2021) 2004588:2004588. doi: 10.1002/advs.202004588
191. Singh AV, Ansari MHD, Rosenkranz D, Maharjan RS, Kriegel FL, Gandhi K, et al. Artificial Intelligence and Machine Learning in Computational Nanotoxicology: Unlocking and Empowering Nanomedicine. *Adv Healthc Mater* (2020) 9:1901862. doi: 10.1002/adhm.201901862
192. Murugadoss S, Das N, Godderis L, Mast J, Hoet PH, Ghosh M. Identifying Nanodescriptors to Predict the Toxicity of Nanomaterials: A Case Study on Titanium Dioxide. *Environ Sci Nano* (2021) 8(2):580–90. doi: 10.1039/D0EN01031F
193. Papadiamantis AG, Jänes J, Voyiatzis E, Sikk L, Burk J, Burk P, et al. Predicting Cytotoxicity of Metal Oxide Nanoparticles Using Isalos Analytics Platform. *Nanomaterials* (2020) 10:1–19. doi: 10.3390/nano10102017
194. Milosevic A, Romeo D, Wick P. Understanding Nanomaterial Biotransformation: An Unmet Challenge to Achieving Predictive Nanotoxicology. *Small* (2020) 1907650. doi: 10.1002/smll.201907650
195. Papadiamantis AG, Klaessig FC, Exner TE, Hofer S, Hofstaetter N, Himly M, et al. Metadata Stewardship in Nanosafety Research: Community-Driven Organisation of Metadata Schemas to Support Fair Nanoscience Data. *Nanomaterials* (2020) 10:2033. doi: 10.3390/nano10102033
196. Martinez DST, Da Silva GH, de Medeiros AMZ, Khan LU, Papadiamantis AG, Lynch I. Effect of the Albumin Corona on the Toxicity of Combined Graphene Oxide and Cadmium to Daphnia Magna and Integration of the

Datasets Into the NanoCommons Knowledge Base. *Nanomaterials* (2020) 10:1936. doi: 10.3390/nano10101936

197. Worth A, Aschberger K, Asturiol D, Bessems J, Gerloff K, Graepel R, et al. *Evaluation of the Availability and Applicability of Computational Approaches in the Safety Assessment of Nanomaterials*. Publications Office of the European Union, Luxembourg (2017). doi: 10.2760/248139
198. Varsou DD, Afantitis A, Tsoumanis A, Melagraki G, Sarimveis H, Valsami-Jones E, et al. A Safe-by-Design Tool for Functionalised Nanomaterials Through the Enalos Nanoinformatics Cloud Platform. *Nanoscale Adv* (2019) 1:706–18. doi: 10.1039/c8na00142a
199. Gazzi A, Fusco L, Orecchioni M, Ferrari S, Franzoni G, Yan JS, et al. Graphene, Other Carbon Nanomaterials and the Immune System: Toward Nanoimmunity-by-Design. *J Phys Mater* (2020) 3:034009. doi: 10.1088/2515-7639/ab9317
200. Pinsino A, Bastús NG, Busquets-Fité M, Canesi L, Cesaroni P, Drobne D, et al. Probing the Immune Responses to Nanoparticles Across Environmental Species. A Perspective of the EU Horizon 2020 Project PANDORA. *Environ Sci Nano* (2020) 7:3216–32. doi: 10.1039/D0EN00732C

Conflict of Interest: The authors declare that the research was conducted in the absence of any commercial or financial relationships that could be construed as a potential conflict of interest.

frontiers in Immunology

MINI REVIEW
published: 15 June 2021
doi: 10.3389/fimmu.2021.688927

Iron Oxide Nanoparticles in Bioimaging – An Immune Perspective

Mark Geppert and Martin Himly*

Division of Allergy and Immunology, Department of Biosciences, University of Salzburg, Salzburg, Austria

Iron oxide nanoparticles (IONPs) bear big hopes in nanomedicine due to their (potential) applications in tumor therapy, drug delivery or bioimaging. However, as foreign entities, such particles may be recognized by the immune system and, thus, lead to inflammation, hypersensitivity or anaphylactic shock. In addition, an overload with iron is known to cause oxidative stress. In this short review, we summarize the biological effects of such particles with a major focus on IONP-formulations used for bioimaging purposes and their effects on the human immune system. We conclude that especially the characteristics of the particles (size, shape, surface charge, coating, *etc.*) as well as the presence of bystander substances, such as bacterial endotoxin are important factors determining the resulting biological and immunological effects of IONPs. Further studies are needed in order to establish clear structure-activity relationships.

Keywords: SPIONs, inflammation, oxidative stress, ROS, MRI contrast agent, endotoxin

Edited by:
Yang Li,
Shenzhen Institutes of Advanced Technology (CAS), China

Reviewed by:
Paola Italiani,
National Research Council (CNR), Italy
Liming Wang,
Institute of High Energy Physics (CAS), China

****Correspondence:***
Mark Geppert
mark.geppert@sbg.ac.at

Specialty section:
This article was submitted to Molecular Innate Immunity, a section of the journal Frontiers in Immunology

Received: *31 March 2021*
Accepted: *01 June 2021*
Published: *15 June 2021*

Citation:
Geppert M and Himly M (2021) Iron Oxide Nanoparticles in Bioimaging – An Immune Perspective. Front. Immunol. 12:688927. doi: 10.3389/fimmu.2021.688927

INTRODUCTION

Nanoparticles (NPs) are defined as particular entities with a maximum size of 100 nm in two or three dimensions (1). They can be composed of different organic and inorganic materials such as liposomes, micelles, carbon nanotubes, fullerenes, metalloids, metals and metal oxides. Iron oxide nanoparticles (IONPs) typically consist of a core of a magnetic iron oxide (magnetite, Fe_3O_4 or maghemite, γ-Fe_2O_3), surrounded by a coating for their stabilization and can be synthesized by a huge variety of chemical approaches (2, 3). During the last decades, IONPs became more and more popular due to their numerous biomedical applications, such as cancer therapy by magnetic-field mediated hyperthermia, drug-delivery, iron replacement therapy or bioimaging techniques (4–6). Although IONPs are generally considered as biocompatible and possess only low cytotoxic potential (7), it is evident that such particles are considered as foreign entities and, thus, may have a variety of effects on the immune system, such as hypersensitivity reactions, immunosuppression or immune stimulation (8, 9). The aim of this review is to give an overview on different IONP formulations that are (or have been) clinically applied for imaging purposes and to elaborate on the effects of these particles on human health and the immune system.

IRON OXIDE NANOPARTICLES IN BIOIMAGING

Due to the magnetic properties of the core and the small particle size, IONPs are superparamagnetic and undergo magnetization only in presence of a magnetic field. This special properties have shown to be beneficial for use of such particles as contrast agents in magnetic resonance imaging (MRI) where IONPs produce hypointense (dark) signals in T_2-weighted MR images (10, 11). As such, they represent the counterpart to the classical Gadolinium (Gd)-based contrast agents which increase T_1 relaxation rates leading to positive (bright) image contrast (12). In recent literature, there is also evidence that ultra-small IONPs (<5 nm) can be used in both T_1- and T_2-weighted MRI (13, 14). These findings could appear to be beneficial in the future since Gd-based contrast agents are known to be less biocompatible and can raise the possibility of nephrotoxicity, especially in patients with advanced acute or chronic kidney disease (15, 16).

MRI contrast agents can be administered orally or intravenously (17). An example for an orally administered IONP-based contrast agent is Ferumoxsil (Lumirem®, GastroMARK®), which was approved for imaging of the gastrointestinal (GI) tract by the FDA in 1996 but later withdrawn from the market. However, most IONP-based imaging agents are administered *via* injection. Ferumoxide (Feridex®, Endorem®) and Ferucarbotran (Ciavist™, Resovist®) were two contrast agents designed for liver imaging which both became approved in the US as well as in Europe. However, due to different side effects, both were withdrawn from the market in 2008/2009 and only Resovist® is still available in limited countries (9, 18, 19). Ferumoxtran-10 (Sinerem®, Combidex®) was designed for lymph node imaging in prostate cancer metastasis (20). However, also this earlier FDA-approved agent was withdrawn from the market due to a lack of improved efficacy (19). Ferumoxytol (Feraheme®, Rienso®) was initially approved for treatment of iron deficiency for patients with chronic kidney disease but recently has also been shown to be suitable as contrast aging in MRI, however with no clinical approval yet (21). VSOP C184 and Feruglose (Clariscan®) were both designed and clinically tested for MR angiography and blood pool imaging but did not reach the level of approval (22, 23). **Table 1** lists a selection of iron oxide-based contrast agents applied for bioimaging.

Aside from MRI, IONPs can also be applied for a similar but different technique, named magnetic particle imaging (MPI). Here, the particles do not act as a contrast agent but rather are the only source of the signal and the only visualized element (24). By using static and dynamic magnetic fields, the unique magnetic characteristics of IONPs can be used to acquire detailed images without using harmful ionizing radiation. In contrast to MRI, MPI thereby only images the anatomical sections which were labelled with the IONP tracer (25, 26). Thereby it offers three-dimensional images with high sensitivity, temporal and spatial resolution. However, to date, MPI is rather experimental, and available scanners are designed for investigation of mouse- and rat-sized animals (26). IONP-formulations like Ferucarbotran (Resovist®) have been shown suitable for MPI, however, other formulations of IONPs (IONP-micelles) seemed to perform better for this novel technique (27).

BIOCOMPATIBILITY OF IRON OXIDE NANOPARTICLES

Iron is an essential element and, thus, a life without iron would not be possible. However, overload of iron is also hazardous since it can increase reactive oxygen species (ROS) production *via* Fenton and Haber-Weiss reactions (28). In the Fenton reaction (1), ferrous iron (Fe^{2+}) reacts with hydrogen peroxide (H_2O_2) – which is, for instance, produced as a side product in mitochondrial respiration (29) – forming ferric iron (Fe^{3+}), a hydroxide anion (OH^-) and the extremely reactive hydroxyl radical ($OH\cdot$). The oxidized Fe^{3+} can be reduced to Fe^{2+} again by the involvement of a superoxide anion, which will be converted to oxygen (2). The scheme below depicts the reaction equations of both reactions. The concluding final reaction is termed the Haber Weiss reaction – an iron catalyzed reaction, which generates hydroxyl radicals using hydrogen peroxide and superoxide radicals as substrates (3).

$$\mathrm{Fe}^{2+} + \mathrm{H_2O_2} \rightarrow \mathrm{Fe}^{3+} + \mathrm{OH}^- + \mathrm{OH}\cdot \tag{1}$$

$$\mathrm{Fe}^{3+} + \mathrm{O}_2^- \cdot \rightarrow Fe^{2+} + \mathrm{O_2} \tag{2}$$

$$\mathrm{H_2O_2} + \mathrm{O}_2^- \cdot \rightarrow \mathrm{O_2} + \mathrm{OH}^- + \mathrm{OH}\cdot \tag{3}$$

Due to this reactions, cells have to tightly regulate iron metabolism and have developed numerous pathways and antioxidative defense mechanisms to compete iron-induced stress such as detoxification of H_2O_2 by the enzyme catalase or by involvement of the antioxidant glutathione and the enzymes glutathione peroxidase and glutathione reductase or by storing excess of free intracellular iron in the iron storage protein ferritin (30–32). Nevertheless, if these different antioxidative

TABLE 1 | Selected IONP-based contrast agents for MRI.

Formulation	Trade name(s)	Coating	Application(s)
Ferumoxide	Feridex®, Endorem®	Dextran	Liver imaging
Ferucarbotran	Ciavist™, Resovist®	Carboxydextran	Liver imaging
Ferumoxtran-10	Sinerem®, Combidex®	Dextran	Lymph node imaging
Ferumoxytol	Feraheme®, Rienso®	Polyglucose sorbitol carboxymethyl ether	CNS imaging, blood pool imaging, lymph node imaging, Iron deficiency treatment
Citrate-coated very small iron oxide NP	VSOP C184	Citrate	MR angiography, Blood pool imaging
Feruglose	Clariscan®	PEGylated starch	MR angiography, Blood pool imaging
Ferumoxsil	Lumirem®, GastroMARK®	Siloxane	Oral GI imaging

mechanisms become overcharged and fail, OH· radicals can induce intracellular damage such as lipid peroxidation, protein oxidation and subsequent degradation and DNA damage, which will lead to cell death through a process called ferroptosis (33). IONPs can be responsible in Fenton reaction-mediated ROS generation either at the particle surface or by intracellular liberation of Fe^{2+}/Fe^{3+} ions (34–36). Oxidative stress is frequently described as the main reason for IONP-mediated cytotoxicity as extensively reviewed earlier (7, 37, 38).

Cellular and Molecular Effects Determined *In Vitro*

Cytotoxicity of NPs can be assessed *in vitro* by a number of different assays addressing different cellular markers. The most prominent assays are the MTT-assay and the WST-1 assay to address the cellular metabolic activity, the LDH assay to address the cell membrane integrity and the Neutral Red uptake assay to assess lysosomal integrity. In general, the cytotoxicity of IONPs is considered rather low, especially when comparing them with other metal/metal oxide NPs such as silver or copper oxide (39, 40) and only a limited number of studies exists that report toxicity at lower (<100µg/mL) concentrations (41, 42). Interestingly, when moving away from the field of human toxicology, IONPs become much more critical. For example, Zhu and colleagues found that IONPs in concentrations of 10 µg/mL and higher severely affected hatching rate and survival from zebrafish (*Danio rerio*) while García and co-workers published EC50 values of even less than 1 µg/mL for IONP-toxicity towards *Daphnia magna* (43, 44).

Aside from classical cytotoxicity studies, numerous studies exist that in greater depth investigate the cellular and molecular effects of IONP exposure towards different cell types. As already mentioned above, oxidative stress plays a major role for IONP-related effects. For example, increase of ROS production was found for the IONP formulation Endorem® in human liver cells (45), for Endorem®, Resovist® and VSOP C200 in C17.2 neural progenitor cells and PC12 rat pheochromocytoma cells (46) or Feraheme® in human T cells (47). However, also studies exist that show only minor or no ROS production after incubation of human cells with IONPs for bioimaging. Müller and colleagues showed that Ferumoxtran-10 was not toxic to human macrophages, nor did it activate them to produce pro-inflammatory cytokines or induce ROS production (48) and Lindemann and co-workers showed that Ferucarbotran (Resovist®) did not lead to increased ROS production in head and neck squamous cancer cells (HNSCCs) despite they induced apoptosis (49).

In addition to ROS formation and cytotoxicity, other adverse effects have been reported being caused by IONPs. Dissanayake and co-workers extensively reviewed the potential of IONPs to induce genomic alterations (50). Genotoxicity of IONPs was observed by different types of DNA damage, such as chromosomal aberrations, DNA strand breakage, oxidative DNA damage and mutations (51) or by the formation of micronuclei (52). Jin and colleagues showed that the commercial IONP formulation Feridex® exerted genetic toxicity in human hepatoma (HepG2) cells (53). Soenen and colleagues demonstrated that high concentrations of Endorem®, Resovist® and citrate-coated IONPs induced important cytoskeleton and morphology alterations and affected the proliferation of C17.2 neural progenitor cells and primary human blood outgrowth endothelial cells (46, 54). Other IONP-related effects that have been reported are cell cycle alterations (55), autophagy (56) or apoptosis (49, 57). **Figure 1** summarizes entry routes and cellular fate of IONPs in human cells.

Biodistribution, Clearance and Toxicity Determined *In Vivo*

Understanding the biodistribution of NPs is a critical point when evaluating their biological and immunological safety (58). The disposition of any compound within an organism can be described by the ADME principle, which stands for **a**bsorption, **d**istribution, **m**etabolism and **e**xcretion. For IONPs, all these four criteria are strongly dependent on particle characteristics, such as size, size distribution, surface charge, coating molecules and protein corona formation (59). Already more than 30 years ago, the biodistribution of radioactive-labelled Ferumoxide (AMI-25) after injection in rats was studied, with the result that the majority of the particles accumulated in the liver and spleen 1 h after injection (60). While the clearance of the particles of these organs occurs with half-lives of 3-4 days, the whole body clearance was much longer (44.9 days). In contrast, the blood half-life of these particles was determined to be only 6 min, indicating the rapid uptake and clearance by the mononuclear phagocyte system (MPS) (61). In the same report, the authors also investigated the blood half-life of a second ultrasmall IONP type (size <10 nm, while AMI-25 was 72 nm) and found that these particles remain in the bloodstream with half-lives of 81 min, indicating that IONP size plays a crucial role in particle clearance. This finding was also confirmed by Bourrinet and colleagues who compared 30 nm Ferumoxtran-10 with the larger Ferumoxides (62).

Apart from IONP size, also the coating and surface charge play a major role in their blood clearance, pharmacokinetics and biodistribution (58, 59). In general, IONPs with neutral surface charge are considered having a longer circulation time and a reduced uptake by the MPS due to less opsonization (63, 64). Polyethylene glycol (PEG) is often used as a coating agent for IONPs, since it provides a steric stabilization of the particles by a shielding of their surface charge that strongly reduces opsonization and subsequent macrophage uptake (65). Another polymeric coating agent, which is often used as alternative to PEG, is polyvinyl pyrrolidone (PVP) (66). IONPs with positively charged coatings are often cleared much faster from the bloodstream due to differences in protein absorption in comparison with neutral or negatively charged particles (67). It is well known that protein absorption and subsequent protein corona formation has a great impact on the biological identity of NPs and on their effects on living organisms (68). When cleared from the bloodstream, injected IONPs are mainly found in the liver and spleen. However, there is also evidence of IONPs present in the lungs (69), kidney (70), heart (71) and even the brain (72).

IONPs are generally considered as safe and non-toxic *in vivo* (59), however, such particles can have side effects such as local pain, hypotension, hypersensitivity, anaphylactic shock, vasodilatation and paraesthesia (9) which were the reasons for withdrawal of the earlier clinical applied dextran/carboxydextran-coated IONP-formulations (Feridex®/Endorem®, Resovist®/Cliavist®, Sinerem®/Combidex®). A still approved formulation is

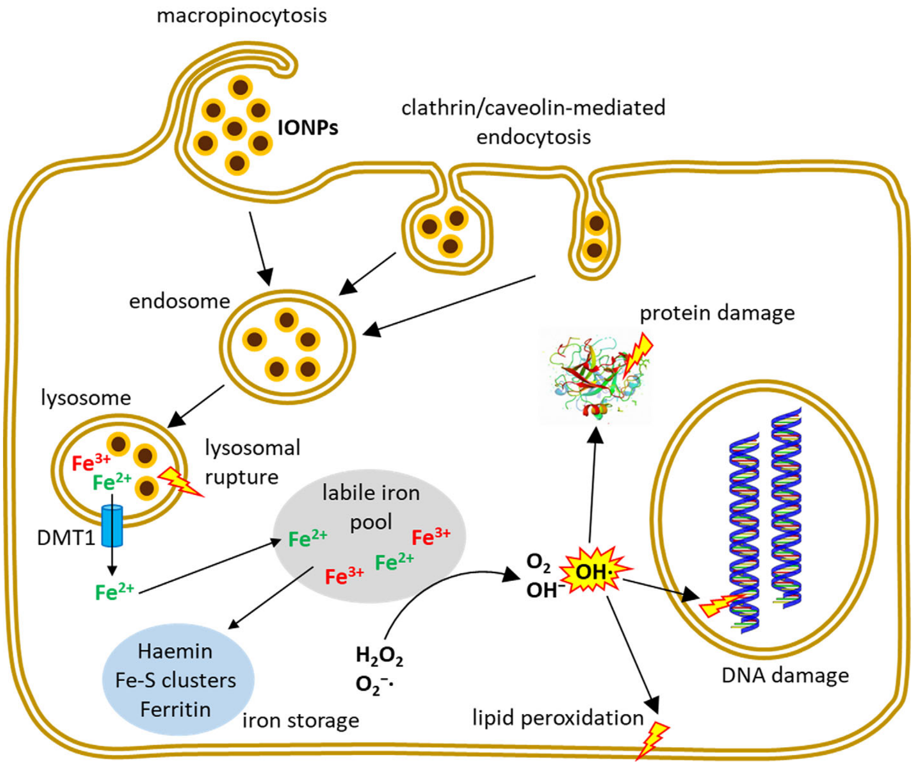

FIGURE 1 | Uptake and intracellular fate of IONPs. Depending on IONP-size and coating and on the investigated cell type, different endocytic mechanisms contribute to the uptake of intact IONPs into the cells where the particles typically enter the endo-lysosomal system. Inside the cell, iron can be liberated from the NPs and contribute to several reactions including Fenton- and Haber-Weiss reactions leading to the formation of hydroxyl radicals which can induce cell damage.

Ferumoxytol (Feraheme®, Rienso® in the EU) which is primarily used as iron therapy and has been shown to be tolerable in high doses up to 510 mg per injection (73). However, there is also evidence of risks of hypersensitivity reactions and also the long-term effects seem to be not fully evaluated (74).

IMMUNE EFFECTS OF IRON OXIDE NANOPARTICLES

Besides cytotoxicity induced through particle-mediated or iron-mediated oxidative stress, IONPs may be recognized by the immune system and can, thus, induce different immunological effects. These immune effects are – just like the aforementioned cellular and molecular effects – highly dependent on the particle characteristics. Size, shape, surface charge and particle coating have been described previously to greatly influence the immune effects of IONPs (9). On the one hand, this is explained by the fact that these parameters also influence the IONP biodistribution and toxicokinetic profile (75); one the other hand, certain coatings have been shown to induce certain immune effects. For example, polyethyleneimine (PEI)-coated IONPs have been shown to enhance Th1 polarization of human dendritic cells (DCs) (76), while dextran-coated IONPs have been shown to suppress the proliferation activity of T-lymphocytes (77).

As already mentioned in the previous sections, the first reaction of the human immune system on injected IONPs will be their rapid uptake and elimination by cells of the MPS. One essential component of the MPS are monocytes, which circulate in the peripheral blood and can become activated by different stimuli. Earlier studies have shown that monocytes accumulate dextran-coated IONPs and that this accumulation induces autophagy and an increase in secretion of the pro-inflammatory cytokines Interleukin (IL)-1β, IL-6 and Tumor Necrosis Factor (TNF)-α (78). Contradictory results have been published by Grosse and co-workers who showed that 10 and 30 nm IONPs (coated with a monolayer of oleic acid and a monolayer of amphiphilic polymer) did not lead to elevation of these cytokines end even inhibited LPS-induced pro-inflammatory cytokine production (79). A likely reason for this discrepancy could be the fact that in the latter study, the particles were proven to be free of LPS or other TLR4 agonists, while the authors of the first study did not investigate this. Moreover, the different coatings of the particles can play a role in their different immunological responses. For example, amino-functionalized amino-polyvinyl alcohol-coated IONPs have been shown to increase IL-1β production of human monocytes (80), while starch-coated IONPs did not alter IL-1β and IL-10 secretion but downregulated IL-6 secretion in primary monocytes (81). These differences in observed cytokine profiles shows the need for future studies in order to gain a mechanistic understanding of the stimulatory or suppressive effects of IONPs towards human monocytes.

Macrophages are phagocytes, which can be activated in two different ways: classical (M1) or alternative (M2). The main function of M1 macrophages is the detection, phagocytosis and killing of pathogens, apoptotic cells and damaged host cells while M2 macrophages have important functions in tissue repair (9). Aside from this, macrophages can function as antigen-presenting cells (APCs) and thereby connect innate with adaptive immunity. IONPs have been frequently used to label macrophages for MRI, for example in the brain (82), and have been shown to perform better than conventional Gd-based contrast agents in a model of multiple sclerosis (83). On the other hand, it has been shown *in vitro* that IONPs can also induce oxidative stress and affect cell viability of rat microglia cells (36). Other mechanistic studies reported that IONPs lead to a secretion of IL-12, IL-1β and to upregulation of several genes linked to the M1 phenotype in murine and human macrophages (80, 84, 85). However, it should be noted here that the IONPs in these studies were not checked for endotoxin contaminations. In a study by Yang and colleagues, the clinically applied IONP formulation Ferucarbotran has been shown to activate RAW264.7 macrophages by an increase in oxidative stress, a decrease in mitochondrial membrane potential and an increase in cell proliferation (86).

IONPs can also affect the function of APCs as shown in a study by Park and co-workers (87). They exposed mice intratracheally with IONPs and found that these particles remained in the lungs for at least 90 days and enhanced the expression of antigen presentation-related proteins such as CD80, CD86, and MHC class II, on APCs in bronchoalveolar lavage (BAL) fluid. Another study by Mou and colleagues reported that positively charged IONPs enhanced antigen cross-presentation of murine DCs while negatively charged IONPs inhibited the DCs' functions and rapidly activated autophagy (88). The clinical IONP-formulation Ferumoxide (Feridex®/Endorem®) had been shown earlier to affect the viability and migratory properties of DCs, however, only at high concentrations (89, 90).

The principal cells of humoral and cellular immune response are the lymphocytes, which specifically recognize and respond to antigens and produce antibodies (B cells) or directly kill infected cells or assist the MPS in destroying them (T cells). The ability of these cells to take up NPs is, generally, considered lower than that of monocytes or macrophages (9). A study by Gaharwar and colleagues reports that isolated rat splenic lymphocytes take up IONPs and that the particles affect cell viability, increase intracellular ROS levels and lipid peroxidation while depleting antioxidative enzymes and glutathione (91). Resovist® has been shown to attenuate Th17 responses in ovalbumin (OVA)-sensitized BALB/c mice *in vivo* and in OVA-primed splenocytes isolated from BALB/c mice *in vitro* (92). This was indicated by a decreased infiltration of CCR6+, IL-6+, IL17+ and ROR-γ+ cells in inflamed footpads *in vivo* and by a suppression of the expression of IL-6, IL-17 and ROR-γt *in vitro*. In another study, Feraheme® has been shown to suppress the immune function of human T lymphocytes through mitochondrial damage and ROS production (47). In contrast, a Th1-type immune activation was described by Zhu and co-workers, who exposed mice intratracheally with 4 or 20 μg IONPs and reported that NP-induced exosomes were responsible as signaling mediators for this Th1 immune activation (93).

Taken together, it can be stated that there are a number of open questions regarding the complete understanding of IONPs on the functioning of different immune cells. **Table 2** sums up the IONP-derived immune effects and the cytokines involved of the studies on different immune cells reviewed in this paper. Results presented in literature are sometimes inconsistent which can be attributed to the use of different IONPs, IONP-coatings, -sizes or -shapes or due to different incubation conditions. Structure-activity relationships are not always clear and future studies are definitely needed in order to systematically evaluate the immune effects of IONPs and the influence of different particle characteristics (9).

CONCLUSIONS AND FUTURE PERSPECTIVES

Iron oxide nanoparticles (IONPs) possess a variety of biomedical applications, especially in bioimaging. However, these applications came with a price since many of the IONP-containing formulations have shown to cause different side-effects that later resulted in their withdrawal from the market. We herein reviewed the biological and immunological effects of IONPs and concluded that published results often show inconsistencies regarding the effects of such particles. Theses inconsistencies can often be attributed to the particle characteristics (size, shape, surface coating) or the experimental design and incubation conditions (*e.g.*, the presence of bystander substances such as bacterial endotoxins). Thus, quantitative structure-activity relationships (QSARs) for the analysis of such particles are difficult to draw and require more data from future studies involving systematic analysis of well-characterized particles under clearly defined experimental conditions.

TABLE 2 | IONP-derived immune effects and up-/downregulated cytokines of the studies reviewed in this articles.

Cell type	Immune effects / cytokines up- or downregulated	Reference
Monocytes	Autophagy / IL-1β (+), IL-6 (+), TNFα (+)	(55)
	Suppression of LPS-induced NFκB activation	(79)
	IL-1β (+)	(80)
	IL-6 (–)	(81)
Macrophages	M1 activation, IL-12 (+)	(84)
APCs	IL-1β (+)	(85)
DCs	Upregulation of several proinflammatory cytokines	(80)
Lymphocytes	expression of CD80, CD86 and MHC class II	(87)
	autophagy / antigen cross-presentation	(88)
	oxidative stress, glutathione depletion	(91)
	Attenuation of Th17 cell responses	(91)
	IL-6 (–), IL-17 (–), ROR-γt (–)	(92)
	Suppression of T-lymphocytes	(47)
	Th1 immune activation	(93)

AUTHOR CONTRIBUTIONS

MG performed literature search and prepared first draft and display items of mini review. MH was involved in critical discussions of the content and display items, writing and editing of the mini review. All authors contributed to the article and approved the submitted version.

FUNDING

This work was funded by the H2020 EU research infrastructure for nanosafety projects NanoCommons (Grant Agreement No. 731032) and NanoRigo (Grant Agreement No. 814530) and by the Allergy-Cancer-BioNano Research Center of the Paris Lodron University of Salzburg.

REFERENCES

1. Auffan M, Rose J, Bottero J-Y, Lowry GV, Jolivet J-P, Wiesner MR. Towards a Definition of Inorganic Nanoparticles From an Environmental, Health and Safety Perspective. *Nat Nanotechnol* (2009) 4:634–41. doi: 10.1038/nnano.2009.242
2. Laurent S, Forge D, Port M, Roch A, Robic C, Vander Elst L, et al. Magnetic Iron Oxide Nanoparticles: Synthesis, Stabilization, Vectorization, Physicochemical Characterizations, and Biological Applications. *Chem Rev* (2008) 108:2064–110. doi: 10.1021/cr068445e
3. Dadfar SM, Roemhild K, Drude NI, Von Stillfried S, Knuchel R, Kiessling F, et al. Iron Oxide Nanoparticles: Diagnostic, Therapeutic and Theranostic Applications. *Adv Drug Delivery Rev* (2019) 138:302–25. doi: 10.1016/j.addr.2019.01.005
4. Gupta AK, Gupta M. Synthesis and Surface Engineering of Iron Oxide Nanoparticles for Biomedical Applications. *Biomaterials* (2005) 26:3995–4021. doi: 10.1016/j.biomaterials.2004.10.012
5. Martinkova P, Brtnicky M, Kynicky J, Pohanka M. Iron Oxide Nanoparticles: Innovative Tool in Cancer Diagnosis and Therapy. *Adv Healthc Mater* (2018) 7:1700932. doi: 10.1002/adhm.201700932
6. Vangijzegem T, Stanicki D, Laurent S. Magnetic Iron Oxide Nanoparticles for Drug Delivery: Applications and Characteristics. *Expert Opin Drug Delivery* (2019) 16:69–78. doi: 10.1080/17425247.2019.1554647
7. Patil RM, Thorat ND, Shete PB, Bedge PA, Gavde S, Joshi MG, et al. Comprehensive Cytotoxicity Studies of Superparamagnetic Iron Oxide Nanoparticles. *Biochem Biophys Rep* (2018) 13:63–72. doi: 10.1016/j.bbrep.2017.12.002
8. Dobrovolskaia MA, Shurin M, Shvedova AA. Current Understanding of Interactions Between Nanoparticles and the Immune System. *Toxicol Appl Pharmacol* (2016) 299:78–89. doi: 10.1016/j.taap.2015.12.022
9. Shah A, Dobrovolskaia MA. Immunological Effects of Iron Oxide Nanoparticles and Iron-Based Complex Drug Formulations: Therapeutic Benefits, Toxicity, Mechanistic Insights, and Translational Considerations. *Nanomedicine* (2018) 14:977–90. doi: 10.1016/j.nano.2018.01.014
10. Nakamura H, Ito N, Kotake F, Mizokami Y. And Matsuoka, T. (2000). Tumor-detecting Capacity and Clinical Usefulness of SPIO-MRI in Patients With Hepatocellular Carcinoma. *J Gastroenterol* (2000) 35:849–55. doi: 10.1007/s005350070022
11. Weinstein JS, Varallyay CG, Dosa E, Gahramanov S, Hamilton B, Rooney WD, et al. Superparamagnetic Iron Oxide Nanoparticles: Diagnostic Magnetic Resonance Imaging and Potential Therapeutic Applications in Neurooncology and Central Nervous System Inflammatory Pathologies, a Review. *J Cereb Blood Flow Metab* (2010) 30:15–35. doi: 10.1038/jcbfm.2009.192
12. Zhou Z, Lu ZR. Gadolinium-Based Contrast Agents for Magnetic Resonance Cancer Imaging. *Wiley Interdiscip Rev: Nanomed Nanobiotechnol* (2013) 5:1–18. doi: 10.1002/wnan.1198
13. Shen Z, Wu A, Chen X. Iron Oxide Nanoparticle Based Contrast Agents for Magnetic Resonance Imaging. *Mol Pharm* (2017) 14:1352–64. doi: 10.1021/acs.molpharmaceut.6b00839
14. Ma X, Wang S, Hu L, Feng S, Wu Z, Liu S, et al. Imaging Characteristics of USPIO Nanoparticles (< 5 Nm) as MR Contrast Agent in Vitro and in the Liver of Rats. *Contrast Media Mol Imaging* (2019) 2019:3687537. doi: 10.1155/2019/3687537
15. Ersoy H, Rybicki FJ. Biochemical Safety Profiles of Gadolinium-Based Extracellular Contrast Agents and Nephrogenic Systemic Fibrosis. *J Magnetic Resonance Imaging* (2007) 26:1190–7. doi: 10.1002/jmri.21135
16. Perazella MA. Current Status of Gadolinium Toxicity in Patients With Kidney Disease. *Clin J Am Soc Nephrol* (2009) 4:461–9. doi: 10.2215/CJN.06011108
17. Xiao YD, Paudel R, Liu J, Ma C, Zhang ZS, Zhou SK. MRI Contrast Agents: Classification and Application (Review). *Int J Mol Med* (2016) 38:1319–26. doi: 10.3892/ijmm.2016.2744
18. Wang YX. Superparamagnetic Iron Oxide Based MRI Contrast Agents: Current Status of Clinical Application. *Quant Imaging Med Surg* (2011) 1:35–40. doi: 10.3978/j.issn.2223-4292.2011.08.03
19. Wang YX, Idee JM. A Comprehensive Literatures Update of Clinical Researches of Superparamagnetic Resonance Iron Oxide Nanoparticles for Magnetic Resonance Imaging. *Quant Imaging Med Surg* (2017) 7:88–122. doi: 10.21037/qims.2017.02.09
20. Harisinghani MG, Barentsz J, Hahn PF, Deserno WM, Tabatabaei S, Van De Kaa CH, et al. Noninvasive Detection of Clinically Occult Lymph-Node Metastases in Prostate Cancer. *N Engl J Med* (2003) 348:2491–9. doi: 10.1056/NEJMoa022749
21. Bashir MR, Bhatti L, Marin D, Nelson RC. Emerging Applications for Ferumoxytol as a Contrast Agent in MRI. *J Magnetic Resonance Imaging* (2015) 41:884–98. doi: 10.1002/jmri.24691
22. Klein C, Nagel E, Schnackenburg B, Bornstedt A, Schalla S, Hoffmann V, et al. The Intravascular Contrast Agent Clariscan (TM) (NC 100150 Injection) for 3D MR Coronary Angiography in Patients With Coronary Artery Disease. *Magnetic Resonance Mater Phys Biol Med* (2000) 11:65–7. doi: 10.1007/BF02678498
23. Wagner M, Wagner S, Schnorr J, Schellenberger E, Kivelitz D, Krug L, et al. Coronary MR Angiography Using Citrate-Coated Very Small Superparamagnetic Iron Oxide Particles as Blood-Pool Contrast Agent: Initial Experience in Humans. *J Magnetic Resonance Imaging* (2011) 34:816–23. doi: 10.1002/jmri.22683
24. Dulinska-Litewka J, Lazarczyk A, Halubiec P, Szafranski O, Karnas K, Karewicz A. Superparamagnetic Iron Oxide Nanoparticles-Current and Prospective Medical Applications. *Mater (Basel)* (2019) 12:617. doi: 10.3390/ma12040617
25. Gleich B, Weizenecker R. Tomographic Imaging Using the Nonlinear Response of Magnetic Particles. *Nature* (2005) 435:1214–7. doi: 10.1038/nature03808
26. Panagiotopoulos N, Duschka RL, Ahlborg M, Bringout G, Debbeler C, Graeser M, et al. Magnetic Particle Imaging: Current Developments and Future Directions. *Int J Nanomed* (2015) 10:3097–114. doi: 10.2147/Ijn.S70488
27. Starmans LW, Burdinski D, Haex NP, Moonen RP, Strijkers GJ, Nicolay K, et al. Iron Oxide Nanoparticle-Micelles (ION-Micelles) for Sensitive (Molecular) Magnetic Particle Imaging and Magnetic Resonance Imaging. *PloS One* (2013) 8:e57335. doi: 10.1371/journal.pone.0057335
28. Kehrer JP. The Haber-Weiss Reaction and Mechanisms of Toxicity. *Toxicology* (2000) 149:43–50. doi: 10.1016/s0300-483x(00)00231-6
29. Boveris A, Cadenas E. Mitochondrial Production of Hydrogen Peroxide Regulation by Nitric Oxide and the Role of Ubisemiquinone. *IUBMB Life* (2000) 50:245–50. doi: 10.1080/713803732
30. Aebi H. Catalase In Vitro. *Methods Enzymol* (1984) 105:121–6. doi: 10.1016/s0076-6879(84)05016-3
31. Ursini F, Maiorino M, Brigelius-Flohe R, Aumann KD, Roveri A, Schomburg D, et al. Diversity of Glutathione Peroxidases. *Methods Enzymol* (1995) 252:38–53. doi: 10.1016/0076-6879(95)52007-4
32. Dringen R, Pawlowski PG, Hirrlinger J. Peroxide Detoxification by Brain Cells. *J Neurosci Res* (2005) 79:157–65. doi: 10.1002/jnr.20280

33. Latunde-Dada GO. Ferroptosis: Role of Lipid Peroxidation, Iron and Ferritinophagy. *Biochim Biophys Acta Gen Subj* (2017) 1861:1893–900. doi: 10.1016/j.bbagen.2017.05.019
34. Voinov MA, Sosa Pagan JO, Morrison E, Smirnova TI. And Smirnov, a.I. (2011). Surface-mediated Production of Hydroxyl Radicals as a Mechanism of Iron Oxide Nanoparticle Biotoxicity. *J Am Chem Soc* (2011) 133:35–41. doi: 10.1021/ja104683w
35. Geppert M, Hohnholt MC, Nürnberger S, Dringen R. Ferritin Up-Regulation and Transient ROS Production in Cultured Brain Astrocytes After Loading With Iron Oxide Nanoparticles. *Acta Biomater* (2012) 8:3832–9. doi: 10.1016/j.actbio.2012.06.029
36. Petters C, Thiel K, Dringen R. Lysosomal Iron Liberation is Responsible for the Vulnerability of Brain Microglial Cells to Iron Oxide Nanoparticles: Comparison With Neurons and Astrocytes. *Nanotoxicology* (2016) 10:332–42. doi: 10.3109/17435390.2015.1071445
37. Laffon B, Fernández-Bertólez N, Costa C, Brandão F, Teixeira JP, Pásaro E, et al. Cellular and Molecular Toxicity of Iron Oxide Nanoparticles. In: *Cellular and Molecular Toxicology of Nanoparticles*. Heidelberg, Germany: Springer (2018). p. 199–213.
38. Paunovic J, Vucevic D, Radosavljevic T, Mandic-Rajcevic S, Pantic I. Iron-Based Nanoparticles and Their Potential Toxicity: Focus on Oxidative Stress and Apoptosis. *Chem Biol Interact* (2020) 316:108935. doi: 10.1016/j.cbi.2019.108935
39. Hussain SM, Hess KL, Gearhart JM, Geiss KT, Schlager JJ. In Vitro Toxicity of Nanoparticles in BRL 3A Rat Liver Cells. *Toxicol In Vitro* (2005) 19:975–83. doi: 10.1016/j.tiv.2005.06.034
40. Karlsson HL, Cronholm P, Gustafsson J, Moller L. Copper Oxide Nanoparticles are Highly Toxic: A Comparison Between Metal Oxide Nanoparticles and Carbon Nanotubes. *Chem Res Toxicol* (2008) 21:1726–32. doi: 10.1021/tx800064j
41. Singh N, Jenkins GJS, Asadi R, Doak SH. Potential Toxicity of Superparamagnetic Iron Oxide Nanoparticles (SPION). *Nano Rev Exp* (2010) 1:5358. doi: 10.3402/nano.v1i0.5358
42. Mahmoudi M, Hofmann H, Rothen-Rutishauser B, Petri-Fink A. Assessing the In Vitro and In Vivo Toxicity of Superparamagnetic Iron Oxide Nanoparticles. *Chem Rev* (2012) 112:2323–38. doi: 10.1021/cr2002596
43. García A, Espinosa R, Delgado L, Casals E, González E, Puntes V, et al. Acute Toxicity of Cerium Oxide, Titanium Oxide and Iron Oxide Nanoparticles Using Standardized Tests. *Desalination* (2011) 269:136–41. doi: 10.1016/j.desal.2010.10.052
44. Zhu X, Tian S, Cai Z. Toxicity Assessment of Iron Oxide Nanoparticles in Zebrafish (Danio Rerio) Early Life Stages. *PloS One* (2012) 7:e46286. doi: 10.1371/journal.pone.0046286
45. Raschzok N, Muecke DA, Adonopoulou MK, Billecke N, Werner W, Kammer NN, et al. In Vitro Evaluation of Magnetic Resonance Imaging Contrast Agents for Labeling Human Liver Cells: Implications for Clinical Translation. *Mol Imaging Biol* (2011) 13:613–22. doi: 10.1007/s11307-010-0405-y
46. Soenen SJ, Himmelreich U, Nuytten N, De Cuyper M. Cytotoxic Effects of Iron Oxide Nanoparticles and Implications for Safety in Cell Labelling. *Biomaterials* (2011) 32:195–205. doi: 10.1016/j.biomaterials.2010.08.075
47. Shah A, Mankus CI, Vermilya AM, Soheilian F, Clogston JD, Dobrovolskai MA. Feraheme (R) Suppresses Immune Function of Human T Lymphocytes Through Mitochondrial Damage and mitoROS Production. *Toxicol Appl Pharmacol* (2018) 350:52–63. doi: 10.1016/j.taap.2018.04.028
48. Müller K, Skepper JN, Posfai M, Trivedi R, Howarth S, Corot C, et al. Effect of Ultrasmall Superparamagnetic Iron Oxide Nanoparticles (Ferumoxtran-10) on Human Monocyte-Macrophages In Vitro. *Biomaterials* (2007) 28:1629–42. doi: 10.1016/j.biomaterials.2006.12.003
49. Lindemann A, Lüdtke-Buzug K, Fräderich BM, Gräfe K, Pries R, Wollenberg B. Biological Impact of Superparamagnetic Iron Oxide Nanoparticles for Magnetic Particle Imaging of Head and Neck Cancer Cells. *Int J Nanomed* (2014) 9:5025. doi: 10.2147/IJN.S63873
50. Dissanayake NM, Current KM, Obare SO. Mutagenic Effects of Iron Oxide Nanoparticles on Biological Cells. *Int J Mol Sci* (2015) 16:23482–516. doi: 10.3390/ijms161023482
51. Koedrith P, Boonprasert R, Kwon JY, Kim I-S, Seo YR. Recent Toxicological Investigations of Metal or Metal Oxide Nanoparticles in Mammalian Models In Vitro and In Vivo: DNA Damaging Potential, and Relevant Physicochemical Characteristics. *Mol Cell Toxicol* (2014) 10:107–26. doi: 10.1007/s13273-014-0013-z
52. Singh N, Jenkins GJ, Nelson BC, Marquis BJ, Maffeis TG, Brown AP, et al. The Role of Iron Redox State in the Genotoxicity of Ultrafine Superparamagnetic Iron Oxide Nanoparticles. *Biomaterials* (2012) 33:163–70. doi: 10.1016/j.biomaterials.2011.09.087
53. Jin M, Ryu J-C, Kim Y-J. Investigation of the Genetic Toxicity by Dextran-Coated Superparamagnetic Iron Oxide Nanoparticles (SPION) in HepG2 Cells Using the Comet Assay and Cytokinesis-Block Micronucleus Assay. *Toxicol Environ Health Sci* (2017) 9:23–9. doi: 10.1007/s13530-017-0299-z
54. Soenen SJ, Nuytten N, De Meyer SF, De Smedt SC, De Cuyper M. High Intracellular Iron Oxide Nanoparticle Concentrations Affect Cellular Cytoskeleton and Focal Adhesion Kinase-Mediated Signaling. *Small* (2010) 6:832–42. doi: 10.1002/smll.200902084
55. Wu J, Sun J. Investigation on Mechanism of Growth Arrest Induced by Iron Oxide Nanoparticles in PC12 Cells. *J Nanosci Nanotechnol* (2011) 11:11079–83. doi: 10.1166/jnn.2011.3948
56. Zhang L, Wang X, Miao Y, Chen Z, Qiang P, Cui L, et al. Magnetic Ferroferric Oxide Nanoparticles Induce Vascular Endothelial Cell Dysfunction and Inflammation by Disturbing Autophagy. *J Hazard Mater* (2016) 304:186–95. doi: 10.1016/j.jhazmat.2015.10.041
57. Berry CC, Wells S, Charles S, Aitchison G, Curtis AS. Cell Response to Dextran-Derivatised Iron Oxide Nanoparticles Post Internalisation. *Biomaterials* (2004) 25:5405–13. doi: 10.1016/j.biomaterials.2003.12.046
58. Almeida JPM, Chen AL, Foster A, Drezek R. In Vivo Biodistribution of Nanoparticles. *Nanomedicine* (2011) 6:815–35. doi: 10.2217/nnm.11.79
59. Arami H, Khandhar A, Liggitt D, Krishnan KM. In Vivo Delivery, Pharmacokinetics, Biodistribution and Toxicity of Iron Oxide Nanoparticles. *Chem Soc Rev* (2015) 44:8576–607. doi: 10.1039/c5cs00541h
60. Weissleder RA, Stark DD, Engelstad BL, Bacon BR, Compton CC, White DL, et al. Superparamagnetic Iron Oxide: Pharmacokinetics and Toxicity. *Am J Roentgenol* (1989) 152:167–73. doi: 10.2214/ajr.152.1.167
61. Weissleder R, Elizondo G, Wittenberg J, Rabito C, Bengele H, Josephson L. Ultrasmall Superparamagnetic Iron Oxide: Characterization of a New Class of Contrast Agents for MR Imaging. *Radiology* (1990) 175:489–93. doi: 10.1148/radiology.175.2.2326474
62. Bourrinet P, Bengele HH, Bonnemain B, Dencausse A, Idee J-M, Jacobs PM, et al. Preclinical Safety and Pharmacokinetic Profile of ferumoxtran-10, an Ultrasmall Superparamagnetic Iron Oxide Magnetic Resonance Contrast Agent. *Invest Radiol* (2006) 41:313–24. doi: 10.1097/01.rli.0000197669.80475.dd
63. Owens Iii DE, Peppas NA. Opsonization, Biodistribution, and Pharmacokinetics of Polymeric Nanoparticles. *Int J Pharm* (2006) 307:93–102. doi: 10.1016/j.ijpharm.2005.10.010
64. Aggarwal P, Hall JB, Mcleland CB, Dobrovolskaia MA, Mcneil SE. Nanoparticle Interaction With Plasma Proteins as it Relates to Particle Biodistribution, Biocompatibility and Therapeutic Efficacy. *Adv Drug Delivery Rev* (2009) 61:428–37. doi: 10.1016/j.addr.2009.03.009
65. Jokerst JV, Lobovkina T, Zare RN, Gambhir SS. Nanoparticle PEGylation for Imaging and Therapy. *Nanomedicine* (2011) 6:715–28. doi: 10.2217/nnm.11.19
66. Huang J, Bu L, Xie J, Chen K, Cheng Z, Li X, et al. Effects of Nanoparticle Size on Cellular Uptake and Liver MRI With Polyvinylpyrrolidone-Coated Iron Oxide Nanoparticles. *ACS Nano* (2010) 4:7151–60. doi: 10.1021/nn101643u
67. Sakulkhu U, Mahmoudi M, Maurizi L, Salaklang J. And Hofmann, H. (2014). Protein Corona Composition of Superparamagnetic Iron Oxide Nanoparticles With Various Physico-Chemical Properties and Coatings. *Sci Rep* (2014) 4:5020. doi: 10.1038/srep05020
68. Monopoli MP, Aberg C, Salvati A, Dawson KA. Biomolecular Coronas Provide the Biological Identity of Nanosized Materials. *Nat Nanotechnol* (2012) 7:779–86. doi: 10.1038/nnano.2012.207
69. Sharma A, Cornejo C, Mihalic J, Geyh A, Bordelon DE, Korangath P, et al. Physical Characterization and In Vivo Organ Distribution of Coated Iron Oxide Nanoparticles. *Sci Rep* (2018) 8:4916. doi: 10.1038/s41598-018-23317-2
70. Salimi M, Sarkar S, Fathi S, Alizadeh AM, Saber R, Moradi F, et al. Biodistribution, Pharmacokinetics, and Toxicity of Dendrimer-Coated Iron Oxide Nanoparticles in BALB/c Mice. *Int J Nanomed* (2018) 13:1483–93. doi: 10.2147/IJN.S157293
71. Gaharwar US, Meena R, Rajamani P. Biodistribution, Clearance and Morphological Alterations Of Intravenously Administered Iron Oxide

Nanoparticles In Male Wistar Rats. *Int J Nanomed* (2019) 14:9677–92. doi: 10.2147/IJN.S223142

72. Veiseh O, Sun C, Fang C, Bhattarai N, Gunn J, Kievit F, et al. Specific Targeting of Brain Tumors With an Optical/Magnetic Resonance Imaging Nanoprobe Across the Blood-Brain Barrier. *Cancer Res* (2009) 69:6200–7. doi: 10.1158/0008-5472.CAN-09-1157
73. Fishbane S, Bolton WK, Winkelmayer WC, Strauss W, Li Z, Pereira BJ. Factors Affecting Response and Tolerability to Ferumoxytol in Nondialysis Chronic Kidney Disease Patients. *Clin Nephrol* (2012) 78:181–8. doi: 10.5414/cn107397
74. Pai AB, Garba AO. Ferumoxytol: A Silver Lining in the Treatment of Anemia of Chronic Kidney Disease or Another Dark Cloud? *J Blood Med* (2012) 3:77–85. doi: 10.2147/JBM.S29204
75. Yang L, Kuang H, Zhang W, Aguilar ZP, Xiong Y, Lai W, et al. Size Dependent Biodistribution and Toxicokinetics of Iron Oxide Magnetic Nanoparticles in Mice. *Nanoscale* (2015) 7:625–36. doi: 10.1039/c4nr05061d
76. Hoang MD, Lee HJ, Lee HJ, Jung SH, Choi NR, Vo MC, et al. Branched Polyethylenimine-Superparamagnetic Iron Oxide Nanoparticles (Bpei-Spions) Improve the Immunogenicity of Tumor Antigens and Enhance Th1 Polarization of Dendritic Cells. *J Immunol Res* (2015) 2015:706379. doi: 10.1155/2015/706379
77. Easo SL, Mohanan PV. In Vitro Hematological and In Vivo Immunotoxicity Assessment of Dextran Stabilized Iron Oxide Nanoparticles. *Colloids Surf B Biointerfaces* (2015) 134:122–30. doi: 10.1016/j.colsurfb.2015.06.046
78. Wu Q, Jin R, Feng T, Liu L, Yang L, Tao Y, et al. Iron Oxide Nanoparticles and Induced Autophagy in Human Monocytes. *Int J Nanomed* (2017) 12:3993–4005. doi: 10.2147/IJN.S135189
79. Grosse S, Stenvik J, Nilsen AM. Iron Oxide Nanoparticles Modulate Lipopolysaccharide-Induced Inflammatory Responses in Primary Human Monocytes. *Int J Nanomed* (2016) 11:4625–42. doi: 10.2147/IJN.S113425
80. Strehl C, Gaber T, Maurizi L, Hahne M, Rauch R, Hoff P, et al. Effects of PVA Coated Nanoparticles on Human Immune Cells. *Int J Nanomed* (2015) 10:3429–45. doi: 10.2147/IJN.S75936
81. Gonnissen D, Qu Y, Langer K, Ozturk C, Zhao Y, Chen C, et al. Comparison of Cellular Effects of Starch-Coated SPIONs and Poly(Lactic-Co-Glycolic Acid) Matrix Nanoparticles on Human Monocytes. *Int J Nanomed* (2016) 11:5221–36. doi: 10.2147/IJN.S106540
82. Venneti S, Lopresti BJ, Wiley CA. Molecular Imaging of Microglia/Macrophages in the Brain. *Glia* (2013) 61:10–23. doi: 10.1002/glia.22357
83. Kirschbaum K, Sonner JK, Zeller MW, Deumelandt K, Bode J, Sharma R, et al. In Vivo Nanoparticle Imaging of Innate Immune Cells can Serve as a Marker of Disease Severity in a Model of Multiple Sclerosis. *Proc Natl Acad Sci* (2016) 113:13227–32. doi: 10.1073/pnas.1609397113
84. Mulens-Arias V, Rojas JM, Perez-Yague S, Morales MP, Barber DF. Polyethylenimine-coated Spions Trigger Macrophage Activation Through TLR-4 Signaling and ROS Production and Modulate Podosome Dynamics. *Biomaterials* (2015) 52:494–506. doi: 10.1016/j.biomaterials.2015.02.068
85. Chen S, Chen S, Zeng Y, Lin L, Wu C, Ke Y, et al. Size-Dependent Superparamagnetic Iron Oxide Nanoparticles Dictate interleukin-1beta Release From Mouse Bone Marrow-Derived Macrophages. *J Appl Toxicol* (2018) 38:978–86. doi: 10.1002/jat.3606
86. Yang C-Y, Tai M-F, Lin C-P, Lu C-W, Wang J-L, Hsiao J-K, et al. Mechanism of Cellular Uptake and Impact of Ferucarbotran on Macrophage Physiology. *PloS One* (2011) 6:e25524. doi: 10.1371/journal.pone.0025524
87. Park EJ, Oh SY, Lee SJ, Lee K, Kim Y, Lee BS, et al. Chronic Pulmonary Accumulation of Iron Oxide Nanoparticles Induced Th1-type Immune Response Stimulating the Function of Antigen-Presenting Cells. *Environ Res* (2015) 143:138–47. doi: 10.1016/j.envres.2015.09.030
88. Mou Y, Xing Y, Ren H, Cui Z, Zhang Y, Yu G, et al. The Effect of Superparamagnetic Iron Oxide Nanoparticle Surface Charge on Antigen Cross-Presentation. *Nanoscale Res Lett* (2017) 12:52. doi: 10.1186/s11671-017-1828-z
89. Verdijk P, Scheenen TW, Lesterhuis WJ, Gambarota G, Veltien AA, Walczak P, et al. Sensitivity of Magnetic Resonance Imaging of Dendritic Cells for In Vivo Tracking of Cellular Cancer Vaccines. *Int J Cancer* (2007) 120:978–84. doi: 10.1002/ijc.22385
90. Dekaban GA, Snir J, Shrum B, De Chickera S, Willert C, Merrill M, et al. Semiquantitation of Mouse Dendritic Cell Migration In Vivo Using Cellular MRI. *J Immunother* (2009) 32:240–51. doi: 10.1097/CJI.0b013e318197b2a0
91. Gaharwar US, Meena R, Rajamani P. Iron Oxide Nanoparticles Induced Cytotoxicity, Oxidative Stress and DNA Damage in Lymphocytes. *J Appl Toxicol* (2017) 37:1232–44. doi: 10.1002/jat.3485
92. Hsiao YP, Shen CC, Huang CH, Lin YC, Jan TR. Iron Oxide Nanoparticles Attenuate T Helper 17 Cell Responses In Vitro and In Vivo. *Int Immunopharmacol* (2018) 58:32–9. doi: 10.1016/j.intimp.2018.03.007
93. Zhu M, Tian X, Song X, Li Y, Tian Y, Zhao Y, et al. Nanoparticle-Induced Exosomes Target Antigen-Presenting Cells to Initiate Th1-type Immune Activation. *Small* (2012) 8:2841–8. doi: 10.1002/smll.201200381

Conflict of Interest: The authors declare that the research was conducted in the absence of any commercial or financial relationships that could be construed as a potential conflict of interest.

frontiers
in Bioengineering and Biotechnology

ORIGINAL RESEARCH
published: 15 July 2021
doi: 10.3389/fbioe.2021.682384

Mechanism of Exosomes Involved in Osteoimmunity Promoting Osseointegration Around Titanium Implants With Small-Scale Topography

*Ting Zhang[1], Mengyang Jiang[1], Xiaojie Yin[1], Peng Yao[2] and Huiqiang Sun[1]**

[1] Department of Prosthodontics, School and Hospital of Stomatology, Cheeloo College of Medicine, Shandong University & Shandong Key Laboratory of Oral Tissue Regeneration & Shandong Engineering Laboratory for Dental Materials and Oral Tissue Regeneration, Jinan, China, [2] School of Mechanical Engineering, Shandong University, Jinan, China

Edited by:
Pengfei Zhang,
Shenzhen Institutes of Advanced Technology, Chinese Academy of Sciences (CAS), China

Reviewed by:
Abbas Amini,
Australian College of Kuwait, Kuwait
Chong Wang,
Dongguan University of Technology, China

***Correspondence:**
Huiqiang Sun
whitedove69@163.com

Specialty section:
This article was submitted to Nanobiotechnology, a section of the journal Frontiers in Bioengineering and Biotechnology

Received: *18 March 2021*
Accepted: *15 June 2021*
Published: *15 July 2021*

Citation:
Zhang T, Jiang M, Yin X, Yao P and Sun H (2021) Mechanism of Exosomes Involved in Osteoimmunity Promoting Osseointegration Around Titanium Implants With Small-Scale Topography.
Front. Bioeng. Biotechnol. 9:682384.
doi: 10.3389/fbioe.2021.682384

Exosomes are nanoscale extracellular vesicles. Several studies have shown that exosomes participate in intercellular communication and play a key role in osseointegration. However, it is unclear whether exosomes and their contents participate in the communication between the immune and skeletal systems in the process of osseointegration. In this study, we obtained smooth titanium disks by polishing and small-scale topography titanium disks by sandblasted large-grit acid-etched (SLA) technology combined with alkali thermal reaction. After stimulating mouse RAW264.7 cells with these two kinds of titanium disks, we co-cultured the MC3T3-E1 cells and the RAW264.7 cells, obtained and identified the exosomes derived from RAW264.7 cells, and studied the effect of the osteoimmune microenvironment and the exosomes on the osseointegration of mouse MC3T3-E1 cells. Cell counting kit-8 (CCK-8), real time quantitative PCR, western blotting, alizarin red staining, and quantitative and confocal fluorescence microscopy were used to study the effects of exosomes on MC3T3-E1 cells; RNA sequencing and correlation analysis were performed. We found that the osteoimmune microenvironment could promote the osseointegration of MC3T3-E1 cells. We successfully isolated exosomes and found that RAW264.7 cell-derived exosomes can promote osteogenic differentiation and mineralization of MC3T3-E1 cells. Through RNA sequencing and gene analysis, we found differentially expressed microRNAs that targeted the signal pathways that may be related, such as mTOR, AMPK, Wnt, etc., and thus provide a reference for the mechanism of osteoimmunue regulation of implant osseointegration. The study further elucidated the mechanism of implant osseointegration and provided new insights into the effect of exosomes on implant osseointegration, and provided reference for clinical improvement of implant osseointegration and implant success rate.

Keywords: exosomes, microRNA, osteoimmunity, titanium, osseointegration

INTRODUCTION

In recent years, implant dentures have gradually become an important treatment option for missing teeth. Titanium and titanium alloys have good biocompatibility and mechanical properties and are among the most widely used implant materials in clinics (Xue et al., 2020). However, because titanium is an inert metal with no biological activity, it can easily cause a host inflammatory reaction that can even progress to chronic inflammation, delaying implant osseointegration (Dar et al., 2018). Therefore, many techniques have been applied for titanium surface modification (Dohan Ehrenfest et al., 2010), such as sandblasted large-grit acid etching (SLA) and anodization (Loi et al., 2016; Miron and Bosshardt, 2016). In our previous study, we combined SLA technology with an alkali thermal reaction to construct titanium implants with small-scale topography. It was found that, small-scale topography promoted MC3T3-E1 cell proliferation and osteogenic differentiation better than the polished smooth surface, the micro-surface obtained by SLA technology and the nano-surface obtained by alkali thermal reaction (Yang et al., 2020).

The process of osseointegration of implants involves the coordinated operation of the immune and skeletal systems, namely osteoimmunity (Dar et al., 2018). Macrophages can be differentiated into resident cells or myeloid precursor cells (mainly monocytes) and reside in the bone. The interaction between macrophages and osteocytes is crucial for bone formation and repair (Pieters et al., 2019). Some studies have found that different implant surface morphologies can induce macrophages to polarize to the pro-inflammatory M1 phenotype or anti-inflammatory M2 phenotype (Luu et al., 2015; Quan et al., 2020). In our previous study, we found that the small-scale topography can stimulate RAW264.7 cells to polarize to anti-inflammatory M2 phenotype and regulate the osteoimmune microenvironment to an anti-inflammatory environment, which is more conducive to implant osseointegration (Yang et al., 2020).

Exosomes are nano-sized vesicles that are secreted by most cells. They were first found in reticulocytes in 1983 and named exosome in 1987 (Pan and Johnstone, 1983). The diameter of exosomes is in the range of 30–150 nm, with a lipid bilayer structure (Mathieu et al., 2019); exosomes can be directly absorbed by target cells and affect the phenotype of receptor cells (Rani et al., 2015; Yang et al., 2017). Therefore, they play an important role in cell communication and have attracted increasing attention. Wei et al. (2019) found that the expression of alkaline phosphatase (ALP) and BMP-2 markers of early osteoblast differentiation was significantly increased by using BMP-2/macrophage- derived exosomes to modify titanium nanotube implants, which confirmed that the combination of titanium nanotubes and BMP-2/macrophage-derived exosomes could promote bone formation. Xiong et al. (2020) found that M2 macrophage-derived exosome microRNA-5106 could induce the osteogenic differentiation of bone marrow mesenchymal stem cells.

Exosomes play an important role in target cells, mainly through intercellular communication and the delivery of key bioactive factors. However, it is not clear whether exosomes participate in osteoimmunity and influence osteointegration around titanium implants with small-scale topography. Furthermore, the gene information and function of macrophage-derived exosomes have not been fully clarified. Therefore, we studied the effect of macrophage-derived exosomes stimulated by small-scale topography of titanium implants on MC3T3-E1 cells and screened key microRNAs in exosomes, to further explore the mechanism of macrophages stimulated by exosomal contents in small-scale topography titanium disks on MC3T3-E1 cells, and to provide reference for exploring the effect of osteoimmunity on osseointegration.

MATERIALS AND METHODS

Preparation and Characterization of Titanium Disk

Ti6Al4V disks with a diameter of 19.5 mm and thickness of 1 mm (Taizhou Yutai Metal Materials Co., Ltd., Jiangsu, China) were used and polished to an average roughness of 0.2 mm and a thickness of 0.01 mm. The polishing process of the disks was listed in **Supplementary File 1**. The 60 mesh alumina particles (Gongyi Baolai Water Treatment Material Factory, Henan, China) were sprayed on the polished titanium plate surface at a spray angle of 90° with a spray distance of no more than 5 cm. When the surface of the titanium disk was uniformly gray, it was removed and immersed in 0.5% hydrofluoric acid solution for 15 min at 25°C. For alkali thermal treatment, the titanium disk was immersed in a 10 mol/L sodium hydroxide solution and treated at 80°C for 24 h. All the titanium disks were placed into a 5% concentrated cleaning solution (micro-90, International Products Company, New York, United States), anhydrous ethanol, distilled water, ultrasonic vibration cleaning for 5 min, and air dried at room temperature for standby.

For the surface characterization of the titanium disk, the surface morphology was observed using a cold field emission scanning electron microscope (Carl Zeiss, Germany) and 3D laser scanning microscope (VK-X200 K, Japan). The surface contact angle was measured by the suspension drop method with 2 μL artificial saliva, and the average surface roughness (RA) of the titanium disk was measured using a Wyko nt9300 optical profiler (Veeco, United States). The surface composition of titanium disks was analyzed by X-ray photoelectron spectrometer (Thermo Fisher Scientific, United States).

Cell Culture

RAW264.7 cells, a widely used mouse derived macrophage cell line, were provided by Shandong Key Laboratory of oral tissue. Mouse embryonic osteoblast precursor cells (MC3T3-E1 cells) were purchased from the Cell Bank of the Chinese Academy of Sciences (Shanghai, China). The complete medium was α-minimum essential medium (α-MEM, Hyclone, United States), in which 10% fetal bovine serum (FBS, Hyclone, United States) was added. The culture medium contained double antibodies (100 IU/mL penicillin G and 100 μg/mL streptomycin, Solebo, China). The cells were cultured at 37°C in a 5% CO_2 incubator, and the medium was changed on alternate days.

Osteogenesis induction medium (OM) consisted of complete medium supplemented with 50 mg/L ascorbic acid (Sigma Aldrich), 10 mmol/L β-glycerophosphate (Sigma Aldrich), and 10 nmol/L dexamethasone (Sigma Aldrich). The supernatant of RAW264.7 cell culture medium was centrifuged at 1000 × *g* for 5 min, and then the conditioned medium (CM) was prepared by adding 20% FBS osteogenic induction medium.

Exosome Isolation

The supernatant of RAW264.7 cell culture medium was centrifuged at 1000 × *g* for 5 min, and then 20 mL of each group was added into a 50 mL centrifuge tube. PBS was added to bring it to a total of 40 mL in each tube, centrifuged at 4°C for 10 min at 300 × *g*, and the supernatant was transferred to a new 50 mL, the supernatant was transferred to a centrifuge tube (40 mL), matched with the ultracentrifuge, and centrifuged at 4°C for 30 min at 10,000 × *g*. The supernatant was transferred to a centrifuge tube (40 mL), matched with the ultracentrifuge, and centrifuged at 4°C for 70 min at 10,0000 × *g*. The exosomes were identified by transmission electron microscopy, nanoparticle tracking analysis, and western blotting.

Nanoparticle Tracking Analysis (NTA)

The sample pool was cleaned with deionized water, the instrument was calibrated with polystyrene microspheres (110 nm), and the sample pool was cleaned with 1 × PBS buffer; the exosome solution was diluted with 1 × PBS buffer and injected for detection. Each sample was detected three times, and the data were processed and mapped using the Origin software.

CCK-8 Detection

Cell proliferation was examined using the cell counting kit 8 (CCK-8; Dojindo, Tokyo, Japan). MC3T3-E1 cells were treated with osteogenic induction medium or CM. On days 1, 3, 5, and 7, the original medium was replaced with CCK-8 reagent and complete medium at a ratio of 1:10. MC3T3-E1 cells were incubated at 37°C for 1 h, and the absorbance value was measured at 450 nm.

Alizarin Red S Staining and Cetylpyridinium Chloride Determination

MC3T3-E1 cells were fixed with 4% paraformaldehyde for 30 min and then incubated with alizarin red S (Sigma Aldrich) for 10 min. After washing with deionized water, the calcium deposition was observed using an optical microscope. Cetylpyridinium chloride (10%; Sigma Aldrich) was used for quantification, and the absorbance value was determined at 562 nm.

Real Time Fluorescent Quantitative PCR (qRT-PCR)

Total RNA was extracted using TRIzol reagent (Invitrogen, NY, United States). cDNA was synthesized using the PrimeScript RT Master Mix Kit (Takara Biotechnology, China). GAPDH was selected as the internal reference gene, and the relative gene expression was calculated by the “2−△△CT” method. The primer sequences are listed in **Table 1**.

Western Blot

Cells were lysed with Ripa buffer (Wanleibio, China) containing 10 mM protease inhibitor (PMSF; Wanleibio, China). The lysate was centrifuged at 12,000 rpm and 4°C for 10 min. The supernatant was separated, and the protein concentration was determined using a BCA protein concentration assay kit (Wanleibio, China). Equivalent amounts of protein (40 g) were added to the 8%-15% SDS-PAGE gel and then transferred to a PVDF membrane (Millipore, Billerica, United States). The membrane was sealed in 5% skimmed milk powder solution for 1 h, and then incubated with the following primary antibodies: runt-related transcription factor 2 (Runx2, wl03358; Wanleibio, China), Collagen I (wl0088; Wanleibio, China), β-actin (wl01845; Wanleibio, China), CD9 (ab92726, Abcam, United Kingdom), CD63 (ab216130, Abcam, United Kingdom), and TSG101 (ab125011, Abcam, United Kingdom) at 4°C overnight. After washing with TBST four times, the membrane was incubated with sheep anti-rabbit IgG HRP (wla023; Wanleibio, China) at room temperature for 45 min. An ECL detection kit (Wanleibio, China) was used to visualize the protein bands. Proteins on the same membrane were compared quantitatively by determining the optical density of the target strip using a gel image processing system (Gel-Pro-Analyzer software, Media Cybernetics, United States).

Exosome RNA Sequencing and Gene Analysis

According to the standard procedure provided by Illumina (San Diego, United States), the miRNA sequencing library was prepared using the TruSeq Small RNA Sample Prep Kit (Illumina, San Diego, United States). After library preparation, the constructed library was sequenced using Illumina HiSeq2000/2500, and the reading length was 1 × 50 bp. Clean reads were obtained from original data after quality control. The 3′-linker was removed from the clean reads, and the length of the 3′ linker was screened. Sequences with a base length of 18–25 nt (plant) or 18–26 nt (animal) were retained. The remaining sequences were then aligned to various RNA

TABLE 1 | List of primers used in this study for qRT-PCR.

Genes	Primers	Sequences (5′–3′)
GAPDH	Forward	AGGTCGGTGTGAACGGATTTG
	Reverse	TGTAGACCATGTAGTTGAGGTCA
IL-1β	Forward	GTGTCTTTCCCGTGGACCTT
	Reverse	AATGGGAACGTCACACACCA
IL-10	Forward	GCTCTTGCACTACCAAAGCC
	Reverse	CTGCTGATCCTCATGCCAGT
Runx2	Forward	GGGACTGTGGTTACCGTCAT
	Reverse	ATAACAGCGGAGGCATTTCG
Collagen I	Forward	CCCTGGTCCCTCTGGAAATG
	Reverse	GGACCTTTGCCCCCTTCTTT

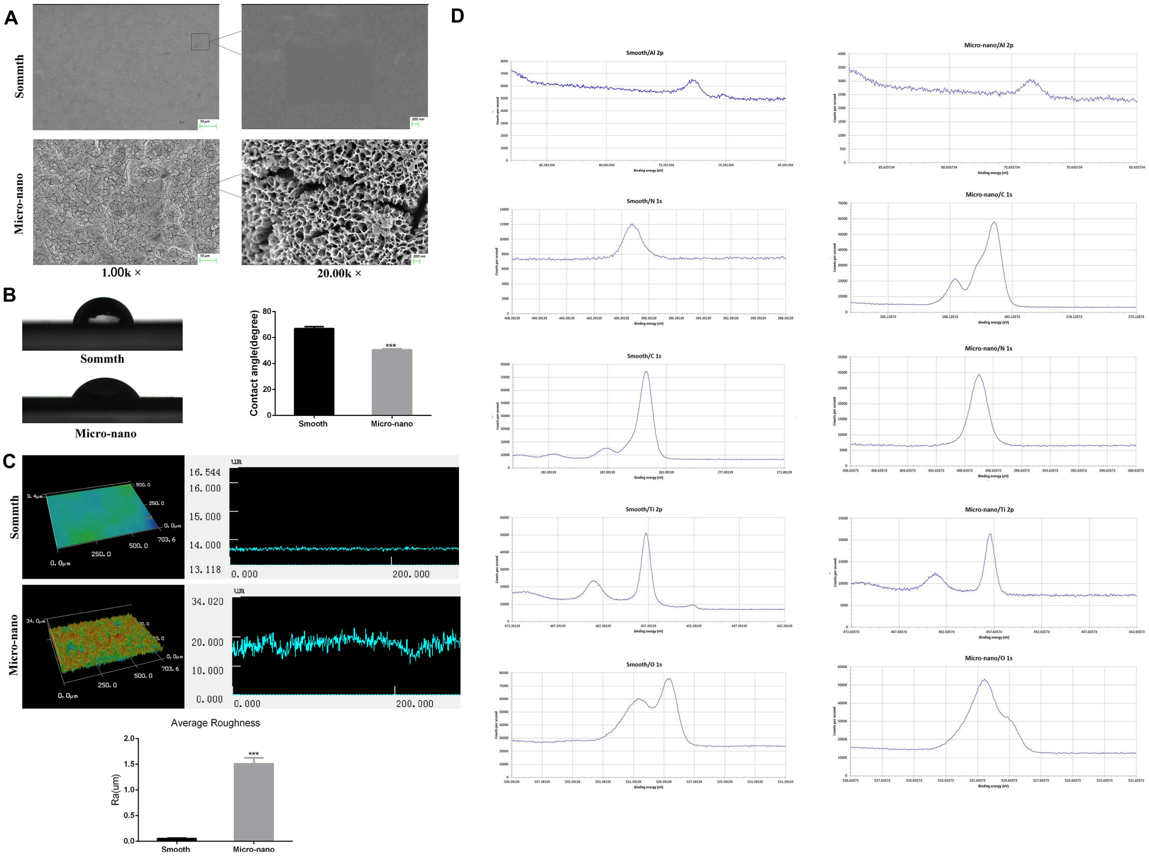

FIGURE 1 | Surface characterization of materials. **(A)** The surface morphology of titanium disk was observed by using a scanning electron microscope. **(B)** Contact angle test. **(C)** Three-dimensional structure diagram observation and roughness test (Yang et al., 2020). **(D)** XPS analysis (smooth: smooth titanium disk; micro-nano: small-scale topography titanium disk. ***$p < 0.001$).

database sequences (excluding miRNA), such as mRNA database, Rfam database (including rRNA, tRNA, snRNA, snoRNA, etc.) and RepBase database (repetitive sequence database), and filtered. Finally, the data obtained were valid. MicroRNA data analysis software Acgt101 Mir Program (LC Sciences, Houston, Texas, United States) was used to analyze the differentially expressed miRNAs.

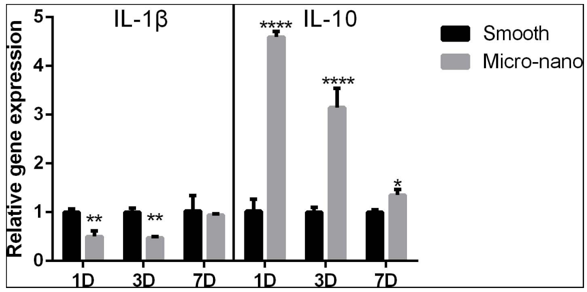

FIGURE 2 | Gene expression of RAW264.7 cells on different titanium disks. (smooth, smooth titanium disk; micro-nano, small-scale topography titanium disk. *$p < 0.05$, **$p < 0.01$, ****$p < 0.0001$).

Bioinformatics Analysis

The number of genes annotated for each function or pathway corresponding to the target genes which were corresponded to the differentially expressed miRNAs was counted, and then the hypergeometric test was applied to determine the number of genes in the Gene ontology (GO) and Kyoto Encyclopedia of Genes and Genomes (KEGG) database corresponding to the target gene mRNAs which were corresponded to all the selected microRNAs. Compared all the gene in the database above (all genes with functional annotation, or all miRNA target genes with functional annotation), the significantly enriched genes or pathways were selected under the standard that p-value less than or equal to 0.05. The formula for calculating the p-value is as follows. $P = 1 - \sum_{i=0}^{s-1} \frac{\begin{pmatrix} B & TB-B \\ i & TS-i \end{pmatrix}}{\begin{pmatrix} TB \\ TS \end{pmatrix}}$ (S: the number of genes with significant differences matched to a single GO/KEGG; TS: the total number of genes with significant differences; B: number of genes matched to a single GO/KEGG; TB: total number of genes.) We used the tool available on this link to draw: https://www.omicstudio.cn/tool?order=complex.

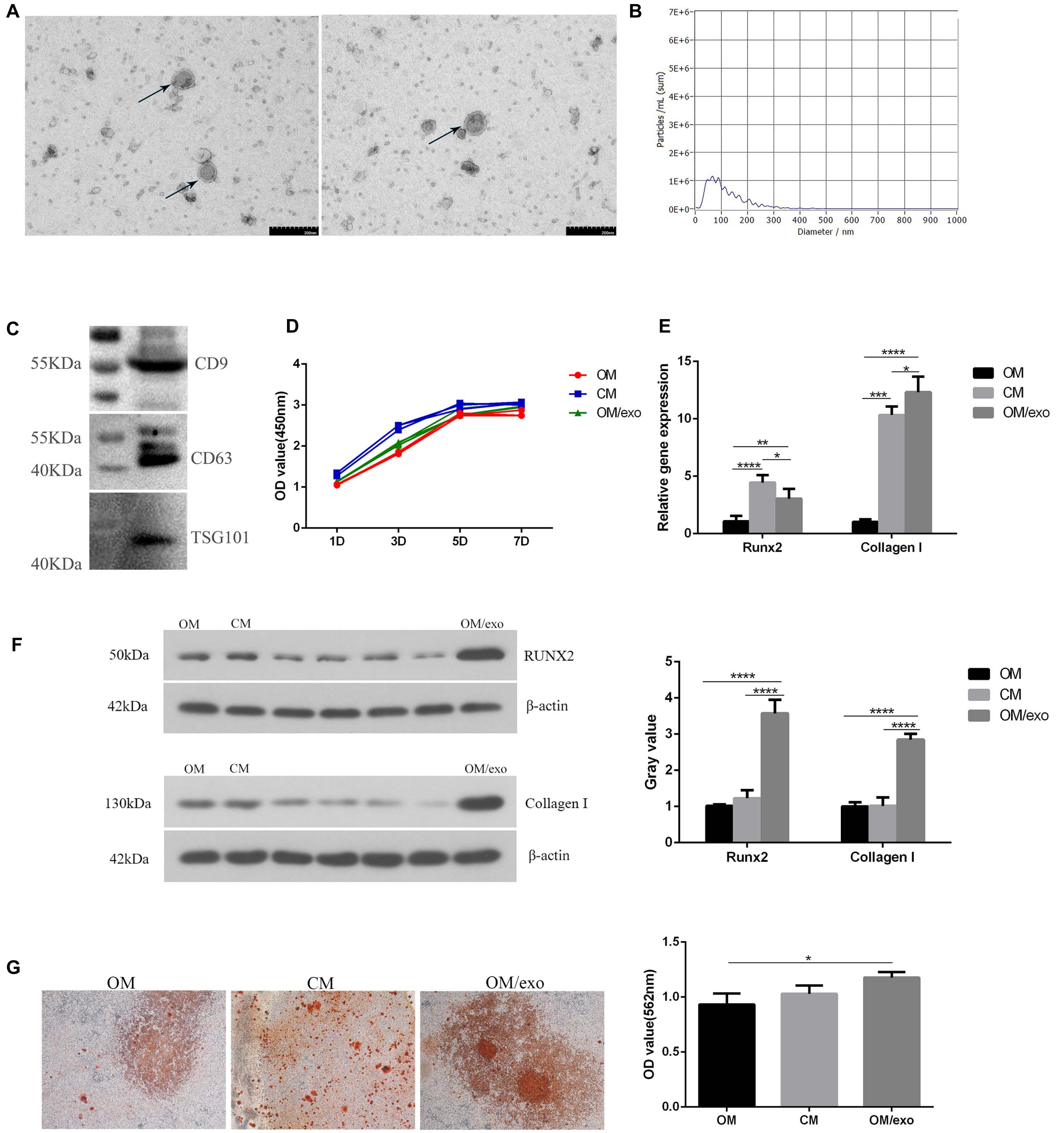

FIGURE 3 | Identification of exosomes and their effects on osteogenic differentiation of MC3T3-E1 cells. **(A)** TEM showed the shape of exosomes; **(B)** NTA showed the diameter of exosomes; **(C)** Western blot showed the expression of exosomes surface marker protein CD9, CD63, and TSG101; **(D)** CCK-8 showed cell proliferation; **(E)** qRT-PCR showed the expression of osteogenic related genes Runx2, Collagen I in MC3T3-E1 cells; **(F)** Western blot showed the expression of osteogenic related genes Runx2 and Collagen I in MC3T3-E1; **(G)** The mineralization of MC3T3-E1 cells was detected by alizarin red. [OM, osteogenic induction medium; CM (osteogenic induction medium + RAW264.7 cell culture medium), OM/exo: CM with RAW264.7 cell-derived exosomes (*$p < 0.05$; **$p < 0.01$; ***$p < 0.001$; ****$p < 0.0001$)].

Statistical Analysis

Quantitative results are expressed as mean ± standard deviation (SD). The experiment was repeated independently at least three times. Univariate analysis of variance and multiple t-tests were used for statistical evaluation, and $p < 0.05$ was set as a statistically significant threshold.

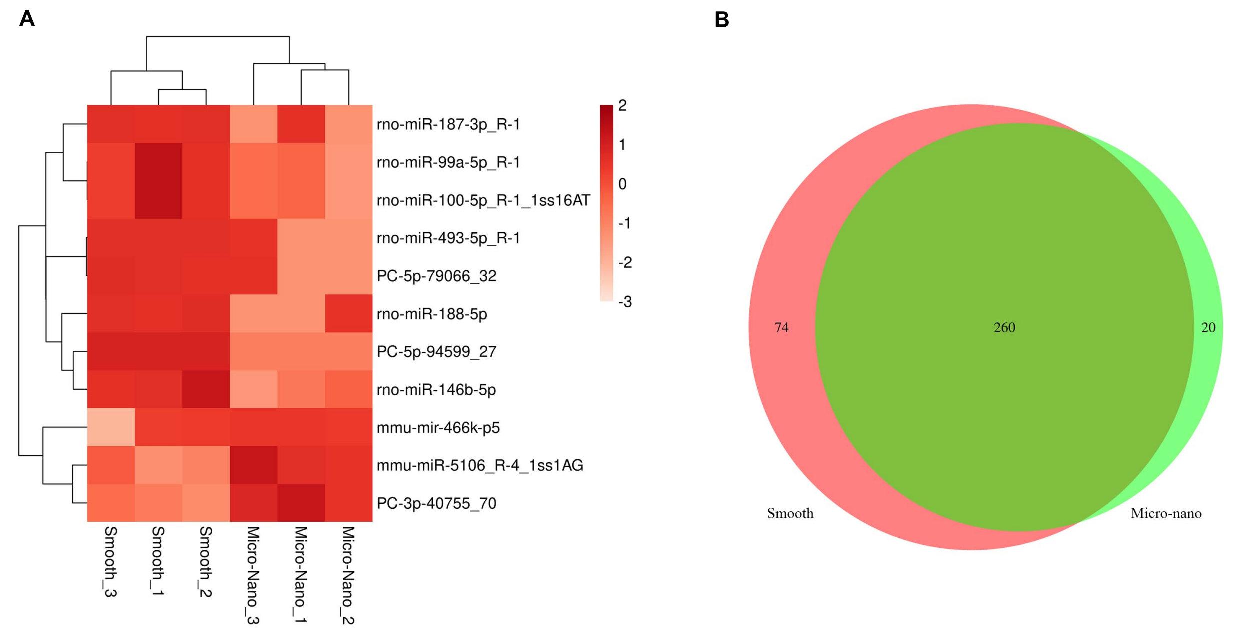

FIGURE 4 | Differentially expressed microRNAs were detected in RAW264.7 cell-derived exosomes stimulated by smooth and small-scale topography titanium disks. **(A)** The heat map of differentially expressed exosome miRNAs; **(B)** Venn map showed that there were 260 common miRNAs and 20 specific miRNAs in the differentially expressed miRNAs.

RESULTS

Surface Characterization of Titanium Disks

Figure 1A and **Supplementary File 2** exhibits that the surface of smooth titanium disk is flat, without scratches; under the low power microscope, the surface of small-scale topography titanium disk is rough, no residual alumina particles are found, and a large number of pits can be seen. The pits are in the form of a multilevel continuous superposition. The secondary depression with a diameter of 2–8 μm is superimposed on the surface of the first depression with a diameter of 10–50 μm, and nanopores with a diameter of approximately 50–200 nm can be viewed under a high-power microscope.

Figure 1B shows the surface droplet morphology and average surface hydrophilicity of the two types of titanium disks. Using 2 μL artificial saliva as a wetting agent, the contact angle of the small-scale topography titanium disk was significantly lower than that of the smooth titanium disk ($p < 0.05$). The superficial 3D microstructure and roughness are shown in **Figure 1C**. The average surface roughness, Ra, of the two kinds of titanium disks was further observed and compared using an optical profiler. In comparison with the smooth titanium disk, the average surface roughness of small-scale topography titanium disk increased significantly ($p < 0.05$; **Figure 1C**, **Supplementary File 3**), which is consistent with the results of scanning electron microscope (Yang et al., 2020). The analysis results of the surface composition of the titanium disc are shown in the **Figure 1D** and **Supplementary Files 4, 5**. All the results above proved that the titanium disk obtained by SLA technology combined with alkali heat treatment was small-scale topography, which increased the surface roughness of the titanium disk and was more conducive to osseointegration.

Small-Scale Topography Titanium Disk Induces Macrophages to Polarize to Anti-inflammatory M2 Type

After RAW264.7 cells were cultured on the surface of smooth and small-scale topography titanium disks, the expression of inflammation-related genes was detected (**Figure 2**). Compared to that on the surface of the smooth titanium disks, the expression level of the anti-inflammatory related gene IL-10 on the surface of small-scale topography titanium disk was increased and the expression level of the pro-inflammatory related gene IL-1β was decreased, with statistical significance, which was consistent with our previous research (Yang et al., 2020), and proved that small-scale topography titanium disk could stimulate the differentiation of RAW264.7 cells into M2 type to form an anti-inflammatory immune microenvironment.

M2 Type RAW264.7 Cells Can Induce Osteogenic Differentiation of MC3T3-E1 Cells, and Exosomes May Play a Key Role in It

In order to study the effect of the osteoimmune microenvironment formed by M2 type RAW264.7 cells on MC3T3-E1 cells, we co-cultured the two types of cells. The CCK-8 result showed that compared with OM, CM could promote MC3T3-E1 cells proliferation better (**Figure 3D**).

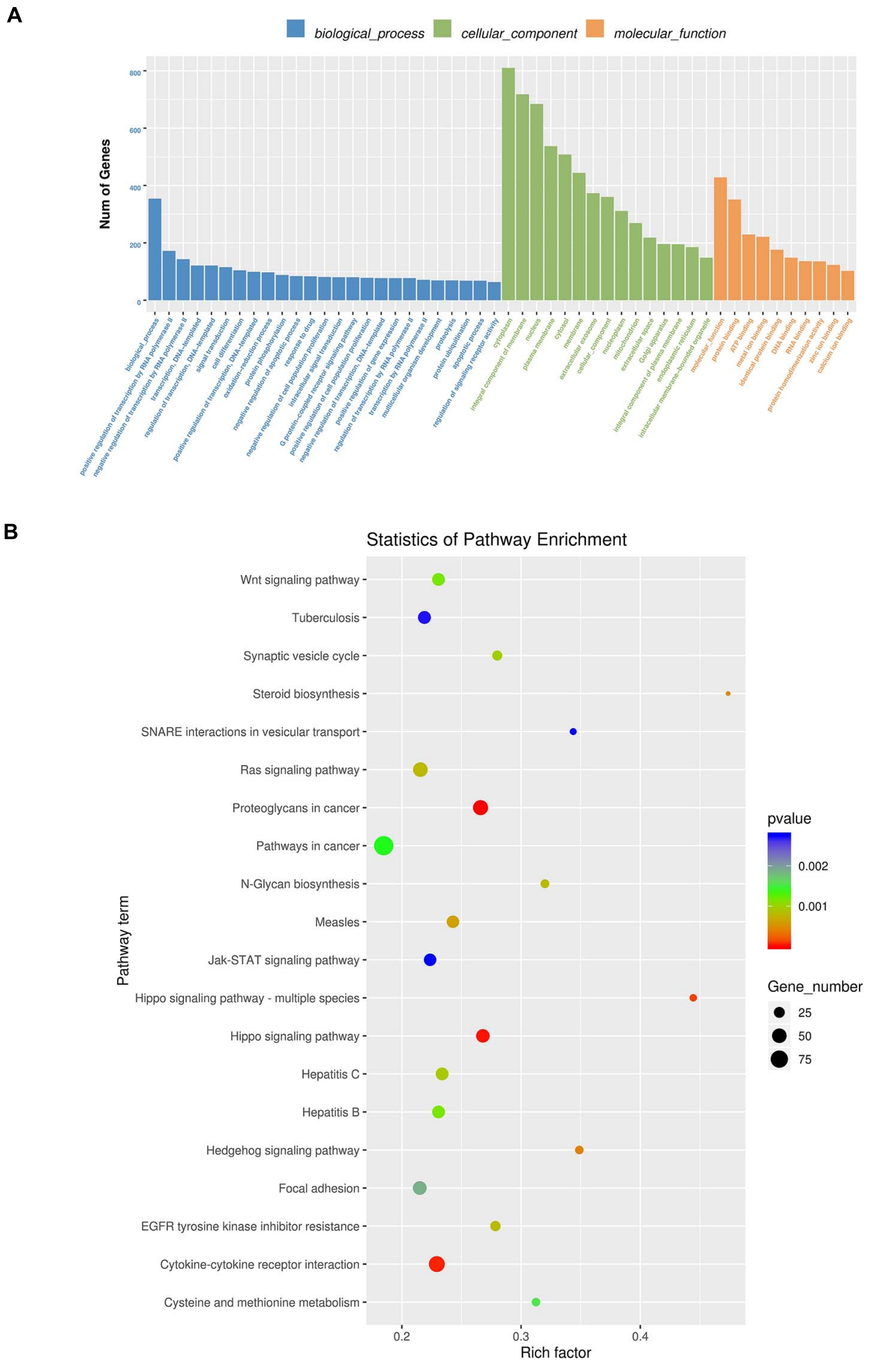

FIGURE 5 | GO analysis and Kyoto Encyclopedia of Genes and Genomes (KEGG) pathway analysis. **(A)** GO analysis enrichment map of biological process, cell composition and molecular function; **(B)** KEGG pathway analysis enrichment map (Blue means $0.002 < p < 0.05$; Green means $0.002 < p < 0.001$; Red means $p < 0.001$).

The qRT-PCR and Western blot results showed that compared with OM, CM enhanced the expression of Collagen I and Runx2 in MC3T3-E1 cells (**Figures 3E,F**). AND the alizarin red staining and semi-quantitative studies showed that the mineral deposition of cells of CM was increased (**Figure 3G**). We speculated that the exosomes played an important role in the process that osteoimmunity promoted the osteogenic differentiation of MC3T3-E1 cells. Therefore, the exosomes derived from RAW264.7 cells stimulated by the two kinds of titanium disks were separated and studied.

First, we characterized the exosomes derived from RAW264.7 cell. Transmission electron microscopy (TEM) results showed that the separated vesicles had a round bilayered membrane structure (**Figure 3A**). NTA results showed that the peak diameter of vesicles was 63.3 nm, accounting for 64.9% of the total area. The average diameter of vesicles was 117.1 nm, the distribution of vesicles was in the range of 30–200 nm (**Figure 3B**); the expression of exosome surface proteins CD9, CD63 and TSG101 was detected by western blot (**Figure 3C**); the above results demonstrated that the vesicles isolated from RAW264.7 cells were exosomes.

Next, we studied the effect of the exosomes on osteogenic differentiation of MC3T3-E1 cells. The CCK-8 assay was used to study the effect of cell proliferation (**Figure 3D**). In comparison with the control group, exosomes promoted the proliferation of MC3T3-E1 cells, but the effect was not as pronounced as that of the CM. qRT-PCR and western blotting were used to detect the expression of osteogenesis-related marker genes and proteins (**Figures 3E,F**). The results showed that compared to OM and CM, the expression of Collagen I and Runx2 in exosome-stimulated MC3T3-E1cells had significantly increased. Alizarin red staining and semi-quantitative studies showed that the effect of exosomes on promoting extracellular mineralization was similar to that of the MC3T3-E1 cells in CM (**Figure 3G**). The above studies had proved that exosomes played a key role in the process of oateoimmunity to promote osseointegration.

Differentially Expressed MicroRNA Detected in RAW264.7 Cell-Derived Exosomes Stimulated by Smooth Titanium Disk and Small-Scale Topography Titanium Disk

By RNA sequencing, we analyzed the differentially expressed microRNAs in RAW264.7 cell-derived exosomes stimulated by two kinds of titanium disks. The abscissa of the heat map represents the sample cluster, and the ordinate represents the gene cluster (**Figure 4A**). A total of 260 mature miRNAs and 20 specific miRNAs were expressed in RAW264.7 cell-derived exosomes (**Figure 4B**). Exosome microRNAs can regulate related signaling pathways by targeting downstream target genes, thereby affecting successful differentiation. According to further GO and KEGG pathway analyses, differentially expressed miRNAs are involved in most biological processes, and are mainly regulated in the Hippo signaling pathway, Wnt signaling pathway, and mTOR signaling pathway (**Figures 5A,B**). **Table 2** summarizes and lists the 11 upregulated and downregulated miRNAs and generates the regulatory network of these 11 miRNAs (**Figure 6**). Some genes involved in cell proliferation and differentiation are involved, which helps to further clarify the mechanism of differential expression of microRNAs in regulating osteoimmunity and promoting osseointegration.

DISCUSSION

In this study, we used titanium disks to stimulate RAW264.7 cells to polarize into anti-inflammatory M2 phenotype, and isolated exosomes from RAW264.7 cells. We found that exosomes induced osteogenic differentiation, and mineralization of MC3T3-E1 cells. Meanwhile, we summarized the expression of microRNA of RAW264.7 cell-derived exosomes, which could provide a basis for exploring the mechanism of RAW264.7 cell-derived exosomes involved in the osteogenic differentiation of MC3T3-E1 cells.

Titanium and titanium alloys are the most widely used dental implant materials in clinics. The surface morphology of the implant has an important influence on osseointegration. A large number of studies have shown that the small-scale topography of the implant surface is more conducive to the biological behavior of osteoblasts than the simple micro-or nano- morphology (Wang et al., 2012, 2016; Ren et al., 2018). Micro-morphology can improve the mechanical properties of the implant by increasing the surface area of the implant and enhancing the mechanical chimerism between the implant and the bone cells (Dohan Ehrenfest et al., 2010). Nano-morphology can regulate the behavior of the implant by regulating the information transmission between cells (Chen et al., 2018). Compared to the traditional SLA technology, small-scale topography has a stronger ability to form hydroxyapatite *in vitro*, which can better promote the adhesion and extension of bone cells and promote osteogenesis cell proliferation and differentiation (Wang et al., 2012, 2016; Ren et al., 2018; Yang et al., 2020).

TABLE 2 | Differentially expressed microRNAs.

miR name	miR seq	Log2 ratio	Up/down	*P*-value
mmu-miR-5106_R-4_1ss1AG	GGGTCTGTAGCTCAGTTGG	0.60	Up	1.22E-02
mmu-mir-466k-p5	GTGTGTGTGTGTGTGTGTG	2.02	Up	1.36E-02
PC-3p-40755_70	GCGTGAGGAAGGAGGGGA	1.39	Up	2.43E-02
PC-5p-94599_27	GCATTGCCGGGTAGCTAA	-inf	Down	8.77E-03
rno-miR-493-5p_R-1	TTGTACATGGTAGGCTTTCAT	–2.72	Down	1.65E-02
rno-miR-146b-5p	TGAGAACTGAATTCCATAGGCTGT	–1.31	Down	2.14E-02
rno-miR-99a-5p_R-1	AACCCGTAGATCCGATCTTGT	–0.27	Down	3.27E-02
rno-miR-100-5p_R-1_1ss16AT	AACCCGTAGATCCGATCTTGT	–0.27	Down	3.27E-02
PC-5p-79066_32	GAGGAGTACTAGTCGGCA	–2.35	Down	3.61E-02
rno-miR-188-5p	CATCCCTTGCATGGTGGAGGG	–2.72	Down	4.16E-02
rno-miR-187-3p_R-1	TCGTGTCTTGTGTTGCAGCCG	–2.24	Down	4.79E-02

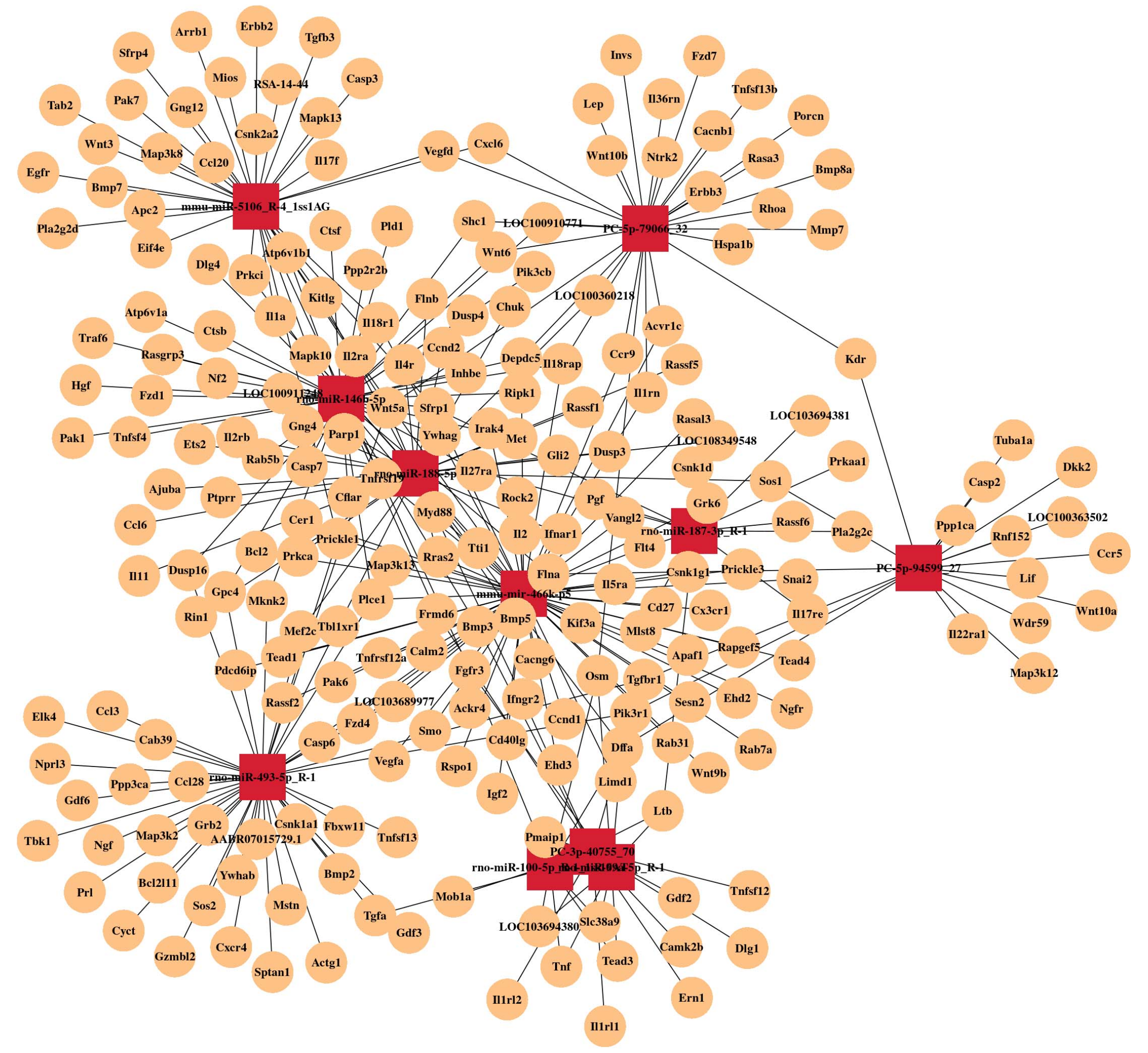

FIGURE 6 | MicroRNA mRNA network. The relationship between differentially expressed miRNAs and their target genes.

During osseointegration, there is a close relationship between the immune system and skeletal system. The immune system plays a key role in tissue repair and regeneration (Forbes and Rosenthal, 2014); macrophages and myeloid heterogeneous immune cells play an important role in the process of osseointegration. They can polarize to the pro-inflammatory M1 phenotype or anti-inflammatory M2 phenotype according to different stimuli (Gordon and Taylor, 2005; Gordon and Martinez, 2010; Michalski and McCauley, 2017). Many studies have shown that immune cells can be affected by various factors of the implant, including surface morphology (Fink et al., 2008; Spiller et al., 2009). In our previous study, we found that the small-scale topography titanium disk can stimulate RAW264.7 cells to polarize to the M2 phenotype, secrete IL-10 and VEGF, regulate the immune environment, and promote the osteogenic differentiation of MC3T3-E1 cells (Yang et al., 2020).

Exosome biogenesis is a dynamic but highly ordered process involving two invasions of the plasma membrane and the formation of intraluminal vesicles (ILVs) and intracellular multivesicular bodies (MVBs) (Li et al., 2019; Kalluri and LeBleu, 2020). Then, MVBs fuse with lysosomes to degrade, or with the plasma membrane to release ILV into the extracellular environment and become exosomes (van Niel et al., 2018; Mathieu et al., 2019), which then actively participate in the functional changes of many cells. The nature and content of exosomes are cell type-specific (Kalra et al., 2016), which are usually influenced by the physiological or pathological state of donor cells, the stimulation, and the molecular mechanism of biogenesis (Minciacchi et al., 2015). Studies have shown that many cell types and molecular mechanisms contribute to the coupling between bone resorption and bone formation (Sims and Martin, 2014). Exosomes from mononuclear phagocytes are most likely to play a role in maintaining bone homeostasis (Silva et al., 2017). Belonging to Runx family, expressed in osteoblasts, Runx2 is responsible for activating osteoblast differentiation marker genes, and plays a key role in the process of osteogenic differentiation (Vimalraj et al., 2015). Ekström et al. (2013) showed that LPS-stimulated monocytes can communicate with mesenchymal stem cells through exosomes, which can increase the expression of Runx2 and BMP-2 in mesenchymal stem cells. This is considered to be an intercellular signal transduction mode from the stages of injury and inflammation till bone regeneration. Qin et al. (2016) confirmed that the secretion of human bone marrow mesenchymal stem cells can effectively promote the proliferation and differentiation of rat bone marrow mesenchymal stem cells. Qi et al. (2016) combined human induced pluripotent stem cell-derived exosomes with β-tricalcium phosphate (β-TCP) scaffolds to repair rat skull defects. It was found that the repair effect of the exosome composite scaffolds was significantly better than that of the β-TCP scaffolds alone, and exosomes could promote the osteogenic differentiation of bone marrow mesenchymal stem cells by activating the PI3K/Akt signaling pathway. In this study, exosomes derived from M2 RAW264.7 cells induced upregulation of Runx2 and Collagen I expression in MC3T3-E1 cells, and the effect was significantly better than that in the macrophage co-culture group, indicating that exosomes play an important role in the process of osteoimmunity-promoting osseointegration. At the same time, we found that three miRNAs were upregulated and eight miRNAs were downregulated in M2 RAW264.7 cell-derived exosomes, and the corresponding target genes involved in the regulation of multiple signaling pathways, such as mTOR, AMPK and Wnt signaling pathways, which play an important role in the process of osseointegration. After RNA sequencing of exosomes derived from hMSCs induced by osteogenesis, Zhai et al. (2020) found that exosomes induce osteogenic differentiation through microRNA, among which the miRNAs HAS-Mir-146a-5p, HAS-Mir-503-5p, HAS-Mir-483-3P, and HAS-MIR) that contribute to bone formation. The upregulation of HAS-Mir-32-5p, HAS-Mir-133a-3P, and HAS-Mir-204-5p activated the PI3K/Akt and MAPK signaling pathways related to osteogenesis.

CONCLUSION

In conclusion, we successfully isolated exosomes from RAW264.7 cells, which were induced to polarize to the M2 phenotype by preparing small-scale topography titanium disks. After co-culture with MC3T3-E1 cells, we found that exosomes significantly promoted the osteogenic differentiation and mineralization of MC3T3-E1 cells. Through RNA sequencing and gene analysis, we found differentially expressed microRNAs that targeted the signal pathways that may be related, such as mTOR, AMPK, Wnt, etc., and thus provide a reference for the mechanism of osteoimmunue regulation of implant osseointegration. The deficiency of this study is that the selection of RAW264.7 cells and MC3T3-E1 cells has certain limitations, and the related research is still insufficient. In the next research, we will focus on the exosome microRNA and its downstream key factors, and further study the molecular mechanism of osteoimmune effect on small-scale topography implant osseointegration through exosomes.

DATA AVAILABILITY STATEMENT

The datasets presented in this study can be found in online repositories. The names of the repository/repositories and accession number(s) can be found below: GSE175428, https://www.ncbi.nlm.nih.gov/geo/query/acc.cgi?acc=GSE175428.

AUTHOR CONTRIBUTIONS

HS, PY, and TZ conceived the project and designed experiments. TZ, MJ, and XY performed the experiments. TZ and MJ analyzed the data. TZ wrote the manuscript. All authors commented on the manuscript.

FUNDING

This work was funded and supported by the Key Research and Development Program of Shandong Province (2019GSF107001), Jinan Clinical Medical Science and Technology Innovation Plan (202019167), and Laboratory Construction and Management Research Project of Shandong University (sy20212401).

ACKNOWLEDGMENTS

Thanks to the School of Mechanical Engineering, Shandong University for providing technical support for this research.

SUPPLEMENTARY MATERIAL

The Supplementary Material for this article can be found online at: https://www.frontiersin.org/articles/10.3389/fbioe.2021.682384/full#supplementary-material

REFERENCES

Chen, S., Guo, Y., Liu, R., Wu, S., Fang, J., Huang, B., et al. (2018). Tuning surface properties of bone biomaterials to manipulate osteoblastic cell adhesion and the signaling pathways for the enhancement of early osseointegration. *Colloids Surf B Biointerfaces* 164, 58–69. doi: 10.1016/j.colsurfb.2018.01.022

Dar, H. Y., Azam, Z., Anupam, R., Mondal, R. K., and Srivastava, R. K. (2018). Osteoimmunology: the nexus between bone and immune system. *Front. Biosci.* 23:464–492. doi: 10.2741/4600

Dohan Ehrenfest, D. M., Coelho, P. G., Kang, B. S., Sul, Y. T., and Albrektsson, T. (2010). Classification of osseointegrated implant surfaces: materials, chemistry and topography. *Trends Biotechnol.* 28, 198–206.

Ekström, K., Omar, O., Granéli, C., Wang, X., Vazirisani, F., and Thomsen, P. (2013). Monocyte exosomes stimulate the osteogenic gene expression of mesenchymal stem cells. *PloS One* 8:e75227. doi: 10.1371/journal.pone.0075227

Fink, J., Fuhrmann, R., Scharnweber, T., and Franke, R. P. (2008). Stimulation of monocytes and macrophages: possible influence of surface roughness. *Clin. Hemorheol. Microcirc.* 39, 205–212.

Forbes, S. J., and Rosenthal, N. (2014). Preparing the ground for tissue regeneration: from mechanism to therapy. *Nat. Med.* 20, 857–869. doi: 10.1038/nm.3653

Gordon, S., and Martinez, F. O. (2010). Alternative activation of macrophages: mechanism and functions. *Immunity* 32, 593–604. doi: 10.1016/j.immuni.2010.05.007

Gordon, S., and Taylor, P. R. (2005). Monocyte and macrophage heterogeneity. *Nat. Rev. Immunol.* 5, 953–964. doi: 10.1038/nri1733

Kalluri, R., and LeBleu, V. S. (2020). The biology, function, and biomedical applications of exosomes. *Science* 367:eaau6977. doi: 10.1126/science.aau6977

Kalra, H., Drummen, G. P., and Mathivanan, S. (2016). Focus on extracellular vesicles: introducing the next small big thing. *Int. J. Mol. Sci.* 17:170. doi: 10.3390/ijms17020170

Li, Q., Wang, H., Peng, H., Huyan, T., and Cacalano, N. A. (2019). Exosomes: versatile nano mediators of immune regulation. *Cancers* 11:1557. doi: 10.3390/cancers11101557

Loi, F., Córdova, L. A., Pajarinen, J., Lin, T. H., Yao, Z., and Goodman, S. B. (2016). Inflammation, fracture and bone repair. *Bone* 86, 119–130. doi: 10.1016/j.bone.2016.02.020

Luu, T. U., Gott, S. C., Woo, B. W., Rao, M. P., and Liu, W. F. (2015). Micro- and nanopatterned topographical cues for regulating macrophage cell shape and phenotype. *ACS Appl. Mater. Interfaces* 7, 28665–28672. doi: 10.1021/acsami.5b10589

Mathieu, M., Martin-Jaular, L., Lavieu, G., and Théry, C. (2019). Specificities of secretion and uptake of exosomes and other extracellular vesicles for cell-to-cell communication. *Nat. Cell Biol.* 21, 9–17. doi: 10.1038/s41556-018-0250-9

Michalski, M. N., and McCauley, L. K. (2017). Macrophages and skeletal health. *Pharmacol. Ther.* 174, 43–54. doi: 10.1016/j.pharmthera.2017.02.017

Minciacchi, V. R., Freeman, M. R., and Di Vizio, D. (2015). Extracellular vesicles in cancer: exosomes, microvesicles and the emerging role of large oncosomes. *Semin. Cell Dev. Biol.* 40, 41–51. doi: 10.1016/j.semcdb.2015.02.010

Miron, R. J., and Bosshardt, D. D. (2016). OsteoMacs: key players around bone biomaterials. *Biomaterials* 82, 1–19. doi: 10.1016/j.biomaterials.2015.12.017

Pan, B. T., and Johnstone, R. M. (1983). Fate of the transferrin receptor during maturation of sheep reticulocytes in vitro: selective externalization of the receptor. *Cell* 33, 967–978. doi: 10.1016/0092-8674(83)90040-5

Pieters, B., Cappariello, A., van den Bosch, M., van Lent, P., Teti, A., and van de Loo, F. (2019). Macrophage-derived extracellular vesicles as carriers of alarmins and their potential involvement in bone homeostasis. *Front. Immunol.* 10:1901. doi: 10.3389/fimmu.2019.01901

Qi, X., Zhang, J., Yuan, H., Xu, Z., Li, Q., Niu, X., et al. (2016). Exosomes secreted by human-induced pluripotent stem cell-derived mesenchymal stem cells repair critical-sized bone defects through enhanced angiogenesis and osteogenesis in osteoporotic rats. *Int. J. Biol. Sci.* 12, 836–849. doi: 10.7150/ijbs.14809

Qin, Y., Wang, L., Gao, Z., Chen, G., and Zhang, C. (2016). Bone marrow stromal/stem cell-derived extracellular vesicles regulate osteoblast activity and differentiation in vitro and promote bone regeneration in vivo. *Sci. Rep.* 6:21961. doi: 10.1038/srep21961

Quan, H., Kim, Y., Wu, L., Park, H. C., and Yang, H. C. (2020). Modulation of macrophage polarization by phospholipids on the surface of titanium. *Molecules* 25:2700. doi: 10.3390/molecules25112700

Rani, S., Ryan, A. E., Griffin, M. D., and Ritter, T. (2015). Mesenchymal stem cell-derived extracellular vesicles: toward cell-free therapeutic applications. *Mol. Ther.* 23, 812–823. doi: 10.1038/mt.2015.44

Ren, B., Wan, Y., Wang, G., Liu, Z., Huang, Y., and Wang, H. (2018). Morphologically modified surface with hierarchical micro-/nano-structures for enhanced bioactivity of titanium implants. *J. Mater. Sci.* 53, 12679–12691. doi: 10.1007/s10853-018-2554-3

Silva, A. M., Teixeira, J. H., Almeida, M. I., Gonçalves, R. M., Barbosa, M. A., and Santos, S. G. (2017). Extracellular vesicles: immunomodulatory messengers in the context of tissue repair/regeneration. *Eur. J. Pharm. Sci.* 98, 86–95. doi: 10.1016/j.ejps.2016.09.017

Sims, N. A., and Martin, T. J. (2014). Coupling the activities of bone formation and resorption: a multitude of signals within the basic multicellular unit. *Bonekey Rep.* 3:481. doi: 10.1038/bonekey.2013.215

Spiller, D., Mirtelli, C., Losi, P., Briganti, E., Sbrana, S., Counoupas, S., et al. (2009). In vitro evaluation of the PEtU-PDMS material immunocompatibility: the influence of surface topography and PDMS content. *J. Mater. Sci. Mater. Med.* 20, 2511–2520. doi: 10.1007/s10856-009-3823-0

van Niel, G., D'Angelo, G., and Raposo, G. (2018). Shedding light on the cell biology of extracellular vesicles. *Nat. Rev. Mol. Cell Biol.* 19, 213–228. doi: 10.1038/nrm.2017.125

Vimalraj, S., Arumugam, B., Miranda, P. J., and Selvamurugan, N. (2015). Runx2: structure, function, and phosphorylation in osteoblast differentiation. *Int. J. Biol. Macromol.* 78, 202–208. doi: 10.1016/j.ijbiomac.2015.04.008

Wang, T., Wan, Y., and Liu, Z. (2016). Fabrication of hierarchical micro/nanotopography on bio-titanium alloy surface for cytocompatibility improvement. *J. Mater. Sci.* 51, 9551–9561. doi: 10.1007/s10853-016-0219-7

Wang, W., Zhao, L., Ma, Q., Wang, Q., Chu, P. K., and Zhang, Y. (2012). The role of the Wnt/β-catenin pathway in the effect of implant topography on MG63 differentiation. *Biomaterials* 33, 7993–8002. doi: 10.1016/j.biomaterials.2012.07.064

Wei, F., Li, M., Crawford, R., Zhou, Y., and Xiao, Y. (2019). Exosome-integrated titanium oxide nanotubes for targeted bone regeneration. *Acta Biomater.* 86, 480–492. doi: 10.1016/j.actbio.2019.01.006

Xiong, Y., Chen, L., Yan, C., Zhou, W., Yu, T., Sun, Y., et al. (2020). M2 macrophagy-derived exosomal miRNA-5106 induces bone mesenchymal stem cells towards osteoblastic fate by targeting salt-inducible kinase 2 and 3. *J. Nanobiotechnol.* 18:66. doi: 10.1186/s12951-020-00622-5

Xue, T., Attarilar, S., Liu, S., Liu, J., Song, X., Li, L., et al. (2020). Surface modification techniques of titanium and its alloys to functionally optimize their biomedical properties: thematic review. *Front. Bioeng. Biotechnol.* 8:603072. doi: 10.3389/fbioe.2020.603072

Yang, F., Liao, X., Tian, Y., and Li, G. (2017). Exosome separation using microfluidic systems: size-based, immunoaffinity-based and dynamic methodologies. *Biotechnol. J.* 12:1600699. doi: 10.1002/biot.201600699

Yang, Y., Zhang, T., Jiang, M., Yin, X., Luo, X., and Sun, H. (2020). Effect of the immune responses induced by implants in a integrated three-dimensional micro-nano topography on osseointegration. *J. Biomed. Mater. Res. A* 109, 1429–1440. doi: 10.1002/jbm.a.37134

Zhai, M., Zhu, Y., Yang, M., and Mao, C. (2020). Human mesenchymal stem cell derived exosomes enhance cell-free bone regeneration by altering their miRNAs profiles. *Adv. Sci.* 7:2001334. doi: 10.1002/advs.202001334

Conflict of Interest: The authors declare that the research was conducted in the absence of any commercial or financial relationships that could be construed as a potential conflict of interest.

frontiers
in Immunology

ORIGINAL RESEARCH
published: 06 August 2021
doi: 10.3389/fimmu.2021.692165

Personalised Profiling of Innate Immune Memory Induced by Nano-Imaging Particles in Human Monocytes

Giacomo Della Camera[1], *Mariusz Madej*[1†], *Anna Maria Ferretti*[2], *Rita La Spina*[3], *Yang Li*[1†], *Annunziata Corteggio*[1], *Tommaso Heinzl*[1], *Benjamin J. Swartzwelter*[1†], *Gergö Sipos*[1], *Sabrina Gioria*[3], *Alessandro Ponti*[2], *Diana Boraschi*[1,4*†] and *Paola Italiani*[1*]

[1] Institute of Biochemistry and Cell Biology (IBBC), National Research Council (CNR), Napoli, Italy, [2] Istituto di Scienze e Tecnologie Chimiche "Giulio Natta" (SCITEC), National Research Council (CNR), Milano, Italy, [3] European Commission, Joint Research Centre (JRC), Ispra, Italy, [4] Stazione Zoologica Anton Dohrn, Napoli, Italy

Edited by:
Cheol-Heui Yun,
Seoul National University, South Korea

Reviewed by:
David Ashley,
Duke University, United States
Marc Pallardy,
Université Paris-Saclay, France
Laura Rodriguez-Lorenzo,
International Iberian Nanotechnology Laboratory (INL), Portugal

***Correspondence:**
Diana Boraschi
diana.boraschi@ibbc.cnr.it
Paola Italiani
paola.italiani@ibbc.cnr.it

†Present address:
Mariusz Madej,
OcellO B.V., Leiden, Netherlands
Yang Li and Diana Boraschi,
Shenzhen Institute of Advanced Technology (SIAT), Chinese Academy of Sciences (CAS), Shenzhen, China
Benjamin J. Swartzwelter,
Lab Microbiology, Immunology and Pathology, Colorado State University, Fort Collins, CO, United States

Specialty section:
This article was submitted to Molecular Innate Immunity, a section of the journal Frontiers in Immunology

Received: 07 April 2021
Accepted: 14 July 2021
Published: 06 August 2021

Citation:
Della Camera G, Madej M, Ferretti AM, La Spina R, Li Y, Corteggio A, Heinzl T, Swartzwelter BJ, Sipos G, Gioria S, Ponti A, Boraschi D and Italiani P (2021) Personalised Profiling of Innate Immune Memory Induced by Nano-Imaging Particles in Human Monocytes. Front. Immunol. 12:692165. doi: 10.3389/fimmu.2021.692165

Engineered nanoparticles used for medical purposes must meet stringent safety criteria, which include immunosafety, *i.e.*, the inability to activate possibly detrimental immune/inflammatory effects. Even medical nanomaterials devoid of direct immunotoxic or inflammatory effects may have an impact on human health if able to modify innate memory, which is the ability to "prime" future immune responses towards a different, possibly more detrimental reactivity. Although innate memory is usually protective, anomalous innate memory responses may be at the basis of immune pathologies. In this study, we have examined the ability of two nanomaterials commonly used for diagnostic imaging purposes, gold and iron oxide nanoparticles, to induce or modulate innate memory, using an *in vitro* model based on human primary monocytes. Monocytes were exposed in culture to nanoparticles alone or together with the bacterial agent LPS (priming phase/primary response), then rested for six days (extinction phase), and eventually challenged with LPS (memory/secondary response). The memory response to the LPS challenge was measured as changes in the production of inflammatory (TNFα, IL-6) and anti-inflammatory cytokines (IL-10, IL-1Ra), as compared to unprimed monocytes. The results show that both types of nanoparticles can have an effect in the induction of memory, with changes observed in the cytokine production. By comparing nanomaterials of different shapes (spherical *vs*. rod-shaped gold particles) and different size (17 *vs*. 22 nm diameter spherical iron oxide particles), it was evident that innate memory could be differentially induced and modulated depending on size, shape and chemical composition. However, the main finding was that the innate memory effect of the particles was strongly donor-dependent, with monocytes from each donor showing a distinct memory profile upon priming with the same particles, thereby making impossible to draw general conclusions on the particle effects. Thus, in order to predict the effect of imaging nanoparticles on the innate memory of patients, a personalised profiling would be required, able to take in consideration the peculiarities of the individual innate immune reactivity.

Keywords: innate immunity, innate memory, nanoparticles, imaging materials, monocytes

INTRODUCTION

Among the several biomedical applications of nanomaterials, nanoparticles (NP) of various composition and characteristics represent contrast agents of new generation, with improved sensitivity and imaging capacity (1). Medical imaging technologies in which NP are applied go from fluorescence imaging to positron emission tomography, and include magnetic resonance imaging, ultrasound, computed tomography and single-photon emission computed tomography (2). Among nanoimaging materials, iron oxide and gold NP are widely used for a number of reasons: they are easy to synthesize and have high colloidal stability, can be easily functionalized thereby acquiring new desired surface characteristics, and are safe and biocompatible, as proven by many years of use in different diagnostic and therapeutic approaches (3–5).

Iron oxide nanoparticles (FeOxNP) have been long applied in both therapeutic and diagnostic approaches (6). Therapeutically, they are used in treatment of anaemia (7) and in magnetic fluid hyperthermia (8). In diagnostic imaging, FeOxNP are applied in magnetic resonance angiography (9–11) and imaging of organs/tissues such as liver (12), lymph nodes (13–15) and bone marrow (16), and imaging in pathological situations, *e.g.*, tumour perfusion (17–19), atherosclerotic plaques and thrombosis (20–22) and various types of inflammation (23–25). Importantly, FeOxNP are useful for identifying macrophages in atherosclerotic plaques (26) and in other organs/tissues, and they have been reported able to polarize macrophages towards an anti-tumoral phenotype (27, 28).

Gold nanoparticles (AuNP) are also used in several imaging approaches, in particular X-ray imaging and computed tomography (29), exploiting the high gold atomic number that allows for a higher X-ray absorption efficiency compared to other agents and tissues (bone, soft tissues) (2, 30). They are also applied in other approaches, such as the photoacoustic imaging of brain vasculature (31). AuNP are considered safe and biocompatible, are easy to produce in various sizes and shapes, and can be surface-modified to display different functionalities. AuNP can act as cell tracers, once taken up by cells (29), and therefore they have been used for monitoring tumour growth (32), to image blood flow (33) and to visualise monocyte migration into atherosclerotic plaques (34).

Despite their wide range of applications, our understanding of the biological interactions, toxicity, uptake and clearance routes of these NP is still incomplete, in particular regarding their long-term interaction with the immune defensive system. By focusing in particular on inflammation/innate immunity, the effects of FeOxNP are variable and likely depending on type/shape/size of particles, concentration, route of administration and target immune cells (35). As already mentioned, FeOxNP were shown able to drive intratumor macrophage polarization towards the M1 inflammatory and tumoricidal phenotype (28), supporting their ability to induce innate/inflammatory activation, as shown *in vitro* by the release of inflammatory cytokines (IL-1β, IL-12, TNFα and IFN-γ) from macrophages and immature dendritic cells (36, 37). Several studies report the capacity of FeOxNP to induce the production of inflammatory/toxic reactive oxygen species [reviewed in (35, 38)]. Other studies, however, do not find inflammation-related effects on macrophages, dendritic cells and microglial cells *in vitro* (36, 39–42). While AuNP are generally considered biocompatible, variable results have been obtained, depending on the experimental model/cell type used, the dose, size and shape of the NP (43–46). On immune cells such as monocytes, macrophages and dendritic cells, AuNP in general show limited or no immunotoxic/inflammatory effect *in vitro* [(43, 44), reviewed in (47, 48)]. An important issue, when examining the inflammatory effects of NP on immune cells *in vitro*, in particular on human cells, is the possible presence of contaminating endotoxin, a ubiquitous bacterial product with high inflammatory activity present also in conditions of microbiological sterility. The presence of endotoxin on the surface of many NP types can confer to the NP a potent inflammatory activity that is undetectable in clean NP (49–52).

In this study, we have examined the capacity of AuNP and FeOxNP to interact with cells of the innate immune system and induce their inflammatory activation (53–55). To increase the reliability of results, we have selected an *in vitro* model based on primary human cells (blood monocytes), thereby avoiding the unrealistic experimental systems based on non-human or transformed/tumour cell lines, and we have used particles that were endotoxin-free at the concentrations used. The use of two different shapes for AuNP (spheres and rods) and two different sizes for FeOxNP (17 and 22 nm) would allow for detecting the capacity of human innate immune cells to distinguish between chemistry, shape and size of the interacting particles.

Besides a direct effector function based on non-specific inflammation-related activities (production of inflammatory factors, prostaglandins and other lipid mediators, reactive oxygen and nitrogen species, lytic enzymes, etc.), innate immune cells have the capacity of developing “memory”. Innate immune memory is a phenomenon known since several decades, which has been recently re-discovered under the name of trained immunity (56–61). Similar to the well-known adaptive immune memory at the basis of vaccine efficacy, innate memory implies that innate cells exposed to a stimulus can retain the memory of such exposure and react to a subsequent stimulation differently, compared to cells that had not been previously exposed. This optimized secondary “memory” response could be stronger (potentiation, trained immunity) or weaker (tolerance) compared to the primary response, in order to attain the best protection against infectious/stressful challenges and at the same time preserve the structural and functional integrity of the affected tissues/organs. At variance with adaptive immune memory, innate memory is at least partially non-specific, meaning that the memory reaction is independent of the challenge, *i.e.*, the optimized memory reaction occurs also in response to a challenge that is different from the memory-inducing “priming” stimulus.

Few studies have examined the capacity of NP to induce innate memory. In mouse macrophages, pristine graphene could induce a memory profile that resulted in an increased innate/inflammatory response to subsequent stimulations (62). In human monocytes and macrophages, AuNP could induce memory responses either directly, by priming cells for a different secondary response, or by modulating the memory-inducing capacity of strong stimuli such as LPS (which induces tolerance) and BCG (the *Mycobacterium bovis* strain used as tuberculosis vaccine, which induces a potentiated secondary responses) (63–67). Thus, in this study we have focused on the ability of FeOxNP and AuNP of different sizes and shapes not only to induce a primary innate response (measured as balance between the induction of inflammatory *vs*. anti-inflammatory cytokines) but in particular to induce and/or modulate innate memory.

MATERIALS AND METHODS

Nanoparticle Synthesis and Characterisation

Rod-shaped AuNP (AuNP ROD) were purchased by Nanopartz Inc. (cat. A12-5-780-CIT-DIH-1-100-CS-EP, lot. J7251; Nanopartz Inc., Loveland, CO, USA). Declared characteristics were: capping with citrate (3 mM), diameter 5 nm, length 18 nm, ζ-potential -35 mV, concentration 39 µg/mL in water, pH 7.0, sterile and endotoxin-free. Particles were re-characterised before use in the biological experiments. The company refused to release information on the synthesis procedure.

Spherical AuNP (AuNP SPH) were prepared using the procedure of Turkevich et al. (68), with slight modifications. All reagents and solutions were prepared in LAL Reagent Water (LRW; Associates of Cape Code, Inc., East Falmouth, MA, USA), to ensure endotoxin-free conditions. Briefly, 5 mL of 0.01 M tetrachloroauric acid tri-hydrate (HAuCl4·3H2O; Sigma-Aldrich, Merck KGaA, St. Louis, MO, USA) were diluted in 90 mL water. The solution was rapidly heated to 97°C in a microwave heating system (Discover S; CEM Corporation, Matthews, NC, USA), using a maximum power of 250 W, and allowed to equilibrate for 5 min under constant mechanical stirring. The reduction reaction was started by injecting 2.5 mL 0.1 M trisodium citrate di-hydrate (Sigma-Aldrich) into the gold solution, in order to reach a 2.5 mM final citrate concentration. The reaction mixture was kept at 97°C for 20 min under stirring, then the reaction vessel was rapidly cooled on ice, and the NP solution stored at +4°C until use.

Details of the synthesis and characterisation of FeOxNP coated with zwitterionic dopamine sulfonate (ZDS) have been published elsewhere (42). For all NP types, the main physico-chemical characteristics are reported in **Figure 1** and **Tables 1**, **2**.

All NP were pre-coated with human AB serum (Sigma-Aldrich) immediately before use in monocyte stimulation experiments. Briefly, NP suspensions were admixed 1:1 with heat-inactivated serum and incubated for 2 h at 37°C in an orbital shaker at 500 rpm. NP were then diluted in culture medium to the concentration required for use in the biological assays, and serum concentration was adjusted to 5%. As already described elsewhere (52), coating with serum significantly increased the colloidal stability of AuNP (data not shown).

Transmission electron microscopy (TEM) images of untreated NP were recorded using a JEOL-JEM 2100 microscope operated in transmission mode at an acceleration voltage of 120 kV. TEM specimens were prepared by depositing 3 µL of non-treated NP dispersion onto Formvar carbon-coated grids (S162 Formvar/Carbon, 200 mesh copper grids; Agar Scientific Ltd, Stansted, UK) and left to dry at room temperature in a desiccator (overnight) and under vacuum for 2 h. TEM images from different regions of the grid were analysed using the ImageJ Software (http://rsb.info.nih.gov/ij/). NP size distributions and shapes were evaluated using the Particle Size Analyzer imageJ macro or by manual processing. More than 350 isolated primary NP were assessed for each sample.

Dynamic light scattering (DLS) experiments were carried out using a Malvern Zetasizer Nano-ZS instrument (Malvern Panalytical Ltd, Malvern, UK) equipped with a light source of 632.8 nm wavelength at a fixed scattering angle of 173°. Data were analysed by the CONTIN software (69, 70). The ζ-potential was measured by electrophoretic light scattering (ELS), using the same instrumentation. For each NP suspension, dilutions were prepared in water for injection (WFI), PBS, and RPMI. Then, 0.6 mL of each sample dilution were transferred to a disposable cuvette (cat. ZE0040; BrandTech Scientific, Inc., Essex, CT, USA) for DLS measurement, whereas 1.2 mL was loaded in a disposable folded capillary cell (cat. DTS1070, Malvern) for ELS measurement. Each sample was measured twice at 25°C, after an equilibration step of 120 sec with an acquisition time of 80 sec. The hydrodynamic diameter was reported as the volume-weighted mean diameter (D_V).

Human Monocyte Isolation and Differentiation of Monocyte-Derived Macrophages

Blood was obtained from healthy donors, upon informed consent and in agreement with the Declaration of Helsinki. The protocol was approved by the Regional Ethics Committee for Clinical Experimentation of the Tuscany Region (Ethics Committee Register n. 14,914 of May 16, 2019). Monocytes were isolated by CD14 positive selection with magnetic microbeads (Miltenyi Biotec, Bergisch Gladbach, Germany) from peripheral blood mononuclear cells (PBMC), obtained by Ficoll-Paque gradient density separation (GE Healthcare, Bio-Sciences AB, Uppsala, Sweden). Monocyte preparations used in the experiments were > 95% viable and > 95% pure (assessed by trypan blue exclusion and cytosmears). Monocytes isolated with this method were not activated, based on analysis of expression of inflammation-related genes (*IL1B*, *TNFA*) and release of the encoded proteins, compared to monocytes within PBMC (*i.e.*, after Ficoll-Paque separation) and whole blood (*i.e.*, after withdrawal with anticoagulants) (data not shown).

Monocytes were cultured in culture medium (RPMI 1640 + Glutamax-I; GIBCO by Life Technologies, Paisley, UK) supplemented with 50 µg/mL gentamicin sulfate (GIBCO) and 5% heat-inactivated human AB serum (Sigma-Aldrich). Cells

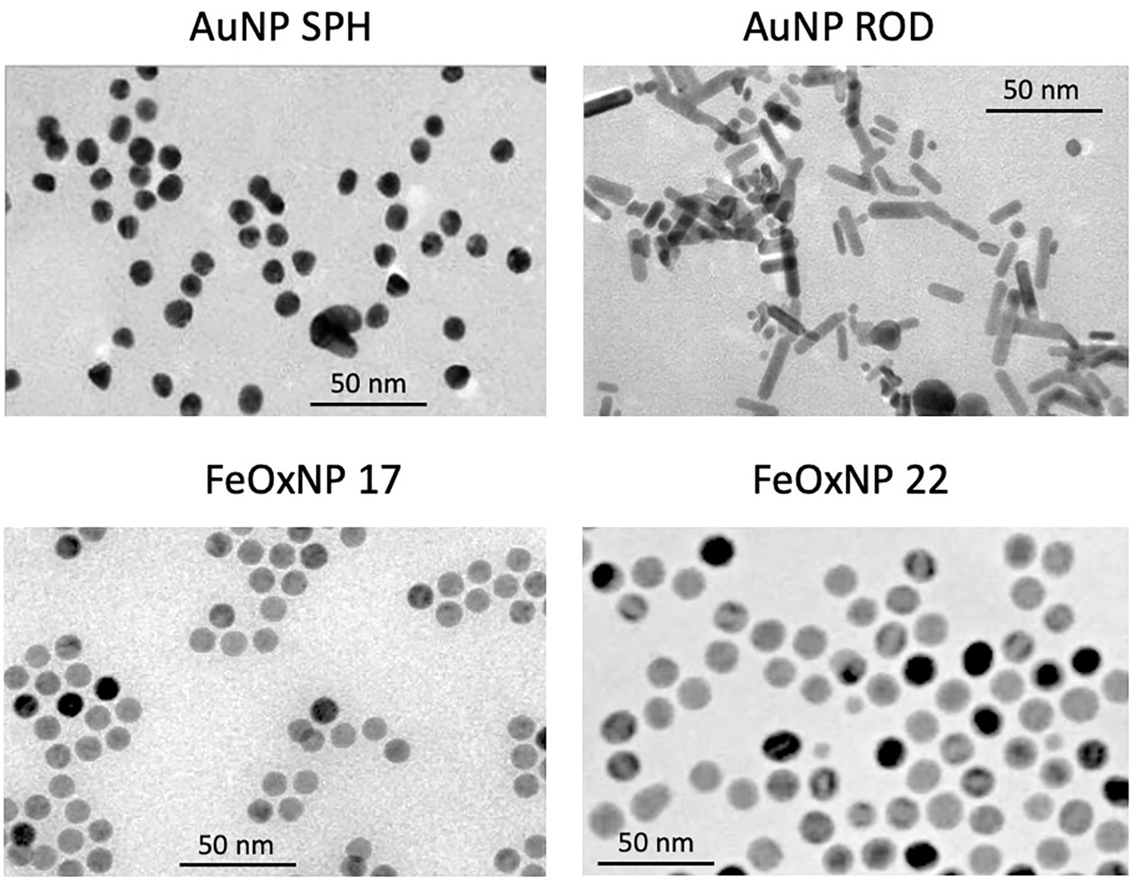

FIGURE 1 | Size and morphology of the AuNP and FeOxNP used in this study. TEM images of spherical AuNP (upper left panel), rod-shaped AuNP (upper right panel), FeOxNP 17 (lower left panel) and FeOxNP 22 (lower right panel). Size bars (50 nm) are shown in each panel.

TABLE 1 | NP morphology.

Parameter	AuNP SPH	AuNP ROD[a]	FeOxNP 17	FeOxNP 22
<*d*>(nm)	13.0	20.0, 6.5	16.8	22.4
σ_d (nm)	0.8	13.0, 0.8	0.9	1.5
σ_d/<*d*>	6%	7%, 12%	5%	7%

The mean diameter <d> is reported along with the standard deviation of the diameter σ_d *and the coefficient of variation* σ_d*/<d>.*

[a] *Length, width.*

TABLE 2 | NP hydrodynamic features.

Parameter	AuNP SPH	AuNP ROD	FeOxNP 17	FeOxNP 22
Dv (nm)[a]	16 ± 2 (WFI)[b]	17 ± 4 (WFI)	20 ± 1 (WFI)	21 ± 3 (WFI)
	17 ± 7 (PBS 1x)	22 ± 4 (PBS 1x)	NA	NA
	100 ± 20 (RPMI)	120-170 (RPMI)	18 ± 2 (RPMI)[d]	17 ± 5 (RPMI)[d]
	38 ± 2 (RPMI)[c]	22 ± 2 (RPMI)[c]	NA	NA
ζ-potential (mV)[e]	–53 ± 2	–39 ± 4	–18 ± 2	–29 ± 3
Endotoxin activity	0.45 EU/mg	30.8 EU/mg	58.3 EU/mg	<16 EU/mg

[a] *Volume-weighted hydrodynamic diameter; for Au nanorods, it is the volume-weighted hydrodynamic diameter of spherical NP having the same average diffusion coefficient of the nanorods.*

[b] *WFI, water for injection.*

[c] *NP were pre-treated with 50% human serum.*

[d] *RPMI plus 5% FBS.*

[e] *in PBS 1x.*

NA, not available.

($5x10^5$) were seeded in a final volume of 1.0 mL in wells of 24-well flat bottom plates (Corning® Costar®; Corning Inc. Life Sciences, Oneonta, NY, USA) at 37°C in moist air with 5% CO_2. Monocyte stimulation was performed after overnight resting.

Human Monocyte Activation and Induction of Innate Memory

For assessing the primary response to stimulation, monocytes were exposed for 24 h to culture medium alone (medium/negative control) or containing 1 ng/mL LPS (positive control; from *E. coli* O55:B5; Sigma-Aldrich), serum pre-coated NP, or LPS in the presence of NP.

For memory experiments, after the first exposure to stimuli for 24 h and supernatant collection, cells were washed and cultured with fresh culture medium for 7 additional days (one medium change after 4 days). During this period, the activation induced by previous stimulation subsides, and cells return to their baseline status (as determined by evaluation of inflammation-related cytokines in the supernatant). After this resting phase, the supernatant was collected, and cells were challenged for 24 h with fresh medium alone or containing 5 ng/mL LPS (a 5x higher concentration than in the primary stimulation).

All supernatants (after the first stimulation, after the resting phase and after the challenge phase) were frozen at −20°C for subsequent cytokine analysis. By visual inspection, cell viability and cell number did not substantially change in response to the different treatments.

Cytotoxicity Evaluation

The direct toxicity of NP on monocytes was tested as release of lactate dehydogenase (LDH). Briefly, monocytes (1.2x105 cells/well of 96-well plates; Corning Inc.) were incubated for 24 h in 200 µL culture medium alone or containing serum-coated NP in triplicate. Positive control wells received 200 µL of 0.1% Triton-X 100. At the end of the incubation, release of the cytoplasmic enzyme LDH was measured in the supernatant using a colorimetric assay (LDH-Cytotoxicity Colorimetric Assay Kit; BioVision, Inc., Milpitas, CA, USA).

Assessment of Endotoxin Contamination

Endotoxin contamination in NP was assessed with a commercial chromogenic LAL assay (Pyros Kinetix® Flex (Associates of Cape Cod, Inc.), following a protocol adapted for use with particulate agents (71). As the assay readout is paranitroaniline (pNA) at 405 nm, preliminary controls were run to assess the possible interference of NP (direct optical reading at 405 nm and interference with detection of different concentrations of synthetic pNA). NP were used in the LAL assay at concentrations that did not interfere with the assay readout. An additional control was run, to assess the possible interference of NP with the assay components/reagents, which consisted in spiking the NP samples with a known amount of LPS (0.5 EU/mL) and assessing the recovery of spiked endotoxin. A recovery rate between 80 and 120% was considered acceptable. The endotoxin contamination was therefore reliably assessed at NP dilutions that did not interfere with the 405 nm readout and in which 80-120% spiked endotoxin could be recovered. The LAL assay was run with Glucashield® (Associates of Cape Cod, Inc.), to eliminate possible false positives due to the presence of glucans, using a dedicated tube reader and software (Associates of Cape Cod, Inc.). The assay sensitivity was 0.001 EU/mL.

Transmission Electron Microscopy for NP Uptake

Cells ($1x10^6$ in wells of 6-well flat bottom plates) were exposed to AuNP for 24 h, then fixed, stained and embedded in EPON resin for sectioning (EM UC7 ultramicrotome; Leica Microsystems, Wetzlar, Germany) (65). TEM images were obtained using a Tecnai 12 transmission electron microscope (FEI Company, Hillsboro, OR, USA).

Cytokine Analysis

The levels of the human inflammatory cytokines TNFα and IL-6 and of the anti-inflammatory factors IL-10 and IL-1Ra were assessed by ELISA (R&D Systems), using a Cytation 3 imaging multi-mode reader (BioTek, Winooski, VT, USA).

Statistical Analysis

Data were analyzed using the GraphPad Prism6.01 software (GraphPad Inc., La Jolla, CA, USA). For cytokine production, results are presented as ng produced cytokine/10^6 plated monocytes. Results are reported as mean ± SD of values from 2-6 replicate samples from the same donor. Statistical significance of differences is indicated by p values, calculated using unpaired and two-tailed Student's t-test (**Figures 4**, **5**).

RESULTS AND DISCUSSION

Physico-Chemical Characterisation of the NP Used in This Study

Two types of nano-imaging materials have been evaluated in this study, gold and iron oxide ($Fe_{3-x}O_{4-x}$, $0 \le x \le 1$, cubic ferrite structure). Gold (Au) NP of two different shapes have been assessed, quasi-spheres with a diameter of 13 nm (surface area 531 nm^2), and rods of 20 x 6.5 nm (surface area 408 nm^2). Both AuNP types are stabilized by citrate. Spherical iron oxide (FeOx) NP of different size were used, 16.8 and 22.4 nm diameter (the latter having a surface area almost double *vs.* the former, 1576 *vs.* 887 nm^2), both stabilized by zwitterionic dopamine sulfonate (ZDS). The morphology of the inorganic core of AuNP and FeOxNP is depicted in the **Figure 1** (TEM images), and their morphological characteristics summarised in **Table 1**. The corresponding size histograms are reported in **Supplementary Figure 1**. All NP are monodispersed, with size varying by less than (or close to) 10% from the average value.

The hydrodynamic features of the AuNP and FeOxNP are reported in **Table 2**, in which their endotoxin contamination is also shown. AuNP and FeOxNP are well-dispersed and colloidally stable in water, and their volume-weighted hydrodynamic diameter (D_V) is consistent with the TEM-derived core size <*d*>. Both types of AuNP are well-dispersed also in PBS 1x, with similar D_V, but they aggregate in RPMI-1640 medium, as shown by the strong increase in D_V. When AuNP are pre-treated with human serum before dispersion in RPMI medium, they have D_V close to those they display in WFI and PBS. Both types of FeOxNP do not aggregate for at least 6 h in RPMI-1640 medium added with 5% foetal bovine serum (FBS). Furthermore, their D_V shows that they do not adsorb proteins.

The colloidal stability of AuNP and FeOxNP is due to their negative ζ-potential that ensures electrostatic repulsion between NP. The different stability of AuNP *vs*. FeOxNP is due to their coating. The citrate anions are weakly bound (physisorbed) to the AuNPs, and are thus not able to prevent aggregation in RPMI-1640 medium, probably because they are displaced by the non-salt components in the culture medium. Conversely, the zwitterionic sulfobetaine ZDS is strongly bonded to the FeOxNP and is able to protect NP from aggregation and protein adsorption (42), thanks to its hydrophilicity and overall neutrality. The pre-treatment with human serum afforded colloidal stability in culture medium for spherical AuNP and, up to a concentration of 1.4 μg/mL, also for rod-shaped AuNP. The similarity of the D_V between untreated AuNP in WFI and PBS and serum-coated AuNP in RPMI-1640 medium suggests that the latter are stabilized by a protein coating. However, the position of the major peak of the intensity-weighted size distribution of AuNP SPH increases by about 6 nm when they are pre-treated with human serum, suggestive of the formation of a biocorona on the NP surface (**Supplementary Figure 2**). The major serum component within the NP biocorona was a 60 kDa protein, most likely albumin (data not shown).

Selection of the NP Concentrations for Biological Studies

The NP concentrations to be used in biological experiments were selected based on two criteria, *i.e.*, the endotoxin contamination (in order to use of the highest possible concentration with endotoxin contamination not exceeding 0.1 EU/mL, *i.e.*, the concentration at which there is little/no human monocyte activation *in vitro*; 45) and the surface area (in order to use NP concentrations comparable by total surface area). The latter criterion is based on the fact that NP are incubated with human serum before being added to human monocytes in culture, to reproduce the *in vivo* conditions in which NP are exposed to biological fluids and expected to form a biomolecular coating of adsorbed proteins/molecules on their surface, which may change the mode of their interaction with living cells. Thus, a comparable NP surface area may allow for a more comparable interaction with microenvironmental molecules (the biocorona) and with cells in the experimental system. We have calculated a surface area of 27 mm^2 as the optimal dose to compare the different NP types, which corresponds to 5.7 μg AuNP SPH (with an endotoxin contamination of 0.003 EU), 2 μg FeOxNP 17 (endotoxin 0.117 EU) and 2.7 μg FeOxNP 22 (endotoxin <0.043 EU), the dose-limiting factor being the endotoxin contamination of FeOxNP 17. For AuNP ROD, a 2.7x lower dose was used (surface area 10 nm^2, 1.4 μg NP, endotoxin 0.043 EU), because of problems of aggregation at higher concentrations. Thus, the NP concentrations used in culture were 5.7 μg/mL for AuNP SPH, 1.4 μg/mL for AuNP ROD, 2.0 μg/mL for FeOxNP 17 and 2.7 μg/mL for FeOxNP 22.

Primary Response of Human Monocytes to NP Exposure

NP aggregation during *in vitro* assays is a common disturbing factor when studying NP-cell interactions. In our case, aggregation is a very minor factor since (i) both AuNP types are colloidally stabilized by the pre-treatment with human serum (likely due to protein adsorption), and (ii) both FeOxNP types are coated with ZDS, which is known to endow high colloidal stability (42). Therefore, we hold that NP aggregation is of minor importance in the present study, in particular at the selected concentrations.

Before assessing the effects of the selected NP on innate/inflammatory responses of human monocytes, their possible direct toxicity was examined. As already mentioned, all NP were pre-coated with human AB serum (see *Materials and Methods*).

Monocytes isolated from blood of individual donors were exposed to NP at the established concentrations for 24 h. Cell death was assessed in terms of release of the cytoplasmic enzyme LDH. No toxicity was detected for any of the NP type on monocytes of any donor (data not shown). Uptake of NP by monocytes was monitored visually. Cells took up the NP abundantly, as expected for professional phagocytes, and stored them within vesicles (see examples for AuNP SPH in **Supplementary Figure 3**). Since NP were not toxic for monocytes, there was no correlation between the NP uptake and the NP toxicity.

The primary response of human monocytes to NP was assessed after exposure in culture for 24 h. Monocytes are cells of the innate immune system, involved in immediate defensive reactions that include inflammatory responses. Thus, monocyte activation was evaluated in terms of production of four innate cytokines, the inflammatory factors TNFα and IL-6, and the anti-inflammatory cytokines IL-10 and IL-1Ra. As positive control, cells were exposed to LPS, which is an excellent activator of human monocyte innate/inflammatory responses. Cells were also co-exposed to LPS and NP, in order to detect possible NP-dependent modulation of LPS-induced activation. For this reason, a sub-optimal LPS concentration was selected (1 ng/mL), in order to allow us to detect both positive and negative NP effects.

In line with previous evidence, none of the NP could induce a measurable reactivity in human monocytes, being inactive in inducing inflammatory cytokines (**Figure 2**, upper panels), apart from a measurable induction with FeOxNP 17 in one donor. When examining anti-inflammatory cytokines, it should be noted that, similar to inflammatory factors, no detectable IL-10 levels were produced in baseline unstimulated conditions, whereas the baseline levels of IL-1Ra were measurable (**Figure 2**, lower panels). Neither AuNP nor FeOxNP could

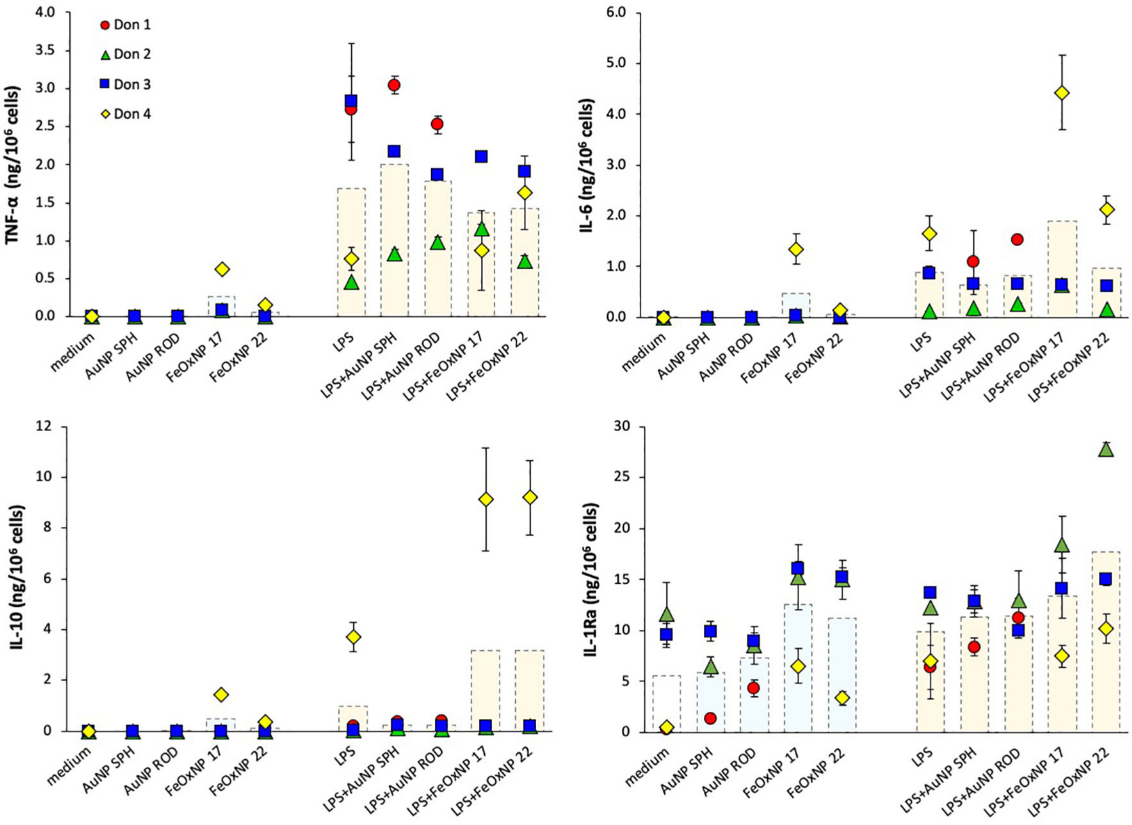

FIGURE 2 | Innate immune primary response of human monocytes to NP alone or upon co-exposure with LPS. Human monocytes isolated from blood of four individual donors (red, green, blue, and yellow symbols) were cultured for 24 h in culture medium alone (empty columns) or containing serum-precoated NP: 5.7 μg/ml spherical AuNP (AuNP SPH), 1.4 μg/ml rod-shaped AuNP (AuNP ROD), 2 μg/ml spherical FeOxNP of 16.8 nm diameter (FeOxNP 17) and 2.7 μg/ml spherical FeOxNP of 22.4 nm diameter (FeOxNP 22) alone (light blue columns) or together with 1 ng/ml LPS (orange columns). The production of TNFα (upper left), IL-6 (upper right), IL-10 (lower left) and IL-1Ra (lower right) was measured in the 24 h supernatants by ELISA. Data are presented as individual donors' values (coloured symbols) ± SD and as mean of the individual values (dotted columns).

stimulate monocytes to produce IL-10 (again with the exception of FeOxNP 17 for one donor), whereas a tendency to increase in IL-1Ra production was detected in response to FeOxNP in all donors (while AuNP are essentially inactive, regardless of shape). LPS significantly activated the production of inflammatory factors in monocytes, although with a substantial donor-to-donor variability. Such variability was also evident in the ability of NP to modulate the response to LPS, with donors showing a NP-dependent amplification of the response to LPS, others showing a decrease and others no substantial changes. In the case of the anti-inflammatory cytokine IL-10, it should be noted that, as expected, its induction by the selected LPS concentration was null, except for one donor. Only in this donor, FeOxNP seemed able to directly induce detectable IL-10 levels, as well as to increase LPS-induced IL-10 production. In the case of the other anti-inflammatory factor, IL-1Ra, the significant baseline production was variably affected by NP and only partly increased by LPS (in 2/4 donors). Co-exposure to LPS and NP did not substantially affect IL-1Ra production, although with some donor-to-donor variability, as in the case of the high IL-1Ra increase in response to LPS plus FeOxNP 22 in one donor. The donor-dependent NP activities, already observed in previous studies, suggest the need for a personalised evaluation of NP effects when safety assessment is required, *e.g.*, before their clinical diagnostic use.

Memory Response of Human Monocytes Exposed to NP

After exposure for 24 h to NP, LPS or their mixture, cells were washed (to eliminate the priming agents) and cultured for 7 days in fresh culture medium to allow return to baseline. The culture medium was refreshed after 4 days. The extinction of cell activation was confirmed by examining the production of cytokines released in the culture medium at the end of the resting period (representing the cytokine release in the last 3 days of resting) (data not shown). After the extinction period, cells were either exposed to medium alone or challenged with 5x higher LPS concentration, relative to priming, in agreement with the concept that memory can shape the host capacity to react to more severe challenges.

As for the primary response, the memory response was assessed in terms of production of inflammatory and anti-inflammatory cytokines, and the results are reported in **Figure 3**. Similar to the primary response, LPS challenge of medium-primed cells showed a general induction of TNFα, IL-6 and IL-10 production, and a small increase over the substantial baseline production of IL-1Ra (compare the columns "CTR", no challenge, and "medium", medium-primed challenged with LPS). It is interesting to note that cells primed with LPS responded to challenge with a lower production of the inflammatory cytokines TNFα and IL-6 in all donors, while there was no change in the production of the anti-inflammatory factors relative to the response of medium-primed cells (**Figure 3**, orange column "LPS" *vs*. light blue column "medium" in the priming line). This is in line with the features of the "endotoxin tolerance" that implies a reduced inflammatory response upon repeated exposures in order to avoid a destructive inflammatory reaction to a recurrent challenge. Priming with NP showed variable effects, which seem to depend more on the donor than on the NP chemistry, size or shape. The innate memory induced by co-priming with LPS and NP generally shows distinct features from those induced by either agent alone. In the case of TNFα production, priming with LPS + AuNP abolished the tolerance observed in LPS-primed cells and reconducted the response to the levels shown by unprimed cells in 2/3 donors. Conversely, priming with LPS + FeOxNP showed variable, donor-dependent and NP size-dependent effects. The LPS-induced decrease of IL-6 production was differentially affected by different NP in different donors. Likewise, the memory production of the two anti-inflammatory cytokines IL-10 and IL-1Ra showed a substantial donor-to-donor variability that did not allow for a global evaluation.

From the data shown above, it is clear that the significant donor-to donor variability prevents drawing general conclusions. By examining the individual responses, it is evident that each donor has her/his own capacity to discriminate between different NP. The results in **Figures 4**, **5** (data taken from **Figure 3**)

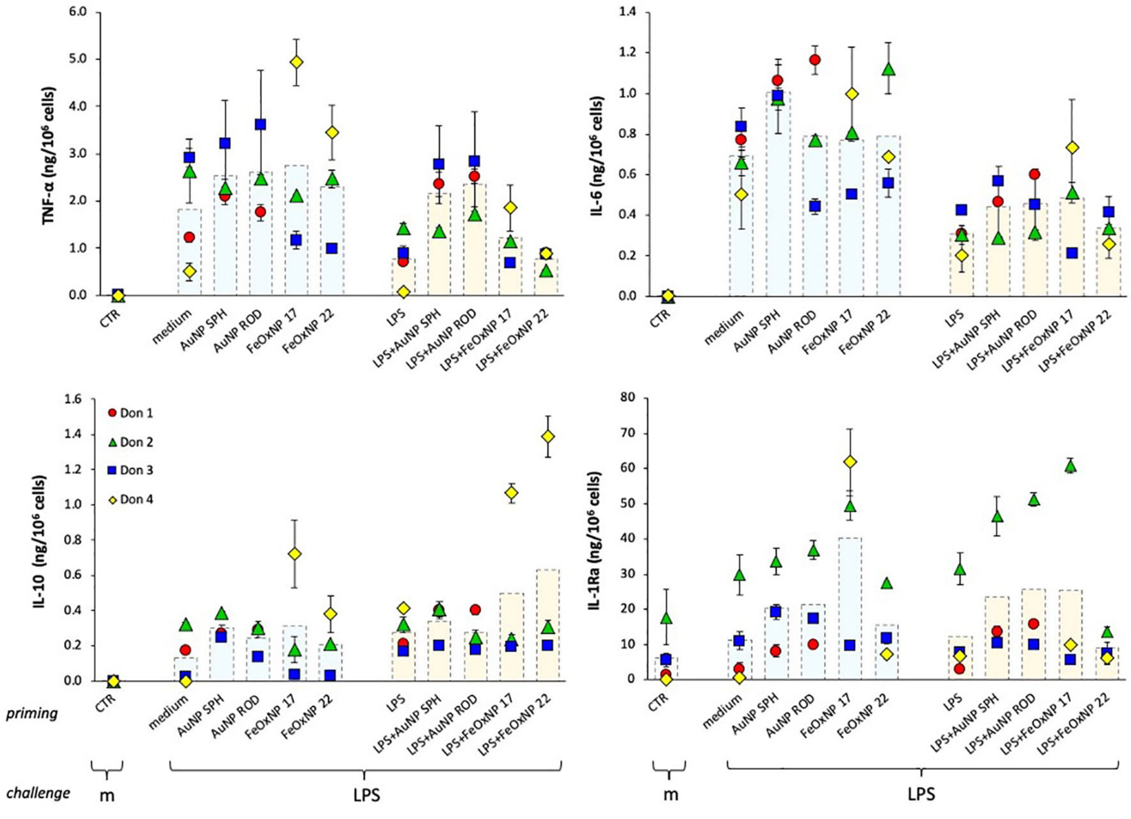

FIGURE 3 | Innate immune memory response of human monocytes primed with NP alone or together with LPS. Human monocytes isolated from blood of four individual donors (red, green, blue, and yellow symbols) were cultured for 24 h in culture medium alone or containing serum-precoated NP: 5.7 µg/ml AuNP SPH, 1.4 µg/ml AuNP ROD, 2 µg/ml FeOxNP 17 and 2.7 µg/ml FeOxNP 22 alone (light blue columns) or together with 1 ng/ml LPS (orange columns) (line *priming in* abscissa). Cells were then washed and rested for 6 days in the absence of stimuli, then challenged for 24 h in fresh medium alone or containing 5 ng/mL LPS (m and LPS in the abscissa line *challenge*). The production of TNFα (upper left), IL-6 (upper right), IL-10 (lower left) and IL-1Ra (lower right) was measured in the 24 h supernatants by ELISA. Data are presented as individual donors' values (coloured symbols) ± SD and as mean of the individual values (dotted columns). The basal response of control cells (CTR), *i.e.*, primed or unprimed cells rested for 6 days and then exposed for 24 h to medium alone, is shown at the extreme left in each panel (empty columns).

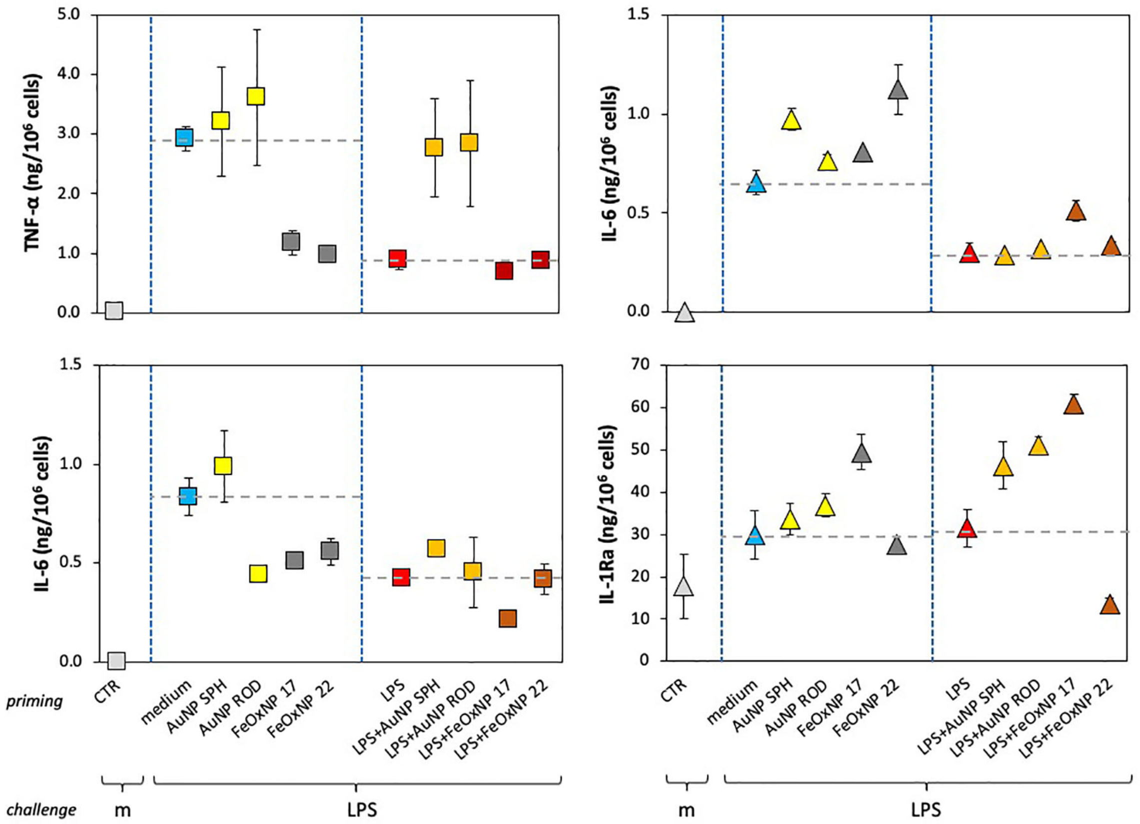

FIGURE 4 | Innate memory response of human monocytes from individual donors, primed with AuNP or FeOxNP alone or together with LPS. Human monocytes isolated from blood of two individual donors (donor 3, square symbols, left panels; donor 2, triangle symbols, right panels) were cultured for 24 h in culture medium alone or containing serum-precoated NP: 5.7 µg/ml AuNP SPH, 1.4 µg/ml AuNP ROD, 2 µg/ml FeOxNP 17 and 2.7 µg/ml FeOxNP 22, alone or together with 1 ng/ml LPS (line *priming in* abscissa). Cells were then washed and rested for 6 days in the absence of stimuli, then challenged for 24 h in fresh medium alone or containing 5 ng/mL LPS (m and LPS in the abscissa line *challenge*). The production of TNFα (upper left), IL-6 (upper right and lower left), and IL-1Ra (lower right) was measured in the 24 h supernatants by ELISA. Data are reported as mean ± SD of replicate determination from individual donors out of four tested (all shown in **Figure 3**). Horizontal dotted lines represent the reference values of cells primed with medium alone and cells primed with LPS in the two parts of each panel. The basal response of control cells (CTR), *i.e.*, primed or unprimed cells rested for 6 days and then exposed for 24 h to medium alone, is shown at the extreme left in each panel (grey symbols). Statistical significance is as follows. Upper left panel: CTR *vs*. medium, $p < 0.0001$; medium *vs.* LPS, $p < 0.005$; medium *vs*. FeOxNP, $p < 0.005$; LPS *vs*. LPS + AuNP, $p < 0.05$. Upper right: CTR *vs*. medium, $p < 0.0001$; medium *vs.* LPS, $p < 0.005$; medium *vs*. AuNP SPH and FeOxNP 22, $p < 0.05$; LPS vs. LPS + FeOxNP 17, $p < 0.05$. Lower left: CTR *vs*. medium, $p < 0.0001$; medium *vs.* LPS, $p < 0.01$; medium *vs*. AuNP ROD, FeOxNP 17 and FeOxNP 22, $p < 0.05$; LPS *vs*. LPS + FeOxNP 17, $p < 0.05$. Lower right: medium *vs*. FeOxNP 17, $p < 0.05$; LPS *vs*. LPS + all NP, $p < 0.05$. All other relevant comparisons are not significant.

underline such donor-specific capacity to distinguish between NP chemistry, shape and size. **Figure 4** reports the production of an inflammatory and an anti-inflammatory cytokine in the memory response of two individual donors, donor 2 (triangles, right panels) and donor 3 (squares, left panels). The secondary (memory) production of TNFα by donor 3 showed no significant changes in cells primed with AuNP but a substantial decrease in cells primed with FeOxNP. In addition, the decrease of TNFα in LPS-primed cells (a typical "tolerance" type memory response) was abolished if cells were co-primed with AuNP, while co-priming with FeOxNP had no effect (**Figure 4**, upper left panel). Thus, it seems that cells from donor 3 "see" the difference in the NP chemical composition but do not distinguish between shapes and size, as spherical and rod-shaped AuNP have comparable effects, and FeOxNP of both sizes equally decrease the TNFα production at challenge. However, when examining the NP effects on the IL-6 memory response, it becomes clear that cells from donor 3 also recognise size and shape. The memory production of IL-6 in cells primed with AuNP ROD was significantly decreased, while priming with AuNP SPH had no effect. Also, co-priming with LPS and FeOxNP shows that while FeOxNP 22 have no effect, co-priming with FeOxNP 17 substantially decreased IL-6 production (**Figure 4**, lower left panel).

When examining the memory responses of donor 2 (**Figure 4**, right panels), we can see a different picture. Priming with AuNP SPH increased the memory production of inflammatory IL-6 (upper right panel), while AuNP ROD were ineffective; FeOxNP 17 were likewise ineffective, while FeOxNP 22 increased the response. This suggests that donor 2 can distinguish between

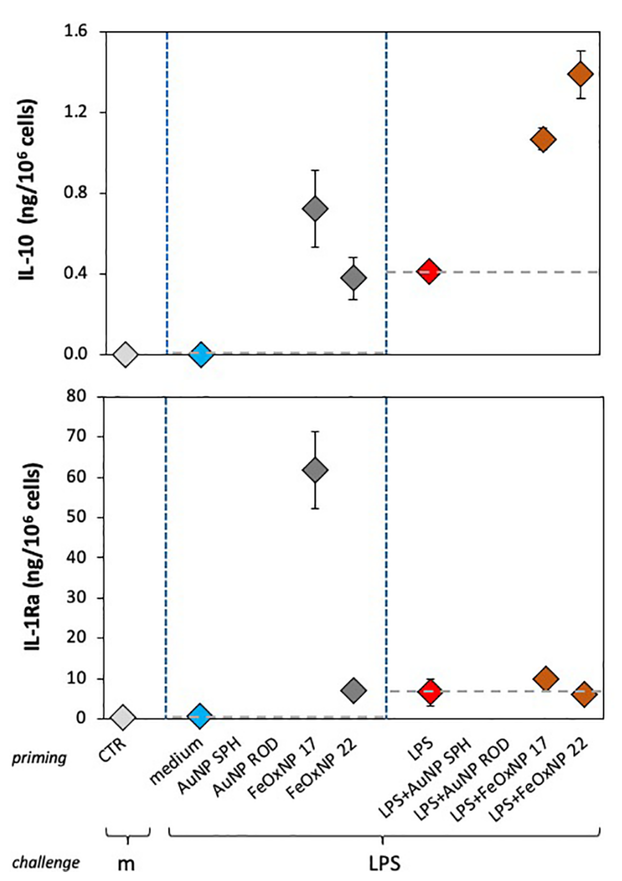

FIGURE 5 | Anti-inflammatory innate memory response of human monocytes from one individual donor, primed with FeOxNP alone or together with LPS. Human monocytes isolated from blood of one individual donor (donor 4, diamond symbols); were cultured for 24 h in culture medium alone or containing serum-precoated FeOxNP (2 µg/ml FeOxNP 17 and 2.7 µg/ml FeOxNP 22) alone or together with 1 ng/ml LPS (line *priming in* abscissa). Cells were then washed and rested for 6 days in the absence of stimuli, then challenged for 24 h in fresh medium alone or containing 5 ng/mL LPS (m and LPS in the abscissa line *challenge*). The production of IL-10 (upper panel) and IL-1Ra (lower panel) was measured in the 24 h supernatants by ELISA (complete data shown in **Figure 3**). Horizontal dotted lines represent the reference values of cells primed with medium alone and cells primed with LPS in the two parts of each panel. The basal response of control cells (CTR), *i.e.*, primed or unprimed cells rested for 6 days and then exposed for 24 h to medium alone, is shown at the extreme left in each panel (grey symbols). Data are reported as mean ± SD of replicate determination from individual donors out of four tested (all shown in **Figure 3**). Statistical significance is as follows. Upper panel: medium *vs*. LPS, $p < 0.05$; medium *vs*. both FeOxNP, $p < 0.05$; LPS *vs*. LPS + FeOxNP, $p < 0.05$; FeOxNP 17 *vs*. LPS + FeOxNP 17, $p < 0.05$. Lower panel: medium *vs*. FeOxNP 17, $p < 0.05$; FeOxNP 17 *vs*. FeOxNP22, $p < 0.05$. All other relevant comparisons are not significant.

shapes and sizes. Interestingly, none of the NP had a significant effect on the tolerance type of memory induced by LPS priming, except for FeOxNP 17, which partially reverted tolerance. The memory effects on the anti-inflammatory factor IL-1Ra are very different: only priming with FeOxNP 17 increased the secondary production of IL-1Ra, while all NP interfered with the LPS priming (a priming that *per se* did not significantly change the cytokine production). Thus, priming with LPS plus AuNP SPH, AuNP ROD or FeOxNP17 increased the secondary production of IL-1Ra, while co-priming with FeOxNP 22 decreased it. Therefore, donor 2 seems able to discriminate between both size and shape.

In the present study, four cytokines were evaluated, two with inflammatory activity and two with anti-inflammatory effects. The data in **Figure 4** compare, in two individual donors, two inflammatory factors (TNFα and IL-6 for donor 3) and an inflammatory factor with an anti-inflammatory cytokine (IL-6 and IL-1Ra for donor 2), as example of the different capacity of different donors to recognise the NP chemistry, size and shape. In **Figure 5** we show that also between two anti-inflammatory factors the NP-induced memory can be different. Control medium-primed cells of donor 4 produced essentially undetectable levels of both anti-inflammatory factors IL-10 (upper panel) and IL-1Ra (lower panel) in response to an LPS challenge. If cells were primed with FeOxNP (no AuNP priming was included in this experiment), the production of IL-10 was significant and comparable between the two NP sizes, while the production of IL-1Ra was significantly higher in FeOxNP 17- *vs*. FeOxNP 22-primed cells. In LPS-primed cells, co-priming with both FeOxNP types increased IL-10 production, while no effect was detectable for IL-1Ra. Thus, the strong anti-inflammatory effect of FeOxNP 17 priming (increase in IL-10 and strong increase in IL-1Ra) was partially abolished if priming occurred in the presence of LPS, as priming with LPS + FeOxNP 17 induced similar IL-10 and much lower IL-1Ra levels than priming with FeOxNP 17 alone. Conversely, the more limited anti-inflammatory effect of FeOxNP 22 (a small induction of both IL-10 and IL-1Ra) was increased in LPS co-primed cells (increase in IL-10, no change in IL-1Ra).

CONCLUSIONS

This study confirms previous observations that engineered NP can modulate human innate memory (62–66). A direct capacity of inducing memory, thereby changing the secondary response of human monocytes to a microbial challenge, was observed with AuNP of two different shapes (both coated with citrate and serum proteins), and with iron oxide NP of two different sizes (both coated with the sulfobetaine ZDS and pre-treated with serum). In addition, all four NP types were able to modulate the memory response induced by LPS. Our data also show that memory can be differently induced depending on the NP shape (in cells from the same donor the memory profile induced by AuNP SPH is different from that induced by AuNP ROD) and on the NP size (in the same donor the memory profile induced by FeOxNP 17 is different from that induced by FeOxNP 22). Dependence on the surface chemistry is more difficult to ascertain since in our NP different coating is associated with different composition, size and shape of the inorganic core. However, when the response difference between the AuNP pair and the FeOx NP pair is much larger than those within the pairs, as occurs for the TNFα memory effect, the main causal factor most likely is the surface chemistry. Overall, the most important observation is that the memory effects are strongly donor-dependent, thereby preventing a generalisation of the NP effects.

We examined the global scenario of NP-generated memory in this study by simplifying the memory responses to NP as increase of inflammation/immunostimulation (+), no change (=) and decrease (–) *vs*. the response of control cells primed in the absence of NP. The results are shown in **Table 3**. Since for every NP we have tested the memory effects on the production of two inflammatory and two anti-inflammatory factors, we have assessed the overall memory effect in each donor by considering the balance between changes in the production of inflammatory *vs*. anti-inflammatory factors, in order to obtain an individual profile of the NP-induced memory responses. The summary in **Table 4** depicts the NP-specific donor-specific memory profiles based on the data summarised in **Table 3**. The general finding is that each donor reacts differently to the same NP. For instance, memory induced by priming with AuNP SPH induces no overall change in the response of donor 1 (the lack of change being due to the increase of two inflammatory markers balanced by the increase in two anti-inflammatory markers), a more inflammatory response in donor 2 and a more anti-inflammatory response in donor 3. Strikingly, the memory profile induced by AuNP SPH together with LPS is different from that induced by NP alone, being more anti-inflammatory for donor 1 (*vs*. no change with NP alone), and opposite for donor 2 (more anti-inflammatory) and donor 3 (more inflammatory).

Memory-dependent changes are detected in most cases, both in the direction of an enhanced secondary response (potentiation) and in the direction of a reduced secondary response (tolerance). In general, however, these changes do not seem substantial, as they are based on the change of one parameter out of four measured. Thus, we have defined such partial changes as "towards potentiation" and "towards

TABLE 3 | Changes in cytokine production in NP-induced innate memory responses.

Priming[1]		Cytokine[2]	Donors[3]			
LPS	NP		D1	D2	D3	D4
No	AuNP SPH	TNFα	+	=	=	*nt*
		IL-6	+	+	=	*nt*
		IL-10	+	=	+	*nt*
		IL-1Ra	+	=	=	*nt*
	AuNP ROD	TNFα	=	=	=	*nt*
		IL-6	+	=	–	*nt*
		IL-10	+	=	+	*nt*
		IL-1Ra	+	=	=	*nt*
	FeOxNP 17	TNFα	*nt*	=	–	–
		IL-6	*nt*	=	–	+
		IL-10	*nt*	=	=	+
		IL-1Ra	*nt*	+	=	+
	FeOxNP 22	TNFα	*nt*	=	–	+
		IL-6	*nt*	+	–	=
		IL-10	*nt*	=	=	+
		IL-1Ra	*nt*	=	=	+
Yes	AuNP SPH	TNFα	+	=	+	*nt*
		IL-6	=	=	=	*nt*
		IL-10	+	=	=	*nt*
		IL-1Ra	+	+	=	*nt*
	AuNP ROD	TNFα	+	=	+	*nt*
		IL-6	+	=	=	*nt*
		IL-10	+	=	=	*nt*
		IL-1Ra	+	+	=	*nt*
	FeOxNP 17	TNFα	*nt*	=	=	–
		IL-6	*nt*	+	–	+
		IL-10	*nt*	=	=	+
		IL-1Ra	*nt*	+	=	=
	FeOxNP 22	TNFα	*nt*	–	=	–
		IL-6	*nt*	=	=	=
		IL-10	*nt*	=	=	+
		IL-1Ra	*nt*	–	=	=

[1] *Human monocytes were primed in vitro with NP alone or in the presence of 1 ng/mL LPS for 24 h, then washed, rested for 6 days and eventually challenged for 24 h with 5 ng/mL LPS.*

[2] *The two inflammatory cytokines TNFα and IL-6, and the two anti-inflammatory cytokines IL-10 and IL-1Ra were measured in the 24 h supernatant of LPS-challenged monocytes.*

[3] *The NP effects on memory responses were assessed in four individual donors, indicated as D1, D2, D3 and D4, and expressed as statistically significant changes (increase, +; decrease, –; no change, =) vs. control cells (medium-primed or LPS-primed). Actual values are shown in* ***Figure 3****.*

nt, not tested.

TABLE 4 | Individual profiling of the NP-induced innate memory responses.

NP[1]	Donor	Memory profiling[2] upon priming with[3]			
		NP		LPS + NP	
AuNP SPH	D1	2+/2−	Balance	1+/2−/1=	Towards Tolerance
	D2	1+/3=	Towards Potentiation	1−/3=	Towards Tolerance
	D3	1−/3=	Towards Tolerance	1+/3=	Towards Potentiation
AuNP ROD	D1	1+/2−/1=	Towards Tolerance	2+/2−	Balance
	D2	4=	Balance	1−/3=	Towards Tolerance
	D3	2−/2=	Tolerance	1+/3=	Towards Potentiation
FeOxNP 17	D2	1−/3=	Towards Tolerance	1+/1−/2=	Balance
	D3	2−/2=	Tolerance	1−/3=	Towards Tolerance
	D4	1+/3−	Tolerance	1+/2−/1=	Towards Tolerance
FeOxNP 22	D2	1+/3=	Towards Potentiation	1+/1−/2=	Balance
	D3	2−/2=	Tolerance	4=	Balance
	D4	1+/2−/1=	Towards Tolerance	2−/2=	Tolerance

[1] *The four types of NP used for priming (memory induction) are indicated.*

[2] *The overall NP effects on memory responses are described as potentiation (i.e., increased inflammation/immunostimulation) or tolerance (i.e., increased anti-inflammation/immunosuppression) or balance, based on the changes in the production of inflammation-related cytokines in comparison to control cells (all listed in* ***Table 3****). For the individual memory profiling, four cytokines were assessed in cells from each donor and their NP-induced memory changes indicated as + (when observing an increase in the production of the inflammatory factors TNFα and IL-6, or a decrease in the production of the anti-inflammatory cytokines IL-10 and IL-1Ra), − (when observing a decrease in the production of the inflammatory factors TNFα and IL-6, or an increase in the production of the anti-inflammatory cytokines IL-10 and IL-1Ra) or = (no change in the cytokine production). Cytokines were measured in the 24 h supernatant of LPS-challenged monocytes. Potentiation and tolerance were considered clear when at least 2/4 parameters were changed in the same direction, and as a tendency when only 1/4 parameters was changed.*

[3] *The memory responses were assessed in cells primed with NP alone or NP and LPS and all challenged with LPS.*

tolerance", to define a tendency rather than a full change of reactivity. Only in few cases we have observed a clear tolerance (change in at least 2/4 parameters), while we could never detect a clear potentiation. This may be interpreted as a general inability of NP to induce a potentiation of subsequent reactivity, *i.e.*, we should not expect excessive inflammation upon subsequent challenges. On the other hand, there is the possibility, in some donors with some NP types, of a lower/inadequate secondary response, which might imply higher susceptibility to infections/diseases. Interestingly, in several cases we can observe a similar overall response between donors, as for instance in cells from donors 2 and 3 primed with FeOxNP 22 together with LPS, which showed an unchanged overall response. However, there is a difference between the two donors for attaining the same overall effects, with donor 3 showing no change in the four parameters, while donor 2 showed a decrease in one inflammatory parameter (TNFα) counterbalanced by a decrease in one anti-inflammatory parameter (IL-1Ra).

As general conclusion, we have observed a strongly individual memory response of human innate cells primed with NP, to confirm previous indications (62, 64, 66). The NP-induced memory response can differ between donors for the same type of NP, a finding that supports the need for a personalised memory profiling, before administration of nanoimaging materials for diagnostic scopes. This would allow us to predict the possible impact of NP on the capacity of the patient to adequately react to future challenges, thereby allowing for selecting patients unlikely to develop innate memory alterations and avoiding treating those at risk of developing health-impairing reactivities. In the case of both nanoimaging and nanotherapeutic materials, a preventive innate memory profiling of the patient will contribute to implementing a better targeted treatment and a safer patient management.

DATA AVAILABILITY STATEMENT

The original contributions presented in the study are included in the article/**Supplementary Material**. Further inquiries can be directed to the corresponding authors.

ETHICS STATEMENT

The studies involving human participants were reviewed and approved by Regional Ethics Committee for Clinical Experimentation of the Tuscany Region (Ethics Committee Register n. 14,914 of May 16, 2019). Written informed consent for participation was not required for this study in accordance with the national legislation and the institutional requirements.

AUTHOR CONTRIBUTIONS

GDC, AF, RLS and AP synthesized and characterised the nanomaterials. GDC, MM, YL, AC, TH, BJS and GS contributed to the experimental work. DB and PI planned the study. DB wrote the manuscript. AP and MM contributed to writing the manuscript. GDC, AP, DB and PI prepared the figures. PI performed the statistical analysis. All authors contributed to the article and approved the submitted version.

FUNDING

This work was supported by the EU Commission H2020 projects ENDONANO (GA 812661) and PANDORA (GA 671881), the FP7 project HUMUNITY (GA 316383), the Italian MIUR InterOmics Flagship projects MEMORAT and MAME, and the Italian MIUR/PRIN-20173ZECCM. This work was partially carried out in the frame of the JRC Visiting Scientist agreement no. 05/JRC.F.2/2019 (Directorate F - Health, Consumers and Reference Materials, Consumer Products Safety, Nanobiotechnology Lab).

ACKNOWLEDGMENTS

The authors would like to thank Prof. Paola Migliorini (University of Pisa) for the organisation of the human blood collection and ethical study approval, and Dora Mehn (JRC) for the support and helpful discussion. We thank Marinella Pirozzi and Anna Chiara De Luca (EuroBioImaging facility at CNR) for the TEM images of NP uptake and Jessica Ponti (JRC) for the AuNP TEM images.

SUPPLEMENTARY MATERIAL

The Supplementary Material for this article can be found online at: https://www.frontiersin.org/articles/10.3389/fimmu.2021.692165/full#supplementary-material

Supplementary Figure 1 | TEM (number-weighted) NP size distribution. Histograms representing the size distribution from TEM images. **(A)** AuNP SPH; **(B)** AuNP ROD (the distribution of both length and width are shown in the left and right panels, respectively); **(C)** FeOxNP 17; and d) FeOxNP 22. The red line in **(C, D)** is the best-fit log-normal distribution. The size data are reported in the inserts and in **Table 1**.

Supplementary Figure 2 | DLS intensity-weighted distribution of the hydrodynamic diameter of AuNP SPH. Intensity-weighted distribution (P_I) of the hydrodynamic diameter of AuNP SPH in WFI (black), PBS (blue) and RPMI-1640 after pre-treatment with human serum (red). Error bars are shown. The largest PI peak is centered at 16 nm for AuNP SPH in WFI, 15 nm for AuNP SPH in PBS, and 21 nm for AuNP SPH in RPMI-1640 after pre-treatment with human serum.

Supplementary Figure 3 | AuNP uptake by monocytes. TEM images of AuNP SPH internalized by monocytes and associated within vesicles. Size bars are 1 mm in the left panel and 500 nm in the right panel.

REFERENCES

1. Rosen JE, Yoffe S, Meerasa A, Verma M, Gu FX. Nanotechnology and Diagnostic Imaging: New Advances in Contrast Agent Technology. *J Nanomed Nanotechnol* (2011) 2:1000115. doi: 10.4172/2157-7439.1000115
2. Han X, Xu K, Taratula O, Farsad K. Applications of Nanoparticles in Biomedical Imaging. *Nanoscale* (2019) 11:799–819. doi: 10.1039/c8nr07769j
3. Nune SK, Gunda P, Thallapally PK, Lin Y-Y, Forrest ML, Berkland CJ. Nanoparticles for Biomedical Imaging. *Expert Opin Drug Deliv* (2009) 6:1175–94. doi: 10.1517/17425240903229031
4. Dadfar SM, Roemhild K, Drude NI, von Stillfried S, Knüchel R, Kiessling F, et al. Iron Oxide Nanoparticles: Diagnostic, Therapeutic and Theranostic Applications. *Adv Drug Deliv Rev* (2019) 138:302–25. doi: 10.1016/j.addr.2019.01.005
5. Bagheri S, Yasemi M, Safaie-Qamsari E, Rashidiani J, Abkar M, Hassani M, et al. Using Gold Nanoparticles in Diagnosis and Treatment of Melanoma Cancer. *Artif Cells Nanomed Biotechnol* (2018) 46:462–71. doi: 10.1080/21691401.2018.1430585
6. Daldrup-Link HE. Ten Things You Might Not Know About Iron Oxide Nanoparticles. *Radiology* (2017) 284:616–29. doi: 10.1148/radiol.2017162759
7. Coyne DW. Ferumoxytol for Treatment of Iron Deficiency Anemia in Patients With Chronic Kidney Disease. *Expert Opin Pharmacother* (2009) 10:2563–8. doi: 10.1517/14656560903224998
8. Thiesen B, Jordan A. Clinical Applications of Magnetic Nanoparticles for Hyperthermia. *Int J Hyperthermia* (2008) 24:467–74. doi: 10.1080/02656730802104757
9. Li W, Tutton S, Vu AT, Pierchala L, Li BSY, Lewis JM, et al. First-Pass Contrast-Enhanced Magnetic Resonance Angiography in Humans Using Ferumoxytol, a Novel Ultrasmall Superparamagnetic Iron Oxide (USPIO)-Based Blood Pool Agent. *J Magn Reson Imaging* (2005) 21:46–52. doi: 10.1002/jmri.20235
10. Ahlström KH, Johansson LO, Rodenburg JB, Ragnarsson AS, Akeson P, Börseth A. Pulmonary MR Angiography With Ultrasmall Superparamagnetic Iron Oxide Particles as a Blood Pool Agent and a Navigator Echo for Respiratory Gating: Pilot Study. *Radiology* (1999) 211:865–9. doi: 10.1148/radiology.211.3.r99jn10865
11. Fananapazir G, Marin D, Suhocki PV, Kim CY, Bashir MR. Vascular Artifact Mimicking Thrombosis on MR Imaging Using Ferumoxytol as a Contrast Agent in Abdominal Vascular Assessment. *J Vasc Interv Radiol* (2014) 25:969–76. doi: 10.1016/j.jvir.2013.12.019
12. Smits LP, Coolen BF, Panno MD, Runge JH, Nijhof WH, Verheij J, et al. Non-Invasive Differentiation Between Hepatic Steatosis and Steatohepatitis With MR Imaging Enhanced With USPIOs in Patients With Non-Alcoholic Fatty Liver Disease: A Proof-of-Concept Study. *Radiology* (2016) 278:782–91. doi: 10.1148/radiol.2015150952
13. Turkbey B, Agarwal HK, Shih J, Bernardo M, McKinney YL, Daar D, et al. A Phase I Dosing Study of Ferumoxytol for MR Lymphography at 3 T in Patients With Prostate Cancer. *Am J Roentgenol* (2015) 205:64–9. doi: 10.2214/AJR.14.13009
14. Harisinghani MG, Barentsz J, Hahn PF, Deserno WM, Tabatabaei S, van de Kaa CH, et al. Noninvasive Detection of Clinically Occult Lymph-Node Metastases in Prostate Cancer. *N Engl J Med* (2003) 348:2491–9. doi: 10.1056/NEJMoa022749
15. Harisinghani MG, Saini S, Weissleder R, Hahn PF, Yantiss RK, Tempany C, et al. MR Lymphangiography Using Ultrasmall Superparamagnetic Iron Oxide in Patients With Primary Abdominal and Pelvic Malignancies: Radiographic-Pathologic Correlation. *Am J Roentgenol* (1999) 172:1347–51. doi: 10.2214/ajr.172.5.10227514
16. Daldrup-Link HE, Rummeny EJ, Ihssen B, Kienast J, Link TM. Iron-Oxide-Enhanced MR Imaging of Bone Marrow in Patients With Non-Hodgkin's Lymphoma: Differentiation Between Tumor Infiltration and Hypercellular Bone Marrow. *Eur Radiol* (2002) 12:1557–66. doi: 10.1007/s00330-001-1270-5
17. Neuwelt EA, Várallyay CG, Manninger S, Solymosi D, Haluska M, Hunt MA, et al. The Potential of Ferumoxytol Nanoparticle Magnetic Resonance Imaging, Perfusion, and Angiography in Central Nervous System Malignancy: A Pilot Study. *Neurosurgery* (2007) 60:601–12. doi: 10.1227/01.NEU.0000255350.71700.37
18. Daldrup-Link HE, Rydland J, Helbich TH, Bjørnerud A, Turetschek K, Kvistad KA, et al. Quantification of Breast Tumor Microvascular Permeability With Feruglose-Enhanced MR Imaging: Initial Phase II Multicenter Trial. *Radiology* (2003) 229:885–92. doi: 10.1148/radiol.2293021045
19. Gahramanov S, Raslan AM, Muldoon LL, Hamilton BE, Rooney WD, Varallyay CG, et al. Potential for Differentiation of Pseudoprogression From True Tumor Progression With Dynamic Susceptibility-Weighted Contrast-Enhanced Magnetic Resonance Imaging Using Ferumoxytol vs. Gadoteridol: A Pilot Study. *Int J Radiat Oncol Biol Phys* (2011) 79:514–23. doi: 10.1016/j.ijrobp.2009.10.072
20. Vazquez-Prada KX, Lam J, Kamato D, Xu ZP, Little PJ, Ta HT. Targeted Molecular Imaging of Cardiovascular Diseases by Iron Oxide Nanoparticles. *Arterioscler Thromb Vasc Biol* (2021) 41:601–13. doi: 10.1161/ATVBAHA.120.315404
21. Herborn CU, Vogt FM, Lauenstein TC, Dirsch O, Corot C, Robert P, et al. Magnetic Resonance Imaging of Experimental Atherosclerotic Plaque:

Comparison of Two Ultrasmall Superparamagnetic Particles of Iron Oxide. *J Magn Reson Imaging* (2006) 24:388–93. doi: 10.1002/jmri.20649

22. Schmitz SA, Taupitz M, Wagner S, Wolf KJ, Beyersdorff D, Hamm B. Magnetic Resonance Imaging of Atherosclerotic Plaques Using Superparamagnetic Iron Oxide Particles. *J Magn Reson Imaging* (2001) 14:355–61. doi: 10.1002/jmri.1194
23. Gaglia JL, Harisinghani M, Aganj I, Wojtkiewicz GR, Hedgier S, Benoist C, et al. Noninvasive Mapping of Pancreatic Inflammation in Recent-Onset Type-1 Diabetes Patients. *Proc Natl Acad Sci USA* (2015) 112:2139–44. doi: 10.1073/pnas.1424993112
24. Simon GH, von Vopelius-Feldt J, Fu Y, Schlegel J, Pinotek G, Wendland MF, et al. Ultrasmall Supraparamagnetic Iron Oxide-Enhanced Magnetic Resonance Imaging of Antigen-Induced Arthritis: A Comparative Study Between SHU 555 C, ferumoxtran-10, and Ferumoxytol. *Invest Radiol* (2006) 41:45–51. doi: 10.1097/01.rli.0000191367.61306.83
25. Vellinga MM, Vrenken H, Hulst HE, Polman CH, Uitdehaag BMJ, Pouwels PJW, et al. Use of Ultrasmall Superparamagnetic Particles of Iron Oxide (USPIO)-Enhanced MRI to Demonstrate Diffuse Inflammation in the Normal-Appearing White Matter (NAWM) of Multiple Sclerosis (MS) Patients: An Exploratory Study. *J Magn Reson Imaging* (2009) 29:774–9. doi: 10.1002/jmri.21678
26. Kooi ME, Cappendijk VC, Cleutjens KBJM, Kessels AGH, Kitslaar PJEHM, Borgers M, et al. Accumulation of Ultrasmall Superparamagnetic Particles of Iron Oxide in Human Atherosclerotic Plaques Can Be Detected by *In Vivo* Magnetic Resonance Imaging. *Circulation* (2003) 107:2453–8. doi: 10.1161/01.CIR.0000068315.98705.CC
27. Costa da Silva M, Breckwoldt MO, Vinchi F, Correia MP, Stojanovic A, Thielmann CM, et al. Iron Induces Anti-Tumor Activity in Tumor-Associated Macrophages. *Front Immunol* (2017) 8:1479. doi: 10.3389/fimmu.2017.01479
28. Zanganeh S, Hutter G, Spitler R, Lenkov O, Mahmoudi M, Shaw A, et al. Iron Oxide Nanoparticles Inhibit Tumour Growth by Inducing Pro-Inflammatory Macrophage Polarization in Tumour Tissues. *Nat Nanotechnol* (2016) 11:986–94. doi: 10.1038/NNANO.2016.168
29. Cole LE, Ross RD, Tilley JMR, Vargo-Gogola T, Roeder RK. Gold Nanoparticles as Contrast Agents in X-Ray Imaging and Computed Tomography. *Nanomed (Lond)* (2015) 10:321–41. doi: 10.2217/NNM.14.171
30. Ahn S, Jung SY, Lee SJ. Gold Nanoparticle Contrast Agents in Advanced X-Ray Imaging Technologies. *Molecules* (2013) 18:5858–90. doi: 10.3390/molecules18055858
31. Lu W, Huang Q, Ku G, Wen X, Zhou M, Guzatov D, et al. Photoacoustic Imaging of Living Mouse Brain Vasculature Using Hollow Gold Nanospheres. *Biomaterials* (2010) 31:2617–26. doi: 10.1016/j.biomaterials.2009.12.007
32. Chien CC, Chen HH, Lai SF, Hwu Y, Petibois C, Yang CS, et al. X-Ray Imaging of Tumor Growth in Live Mice by Detecting Gold-Nanoparticle-Loaded Cells. *Sci Rep* (2012) 2:610. doi: 10.1038/srep00610
33. Ahn S, Jung SY, Seo E, Lee SJ. Gold Nanoparticle-Incorporated Human Red Blood Cells (Rbcs) for X-Ray Dynamic Imaging. *Biomaterials* (2011) 32:7191–9. doi: 10.1016/j.biomaterials.2011.05.023
34. Chhour P, Naha PC, O'Neill SM, Litt HI, Reilly MP, Ferrari VA, et al. Labeling Monocytes With Gold Nanoparticles to Track Their Recruitment in Atherosclerosis With Computed Tomography. *Biomaterials* (2016) 87:93–103. doi: 10.1016/j.biomaterials.2016.02.009
35. Shah A, Dobrovolskaia M. Immunological Effects of Iron Oxide Nanoparticles and Iron-Based Complex Drug Formulations: Therapeutic Benefits, Toxicity, Mechanistic Insights, and Translational Considerations. *Nanomedicine* (2018) 14:977–90. doi: 10.1016/j.nano.2018.01.014
36. Raynal I, Prigent P, Peyramaure S, Najid A, Rebuzzi C, Corot C. Macrophage Endocytosis of Superparamagnetic Iron Oxide Nanoparticles: Mechanisms and Comparison of Ferumoxides and Ferumoxtran-10. *Invest Radiol* (2004) 39:56–63. doi: 10.1097/01.rli.0000101027.57021.28
37. Zhu M, Tian X, Song X, Li Y, Tian Y, Zhao Y, et al. Nanoparticle-Induced Exosomes Target Antigen-Presenting Cells to Initiate Th1-Type Immune Activation. *Small* (2012) 8:2841–8. doi: 10.1002/smll.201200381
38. Valdiglesias V, Kiliç G, Costa C, Fernández-Bertólez N, Pasaro E, Teixeira JP, et al. Effects of Iron Oxide Nanoparticles: Cytotoxicity, Genotoxicity, Developmental Toxicity, and Neurotoxicity. *Environ Mol Mutagenesis* (2015) 56:125–48. doi: 10.1002/em.21909
39. Yang CY, Tai MF, Lin CP, Lu CW, Wang JL, Hsiao JK, et al. Mechanism of Cellular Uptake and Impact of Ferucarbotran on Macrophage Physiology. *PLoS One* (2011) 6:e25524. doi: 10.1371/journal.pone.0025524
40. Müller K, Skepper JN, Posfai M, Trivedi R, Howarth S, Corot C, et al. Effect of Ultrasmall Superparamagnetic Iron Oxide Nanoparticles (Ferumoxtran-10) on Human Monocyte-Macrophages In Vitro. *Biomaterials* (2007) 28:1629–42. doi: 10.1016/j.biomaterials.2006.12.003
41. Kunzmann A, Andersson B, Vogt C, Feliu N, Ye F, Gabrielsson S, et al. Efficient Internalization of Silica-Coated Iron Oxide Nanoparticles of Different Sizes by Primary Human Macrophages and Dendritic Cells. *Toxicol Appl Pharmacol* (2011) 253:81–93. doi: 10.1016/j.taap.2011.03.011
42. Ferretti AM, Usseglio S, Mondini S, Drago C, La Mattina R, Chini B, et al. Towards Bio-Compatible Magnetic Nanoparticles. Immune-related Effects, *In Vitro* Internalization, and *In Vivo* Bio-Distribution of Zwitterionic Ferrite Nanoparticles With Unexpected Renal Clearance. *J Coll Interf Sci* (2021) 582:678–700. doi: 10.1016/j.jcis.2020.08.026
43. Villiers C, Freitas H, Courderc R, Villiers M-B, Marche P. Analysis of the Toxicity of Gold Nano Particles on the Immune System: Effect on Dendritic Cell Functions. *J Nanopart Res* (2010) 12:55–60. doi: 10.1007/s11051-009-9692-0
44. Pfaller T, Colognato R, Nelissen I, Favilli F, Casals E, Ooms D, et al. The Suitability of Different Cellular *In Vitro* Immunotoxicity and Genotoxicity Methods for the Analysis of Nanoparticle-Induced Events. *Nanotoxicology* (2010) 4:52–72. doi: 10.3109/17435390903374001
45. Oostingh GJ, Casals E, Italiani P, Colognato R, Stritzinger R, Ponti J, et al. Problems and Challenges in the Development and Validation of Human Cell-Based Assays to Determine Nanoparticle-Induced Immunomodulatory Effects. *Particle Fibre Toxicol* (2011) 8:8. doi: 10.1186/1743-8977-8-8s
46. Adewale OB, Davids H, Cairncross L, Roux S. Toxicological Behavior of Gold Nanoparticles on Various Models: Influence of Physicochemical Properties and Other Factors. *Int J Toxicol* (2019) 38:357–84. doi: 10.1177/1091581819863130
47. Carnovale C, Bryant G, Shukla R, Bansal V. Identifying Trends in Gold Nanoparticle Toxicity and Uptake: Size, Shape, Capping Ligand, and Biological Corona. *ACS Omega* (2019) 4:242–56. doi: 10.1021/acsomega.8b03227
48. Dykman LA, Khlebtsov NG. Immunological Properties of Gold Nanoparticles. *Chem Sci* (2017) 8:1719–35. doi: 10.1039/c6sc03631g
49. Li Y, Boraschi D. Endotoxin Contamination*: A* Key Element in the Interpretation of Nanosafety Studies. *Nanomed (Future Med)* (2016) 11:269–87. doi: 10.2217/nnm.15.196
50. Li Y, Italiani P, Casals E, Valkenborg D, Mertens I, Baggerman G, et al. Assessing the Immunosafety of Engineered Nanoparticles With a Novel *In Vitro* Model Based on Human Primary Monocytes. *ACS Appl Mater Interfaces* (2016) 8:28437–47. doi: 10.1021/acsami.6b06278
51. Li Y, Fujita M, Boraschi D. Endotoxin Contamination in Nanomaterials Leads to the Misinterpretation of Immunosafety Results. *Front Immunol* (2017) 8:472. doi: 10.3389/fimmu.2017.00472
52. Li Y, Shi Z, Radauer-Preiml I, Andosch A, Casals E, Luetz-Meindl U, et al. Bacterial Endotoxin (Lipopolysaccharide) Binds to the Surface of Gold Nanoparticles, Interferes With Biocorona Formation and Induces Human Monocyte Inflammatory Activation. *Nanotoxicology* (2017) 11:1157–75. doi: 10.1080/17435390.2017.1401142
53. Boraschi D, Costantino L, Italiani P. Interaction of Nanoparticles With Immunocompetent Cells: Nanosafety Considerations. *Nanomed (Future Med)* (2012) 7:121–31. doi: 10.2217/nnm.11.169
54. Boraschi D, Italiani P, Palomba R, Decuzzi P, Duschl A, Fadeel B, et al. Nanoparticles and Innate Immunity: New Perspectives on Host Defence. *Sem Immunol* (2017) 34:33–51. doi: 10.1016/j.smim.2017.08.013
55. Boraschi D, Swartzwelter BJ, Italiani P. Interaction of Engineered Nanomaterials With the Immune System: Health Related Safety and Possible Benefits. *Curr Opin Toxicol* (2018) 10:74–83. doi: 10.1016/j.cotox.2018.02.002
56. Netea MG, Quintin J, van der Meer JW. Trained Immunity: A Memory for Innate Host Defense. *Cell Host Microbe* (2011) 9:355–61. doi: 10.1016/j.chom.2011.04.006
57. Ifrim DC, Quintin J, Joosten LA, Jacobs C, Jansen T, Jacobs L, et al. Trained Immunity or Tolerance: Opposing Functional Programs Induced in Human

Monocytes After Engagement of Various Pattern Recognition Receptors. *Clin Vaccine Immunol* (2014) 21:34–45. doi: 10.1128/CVI.00688-13

58. Quintin J, Cheng SC, van der Meer JWM, Netea MG. Innate Immune Memory: Towards a Better Understanding of Host Defense Mechanisms. *Curr Opin Immunol* (2014) 29:1–7. doi: 10.1016/j.coi.2014.02.006
59. Saeed S, Quintin J, Kerstens HH, Rao NA, Aghajanirefah A, Matarese F, et al. Epigenetic Programming of Monocyte-to-Macrophage Differentiation and Trained Innate Immunity. *Science* (2014) 345:1251086. doi: 10.112/science.1251086
60. Gourbal B, Pinaud S, Beckers GJM, van der Meer JWM, Conrath U, Netea MG. Innate Immune Memory: An Evolutionary Perspective. *Immunol Rev* (2018) 283:21–40. doi: 10.1111/imr.12647
61. Boraschi D, Italiani P. Innate Immune Memory: Time for Adopting a Correct Terminology. *Front Immunol* (2018) 9:799. doi: 10.3389/fimmu.2018.00799
62. Lebre F, Boland JB, Gouveia P, Gorman AL, Lundahl MLE, Lynch RI, et al. Pristine Graphene Induces Innate Immune Training. *Nanoscale* (2020) 12:11192–200. doi: 10.1039/c9nr09661b
63. Italiani P, Boraschi D. Induction of Innate Immune Memory by Engineered Nanoparticles, an Hypothesis That May Become True. *Front Immunol* (2017) 8:734. doi: 10.3389/fimmu.2017.00734
64. Italiani P, Della Camera G, Boraschi D. Induction of Innate Immune Memory by Engineered Nanoparticles in Monocytes/Macrophages: From Hypothesis to Reality. *Front Immunol* (2020) 11:566309. doi: 10.3389/fimmu.2020.566309
65. Swartzwelter BJ, Barbero F, Verde A, Mangini M, Pirozzi M, De Luca AC, et al. Gold Nanoparticles Modulate BCG-Induced Innate Immune Memory in Human Monocytes by Shifting the Memory Response Towards Tolerance. *Cells* (2020) 9:284. doi: 10.3390/cells9020284
66. Swartzwelter BJ, Fux AC, Johnson L, Swart E, Hofer S, Hofstätter N, et al. The Impact of Nanoparticles on Innate Immune Activation by Live Bacteria. *Int J Mol Sci* (2020) 21:9695. doi: 10.3390/ijms21249695
67. Swartzwelter BJ, Verde A, Rehak L, Madej M, Puntes VF, De Luca AC, et al. Interaction Between Macrophages and Nanoparticles: *In Vitro* 3D Cultures for the Realistic Assessment of Inflammatory Activation and Modulation of Innate Memory. *Nanomaterials* (2021) 11:207. doi: 10.3390/nano11010207
68. Turkevich J, Stevenson PC, Hillier J. A Study of the Nucleation and Growth Processes in the Synthesis of Colloidal Gold. *Discuss Faraday Soc* (1951) 11:55–75. doi: 10.1039/DF9511100055
69. Provencher SW. A Constrained Regularization Method for Inverting Data Represented by Linear Algebraic or Integral-Equations. *Comput Phys Commun* (1982) 27:213–27. doi: 10.1016/0010-4655(82)90173-4
70. Provencher SW. CONTIN - A General-Purpose Constrained Regularization Program for Inverting Noisy Linear Algebraic and Integral-Equations. *Comput Phys Commun* (1982) 27:229–42. doi: 10.1016/0010-4655(82)90174-6
71. Li Y, Italiani P, Casals E, Tran N, Puntes VF, Boraschi D. Optimising the Use of Commercial LAL Assays for the Analysis of Endotoxin Contamination in Metal Colloids and Metal Oxide Nanoparticles. *Nanotoxicology* (2015) 9:462–73. doi: 10.3109/17435390.2014.948090

Conflict of Interest: The authors declare that the research was conducted in the absence of any commercial or financial relationships that could be construed as a potential conflict of interest.

frontiers in Immunology

PERSPECTIVE
published: 14 September 2021
doi: 10.3389/fimmu.2021.684605

Do Engineered Nanomaterials Affect Immune Responses by Interacting With Gut Microbiota?

Mingxing Tang[1,2,3†], *Shuo Li*[1,3†], *Lan Wei*[2,4], *Zhaohua Hou*[5], *Jing Qu*[2*] and *Liang Li*[2*]

[1] Huazhong University of Science and Technology Union Shenzhen Hospital, Shenzhen, China, [2] Institute of Biomedicine and Biotechnology, Shenzhen Institutes of Advanced Technology, Chinese Academy of Sciences, Shenzhen, China, [3] The 6th Affiliated Hospital of Shenzhen University Health Science Center, Shenzhen, China, [4] School of Biomedical Science and Pharmacy, Faculty of Health and Medicine, Hunter Medical Research Institute, University of Newcastle, New Lambton Heights, NSW, Australia, [5] Department of Surgery, Sloan Kettering Institute Z427-D, Mortimer B. Zuckerman Research Center, Memorial Sloan Kettering Cancer Center, New York, NY, United States

Edited by:
Diana Boraschi,
Shenzhen Institutes of Advanced
Technology (CAS), China

Reviewed by:
Benjamin Swartzwelter,
Colorado State University,
United States
Mariusz Piotr Madej,
OcellO B.V., Netherlands

***Correspondence:**
Liang Li
liang.li@siat.ac.cn
Jing Qu
jing.qu@siat.ac.cn

[†]*These authors have contributed equally to this work and share first authorship*

Specialty section:
This article was submitted to Molecular Innate Immunity, a section of the journal Frontiers in Immunology

Received: *23 March 2021*
Accepted: *26 August 2021*
Published: *14 September 2021*

Citation:
Tang M, Li S, Wei L, Hou Z, Qu J and Li L (2021) Do Engineered Nanomaterials Affect Immune Responses by Interacting With Gut Microbiota? Front. Immunol. 12:684605. doi: 10.3389/fimmu.2021.684605

Engineered nanomaterials (ENMs) have been widely exploited in several industrial domains as well as our daily life, raising concern over their potential adverse effects. While in general ENMs do not seem to have detrimental effects on immunity or induce severe inflammation, their indirect effects on immunity are less known. In particular, since the gut microbiota has been tightly associated with human health and immunity, it is possible that ingested ENMs could affect intestinal immunity indirectly by modulating the microbial community composition and functions. In this perspective, we provide a few pieces of evidence and discuss a possible link connecting ENM exposure, gut microbiota and host immune response. Some experimental works suggest that excessive exposure to ENMs could reshape the gut microbiota, thereby modulating the epithelium integrity and the inflammatory state in the intestine. Within such microenvironment, numerous microbiota-derived components, including but not limited to SCFAs and LPS, may serve as important effectors responsible of the ENM effect on intestinal immunity. Therefore, the gut microbiota is implicated as a crucial regulator of the intestinal immunity upon ENM exposure. This calls for including gut microbiota analysis within future work to assess ENM biocompatibility and immunosafety. This also calls for refinement of future studies that should be designed more elaborately and realistically to mimic the human exposure situation.

Keywords: engineered nanomaterials (ENMs), gut microbiota, intestinal permeability, immunomodulation, bacterial components

INTRODUCTION

Unique properties including large surface area, high catalytic properties and antimicrobial efficacy confer to engineered nanomaterials (ENMs) a significant range of applications in nanomedicine and consumer products (1, 2), raising public concerns about their biosafety. For example, nanoparticulate Ag, TiO_2, ZnO and plastics are widely used in food additives (3), components of food packaging and containers (4, 5), and toothpaste (6). Oral exposure to these ENMs in our daily life is therefore likely through ingestion of food or water that deliberately or inadvertently contain ENMs. ENMs might therefore reach the gastro-intestinal tract (GIT) and interact with mucosal cells. Indeed, endocytosis of ENMs by intestinal epithelial cells (IECs) and various immune cells is observed using either conventional 2D *in vitro* models such as tumor cell lines (7, 8) or *in vivo* animal models (9). Moreover, it has been reported that ENMs could modulate innate/inflammatory immune responses upon direct interactions with neutrophils, macrophages, dendritic cells (DCs) and the complement system (10–13). Upon ingestion, ENMs most likely also come in contact with gut microbiota, *i.e.*, the population of microbes residing in the intestinal lumen and mucosa. It has been long known that the gut microbiota is essential for the development of the immune system and for immune homeostasis (14). Recent observations suggest that the ENM effects on innate/inflammatory responses largely depend on the co-presence of bacterial agents such as lipopolysaccharide (LPS) (15, 16). Thus, it is a logical assumption that ENMs could affect immunity by altering gut microbiota, a concept that is currently unexplored.

Herein, we provide an overview of the current state-of-the-art, and discuss a hypothetical scenario in which ingested EMNs may affect host immunity by modulating the gut microbiota. From published *in vivo* studies in different models and with different ENMs, a high level of variability is found regarding the ENM effects on gut microbiota and local/systemic immunity (**Table 1**).

LPS AND SCFAS: TWO REPRESENTATIVE MICROBIAL MOLECULES BRIDGING GUT MICROBIOTA AND INTESTINAL IMMUNITY

Mounting evidence has highlighted the tremendous contribution of gut microbiota to human physiology (30–35). Within this microbiota-immune system interaction, a large amount of microbial metabolites and components serve as potent effectors to orchestrate their communication (36, 37). We will specifically discuss hereafter the immunomodulatory effects of short-chain fatty acids (SCFAs) and LPS. More comprehensive information is shown in **Figure 1** and extensively discussed in other excellent reviews (32, 33, 36–39). SCFAs are generated from indigestible oligosaccharides by gut commensals, including *Lactobacillus*, *Bacteroides*, *Bifidobacterium*, *Feacalibacterium*, *etc.* (40). LPS is the major membrane component of Gram-negative bacteria and has profound immunostimulatory and inflammatory capacity (41). The immunological effects of these microbiota-derived molecules are manifold, covering innate and adaptive immunity.

Regulation of Innate Immunity

As a physical barrier at the intestinal surface, IECs are equipped with an array of immune receptors to sense and integrate microbiota-derived metabolites and components for maintaining immune homeostasis. By activating G-protein-coupled-receptors (GPR41, GPR43, GPR109A) on IECs, SCFAs can promote the activation of the NOD-like-receptor-protein 3 (NLRP3) inflammasome, inducing production of the homeostatic cytokine interleukin-18 (IL-18) (42). SCFAs can also stimulate goblet cell differentiation, mucin gene transcription and mucus secretion (43). Pattern recognition receptors (PRRs) on the IEC surface, such as Toll-like receptors (TLRs), can sense microbial antigens. Notably, a number of homeostatic mechanisms ensure immune tolerance towards commensals, such as the basolateral location of the LPS receptor TLR4 that allows binding and activation only to invading bacteria (44) and the constitutive expression of the anti-inflammatory IL-1R8, which binds to and inhibits TLR and IL-1 receptors (45).

Intriguingly, the commensal gut microbiota also interacts with IECs to maintain an effective gut barrier. SCFAs, particularly butyrate, have crucial roles in regulating tight junction (TJ) proteins *via* multifaceted signaling pathways (46), such as HIF-1 stabilization (47), and histone deacetylase (HDAC) inhibition (48). By contrast pathogenic *E. coli* Shiga-toxins and LPS (49) could compromise the epithelial barrier by disrupting TJ. LPS increases intestinal epithelium permeability through the TLR4/MyD88/TGF-β activated kinase 1 (TAK1)/nuclear-factor-κB (NF-κB) cascade in both *in vitro* and *in vivo* models (50).

Immunoregulation of gut microbiota also covers innate lymphoid cells (ILCs), a subpopulation of innate cells (natural killer cells, ILC1, ILC2, ILC3) specialized in recognizing and reacting to infectious challenges. SCFAs can modulate ILC3 proliferation and stimulate IL-22 production in an AKT/STAT3-dependent manner. IL-22 promotes antimicrobial peptide (AMP) production, mucin secretion and colonization of commensal microbes (51).

Intestinal resident macrophages maintain the tissue homeostasis by removing senescent and anomalous cells, and contribute to tissue defense by eliminating invading pathogens and foreign objects. Upon binding to TLR4, LPS can promote inflammatory macrophage activation (M1 polarization), with the production of an array of inflammatory cytokines, IL-1β, IL-6, IL-12 and tumor necrosis factor-α (TNF-α) (52). Conversely, SCFA butyrate facilitates the anti-inflammatory/tissue-healing macrophage polarization, probably by activation of the H3K9/STAT6 signaling pathway (53).

Regulation of Adaptive Immunity

The impact of gut microbiota goes beyond the innate immunity, through its ability to affect the activation of antigen-presenting cells (APCs), which are the link between innate and adaptive immunity. APCs in the gut encompass resident DCs and tissue macrophages, which are involved in antigen presentation to naïve and primed T cells. Activation, maturation and functionality of DCs and macrophages can be influenced by LPS and SCFAs. As the major APCs in the intestine (54), macrophages can be regulated by microbial niacin and butyrate *via* activating GPR109A, which in turn increases production of anti-inflammatory IL-10 and Aldehyde-Dehydrogenase-1-Family-Member-A1 (ALDH1A), and induces differentiation of T cells (55). LPS is a potent elicitor of DC

TABLE 1 | Representative *in vivo* assays studying the impact of ENMs on gut microbiota and subsequent influences on intestinal immunity.

Engineered NanoMaterials	Animal model	Exposure dose	Exposure way and duration	Analysis methods of gut microbiota	Gut microbiota changes by ENM treatment	Immune markers	Clinical effect/Immune response	References
Silver nanoparticles with a diameter of 55 ± 3 nm	3 mo-old C57BL/6 female mice	0, 11.4, 114 and 1140 µg/kg bw/dy	Dietary exposure for 28 days	16S rRNA Sequencing of Bacterial DNA from Fecal Samples	*Odoribacteraceae, Bacteroidaceae* and S24-7 family decreased while *Lactobacillaceae* and *Lachnospiraceae* increased	Serum C-reactive protein level; histology of ileum villi, intestinal goblet cells, glycocalyx and colon	No overt effect on body weight gain, the intestinal histology as well as the serum C-reactive protein level.	(17)
Silver nanoparticles with a diameter of 12 ± 3 nm	7 wk-old CD-1 (ICR) male mice	2.5 mg/kg bw/dy	Oral gavage daily for 7 days	Pyrosequencing of 16S rRNA genes in fecal samples	*Firmicutes/Bacteroidetes* ratio reduced. *Alistipes*, *Bacteroides* and *Prevotella* increased, while *Lactobacillus* decreased	Blood cell level, serum lymphocyte level. colon length, disease activity index (DAI), histology of colon; intestinal permeability; IL-1β, IL-6 and TNF-α in small bowel and colon	The level of blood cells and lymphocytes was increased; Body weight decreased and colon length was shortened by Ag NP; The epithelial architecture and crypts in colon was destroyed. Intestinal permeability was significantly increased; Pro-inflammatory cytokines: IL-1β, IL-6 and TNF-α were upregulated.	(18)
Silver nanoparticle with a diameter of 294 nm	6 wk-old BALB/c male mice	5 ng/dy	Oral gavage daily for 4 days	A few specific bacteria from the colon mucosa were isolated and counted by selective plates	*Lactobacillus* sp. decreased, while *Clostridium perfringens* and *Escherichia coli increased but not significantly*	Stool consistence; colon length and weight; colon epithelial histology; myeloperoxidase activity in the colon. Colon smooth muscle thickness; Presence of ulcers, hemorrhage, fecal blood, and diarrhea.	NanoAg1 displayed weaker anti-inflammatory effect and alleviated the TNBS-induced severe colonic injury.	(19)
Silver nanoparticle with a diameter of 122 nm					*Lactobacillus* sp. increased while *Clostridium perfringens and Escherichia coli* decreased		NanoAg2 significantly attenuated DSS-induced colitis and alleviated the TNBS-induced severe colonic injury.	
PVP-stabilized silver nanoparticulate with a diameter of 14 nm	4 wk-old Wistar Hannover Galas rats	2.25, 4.5 or 9 mg/kg bw/dy	Oral gavage daily for 14 days and 28 days	Bacterial phyla in caecum content were quantified by qPCR	No significant change	Histology of liver, kidney, ileum and myocardium. Twenty-four-hour urine and feces.	No overt effect on body weight gain, organ weight, organ histology and leucocyte infiltration	(20)
PVP- or citrate-coated silver nanoparticles with a diameter of 20 and 110 nm	10-12 wk-old C57BL/6NCrl male mice	10 mg/kg bw/dy	Oral gavage daily for 28 days	16S rRNA sequencing of contents in the cecal tips	No significant change	Not studied	Not studied	(21)
TiO$_2$ nanoparticles with a diameter of 17 ± 2 nm	7 wk-old CD-1 (ICR) male mice	2.5 mg/kg bw/dy	Oral gavage daily for 7 days	Pyrosequencing of 16S rRNA genes in fecal samples	*Bacteroides* decreased	Blood cell level, serum lymphocyte level. colon length, histology of colon; intestinal permeability; IL-1β, IL-6 and TNF-α in small bowel and colon	TiO$_2$ ENMs were deposited in the stomach and the colon; no effect on body weight, no significant change in DAI index and colon length, loss and shortening of crypts, inflammatory cell infiltration and mucosal erosions but a few inflammatory cells scattered within duodenal and colonic sections; The integrity of the GIT epithelium is intact; IL-1β level was increased in the small bowel and colon.	(18)
Spherical anatase TiO$_2$ nanoparticles with a diameter of 20 nm in water, of 134 ± 22 nm in gastric fluid, of 420 ± 25 nm in intestinal fluid	8 wk-old C57BL/6 male mice	100 mg/kg bw/dy	Oral gavage daily for 28 days	16S rRNA Sequencing of Bacterial DNA from Fecal Samples	*Bacteroides* and *Akkermansia* increased	Histology of liver, spleen, kidney, lung, heart, brain, jejunum and colon. NP deposition in these organs mentioned.	No effect on body weight or histology of key organs	(22)
Edged conner rutile TiO$_2$ nanoparticles with a diameter of 16 nm in water, of 148± 30 in gastric fluid, of 361 ± 8 nm in intestinal fluid					*Escherichia-Shigella and Rhodococcus* increased, while *Bacteroidetes* and *Firmicutes* decreased		Intestinal villi length increased and villus epithelium cells became irregularly arranged	
Spherical anatase TiO$_2$ nanoparticles with a diameter 29 ± 9 nm	3 wk-old Sprague-Dawley rats	0, 2, 10, 50 mg/kg bw	Oral gavage daily for 30 days	16S rRNA Sequencing of Bacterial DNA from Fecal Samples	Increased abundance of *L. gasseri*, *Turicibacter*, and *L.* NK4A136_group and decreased abundance of *Veillonella*	Body weight; LPS and short-chain fatty acids content in the feces; colon histology; fecal metabolites; presence of glutathione, glutathione peroxidase, lipid peroxidation products, superoxide dismutase, and sulfhydryl groups in tissue homogenates; Inflammatory cytokines in serum	Accumulation of malondialdehyde and decreased activity of superoxide dismutase were detected in colon tissues; Increased concentration of IL-6 in the serum. The number of goblet cells decreased and inflammatory cells infiltrated in colon epithelium.	(23)
ZnO nanoparticles with a diameter of average 71.61 nm	28 dy-old weaned piglets	150, 300, or 450 mg/kg in diet	Dietary exposure for 21 days	The cecal, colonic and rectal contents were spread on selective plates to assess *E. coli, Salmonella, Lactobacillus, and Bacillus bifidus*	*E. coli* decreased	Histology of the jejunum, duodenum and ileum; serum cytokines and immunoglobins	Significant improvements in average daily weight gain, average daily feed intake and gain to feed ratio were observed. The diarrhea rate was reduced. The villus height in the jejunum, duodenum and ileum was increased. The blood concentration of IgA, serum concentrations of IL-6 and TNF-α was increased; while the blood concentration of IgM was decreased.	(24)

(Continued)

TABLE 1 | Continued

Engineered NanoMaterials	Animal model	Exposure dose	Exposure way and duration	Analysis methods of gut microbiota	Gut microbiota changes by ENM treatment	Immune markers	Clinical effect/Immune response	References
ZnO nanoparticles with a diameter of 23-25 nm	27 dy-old weaned piglets	600 mg/kg in diet	Dietary exposure for 14 days	16S rRNA sequencing of the intestinal contents	*Lactobacillus* increased while *Prevotella* and *Oscillospira* decreased in the colon	Histology of jejunal tissue; gene expression of pro-inflammatory cytokines, cell proliferation markers, antioxidant markers, tight junction proteins and cell death markers in the jejunal tissue	The diarrhea incidence was reduced; average daily gain and feed intake were unaltered; villus height as well as the ratio of villus height to crypt depth was increased; the expression of antioxidant enzymes and tight junction in the jejunal tissues was increased significantly; the expression of cell proliferation markers was increased; the expression of pro-inflammatory markers was reduced.	(25)
SWCNT with a diameter of 1nm and a length of 1-5 μm	7 wk-old CD-1 (ICR) male mice	0.05, 0.5, and 2.5 mg kg/bw/dy	Oral gavage daily for 7 days	16S rRNA sequencing of fecal samples	*Bacteroides, Prevotella*, and *Alistipes* increased, while *Bacteroidales, Lachnospriaceae* and *Lactobacillus* decreased	Intestine histology, intestinal epithelium permeability, cytokine production in both duodenum and colon and lymphocyte abundance in the serum.	Ulceration, crypt damage, and inflammatory cell infiltration were observed in the duodenum and colon. The intestinal permeability was significantly increased. IL-1β, IL-6, and TNF-α increased in the duodenum and the colon. White blood cell, lymphocytes, and intermediate cell counts significantly elevated in the serum.	(26)
MWCNT with a diameter of 8 ± 1 nm and a length of 0.5-2 μm		2.5 mg kg/bw/day		16S rRNA sequencing of fecal samples	*Bacteroides, Prevotella, Alistipes*, and *Ruminococcaceae* increased, whereas *Bacteroidales, Lachnospriaceae* and *Lactobacillus* decreased		Slight microvilli damage and inflammatory cell infiltration in duodenum and a few inflammatory cell infiltrations in colon. Significant increase of intestinal permeability and the elevated levels of proinflammatory cytokines IL-1β, IL-6, and TNF-α in duodenum and colon were observed.	
Graphene oxide nanoparticles with a thickness of 1-2 μm and a dimension area of 1-14 μm^2		2.5 mg kg/bw/dy		16S rRNA sequencing of fecal samples	*Lachnospriaceae, Lactobacillus, Ruminococcus, Alistipes, Oscillibactyer*, and *Prevotella* increased; while *Bacteroidales* and *Bacteroides* decreased		Slightly pathological changes of epithelium loss and inflammatory cell infiltration in duodenum. Significant increase of intestinal permeability and the elevated levels of proinflammatory cytokines IL-1β, IL-6, and TNF-α in duodenum and colon were observed.	
Lysine-modified SWCNT with a length of 400 nm and a diameter of 2-3 nm	23-30 dy-old BALB/c mice	4.25 mg/wk	Oral gavage or intraperitoneal dosing weekly for 7 or 8 weeks	16S rRNA sequencing of fecal samples	The α- and β-diversity of the mouse microbiota reduced in the cecum but not in colon or ileum.	Body weight, liver and kidney weight.	No overt effect on body weight as well as liver and kidney weights	(27)
Polyethylene microplastics with a diameter of 10-150 μm	C57BL/6 mice	6, 60, and 600 μg/dy	Dietary exposure for 5 weeks	16S rRNA sequencing of fecal samples	The α- and β-diversity of the mouse microbiota increased. Staphylococcus increased, while Parabacteroides decreased	Serum cytokine; T cells in the spleen; TLR4, AP-1, and IRF5 expression; intestinal histology.	Serum concentrations of IL-1α increased; the percentage of Th17 and T_{regs} cells among $CD4^+$ cells decreased; edema occurred and lymphocyte and plasma cell infiltration was observed in the lamina propria of the colon and duodenum; TLR4, AP-1, and IRF5 expression significantly increased in the colon and duodenum.	(28)
Cuboid CuO nanoparticles with a dimension area of 20 nm by 50 nm	*Eisenia fetida* with a weight range between 300 and 600 mg	160 mg/kg soil	Exposure to soil containing ENMs for 28 days	16S rRNA sequencing of microbiota in gut tissue	*Candidatus Lumbricincola* and *Luteolibacter* decreased	Histology of the gut epithelium and longitudinal muscle tissue; expression of coelomic cytolytic factor, lysenin/fetidin and lysozyme.	No overt effect on tissue integrity, and immune responses	(29)

Doses relevant for human exposure level are marked using underline. AP-1, activating protein-1; Bw, body weight; CuO, copper oxide; DSS, dextran sulfate sodium; Dy, day; GIT, gastrointestinal tract; IL, interleukin; Ig, immunoglobin; IRF5, interferon regulatory factor 5; LPS, lipopolysaccharide; Mo, month; MWCNT, multiple-walled carbon nanotubes; PVP, polyvinyl pyrrolidone; SWCNT, single-walled carbon nanotubes; Th17, T helper type 17; TNBS, trinitrobenzene sulfonic acid; TLR4, Toll-like receptor 4; TNF, tumour necrosis factor; Wk, week; ZnO, zinc oxide.

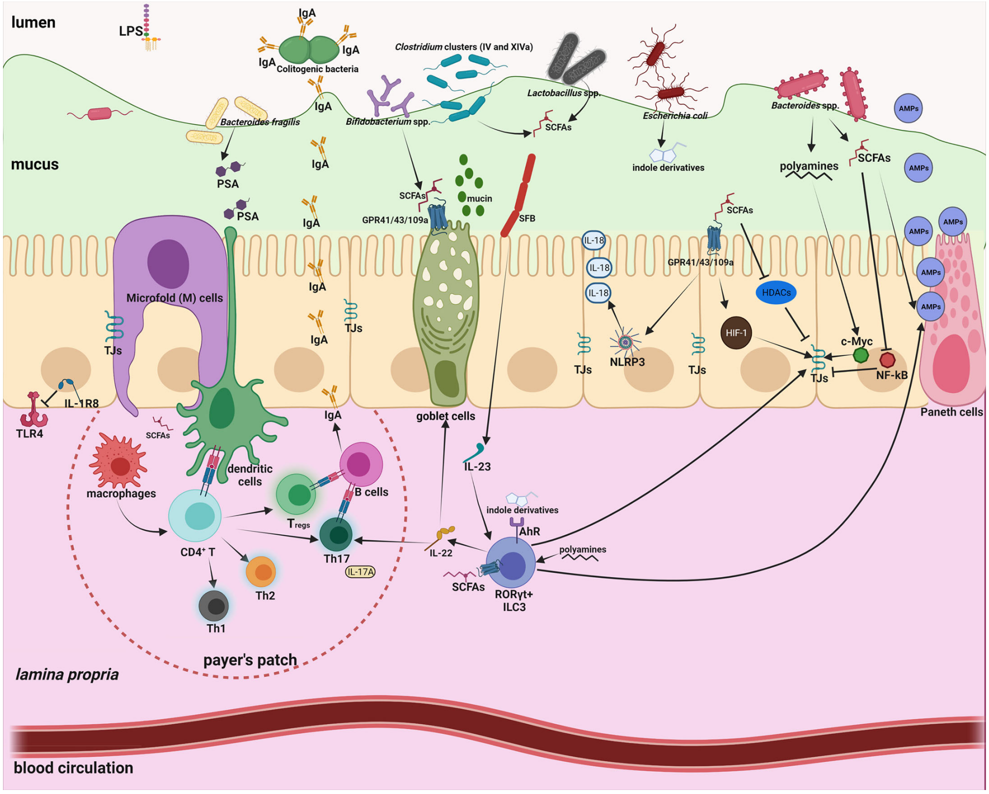

FIGURE 1 | Intestinal homeostasis is tightly controlled by gut microbiota through a large number of microbial metabolites/components. Intestinal mucus not only provides a habitat for bacterial colonization but also serves as a lubricant barrier to restrict most gut microbes in the outer layer. Microfold (M) cells above the Peyer's patch are essential to transport microbiota-derived metabolites/components to maintain the homeostasis of the mucosal immune system. 1) The effects of short-chain-fatty-acids (SCFAs) are manifold, including enhanced mucus production; inhibition of nuclear factor-κB (NF-κB); activation of NLR-family-pyrin-domain-containing-3 (NLRP3) inflammasomes and subsequent production of interleukin-18 (IL-18); enhanced antimicrobial peptide (AMP) production; polarization of anti-inflammatory macrophages; increased Immunoglobulin A (IgA) secretion; reduced expression of T cell-activating molecules on antigen-presenting cells; and increased number and function of colonic regulatory T (T_{regs}) cells. 2) Polyamines can activate $ROR^{γt+}$ group 3 innate lymphoid cells (ILC3) and induce production of IL-22, which promote mucus and AMP secretion, and ensure commensal compartmentalization from the intestinal epithelium. 3) Indole derivatives produced by gut commensals can stimulate Aryl-Hydrocarbon-Receptor (AhR) to activate ILC3 and fortify the epithelium barrier function. 4) Polysaccharide A (PSA) from *Bacteroides fragilis* is taken up by DCs, processed and presented to naive $CD4^+$ T cells, inducing the expansion of $FOXP3^+$ T_{reg} cells. 5) Attachment of segmented filamentous bacteria (SFB) to the epithelium enhances differentiation and expansion of $CD4^+$ Th17 cells. $Foxp3^+$ Treg cells and Th17 cells localize in the Peyer's patches, and induce B cell class-switch and IgA production, which in turn remodels microbiota. 6) Basolateral location of the LPS receptor TLR4 on IECs and expression of the anti-inflammatory IL-1R8 allow proper immune tolerance.

migration and maturation by activating mitogen-activated protein kinase (MAPK) and NF-κB signaling pathways (56). SCFAs can block the DC generation from bone marrow stem cells (57), and down-regulate expression of the T cell-stimulatory proteins CD80, CD83 and major-histocompatibility-complex class II (MHCII) (58).

Through its effects on APCs that produce several cytokines necessary for T cell activation, the gut microbiota is also involved in differentiation of naïve $CD4^+$ T cells into defined subsets, including T helper (Th1, Th2 and Th17) and regulatory T cells (T_{regs}). Inhibition of HDAC by SCFAs can regulate the mTOR–S6K pathway required for generation of Th17, Th1, and IL-10^+ T cells (59). T_{regs} have important anti-inflammatory roles, allowing the immune system to tolerate antigens derived from gut microbiota and diet. Through binding to GPR43, SCFAs can stimulate T_{regs} proliferation (60). Additionally, SCFAs control the expression of genes necessary for plasma B cell differentiation and Immunoglobulin A (IgA) production (61). As the largest class of immunoglobulins in the intestinal mucosa, IgA targets microbial antigens and preferentially coats colitogenic bacteria, therefore preventing inflammation and perturbation of intestinal homeostasis (62).

NUMEROUS ENMs COULD RESHAPE THE GUT MICROBIOTA SIGNATURE BUT IT IS NOT A GENERAL EFFECT

ENMs might interact with gut microbes in different manners (**Figure 2**). Of special concern is the intrinsic antimicrobial potency of some ENMs. Nanoparticulate Au, Ag, TiO_2 and

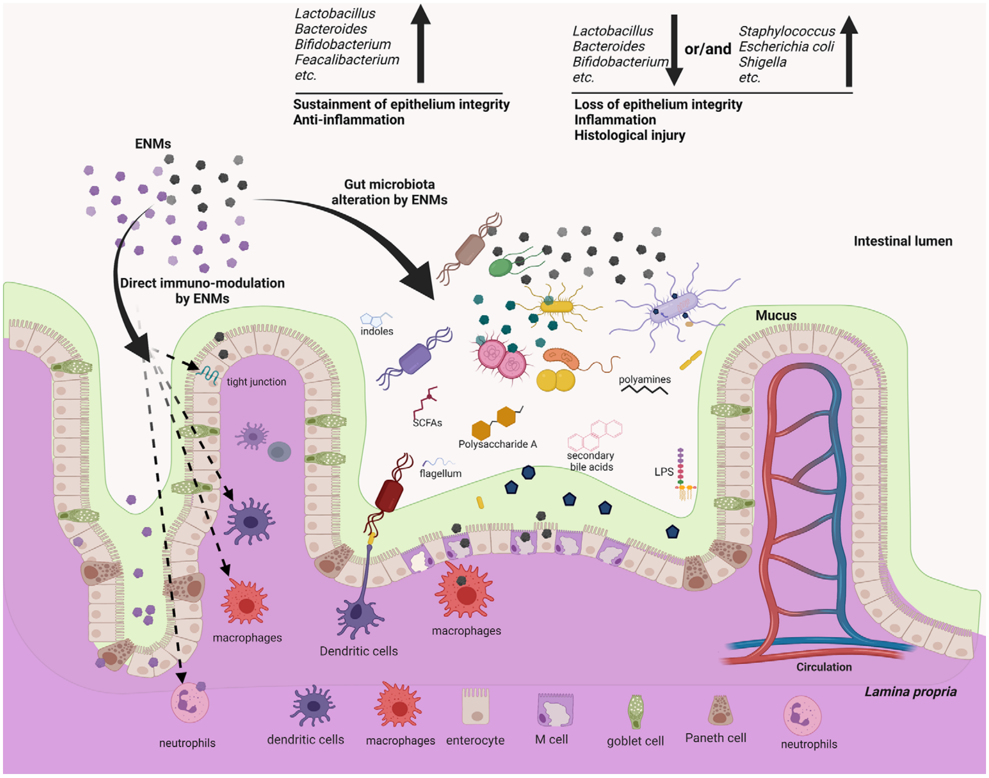

FIGURE 2 | ENMs could not only modulate several components of the mucosal immune systems directly, but also reshape the gut microbiota, which may potentially act as an alternative but important regulator to mediate the immuno-modulatory effects of ENMs. ENMs could accumulate and directly interact with neutrophils, macrophages, dendritic cells (DCs) and the complement system to modulate innate/inflammatory immune responses. On the other hand, several metallic and non-metallic ENMs are proved to be bactericidal, either impairing the bacterial membrane, or causing intracellular oxidative stress, or generating genotoxicity. As responses to the ENM bactericidal effects, members of gut microbiota may rapidly develop resistance, but the associated molecular strategies and efficacy often differ among distinct members. Many *in vitro* and *in vivo* assays showed that ENMs can alter the gut microbiota profile, enrich the relative abundance of pathogens or decrease that of gut commensals. This effect often associates with intestinal inflammation and tissue injury. While some ENMs could increase gut commensals, which in turn exert anti-inflammatory effects. Conversely, a few works show that the gut microbiota remains resilient following oral exposure to ENMs, indicating that the ENM effect on gut microbiota/mucosal immunity is not general.

ZnO can exert bactericidal activity by disrupting the bacterial membrane (63, 64), inducing intracellular reactive oxygen species (64, 65) and causing direct genotoxicity (66). Conversely, iron oxide and graphene ENMs can promote the growth of some bacterial species, with mechanisms still largely unknown (67, 68). Adding to the complexity is that many gut microbes could rapidly develop strategies to resist ENM bactericidal actions (69). Gram-negative bacteria are thought to be more tolerant to ENMs, in that a lower amount of the negatively charged peptidoglycan may be less effective in trapping the positively-charged metal ions, while other studies argue that Gram-positive bacteria have thicker membranes to ensure stronger protection (69, 70). The resistance mechanism to ENMs could be specific at the bacterial species/strain level. The gut microbiota remodeling effect of ENMs has been substantiated by a panel of *in vivo* assays. For instance, dietary Ag ENMs for mice decreased *Odoribacteraceae, Bacteroidaceae* and the S24-7 family while increasing *Lactobacillaceae* and *Lachnospiraceae* (17). Oral gavage of TiO_2 ENMs in mice also modulated the gut microbiota, with *Bacteroides* and *Akkermansia* increased (22). Oral administration of non-metallic single-walled carbon nanotubes (SWCNTs) modestly altered the α- and β-diversity of the mouse microbiome (27). The modulation of animal gut microbiota by other ENMs is systemically summarized in recent reviews, which include nanoparticulate plastics, graphene oxide, multi-walled carbon nanotubes (MWCNT), SWCNT, Ag, ZnO, MoO_3, MoS_2, TiO_2, CuO and SiO_2 (5, 71, 72). Numerous *in vitro* assays also validate the ENM modulatory effect on gut microbiota samples (68, 73–75). Importantly, there appears to be no consensus effect, as multiple ENM-related factors (dose, physicochemical nature, particle size, surface charge, shape and stability) might dictate their modulatory mechanisms and efficacy (64, 76). In addition, the gut microbiota signature varies among individuals, and even within the same subject it changes with time, food intake and health conditions (77–79).

One may suspect the modulatory effect of ENMs on gut microbiota. Because the link between immunity and microbiota is bidirectional (32), could it be possible that ENMs affect immunity and as a consequence the microbiota? Indeed, ENMs could accumulate in the intestine, favor inflammatory responses and impair the barrier function, including IEC apoptosis, tight junction opening, decreased AMP production, Th1/T_{regs} imbalance, aberrant IgA secretion and inflammatory activation of macrophages (72). In this situation, the gut microbiota can be in turn altered by the mucosal immunity. But, a considerable number of ENMs (Ag, SWCNT, CuO, TiO_2) are shown to alter the gut microbiota without inducing any detectable changes in intestinal immunity (17, 22, 27, 29). These data suggest that ENMs may cooperate with the mucosal immunity to modulate the gut microbiota.

THE POTENTIAL EFFECT OF ENM-ALTERED MICROBIOTA ON INTESTINAL INFLAMMATION

As discussed above, microbiota-derived metabolites such as SCFAs have important roles in the regulation of gut immunity (**Figure 1**), while ENM exposure that reduces SCFA-producing bacteria may perturb the immune homeostasis and cause inflammation (**Table 1**). Indeed, gut microbiota dysbiosis appears to tightly associate with inflammatory bowel disease (IBD), a chronic and relapsing inflammatory disorder of the intestine (80). This link has been observed in several *in vivo* assays that model GIT exposure to ENMs. Oral administration of Ag ENM (2.5 mg/kg body weight daily) in mice profoundly reduced the *Firmicutes* to *Bacteroidetes* ratio, specifically due to an increase in *Alistipes*, *Bacteroides* and *Prevotella*, and a significant decrease in SCFA-producing *Lactobacillus*. The altered microbiota could cause some IBD-like symptoms, including disrupted epithelium structure, increased intestinal permeability and upregulation of inflammatory cytokines (IL-1β, IL-6 and TNF-α) (18). In the same study, oral gavage of TiO_2 ENMs (2.5 mg/kg body weight daily) significantly decreased the probiotic *Bacteroides* and triggered a low-grade colonic inflammation (18). Likewise, administration of SWCNT, MWCNT and graphene oxide ENMs (2.5 mg/kg body weight daily) in mice disrupted the gut microbiota signature, with commensal *Lactobacillus* and *Bacteroides* decreased. The exposed mice displayed tissue injury, increased intestinal permeability and elevated production of inflammatory IL-1β, IL-6, and TNF-α (26).

Moreover, enrichment of pathogens and associated virulence factors following ENM administration could also cause intestinal inflammation (81). The work of Chen et al. showed that oral administration of TiO_2 ENMs (50 mg/kg body weight) in rats decreased the number of goblet cells, elicited immune cell infiltration and mitochondrial abnormalities in the colon tissues, suggesting redox imbalance and inflammation. TiO_2 ENM treatment remarkably affected the fecal metabolite profile, and particularly enriched the LPS content (23). In another work, oral gavage of TiO_2 ENM (100 mg/kg body weight daily) in mice impaired the intestinal microvilli structure, and increased *Escherichia* and *Shigella*, two potential pathogens for elicitation of intestinal inflammation (22). Dietary nanoplastics (600 μg daily) for mice significantly increased pathogenic *Staphylococcus* abundance alongside a decrease in *Parabacteroides* (28). The ENM-feeding group displayed a chronic intestinal inflammation, such as increased serum IL-1α, abnormal ratio of Th17 and T_{regs} among $CD4^+$ cells, infiltration of lymphocytes and plasma B cells in the *lamina propria*, and higher expression of inflammatory markers (TLR4, AP-1, and IRF5) (28). In these cases, ENMs may enrich opportunistic pathogens or liberate the membrane-bound PAMPs from bacterial cells (82). The inflammatory antigens, such as LPS, exotoxin and flagellin, would bind to PRRs on IECs and immune cells, thus activating inflammatory pathways and promoting an excessive intestinal inflammation (83–86). However, most of these *in vivo* studies based on animal models rarely simulated the realistic human exposure condition. **Table 1** details such shortcomings: either subjects were exposed to an excessive dose of ENMs, or ENMs were administered alone without food which is not a real-life fashion. Whether ENMs were contaminated by LPS was not checked, either.

There is no general effect of ENMs on gut microbiota and intestinal immunity. Contrary to the aforementioned adverse effects, other studies showed that ENM ingestion can increase commensal microbes and exert anti-inflammatory effects. Dietary ZnO ENMs (600 mg/kg food) for weaned piglets increased *Lactobacillus*, leading to upregulation of tight junction proteins and antioxidant enzymes, and decreased expression of inflammatory interferon-γ (IFN-γ), IL-1β, TNF-α and NF-κB (25). Similarly, oral gavage of Ag ENMs (5ng daily) attenuated the dextran sodium sulfate (DSS)-induced IBD symptoms in mice, probably by increasing *Lactobacillus* and decreasing *Clostridium perfringens* and *Escherichia coli* (19). Enrichment of *Lactobacillus* was found in these works, again highlighting the protective role of SCFA-producers in epithelium integrity and anti-inflammatory responses.

Strikingly, several studies found no significant effect of ENMs (Au, CuO, Ag and lysine-modified SWCNTs) on intestinal immunity (17, 20, 21, 27, 29, 87). One possibility is that most ENMs may be rapidly excreted following ingestion, so few accumulate in the GIT and they are insufficient to modulate the immune responses. Indeed, 270-day consecutive dietary supplementation with ZnO ENMs (1600 mg/kg food) for mice revealed no detectable ENM distribution in the GIT (88). Hence, this work indicates that there is no general effect regarding the biodistribution and accumulation, it should be specific to each ENM. Additionally, the mucus layer that is mainly composed of highly-glycosylated secreted proteins overlying the intestinal epithelium could trap ENMs and minimize their contact with gut microbes and mucosal cells (8). This can explain why the modulatory effect of ENMs on gut microbes *in vitro* is always greater than that *in vivo*. When the earthworms were exposed to soil with CuO or Ag ENMs, the gut microbiota remained largely resilient, whereas both ENMs significantly changed the soil bacterial community composition (89). Moreover, though some ENMs can modify the gut microbiota, members of the core commensal consortium are not affected; or the roles of redundant symbionts affected by ENMs could be compensated by other unchanged commensals. For example, exposure of earthworms to soil supplemented with CuO ENMs (160 mg/kg) induced substantial changes in the gut microbiota with a significant decrease in the symbiont *Candidatus Lumbricincola*, but it had no effect on the immune competence (29). Thereby, the gut microbiota might adapt itself in a way (which needs to be demonstrated) that ensures maintaining a proper immune homeostasis.

CONCLUSIONS AND PERSPECTIVES

To summarize, increasing observations have claimed a link between GIT exposure to ENMs, gut microbiota dysbiosis and intestinal inflammation (**Figure 2**). Such effects of ENMs are often dose-dependent. We acknowledge that in a few cases ENMs could induce microbiota dysbiosis characterized by a decrease in commensals (*Lactobacillus, Bacteroides*, *Bifidobacterium*, *etc.*) and/or an enrichment of other members (*E. coli, Shigella, Listeria, etc.*), which in turn cause an intestinal inflammation, compromise epithelium integrity and induce IBD-like symptoms (**Figure 2**). But these works suffer shortcomings and are not relevant for human exposure doses or uptake conditions. By contrast, little or no overt effect on intestinal immunity has been found in a large number of *in vivo* assays, where ENMs are orally administered in a more realistic dose or fashion. Notably, most *in vivo* studies investigate the immunotoxicity of ENMs in healthy individuals, while it might be more prominent in those with intestinal inflammation (such as IBD). Indeed, inflammatory symptoms like mucus defects (90), dysfunctional macrophages (91), *etc.* could increase and extend the exposure of intestinal epithelium to ENMs. Interestingly, the DSS-induced IBD symptoms in mice can be either exacerbated (92) or attenuated (19) following oral intake of ENMs, suggesting that ENM exposure do not necessarily have detrimental consequences, even for those with inflamed intestine. Future works should cover more types of ENMs, simulate the real-life ENM exposure situation, exploit both healthy and inflammatory host model, and draw cautious conclusions.

The *in vivo* studies on different animal models show extensive variation regarding the ENM effects on gut microbiota or intestinal immunity (**Table 1**). This may be due to discrepancies in the overall experimental settings (animal species, age, EMN exposure time, dose and uptake manner), the ENM physicochemical nature (size, shape, surface decoration and charge), the possible *in vivo* bio-transformation of ENMs and the methodology for gut microbiota analysis (**Table 1**). A unifying exposure model is required.

However, pitfalls of current animal models should be considered when translating gut microbiota research results to humans. The murine gut microbiota resembles the human one at phylum level, but differs at genus and species level (93). The anatomy and physiological functions of several GIT segments in the mouse are also different from those of humans (93). Therefore, a future perspective is to establish human models, necessarily *in vitro*, based on primary cells. To this end, microfluidic intestine-on-chips that can establish a prolonged coculture of human intestinal epithelium and gut microbes could be a promising *in vitro* human model to evaluate the ENM immunotoxicity (94, 95). When supplemented with immune cells, the intestine-on-a-chip could enable us to monitor the dynamics of ENM behavior in the gut tissue, gut microbiota changes, intestinal barrier function, immune cell activation and inflammation, thus providing predictive values on the ENM immunotoxicity. An additional but important point is the variability of gut microbiota, not only inter-individually but also at the intra-individual level (for instance in different health conditions). This calls for the need of a personalized profiling of the ENM effects on gut immunity, as it will depend on the individual microbiota in a given moment. Future immuno-nanosafety models, like the intestine-on-a-chip mentioned above, will therefore need to include the individual microbiota and the innate immune cells (in particular macrophages) derived from the individual subject.

AUTHOR CONTRIBUTIONS

MT, JQ, and LL devised the study and wrote the manuscript. SL, LW, and ZH contributed to literature search and gave insightful suggestions in revising this work. All authors contributed to the article and approved the submitted version.

FUNDING

This work was supported by the National Natural Science Foundation of China (81900071).

ACKNOWLEDGMENTS

BioRender was used to create schematic representations.

REFERENCES

1. De Jong WH, Borm PJA. Drug Delivery and Nanoparticles: Applications and Hazards. *Int J Nanomed* (2008) 3(2):133–49. doi: 10.2147/ijn.s596
2. Ge L, Li Q, Wang M, Ouyang J, Li X, Xing MMQ. Nanosilver Particles in Medical Applications: Synthesis, Performance, and Toxicity. *Int J Nanomed* (2014) 9:2399–407. doi: 10.2147/IJN.S55015
3. Weir A, Westerhoff P, Fabricius L, Hristovski K, Von Goetz N. Titanium Dioxide Nanoparticles in Food and Personal Care Products. *Environ Sci Technol* (2012) 46(4):2242–50. doi: 10.1021/es204168d
4. Vance ME, Kuiken T, Vejerano EP, Mcginnis SP, Hochella MFJr., Rejeski D, et al. Nanotechnology in the Real World: Redeveloping the Nanomaterial Consumer Products Inventory. *Beilstein J Nanotechnol* (2015) 6:1769–80. doi: 10.3762/bjnano.6.181
5. Hirt N, Body-Malapel M. Immunotoxicity and Intestinal Effects of Nano- and Microplastics: A Review of the Literature. *Part Fibre Toxicol* (2020) 17(1):57. doi: 10.1186/s12989-020-00387-7
6. Carrouel F, Viennot S, Ottolenghi L, Gaillard C, Bourgeois D. Nanoparticles as Anti-Microbial, Anti-Inflammatory, and Remineralizing Agents in Oral Care Cosmetics: A Review of the Current Situation. *Nanomater (Basel Switzerland)* (2020) 10(1):140. doi: 10.3390/nano10010140

7. Park E-J, Yi J, Kim Y, Choi K, Park K. Silver Nanoparticles Induce Cytotoxicity by a Trojan-Horse Type Mechanism. *Toxicol In Vitro* (2010) 24(3):872–8. doi: 10.1016/j.tiv.2009.12.001
8. Georgantzopoulou A, Serchi T, Cambier S, Leclercq CC, Renaut J, Shao J, et al. Effects of Silver Nanoparticles and Ions on a Co-Culture Model for the Gastrointestinal Epithelium. *Part Fibre Toxicol* (2016) 13(1):9. doi: 10.1186/s12989-016-0117-9
9. Mortensen NP, Moreno Caffaro M, Aravamudhan S, Beeravalli L, Prattipati S, Snyder RW, et al. Simulated Gastric Digestion and In Vivo Intestinal Uptake of Orally Administered CuO Nanoparticles and TiO_2 E171 in Male and Female Rat Pups. *Nanomater (Basel Switzerland)* (2021) 11(6):1487. doi: 10.3390/nano11061487
10. Zolnik BS, GonzíLez-FerníNdez AF, Sadrieh N, Dobrovolskaia MA. Minireview: Nanoparticles and the Immune System. *Endocrinology* (2010) 151(2):458–65. doi: 10.1210/en.2009-1082
11. Boraschi D, Italiani P, Palomba R, Decuzzi P, Duschl A, Fadeel B, et al. Nanoparticles and Innate Immunity: New Perspectives on Host Defence. *Semin Immunol* (2017) 34:33–51. doi: 10.1016/j.smim.2017.08.013
12. Dobrovolskaia MA, Shurin M, Shvedova AA. Current Understanding of Interactions Between Nanoparticles and the Immune System. *Toxicol Appl Pharmacol* (2016) 299:78–89. doi: 10.1016/j.taap.2015.12.022
13. David CA, Owen A, Liptrott NJ. Determining the Relationship Between Nanoparticle Characteristics and Immunotoxicity: Key Challenges and Approaches. *Nanomedicine* (2016) 11(11):1447–64. doi: 10.2217/nnm-2016-0017
14. Tlaskalova-Hogenova H, Vetvicka V, Sterzl J, Stepankova R. Development of Immune Potential and Migration Pattern of Cells From Germfree (Gf) and Conventionally (Conv) Reared Rats. *Adv Exp Med Biol* (1982) 149:515–20. doi: 10.1007/978-1-4684-9066-4_72
15. Li Y, Fujita M, Boraschi D. Endotoxin Contamination in Nanomaterials Leads to the Misinterpretation of Immunosafety Results. *Front Immunol* (2017) 8:472. doi: 10.3389/fimmu.2017.00472
16. Li Y, Shi Z, Radauer-Preiml I, Andosch A, Casals E, Luetz-Meindl U, et al. Bacterial Endotoxin (Lipopolysaccharide) Binds to the Surface of Gold Nanoparticles, Interferes With Biocorona Formation and Induces Human Monocyte Inflammatory Activation. *Nanotoxicology* (2017) 11(9-10):1157–75. doi: 10.1080/17435390.2017.1401142
17. Van Den Brule S, Ambroise J, Lecloux H, Levard C, Soulas R, De Temmerman PJ, et al. Dietary Silver Nanoparticles Can Disturb the Gut Microbiota in Mice. *Part Fibre Toxicol* (2016) 13(1):38. doi: 10.1186/s12989-016-0149-1
18. Chen H, Zhao R, Wang B, Cai C, Zheng L, Wang H, et al. The Effects of Orally Administered Ag, TiO_2 and SiO_2 Nanoparticles on Gut Microbiota Composition and Colitis Induction in Mice. *NanoImpact* (2017) 8:80–8. doi: 10.1016/j.impact.2017.07.005
19. Siczek K, Zatorski H, Chmielowiec-Korzeniowska A, Pulit-Prociak J, Smiech M, Kordek R, et al. Synthesis and Evaluation of Anti-Inflammatory Properties of Silver Nanoparticle Suspensions in Experimental Colitis in Mice. *Chem Biol Drug Des* (2017) 89(4):538–47. doi: 10.1111/cbdd.12876
20. Hadrup N, Loeschner K, Bergstrom A, Wilcks A, Gao X, Vogel U, et al. Subacute Oral Toxicity Investigation of Nanoparticulate and Ionic Silver in Rats. *Arch Toxicol* (2012) 86(4):543–51. doi: 10.1007/s00204-011-0759-1
21. Wilding LA, Bassis CM, Walacavage K, Hashway S, Leroueil PR, Morishita M, et al. Repeated Dose (28-Day) Administration of Silver Nanoparticles of Varied Size and Coating Does Not Significantly Alter the Indigenous Murine Gut Microbiome. *Nanotoxicology* (2016) 10(5):513–20. doi: 10.3109/17435390.2015.1078854
22. Li J, Yang S, Lei R, Gu W, Qin Y, Ma S, et al. Oral Administration of Rutile and Anatase Tio2 Nanoparticles Shifts Mouse Gut Microbiota Structure. *Nanoscale* (2018) 10(16):7736–45. doi: 10.1039/c8nr00386f
23. Chen Z, Han S, Zhou D, Zhou S, Jia G. Effects of Oral Exposure to Titanium Dioxide Nanoparticles on Gut Microbiota and Gut-Associated Metabolism in Vivo. *Nanoscale* (2019) 11(46):22398–412. doi: 10.1039/c9nr07580a
24. Pei X, Xiao Z, Liu L, Wang G, Tao W, Wang M, et al. Effects of Dietary Zinc Oxide Nanoparticles Supplementation on Growth Performance, Zinc Status, Intestinal Morphology, Microflora Population, and Immune Response in Weaned Pigs. *J Sci Food Agric* (2019) 99(3):1366–74. doi: 10.1002/jsfa.9312
25. Xia T, Lai W, Han M, Han M, Ma X, Zhang L. Dietary Zno Nanoparticles Alters Intestinal Microbiota and Inflammation Response in Weaned Piglets. *Oncotarget* (2017) 8(39):64878–91. doi: 10.18632/oncotarget.17612
26. Chen H, Zhao R, Wang B, Zheng L, Ouyang H, Wang H, et al. Acute Oral Administration of Single-Walled Carbon Nanotubes Increases Intestinal Permeability and Inflammatory Responses: Association With the Changes in Gut Microbiota in Mice. *Adv Healthc* (2018) 7(13):1701313. doi: 10.1002/adhm.201701313
27. Mulvey JJ, Littmann ER, Ling L, Mcdevitt MR, Pamer EG, Scheinberg DA. The Effects of Amine-Modified Single-Walled Carbon Nanotubes on the Mouse Microbiota. *Int J Nanomed* (2018) 13:5275–86. doi: 10.2147/IJN.S168554
28. Li B, Ding Y, Cheng X, Sheng D, Xu Z, Rong Q, et al. Polyethylene Microplastics Affect the Distribution of Gut Microbiota and Inflammation Development in Mice. *Chemosphere* (2020) 244:125492. doi: 10.1016/j.chemosphere.2019.125492
29. Swart E, Dvorak J, Hernádi S, Goodall T, Kille P, Spurgeon D, et al. The Effects of in Vivo Exposure to Copper Oxide Nanoparticles on the Gut Microbiome, Host Immunity, and Susceptibility to a Bacterial Infection in Earthworms. *Nanomater (Basel)* (2020) 10(7):1337. doi: 10.3390/nano10071337
30. Kamada N, Kim Y-G, Sham HP, Vallance BA, Puente JL, Martens EC, et al. Regulated Virulence Controls the Ability of a Pathogen to Compete With the Gut Microbiota. *Science* (2012) 336(6086):1325–9. doi: 10.1126/science.1222195
31. Donohoe DR, Garge N, Zhang X, Sun W, O'connell TM, Bunger MK, et al. The Microbiome and Butyrate Regulate Energy Metabolism and Autophagy in the Mammalian Colon. *Cell Metab* (2011) 13(5):517–26. doi: 10.1016/j.cmet.2011.02.018
32. Zheng D, Liwinski T, Elinav E. Interaction Between Microbiota and Immunity in Health and Disease. *Cell Res* (2020) 30(6):492–506. doi: 10.1038/s41422-020-0332-7
33. Belkaid Y, Harrison OJ. Homeostatic Immunity and the Microbiota. *Immunity* (2017) 46(4):562–76. doi: 10.1016/j.immuni.2017.04.008
34. Albhaisi SM, Bajaj JS, Sanyal AJ. Role of Gut Microbiota in Liver Disease. *Am J Physiol Gastrointest Liver Physiol* (2020) 318(1):84–98. doi: 10.1152/ajpgi.00118.2019
35. Morais LH, Schreiber HL, Mazmanian SK. The Gut Microbiota–Brain Axis in Behaviour and Brain Disorders. *Nat Rev Microbiol* (2021) 19(4):241–55. doi: 10.1038/s41579-020-00460-0
36. Rooks MG, Garrett WS. Gut Microbiota, Metabolites and Host Immunity. *Nat Rev Immunol* (2016) 16(6):341–52. doi: 10.1038/nri.2016.42
37. Wang G, Huang S, Wang Y, Cai S, Yu H, Liu H, et al. Bridging Intestinal Immunity and Gut Microbiota by Metabolites. *Cell Mol Life Sci* (2019) 76 (20):3917–37. doi: 10.1007/s00018-019-03190-6
38. Thaiss CA, Zmora N, Levy M, Elinav E. The Microbiome and Innate Immunity. *Nature* (2016) 535(7610):65–74. doi: 10.1038/nature18847
39. Honda K, Littman DR. The Microbiota in Adaptive Immune Homeostasis and Disease. *Nature* (2016) 535(7610):75–84. doi: 10.1038/nature18848
40. Den Besten G, Van Eunen K, Groen AK, Venema K, Reijngoud D-J, Bakker BM. The Role of Short-Chain Fatty Acids in the Interplay Between Diet, Gut Microbiota, and Host Energy Metabolism. *J Lipid Res* (2013) 54(9):2325–40. doi: 10.1194/jlr.R036012
41. Heine H, Rietschel ET, Ulmer AJ. The Biology of Endotoxin. *Mol Biotechnol* (2001) 19(3):279–96. doi: 10.1385/MB:19:3:279
42. Macia L, Tan J, Vieira AT, Leach K, Stanley D, Luong S, et al. Metabolite-Sensing Receptors Gpr43 and Gpr109a Facilitate Dietary Fibre-Induced Gut Homeostasis Through Regulation of the Inflammasome. *Nat Commun* (2015) 6(1):6734. doi: 10.1038/ncomms7734
43. Wrzosek L, Miquel S, Noordine M-L, Bouet S, Chevalier-Curt MJ, Robert V, et al. *Bacteroides Thetaiotaomicron* and *Faecalibacterium Prausnitzii* Influence the Production of Mucus Glycans and the Development of Goblet Cells in the Colonic Epithelium of a Gnotobiotic Model Rodent. *BMC Biol* (2013) 11(1):61. doi: 10.1186/1741-7007-11-61
44. Fusunyan RD, Nanthakumar NN, Baldeon ME, Walker WA. Evidence for an Innate Immune Response in the Immature Human Intestine: Toll-Like Receptors on Fetal Enterocytes. *Pediatr Res* (2001) 49(4):589–93. doi: 10.1203/00006450-200104000-00023

45. Molgora M, Barajon I, Mantovani A, Garlanda C. Regulatory Role of Il-1r8 in Immunity and Disease. *Front Immunol* (2016) 7:149. doi: 10.3389/fimmu.2016.00149
46. Parada Venegas D, de la Fuente MK, Landskron G, González MJ, Quera R, Dijkstra G, et al. Short Chain Fatty Acids (Scfas)-Mediated Gut Epithelial and Immune Regulation and Its Relevance for Inflammatory Bowel Diseases. *Front Immunol* (2019) 10:277. doi: 10.3389/fimmu.2019.00277
47. Fachi JL, Felipe JDS, Pral LP, Da Silva BK, Corrêa RO, De Andrade MCP, et al. Butyrate Protects Mice From *Clostridium Difficile*-Induced Colitis Through an Hif-1-Dependent Mechanism. *Cell Rep* (2019) 27(3):750–61.e7. doi: 10.1016/j.celrep.2019.03.054
48. Moore R, Pothoulakis C, Lamont JT, Carlson S, Madara JL. C. Difficile Toxin a Increases Intestinal Permeability and Induces Cl- Secretion. *Am J Physiol Gastrointest Liver Physiol* (1990) 259(2):G165–G72. doi: 10.1152/ajpgi.1990.259.2.G165
49. Karve SS, Pradhan S, Ward DV, Weiss AA. Intestinal Organoids Model Human Responses to Infection by Commensal and Shiga Toxin Producing *Escherichia Coli*. *PloS One* (2017) 12(6):e0178966. doi: 10.1371/journal.pone.0178966
50. Guo S, Al-Sadi R, Said HM, Ma TY. Lipopolysaccharide Causes an Increase in Intestinal Tight Junction Permeability In Vitro and In Vivo by Inducing Enterocyte Membrane Expression and Localization of Tlr-4 and Cd14. *Am J Pathol* (2013) 182(2):375–87. doi: 10.1016/j.ajpath.2012.10.014
51. Qiu J, Heller JJ, Guo X, Chen Z-ME, Fish K, Fu Y-X, et al. The Aryl Hydrocarbon Receptor Regulates Gut Immunity Through Modulation of Innate Lymphoid Cells. *Immunity* (2012) 36(1):92–104. doi: 10.1016/j.immuni.2011.11.011
52. Martinez FO, Sica A, Mantovani A, Locati M. Macrophage Activation and Polarization. *Front Biosci* (2008) 13(2):453–61. doi: 10.2741/2692
53. Ji J, Shu D, Zheng M, Wang J, Luo C, Wang Y, et al. Microbial Metabolite Butyrate Facilitates M2 Macrophage Polarization and Function. *Sci Rep* (2016) 6(1):24838. doi: 10.1038/srep24838
54. Smith PD, Smythies LE, Shen R, Greenwell-Wild T, Gliozzi M, Wahl SM. Intestinal Macrophages and Response to Microbial Encroachment. *Mucosal Immunol* (2011) 4(1):31–42. doi: 10.1038/mi.2010.66
55. Singh N, Gurav A, Sivaprakasam S, Brady E, Padia R, Shi H, et al. Activation of Gpr109a, Receptor for Niacin and the Commensal Metabolite Butyrate, Suppresses Colonic Inflammation and Carcinogenesis. *Immunity* (2014) 40(1):128–39. doi: 10.1016/j.immuni.2013.12.007
56. Granucci F, Ferrero E, Foti M, Aggujaro D, Vettoretto K, Ricciardi-Castagnoli P. Early Events in Dendritic Cell Maturation Induced by Lps. *Microbes Infect* (1999) 1(13):1079–84. doi: 10.1016/S1286-4579(99)00209-9
57. Singh N, Thangaraju M, Prasad PD, Martin PM, Lambert NA, Boettger T, et al. Blockade of Dendritic Cell Development by Bacterial Fermentation Products Butyrate and Propionate Through a Transporter (Slc5a8)-Dependent Inhibition of Histone Deacetylases. *J Biol Chem* (2010) 285(36):27601–8. doi: 10.1074/jbc.M110.102947
58. Liu L, Li L, Min J, Wang J, Wu H, Zeng Y, et al. Butyrate Interferes With the Differentiation and Function of Human Monocyte-Derived Dendritic Cells. *Cell Mol Immunol* (2012) 277(1):66–73. doi: 10.1016/j.cellimm.2012.05.011
59. Park J, Kim M, Kang SG, Jannasch AH, Cooper B, Patterson J, et al. Short-Chain Fatty Acids Induce Both Effector and Regulatory T Cells by Suppression of Histone Deacetylases and Regulation of the Mtor–S6k Pathway. *Mucosal Immunol* (2015) 8(1):80–93. doi: 10.1038/mi.2014.44
60. Smith PM, Howitt MR, Panikov N, Michaud M, Gallini CA, Bohlooly –M, et al. The Microbial Metabolites, Short-Chain Fatty Acids, Regulate Colonic T_{reg} Cell Homeostasis. *Science* (2013) 341(6145):569–73. doi: 10.1126/science.1241165
61. Kim M, Qie Y, Park J. And Kim Chang H. Gut Microbial Metabolites Fuel Host Antibody Responses. *Cell Host Microbe* (2016) 20(2):202–14. doi: 10.1016/j.chom.2016.07.001
62. Palm NW, De Zoete MR, Cullen TW, Barry NA, Stefanowski J, Hao L, et al. Immunoglobulin a Coating Identifies Colitogenic Bacteria in Inflammatory Bowel Disease. *Cell* (2014) 158(5):1000–10. doi: 10.1016/j.cell.2014.08.006
63. Smetana AB, Klabunde KJ, Marchin GR, Sorensen CM. Biocidal Activity of Nanocrystalline Silver Powders and Particles. *Langmuir* (2008) 24(14):7457–64. doi: 10.1021/la800091y
64. Guerrero Correa M, Martínez FB, Vidal CP, Streitt C, Escrig J, De Dicastillo CL. Antimicrobial Metal-Based Nanoparticles: A Review on Their Synthesis, Types and Antimicrobial Action. *Beilstein J Nanotechnol* (2020) 11:1450–69. doi: 10.3762/bjnano.11.129
65. Park H, Kim JY, Kim J, Lee J, Hahn J, Gu MB, et al. Silver-Ion-Mediated Reactive Oxygen Species Generation Affecting Bactericidal Activity. *Water Res* (2009) 43(4):1027–32. doi: 10.1016/j.watres.2008.12.002
66. Gulbagca F, Ozdemir S, Gulcan M, Sen F. Synthesis and Characterization of Rosa Canina-Mediated Biogenic Silver Nanoparticles for Anti-Oxidant, Antibacterial, Antifungal, and DNA Cleavage Activities. *Heliyon* (2019) 5(12):e02980. doi: 10.1016/j.heliyon.2019.e02980
67. Borcherding J, Baltrusaitis J, Chen H, Stebounova L, Wu C-M, Rubasinghege G, et al. Iron Oxide Nanoparticles Induce *Pseudomonas Aeruginosa* Growth, Induce Biofilm Formation, and Inhibit Antimicrobial Peptide Function. *Environ Sci Nano* (2014) 1(2):123–32. doi: 10.1039/C3EN00029J
68. Lahiani MH, Gokulan K, Williams K, Khare S. Impact of Pristine Graphene on Intestinal Microbiota Assessed Using a Bioreactor-Rotary Cell Culture System. *ACS Appl Mater Interfaces* (2019) 11(29):25708–19. doi: 10.1021/acsami.9b07635
69. Fröhlich EE, Fröhlich E. Cytotoxicity of Nanoparticles Contained in Food on Intestinal Cells and the Gut Microbiota. *Int J Mol Sci* (2016) 17(4):509. doi: 10.3390/ijms17040509
70. Xie Y, Wu B, Zhang X-X, Yin J, Mao L, Hu M. Influences of Graphene on Microbial Community and Antibiotic Resistance Genes in Mouse Gut as Determined by High-Throughput Sequencing. *Chemosphere* (2016) 144:1306–12. doi: 10.1016/j.chemosphere.2015.09.076
71. Zhang Y, Mortimer M, Guo L-H. Interplay Between Engineered Nanomaterials and Microbiota. *Environ Sci Nano* (2020) 7(9):2454–85. doi: 10.1039/D0EN00557F
72. Lamas B, Martins Breyner N, Houdeau E. Impacts of Foodborne Inorganic Nanoparticles on the Gut Microbiota-Immune Axis: Potential Consequences for Host Health. *Part Fibre Toxicol* (2020) 17(1):19. doi: 10.1186/s12989-020-00349-z
73. Das P, Mcdonald J, Petrof E, Allen-Vercoe E, Walker V. Nanosilver-Mediated Change in Human Intestinal Microbiota. *J Nanomed Nanotechnol* (2014) 5:235. doi: 10.4172/2157-7439.1000235
74. Cattò C, Garuglieri E, Borruso L, Erba D, Cristina M, Cappitelli F, et al. Impacts of Dietary Silver Nanoparticles and Probiotic Administration on the Microbiota of an in-Vitro Gut Model. *Environ Pollut* (2018) 245:754–63. doi: 10.1016/j.envpol.2018.11.019
75. Fondevila M, Herrer R, Casallas MC, Abecia L, Ducha JJ. Silver Nanoparticles as a Potential Antimicrobial Additive for Weaned Pigs. *Anim Feed Sci Technol* (2009) 150(3):259–69. doi: 10.1016/j.anifeedsci.2008.09.003
76. Marambio-Jones C, Hoek EMV. A Review of the Antibacterial Effects of Silver Nanomaterials and Potential Implications for Human Health and the Environment. *J Nanopart Res* (2010) 12(5):1531–51. doi: 10.1007/s11051-010-9900-y
77. Qin J, Li R, Raes J, Arumugam M, Burgdorf KS, Manichanh C, et al. A Human Gut Microbial Gene Catalogue Established by Metagenomic Sequencing. *Nature* (2010) 464(7285):59–65. doi: 10.1038/nature08821
78. Brooks AW, Priya S, Blekhman R, Bordenstein SR. Gut Microbiota Diversity Across Ethnicities in the United States. *PloS Biol* (2018) 16(12):e2006842–e. doi: 10.1371/journal.pbio.2006842
79. Fan Y, Pedersen O. Gut Microbiota in Human Metabolic Health and Disease. *Nat Rev Microbiol* (2021) 19(1):55–71. doi: 10.1038/s41579-020-0433-9
80. Shapiro JM, Subedi S, Leleiko NS. Inflammatory Bowel Disease. *Pediatr Rev* (2016) 37(8):337–47. doi: 10.1542/pir.2015-0110
81. Nishida A, Inoue R, Inatomi O, Bamba S, Naito Y, Andoh A. Gut Microbiota in the Pathogenesis of Inflammatory Bowel Disease. *J Clin Gastroenterol* (2018) 11(1):1–10. doi: 10.1007/s12328-017-0813-5
82. Lepper P, Held T, Schneider E, Bölke E, Gerlach H, Trautmann M. Clinical Implications of Antibiotic-Induced Endotoxin Release in Septic Shock. *J Intensive Care Med* (2002) 28(7):824–33. doi: 10.1007/s00134-002-1330-6
83. Neal MD, Leaphart C, Levy R, Prince J, Billiar TR, Watkins S, et al. Enterocyte Tlr4 Mediates Phagocytosis and Translocation of Bacteria Across the Intestinal Barrier. *J Immunol* (2006) 176(5):3070–9. doi: 10.4049/jimmunol.176.5.3070

84. Elena G, Giovanna D, Brunella P, De Anna F, Alessandro M, Antonietta TM. Proinflammatory Signal Transduction Pathway Induced by *Shigella Flexneri* Porins in Caco-2 Cells. *Braz J Microbiol* (2009) 40(3):701–13. doi: 10.1590/S1517-838220090003000036
85. Ray A, Biswas T. Porin of *Shigella Dysenteriae* Enhances Toll-Like Receptors 2 and 6 of Mouse Peritoneal B-2 Cells and Induces the Expression of Immunoglobulin M, Immunoglobulin G2a and Immunoglobulin A. *Immunology* (2005) 114(1):94–100. doi: 10.1111/j.1365-2567.2004.02002.x
86. Song WS, Jeon YJ, Namgung B, Hong M, Yoon S-I. A Conserved Tlr5 Binding and Activation Hot Spot on Flagellin. *Sci Rep* (2017) 7(1):40878. doi: 10.1038/srep40878
87. Li J, Cha R, Zhao X, Guo H, Luo H, Wang M, et al. Gold Nanoparticles Cure Bacterial Infection With Benefit to Intestinal Microflora. *ACS Nano* (2019) 13 (5):5002–14. doi: 10.1021/acsnano.9b01002
88. Liu J-H, Ma X, Xu Y, Tang H, Yang S-T, Yang Y-F, et al. Low Toxicity and Accumulation of Zinc Oxide Nanoparticles in Mice After 270-Day Consecutive Dietary Supplementation. *Toxicol Res* (2017) 6:134–43. doi: 10.1039/c6tx00370b
89. Swart E, Goodall T, Kille P, Spurgeon DJ, Svendsen C. The Earthworm Microbiome Is Resilient to Exposure to Biocidal Metal Nanoparticles. *Environ Pollut* (2020) 267:115633. doi: 10.1016/j.envpol.2020.115633
90. Johansson MEV. Mucus Layers in Inflammatory Bowel Disease. *Inflamm Bowel Dis* (2014) 20(11):2124–31. doi: 10.1097/mib.0000000000000117
91. Na YR, Stakenborg M, Seok SH, Matteoli G. Macrophages in Intestinal Inflammation and Resolution: A Potential Therapeutic Target in Ibd. *Nat Rev Gastroenterol Hepatol* (2019) 16(9):531–43. doi: 10.1038/s41575-019-0172-4
92. Ogawa T, Okumura R, Nagano K, Minemura T, Izumi M, Motooka D, et al. Oral Intake of Silica Nanoparticles Exacerbates Intestinal Inflammation. *Biochem Biophys Res Commun* (2021) 534:540–6. doi: 10.1016/j.bbrc.2020.11.047
93. Nguyen TLA, Vieira-Silva S, Liston A, Raes J. How Informative Is the Mouse for Human Gut Microbiota Research? *Dis Model Mech* (2015) 8(1):1–16. doi: 10.1242/dmm.017400
94. Jalili-Firoozinezhad S, Gazzaniga FS, Calamari EL, Camacho DM, Fadel CW, Bein A, et al. A Complex Human Gut Microbiome Cultured in an Anaerobic Intestine-on-a-Chip. *Nat BioMed Eng* (2019) 3(7):520–31. doi: 10.1038/s41551-019-0397-0
95. Huh D, Kim HJ, Fraser JP, Shea DE, Khan M, Bahinski A, et al. Microfabrication of Human Organs-on-Chips. *Nat Protoc* (2013) 8 (11):2135–57. doi: 10.1038/nprot.2013.137

Conflict of Interest: The authors declare that the research was conducted in the absence of any commercial or financial relationships that could be construed as a potential conflict of interest.

The Editor declared a shared affiliation with some of the authors MT, LW, JQ, LL at the time of review.

frontiers in Immunology

MINI REVIEW
published: 04 October 2021
doi: 10.3389/fimmu.2021.701485

Applications of Magnetite Nanoparticles in Cancer Immunotherapies: Present Hallmarks and Future Perspectives

Qingle Song[1†], *Amaneh Javid*[1,2†], *Guofang Zhang*[1] *and Yang Li*[1*]

[1] Laboratory of Immunology and Nanomedicine, Shenzhen Institute of Advanced Technology, Chinese Academy of Sciences, Shenzhen, China, [2] Department of Biological Sciences, Faculty of Applied Science and Engineering, Science and Arts University, Yazd, Iran

OPEN ACCESS

Edited by:
Janos G. Filep,
Université de Montréal,
Canada

Reviewed by:
Panagiotis F. Christopoulos,
Oslo University Hospital, Norway
Martin Himly,
University of Salzburg, Austria
Paola Italiani,
National Research Council (CNR), Italy

***Correspondence:**
Yang Li
yang.li@siat.ac.cn

[†]These authors have contributed equally to this work and share first authorship

Specialty section:
This article was submitted to Molecular Innate Immunity, a section of the journal Frontiers in Immunology

Received: *28 April 2021*
Accepted: *14 September 2021*
Published: *04 October 2021*

Citation:
Song Q, Javid A, Zhang G and Li Y (2021) Applications of Magnetite Nanoparticles in Cancer Immunotherapies: Present Hallmarks and Future Perspectives. Front. Immunol. 12:701485. doi: 10.3389/fimmu.2021.701485

Current immuno-oncotherapeutic protocols that inhibit tumor immune evasion have demonstrated great clinical success. However, the therapeutic response is limited only to a percentage of patients, and the immune-related adverse events can compromise the therapeutic benefits. Therefore, improving cancer immunotherapeutic approaches that pursue high tumor suppression efficiency and low side effects turn out to be a clinical priority. Novel magnetite nanoparticles (MNPs) exhibit great potential for therapeutic and imaging applications by utilizing their properties of superparamagnetism, good biocompatibility, as well as the easy synthesis and modulation/functionalization. In particular, the MNPs can exert magnetic hyperthermia to induce immunogenic cell death of tumor cells for effective antigen release and presentation, and meanwhile polarize tumor-associated macrophages (TAMs) to M1 phenotype for improved tumor killing capability, thus enhancing the anti-tumor immune effects. Furthermore, immune checkpoint antibodies, immune-stimulating agents, or tumor-targeting agents can be decorated on MNPs, thereby improving their selectivity for the tumor or immune cells by the unique magnetic navigation capability of MNPs to promote the tumor killing immune therapeutics with fewer side effects. This mini-review summarizes the recent progress in MNP-based immuno-oncotherapies, including activation of macrophage, promotion of cytotoxic T lymphocyte (CTL) infiltration within tumors and modulation of immune checkpoint blockade, thus further supporting the applications of MNPs in clinical therapeutic protocols.

Keywords: magnetite nanoparticles, macrophages, cytotoxic T lymphocytes, immune checkpoint blockade, cancer immunotherapy

INTRODUCTION

Immuno-oncotherapy aims to activate the patient's immune system to recognize and kill tumor cells (1). Immunotherapeutic approaches date back to ancient Egypt, with the observation that tumors could be cured with bacterial infections, an event that we now attribute to immune activation. The modern immunotherapy of cancer started with Willian B. Coley at the end of the

19th century with his "Coley's toxin", a mixture of killed bacteria, which non-specifically activated the immune responses, thereby resulting in tumor regression. Coley's toxin is still used in clinical trials, and pharmaceutical companies are interested in developing modern versions of it (2, 3). Current immunotherapies include several approaches for the non-specific stimulation of innate immune mechanisms on the same line as Coley's toxin (such as the use of BCG in bladder cancer) (4), and strategies aiming at triggering specific anti-tumor immunity. These include the development of cancer vaccines, adoptive cell therapy, and checkpoint inhibitors (5). Indeed, immuno-oncotherapy based on immune checkpoint inhibitors has revolutionized the therapy of advanced and metastatic tumors, leading to an unprecedented rate of cure (6). However, all these therapies need further development and optimization. For instance, non-specific immunological stimulation is often associated with substantial inflammation (the Coley's toxin therapy was dubbed the "fever therapy"), and the therapy with checkpoint inhibitors that releases the block of immunity leads to uncontrolled reactions that can substantially affect the patient's own organism and causes the unwanted immune-related adverse events (irAEs) (7). In addition, in particular for immuno-oncotherapies aiming at activating specific anti-tumor immunity, the therapeutic approach is effective only for a limited number of patients, which depended on the degree of the immunogenicity for various tumor types (8). In an effort to improve the efficacy and safety of the immuno-oncotherapy, many studies have focused on the use of engineered nanoparticles (NPs) (9–12). In this context, magnetite nanoparticles (MNPs) are already in use for medical purposes, e.g., in iron replacement therapy and magnetic resonance imaging (MRI), approved by the US Food and Drug Administration (FDA) (13, 14). The European Medicines Agency (EMA) has also approved the use of iron oxide NPs (NanoTherm®) for the treatment of intermittent glioblastoma multiforme (15). The suitability of MNPs as drug delivery system is based on a number of promising properties, which include their good superparamagnetism and biocompatibility, the easy synthesis and surface modulation/functionalization, and the magnetic hyperthermia and navigation capability (16–18). Based on these characteristics, MNPs can be also applied for theranostics and have been studied for a wide number of new medical applications in oncotherapy. Thus, this brief mini-review tries to report the recent promising applications of MNPs in cancer immunotherapies.

MNPs IN TUMOR IMAGING

Currently, FDA has approved various MNPs for clinical imaging, including Ferumoxide (19), Ferumoxtran-10 (20, 21), Ferumoxsil (22), Ferucarbotran (23), Ferumoxytol (24, 25), and Magtrace (26). However, some of these MNPs have a low performance–price ratio, and some have been withdrawn from the market because of poor clinical results. Therefore, an increasing number of studies have investigated the optimized MNPs to improve the imaging efficiency. Bai et al. (27) reported that the modification with a tumor-targeting peptide (cRGD, a molecule targeting the integrin $\alpha v\beta 3$ overexpressed by endothelium cells of angiogenic tumor vessels) on MNPs could facilitate the effective accumulation of MNPs into the tumor of mice, thus improving the efficiency on MRI application. Moreover, MNPs can be conjugated with other imaging components to realize multi-modal imaging (28). Li et al. (29) incorporated superparamagnetic iron oxide (SPIO) NPs into 1,2-distearoyl-sn-glycero-3-phosphoethanolamine-N-[amino(poly-ethylene glycol)-5000] (DSPE-PEG5k) nanomicelles, which were further conjugated with a near-infrared fluorescence dye (Cy5) and the tumor-targeting peptide bombesin (Bom, used to target the overexpressed G protein-coupled receptors in various malignancies). These nanomicelles could target mouse MDA-MB-231 breast cancer and perform both MRI by the inner SPIO as well as the near-infrared fluorescence imaging by the Cy5 dye (29). These promising outcomes of MNPs in tumor imaging strategies demonstrated their advantages of easy surface modification and functionalization, and these properties could be further integrated into immuno-oncotherapeutic strategies. Recent studies of exploiting MNPs to enhance the efficacy of immunotherapy will be highlighted and discussed in the following paragraphs (30).

MNPs FOR ENHANCING MACROPHAGE ANTI-TUMOR ACTIVITY

Macrophages are the very important component of the innate immune system and first-line defense cells against pathogens and cancers (31). Macrophages are both surveillance and scavenging cells that patrol the tissue and recognize/eliminate senescent, anomalous, and dead cells, and activate effector cells to kill, ingest, and degrade pathogens and tumor cells after having initiated an inflammatory process. The activities of macrophages are mainly influenced by the developmental origin, tissue of residence, and acute microenvironmental cues (32). Although the capacity as antigen-presenting cells (APCs) is weaker than the dendritic cells (DCs), tumor-associated macrophages (TAMs) could re-activate primed T cells by cross-presenting tumor antigens in the tumor microenvironment (TME) rather than in the draining lymph node, thereby contributing to the adaptive immunity in addition to their main role in innate immune responses (33). Besides, the tumor-killing functionality of TAMs should also be ideally achieved through various mechanisms, e.g., the phagocytosis of tumor cells, secretion of cytokines (e.g., IFNγ and TNFα), production of inducible nitric oxide synthase, and induction of anti-tumor inflammation (33, 34). Unfortunately, phagocytosis is partially deactivated owing to the developed escaping mechanism of overexpressing "do-not-eat-me" signal on tumors (35). Furthermore, the most representative TAMs are pro-tumorigenic M2-like phenotype cells, which suppress the anti-tumor capacity of the M1-like phenotype cells, and contribute to the tumor growth, tumor immune evasion, and metastasis (36). Therefore, a bunch of investigations that aim to promote the phagocytosis and the M1 polarization of the TAMs by the application of MNPs have been undertaken.

The expression of the cell surface integrin-associated protein CD47 (ubiquitously expressed on normal cells) is abundantly expressed on most tumor cells and creates a "do-not-eat-me" signal through binding with the signal-regulatory protein alpha (SIRPα) on macrophages (37–39). SIRPα is a regulatory membrane glycoprotein expressed on the macrophage membrane that accumulates at a phagocytic synapse between macrophages and tumor cells upon CD47 binding (37, 40). Thus, the blockade of the CD47–SIRPα interaction by anti-CD47 antibody could restore the macrophage-mediated phagocytosis against tumor (**Figure 1**) (41–43). Accordingly, a combined immunotherapeutic approach was proposed by using indocyanine green and sepantronium bromide co-loaded mesoporous silica NPs for photothermal and chemotherapy with primary tumors. This approach induced a primary tumor destruction that facilitated tumor antigen release and presentation for specific cytotoxic T lymphocyte (CTL) generation (44). Furthermore, MNPs coated by a silica layer conjugated with anti-CD47 antibody were subsequently magnetically guided to be accumulated at metastatic tumor sites to block the interaction of tumor-expressed CD47 with macrophages. As a consequence, macrophages recognized and destroyed/phagocytosed metastatic tumor cells in synergy with activated CTLs (44). In addition, the Fc portion of some CD47 antibody could also drive macrophage for the antibody-dependent cellular phagocytosis (ADCP), which could further strengthen the macrophage-mediated anti-tumor activity (45). However, since CD47 is an essential molecule for protecting normal cells from macrophage attack, strategies for CD47 inhibition need to be very precisely targeted to tumor cells in order to avoid severe collateral damage, as observed with anti-CD47 antibody infusion that causes thrombocytopenia or anemia (35, 45, 46).

The use of plasma membrane-coated biomimetic NPs was applied for a precise inhibition of tumor CD47 binding to macrophages (47, 48). The MNPs could be coated with membrane from genetically engineered cells that overexpressed a SIRPα variant for CD47 binding and showed a 50,000-fold increased binding affinity. These biomimetic MNPs efficiently accumulated in the TME under external magnetic field guidance and specifically blocked the macrophage-inhibiting CD47–SIRPα binding between tumor cells and macrophages (49). Such magnetic navigation approach with MNPs decreases the risk of inducing severe side effects through enhanced tumor targeting. In addition, it is known that the TME can bias the infiltrating TAMs towards a tumor-promoting M2-like phenotype (50), thereby inhibiting the cytocidal and antigen-presenting capacity of M1 macrophages (51). There are evidences that MNPs could promote the re-polarization of TAMs towards an M1 functional phenotype, which resulted in the activation of the macrophage for tumor killing (49, 52). Ferumoxytol, one of the FDA-approved MNPs, was found able to upregulate the expression of M1-related genes (*CD86* and *TNFA*) and to decrease expression of M2-related genes (*CD206* and *IL10*) in a murine macrophage-like leukemia cell line *in vitro* (52). *In vivo*, experimental tumors were restricted in their growth by treatment with ferumoxytol and showed an increased number of M1-like infiltrating macrophages in comparison to the untreated tumors (52). Other studies also exploited MNPs for inducing M1 polarization of TAMs, as recently shown with polymeric NPs coated with a membrane of LPS treated macrophage, and encapsulating Fe_3O_4 NPs and the imiquimod (Toll-like receptor 7 agonist, a strong macrophage activator), which were able to polarize TAMs towards M1 and achieve a concomitant restriction of experimental tumor growth (53). The membrane was prepared by the LPS stimulated macrophages to specifically target TAMs without direct M1 polarization effects that can be verified from the macrophage polarization results of PLGA-ION (PI) and membrane-coated PLGA-ION (PI@M) NPs. The CD80 expression in PI was 67.55% vs. 74.31% in PI@M. The higher M1 polarization of PI@M may be attributed to the enhanced internalization caused by the coated membrane camouflage and targeting capacity. Furthermore, vitamin C (Vc) was applied to eliminate the polarization capacity induced from the ROS pathway of enhancing p300/CBP acetyltransferase activity and promoting p53 acetylation by iron overload (54). Despite the fact that the ROS level of Vc+PI@M was reduced to 0.69-fold compared to the sole

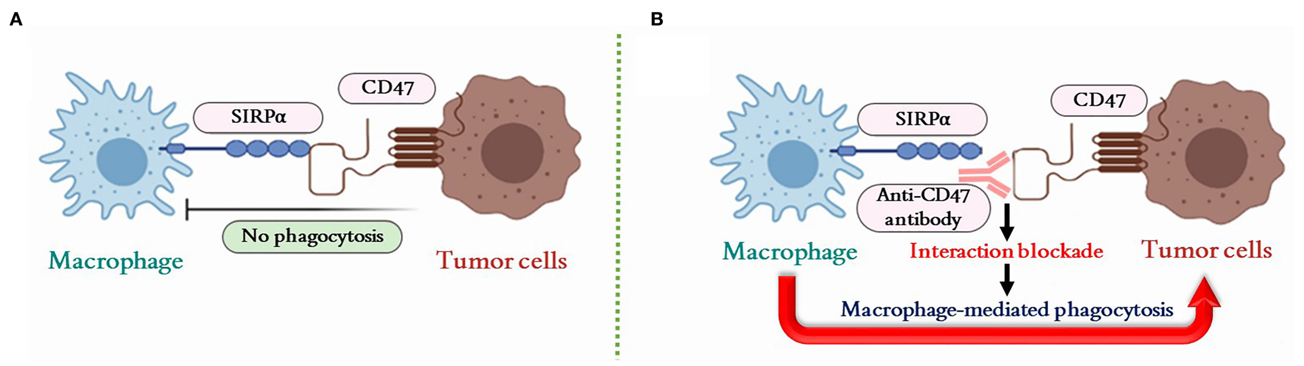

FIGURE 1 | Macrophage-mediated phagocytosis regulated by the CD47–SIRPα pathway. **(A)** The CD47–SIRPα interaction inhibits macrophage-mediated phagocytosis on tumor cells. **(B)** The interaction of CD47–SIRPα can be blocked by the anti-CD47 antibody to restore the macrophage-mediated phagocytosis against tumor cells. SIRPα, signal-regulatory protein alpha; CD47, cluster of differentiation 47.

PI@M treatment, CD80 expression in PI@M (74.31%) and Vc+PI@M (73.24%) was still in a similar range, indicating that the M1 polarization was mainly caused by MNPs rather than the ROS by-product. Besides, a recent study indicated that, after taking a large amount of iron, macrophages could be polarized to M1 type by inhibiting the ERK phosphorylation (55). However, this mechanism still needs to be further investigated and confirmed critically.

Thus, MNPs have proven useful for enhancing the macrophage anti-tumor activity, both in inducing the M1 re-polarization of TAMs and as carriers of inhibitors on tumor CD47 "do-not-eat-me" signal. Although these preliminary results are promising, future research will have to overcome several issues before successfully using MNPs as macrophage activators in cancer immunotherapy. These encompass the heterogeneity of MNP effects on macrophages (56) [may show no activation effects on human primary cells (57)], the need for very accurate tumor targeting to avoid the risk of severe off-target autoimmune and self-destructive effects (which is also the major current problem of immunotherapy with checkpoint inhibitors), the need to reach distant metastatic tumors, and the assessment of efficacy in non-solid tumors.

MNPs FOR TURNING "COLD" TUMOR TO "HOT"

Besides macrophages and the innate immune cells, stimulating CTLs could be considered as another effective approach for improving the anti-tumor immune responses and was also widely studied (58). A solid tumor can be defined as "cold" or "hot", depending on the degree and localization of tumor-infiltrating CTLs and the immunological condition of the TME (59, 60). The "cold" tumor exhibits an immune suppressive TME with an inadequate CTL infiltration and the excessively activated immunosuppressive cells, including regulatory T cells (Tregs), myeloid-derived suppressor cells (MDSCs), and TAMs (61). Meanwhile, the exhaustion of infiltrated CTLs can be induced by the immune suppressive checkpoints in TME, e.g., the programmed cell death protein 1 (PD-1)/programmed cell death ligand 1 (PD-L1) or the cytotoxic T lymphocyte antigen-4 (CTLA-4), which hindered the development of anti-tumor specific CTLs responses (62). Conversely, a "hot" tumor exhibits a high accumulation and infiltration of non-exhausted CTLs, DCs, and natural killer cells (NKs), thus being an ideal target for immuno-oncotherapy (58, 63). Thus, to improve the overall response rate (ORR) of the current immuno-oncotherapy, a growing number of MNP-based immunotherapeutic strategies aim at turning the "cold" tumors to "hot" by enhancing the number of infiltrating CTLs and modulation of immune checkpoint blockade (ICB) in TME (**Figure 2**).

MNPs Improving CTL Tumor Infiltration

In the presence of an alternating magnetic field, MNPs can generate a magnetic hyperthermia by converting the magnetic energy into thermal energy, which can provoke immunogenic/inflammatory cell death in the tumor (64, 65). The hyperthermia may induce immunogenic cell death (ICD) to release tumor-associated neoantigens and danger-associated molecular patterns (DAMPs), including the exposure of calreticulin (CRT), or the release of chromatin-binding protein high mobility group B1 (HMGB1) and the adenosine triphosphate (ATP) (66). Subsequently, the recognition and processing of the neoantigens can be promoted and followed with an effective T-cell priming (67). Thus, after the primary tumor elimination by the magnetic hyperthermia of the ferromagnetic iron oxide nanorings, the "eat-me" signal of CRT was elicited on the surface of the immunogenic dying 4T1 tumor cells and promoted the macrophage activation, which further enhanced the activation and infiltration of CTLs in the re-challenged or metastatic tumor on mice (68). Besides, as the most powerful APCs, the activation of DCs is crucial for promoting the infiltration of CTLs. To achieve a more effective tumor antigen uptaken by DCs, an MNP-based vaccine has been developed using Fe_3O_4 nanocluster core loading with the CpG oligodeoxynucleotide (CpG-ODN, a Toll-like receptor 9 agonist) and tumor cell membrane shell decorated with anti-CD205 for preferentially DC recognition (69). These DC targeting MNPs could extend the retention in lymph nodes by the magnetic control for an increased DC internalization. The CpG-ODN and the various antigens on the tumor cell membrane paved the way of DC maturation, thus facilitating the MHC cross-presentation and T-cell activation, eliciting a tremendous amount of CTL infiltration and responses in the tumor (69). Besides promoting the activation of DCs and CTLs, the possibility of binding MNPs on the surface of CTLs to improve the tumor infiltration by a magnetic field near the tumor site was also explored. By coating Fe_3O_4 nanoclusters with the leucocyte membranes modified with the co-stimulatory ligand CD28 antibody (αCD28) and peptide (SIINFEKL)-loaded major histocompatibility complex class-I (pMHC-I), the artificial antigen-presenting cells (aAPC) were constructed that successfully targeted CTLs for stimulation (70). Then, the CTLs that bound these nanoclusters could be effectively directed to tumor with an increased accumulation and infiltration facilitated upon magnetic guidance, resulting in an enhanced tumor killing efficiency (70).

MNPs Modulating Immune Checkpoint Blockade

Based on the current progress in immuno-oncotherapy, ICB therapy, e.g., PD-1/PD-L1 and CTLA-4, has exerted a major therapeutic effect on patients with advanced cancers (71). Immune checkpoints exhibit crucial functions in adjusting the balance of immune homeostasis and preventing T-cell-mediated autoimmune diseases, while they are also found hijacked by the tumor for suppressing the anti-tumor immune responses (72, 73). The PD-1 on T cells can be activated by binding its ligand PD-L1 on tumors, resulting an exhausted condition of infiltrated CTLs. CTLA-4, a new immunoglobulin superfamily candidate on T cells (including CD4, CD8, and Treg cells), restrains the co-stimulatory signals of CD28-CD80/86 by competitively binding with CD80/86 on antigen-presenting cells (65, 74). In clinical

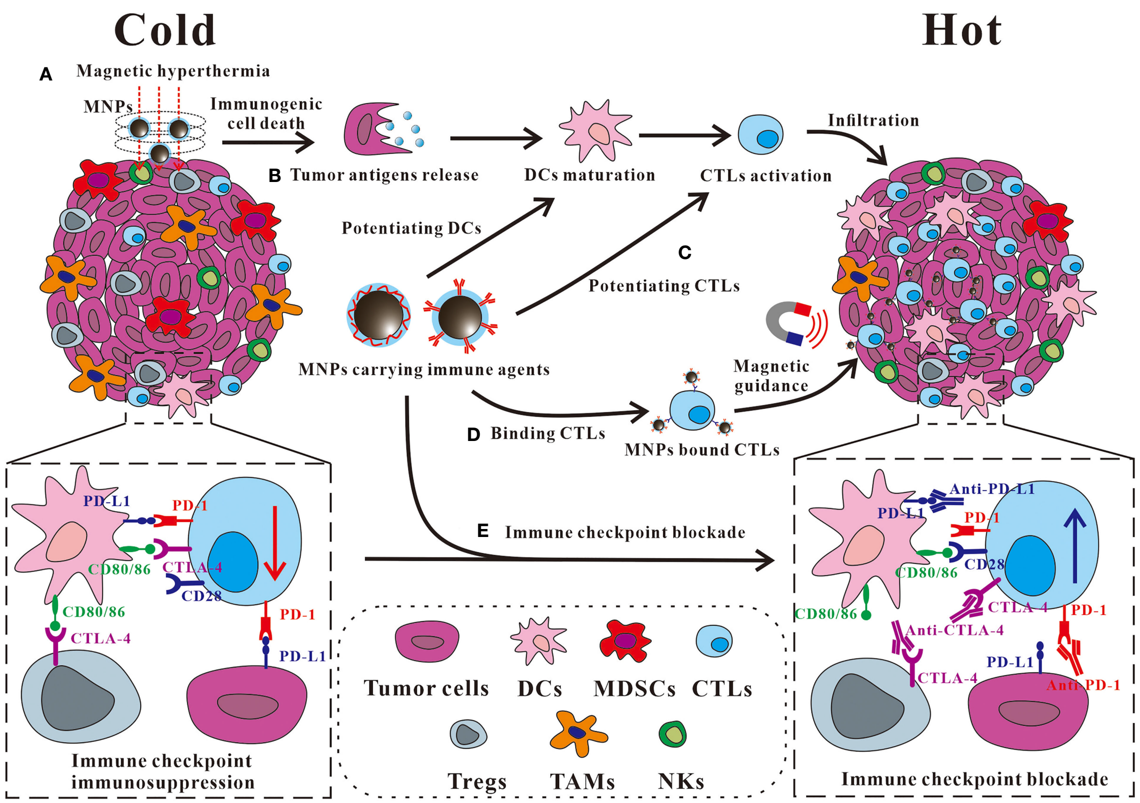

FIGURE 2 | Some representative approaches of MNPs to turn a "cold" tumor into "hot". **(A)** MNP-based magnetic hyperthermia ablation therapy is capable of inducing tumor immunogenic cell death to promote the release of antigen for DC maturation, and the subsequent CTL activation and infiltration in the tumor. **(B, C)** MNPs carrying immune agents such as agonists can be applied **(B)** for potentiating DCs or **(C)** for potentiating CTLs. **(D)** MNPs carrying immune agents such as antibodies can bind CTLs, and direct them to the tumor with an improved accumulation and infiltration by the magnetic guidance. **(E)** The tumor accumulation of the immune checkpoint antibody can be enhanced by the conjugation on MNPs for an improved immunosuppressive pathway modulation with fewer adverse effects. DCs, dendritic cells; MDSCs, myeloid-derived suppressor cells; CTLs, cytotoxic T lymphocytes; Tregs, regulatory T cells; TAM, tumor-associated macrophages; NKs, natural killer cells; PD-1, programmed cell death protein 1; PD-L1, programmed cell death ligand 1; CTLA-4, cytotoxic T lymphocyte-associated protein 4.

practice, anti-PD-1/PD-L1 and anti-CTLA-4 therapy proved effective for restoring the anti-tumor T-cell-mediated immune responses (75). However, ICB therapy only shows limited ORR with commonly associated irAEs, which limited its clinical application (76). Therefore, the combinational immuno-oncotherapy based on the multi-functional MNPs attracts considerable attention because of the immuno-stimulation effects of magnetic hyperthermia and the drug delivery capability of immuno-stimulatory adjuvant or checkpoint antibodies for the improved activation of CTLs and the accumulation of ICB antibodies (77).

The magnetic hyperthermia induced by MNPs could cause tumor ablation and the release of neoantigens. With the help of imiquimod (a toll-like receptor 7 agonist), CTLs were then effectively activated (78, 79). Thus, a further combinational approach by applying immune checkpoint antibodies, such as anti-CTLA-4 for Treg suppression or anti-PD-1/PD-L1 to restore exhausted CTLs, could be used for the synergistic oncotherapy to eliminate primary tumor and inhibit tumor metastasis, or even to generate a robust immunological memory for tumor recurrence prevention without noticeable systemic toxicity (78, 80). Beside the combination with checkpoint inhibitors separately, conjugating checkpoint inhibitors on MNPs demonstrated a better tumor targeting and treatment efficiency. The checkpoint inhibitor (anti-PD-L1) and CTL activators (anti-CD3 and anti-CD28) could be conjugated on the fucoidan-dextran-coated iron oxide NPs for an improved tumor accumulation by the magnetic guidance (81). These MNPs mediated ICB therapy-enhanced PD-L1 blockade and promoted CTL activation that prolonged the median survival time of tumor-bearing mice from 32 to 63 days with minimized adverse events owing to a much lower anti-PD-L1 dosage used than the soluble anti-PD-L1 treatment (81). Remarkably, the superparamagnetic iron nanoclusters were armed with PD-1 antibody by TME pH-sensitive bond and successfully bound on CTLs *in vitro*. These MNP/CTL cells could be magnetically guided to the solid tumors in mice for improved CTL infiltration and tumor killing, and further aided with PD-1 antibody release through acid-mediated MNPs, for a synergistically enhanced immuno-oncotherapy with minimal side effects (82).

As these studies indicated, magnetic hyperthermia therapy induced by functionalized MNPs can effectively promote the immunological stimulation, tumor infiltration of CTLs, and the efficiency of ICB therapy. Moreover, various stimuli or ICB antibodies can be conjugated with the MNPs for improved targeting and immune cell activation in solid tumor. Meanwhile, the targeting cells, such as CTLs, attached with MNPs carrying ICB antibody on their surface, can be magnetically directed to tumor site for improved tumor accumulation. Such strategy has been proved successfully to enhance both CTL infiltration and ICB efficiency in one shot.

CONCLUSIONS AND FUTURE PERSPECTIVES

Taken together, extensive progresses have been made with various MNP platforms toward different applications for the enhanced immuno-oncotherapy. MNPs exhibited good capabilities for magnetic hyperthermia, magnetic navigation, and immuno-agent delivery to enhance macrophage anti-tumor capacity, to increase the tumor infiltration of CTLs, and to improve ICB efficiency. Moreover, the CTLs that adhered to the MNPs carrying immune checkpoint antibodies obtained the ability of magnetic navigation as well, which could greatly improve the CTL infiltration and ICB effects in solid tumors. These MNP-based immunotherapies exhibited higher anti-tumor efficiency with fewer side effects in the experimental studies. In the future therapeutic approaches of MNPs, the combination of these unique properties possessed by MNPs may be the most promising strategy for successful cancer therapeutics. The hyperthermia induced by MNPs can eliminate tumor cells directly, which provokes the ICD from DAMPs and antigen release for the improved anti-tumor immune responses. Moreover, the tumor tissue-retained MNPs could polarize the remaining TAMs to M1 macrophage as a further method to eliminate the residual tumor effectively. Consequently, the tumor metastasis and recurrence may be efficiently and sustainably inhibited by the synergistic strategy. Despite these advantages, disadvantages of high difficulty in mass production, lack of the precise analytic methods for examining the properties, and the complicated usage condition/equipment should be noticed for the future MNP application in oncotherapy. Moreover, in the clinical trials, only few MNP formulations, e.g., ferumoxytol, have shown new progress as an MRI-enhancing agent. Meanwhile, after the withdrawal of some MNPs in clinic, various regulations have currently been announced by the regulatory agencies, to assure a safe, effective, and quality controllable MNPs for fundamental and translational development. With this concern, immense information needs to be researched to cope with the complex challenges, e.g., nano-bio interactions in the body, crossing physiological and tumor-specific technical hurdles, stealth behavior against late endosomal/lysosomal system into the tumor cytosol, and boosting the desired immunity without severe side effects or only with short-term adverse effects. Moreover, MNPs still have to face a number of biological barriers, such as the "Mononuclear Phagocyte System (MPS)", that abate the accumulation and localization of MNPs at the targeted tumor site, and limit their further application as efficacious immunotherapeutic vehicles. However, as promising outcomes have been seen from the current MNP synergetic immuno-oncotherapy, we believe that more potential approaches will be continuously exploited for ideal functionalized MNPs with successful clinical achievements.

AUTHOR CONTRIBUTIONS

YL conceived the idea of the review. QS and AJ performed the literature search, prepared the figures, and wrote the draft. GZ contributed to revising and editing the review. YL contributed to the critical revising, rewriting, and editing of the review. All authors contributed to the article and approved the submitted version.

FUNDING

This work was financially supported by the Shenzhen Science and Technology Program (GJHZ20190821155803877), the National Natural Science Foundation of China (32171390 and 31701005), the China Postdoctoral Science Foundation (2020M672898), the SIAT Innovation Program for Excellent Young Researchers (E1G068), and CAS President's International Fellowship Initiative (PIFI, 2020VBA0028, 2020VBA0022, 2022VBA0008 and 2021PB0060).

ACKNOWLEDGMENTS

We thank Prof. Diana Boraschi (Shenzhen Institute of Advanced Technology, Chinese Academy of Sciences) for her critical reading and helpful English editing of the manuscript.

REFERENCES

1. Steinman RM, Mellman I. Immunotherapy: Bewitched, Bothered, and Bewildered No More. *Science* (2004) 305(5681):197–200. doi: 10.1126/science.1099688
2. Hoption Cann SA, van Netten JP, van Netten C. Dr William Coley and Tumour Regression: A Place in History or in the Future. *Postgrad Med J* (2003) 79(938):672–80.
3. Karbach J, Neumann A, Brand K, Wahle C, Siegel E, Maeurer M, et al. Phase I Clinical Trial of Mixed Bacterial Vaccine (Coley's Toxins) in Patients With NY-ESO-1 Expressing Cancers: Immunological Effects and Clinical Activity. *Clin Cancer Res* (2012) 18(19):5449–59. doi: 10.1158/1078-0432.CCR-12-1116
4. Carlson RD, Flickinger JC, Snook AE. Talkin' Toxins: From Coley's to Modern Cancer Immunotherapy. *Toxins* (2020) 12(4):23. doi: 10.3390/toxins12040241
5. Yousefi H, Yuan J, Keshavarz-Fathi M, Murphy JF, Rezaei N. Immunotherapy of Cancers Comes of Age. *Expert Rev Clin Immunol* (2017) 13(10):1001–15. doi: 10.1080/1744666X.2017.1366315
6. Sharma P, Allison JP. The Future of Immune Checkpoint Therapy. *Science* (2015) 348(6230):56–61. doi: 10.1126/science.aaa8172
7. Naidoo J, Page DB, Li BT, Connell LC, Schindler K, Lacouture ME, et al. Toxicities of the Anti-PD-1 and Anti-PD-L1 Immune Checkpoint Antibodies. *Ann Oncol* (2015) 26(12):2375–91. doi: 10.1093/annonc/mdv383

8. Majidpoor J, Mortezaee K. The Efficacy of PD-1/PD-L1 Blockade in Cold Cancers and Future Perspectives. *Clin Immunol* (2021) 226:108707. doi: 10.1016/j.clim.2021.108707
9. Riley RS, June CH, Langer R, Mitchell MJ. Delivery Technologies for Cancer Immunotherapy. *Nat Rev Drug Discov* (2019) 18(3):175–96. doi: 10.1038/s41573-018-0006-z
10. Zhang Y, Zhang G, Chen L, Li Y. Modulation of the Inflammatory Tumor Microenvironment: A New Approach for Photothermal-Synergized Cancer Immunotherapy. *Nanomed (Lond)* (2019) 14(16):2101–4. doi: 10.2217/nnm-2019-0156
11. Shao X, Ding Z, Zhou W, Li Y, Li Z, Cui H, et al. Intrinsic Bioactivity of Black Phosphorus Nanomaterials on Mitotic Centrosome Destabilization Through Suppression of PLK1 Kinase. *Nat Nanotechnol* (2021). doi: 10.1038/s41565-021-00952-x
12. Zhao J, Lu D, Moya S, Yan H, Qiu M, Chen J, et al. Bispecific T-Cell Engager (BiTE) Immunotherapy of Ovarian Cancer Based on MIL-88a MOF/MC Gene Delivery System. *Appl Materials Today* (2020) 20:100701. doi: 10.1016/j.apmt.2020.100701
13. Zeng Q, Li H, Jiang H, Yu J, Wang Y, Ke H, et al. Tailoring Polymeric Hybrid Micelles With Lymph Node Targeting Ability to Improve the Potency of Cancer Vaccines. *Biomaterials* (2017) 122:105–13. doi: 10.1016/j.biomaterials.2017.01.010
14. Kasturi SP, Skountzou I, Albrecht RA, Koutsonanos D, Hua T, Nakaya HI, et al. Programming the Magnitude and Persistence of Antibody Responses With Innate Immunity. *Nature* (2011) 470(7335):543–7. doi: 10.1038/nature09737
15. Zhu Q, Egelston C, Vivekanandhan A, Uematsu S, Akira S, Klinman DM, et al. Toll-Like Receptor Ligands Synergize Through Distinct Dendritic Cell Pathways to Induce T Cell Responses: Implications for Vaccines. *Proc Natl Acad Sci USA* (2008) 105(42):16260–5. doi: 10.1073/pnas.0805325105
16. López-Castro JD, Maraloiu AV, Delgado JJ, Calvino JJ, Blanchin MG, Gálvez N, et al. From Synthetic to Natural Nanoparticles: Monitoring the Biodegradation of SPIO (P904) Into Ferritin by Electron Microscopy. *Nanoscale* (2011) 3(11):4597–9. doi: 10.1039/c1nr10980d
17. Cho NH, Cheong TC, Min JH, Wu JH, Lee SJ, Kim D, et al. A Multifunctional Core-Shell Nanoparticle for Dendritic Cell-Based Cancer Immunotherapy. *Nat Nanotechnol* (2011) 6(10):675–82. doi: 10.1038/nnano.2011.149
18. Trabulo S, Aires A, Aicher A, Heeschen C, Cortajarena AL. Multifunctionalized Iron Oxide Nanoparticles for Selective Targeting of Pancreatic Cancer Cells. *Biochim Biophys Acta Gen Subj* (2017) 1861 (6):1597–605. doi: 10.1016/j.bbagen.2017.01.035
19. Wang YX. Current Status of Superparamagnetic Iron Oxide Contrast Agents for Liver Magnetic Resonance Imaging. *World J Gastroenterol* (2015) 21 (47):13400–2. doi: 10.3748/wjg.v21.i47.13400
20. Bourrinet P, Bengele HH, Bonnemain B, Dencausse A, Idee JM, Jacobs PM, et al. Preclinical Safety and Pharmacokinetic Profile of Ferumoxtran-10, an Ultrasmall Superparamagnetic Iron Oxide Magnetic Resonance Contrast Agent. *Invest Radiol* (2006) 41(3):313–24. doi: 10.1097/01.rli.0000197669.80475.dd
21. Fortuin AS, Brüggemann R, van der Linden J, Panfilov I, Israël B, Scheenen TWJ, et al. Ultra-Small Superparamagnetic Iron Oxides for Metastatic Lymph Node Detection: Back on the Block. *Wiley Interdiscip Rev Nanomed Nanobiotechnol* (2018) 10(1):e1471. doi: 10.1002/wnan.1471
22. Wáng YX, Idée JM. A Comprehensive Literatures Update of Clinical Researches of Superparamagnetic Resonance Iron Oxide Nanoparticles for Magnetic Resonance Imaging. *Quant Imaging Med Surg* (2017) 7(1):88–122. doi: 10.21037/qims.2017.02.09
23. Reimer P, Balzer T. Ferucarbotran (Resovist): A New Clinically Approved RES-Specific Contrast Agent for Contrast-Enhanced MRI of the Liver: Properties, Clinical Development, and Applications. *Eur Radiol* (2003) 13 (6):1266–76. doi: 10.1007/s00330-002-1721-7
24. Trujillo-Alonso V, Pratt EC, Zong H, Lara-Martinez A, Kaittanis C, Rabie MO, et al. FDA-Approved Ferumoxytol Displays Anti-Leukaemia Efficacy Against Cells With Low Ferroportin Levels. *Nat Nanotechnol* (2019) 14 (6):616–22. doi: 10.1038/s41565-019-0406-1
25. Bullivant JP, Zhao S, Willenberg BJ, Kozissnik B, Batich CD, Dobson J. Materials Characterization of Feraheme/ferumoxytol and Preliminary Evaluation of its Potential for Magnetic Fluid Hyperthermia. *Int J Mol Sci* (2013) 14(9):17501–10. doi: 10.3390/ijms140917501
26. Pouw JJ, Ahmed M, Anninga B, Schuurman K, Pinder SE, Van Hemelrijck M, et al. Comparison of Three Magnetic Nanoparticle Tracers for Sentinel Lymph Node Biopsy in an In Vivo Porcine Model. *Int J Nanomed* (2015) 10:1235–43. doi: 10.2147/IJN.S76962
27. Bai C, Jia Z, Song L, Zhang W, Chen Y, Zang F, et al. Time-Dependent T1–T2 Switchable Magnetic Resonance Imaging Realized by C(RGDyK) Modified Ultrasmall Fe3O4 Nanoprobes. *Advanced Funct Materials* (2018) 28 (32):1802281.1–.9. doi: 10.1002/adfm.201802281
28. Shin TH, Choi Y, Kim S, Cheon J. Recent Advances in Magnetic Nanoparticle-Based Multi-Modal Imaging. *Chem Soc Rev* (2015) 44(14):4501–16. doi: 10.1039/C4CS00345D
29. Li L, Wu C, Pan L, Li X, Kuang A, Cai H, et al. Bombesin-Functionalized Superparamagnetic Iron Oxide Nanoparticles for Dual-Modality MR/NIRFI in Mouse Models of Breast Cancer. *Int J Nanomed* (2019) 14:6721–32. doi: 10.2147/IJN.S211476
30. Wu X, Zhang H. Therapeutic Strategies of Iron-Based Nanomaterials for Cancer Therapy. *BioMed Mater* (2021) 16(3):032003. doi: 10.1088/1748-605X/abd0c4
31. Demaria O, Cornen S, Daëron M, Morel Y, Medzhitov R, Vivier E. Harnessing Innate Immunity in Cancer Therapy. *Nature* (2019) 574(7776):45–56. doi: 10.1038/s41586-019-1593-5
32. DeNardo DG, Ruffell B. Macrophages as Regulators of Tumour Immunity and Immunotherapy. *Nat Rev Immunol* (2019) 19(6):369–82. doi: 10.1038/s41577-019-0127-6
33. Lecoultre M, Dutoit V, Walker PR. Phagocytic Function of Tumor-Associated Macrophages as a Key Determinant of Tumor Progression Control: A Review. *J Immunother Cancer* (2020) 8(2):e001408. doi: 10.1136/jitc-2020-001408
34. Najafi M, Hashemi Goradel N, Farhood B, Salehi E, Nashtaei MS, Khanlarkhani N, et al. Macrophage Polarity in Cancer: A Review. *J Cell Biochem* (2019) 120(3):2756–65. doi: 10.1002/jcb.27646
35. Feng M, Jiang W, Kim BYS, Zhang CC, Fu YX, Weissman IL. Phagocytosis Checkpoints as New Targets for Cancer Immunotherapy. *Nat Rev Cancer* (2019) 19(10):568–86. doi: 10.1038/s41568-019-0183-z
36. Pathria P, Louis TL, Varner JA. Targeting Tumor-Associated Macrophages in Cancer. *Trends Immunol* (2019) 40(4):310–27. doi: 10.1016/j.it.2019.02.003
37. Chao MP, Alizadeh AA, Tang C, Myklebust JH, Varghese B, Gill S, et al. Anti-CD47 Antibody Synergizes With Rituximab to Promote Phagocytosis and Eradicate non-Hodgkin Lymphoma. *Cell* (2010) 142(5):699–713. doi: 10.1016/j.cell.2010.07.044
38. Majeti R, Chao MP, Alizadeh AA, Pang WW, Jaiswal S, Gibbs KDJr., et al. CD47 is an Adverse Prognostic Factor and Therapeutic Antibody Target on Human Acute Myeloid Leukemia Stem Cells. *Cell* (2009) 138(2):286–99. doi: 10.1016/j.cell.2009.05.045
39. Jaiswal S, Jamieson CH, Pang WW, Park CY, Chao MP, Majeti R, et al. CD47 is Upregulated on Circulating Hematopoietic Stem Cells and Leukemia Cells to Avoid Phagocytosis. *Cell* (2009) 138(2):271–85. doi: 10.1016/j.cell.2009.05.046
40. Rezaei G, Habibi-Anbouhi M, Mahmoudi M, Azadmanesh K, Moradi-Kalbolandi S, Behdani M, et al. Development of Anti-CD47 Single-Chain Variable Fragment Targeted Magnetic Nanoparticles for Treatment of Human Bladder Cancer. *Nanomed (Lond)* (2017) 12(6):597–613. doi: 10.2217/nnm-2016-0302
41. Lu Q, Chen X, Wang S, Lu Y, Yang C, Jiang G. Potential New Cancer Immunotherapy: Anti-CD47-Sirpα Antibodies. *Onco Targets Ther* (2020) 13:9323–31. doi: 10.2147/OTT.S249822
42. Matlung HL, Szilagyi K, Barclay NA, van den Berg TK. The CD47-Sirpα Signaling Axis as an Innate Immune Checkpoint in Cancer. *Immunol Rev* (2017) 276(1):145–64. doi: 10.1111/imr.12527
43. Chen Q, Wang C, Zhang X, Chen G, Hu Q, Li H, et al. In Situ Sprayed Bioresponsive Immunotherapeutic Gel for Post-Surgical Cancer Treatment. *Nat Nanotechnol* (2019) 14(1):89–97. doi: 10.1038/s41565-018-0319-4
44. Zhang Y, Chen H, Wang H, Wang T, Pan H, Ji W, et al. A Synergistic Cancer Immunotherapy Nano-System for Preventing Tumor Growth. *Chem Eng J* (2020) 380:122472. doi: 10.1016/j.cej.2019.122472
45. Pietsch EC, Dong J, Cardoso R, Zhang X, Chin D, Hawkins R, et al. Anti-Leukemic Activity and Tolerability of Anti-Human CD47 Monoclonal Antibodies. *Blood Cancer J* (2017) 7(2):e536. doi: 10.1038/bcj.2017.7
46. Advani R, Flinn I, Popplewell L, Forero A, Bartlett NL, Ghosh N, et al. CD47 Blockade by Hu5F9-G4 and Rituximab in Non-Hodgkin's Lymphoma. *N Engl J Med* (2018) 379(18):1711–21. doi: 10.1056/NEJMoa1807315

47. Xia Q, Zhang Y, Li Z, Hou X, Feng N. Red Blood Cell Membrane-Camouflaged Nanoparticles: A Novel Drug Delivery System for Antitumor Application. *Acta Pharm Sin B* (2019) 9(4):675–89. doi: 10.1016/j.apsb.2019.01.011
48. Liu WL, Zou MZ, Liu T, Zeng JY, Li X, Yu WY, et al. Cytomembrane Nanovaccines Show Therapeutic Effects by Mimicking Tumor Cells and Antigen Presenting Cells. *Nat Commun* (2019) 10(1):3199. doi: 10.1038/s41467-019-11157-1
49. Rao L, Zhao SK, Wen C, Tian R, Lin L, Cai B, et al. Activating Macrophage-Mediated Cancer Immunotherapy by Genetically Edited Nanoparticles. *Adv Mater* (2020) 32(47):e2004853. doi: 10.1002/adma.202004853
50. Mantovani A, Longo DL. Macrophage Checkpoint Blockade in Cancer - Back to the Future. *N Engl J Med* (2018) 379(18):1777–9. doi: 10.1056/NEJMe1811699
51. Italiani P, Boraschi D. From Monocytes to M1/M2 Macrophages: Phenotypical vs. Functional Differentiation. *Front Immunol* (2014) 5:22. doi: 10.3389/fimmu.2014.00514
52. Zanganeh S, Hutter G, Spitler R, Lenkov O, Mahmoudi M, Shaw A, et al. Iron Oxide Nanoparticles Inhibit Tumour Growth by Inducing Pro-Inflammatory Macrophage Polarization in Tumour Tissues. *Nat Nanotechnol* (2016) 11 (11):986–94. doi: 10.1038/nnano.2016.168
53. Liu L, Wang Y, Guo X, Zhao J. Zhou S. A Biomimetic Polymer Magnetic Nanocarrier Polarizing Tumor-Associated Macrophages for Potentiating Immunotherapy. *Small* (2020) 16(38):e2003543 doi: 10.1002/smll.202003543
54. Zhou Y, Que K-T, Zhang Z, Yi ZJ, Zhao PX, You Y, et al. Iron Overloaded Polarizes Macrophage to Proinflammation Phenotype Through ROS/acetyl-P53 Pathway. *Cancer Med* (2018) 7(8):4012–22. doi: 10.1002/cam4.1670
55. Wang S, Cheng M, Peng P, Lou Y, Zhang A, Liu P. Iron Released After Cryo-Thermal Therapy Induced M1 Macrophage Polarization, Promoting the Differentiation of CD4(+) T Cells Into CTLs. *Int J Mol Sci* (2021) 22 (13):7010. doi: 10.3390/ijms22137010
56. Della Camera G, Madej M, Ferretti AM, La Spina R, Li Y, Corteggio A, et al. Personalised Profiling of Innate Immune Memory Induced by Nano-Imaging Particles in Human Monocytes. *Front Immunol* (2021) 12(3053). doi: 10.3389/fimmu.2021.692165
57. Ferretti AM, Usseglio S, Mondini S, Drago C, La Mattina R, Chini B, et al. Towards Bio-Compatible Magnetic Nanoparticles: Immune-Related Effects, in-Vitro Internalization, and in-Vivo Bio-Distribution of Zwitterionic Ferrite Nanoparticles With Unexpected Renal Clearance. *J Colloid Interface Sci* (2021) 582:678–700. doi: 10.1016/j.jcis.2020.08.026
58. Song Q, Zhang G, Wang B, Cao G, Li D, Wang Y, et al. Reinforcing the Combinational Immuno-Oncotherapy of Switching "Cold" Tumor to "Hot" by Responsive Penetrating Nanogels. *ACS Appl Mater Interfaces* (2021) 13 (31):36824–38. doi: 10.1021/acsami.1c08201
59. Chen DS, Mellman I. Elements of Cancer Immunity and the Cancer-Immune Set Point. *Nature* (2017) 541(7637):321–30. doi: 10.1038/nature21349
60. Liu Y-T, Sun Z-J. Turning Cold Tumors Into Hot Tumors by Improving T-Cell Infiltration. *Theranostics* (2021) 11(11):5365–86. doi: 10.7150/thno.58390
61. Hegde PS, Chen DS. Top 10 Challenges in Cancer Immunotherapy. *Immunity* (2020) 52(1):17–35. doi: 10.1016/j.immuni.2019.12.011
62. Pardoll DM. The Blockade of Immune Checkpoints in Cancer Immunotherapy. *Nat Rev Cancer* (2012) 12(4):252–64. doi: 10.1038/nrc3239
63. Hegde PS, Karanikas V, Evers S. The Where, the When, and the How of Immune Monitoring for Cancer Immunotherapies in the Era of Checkpoint Inhibition. *Clin Cancer Res* (2016) 22(8):1865–74. doi: 10.1158/1078-0432.CCR-15-1507
64. Liu X, Zhang Y, Wang Y, Zhu W, Li G, Ma X, et al. Comprehensive Understanding of Magnetic Hyperthermia for Improving Antitumor Therapeutic Efficacy. *Theranostics* (2020) 10(8):3793–815. doi: 10.7150/thno.40805
65. Zhang Y, Zhang G, Wang G, Wu L, Monteiro-Riviere NA, Li Y. The Synergistic Strategies for the Immuno-Oncotherapy With Photothermal Nanoagents. *Wiley Interdiscip Rev Nanomed Nanobiotechnol* (2021) 13(5): e1717. doi: 10.1002/wnan.1717
66. Sweeney EE, Cano-Mejia J, Fernandes R. Photothermal Therapy Generates a Thermal Window of Immunogenic Cell Death in Neuroblastoma. *Small* (2018) 14(20):e1800678. doi: 10.1002/smll.201800678
67. Krysko DV, Garg AD, Kaczmarek A, Krysko O, Agostinis P, Vandenabeele P. Immunogenic Cell Death and DAMPs in Cancer Therapy. *Nat Rev Cancer* (2012) 12(12):860–75. doi: 10.1038/nrc3380
68. Liu X, Zheng J, Sun W, Zhao X, Li Y, Gong N, et al. Ferrimagnetic Vortex Nanoring-Mediated Mild Magnetic Hyperthermia Imparts Potent Immunological Effect for Treating Cancer Metastasis. *ACS nano* (2019) 13 (8):8811–25. doi: 10.1021/acsnano.9b01979
69. Li F, Nie W, Zhang F, Lu G, Lv C, Lv Y, et al. Engineering Magnetosomes for High-Performance Cancer Vaccination. *ACS Cent Sci* (2019) 5(5):796–807. doi: 10.1021/acscentsci.9b00060
70. Zhang Q, Wei W, Wang P, Zuo L, Li F, Xu J, et al. Biomimetic Magnetosomes as Versatile Artificial Antigen-Presenting Cells to Potentiate T-Cell-Based Anticancer Therapy. *ACS Nano* (2017) 11(11):10724–32. doi: 10.1021/acsnano.7b04955
71. Khalil DN, Smith EL, Brentjens RJ, Wolchok JD. The Future of Cancer Treatment: Immunomodulation, CARs and Combination Immunotherapy. *Nat Rev Clin Oncol* (2016) 13(5):273–90. doi: 10.1038/nrclinonc.2016.25
72. Alsaab HO, Sau S, Alzhrani R, Tatiparti K, Bhise K, Kashaw SK, et al. PD-1 and PD-L1 Checkpoint Signaling Inhibition for Cancer Immunotherapy: Mechanism, Combinations, and Clinical Outcome. *Front Pharmacol* (2017) 8:561. doi: 10.3389/fphar.2017.00561
73. Deng H, Zhang Z. The Application of Nanotechnology in Immune Checkpoint Blockade for Cancer Treatment. *J Control Release* (2018) 290:28–45. doi: 10.1016/j.jconrel.2018.09.026
74. Intlekofer AM, Thompson CB. At the Bench: Preclinical Rationale for CTLA-4 and PD-1 Blockade as Cancer Immunotherapy. *J Leukoc Biol* (2013) 94 (1):25–39. doi: 10.1189/jlb.1212621
75. Buchbinder E, Hodi FS. Cytotoxic T Lymphocyte Antigen-4 and Immune Checkpoint Blockade. *J Clin Invest* (2015) 125(9):3377–83. doi: 10.1172/JCI80012
76. Byun DJ, Wolchok JD, Rosenberg LM, Girotra M. Cancer Immunotherapy - Immune Checkpoint Blockade and Associated Endocrinopathies. *Nat Rev Endocrinol* (2017) 13(4):195–207. doi: 10.1038/nrendo.2016.205
77. Jin J, Zhao Q. Engineering Nanoparticles to Reprogram Radiotherapy and Immunotherapy: Recent Advances and Future Challenges. *J Nanobiotechnol* (2020) 18(1):75. doi: 10.1186/s12951-020-00629-y
78. Chao Y, Chen G, Liang C, Xu J, Dong Z, Han X, et al. Iron Nanoparticles for Low-Power Local Magnetic Hyperthermia in Combination With Immune Checkpoint Blockade for Systemic Antitumor Therapy. *Nano Lett* (2019) 19 (7):4287–96. doi: 10.1021/acs.nanolett.9b00579
79. Sobhani N, Tardiel-Cyril DR, Davtyan A, Generali D, Roudi R, Li Y. CTLA-4 in Regulatory T Cells for Cancer Immunotherapy. *Cancers (Basel)* (2021) 13 (6):1440. doi: 10.3390/cancers13061440
80. Wang Z, Zhang F, Shao D, Chang Z, Wang L, Hu H, et al. Janus Nanobullets Combine Photodynamic Therapy and Magnetic Hyperthermia to Potentiate Synergetic Anti-Metastatic Immunotherapy. *Adv Sci (Weinh)* (2019) 6 (22):1901690. doi: 10.1002/advs.201901690
81. Chiang CS, Lin YJ, Lee R, Lai YH, Cheng HW, Hsieh CH, et al. Combination of Fucoidan-Based Magnetic Nanoparticles and Immunomodulators Enhances Tumour-Localized Immunotherapy. *Nat Nanotechnol* (2018) 13 (8):746–54. doi: 10.1038/s41565-018-0146-7
82. Nie W, Wei W, Zuo L, Lv C, Zhang F, Lu GH, et al. Magnetic Nanoclusters Armed With Responsive PD-1 Antibody Synergistically Improved Adoptive T-Cell Therapy for Solid Tumors. *ACS Nano* (2019) 13(2):1469–78. doi: 10.1021/acsnano.8b07141

Conflict of Interest: The authors declare that the research was conducted in the absence of any commercial or financial relationships that could be construed as a potential conflict of interest.

frontiers in Immunology

ORIGINAL RESEARCH
published: 07 October 2021
doi: 10.3389/fimmu.2021.758410

SERS Sensing of Bacterial Endotoxin on Gold Nanoparticles

Alessandro Verde [1,2†], Maria Mangini [1,2†], Stefano Managò [1], Chiara Tramontano [3], Ilaria Rea [3], Diana Boraschi [2,4,5], Paola Italiani [2*] and Anna Chiara De Luca [1,2*]*

[1] Institute for Experimental Endocrinology and Oncology, "G. Salvatore" (IEOS), Second Unit, Consiglio Nazionale Delle Ricerche (CNR), Napoli, Italy, [2] Institute of Biochemistry and Cell Biology (IBBC), Consiglio Nazionale Delle Ricerche (CNR), Napoli, Italy, [3] Institute of Applied Sciences and Intelligent Systems (ISASI), Unit of Napoli, Consiglio Nazionale Delle Ricerche (CNR), Napoli, Italy, [4] Department of Biology and Evolution of Marine Organisms, Stazione Zoologica "Anton Dohrn", Napoli, Italy, [5] The Shenzhen Institutes of Advanced Technology (SIAT), Chinese Academy of Science (CAS), Shenzhen, China

Edited by:
Junji Xing,
Houston Methodist Research Institute,
United States

Reviewed by:
Marco Di Gioia,
Boston Children's Hospital and
Harvard Medical School, United States
Chaojie Wang,
Oregon Health and Science University,
United States
Dheeraj Kumar Singh,
Jacobs University Bremen, Germany

***Correspondence:**
Diana Boraschi
diana.boraschi@cnr.it
Paola Italiani
paola.italiani@ibbc.cnr.it
Anna Chiara De Luca
annachiara.deluca@cnr.it

[†]These authors have contributed equally to this work

Specialty section:
This article was submitted to
Molecular Innate Immunity,
a section of the journal
Frontiers in Immunology

Received: *13 August 2021*
Accepted: *22 September 2021*
Published: *07 October 2021*

Citation:
Verde A, Mangini M, Managò S,
Tramontano C, Rea I, Boraschi D,
Italiani P and De Luca AC (2021) SERS
Sensing of Bacterial Endotoxin on
Gold Nanoparticles.
Front. Immunol. 12:758410.
doi: 10.3389/fimmu.2021.758410

Engineered gold nanoparticles (AuNPs) find application in several fields related to human activities (*i.e.*, food and cosmetic industry or water purification) including medicine, where they are employed for diagnosis, drug delivery and cancer therapy. As for any material/reagent for human use, the safety of AuNPs needs accurate evaluation. AuNPs are prone to contamination by bacterial endotoxin (lipopolysaccharide, LPS), a potent elicitor of inflammatory responses in mammals. It is therefore important, when assessing AuNP immunosafety and immune-related effects, to discriminate between inflammatory effects intrinsic to the NPs from those caused by an undeliberate and undetected LPS contamination. Detection of LPS contamination in AuNP preparations poses different problems when using the current LPS detection assays, given the general interference of NPs, similar to other particulate agents, with the assay reagents and endpoints. This leads to time-consuming search for optimal assay conditions for every NP batch, with unpredictable results, and to the use in parallel of different assays, each with its weaknesses and unpredictability. Thus, the development of highly sensitive, quantitative and accurate assays able to detect of LPS on AuNPs is very important, in view of their medical applications. Surface-enhanced Raman spectroscopy (SERS) is a label-free, sensitive, chemical-specific, nondestructive and fast technique that can be used to directly obtain molecular fingerprint information and a quantitative analysis of LPS adsorbed on AuNPs. Within this study, we describe the use of SERS for the label-free identification and quantitative evaluation - down to few attograms - of the LPS adsorbed on the surface of 50 nm AuNPs. We thus propose SERS as an efficient tool to detect LPS on the AuNP surface, and as the basis for the development of a new sensitive and specific LPS-detection sensor based on the use of AuNPs and SERS.

Keywords: SERS, gold nanoparticles, LPS, biosensor, inflammation, innate immunity

INTRODUCTION

Bacterial endotoxin or lipopolysaccharide (LPS) is the main component of the cell wall of gram-negative bacteria and it is considered a ubiquitous contaminant in the environment, and is resistant to the most common sterilization procedures (1). Human cells are very sensitive to LPS. Upon interaction with membrane receptors (including the Toll-like receptor TLR4, mainly expressed by innate immune cells), LPS triggers the production of inflammatory cytokines such as TNF-α, IL-1β, and chemokines (*e.g.*, CCL2/MCP-1 and CXCL8/IL-8), which all contribute to the inflammatory process (2). One of the most severe effects of LPS in human beings is the septic shock syndrome, a life-threatening disease that accounts for 20% of all global deaths each year (3). For this reason, before being marketed and used in biomedical fields, every drug or biomedical device must undergo accurate testing to determine LPS contamination. The maximum tolerated LPS level in drugs or surgical instruments for human use is 0.5 EU/kg, whilst, if the product comes in contact with the cerebrospinal fluid, the limit is 0.02 EU/kg (4).

In the last years, engineered nanoparticles (NPs) have gained increasing attention in the biomedical field. In particular, gold NPs (AuNPs), owing to their chemical and optical properties, are used in a wide range of different applications in medicine (*e.g.*, drug delivery, diagnostic and imaging procedures) (5–9). As for every biomedical device, also AuNPs must be carefully tested for their immunosafety (inability to trigger immune/inflammatory reactions) and for the presence of LPS contamination. As for many other nanomaterials, AuNPs are very prone to LPS contamination: on one side, because of its amphipathic nature LPS can easily bind NPs with either a cationic or anionic surface; on the other side, LPS binding onto NP surface is facilitated by the high NP surface to volume ratio that increases NP reactivity towards LPS (10). The detection of LPS contamination on AuNPs is crucial for the assessment of particle toxicity and biological properties avoiding misinterpretation of the AuNP impact on human health.

The LPS contamination in pharmaceutical preparations, including AuNPs, is currently detected using regulatory-approved assays: the Limulus amoebocyte lysate (LAL) assay, the monocyte activation test (MAT) and the rabbit pyrogen test (RPT). The application of these assays to the detection of LPS adsorbed on the AuNP surface is not easy, mainly because NPs can interfere with these assays, leading to unreliable results (11–13). Among these methods, the LAL test is the most specific towards LPS. It is based on the capacity of LPS to activate Factor C, an enzyme present in the amoebocytes of the marine arthropod *Limulus polyphemus*. The LAL assay is commercially available in different formats (turbidimetric, gel-clot or chromogenic LAL assays, and most recently the assays based on recombinant factor C). Although LAL assays have a good sensitivity (0.005 EU/mL), NPs can interfere with the assay components or final readout. For this reason, the choice of the most suitable LAL assay is empirical and it can vary case by case (11), or it may be necessary to run different assays in parallel to validate the results (13). Except for the recombinant Factor C assays, all the traditional LAL assays based on the amoebocytes of *L. polyphemus* will soon be abandoned by the regulatory authorities worldwide because of the harm caused to the animals. The RPT and MAT assays measure the response of rabbits *in vivo* or human monocytes *in vitro*, respectively, to inflammatory agents. Their main disadvantage is that they are pyrogen assays, not specific for LPS but sensitive to every inflammatory or pyrogenic agent. Aside from the fact that RPT and MAT are not LPS-specific, particular attention has to be paid to the NP concentration used in these assays to avoid non-specific toxicity for animals or cells. Moreover, these tests are not suitable for NPs carrying cytotoxic drugs. Eventually, as in the case of the LAL assays, the RPT assay will soon be abandoned because of the use of animals. For all these reasons, it is clear that none of the current LPS detection assays is fully suitable for assessing the LPS presence on AuNPs, and that new methods are needed for the reliable and quantitative detection of LPS.

Surface enhanced Raman spectroscopy (SERS) represents an excellent tool for molecular detection, because it can amplify the Raman signals of a given molecule adsorbed onto metallic nanosurfaces, as gold or silver NPs (14). Extraordinary sensing properties of SERS can be achieved by exploiting the metallic NPs' optical amplification mediated by localized surface-plasmon resonances. When an incident laser beam interacts with metallic nanostructures, plasma oscillations of metallic NPs enhance the Raman signals of molecules adsorbed or close to the metallic surface up to 6-7 orders of magnitude (15). Therefore, due to the Raman fingerprint, SERS-based sensing allows to identify and quantify molecules with excellent sensitivity and reproducibility in different environments, thereby enabling the use of the SERS technique for numerous biomedical and biosensing applications (16–20). Indirect SERS sensing, based on the combined use of a SERS tag and a selective aptamer-based binding, has been demonstrated for quantitative detection of endotoxins in a solution (21). Additional advantages of the SERS technique are that it does not require labelling or other specific treatments for sample preparation, measurements can be performed on few μL of desired NP concentration, and the technique is non-destructive, allowing for performing multiple measurements on the same sample. Based on such considerations, the SERS is a good candidate for label-free detection of even minute amounts of LPS directly on metallic NPs.

In this study, we demonstrate the use of the SERS approach for the quantitative detection of LPS contamination in AuNPs. We describe the use of SERS for the direct chemical identification and quantitative evaluation of LPS adsorbed on the surface of 50 nm AuNPs. DLS was used to estimate the number of LPS molecules adsorbed on the surface of AuNPs previously exposed to saturating concentrations of LPS. LPS concentration-dependent SERS signals were collected in order to quantify LPS molecules on AuNPs at low concentration and define the limit of detection (LOD).

MATERIALS AND METHODS

Gold Nanoparticles

LPS-free nanoparticles consisting of 50 nm gold nanospheres (AuNPs) were purchased from Applied Nanoparticles S.L. (Barcelona, Spain). AuNPs are diluted in a 2.2 mM sodium citrate solution at a concentration of 1 mg/mL (corresponding to about $7*10^{11}$ NPs/mL) and stored in sterile endotoxin-free plastic tubes. According to the data sheet, the endotoxin contamination level of these AuNPs was determined to be less than 0.25 EU/mL (roughly corresponding to 25 pg/mL) by the chromogenic LAL assay.

LPS Adhesion to AuNPs

Gel filtration chromatography-purified LPS from *Escherichia coli* O55:B5 (catalogue number L6529) and phenol extraction-purified LPS from *Klebsiella pneumoniae* (catalogue number L4268-10MG) were both obtained by Sigma-Aldrich (Merck KGaA, St. Louis, MO, USA).

Two µL of 50 nm AuNPs (at 1 mg/mL) were incubated with 1 µL of LPS (from *E. coli* or *K. pneumoniae*) at different concentrations (from 0.1 to 5000 µg/mL) in a total volume of 50 µL of 2.2 mM sodium citrate solution for 20 min at 37°C, leading to a stable LPS corona formation (22). In order to remove the non-adsorbed LPS excess, the products were washed twice in sodium citrate solution by centrifugation (22,000 *x g*, 10 min, RT), and pellets were resuspended in sodium citrate solution or cell culture medium, depending on the expected use.

Transmission Electron Microscopy (TEM)

For morphological analysis, an aliquot of bare or LPS-coated AuNPs was drop-casted on a carbon-coated copper grid and allowed to dry at room temperature (RT). TEM images were acquired with an accelerating voltage of 120 kV using a FEI Tecnai 12 Bio Twin Spirit TEM (FEI Company, Hillsboro, OR, USA). Images of bare and LPS-coated AuNPs were analyzed and measured for size distribution using the ImageJ software (Wayne Rasband, NIH, Bethesda, Maryland, USA). Size distribution data were averaged, in order to obtain a mean size both for bare and LPS-coated AuNPs, and their standard deviations (SDs) were calculated.

Dynamic Light Scattering (DLS)

Hydrodynamic diameter and ζ-potential of bare and LPS-AuNPs were measured with a ZetaSizer Nano ZS (Malvern Instruments, Malvern, Worcestershire, UK). The instrument operates with a 633 nm He-Ne laser wavelength and a fixed scattering angle of 173°. For measurements, bare or LPS-AuNPs (20 µL at a concentration of 100 µg/mL) were suspended in 1 mL of distilled water. Data obtained from hydrodynamic diameter and ζ-potential measurements were averaged in order to obtain a mean size and SD both for bare and LPS-coated AuNPs.

The amount of LPS in the corona around AuNPs was estimated as previously described (22). Briefly, the volumes of bare and LPS-coated AuNPs were estimated considering as radius the measured hydrodynamic diameters (sphere model). LPS corona volumes were then obtained by subtracting bare AuNP volumes from concentration-dependent LPS-coated AuNP volumes. Being known the LPS density ρ_{LPS} (1.44 g/cm^3) and the average LPS molecular weight M_{LPS} (20 kDa), the LPS corona masses were estimated by:

$$m_{LPS\,corona} = V_{LPS\,corona} * \rho_{LPS} \tag{1}$$

where:

$$V_{LPS\,corona} = V_{NP+LPS} - V_{NP} = \frac{4}{3}\pi\left(R^3_{NP+LPS} - R^3_{NP}\right) \tag{2}$$

V_{NP+LPS} being the volume of LPS-coated AuNPs and V_{NP} the volume of bare AuNPs. R_{NP+LPS} and R_{NP} are hydrodynamic radii of LPS-coated AuNPs and bare AuNPs, respectively.

The number of LPS molecules was then estimated as follows:

$$LPS\ molecules = m_{LPS\,corona}/M_{LPS} \tag{3}$$

Raman and Surface-Enhanced Raman Spectroscopy and Spectra Analysis

Raman and SERS spectra were acquired with an inverted confocal Raman microscope (XploRA INV, HORIBA Jobin Yvon S.A.S., Villeneuve d'Ascq, France) equipped with a 785 nm wavelength diode laser (23). A 60x/1.2 NA water immersion objective (Nikon) was used to focus the laser light onto the sample and collect the Raman signal. The back scattered light from the sample was spectrally filtered by a notch filter and then directed towards a spectrometer equipped with a holographic grating (600 lines/mm). Finally, Raman signal was detected by a thermoelectrically cooled CCD detector. The pinhole (500 µm) and spectrometer entrance slit (200 µm) were selected to ensure an in-plane spatial resolution (x-y plane) of about 400 nm and 5 µm along z axis.

For Raman experiments, the LPS powder was deposited on a CaF_2 coverslip (Crystran Ltd., Poole, UK), and then the laser was focused onto the sample. Raman spectra were acquired with 8.8 mW laser power at the sample and 30 s integration times per spectra.

For SERS experiments, LPS-coated AuNPs were drop-casted onto a CaF_2 coverslip (Crystran Ltd.) and let dry at RT. SERS spectra were acquired with 0.9 mW laser power and 1 s integration time. The Raman and SERS spectra of the LPS were averaged and background corrected by creating a baseline with the 2nd Derivative method and then subtracting it with the Peak Analyser function available in OriginLab (OriginLab Corporation, Northampton, MA, USA).

Enhancement Factor (EF)

To provide an estimate of the signal amplification experienced by each molecule on the nanostructure, we calculated the enhancement factor (EF) (15). A Byphenil-4-Thiol (BPT) solution in ethanol at a concentration of 1 mM was used for EF estimations. A drop (2 µL) of 50 nm AuNPs (concentration at 1 mg/mL) was drop-casted on a CaF_2 slide and let to dry. By incubating the SERS slide in the BPT solution for 24 h, thanks to the thiol groups showing a strong affinity with the surface, a uniform self-assembled monolayer of BPT molecules on gold surface is obtained (24).

The EF was calculated as:

$$EF = \frac{I_{SERS}}{I_{Raman}}\frac{N_{Raman}}{N_{SERS}} \tag{4}$$

where I_{SERS} and I_{Raman} are the intensities of the SERS and Raman signals normalized to the different laser powers and integration times, N_{Raman} and N_{SERS} are the number of probed molecules.

N_{Raman} can be defined as follows:

$$N_{Raman} = \frac{A_{Laser}\, h\, \rho_{BPT}\, N_A}{M} \tag{5}$$

where A_{Laser} indicates the area of the laser spot size (waist of ~ 800 nm) and h is the Rayleigh length (~ 10 μm). BPT density (1.1 g/cm^3) is indicated with ρ_{BPT} while N_A and M are Avogadro constant (6.022*10^{23} mol^{-1}) and BPT molecular weight (186.3 g/mol), respectively.

On the other hand, N_{SERS} can be defined as:

$$N_{SERS} = \pi R^2 A_{Laser}\, \sigma_{NPs} \sigma_{BPT} \tag{6}$$

where πR^2 is the area occupied by a 50 nm AuNP when lying on a surface (*R is the radius*), σ_{NPs} is the 50 nm AuNPs packing density, *i.e.*, number of AuNPs per area unit (4*10^{-5}/nm^2), in this case the area analysed by Atomic Force Microscopy (AFM)l (**Supplementary Figure 1**) and σ_{BPT} is BPT packing density (considered to be 4 molecules/nm^2) (25).

Limit of Detection (LOD)

Signal to noise ratio (SNR), at each LPS concentration, is a measure related to the quality of the signal and can be defined as:

$$SNR = \frac{I_{Signal}}{I_{Noise}};\ 1 \le SNR \tag{7}$$

where I_{Signal} is the average intensity of the SERS peak at 1610 cm^{-1} an I_{Noise} is the noise intensity, evaluated as the SD in the spectral region between 1700 and 1800 cm^{-1} (26). In order to estimate limit of detection (LOD) of our system, which is the concentration at which SNR becomes equal to unity, we focused our attention on the linear region of SNR *vs.* LPS concentration trend and performed a linear fit of the experimental data.

Human Monocyte Isolation and Macrophage Differentiation

Human peripheral blood mononuclear cells (PBMCs) were isolated from buffy coats of healthy donors by Ficoll-Paque gradient density separation (GE Healthcare, Bio-Sciences AB, Uppsala, Sweden). CD14$^+$ monocytes were separated from PBMCs using magnetic microbeads conjugated with an anti-CD14 antibody (Miltenyi Biotec, Bergisch Gladbach, Germany) according to the manufacturer's instructions. Cell viability was assessed by trypan blue dye exclusion and found to be >95%. Monocytes were plated at 350,000 cells/well in a 24-well plate and cultured in RPMI-1640 + Glutamax-I medium (GIBCO by Life Technologies, Paisley, UK) supplemented with 5% heat-inactivated human AB serum (Sigma-Aldrich) and 50 μg/mL gentamicin sulfate (GIBCO). Cells were cultured in a humidified atmosphere of 5% CO$_2$ and at 37°C. Monocytes were differentiated into macrophages in the presence of 50 ng/mL macrophage colony-stimulating factor (R&D Systems, Minneapolis, MN, USA) for 7 days, refreshing the medium every other day. Differentiation into macrophages was confirmed morphologically and by decreased expression of CD14 and increased expression of CD206 compared to monocytes. Macrophages were treated with LPS, bare AuNPs or LPS-AuNPs for 24 h. After treatment, cells were fixed for 15 min at RT in 4% paraformaldehyde (v/v) for morphological analysis, while culture supernatants were collected and stored at -80°C until testing for cytokine production.

Analysis of Cell Morphology

After fixation, macrophages were permeabilized in 0.02% saponin, 0.5% BSA, and 50 mM ammonium chloride in PBS (blocking solution). Actin cytoskeleton was stained using 33 nM Alexa488-labelled phalloidin (Life Technologies), while nuclei were stained with 2 μg/mL Hoechst 33258 (Sigma Aldrich). Cells were then washed 3x with PBS, and the coverslips were mounted and examined by confocal microscopy (LSM 510; Zeiss, Oberkochen, Germany). Untreated and LPS-activated cells were blind-counted in 30 random fields for each coverslip. Cells were defined as "not activated" when their morphology was regular and without filopodia, and "activated" when filopodia were present on the cell surface.

Cytokine Analysis

The production and release of the inflammatory cytokine TNF-α, the anti-inflammatory factors IL-1Ra and IL-10, and the chemokine CCL2 was assessed by ELISA (R&D Systems) in the culture supernatants, following the manufacturer's instructions. Absorbance of assay wavelength was measured at 450 nm using a Cytation 3 imaging reader (BioTek, Winooski, VT, USA). ELISA data were analyzed by GraphPad Prism 9 (GraphPad Inc., La Jolla, CA, USA), and are presented as percentage, considering LPS 10 ng/mL as 100%. Results are reported as mean ± SD of values from different donors/experiments. Statistical significance of differences is indicated by p values, calculated using a paired Student's two-tail t test.

RESULTS AND DISCUSSION

AuNP Morphological Characterization

Both bare and AuNPs incubated with 5 μL of LPS at a concentration of 1 mg/mL (LPS-AuNPs, see *Materials and Methods* section) were morphologically characterized by TEM, and representative images are reported in **Figure 1**. Bare AuNPs show a diameter of 50 ± 3 nm (**Figure 1A**), confirming the nominal diameter at synthesis. On the other hand, LPS-AuNPs have a diameter of 61 ± 2 nm (**Figure 1B**), corresponding to an increment of 22% compared with bare AuNPs (**Figure 1C**). The increment in the LPS-AuNP diameter is indicative of the LPS adhesion to the NP surface. This finding is also confirmed by TEM images of the LPS-AuNPs, in which it is possible to observe a bright gray halo around NPs, suggestive of an LPS corona with a thickness of ~ 5 nm. Although TEM provides the morphological characteristics of AuNPs, their quantitative analysis for statistical evaluation is extremely difficult and operator dependent, thus highly variable. For these reasons, we have provided an additional evaluation with DLS.

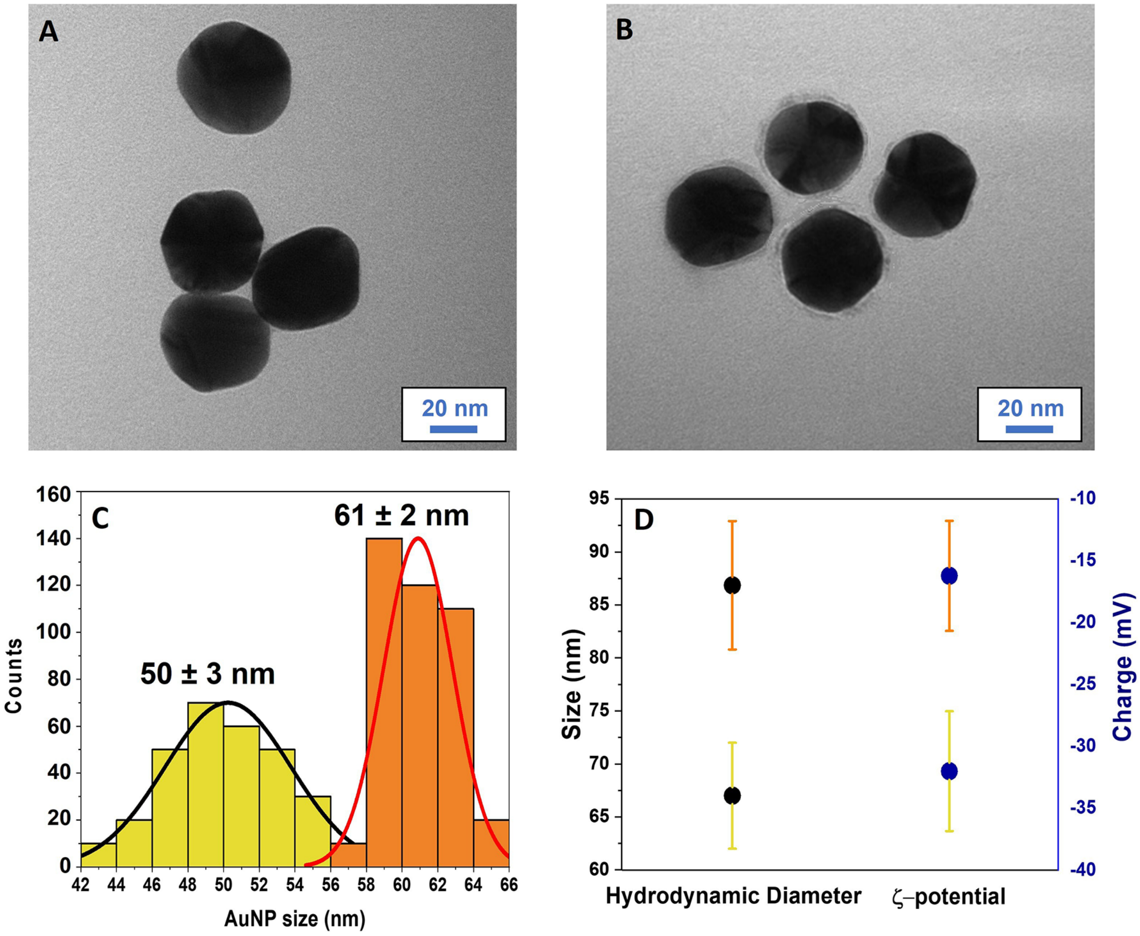

FIGURE 1 | Morphology analysis of the AuNPs and estimation of the LPS corona. TEM images of bare AuNPs **(A)** and LPS-coated AuNPs **(B)**. The LPS corona can be observed as a gray halo around AuNPs. Scale bar: 20 nm. **(C)** Size histograms and Gaussian distribution (black and red lines) related to bare (yellow) and LPS-coated AuNPs (orange). Counts were obtained by measuring the AuNP size in the TEM images. **(D)** Comparison between hydrodynamic diameters and ζ-potentials of bare (yellow SDs) and LPS-coated AuNPs (orange SDs). Results are reported as mean ± SD of data from 5 independent experiments.

DLS Measurements and Estimation of the LPS Corona

DLS measurements were performed in order to characterize the hydrodynamic diameter and ζ-potential changes of AuNPs when incubated with different LPS concentrations. First, we performed the DLS measurements by incubating 2 µL AuNPs (1 mg/mL) with 5 µL LPS (1 mg/mL), in order to ensure the saturation of the NP surface with LPS. The hydrodynamic diameter and ζ-potential of the LPS-coated AuNPs were then compared to those of bare AuNPs (**Figure 1D**). The hydrodynamic diameters of bare and LPS-coated AuNPs were 67 ± 5 nm and 87 ± 6 nm, respectively, while their ζ-potentials were -32 ± 5 mV and -16 ± 4 mV, confirming the LPS corona formation around AuNPs. We then measured the hydrodynamic diameters and ζ-potentials of AuNPs incubated with different concentrations of LPS. The trends of the hydrodynamic diameter and ζ-potential as a function of the LPS concentration are reported in **Figures 2A, B**, respectively. A dose-response function was used to fit both hydrodynamic diameters and ζ-potentials data (27). The hydrodynamic diameter shows a linear increase in the LPS concentration range (10 -100 µg/mL) and reaches a saturation for concentration higher than (500 µg/mL). We suppose that the AuNPs size in the linear range increases linearly with the number of molecules of LPS covering the surface of the AuNPs, allowing for the formation of a surface layer that becomes uniform in the saturation region. When the curve reaches a plateau value (500 -5000 µg/mL), the LPS covers the whole NP surface and a uniform LPS layer coating the AuNPs can be hypothesized (saturation of the AuNP surface). As far ζ-potentials are concerned, **Figure 3B** additionally confirms the adhesion of LPS on the NP surface and a saturation behavior for concentration up to 500 µg/mL. Similar to size, when the LPS layer covering the AuNPs becomes uniform, no further variations of the ζ-potential are detectable. The hydrodynamic diameters measured by DLS in saturation conditions (500 - 5000 µg/mL) were used for estimating the number of LPS molecules composing the uniform corona (22). Estimations of LPS corona volumes and number of LPS molecules in it are reported in the **Supplementary Tables 1**, **2**. The number of LPS molecules composing the LPS corona around a single AuNP in saturation conditions was estimated to be 9000 ± 2000. Finally, the total amount of LPS that could bind to 1 µg of 50 nm AuNPs was estimated by multiplying the LPS corona mass for the number of AuNPs used in the experiments, corresponding to ~10^9 NPs. Thus, the total amount of LPS adhering to 1 µg of AuNPs at saturation was estimated to be 200 ± 50 ng.

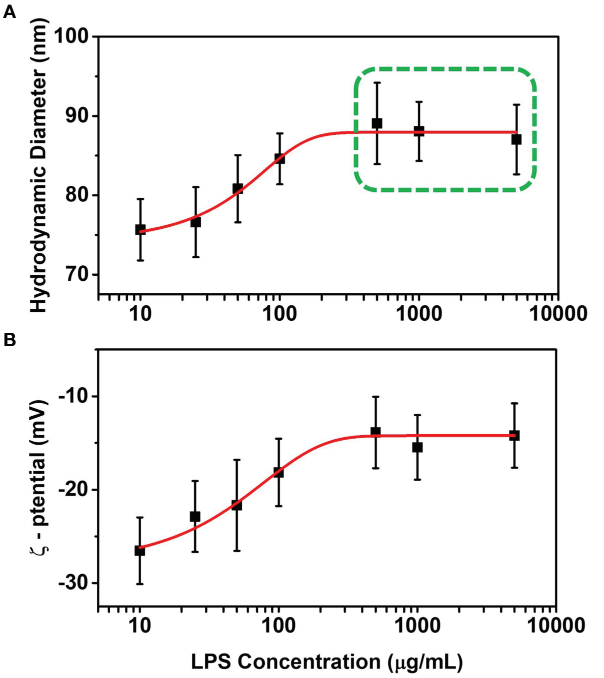

FIGURE 2 | DLS analysis and estimation of the LPS corona. Hydrodynamic diameter **(A)** and ζ-potential **(B)** of AuNPs incubated with different LPS concentrations. The hydrodynamic diameter of bare AuNPs is 67 ± 5 nm, and their ζ-potential is -32 ± 5 mV (see). In panel A, hydrodynamic diameter values used for LPS corona estimation on 50 nm AuNPs in saturation condition are highlighted with a green dashed square. Results are reported as mean ± SD of data from 4 independent experiments.

Biological Effects of LPS-AuNPs on Primary Human Macrophages

In order to verify if the DLS estimation of the amount of LPS bound to AuNPs was reliable, we measured the LPS activity in biological assays, by assessing the activation of innate immune cells. In particular, we used human monocyte-derived macrophages, which are particularly sensitive to LPS (compared to mouse cells or transformed cell lines). First, we examined by confocal microscopy the effect of bare and LPS-coated AuNPs on the macrophage actin cytoskeleton morphology (appearance of lamellipodia and filopodia) (28). **Figure 3** shows the morphology of control untreated macrophages and of macrophages exposed to 200 ng/mL LPS, 1 µg/mL bare AuNPs and 1 µg/mL LPS-coated AuNPs (the amount of LPS of AuNPs calculated as 200 ng, as shown above). Bare AuNPs did not cause morphological changes in macrophages *per se* (**Figure 3**). On the other hand, LPS-coated AuNPs caused the production of filopodia in the same measure as the corresponding concentrations of free LPS (**Figure 3**).

An extensive comparison of free *vs*. NP-bound LPS was performed by examining the inflammatory macrophage

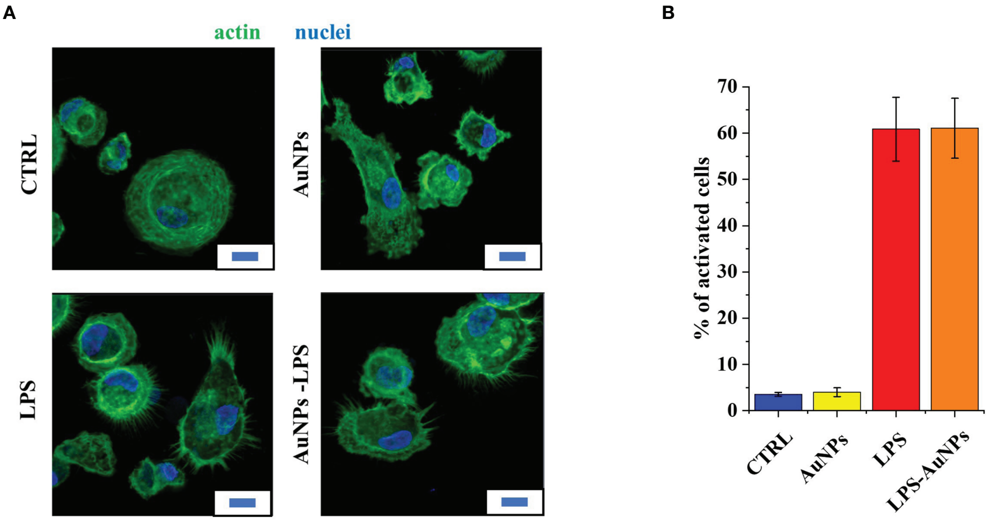

FIGURE 3 | LPS-coated AuNPs induce morphological changes in macrophages. **(A)** Confocal microscopy images showing the morphology of human monocyte-derived macrophages either untreated (CTRL) or exposed to 200 ng/mL free LPS, 1 µg/mL bare AuNPs (AuNPs) and 1 µg/mL LPS-coated AuNPs that contain 200 ng/mL LPS (LPS-AuNPs). The filamentous actin is stained in green, cell nuclei in blue. Scale bar: 10 µm. **(B)** Quantitative evaluation of cells with an activated phenotype for each treatment. Total cell counts for the 3 independent experiments: 2890 cells in the CTRL sample; 2744 cells in the free LPS sample; 2777 cells in the AUNP sample; 2779 cells in the LPS-AuNP sample. Mean ± SD of data from 3 independent experiments.

activation in terms of production of inflammation-related cytokines in response to increasing concentrations of LPS either free or bound to AuNPs. As shown in **Figure 4**, bare AuNPs did not affect the basal production of the inflammatory factors TNF-α (**Figure 4A**) and CCL2 (**Figure 4B**). Conversely, LPS-coated AuNPs induced the production of TNF-α and of CCL2 with an activation profile that fully overlaps with that induced by free LPS. These results indicate that the DLS estimation of the quantity of LPS bound to NPs was realistic. The fact that LPS attached on the surface of AuNPs can induce human macrophage activation with the same concentration-dependent profile as free LPS supports the hypothesis that association to AuNPs does not change the LPS structure in a way that hampers its binding to macrophage receptors and consequent inflammatory activation.

Since LPS-induced inflammatory activation is self-regulating, with the concomitant induction of anti-inflammatory mechanisms (29), we also tested the production of two important anti-inflammatory cytokines, IL-10 and IL-1Ra. As for the other cytokines, bare AuNPs have no effect on the basal levels of IL-1Ra (**Figure 4C**) and IL-10 (**Figure 4D**), while LPS is active in inducing the production of both anti-inflammatory factors. Notably, while exposure to LPS-AuNPs induced a production of IL-1Ra superimposable to that induced by free LPS, LPS-AuNPs were significantly less active than LPS in inducing the production of the other anti-inflammatory cytokine IL-10. We may hypothesize that, while not affecting the activation of plasma membrane TLR4 and its MyD88-dependent activation pathway, the LPS-coated particles may interfere with the intracellular trafficking of TLR4, in particular with the step of LPS-induced endocytosis of TLR4 and the endocytosis-dependent stimulation of the TRIF pathway. Indeed, the LPS-induced production of TNF-α and IL-1Ra is dependent on the MyD88-initiated pathway, whereas IL-10 production is consequent to the production of type I IFN, which is induced by LPS through the TRIF pathway (30). Recently, it has been reported that the E3 ubiquitine ligase TRIM29 is a negative regulator of type I IFN production (31), suggesting the possibility that LPS-AuNPs may inhibit the production of IL-10 through the enhancement of the expression/activity of TRIM29 and consequent decrease of type I IFN production.

It is important to consider that the biological activity of LPS is different depending on its concentration. As also shown in the

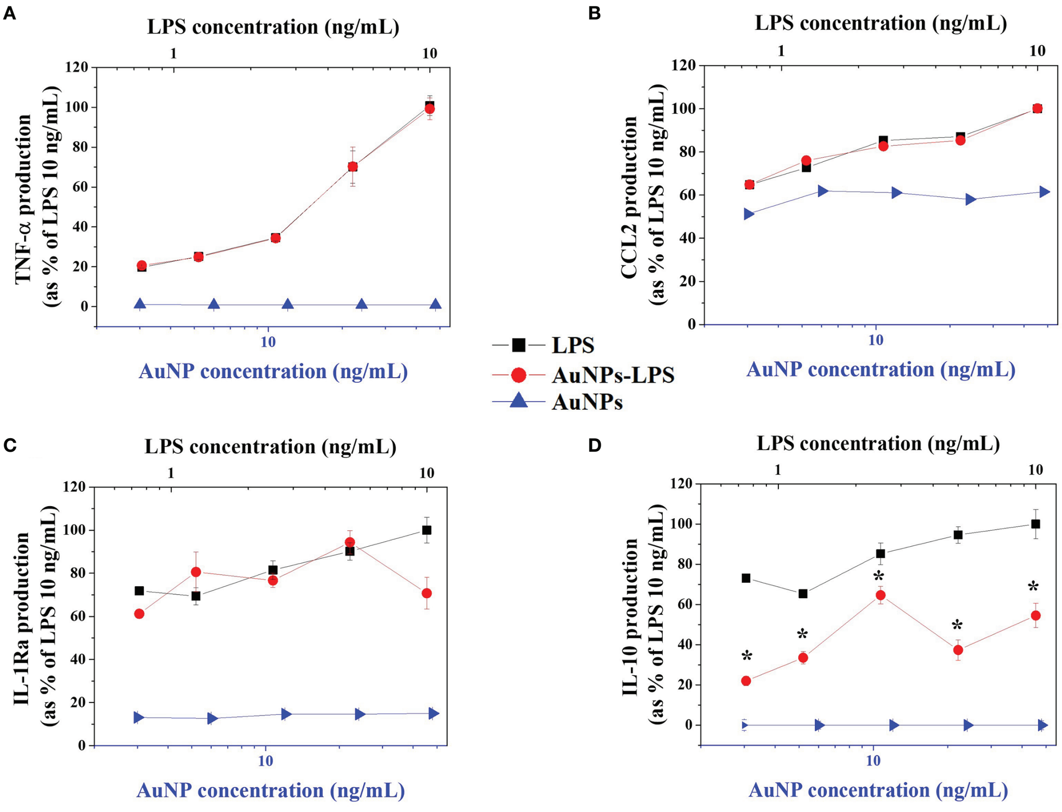

FIGURE 4 | Macrophage activation by LPS-coated AuNPs. Human monocyte-derived macrophages were treated for 24 h with free LPS (black squares), bare (AuNPs; blue triangles) and LPS-coated AuNPs (AuNPs-LPS; red dots). The production of TNF-α **(A)**, CCL2 **(B)**, IL-1Ra **(C)** and IL-10 **(D)** was measured in the culture supernatants by ELISA and normalized as percentage of the maximum value (cytokine levels produced in response to 10 ng/mL LPS). Cytokine concentration ranges were: 0.08-9.40 ng/mL for TNF-α; 0.18-0.38 ng/mL for CCL2; 10.23-78.0 ng/mL for IL-1Ra; 0.28-1.27 ng/mL for IL-10. Results are reported as mean ± SD of data from 3 independent experiments performed on cells from 3 individual donors. *$p < 0.01$ LPS *vs*. LPS-AuNPs (Student's *t* tests).

results reported in **Figure 4**, the induction of potent inflammatory factors requires higher LPS concentrations, in support of the hypothesis that inflammation starts only as reaction to a substantial threat, while the regulation of more homeostatic defensive factors occurs in response to much lower LPS amounts. An example is the inflammatory cytokine IL-1β, whose gene is upregulated in response to as little as 10 pg/mL LPS but that needs much higher LPS concentrations (2-3 ng/mL) for the maturation and secretion of the active inflammatory protein (32). In **Figure 4**, it is evident that high LPS concentrations are necessary for inducing the production of the potent inflammatory factor TNF-α, while at the lowest concentration used (0.65 ng/mL) induction of TNFα is minimal but production of the anti-inflammatory factors IL-1Ra and IL-10 is already at plateau. This implies that a very low number of LPS molecules on NPs can still trigger significant activation of human innate immune cells. An additional issue is that different LPS, coming from different bacteria, have a different inflammation-inducing capacity. LPS detection bioassays provide results in terms of "Endotoxin Units" (EU), based on biological activity (activation of Factor C in the case of LAL assays), while the correspondence between EU and ng is approximate: the conventional correspondence of 1 EU equal to 100 pg holds almost true for the LPS extracted from the *E. coli* serotype O111:B4 but can be 10-100x higher or lower for other LPS. These considerations underline the need of developing an LPS detection assay that could allow us to measure even very low amounts of LPS adsorbed on NP surfaces, to assess the features of their interaction (in order to evaluate possible structural changes) and, very importantly, to distinguish between different LPS. The development of a SERS assay with such characteristics is described below.

Raman and SERS Characterization of LPS Molecules on AuNPs

AuNPs are able to amplify the Raman signals by localized surface plasmon resonance, and these unique optoelectronic properties were used as detection probe for LPS.

To characterize the sensing performances of the AuNPs, we preliminary calculated the enhancement factor (EF) using the BPT as model analyte. We recorded 100 spectra from different locations of the substrate to create a statistically significant relevant data distribution. According to the eq. 4, our 50 nm AuNPs show an excellent enhancement capacity, with an EF of about 10^7 and a good signal uniformity (see **Supplementary Figure 2**).

Because the intensity enhancement is one of the major interests in direct SERS, we investigated the amplification of the LPS Raman profile using SERS technique. **Figure 5** shows a comparison between Raman and SERS spectra of LPS from *E. coli* O55:B5 at a concentration of 1 mg/mL (**Figures 5A, B**). A clear SERS fingerprint of the bacterial endotoxin, similar to its Raman counterpart and in agreement with what found by other groups, is observed. The SERS bands show a shift in frequency compared to Raman ones, which could be ascribed to the specific group absorbed on AuNPs and its orientation respect to the Au surface (33–35). A Raman line broadening during the SERS process is additionally observed, depending from both intermolecular interactions or slightly varying interaction on the AuNPs (35, 36). The LPS molecule is structurally composed by three different parts: a lipid domain called Lipid A, an oligosaccharide core and an extracellular polysaccharide domain called O-antigen (37). Typical bands associated with the O-antigen and core components of the bacterial endotoxin are at 1300–1320 $\mathrm{cm^{-1}}$ and 1350–1370 $\mathrm{cm^{-1}}$, which can be associated to deformation vibration of C-H bond mode (38). The strongest SERS bands are placed at 973 $\mathrm{cm^{-1}}$ and 1610 $\mathrm{cm^{-1}}$ and can be related to the core or Lipid A units of the molecule. The first band can be ascribed to the CH bending/C-O-C stretching vibration mode, while the second SERS band can be related to double C-C bond stretching (37–39). We hypothesize that the AuNP surface interacts with the Lipid A units (the hydrophobic part of the LPS) leading to a strong enhancement of these bands. However, a numerical calculation should be performed to confirm this hypothesis (33–35). A detailed peak assignment is reported in the **Supplementary Table 3**.

In order to evaluate the LPS signal amplification provided by AuNPs, we calculated the ratio between the SERS and the Raman signal intensities, normalized to power, integration time and concentrations of the target molecule. By considering the intensity of the band at 1610 $\mathrm{cm^{-1}}$, we find that SERS provides gains of about 4 orders of magnitude compared to Raman.

Therefore, the AuNPs allows direct sensing of LPS, providing a good enhancement and reproducibility of the signal and avoiding the use of Raman reporters as previously reported (21). At the same time, the proposed approach allows for non-invasive and non-destructive characterization of the local chemical structure of the molecules attached to the AuNPs, avoiding the use of functionalization procedures.

Chemical specificity is an important advantage of the proposed SERS assay because the Raman peaks allow for easier distinction of different molecules and also different LPS types. In order to verify the specificity of the method, SERS characterization of LPS from two different bacteria, *E. coli* serotype O55:B5 and *Klebsiella pneumoniae*, has been performed (**Figures 5B, C**). Both Lipid A and O-antigen largely vary between the different LPS, representing the bacteria fingerprint (37–41). SERS analysis of the two LPS allows us to identify these differences and to distinguish between the two LPS types. Indeed, by comparing the two acquired SERS spectra, differences in peaks at 960 $\mathrm{cm^{-1}}$, 1025 $\mathrm{cm^{-1}}$ and 1610 $\mathrm{cm^{-1}}$ can be observed (**Figures 5B, C**). Since these signals are produced by the LPS lipidic domain, the observed differences can be associated with the different composition of the Lipid A in the two bacterial species (42, 43). Moreover, differences in signals at 1075 $\mathrm{cm^{-1}}$ and 1525 $\mathrm{cm^{-1}}$ are also present (**Figures 5B, C**). Since these signals are associated with the O-antigen, the differences in these Raman bands can be connected to the variability of the O-antigen among the bacterial species (44, 45).

SERS Measurements of LPS-AuNPs and Limit of Detection

A valuable LPS sensor must be capable of detecting pure LPS in a board concentration range of with high chemical specificity, reproducibility and detection limit.

To evaluate sensitivity of our system, we performed SERS measurements of AuNPs (2 μL at a concentration of 1 mg/mL)

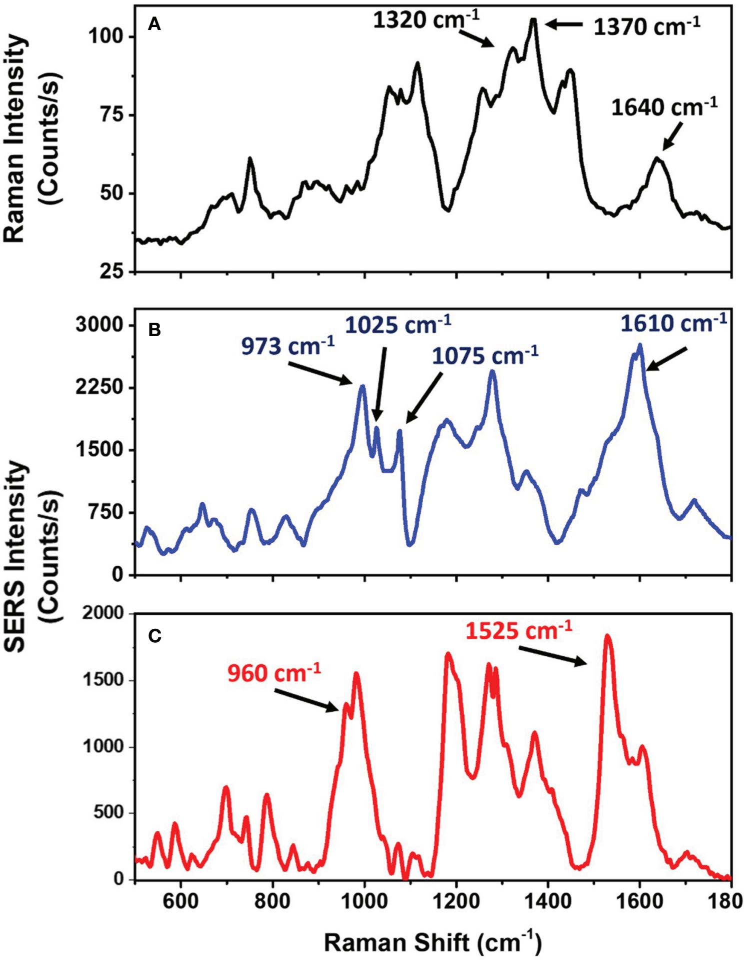

FIGURE 5 | Raman and SERS spectra of LPS from *E. coli* and *K. pneumoniae.* **(A)** Raman spectrum of LPS powder from *E. coli.* **(B)** SERS spectrum of 50 nm AuNPs incubated with 1 mg/mL of LPS from *E. coli*. **(C)** SERS spectrum of 50 nm AuNPs incubated with 1 mg/mL of LPS from *K. pneumoniae.*

incubated with 1 µL of LPS at different concentrations. At each concentration, the SERS signals were collected from 400 randomly selected regions of the substrate, and the mean spectrum was evaluated. **Figure 6A** shows 10 randomly selected spectra and the mean SERS spectrum for the LPS at 1 mg/mL. The spectra variability for this set of measurements was about 10%, which confirms that an excellent reproducibility of SERS technique. The high reproducibility associated to SERS signals could be due to the non-significant conformational changes that the molecules experience as they interact with the gold surface. According to our hypothesis, LPS molecules interact with AuNPs through their hydrophobic part (Lipid A) while the hydrophilic portion (O-antigen) is oriented towards the medium. This hypothesis is further strengthened by the presence of SERS bands at 973 cm^{-1} and 1610 cm^{-1}, ascribed to the Lipid A, in all LPS concentration-dependent SERS spectra (**Figure 6B**). Furthermore, according to this assumption, LPS multilayer formation is not possible because, once the AuNP surface is saturated by LPS molecules, LPS phosphate groups in solution cannot interact with nanoparticles. On the other hand, citrate anions in the sample solution help LPS monomer formation and the consequent interaction with AuNPs. As a matter of fact, citrate anions are able to remove divalent cations in LPS micelles thereby weakening aggregate structures (46).

The SNR at each LPS concentration was evaluated by taking into account the ratio of the average of the peak intensity value at 1610 cm^{-1} to the SD of the spectral region between 1700 and 1800 cm^{-1}. **Figure 6C** shows the measured SNR as a function of LPS concentration. The SERS spectra are reproducible at all the LPS concentrations. The signal intensities at lower LPS concentrations are good enough to detect and distinguish LPS at different concentrations from 0.1 to 1000 µg/mL, overcoming the limitation of the DLS measurements. It can be noted that the SNR values follow a positive increasing correlation with the LPS concentration in the range (0.1-100 µg/mL) and then reaches a plateau at LPS concentrations > 500 µg/mL. These results confirm the DLS data, suggesting that for concentrations > 500 µg/mL LPS uniformly covers the NP surface without the creation of multilayers.

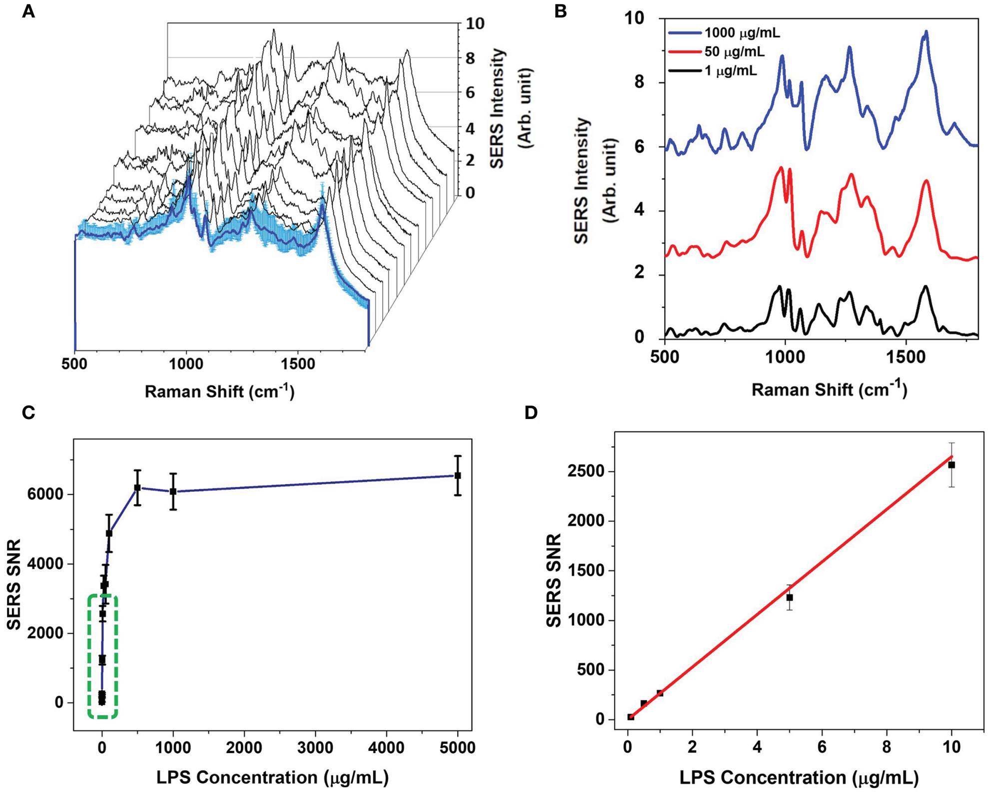

FIGURE 6 | SERS measurements of the LPS-AuNPs. **(A)** Variability of raw SERS signals acquired on AuNP clusters related to a single concentration of LPS (1 mg/mL). **(B)** Average background-corrected SERS signals of AuNPs incubated with different LPS concentrations. LPS concentration (μg/mL) associated to each average SERS spectra are indicated on the right. Every SERS signal is obtained by averaging 30 spectra. **(C)** 1610 cm^{-1} peak SERS intensity signal to noise ratio (SNR) as a function of LPS concentration. The blue line represents the theoretical trend for concentration-dependent SERS signals. Green dashed square highlights the linear region of the trend, reported in the panel **(D)**. **(D)** Linear region of SNR on which LOD was estimated. Means ± SD of 1610 cm^{-1} peak SNR are reported. The red line represents the linear fit of the experimental data.

The limit of detection (LOD), that is the concentration value at which the SNR becomes equal to unity (26), was estimated from a linear fit of the experimental data in the range (0.1-10 μg/mL) to be 2.6 ± 0.1 ng/mL (**Figure 6D**), comparable to the range obtained with colorimetric LAL assays (13). This LOD value has been obtained by considering the nominal concentration of LPS and AuNPs in the whole solution. However, the SERS system detects the signal from the few NPs available in the laser area - that is about 1000 AuNPs – providing a real LOD of 160 (± 10) fg/mL, that is lower than the detection limit of LAL assays (13). Furthermore, the proposed SERS approach does not suffer the limit of the fluorophore quenching, which is a serious issue in colorimetric and fluorogenic LPS detection assays, especially for nanoparticles, and allows to measure the number of LPS molecules directly on the single AuNP, without the use of SERS tag or functionalization procedures, as previously reported (21). Indeed, since the number of LPS molecules adsorbed on the NPs, in saturation condition, can be evaluated by the DLS measurements, as reported in the **Supplementary Table 1**, it is possible to estimate the SERS SNR as a function of the number of LPS molecules per AuNP (47). Therefore, we demonstrated that the minimum detectable number of LPS molecules per each AuNP is 5 ± 1, corresponding to about 0.16 ± 0.01 ag of LPS (see **Supplementary Table 2** and **Supplementary Figures 3**, **4**).

CONCLUSIONS

In this study, an ultra-sensitive direct SERS sensing method was successfully developed, demonstrating the excellent ability of SERS technique to detect LPS directly on AuNPs without the use of any tag or functionalization procedure. We exploited the nanoparticles itself to detect the SERS signal of the endotoxin, to specifically identify the type of endotoxin and to quantitatively measure the amount of LPS on a single AuNP. Compared with existing approaches, SERS sensing showed good chemical specificity (allowing for an easy distinction of different molecules and different LPS types, without the use of functionalization procedures), broad detection range (0.1-1000 μg/mL), low detection limit (LOD of 5 LPS molecules per AuNP), high reproducibility and little sample volume required. The simple spectroscopic detection mechanism of SERS is low cost and reliable, and there is no need to select appropriate NP concentrations or functionalize/stain the sample before preforming measurements. Moreover, high enhancement of the Raman signal is inherently built into the assay, allowing for easy, direct and rapid detection of low LPS concentrations compared to other assays. The proposed sensor can be used to quantify the amount of LPS molecules attached on a single AuNP, that is 5 ± 1 LPS molecules at the minimum detectable signal, corresponding to about 0.16 ± 0.01 ag of LPS. These results pave the way to develop a robust bio-sensor based on the use AuNPs and SERS for LPS detection and quantification, with high sensitivity and specificity, which can complement the current LPS detection assays based on biological activity (recombinant Factor C assay and MAT).

DATA AVAILABILITY STATEMENT

The raw data supporting the conclusions of this article will be made available by the authors, without undue reservation.

AUTHOR CONTRIBUTIONS

AV and MM are joint first authors. ACDL, PI and DB conceptualized and designed the study. AV, MM, and SM designed, performed the experiments and analyses under the supervision of ACDL and PI. CT and IR performed DLS experiments. All the authors analyzed and discussed the data. AV and MM wrote the first draft. All authors contributed to the article and approved the submitted version.

FUNDING

This work was supported by the EU Commission H2020 project ENDONANO (GA 812661) and PANDORA (GA671881). ACLL acknowledges financial support from the Italian Association for Cancer Research (AIRC) IG grant no. 21420, Italian Ministry for University and Research (project PON-NeON) and POR Campania FESR 2014/2020 (project POR-PLATT).

ACKNOWLEDGMENTS

The authors acknowledge the Department of Environmental, Biological and Pharmaceutical Sciences and Technologies of the Università della Campania Luigi Vanvitelli (Napoli, Italy) that coordinates the PhD programme of AV. The authors also thank Dr. G. Coppola of ISASI-CNR for the AFM analysis and Marinelli Pirozzi of the EuroBioimaging Infrastructure for the TEM analysis. The authors would like to thank Dr. G. Zito of ISASI-CNR for the constructive discussion.

SUPPLEMENTARY MATERIAL

The Supplementary Material for this article can be found online at: https://www.frontiersin.org/articles/10.3389/fimmu.2021.758410/full#supplementary-material

REFERENCES

1. Gorbet MB, Sefton MV. Endotoxin: The Uninvited Guest. *Biomaterials* (2005) 26:6811–7. doi: 10.1016/j.biomaterials.2005.04.063
2. Pober JS, Cotran RS. Cytokines and Endothelial Cell Biology. *Physiol Rev* (1990) 70:427–51. doi: 10.1152/physrev.1990.70.2.427
3. Rudd KE, Johnson SC, Agesa KM, Shackelford KA, Tsoi D, Kievlan DR, et al. Global, Regional, and National Sepsis Incidence and Mortality, 1990-2017: Analysis for the Global Burden of Disease Study. *Lancet* (2020) 395:200–11. doi: 10.1016/S0140-6736(19)32989-7
4. The Unites States Pharmacopoeia Convention. *<85> Bacterial Endotoxin Test*. (2012). US Pharmacopeial Convention
5. Aminabad NS, Farshbaf M, Akbarzadeh A. Recent Advances of Gold Nanoparticles in Biomedical Applications: State of the Art. *Cell Biochem Biophys* (2019) 77:123–37. doi: 10.1007/s12013-018-0863-4
6. Elahi N, Kamali M. Baghersad MHRecent Biomedical Applications of Gold Nanoparticles: A Review. *Talanta* (2018) 184:537–56. doi: 10.1016/j.talanta.2018.02.088
7. Jeong H-H, Choi E, Ellis E, Lee T-C. Recent Advances in Gold Nanoparticles for Biomedical Applications: From Hybrid Structures to Multi-Functionality. *J Mater Chem B* (2019) 7:3480–96. doi: 10.1039/C9TB00557A
8. Guo J, Rahme K, He Y, Li LL, Holmes JD, O'Driscoll CM. Gold Nanoparticles Enlighten the Future of Cancer Theranostics. *Int J Nanomedicine* (2017) 12:6131–52. doi: 10.2147/IJN.S140772
9. Khandelwal P, Singh DK, Poddar P. Advances in the Experimental and Theoretical Understandings of Antibiotic Conjugated Gold Nanoparticles for Antibacterial Applications. *ChemistrySelect* (2019) 4:6719–38. doi: 10.1002/slct.201900083
10. Jones CF, Grainger DW. *In Vitro* Assessments of Nanomaterial Toxicity. *Adv Drug Deliv Rev* (2009) 61:438–56. doi: 10.1016/j.addr.2009.03.005
11. Li Y, Italiani P, Casals E, Tran N, Puntes VF, Boraschi D. Optimising the Use of Commercial LAL Assays for the Analysis of Endotoxin Contamination in Metal Colloids and Metal Oxide Nanoparticles. *Nanotoxicology* (2015) 9:462–73. doi: 10.1080/17435390.2017.1401142
12. Li Y, Boraschi D. Endotoxin Contamination: A Key Element in the Interpretation of Nanosafety Studies. *Nanomedicine* (2016) 11:269–87. doi: 10.2217/nnm.15.196
13. Mangini M, Verde A, Boraschi D, Puntes VF, Italiani P, De Luca AC. Interaction of Nanoparticles With Endotoxin Importance in Nanosafety Testing and Exploitation for Endotoxin Binding. *Nanotoxicology* (2021) 15:558–76. doi: 10.1080/17435390.2021.1898690
14. Le Ru EC, Etchegoin PG. *Principles of Surface-Enhanced Raman Spectroscopy and Related Plasmonic Effects. 1st edition*. Amsterdam: Elsevier Science (2008). p. 688.
15. Campion A, Kambhampati P. Surface-Enhanced Raman Scattering. *Chem Soc Rev* (1998) 27:241–50. doi: 10.1039/A827241Z
16. Schlucker S. SERS Microscopy: Nanoparticle Probes and Biomedical Applications. *ChemPhysChem* (2009) 10:1344–54. doi: 10.1002/cphc.200900119
17. Cialla D, März A, Böhme R, Theil F, Weber K, Schmitt M, et al. Surface-Enhanced Raman Spectroscopy (SERS): Progress and Trends. *Anal Bioanal Chem* (2011) 403:27–54. doi: 10.1007/s00216-011-5631-x
18. Han L, Duan W, Li X, Wang C, Jin Z, Zhai Y, et al. Surface-Enhanced Resonance Raman Scattering-Guided Brain Tumor Surgery Showing Prognostic Benefit in Rat Models. *ACS Appl Mater Interfaces* (2019) 11:15241–50. doi: 10.1021/acsami.9b00227
19. Managò S, Quero G, Zito G, Tullii G, Galeotti F, Pisco M, et al. Tailoring Lab-on-Fiber SERS Optrodes Towards Biological Targets of Different Sizes. *Sens Actuators B Chem* (2021) 339:129321. doi: 10.1016/j.snb.2020.129321
20. Managò S, Tramontano C, Delle Cave D, Chianese G, Zito G, De Stefano L, et al. SERS Quantification of Galunisertib Delivery in Colorectal Cancer Cells

by Plasmonic-Assisted Diatomite Nanoparticles. *Small* (2021) 2101711:1–15. doi: 10.1002/smll.202101711

21. Xiang S, Ge C, Li S, Chen L, Wang L, Xu Y. *In Situ* Detection of Endotoxin in Bacteriostatic Process by SERS Chip Integrated Array Microchambers Within Bioscaffold Nanostructures and SERS Tags. *ACS Appl Mater Interfaces* (2020) 12(26):28985–92. doi: 10.1021/acsami.0c04897
22. Li Y, Shi Z, Radauer-Preiml I, Andosch A, Casals E, Luetz-Meindl U, et al. Bacterial Endotoxin (Lipopolysaccharide) Binds to the Surface of Gold Nanoparticles, Interferes With Biocorona Formation and Induces Human Monocyte Inflammatory Activation. *Nanotoxicology* (2017) 11:1157–75. doi: 10.1080/17435390.2017.1401142
23. Managò S, Migliaccio N, Terracciano M, Napolitano M, Martucci NM, De Stefano L, et al. Internalization Kinetics and Cytoplasmic Localization of Functionalized Diatomite Nanoparticles in Cancer Cells by Raman Imaging. *J Biophotonics* (2018) 11:e201700207. doi: 10.1002/jbio.201700207
24. Quero G, Zito G, Manago S, Galeotti F, Pisco M, De Luca AC, et al. Nanosphere Lithography on Fiber: Towards Engineered Lab-On-Fiber SERS Optrodes. *Sensors* (2018) 18:680. doi: 10.3390/s18030680
25. Managò S, Zito G, Rogato A, Casalino M, Esposito E, De Luca AC, et al. Bioderived Three-Dimensional Hierarchical Nanostructures as Efficient Surface-Enhanced Raman Scattering Substrates for Cell Membrane Probing. *ACS Appl Mater Interfaces* (2018) 10:12406–16. doi: 10.1021/acsami.7b19285
26. De Luca AC, Reader-Harris P, Mazilu M, Mariggio S, Corda D, Di Falco A. Reproducible Surface-Enhanced Raman Quantification of Biomarkers in Multicomponent Mixtures. *ACS Nano* (2014) 8:2575–83. doi: 10.1021/nn406200y
27. Altshuler B. Modeling of Dose-Response Relationships. *Environ Health Perspect* (1981) 42:23–7. doi: 10.1289/ehp.814223
28. Williams LM, Ridley AJ. Lipopolysaccharide Induces Actin Reorganization and Tyrosine Phosphorylation of Pyk2 and Paxillin in Monocytes and Macrophages. *J Immunol* (2000) 164:2028–36. doi: 10.4049/jimmunol.164.4.2028
29. Murphy K, Weaver C, Berg L. *Janeway's Immunobiology*. *10th edition*. New York: Garland Science (2022).
30. Chang EY, Guo B, Doyle SE, Cheng G. Cutting Edge: Involvement of the Type I IFN Production and Signaling Pathway in Lipopolysaccharide-Induced IL-10 Production. *J Immunol* (2007) 178:6705–9. doi: 10.4049/jimmunol.178.11.6705
31. Xing J, Weng L, Yuan B, Wang Z, Jia L, Rui J, et al. Identification of a Role for TRIM29 in the Control of Innate Immunity in the Respiratory Tract. *Nat Immunol* (2016) 17:1373–80. doi: 10.1038/ni.3580
32. Oostingh GJ, Casals E, Italiani P, Colognato R, Stritzinger R, Ponti J, et al. Problems and Challenges in the Development and Validation of Human Cell-Based Assays to Determine Nanoparticle-Induced Immunomodulatory Effects. *Part Fibre Toxicol* (2011) 8:8. doi: 10.1186/1743-8977-8-8
33. Lam ATN, Yoon J, Ganbold E-O, Singh DK, Kim D, Cho K, et al. Colloidal Gold Nanoparticle Conjugates of Gefitinib. *Colloids Surf B* (2014) 123:61–7. doi: 10.1016/j.colsurfb.2014.08.021
34. Lam ATN, Yoon J, Ganbold E-O, Singh DK, Kim D, Cho K, et al. Adsorption and Desorption of Tyrosine Kinase Inhibitor Erlotinib on Gold Nanoparticles. *J Colloid Interface Sci* (2014) 425:96–101. doi: 10.1016/j.jcis.2014.03.032
35. Singh DK, Ganbold E-O, Cho E-M, Lee CM, Yang SI, Joo S. Tautomerism of a Thiabendazole Fungicide on Ag and Au Nanoparticles Investigated by Raman Spectroscopy and Density Functional Theory Calculations. *J Mol Struct* (2013) 1049:464–72. doi: 10.1016/j.molstruc.2013.06.060
36. Artur C, Le Ru EC, Etchegoin PG. Temperature Dependence of the Homogeneous Broadening of Resonant Raman Peaks Measured by Single-Molecule Surface-Enhanced Raman Spectroscopy. *J Phys Chem Lett* (2011) 2:3002–5. doi: 10.1021/jz2013787
37. Rietschel ET, Brade H, Holst O, Brade L, Muller-Loennies S, Mamat U, et al. Bacterial Endotoxin: Chemical Constitution, Biological Recognition, Host Response, and Immunological Detoxification. *Curr Top Microbiol Immunol* (1996) 216:39–81. doi: 10.1007/978-3-642-80186-0_3
38. Osorio-Roman IO, Aroca RF, Astudillo J, Matsuhiro B, Vasquez C, Pérez JM. Characterization of Bacteria Using Its O-Antigen With Surface-Enhanced Raman Scattering. *Analyst* (2010) 135:1997–2001. doi: 10.1039/c0an00061b
39. Barret TW. Laser Raman Spectra of Mono-, Oligo- and Polysaccharides in Solution. *Spectrochim Acta A Mol Biomol Spectrosc* (1981) 37:7. doi: 10.1016/0584-8539(81)80168-7
40. Czamara K, Majzner K, Pacia MZ, Kochan K, Kaczor A, Baranska M. Raman Spectroscopy of Lipids: A Review. *J Raman Spectrosc* (2015) 46:4–20. doi: 10.1002/jrs.4607
41. Steimle A, Autenrieth IB, Frick JS. Structure and Function: Lipid A Modifications in Commensals and Pathogens. *Int J Med Microbiol* (2016) 306:290–301. doi: 10.1016/j.ijmm.2016.03.001
42. Kawahara K. Variation, Modification and Engineering of Lipid A in Endotoxin of Gram-Negative Bacteria. *Int J Mol Sci* (2021) 22(5):2281. doi: 10.3390/ijms22052281
43. Mills G, Dumigan A, Kidd T, Hobley L, Bengoechea JA. Identification and Characterization of Two Klebsiella Pneumoniae lpxL Lipid A Late Acyltransferases and Their Role in Virulence. *Infect Immun* (2017) 85: e00068–17. doi: 10.1128/IAI.00068-17
44. Hansen DS, Mestre F, Alberti S, Hernandez-Alles S, Alvarez D, Merino S, et al. Klebsiella Pneumoniae Lipopolysaccharide O Typing: Revision of Prototype Strains and O-Group Distribution Among Clinical Isolates From Different Sources and Countries. *J Clin Microbiol* (1999) 37:56–62. doi: 10.1128/JCM.37.1.56-62.1999
45. Liu B, Furevi A, Perepelov AV, Guo X, Cao H, Wang Q, et al. Structure and Genetics of Escherichia Coli O Antigens. *FEMS Microbiol Rev* (2020) 44:655–83. doi: 10.1093/femsre/fuz028
46. Schwarz H, Gornicec J, Neuper T, Parigiani MA, Wallner M, Duschl A, et al. Biological Activity of Masked Endotoxin. *Sci Rep* (2017) 7:44750. doi: 10.1038/srep44750
47. Massarini E, Wästerby P, Landstrom L, Lejon C, Beckc O, Andersson PO. Methodologies for Assessment of Limit of Detection and Limit of Identification Using Surface-Enhanced Raman Spectroscopy. *Sens Actuators B Chem* (2015) 207:437–46. doi: 10.1016/j.snb.2014.09.116

Conflict of Interest: The authors declare that the research was conducted in the absence of any commercial or financial relationships that could be construed as a potential conflict of interest.

frontiers in Immunology

MINI REVIEW
published: 06 January 2022
doi: 10.3389/fimmu.2021.795232

Applications and Immunological Effects of Quantum Dots on Respiratory System

Laibin Ren[1,2†], **Lingwei Wang**[1,2†], **Markus Rehberg**[3], **Tobias Stoeger**[3], **Jianglin Zhang**[2,4*] and **Shanze Chen**[1,2*]

[1] Institute of Respiratory Diseases, Shenzhen People's Hospital, Jinan University, Shenzhen, China, [2] The First Affiliated Hospital, Southern University of Science and Technology, Shenzhen, China, [3] Comprehensive Pneumology Center, Institute of Lung Biology and Disease, Helmholtz Center Munich, German Research Center for Environmental Health, Neuherberg and Member of the German Center for Lung Research, Munich, Germany, [4] Department of Dermatology, Shenzhen People's Hospital, Jinan University, Shenzhen, China

Edited by:
Yang Li,
Chinese Academy of Sciences (CAS),
China

Reviewed by:
Lang Rao,
Shenzhen Bay Laboratory, China
Xiang Gao,
Sichuan University, China
Martin Himly,
University of Salzburg, Austria

***Correspondence:**
Jianglin Zhang
zhangjl@csu.edu.com
Shanze Chen
chenshanze@mail.sustech.edu.cn

†These authors have contributed equally to this work and share first authorship

Specialty section:
This article was submitted to Molecular Innate Immunity, a section of the journal Frontiers in Immunology

Received: *14 October 2021*
Accepted: *13 December 2021*
Published: *06 January 2022*

Citation:
Ren L, Wang L, Rehberg M, Stoeger T, Zhang J and Chen S (2022) Applications and Immunological Effects of Quantum Dots on Respiratory System. Front. Immunol. 12:795232. doi: 10.3389/fimmu.2021.795232

Quantum dots (QDs), are one kind of nanoscale semiconductor crystals with specific electronic and optical properties, offering near-infrared mission and chemically active surfaces. Increasing interest for QDs exists in developing theranostics platforms for bioapplications such as imaging, drug delivery and therapy. Here we summarized QDs' biomedical applications, toxicity, and immunological effects on the respiratory system. Bioapplications of QDs in lung include biomedical imaging, drug delivery, bio-sensing or diagnosis and therapy. Generically, toxic effects of nanoparticles are related to the generation of oxidative stresses with subsequent DNA damage and decreased lung cells viability *in vitro* and *in vivo* because of release of toxic metal ions or the features of QDs like its surface charge. Lastly, pulmonary immunological effects of QDs mainly include proinflammatory cytokines release and recruiting innate leukocytes or adaptive T cells.

Keywords: quantum dot, respiratory system, biomedical applications, cytotoxicity, immunological effects

INTRODUCTION

Quantum dots (QDs), one of the extensively studied nanoparticle material forms, have specific optical, photochemical, and electronic properties. The quantum confinement effect was firstly reported by Ekimov and Onushchenko in 1981, when they observed a size effect on the absorption characteristics of CuCl crystals dispersed in silicate glasses (1). The application of QDs on biological system for bioimaging started in1998 (2).

Generally, traditional organic label dyes have no ability of producing the near-infrared emission highly desired for biological imaging because of its high tissue penetration (low light scattering and absorption), and for this reason tunable optical QDs have gained utmost interests. Depending on specific properties of the material, different kinds of QDs could even be excited by the very same wavelength light, and their narrow emission stripes could be detected in parallel at individual wavelengths, allowing the conduction of different assays simultaneously. The compositions, shell thickness, and size of QDs determine the fluorescence bands (3). Generally QDs, like CdTeS, PbS, and HgTe, consist of elements such as Cd, Pb, and Hg from the II–VI, III–IV and IV–VI groups of the periodic table. Additionally, ternary I–III–VI elements (such as Ag, Cu, and Se)-related QDs like Ag2S, CuInS2, and CdZnSe have been developed (4). Besides, massive research regarding QDs has shifted to new emerging materials. Among them silicon- and carbon-based QDs have attracted great attention. Especially, the carbon-based QDs, namely, carbon dots, carbon nanotube dots, and graphene QDs have characteristics such as improved biocompatibility, nontoxicity or low toxicity, eco-friendly, stable and photobleaching-resistant compared to conventional QDs (5, 6). It was reported that the distribution of carbon-based QDs in the organ is related to its volume size: the smaller, the harder to clear. Besides, the surface charge of QDs affects their distribution: charged QDs are more capable of protein adsorption, accumulating in organs like liver. On the contrary, the neutral ones without protein adsorption are safely removed by renal filtration (7).

BIOAPPLICATIONS OF QDS IN LUNG

Pulmonary System Related Bioimaging

Though bio-imaging with fluorescence has been employed in cells or animal for decades, broader clinical applications are limited for the visible light poor transmission through biological tissues, which promoted scientists to employ the optical window of Near Infrared (NIR) to carry out deep-tissue optical imaging (8, 9). Many formulations of QDs for bio-imaging lung cell signaling, tissue structures or related lung diseases in respiratory system are currently available in the literature.

Overcoming traditional chest radiology by radiation-free, noninvasive imaging is an important field in nanotechnology. DNA methylation is an essential part of human epigenetic modifications. The abnormal patterns of DNA methylation are tightly connected with lots of cancers or genetic diseases of liver, colon, and lung (10). Wang et al. reported that fluorescence resonance energy transfer (FRET) based on QDs mediated by tricyclic ligation chain reaction (LCR) were employed to image and examine DNA methylation in H157 non-small cell lung cancer cells, detecting DNA methylation with single 5-methylcytosine resolution low to 1.0 aM and a 7-order dynamic magnitude scope, which held great potential for precisely epigenetically evaluating lung cancers (11).

As QDs could in real-time image and reflect biological molecular activities in cells, some attempts have been taken to study lung cellular signaling pathways. In lung vascular cell adhesion molecule-1 (VCAM) is central to lung inflammation because it facilitates recruiting and anchoring phagocytes to the pulmonary endothelium, potentially aggravating endothelial damages and eventual pulmonary dysfunction (12). NADPH oxidase 2 (Nox2) is the major source of inflammation-associated reactive oxygen species (ROS) production. Orndorff et al. showed that endothelial Nox2 induced VCAM expression associated with lung inflammation *in vivo* through functionalizing fluorescent QDs with antibodies toward VCAM to detect its expression in a mouse model, demonstrates the relationship between Nox2 and VCAM during lung inflammation (13).

Light microscopic imaging of blood vessels is a good way to observe the hemodynamics of lungs under normal or pathologic conditions. Saitoh et al. captured precise peripheral pulmonary alveoli blood flow time-courses by injecting glutathione-decorated QDs into heart right ventricles and at different time-points performing *in vivo* cryotechnique (IVCT) in normal or abnormal lung stages (acute pulmonary hypertension mouse model) (14), thereby facilitating the investigation of mice lung microvascular hemodynamics and the altered structures.

Several reports attempted to image lung tumor-related markers *in vitro* or *in vivo* by employing QDs. Liu et al. produced "Affibody" QDs (AF-QDs) to bio-image the human epidermal growth factor receptor type 2 (HER2) in human pulmonary tumor cells. The approach avoided complicated chemical conjugation process and demonstrated to be a promising way of fluorescent nanoprobes for imaging cancer targets (15). Xue et al. employed CdTeS QDs decorated by folate–polyethylene glycol (FA–PEG) to image the overexpressed folate receptor (FR) in the tumors, demonstrating good biocompatibility, excellent specificity, and sensitivity for tumors imaging. Su et al. reported iodine doped carbon dots conjugated with cetuximab as a dual fluorescent/CT probe for bioimaging lung cancer cells epidermal growth factor receptor (EGFR) (16). Additionally, QDs immunofluorescence histochemistry (QDs-IHC) was employed to detect EGFR mutant, RRM2 and Bcl2, and Monocarboxylate transporter 4 (MCT-4) in non-small cell lung cancer patients (17).

Moreover, QDs also have been used to image and detect lung-related viral infections. Using a three-dimensional single-particle tracking technique (SPT) and through labeling avian influenza H9N2 virus with QDs, Wang et al. found that the sialic acid receptors were highly consistent with the number of influenza virus in human bronchial epithelial (HBE) cells, indicating sialic acid receptors may facilitate monitoring the situation that avian influenza viruses infected humans beings (18). Furthermore, by *in vivo* labeling H5N1 pseudotype of avian influenza virus with QDs, Pan et al. found that QD-labeled H5N1p showed sustained and bright fluorescent intensity in mice pulmonary tissues, enabling them to observe respiratory viral infection noninvasively and in real-time (19). Importantly, Gorshkov et al. produced a probe (fluorescent QDs-conjugated recombinant Spike receptor binding domain which could bind to Angiotensin Converting Enzyme 2 (ACE2)) for tracking SARS-CoV-2 virus. By employing the probe, they found the probe immediately bound on the surface of ACE2-GFP-transfected cells with subsequent endocytosis (20).

Drug Delivery Into Lung Tumors

QDs are desired candidates as drug nano-platforms because they can be part of a more complex architecture or as the main carrier. Currently, trials on the application of QDs for drug delivery in the respiratory system mainly focused on pulmonary tumors.

5-Fluorouracil (5FU), an analogue of pyrimidine inhibiting cell metabolism, is a widely employed chemotherapy drug in cancer treatment. Duman et al. developed PEGylated Ag_2S QDs which were decorated with Cetuximab and carried with 5-fluorouracil (5FU) (an anticancer drug). PEGylated Ag_2S QDs demonstrated effectively and selectively delivering 5FU into A549 cells with subsequently significantly increased apoptosis, and also overcame better the cell protective effect of better 5FU-induced autophagy (21).

The folate receptor (FR), highly overexpressing on human pulmonary cancer cells surface, represents another potential candidate for targeted tumor treatment. Ruzycka–Ayoush et al. showed that Ag–In–Zn–S QDs nanocrystals which were decorated with L–cysteine, 11–mercaptoundecanoic acid (MUA), and lipoic acid modified with folic acid (FA) can be employed as a good approach for engaging doxorubicin (DOX) to FRs in A549. The QD–MUA–FA–DOX complex had a great genotoxicity and cytotoxicity, and also inhibited the migration of A549 significantly (22).

Cai et al. presented NH_2-ZnO QDs with hyaluronic acid (HA) decorated with the dicarboxyl-terminated PEG specifically bound to cancer cells glycoprotein CD44. DOX were introduced to PEG modified ZnO QDs decorated with PEG *via* covalent interactions and metal–DOX complex. After uptake, the pH-sensitive QDs dissolved and released Zn^{2+} ion into the endosome and lysosome, followed by a controlled DOX releasing and the metal–drug complex dissociating (23). Importantly, the results showed that Zn^{2+} preferentially killed the tumor cells but had little impact on the healthy control cells.

The development of efficient combination therapy has drawn great attention in the oncotherapy field. Based on QDs nanoparticles, Li et al. delivered small interfering RNA (siRNA), paclitaxel, carboplatin, and doxorubicin for targeting lung tumor. QD nanocarriers delivering Bcl-2-targeted siRNA with other anticancer drugs not only induced greatly higher inhibition in A549 viability than single but furthermore enabled the real-time bioimaging of the delivery of the medicants and release by employing the special fluorescence characteristics (24).

Chronic obstructive pulmonary disease is a nonmalignant but intractable ill condition, manifested by airway obstruction and the increase of sticky mucus layers. Accordingly, QDs material with mucus-penetrating ability offered a novel approach to therapeutically give medicants. Li et al. reported that black phosphorus QDs (BPQDs) modified with PEG-decorated chitosan nano-particle with amikacin, which facilitated deep penetration of nano-vehicles into the mucus layer. The rapid degradation of BPQDs promoted dissociation of PEGylated QDs, accelerated release of amikacin, and eventually destroyed the biofilms (25).

Biosensor and Diagnosis of Lung Tumors

Based on QDs unique light properties, recently the new relevant molecules detection and quantification strategies have arisen. Currently, developing and exploring novel QDs diagnosis methods in respiratory system mainly focused on lung cancers.

For EGFRs overexpressed in the lung cancer cells, Chen et al. developed a novel DNA electrochemiluminescence (ECL) sensor combining with CuZnInS QDs and gold-nanoparticles to detect highly sensitively EGFR gene. The range of target DNA concentration was from 0.05 to 1 nmol/L, and the detection limit reached low enough to 0.0043 nmol/L (26).

Silencing or decreasing tumor suppressor genes expressions always helps the initiation and progression of cancers (27), and DNA methylation is tightly related to the initiation of cancers. Ma et al. utilized the QDs-based FRET nanosensor technology to detect the tumor suppressor genes—protocadherin gamma subfamily B, 6 (PCDHGB6), Homeobox A9 (HOXA9) and Ras association domain family 1 isoform A (RASSF1A)-promoters methylation in non-small-cell lung carcinoma (NSCLC) early-stage specimens or noninvasive bronchial brushing tissues. The method could identify pulmonary tumor tissue samples and noninvasive bronchial brushing tissues from healthy controls with an excellent sensitivity of 92 and 80% respectively (28).

CYFRA 21-1 (a cytokeratin 19 fragment) is part of intermediate filament proteins stabilizing epithelial cells. Its expression on various epithelial cells makes it a useful biomarker in lung or other organ cancers (29). Several studies attempted to develop QDs related methods for detecting CYFRA 21-1 for helping diagnose lung cancer. Firstly, Chen et al. reported that a novel lateral flow test strips (QPs-LFTS) system based on polystyrene QDs particles was generated to examine human serum carcinoembryonic antigen (CEA) and CYFRA 21-1 simultaneously. The limit of detection for CEA or CYFRA 21-1 was 0.35 or 0.16 ng/ml respectively, indicating the system is highly efficient enough to be employed for the early screening and prognosis of lung cancer patients (30). Also, Meng et al. reported that molybdenum oxide QDs (MoOx QDs) were generated in one-pot manner and employed as a versatile probe in an ECL immunoassay of CYFRA21-1 as a model analyte (31). Besides, Alarfaj reported a different way of detecting CYFRA 21-1 that the green synthesized carbon QDs conjugated ZnO nanocomposite using Citrus lemon pericarp quickly determinate human serum CYFRA 21-1 antigen (32). Additionally, Liu et al, presented a method by combining the suspension and planar microarray formats in a single polydimethylsiloxane layer. On the basis of the target proteins, they formed a sandwich structure between the QD probes and the magnetic beads by specific antigen–antibody interactions, which could be used for simultaneous detecting pulmonary tumor biomarkers (CEA, CYFRA21-1 and neuron-specific enolase) with a broad linear dynamic scope and a low detection limit (33).

Therapy Against Lung Tumors, Infection and Pulmonary Arterial Hypertension

QDs have been shown in various applications from the treatment of lung tumors to kill pulmonary infection-related bacteria and also alleviate pulmonary arterial hypertension.

In this context, Sun et al. reported that CdSe/ZnS-3-mercaptopropionic acid and CdSe/ZnS-glutathione QDs could inhibit the expressions of P-glycoprotein gene and protein accounting for multidrug resistance of lung cancer cells by inducing miR-185 and miR-34b, indicating miR-185 and miR-34b could be also interesting and potential targets for lung cancer treatment (34). Moreover, Green Synthesis Derived CdS QDs with *Camellia sinensis* leaf extracts arrested lung tumor cells cycle and decreased cell viability (35). In addition they showed that leaf extract-mediated CdS QDs inhibited pulmonary infection-related gram positive *Streptococcus pyogens* and gram negative *Serratia marcescens in vitro* (36). Besides, Zhao et al. reported that nitrogen-doped carbon QDs (NDQDs) generated from diethylenetriamine (DETA) and D (+)-Glucose monohydrate had specific antibacterial activity against *Staphylococcus* by inducing the rupture and integrity loss of cytoplasmic membrane of methicillin-resistant *Staphylococcus aureus* (37).

Photodynamic therapy (PDT) is a novel and innovative method for treating tumor in which a photosensitizing agent is administered and then exposed to visible or invisible light (38). Hsu et al. reported that Renilla luciferase-immobilized QDs-655 was employed for bioluminescence resonance energy transfer-mediated PDT to efficiently generate ROS, *in vitro* killing tumor cells and *in vivo* inhibiting tumor growth (39). Additionally, Choi et al. found CdSe/ZnS QDs irradiated by ultraviolet A/B inhibited the viability of lung tumor cells and induced cell apoptosis, suggesting that UV irradiation enhanced the efficacy of QDs in photodynamic cancer therapy (40). Besides, Liu et al. encapsulated BPQDs with exosomes (hEX) and found that hEX@BP showed evident tumor cells inhibition in a mice subcutaneous lung cancer model. When combined with photothermal therapy, hEX@BP got a more evident inhibitory effects against tumor cells (41), demonstrating great potentials for clinical applications.

Pulmonary arterial hypertension (PAH) is known as hypertension with high blood pressure in the lungs and primarily affects the pulmonary vasculature (42). In this regard, Zhu et al. reported that amorphous nano-selenium QDs (A-SeQDs) increased cellular tetrahydrobiopterin to protect against PAH through reuniting endothelial nitric oxide synthase (43). Specifically, A-SeQDs not only enhanced nitric oxide production and intracellular BH4 levels, but increased the activity of dihydrofolate reductase in lungs, above of which upregulated pulmonary arterial remodeling. The role of dihydrofolate reductase in preventing PAH was verified by gene knockout mice. In addition, clinical studies showed that the reduced tetrahydrobiopterin and selenium in the blood of patients with PAH confirmed the role of dihydrofolate reductase in the protection from pulmonary arterial hypertension.

TOXICITIES OF QDS IN LUNG

The toxicity concerns regarding QDs are mostly connected with their chemical compositions, especially heavy metal ions in the core of QD such as Cd and Hg which might be released upon endocytic uptake into the cytoplasm of cells (**Figure 1**). However as for all nanoparticles with an extreme high surface to mass ratio, the surface reactivity of QDs is of toxicological concerns and accordingly often modified by surface passivation, e.g., *via* PEGylation.

In Vitro Pulmonary Cytotoxicity

CdTe QDs are a kind of widely employed QDs in biomedicine, and their safety concerns people most. Zheng et al. presented findings about effects of CdTe QDs with different particle sizes on normal human bronchial epithelial cells (44). Acute exposure to CdTe QD induced dose-dependent cytotoxicity and carcinogenicity in BEAS-2B; chronic exposure induced BEAS-2B cell transformation including enhancing cell migration. They further examined the cellular response at the proteome level treated with CdTe QDs. 520Q with 520 nm emission maximum and 580Q with 580 nm emission maximum treatment changed cells proteome greatly in a very similar magnitude. Pre-treatment of cells with glutathione impeded the different upregulated/downregulated proteins and blocked cell death, indicating that ROS mediated QDs-induced cytotoxicity (45).

Besides, Chen et al. present the cytotoxicity of InP/ZnS QDs decorated with NH_2, COOH, OH in human lung cancer cell and alveolar type II epithelial cell (46). High doses of all three QDs decreased the cell viability, causing intracellular ROS generation and cell apoptosis. Additionally, COOH QDs and NH2 QDs were more toxic than OH QDs, suggesting that surface decoration and concentration of InP/ZnS QDs should be optimized well for therapeutic purpose or biological imaging.

Stan et al. reported effects of Si/SiO_2 QDs on human lung fibroblasts MRC-5 cells. They found Si/SiO_2 QDs increased ROS and malondialdehyde (MDA) levels and decreased glutathione contents, suggesting that Si/SiO_2 QDs' cytotoxicity on human lung fibroblast was caused by disturbing cellular homeostasis (47). Furthermore, they found Si/SiO_2 QDs induced MRC-5 cellular membrane disruption, changed cell morphology as actin filaments disrupted. Besides, matrix metalloproteinase (MMP)-1 and MMP-2 and also MMP-9 activity decreased which resulted in an unbalanced extracellular matrix turnover, for which MMPs might be risk factors of pulmonary fibrosis as SiO_2 is a well-known harmful silica agent closely related to silicosis (48).

Because of GQDs biocompatibility and safety, GQDs-related nanomaterials received much more attention. Yuan et al. explored the cytotoxicity of GQDs decorated with COOH, NH2, and CO-N (CH3)2 in A549 cells. By employing trypan blue and thiazoyl blue colorimetric (MTT) assays in order to detect cell viability or flow cytometry analysis to detect cellular apoptosis or necrosis, they found all three GQDs had excellent biocompatibility and low cytotoxicity independent of chemical modifications (49). However, there are also some reports about the harmful effects of GQDs. Tian et al. explored the effects of hydroxyl-decorated GQDs (OH-GQDs) on A549 ($p53^{+/+}$) and H1299 ($p53^{-/-}$) cells. They found OH-GQDs enhanced intracellular ROS generation, led to cell cycle arrest and cells senescence (50). Besides, Xu et al. reported that aminated graphene GQDs (AG-QD) accumulated in rat alveolar macrophages nuclei, further resulting in nuclear damages and DNA cleavage. The detailed mechanisms were that AG-QD induced oxidative damage mediated by directly contacted *via* H-bonding and π–π stacking between AG-QD and DNA and promoted the upregulation of caspase genes (51) (**Figure 1**).

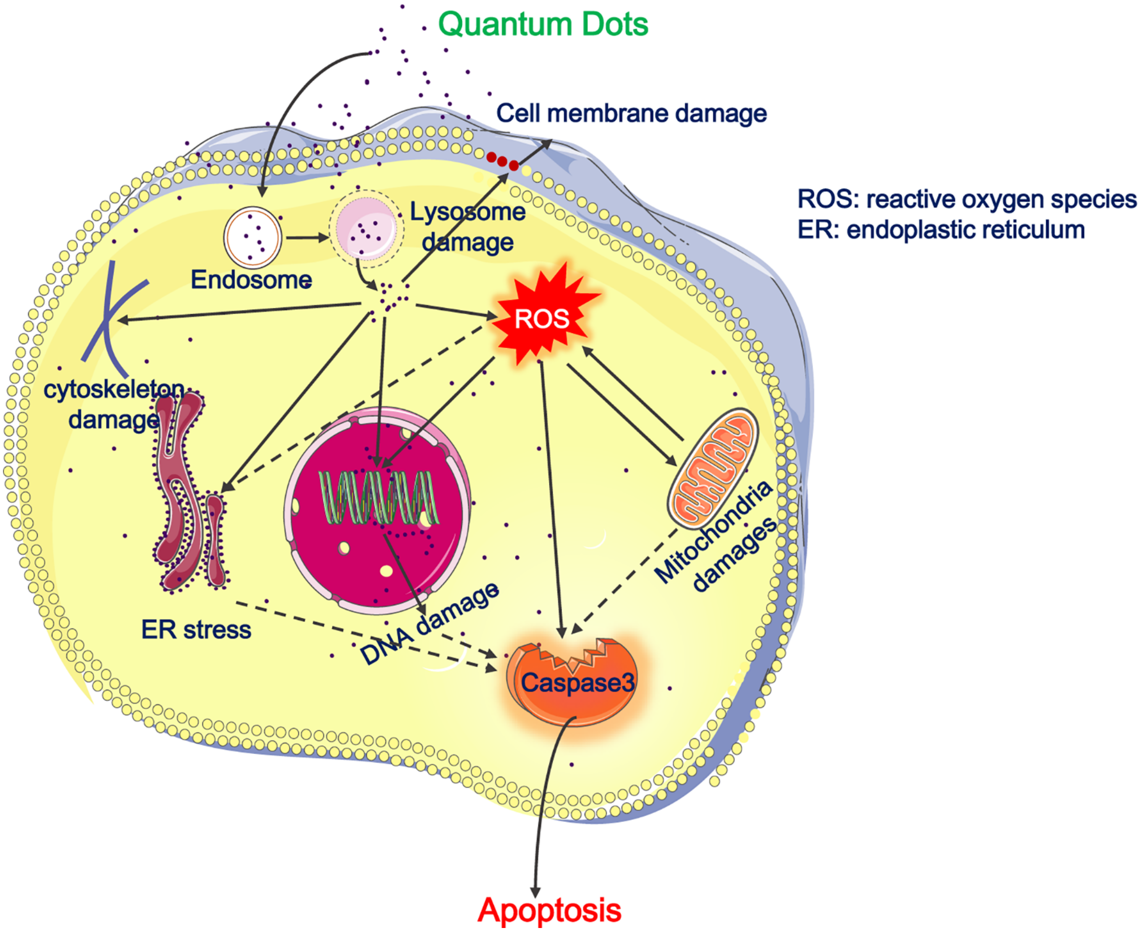

FIGURE 1 | Cytotoxicity of QDs on the respiratory system. The picture illustrates that QDs entered the endo-lysosomal system and then are released into cytoplasm, resulting in cell membrane damages, depolymerization or disruption of cytoskeleton, ROS generation, mitochondrial damages, ER stress, DNA damage, and apoptosis. Besides, QDs-induced ROS promotes mitochondrial damages, ER stress, and apoptosis. Full lines represent the situation demonstrated and dotted lines represent our deductions.

In Vivo Pulmonary Tissue Toxicity

There are several reports indicating QDs depositions resulting in lung tissue damages.

Roberts et al. reported that CdSe/ZnS QDs led to lung abnormities accompanied with increased lactate dehydrogenase, lung injury parameters and albumin. The injury was at its severest at days 7 and 14 after inhalation. QDs dose had a positive correlation with the lung damage severity (52). Also researchers started to get interested in QDs effects on lung mechanics. Scoville et al. reported that amphiphilic polymercoated CdSe/ZnS QDs affected lung mechanics in A/J mice only but not C57BL/6J through using forced oscillation. Besides, they found significant inverse relationships between lung glutathione levels and the lung mechanics by measuring Resistance and Tissue Damping in QD-treated mice (53). Tang et al. reported that CdSe/ZnS QDs decorated with cationic polydiallyldimethylammonium chloride showed acute severe toxicity because of pulmonary embolism. All QDs caused injuries in specific tissues such as lung and liver after acute or long-term exposure, however, the injury degree was determined by their surface properties (54). Yang et al, found that 218 genes were significantly differentially expressed in the lung after ZnO QDs treatment by RNA sequencing. Related signaling and pathways mainly included cell DNA replication, peroxisome proliferator-activated receptor (PPAR) signaling, retinol metabolism, p53 signaling pathway and cellular senescence (55).

The surface modification of QDs could influence *in vivo* toxicity and the biological behavior. In this context, Li et al. explored the *in vivo* toxicity and distributions of InP/ZnS QDs decorated with COOH, NH2, and OH, in BALB/c mice after being intravenously injected. They found there were no evident histopathological abnormalities in all mice tissues after exposure to these three QDs. However, high dose of QDs-NH2 and QDs-COOH resulted in acute inflammation of the whole body but not QDs-OH. In addition, high-dose QDs-COOH induced mice death and slight liver function alternations (56). Moreover, in

BALB/c mice Lin et al. also explored acute toxicity of the above three InP/ZnS QDs with aerosol inhalation. All QDs deposited in the lung, but the amount of QDs-OH was the most abundant possibly because of its largest size in aqueous solutions. Similarly, there were no histopathological conditions in the main mice organs. However, QDs-NH2 led to obvious hyperemia in alveoli septum (57). Additionally, Rehberg et al. reported that amine-modified CdSe/ZnS QDs (PEG), but not carboxyl-CdSe/ZnS QDs (PEG), accumulated in the postcapillary venule vessel wall and increased ischemia–reperfusion-induced leukocyte transmigration in postischemic heart and skeletal muscle (58). Therefore, the surface chemistry of QDs should be given adequate attention to for their biomedical applications.

IMMUNOLOGICAL EFFECTS OF QDs

QDs immunological effects have been studied at the cellular level, organs and the whole body as well in mice. After exposure, QDs are recognized and "swallowed" by lung tissue cells such as epithelial cells and immune cells. Generally, QDs would pose damages to them and induce inflammatory responses, which would recruit innate leukocyte cells (e.g., macrophages and neutrophils) and also adaptive immune T cells.

Several literatures showed the potential of QDs to modulate lung epithelial cells, fibroblast cells or alveolar macrophages inflammatory response, like the activation of proinflammatory signaling or the promotion of cytokines release *in vitro*. For example, Stan et al. reported that Si/SiO_2 QDs enhanced the production of nitric oxide, interleukin-6 (IL-6) and IL-8 expressions in human fibroblast MRC-5 cells (47). Besides, in cellular levels Lee et al. showed TOPO-PMAT CdSe/ZnS QDs induced expressions of neutrophil chemokines Chemokine (C-X-C motif) ligand (CXCL) -1, CXCL-2, IL-6, IL-12, and other proinflammatory factors in mice tracheal epithelial cells, alveolar macrophages, and bone marrow-derived macrophages (59).

In vivo, Ho et al. discovered intratracheal instillation of QD705-COOH induced acute neutrophils infiltration, interstitial lymphocytes infiltration, and a granulomatous reaction with cytokines, chemokines, and metalloproteinase 12 expressions (60). Furthermore, they found QD705-COOH-induced IFN-β expression might be dependent on Toll-like receptor pathways which was dependent on Toll/interleukin-1 receptor domain-containing adapter protein (61).

Besides, Roberts et al. showed that the treatment of CdSe/ZnS induced rat pulmonary inflammatory chemokines, increased innate immune cells (polymorphonuclear cells and alveolar macrophages) and also adaptive immune lymphocytes, indicating the leading to strong immune responses of CdSe/ZnS QDs (52). McConnachie et al. also showed that TOPO-PMAT CdSe/ZnS QDs induced the releasing of CXCL-1, GM-CSF, MIP-1α, and MIP-1γ, and in mouse bronchoalveolar lavage fluid (BALF), and also increased neutrophils infiltration but not alveolar macrophages. They found significantly inverse association between lung tissue cytokines levels, glutathione and BALF neutrophils and deposited pulmonary Cd QDs, indicating decreased glutathione might be the reason of QDs-induced lung inflammation (62). Also, Scoville et al. reported similar findings in NOD/ShiLtJ or NZO/HlLtJ mice (63).

Except for research about QDs direct treatment on lung, Scoville et al. explored the combined effects of house dust mite (HDM) and TOPO-PMAT CdSe/ZnS QDs on allergic airway disease (AAD) of C57BL/6J and A/J mice. Compared with C57BL/6J, they found that HDM plus QD group of A/J mice had more significantly enhanced levels of BALF IL-33 than that in HDM and saline controls. Moreover, A/J mice had greatly more innate lymphoid 2 cells (ILC2s) cells than C57BL/6J mice. ILC2s in A/J mice lung were negatively related to lung glutathione and resident macrophages with high MHC-II, and positively related to resident macrophages with low MHC-II, suggesting QDs could aggravate HDM-induced the development of AAD by recruiting ILC2s and increasing selected cytokines production (64).

In the above literatures, QDs' proinflammatory and immune responses activation roles have been reported. However, there are also reports that QDs negatively regulate inflammation or immunological responses. Firstly, Volarevic et al. showed that GQDs significantly inhibited concanavalin A-induced mouse hepatitis. Specifically, GQDs decreased both apoptosis and autophagy in liver tissue which were associated with the reduced liver T cells producing IFN-γ and a serum IFN-γ decrease (65). Also, recently, Lee et al. reported that GQDs effectively alleviated dextran sulfate sodium-mediated acute and chronic colitis model by inhibiting TH1/TH17 polarization, switching macrophage M1 polarization to M2, and enhancing intestinal regulatory T cell infiltration (66). However, whether GQDs also show anti-inflammatory effects on lung inflammatory diseases like AAD or bacterial or virus infection-induced inflammation and cytokine storm is still unknown and needs to be investigated in the future.

Based on the above, different kinds of QDs would induce respiratory inflammatory response, but the related further details or the underlying mechanisms need to be examined carefully. For example, QDs caused DNA damages in A549 and Beas-2B cell lines (67, 68), and DNA damages reagents-induced cells inflammation are dependent on Toll-like receptors 9 (TLR9) receptor or Cyclic GMP-AMP synthase (cGAS)-Stimulator of Interferon Genes (STING) pathway (69). Therefore it might be possible that QDs-induced cell damage also activates nucleic acid receptor TLR9 or cGAS-STING to mediate inflammatory responses. Alveolar macrophages include proinflammatory M1 type and anti-inflammatory M2 type (**Figure 2**). Whether QDs-induced lung inflammation could be attributed to excessive M1 macrophages activation and damaged M2 macrophages functions also needs to be explored in the future.

Collectively, employing QDs would perturb normal cell signals and cytoskeleton homeostasis, damage essential organelles, e.g., mitochondria and endoplasmic reticulum, and even activate related programmed cell death, which were mainly attributed to QDs' heavy metal cores. Since pulmonary delivered particles are cleared from the lungs only very slowly and thus persist over a long period of time (70), the use of biopersistent

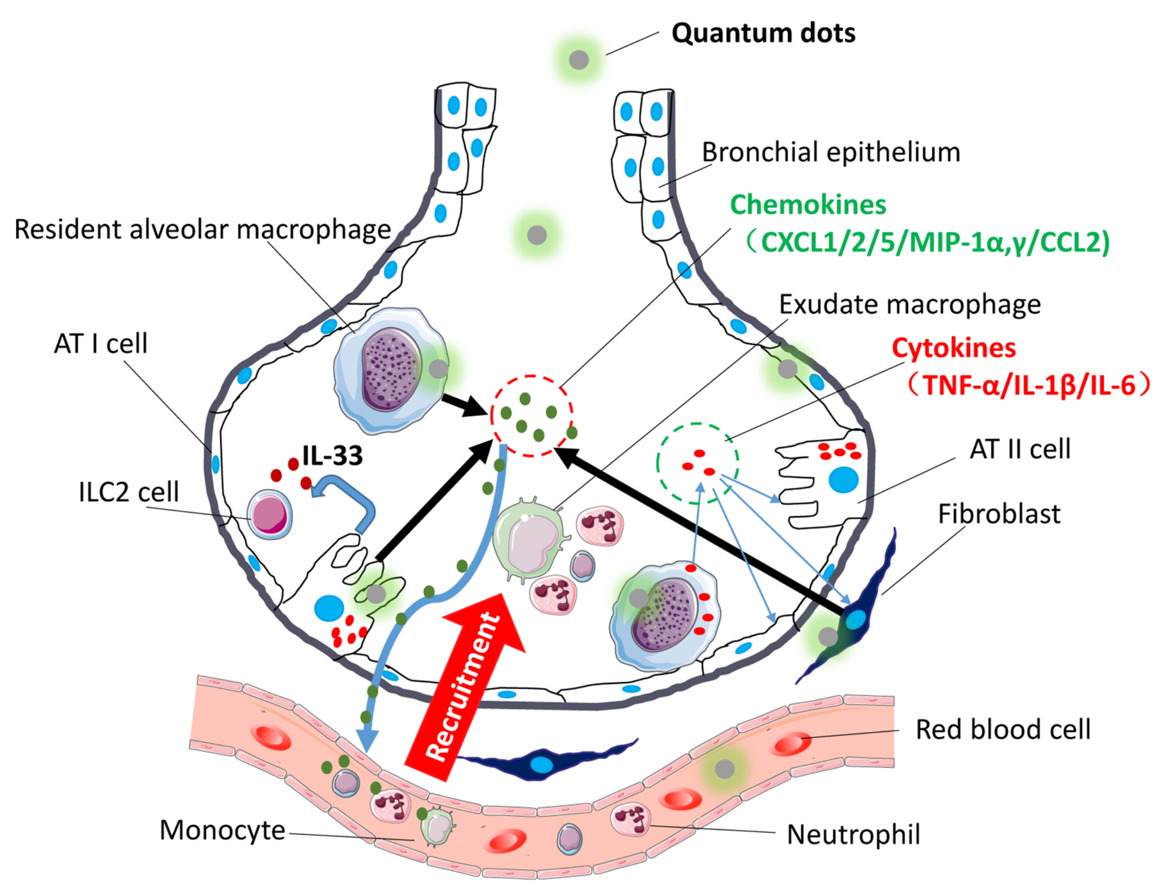

FIGURE 2 | Immune modulatory effects of QDs on the respiratory system. The picture shows that after being exposed to QDs, resident pulmonary macrophages, lung epithelial cells, and fibroblast swallowed QDs, and then QDs would activate inflammatory-related pathway like TLR signaling, which promoted cells to release proinflammatory cytokines (TNF-α, IL-1β, and IL-6) and chemokines (CXCL-1/2/5/MIP-1α,γ/CCL-2). Sequentially neutrophils would be recruited firstly, and then monocyte and adaptive immune T cells would follow. Besides, QDs activated AT II cells and released IL-33 which activated ILC2 cells.

materials such as QDs for diagnosis or therapy has to be balanced for its pros and cons.

CONCLUSION

QDs have high potentials for biomedical applications in areas like bio-imaging, drug delivery, and diagnosis in the pulmonary system. For QDs to be realistically translated into clinical applications, issues such as pulmonary toxicity and immunological responses triggered by QDs should be addressed. Decreasing the toxicity of QDs for example by surface coating with more safe and biocompatible materials or replacing the heavy metal core, or the usage of low toxicity chemical cores such as Zn and graphene still should to be taken into account. In this mini review, we summarized the newest progress in the literature about the employment and the shortcomings of QDs for bioapplications to the respiratory system.

AUTHOR CONTRIBUTIONS

LR and LW performed literature search and prepared the first draft and displayed items of the mini review. MR and TS were involved in critical discussions of the content and display items and revising the draft. JZ and SC were involved in critical discussions of the content and displaying items, writing, and editing of the manuscript. All authors contributed to the article and approved the submitted version.

FUNDING

This work was supported by the National Natural Science Foundation of China (81803183) and the Clinical research of Health and Family Planning Commission of Shenzhen Municipality (SZLY 2017024 to LW).

REFERENCES

1. Ekimov A, Onushenko AA. Quantum Size Effect in Three-Dimensional Microscopic Semiconductor. *JETP Lett* (1981) 34:363–6.
2. Rocha TL, Mestre NC, Saboia-Morais SMT, Bebianno MJ. Environmental Behaviour and Ecotoxicity of Quantum Dots at Various Trophic Levels: A Review. *Environ Int* (2017) 98:1–17. doi: 10.1016/j.envint.2016.09.021
3. Xing SG, Xiong QR, Zhong Q, Zhang Y, Bian SM, Jin Y, et al. Recent Research Advances of Antibody-Conjugated Quantum Dots. *Chin J Anal Chem* (2013) 41:949–55. doi: 10.1016/S1872-2040(13)60663-5
4. Ji X, Pen F, Zhong Y, Su Y, He Y. Fluorescent Quantum Dots: Synthesis, Biomedical Optical Imaging, and Biosafety Assessment. *Colloids Surf B Biointerfaces* (2014) 124:132–9. doi: 10.1016/j.colsurfb.2014.08.036
5. Ge J, Lan M, Zhou B, Liu W, Guo L, Wang H, et al. A Graphene Quantum Dot Photodynamic Therapy Agent With High Singlet Oxygen Generation. *Nat Commun* (2014) 5:1–8. doi: 10.1038/ncomms5596
6. Pang W, Jiang P, Ding S, Bao Z, Wang N, Wang H, et al. Nucleolus-Targeted Photodynamic Anticancer Therapy Using Renal-Clearable Carbon Dots. *Adv Healthc Mater* (2020) 9(16):e2000607. doi: 10.1002/adhm.202000607
7. Liu J, Li R, Yang B. Carbon Dots: A New Type of Carbon-Based Nanomaterial With Wide Applications. *ACS Cent Sci* (2020) 6(12):2179–95. doi: 10.1021/acscentsci.0c01306
8. Smith AM, Duan H, Mohs AM, Nie S. Bioconjugated Quantum Dots for *In Vivo* Molecular and Cellular Imaging. *Adv Drug Delivery Rev* (2008) 60 (11):1226–40. doi: 10.1016/j.addr.2008.03.015
9. Weissleder R. A Clearer Vision for *In Vivo* Imaging: Progress Continues in the Development of Smaller, More Penetrable Probes for Biological Imaging. *Nat Biotechnol* (2001) 19(4):316–7. doi: 10.1038/86684
10. Kulis M, Esteller M. DNA Methylation and Cancer. *Adv Genet* (2010) 70:27–56. doi: 10.1016/B978-0-12-380866-0.60002-2
11. Wang Z, Wang L, Zhang Q, Tang B, Zhang CY. Single Quantum Dot-Based Nanosensor for Sensitive Detection of 5-Methylcytosine at Both CpG and non-CpG Sites. *Chem Sci* (2017) 9(5):1330–8. doi: 10.1039/c8sc90012d
12. Orndorff RL, Hong N, Yu K, Feinstein FS, Zern BJ, Fisher AB, et al. NOX2 in Lung Inflammation: Quantum Dot Based *in Situ* Imaging of NOX2-Mediated Expression of Vascular Cell Adhesion Molecule-1. *Am J Physiol Lung Cell Mol Physiol* (2014) 306(3):L260–8. doi: 10.1152/ajplung.00278.2013
13. Lee IT, Yang CM. Role of NADPH Oxidase/ROS in Pro-Inflammatory Mediators-Induced Airway and Pulmonary Diseases. *Biochem Pharmacol* (2012) 84:581–90. doi: 10.1016/j.bcp.2012.05.005
14. Saitoh Y, Terada N, Saitoh S, Ohno N, Jin T, Ohno S. Histochemical Analyses and Quantum Dot Imaging of Microvascular Blood Flow With Pulmonary Edema in Living Mouse Lungs by "*In Vivo* Cryotechnique". *Histochem Cell Biol* (2012) 137(2):137–51. doi: 10.1007/s00418-011-0892-1
15. Zhao N, Liu S, Jiang Q, Lan T, Cheng Z, Liu H. Small Protein Stabilized Semiconductor Nanoprobe for Targeted Imaging of Cancer Cells. *Chembiochem* (2016) 17(13):1202–6. doi: 10.1002/cbic.201600219
16. Rahman MA, Ruhul Amin AR, Wang D, Koenig L, Nannapaneni S, Chen Z, et al. RRM2 Regulates Bcl-2 in Head and Neck and Lung Cancers: A Potential Target for Cancer Therapy. *Clin Cancer Res* (2013) 19(13):3416–28. doi: 10.1158/1078-0432.CCR-13-0073
17. Qu YG, Zhang Q, Pan Q, Zhao XD, Huang YH, Chen FC, et al. Quantum Dots Immunofluorescence Histochemical Detection of EGFR Gene Mutations in the non-Small Cell Lung Cancers Using Mutation-Specific Antibodies. *Int J Nanomed* (2014) 9:5771–8. doi: 10.2147/IJN.S71310
18. Wang Z, Liu S, Zhang Z. Exploring Sialic Acid Receptors-Related Infection Behavior of Avian Influenza Virus in Human Bronchial Epithelial Cells by Single-Particle Tracking. *Small* (2014) 10(13):2712–20. doi: 10.1002/smll.201303532
19. Pan H, Zhang P, Gao D, Zhang Y, Li P, Liu L, et al. Noninvasive Visualization of Respiratory Viral Infection Using Bioorthogonal Conjugated NearInfrared-Emitting Quantum Dots. *ACS Nano* (2014) 8(6):5468–77. doi: 10.1021/nn501028b
20. Gorshkov K, Susumu K, Chen J, Xu M, Pradhan M, Zhu W, et al. Quantum Dot-Conjugated SARS-CoV-2 Spike Pseudo-Virions Enable Tracking of Angiotensin Converting Enzyme 2 Binding and Endocytosis. *ACS Nano* (2020) 14(9):12234–47. doi: 10.1021/acsnano.0c05975
21. Duman FD, Akkoc Y, Demirci G, Bavili N, Kiraz A, Gozuacik D, et al. Bypassing Pro-Survival and Resistance Mechanisms of Autophagy in EGFR-Positive Lung Cancer Cells by Targeted Delivery of 5FU Using Theranostic Ag2S Quantum Dots. *J Mater Chem B* (2019) 7(46):7363–76. doi: 10.1039/c9tb01602c
22. Matysiak-Brynda E, Bujak P, Augustin E, Kowalczyk A, Mazerska Z, Pron A, et al. Stable Nanoconjugate of Transferrin With Alloyed Quaternary Nanocrystals Ag-In-Zn-S as Biological Entity for Tumor Recognition. *Nanoscale* (2018) 10(3):1286–96. doi: 10.1039/c7nr07819f
23. Ruzycka–Ayoush M, Kowalik P, Kowalczyk A, Bujak P, Nowicka AM, Wojewodzka M, et al. Quantum Dots as Targeted Doxorubicin Drug Delivery Nanosystems in Human Lung Cancer Cells. *Cancer Nanotechnol* (2021) 12:8. doi: 10.1186/s12645-021-00077-9
24. Cai X, Luo Y, Zhang W, Du D, Lin Y. pH-Sensitive ZnO Quantum Dots-Doxorubicin Nanoparticles for Lung Cancer Targeted Drug Delivery. *ACS Appl Mater Interfaces* (2016) 8(34):22442–50. doi: 10.1021/acsami.6b04933
25. Li J, Wang Y, Xue S, Sun J, Zhang W, Hu P, et al. Effective Combination Treatment of Lung Cancer Cells by Single Vehicular Delivery of siRNA and Different Anticancer Drugs. *Int J Nanomed* (2016) 11:4609–24. doi: 10.2147/IJN.S107345
26. Li Z, Luo G, Hu W, Hua J, Geng S, Chu PK, et al. Mediated Drug Release From Nano-Vehicles by Black Phosphorus Quantum Dots for Efficient Therapy of Chronic Obstructive Pulmonary Disease. *Angew Chem Int Ed Engl* (2020) 59 (46):20568–76. doi: 10.1002/anie.202008379
27. Maria Abreu Velez A, Howard MS. Tumor-Suppressor Genes, Cell Cycle Regulatory Checkpoints, and the Skin. *N Am J Med Sci* (2015) 7(5):176–88. doi: 10.4103/1947-2714.157476
28. Chen X, Gui W, Ma Q. Ultrasensitive Detection of EGFR Gene Based on Surface Plasmon Resonance Enhanced Electrochemiluminescence of CuZnInS Quantum Dots. *Anal Chim Acta* (2018) 1009:73–80. doi: 10.1016/j.aca.2018.01.011
29. Ma Y, Bai Y, Mao H, Hong Q, Yang D, Zhang H, et al. A Panel of Promoter Methylation Markers for Invasive and Noninvasive Early Detection of NSCLC Using a Quantum Dots-Based FRET Approach. *Biosens Bioelectron* (2016) 85:641–8. doi: 10.1016/j.bios.2016.05.067
30. Boeck S, Wittwer C, Heinemann V, Haas M, Kern C, Stieber P, et al. Cytokeratin 19-Fragments (CYFRA 21-1) as a Novel Serum Biomarker for Response and Survival in Patients With Advanced Pancreatic Cancer. *Br J Cancer* (2013) 108(8):1684–94. doi: 10.1038/bjc.2013.158
31. Chen Z, Liang R, Guo X. Simultaneous Quantitation of Cytokeratin-19 Fragment and Carcinoembryonic Antigen in Human Serum *via* Quantum Dot-Doped Nanoparticles. *Biosens Bioelectron* (2017) 91:60–5. doi: 10.1016/j.bios.2016.12.036
32. Meng X, Chen X, Wu W, Zheng W, Deng H, Xu L, et al. Electrochemiluminescent Immunoassay for the Lung Cancer Biomarker CYFRA21-1 Using MoO X Quantum Dots. *Mikrochim Acta* (2019) 186 (12):855. doi: 10.1007/s00604-019-3917-4
33. Alarfaj NA, El-Tohamy MF, Oraby HF. New Immunosensing-Fluorescence Detection of Tumor Marker Cytokeratin-19 Fragment (CYFRA 21-1) *via* Carbon Quantum Dots/Zinc Oxide Nanocomposite. *Nanoscale Res Lett* (2020) 15(1):12. doi: 10.1186/s11671-020-3247-9
34. Liu L, Wu S, Jing F, Zhou H, Jia C, Li G, et al. Bead-Based Microarray Immunoassay for Lung Cancer Biomarkers Using Quantum Dots as Labels. *Biosens Bioelectron* (2016) 80:300–6. doi: 10.1016/j.bios.2016.01.084
35. Sun Y, Zhang J, Yin H, Yin J. MicroRNA-Mediated Suppression of P-Glycoprotein by Quantum Dots in Lung Cancer Cells. *J Appl Toxicol* (2020) 40(4):525–34. doi: 10.1002/jat.3924
36. Shivaji K, Mani S, Ponmurugan P, De Castro CS, Davies ML, Balasubramanian MG, et al. Green-Synthesis-Derived CdS Quantum Dots Using Tea Leaf Extract: Antimicrobial, Bioimaging, and Therapeutic Applications in Lung Cancer Cells. *ACS Appl Nano Mater* (2018) 1, 4:1683–93. doi: 10.1021/acsanm.8b00147
37. Zhao C, Wang X, Wu L, Wu W, Zheng Y, Lin L, et al. Nitrogen-Doped Carbon Quantum Dots as an Antimicrobial Agent Against Staphylococcus for the Treatment of Infected Wounds. *Colloids Surf B Biointerfaces* (2019) 179:17–27. doi: 10.1016/j.colsurfb.2019.03.042

38. Gunaydin G, Emre Gedik M, Ayan S. Photodynamic Therapy for the Treatment and Diagnosis of Cancer-A Review of the Current Clinical Status. *Front Chem* (2021) 9:686303. doi: 10.3389/fchem.2021.686303
39. Hsu C, Chen C, Yu H, Lin Y, Lai P. Bioluminescence Resonance Energy Transfer Using Luciferase-Immobilized Quantum Dots for Self-Illuminated Photodynamic Therapy. *Biomaterials* (2013) 34(4):1204–12. doi: 10.1016/j.biomaterials.2012.08.044
40. Choi YJ, Kim YJ, Lee JW, Lee Y, Lim YB, Chung HW. Cyto-/Genotoxic Effect of CdSe/ZnS Quantum Dots in Human Lung Adenocarcinoma Cells for Potential Photodynamic UV Therapy Applications. *J Nanosci Nanotechnol* (2012) 12(3):2160–8. doi: 10.1166/jnn.2012.5781
41. Liu Q, Fan T, Zheng Y, Yang SL, Yu Z, Duo Y, et al. Immunogenic Exosome-Encapsulated Black Phosphorus Nanoparticles as an Effective Anticancer Photo-Nanovaccine. *Nanoscale* (2020) 12(38):19939–52. doi: 10.1039/d0nr05953f
42. Lai YC, Potoka KC, Champion HC, Mora AL, Gladwin MT. Pulmonary Arterial Hypertension: The Clinical Syndrome. *Circ Res* (2014) 115(1):115–30. doi: 10.1161/CIRCRESAHA.115.301146
43. Zhu M, Gao Z, Lu J, Wang Y, Wang G, Zhu TT, et al. Amorphous Nano-Selenium Quantum Dots Prevent Pulmonary Arterial Hypertension Through Recoupling Endothelial Nitric Oxide Synthase. *Aging (Albany NY)* (2020) 13 (3):3368–85. doi: 10.18632/aging.202215
44. Zheng W, Xu Y, Wu D, Yao Y, Liang Z, Tan HW, et al. Acute and Chronic Cadmium Telluride Quantum Dots-Exposed Human Bronchial Epithelial Cells: The Effects of Particle Sizes on Their Cytotoxicity and Carcinogenicity. *Biochem Biophys Res Commun* (2018) 495(1):899–903. doi: 10.1016/j.bbrc.2017.11.074
45. Xu Y-M, Tan HW, Zheng W, Liang Z, Yu F, Wu D, et al. Cadmium Telluride Quantum Dot-Exposed Human Bronchial Epithelial Cells: A Further Study of the Cellular Response by Proteomics. *Toxicol Res (Camb* (2019) 8(6):994–100. doi: 10.1039/c9tx00126c
46. Chen T, Li L, Xu G, Wang X, Wang J, Chen Y, et al. Cytotoxicity of InP/ZnS Quantum Dots With Different Surface Functional Groups Toward Two Lung-Derived Cell Lines. *Front Pharmacol* (2018) 9:763. doi: 10.3389/fphar.2018.00763
47. Stan M, Memet I, Sima C, Popescu T, Teodorescu VS, Hermenean A, et al. Si/SiO_2 Quantum Dots Cause Cytotoxicity in Lung Cells Through Redox Homeostasis Imbalance. *Chem Biol Interact* (2014) 220:102–15. doi: 10.1016/j.cbi.2014.06.020
48. Stan M, Sima C, Cinteza LO, Dinischiotu A. Silicon-Based Quantum Dots Induce Inflammation in Human Lung Cells and Disrupt Extracellular Matrix Homeostasis. *FEBS J* (2015) 282(15):2914–29. doi: 10.1111/febs.13330
49. Yuan X, Liu Z, Guo Z, Ji Y, Jin M, Wang X. Cellular Distribution and Cytotoxicity of Graphene Quantum Dots With Different Functional Groups. *Nanoscale Res Lett* (2014) 9(1):108. doi: 10.1186/1556-276X-9-108
50. Tian X, Xiao B, Wu A, Yu L, Zhou J, Wang Y, et al. Hydroxylated-Graphene Quantum Dots Induce Cells Senescence in Both P53-Dependent and -Independent Manner. *Toxicol Res (Camb* (2016) 5(6):1639–48. doi: 10.1039/c6tx00209a
51. Xu L, Dai Y, Wang Z, Zhao J, Li F, White JC, et al. Graphene Quantum Dots in Alveolar Macrophage: Uptake-Exocytosis, Accumulation in Nuclei, Nuclear Responses and DNA Cleavage. *Part Fibre Toxicol* (2018) 15(1):45. doi: 10.1186/s12989-018-0279-8
52. Roberts JR, Antonini AJ, Porter DW, Chapman RS, Scabilloni JF, Young S, et al. Lung Toxicity and Biodistribution of Cd/Se-ZnS Quantum Dots With Different Surface Functional Groups After Pulmonary Exposure in Rats. *Part Fibre Toxicol* (2013) 10:5. doi: 10.1186/1743-8977-10-5
53. Scoville DK, White CC, Botta D, An D, Afsharinejad Z, Bammler TK, et al. Quantum Dot Induced Acute Changes in Lung Mechanics are Mouse Strain Dependent. *Inhal Toxicol* (2018) 30(9-10):397–403. doi: 10.1080/08958378.2018.1542046
54. Tang Y, Han S, Liu H, Chen X, Huang L, Li X, et al. The Role of Surface Chemistry in Determining *In Vivo* Biodistribution and Toxicity of CdSe/ZnS Core-Shell Quantum Dots. *Biomaterials* (2013) 34(34):8741–55. doi: 10.1016/j.biomaterials.2013.07.087
55. Yang Y, Li P, Lin Y, Li Z, Cui T, Song Z, et al. Gene Expression Profiling of the Liver and Lung in Mice After Exposure to ZnO Quantum Dots. *Int J Nanomed* (2020) 15:2947–55. doi: 10.2147/IJN.S246754
56. Li L, Chen Y, Xu G, Liu D, Yang Z, Chen T, et al. *In Vivo* Comparison of the Biodistribution and Toxicity of InP/ZnS Quantum Dots With Different Surface Modifications. *Int J Nanomed* (2020) 15:1951–65. doi: 10.2147/IJN.S241332
57. Lin G, Chen T, Pan Y, Yang Z, Li L, Yong KT, et al. Biodistribution and Acute Toxicity of Cadmium-Free Quantum Dots With Different Surface Functional Groups in Mice Following Intratracheal Inhalation. *Nanotheranostics* (2020) 4 (3):173–83. doi: 10.7150/ntno.42786
58. Rehberg M, Leite CF, Mildner K, Horstkotte J, Zeuschner D, Krombach F. Surface Chemistry of Quantum Dots Determines Their Behavior in Postischemic Tissue. *ACS Nano* (2012) 6(2):1370–9. doi: 10.1021/nn204187c
59. Lee V, McMahan RS, Hu X, Gao X, Faustman EM, Griffith WC, et al. Amphiphilic Polymer-Coated CdSe/ZnS Quantum Dots Induce Pro-Inflammatory Cytokine Expression in Mouse Lung Epithelial Cells and Macrophages. *Nanotoxicology* (2015) 9(3):336–43. doi: 10.3109/17435390.2014.930532
60. Ho C, Chang H, Tsai H, Tsai M, Yang C, Ling Y, et al. Quantum Dot 705, a Cadmium-Based Nanoparticle, Induces Persistent Inflammation and Granuloma Formation in the Mouse Lung. *Nanotoxicology* (2013) 7(1):105–15. doi: 10.3109/17435390.2011.635814
61. Ho C, Luo Y, Chuang T, Lin P. Quantum Dots Induced Interferon Beta Expression *via* TRIF-Dependent Signaling Pathways by Promoting Endocytosis of TLR4. *Toxicology* (2016) 344-346:61–70. doi: 10.1016/j.tox.2016.02.005
62. McConnachie LA, Botta D, White CC, Weldy CS, Wilkerson H, Yu J, et al. The Glutathione Synthesis Gene Gclm Modulates Amphiphilic Polymer-Coated CdSe/ZnS Quantum Dot-Induced Lung Inflammation in Mice. *PloS One* (2013) 8(5):e64165. doi: 10.1371/journal.pone.0064165
63. Scoville DK, White CC, Botta D, McConnachie LA, Zadworny ME, Schmuck SC, et al. Susceptibility to Quantum Dot Induced Lung Inflammation Differs Widely Among the Collaborative Cross Founder Mouse Strains. *Toxicol Appl Pharmacol* (2015) 289(2):240–50. doi: 10.1016/j.taap.2015.09.019
64. Scoville DK, Nolin JD, Ogden HL, An D, Afsharinejad Z, Johnson BW, et al. Quantum Dots and Mouse Strain Influence House Dust Mite-Induced Allergic Airway Disease. *Toxicol Appl Pharmacol* (2019) 368:55–62. doi: 10.1016/j.taap.2019.01.018
65. Volarevic V, Paunovic V, Markovic Z, Markovic BS, Misirkic-Marjanovic M, Todorovic-Markovic B, et al. Large Graphene Quantum Dots Alleviate Immune-Mediated Liver Damage. *ACS Nano* (2014) 8(12):12098–109. doi: 10.1021/nn502466z
66. Lee B, Lee JY, Kim J, Yoo JM, Kang I, Kim JJ, et al. Quantum Dots as Anti-Inflammatory Therapy for Colitis. *Sci Adv* (2020) 6(18):eaaz2630. doi: 10.1126/sciadv.aaz2630
67. Jigyasu AK, Siddiqui S, Lohani M, Khan IA, Arshad M. Chemically Synthesized CdSe Quantum Dots Inhibit Growth of Human Lung Carcinoma Cells *via* ROS Generation. *EXCLI J* (2016) 15:54–63. doi: 10.17179/excli2015-705
68. Nagy A, Hollingsworth JA, Hu B, Steinbrück A, Stark PC, Valdez CR, et al. Functionalization-Dependent Induction of Cellular Survival Pathways by CdSe Quantum Dots in Primary Normal Human Bronchial Epithelial Cells. *ACS Nano* (2013) 7(10):8397–411. doi: 10.1021/nn305532k
69. Kumar V. The Trinity of cGAS, TLR9, and ALRs Guardians of the Cellular Galaxy Against Host-Derived Self-DNA. *Front Immunol* (2021) 11:624597. doi: 10.3389/fimmu.2020.624597
70. Kreyling WG, Semmler M, Erbe F, Mayer P, Takenaka S, Schulz H, et al. Translocation of Ultrafine Insoluble Iridium Particles From Lung Epithelium to Extrapulmonary Organs is Size Dependent But Very Low. *J Toxicol Environ Health A* (2002) 65(20):1513–30. doi: 10.1080/00984100290071649

Conflict of Interest: The authors declare that the research was conducted in the absence of any commercial or financial relationships that could be construed as a potential conflict of interest.

Advantages of publishing in Frontiers

OPEN ACCESS
Articles are free to read for greatest visibility and readership

FAST PUBLICATION
Around 90 days from submission to decision

HIGH QUALITY PEER-REVIEW
Rigorous, collaborative, and constructive peer-review

TRANSPARENT PEER-REVIEW
Editors and reviewers acknowledged by name on published articles

Frontiers
Avenue du Tribunal-Fédéral 34
1005 Lausanne | Switzerland

Visit us: www.frontiersin.org
Contact us: frontiersin.org/about/contact

REPRODUCIBILITY OF RESEARCH
Support open data and methods to enhance research reproducibility

DIGITAL PUBLISHING
Articles designed for optimal readership across devices

FOLLOW US
@frontiersin

IMPACT METRICS
Advanced article metrics track visibility across digital media

EXTENSIVE PROMOTION
Marketing and promotion of impactful research

LOOP RESEARCH NETWORK
Our network increases your article's readership